

UNCLASSIFIED

AD 264 140

*Reproduced  
by the*

ARMED SERVICES TECHNICAL INFORMATION AGENCY  
ARLINGTON HALL STATION  
ARLINGTON 12, VIRGINIA



UNCLASSIFIED

NOTICE: When government or other drawings, specifications or other data are used for any purpose other than in connection with a definitely related government procurement operation, the U. S. Government thereby incurs no responsibility, nor any obligation whatsoever; and the fact that the Government may have formulated, furnished, or in any way supplied the said drawings, specifications, or other data is not to be regarded by implication or otherwise as in any manner licensing the holder or any other person or corporation, or conveying any rights or permission to manufacture, use or sell any patented invention that may in any way be related thereto.

CALCULATED  
AS AD NO. 264140

EC  
7



SYMPOSIUM PROCEEDINGS

# STRUCTURAL DYNAMICS OF HIGH SPEED FLIGHT

LOS ANGELES, CALIFORNIA

APRIL 24, 25, 26, 1961

NOX  
41-4-6

657400

ASTIA  
RECEIVED  
OCT 12 1961  
JIPDB

ACR-62  
VOLUME 1

OTS \$ 9.00

Statements and opinions contained herein  
are those of the authors and are not necessarily  
to be construed as official or reflecting the  
views of the sponsors.

Copies available at OTS \$9.00



SYMPOSIUM PROCEEDINGS

**STRUCTURAL DYNAMICS OF HIGH SPEED FLIGHT**

LOS ANGELES, CALIFORNIA - APRIL 24, 25, 26, 1961

SPONSORED BY

AEROSPACE INDUSTRIES ASSOCIATION  
OFFICE OF NAVAL RESEARCH

## PREFACE

In line with its objectives of advancing the frontiers of scientific knowledge closely related to the operational mission of the United States Navy, and of disseminating these advances to designers of our Nation's weapon systems, the Office of Naval Research welcomes this opportunity to join with the Aerospace Industries Association in the sponsorship of this very timely symposium on the Structural Dynamics of High Speed Flight.

That the symposium succeeded in disseminating new and needed technical information in this challenging and complex field was amply attested by the definitely favorable comments of many of the two hundred and thirty-five scientists and engineers who attended. Some forty-five organizations were represented by these participants, namely: Army - two; Navy - fifteen; Air Force - twelve; NASA - twenty-six, the Federal Aviation Agency - two; the National Science Foundation - one; Universities - seven; Research Institutes - six; and some thirty five Industrial Concerns - one hundred and sixty-four.

In order to facilitate discussion, all of the sessions of the symposium were classified confidential, but only five of the thirty formal papers were so classified. Accordingly, the Proceedings are issued in two volumes, Volume 1 containing the twenty-five unclassified papers and Volume 2 containing the five classified talks.

In conclusion, the personnel of the Structural Mechanics Branch of this Office wish to commend the efforts of those members of the Aerospace Industries Association's Panel on Dynamics and Aeroelasticity Research whose technical and organizational excellence contributed so effectively to the success of this symposium.

JOHN M. CROWLEY

Structural Mechanics Branch  
Office of Naval Research

# CONTENTS

## Volume 1

Foreword . . . . .	vi
Welcome . . . . .	vii

### SESSION I. FLUTTER AND VIBRATION

New Dynamic System Concepts and Their Application to Aeroelastic System Approximations . . . . .	3
Melvin B. Zisfein and Frank J. Frueh, Giannini Controls Corp.	
Elementary Static Aerodynamics Adds Significance and Scope in Flutter Analyses . . . . .	28
Norman H. Zimmerman, McDonnell Aircraft Corp.	
New Techniques in Flutter at High Mach Numbers . . . . .	85
J. Stuart Keith, Chance Vought Corporation	
An Indicial Flutter Analysis Procedure for Hypersonic Delta Wings . . . . .	135
Bernard Mazelsky and Harry B. Amey, Jr., Aerojet-General Corporation	

### SESSION II. FLUTTER AND VIBRATION

Application of a Modified Low-Aspect Ratio Theory to Aeroelastic Studies of Flexible Delta Lifting Surfaces . . . . .	175
D. O. Neilson and I. Jaszlics, Boeing Airplane Company	
A Comparative Experimental and Theoretical Study of the Flutter of Flat Panels in a Low Supersonic Flow . . . . .	209
M. H. Lock and Y. C. Fung, California Institute of Technology	
The Effect of Some Practical Complications on the Flutter of Rectangular Panels . . . . .	252
H. M. Voss, Boeing Airplane Company	
Scale-Model Flight Dynamics Testing on High-Speed Tracks . . .	268
Charles E. Woods, U.S. Naval Ordnance Test Station	

### SESSION III. MISSILE SYSTEM DYNAMICS

Liquid Dynamic Behavior in Rocket Propellant Tanks . . . . .	287
H. Norman Abramson, Southwest Research Institute	
Dynamics of Liquid Propellant Vehicles . . . . .	319
Helmut F. Bauer, NASA, Marshall Space Flight Center	

Discussion of an Aero-Inertial Control System . . . . .	356
Robert M. Hunt, NASA, Marshall Space Flight Center	
A Dynamic Loads Comparison for a Range of Missile Configurations Utilizing Two Control System Concepts . . . . .	376
R. T. Wagner, Boeing Airplane Company	

#### SESSION IV. DYNAMIC LOADS

Wind Loads on a Vertically Rising Vehicle Including Effects of Time-Varying Parameters . . . . .	413
Homer G. Morgan and Sheldon Baron, NASA, Langley Research Center	
Calculation of Random Gust and Taxi Response and Development of Fatigue Test Loading for Delta Wing Aircraft . . . . .	447
R. P. Peloubet, Convair	
Shock-Tube Studies of Blast-Loading on Airfoils . . . . .	477
J. R. Ruetenik, W. Herrmann, and E. A. Witmer, Massachusetts Institute of Technology	
Airplane Response to Stall Buffeting Loads . . . . .	497
J. R. Post, North American Aviation, Inc.	

#### SESSION V. HIGH TEMPERATURE EFFECTS

A Matrix Force Method for Analyzing Heated Wings, Including Large Deflections . . . . .	533
W. Lansing, I. W. Jones, and P. Ratner, Grumman Aircraft Engineering Corporation	
Deformational Response Determinations for Practical Heated Wing Structures . . . . .	567
Richard H. Gallagher, James F. Quinn, and Joseph Padlog, Bell Aerosystems Company	
An Approach to the Thermal Stiffness Problem . . . . .	609
L. J. Topp, D. L. Grande, R. R. June, and C. D. Newsom, Boeing Airplane Company	
Acoustic Fatigue Tests Relating to the Design of Structures for Elevated Temperatures . . . . .	629
Philip M. Edge, Jr., NASA, Langley Research Center	

#### SESSION VI. ENVIRONMENTAL VIBRATION

Structural Vibration in Space Vehicles . . . . .	649
Kenneth McK. Eldred, Western Electro-Acoustic Laboratory, Inc., William Roberts and Robert W. White, Northrop Corporation	

Structural Response to Random and Discrete Noise Inputs . . . . .	686
G. L. Getline, Convair	
Captive Missile Response Due to Random Pressures . . . . .	698
H. L. Leve, Hughes Aircraft Company	
Structural Response to the Noise Input of the Saturn Engines . . .	710
J. H. Farrow, NASA, George C. Marshall Space Flight Center, R. E. Jewell and G. A. Wilhold, Chrysler Corporation	
A Rational Approach to the Environmental Vibration Problem . .	721
P. T. Mahaffey, Convair	
Attendance List . . . . .	733
Author Index . . . . .	746

## FOREWORD

The rapidly expanding aerospace vehicle flight regime has created many new and unique design requirements. In the field of structural dynamics the industry has encountered an increasing number of problems which have required new research to develop satisfactory methods of solution. Although considerable progress has been made in the past few years in advancing the state of the art in structural dynamics, there has been a need for a more adequate dissemination of this information to permit a wider and more immediate application of the new techniques and to serve as a guide and stimulant for additional research.

Recognizing this need, the ARTC Dynamics and Aeroelasticity Research Panel of the Aerospace Industries Association conceived and planned a symposium on Structural Dynamics of High Speed Flight. The symposium was held on 24-26 April 1961 at the auditorium of the Institute of the Aerospace Sciences in Los Angeles, California, and was sponsored jointly by the Aerospace Industries Association and the Office of Naval Research. These proceedings, in two volumes, contain the papers presented at the symposium.

On behalf of the Dynamics and Aeroelasticity Research Panel, I would like to express my thanks to the many people who so ably contributed to the success of the symposium: to Captain Harold E. Ruble, Deputy and Assistant Chief of Naval Research, for a most inspiring welcoming address; to Mr. John M. Crowley and Mr. Ben J. Cagle of the Office of Naval Research and Mr. H. Dana Moran of the Aerospace Industries Association for their invaluable aid in attending to the many details of arranging the symposium; to Mr. Irving Rudin of the Office of Naval Research for the all-important job of publishing these proceedings; to the speakers and co-authors for supplying the basic ingredient of the symposium; and finally, to the six session chairmen, Mr. Walter J. Mykytow of WADD, Professor John W. Miles of UCLA, Dr. Millard V. Barton of STL, Mr. I. Edward Garrick of NASA, Dr. Harold Liebowitz of ONR, and Dr. Charles T. Morrow of Aerospace Corp. for supplying a unifying thread which gave added significance to the papers, and for interjecting a bit of humor which made the symposium enjoyable as well as informative.

Eugene F. Baird  
Chairman  
ARTC Panel 58-A  
Dynamics & Aeroelasticity Research  
Aerospace Industries Association

## WELCOME

Captain H. E. Ruble, USN  
Deputy and Assistant Chief  
Office of Naval Research

Mr. Baird, Distinguished Guests and Participants in this Symposium:

On behalf of the Aerospace Industries Association and the Office of Naval Research, I wish to welcome you to this Symposium. I extend to you, also, the best wishes of Admiral Coates, Chief of Naval Research, who deeply regrets that sudden demands of business in Washington have prevented his appearance here this morning.

I would like each of you to know that it is a pleasure for the Department of the Navy to cooperate with the Aerospace Industries Association in arranging for the conduct of the excellent program planned for this meeting. Indeed, the joining of research and technology as symbolized by this Symposium may be said to mirror the goal of all progressive research and engineering activities, which is to effectively integrate these two allies for progress. The dynamics problems scheduled for presentation and critical discussion here appear to be timely and of particular technical significance to the defense needs of the Nation in this period of rapid technological development.

The Navy's needs in the area of structural mechanics are quite comprehensive and varied, since we are concerned with vehicles operating deep beneath the sea, on the surface of the ocean and in the air above. In the case of the Polaris missile, we have a weapon that must function in all three environments.

In the regime of high speed flight particularly, severe situations have arisen which require urgent solution. Recognizing this, the Office of Naval Research and the Bureau of Naval Weapons have planned and coordinated a structures research program which reflects the future needs of both the Navy and the prime aircraft and missile companies engaged in missile structural design. Out of this program

has come the present broad Navy support of research tasks which are certain to lead to the development of more effective and reliable military structures.

Testing apparatus and experimental techniques, previously unavailable, have been developed as part of a high temperature program to determine physical properties of materials of interest at temperatures up to 4000°F. This engineering data is necessary in order to analyze in a rational manner the thermal stresses and deformations encountered by missile and aircraft structures in supersonic and hypersonic flight.

Similitude requirements for the experimental study of aerothermoelastic phenomena associated with flight at hypersonic speeds have been devised as a result of research sponsored under this program. Studies have also been made of the type and minimum sizes of facilities for studying aeroelasticity phenomena in the presence of aerodynamic heating.

In the area of research coordination, the present DOD centralizing activity for Shock, Vibration and Associated Environments was originally established by the Office of Naval Research specifically for Naval needs in Shock and Vibration. With the encouragement of the other services and the endorsement of the Office of the Director of Defense Research and Engineering, the function of this activity has grown to serve, we believe effectively, the entire National defense community.

Augmenting our research efforts in the more usual areas of structural mechanics and dynamics, the Office of Naval Research has recently instituted a program of study in viscoelasticity as related to the design of solid propellants in rocket motors. As solid propellant grains, chemically potent but mechanically weak, continue to grow in size, we are becoming increasingly concerned about their reliability. We must gain a better understanding of what it is that causes cracks to form and dimensional instabilities to occur at various times during the grain life including the combustion phase. Both the static and dynamic aspects of this problem are important.

The purpose of this research is to provide engineers with basic and design information on the viscoelastic structural response of high-energy solid propellant materials under realistically simulated service conditions.

Most of the papers to be presented by industry at this symposium are based on research sponsored by various government agencies, particularly the Air Force and the Navy. Previous structural dynamics research so conducted has been intelligently executed and shows encouraging results. Nevertheless, the need for additional knowledge in this area continues to be pressing. It is hoped that Government and Industry will continue to cooperate effectively toward this goal of enhancing our military capability.



Ruble

Initiative must be partnered with aggressiveness to achieve any really solid advances in military technology. This is particularly true in the area of structural dynamics; we are dealing with new forces and new environments where we cannot even be sure of the parameters. The close association and partnership of government and industry is the only way we can be sure of generating steady significant progress.

I am glad to have had this opportunity to say a few words to this distinguished assembly, and I am sure that this symposium is a harbinger of greater things to come.

**SESSION I | FLUTTER AND VIBRATION**

Chairman: Mr. Walter Mykytow  
Wright Air Development Division  
Wright-Patterson Air Force Base

NEW DYNAMIC SYSTEM CONCEPTS  
AND THEIR APPLICATION TO  
AEROELASTIC SYSTEM APPROXIMATIONS

Melvin B. Zisfein\* & Frank J. Frueh\*\*  
Astromechanics Research Division  
Giannini Controls Corporation  
Buffalo, New York

We present here some results of a study which is directed at a better understanding of flutter and its relation to the sub and supercritical dynamic behavior of an aeroelastic system. All of this work was sponsored by the Air Force Office of Scientific Research and monitored by Mr. Howard Wolko of that organization. This work has recently been summarized and published in Air Force Office of Scientific Research Technical Report 60-182. In addition, both the authors and the Air Force are happy to thank the AIA 58-A Dynamics and Aeroelasticity Panel through which practical examples were obtained for the comparisons which we will show. In this paper we will not attempt to condense the detail of AFOSR TR 60-182. Rather, we hope to explain our motivations and conclusions and to elaborate on the important points. For detail we refer the listener to the AFOSR Technical Report.

The project upon which we report grew out of an attempt to explain some apparent contradictions between the conventional flutter damping solution (sometimes known as the AMC type solution because it is classically exemplified in AMC Technical Report 4798) and the true dynamic response of the aeroelastic system. As our work progressed, and these apparent contradictions were explained, a new logical approach to the dynamics of aeroelastic systems began to evolve. This approach was first formulated qualitatively and later employed quantitatively to develop some new and useful approximations which relate flutter to true system dynamic response. In the opinions of the authors, this new dynamics logic is the principal contribution of the study to date. It makes extensive qualitative and quantitative use of the roots coalescence property noticed by many authors and should be differentiated here from the very valuable recent contributions of authors such as Pines and Laidlaw. We have not sought

\*Division Manager

\*\*Senior Staff Scientist

means of accurate approximate flutter prediction, nor have we employed roots coalescence thinking to examine flutter trends as such. Rather, our unique contribution has been in the relating of flutter and flutter-type calculations to the true sub and super-critical system dynamic response, sometimes referred to as true system damping.

Before we show the algebraic and numerical results of our studies, let us introduce some new concepts. In our first slide we show the loci of the roots of a typical, "AMC" flutter solution. We show these roots in the upper portion of the slide plotted as structural damping required for neutral stability versus air speed and in the lower portion of the slide as corresponding values of coupled frequency versus air speed. If these binary roots represented simple bending torsion flutter, branch A might be the bending branch and branch B might be the torsion branch. If the roots represented a two-mode approximation to panel flutter, branch A would be the lower frequency panel mode and branch B the high frequency panel mode. Now, let us define a curve which in this binary case is a closed curve which travels in the  $V-\omega$  plane from one zero-airspeed natural frequency to the other zero-airspeed natural frequency, and which does this by approximating as closely as it can in simple fashion the lower air speed values of the roots loci. We superimpose this curve on our roots loci in the next slide. Let us call this the Base Curve and call any points along it values of  $\omega$  and  $V_0$  rather than values of  $\omega$  and  $V$ . We will see later that this base curve may be found as a very good approximation to the roots loci if we let damping be at all times very low.

Now what about points along the roots loci when damping is not very low. We see from the slide that there is an intermediate region and then a region where damping becomes very high and the roots loci become asymptotic to a line. Let us, in the next slide, add this line and call it the High Damping Asymptote.

Note that we are speaking here about a conventional or AMC type of flutter solution which deals with values of velocity and frequency corresponding to neutral stability or simple harmonic motion and with values of the structural damping which would be required in the system to bring about this condition. Instead of requiring structural damping we could require viscous damping. We would find that our roots loci fell along essentially the same base curve but departed from this base curve at a different place and followed a different high damping asymptote. We could also think in terms of still different roots loci, namely, the roots loci of so-called true system damping. This true system damping is, at any air speed, the rate at which a disturbed mode would subside or decay. In our studies we certainly considered this kind of motion, however, we avoided the nomenclature confusion which almost always results by referring to its amplification magnitude not as amount of true system damping but rather as the Decay Coefficient. We will henceforth

describe subsiding or increasing motions by their decay coefficients which are nothing more than the coefficients of their exponential envelopes. Hence, in the next slide we show decay roots for the same binary system that we have discussed previously. Note that the envelope of motion in any mode is given by values of  $e^{\gamma\omega t}$ . Note that for the same system, these roots will, in the  $V-\omega$  plane, also tend to follow essentially the same base curve but that they tend to depart from this base curve at a different point and thenceforth to follow a different asymptote which we have named the High Decay Asymptote. It is interesting and comforting to note that this high decay asymptote will always intersect a base curve at the point where its slope is infinite, a point which we have termed the Nose of the base curve. We say comforting because this fact ensures that regardless of double valued damping roots, neither of the two decay roots will be double valued at any velocity; a fact which corresponds with all known experiment. We should emphasize another important point at this time, namely, that all of our algebra and our subsequent numerical computations (and these have been considerable) shows us that there is no reason to expect the flutter point to lie at the intersection of any of these asymptotes with the base curve, especially the intersection of the high decay asymptote with the nose of the base curve. In other words there is no reason to expect the flutter point to fall at the coalescence point and this fact in no way diminishes any of the useful properties of this coalescence point of view. In the next slide we superimpose the two velocity-damping and velocity-decay curves that we have shown and we see that despite the fact that in the  $V-\omega$  plane they tend to follow the same base curve and depart neatly along asymptotes, in the  $V-g$  or  $V-\gamma$  planes, they do not, in general, correspond to each other nor should they be expected to correspond to each other except in some special cases.

Now that we have described these new basic concepts to you we can demonstrate how they have been and how they can be employed to better understand dynamic response and relate dynamic response to the flutter solution. Let us consider our first two binary systems, a pitch-plunge wing and a two-mode simply-supported infinite panel. These systems are pictured in the sketches on the auxiliary slide which we now show. This slide also contains some of the necessary algebra and we really should apologize for the clutter. The characteristic equation of each of our binary systems is given directly below the sketch of the system. We derived these equations using a conventional Lagrangean approach with aerodynamic inputs of first order piston theory. The notation is that of our AFOSR TR 60-182 which also lists all of our assumptions. The characteristic equation is phrased in terms of system natural frequencies, coupled frequencies, system parameters such as  $r_\alpha$  and  $x_\alpha$ , velocity,  $V$ , and values of the structural damping  $g_s$ , and viscous damping  $\zeta_s$ . Each mode is free to vibrate as  $e^{st}$  where  $s = \gamma\omega + i\omega$  and where  $\gamma$  is the decay coefficient. We solved these characteristic equations in conventional fashion for the cases that we have just discussed, Case A being a

conventional flutter solution, Case B being a required viscous damping flutter solution, Case C being a true system damping solution or as we call it decay solution for the system if we assume that it has no structural or viscous damping, and Case D being a decay solution for the system if we admit the presence of its actual structural damping. For all of these cases, velocity is related to frequency for very low damping by the relations shown at the bottom of the chart, hence these relations are the equations of the applicable base curves. Now let us examine some of the solutions for Cases A, B, C, and D. The solution for flutter damping,  $g_R$ , in Case A for both the pitch-plunge wing and simply-supported panel turns out to be a coefficient times frequency to the first power times some function of frequency which we call  $F_1(\omega)$  or  $G_1(\omega)$  all divided by a different function of frequency which we call  $F_2(\omega)$  or  $G_2(\omega)$ . Note the similarity of the wing and panel solutions. The Case B solution for  $\zeta_R$ , the required viscous damping, is quite similar in form to Case A except for the denominator frequency polynomial which we call  $F_3(\omega)$  or  $G_3(\omega)$ . The Case C solution for  $\gamma_0$ , decay rate without material damping, has still the same frequency polynomials in the numerator but now frequency times a still different frequency polynomial  $F_4(\omega)$  or  $G_4(\omega)$  in the denominator. The Case D solution for  $\gamma$ , decay rate with structural damping is similar to Case C except that the numerator has an additive frequency polynomial which turns out to be the denominator frequency polynomial of Case A. The important thing about Case D is that it reduces to a very useful relation shown as the right-hand equation in the Case D blocks, namely, that for either binary wing or panel,  $\gamma$ , the true system decay rate equals  $\gamma_0$  (that is, the decay rate in the absence of any structural or viscous damping) times the quantity one minus  $g_s$  (the structural damping actually present) divided by  $g_R$  (the AMC flutter solution). Note also that from these solutions we can get the equation of the high structural damping asymptote by setting  $F_2(\omega)$  or  $G_2(\omega)$ , the denominator of the  $g_R$  polynomial equal to zero and then solving for  $\omega$ . We can get the equation for the high viscous damping asymptote by setting the  $\zeta_R$  expression's denominator polynomials  $F_3(\omega)$  or  $G_3(\omega)$  equal to zero and solving for frequency. We can similarly obtain the high decay asymptote from either Case C or Case D by setting their denominator polynomials  $F_4(\omega)$  or  $G_4(\omega)$  equal to zero and again solving for  $\omega$ .

We must apologize here for our hasty treatment of this topic and explain that it is thoroughly documented in our previous report, AFOSR Technical Note 59-969, which introduces these concepts and presents a number of numerical examples.

Having defined our basic concepts and presented simple binary solutions we can now illustrate their use in more complex solutions. Let us turn our attention to some ternary systems. In our study, three ternary systems were chosen -- a uniform simply-supported panel, a uniform cantilever wing capable of bending in two modes and twisting in one, and a uniform cantilever wing capable of

both bending and torsion in one mode each and containing a control surface which is free to twist with respect to the wing. By employing our basic concepts and assuming an algebraic similarity of form between the binary solution on the auxiliary slide and our desired ternary solution, we were able to calculate ternary system approximations which agreed quite well with exact solutions. Algebraic complexity prevents us from going through the details of this work here, but the work has been carefully documented in AFOSR Technical Report 60-182. We should particularly emphasize that our derivations of the denominators of these approximations were made possible only by a knowledge of the base curve equation and the properties that should be expected of the base curve. We illustrate this use of "base curve reasoning" here with a description of how we approximated the ternary decay,  $\gamma_0$ , solution for the three mode panel. From our study of binaries (shown in the auxiliary slide) we noted the relation between modal coalescence and the flutter point. From extensive previous experience with aircraft flutter it seemed proper to expect only one coalescence in the vicinity of a flutter point for any reasonable number of degrees of freedom. In view of this "physical" similarity it was at least worthy of investigation to ascertain whether or not the solution of the ternary system was not similar in essential algebraic form to the corresponding binary solution. First, the form of  $\gamma_0$ , by analogy to the binary solution in the auxiliary slide, is postulated to be equation A in the next slide, where  $H_x(\omega)$  and  $H_y(\omega)$  are frequency polynomials to be determined.

The identity of  $H_x(\omega)$  and  $H_y(\omega)$  can be established by the use of some clues obtainable from the auxiliary slide. The study of the binary systems showed that the expressions for  $g_R$  and  $\gamma_0$  have the common numerator  $G_1(\omega)$ . We observe that the ternary  $g_R$  and  $\gamma_0$  are also required to be zero at the same velocity and frequency. Then, by analogy, the numerator polynomial  $H_x(\omega)$  was assumed to be  $H_1(\omega)$ , the numerator of the ternary  $g_R$  solution which we were able to find analytically. As for  $H_y(\omega)$ , we noted in our binary work that  $\gamma_0$  was caused to become infinite at a frequency where its denominator frequency polynomial  $G_4(\omega)$  became zero. This fact, as I explained a short while ago, determined the frequency of the high decay asymptote. We further found that this high decay asymptote intersected our base curve at its nose, i.e. the frequency of its maximum velocity point. This then means that an expression for the inverse slope of the base curve  $dV_0/d\omega$  (obtained by differentiating the base curve equation) should become zero at this same frequency. Performing this differentiation for the binary system yielded the information that the frequency polynomial in  $dV_0/d\omega$  which caused this to happen was our same  $G_4(\omega)$ . Using this clue to formulate a ternary approximation we contrived a frequency polynomial  $H_4(\omega)$ , which we found by differentiation (for  $dV_0/d\omega$ ) of the ternary system base curve equation. The differentiated expression is shown here as Equation B. The frequency polynomial we want is the frequency polynomial in this differentiated expression which causes it to become zero at the right place. We

show this polynomial as equation C. We therefore put this new frequency polynomial  $H_4(\omega)$  into the denominator of our postulated approximation for ternary  $\gamma_0$  in place of  $H_Y(\omega)$  to get our completed approximation, equation D.

This derivation, in itself, did not establish the validity of equation D. In fact, recalling some of the intuitive leaps involved, extensive numerical comparison of equation D with an "exact" numerical solution of the characteristic equation was required to establish such validity. These numerical comparisons were made and they are presented in the next slide. Here our approximate solutions for the  $\gamma_0$  roots are the lines and the "exact" solutions are the points. You will note that the correlation between our approximation and the "exact" values is rather remarkable. These numerical comparisons also give strong support to the validity of our "basic concepts".

We also show here a comparison between another one of our approximations and some "exact" calculations which we obtained numerically directly from the characteristic equation. These are shown in the next slide for the three-degree-of-freedom wing case. Note in the  $V-\omega$  plane our approximations to the first bending, torsion, and second bending decay roots. Note further in the velocity-decay plane that correspondence between our approximations and the exact solutions are almost as good to a point considerably beyond the flutter point. Note further that the flutter point does not in this case fall at the point of coalescence of the coupling modes. In the next slide we have similar comparisons for the same wing for approximate and exact solutions for the total decay rate,  $\gamma$ , for two values of the structural damping coefficient,  $g_s$ , namely, .05 and .1. Here the correspondence between approximate and exact solutions is similarly good.

We should point out here that all the work which I have described so far was characterized by the need for knowing in advance the system's characteristic equation and also the values of the many system parameters which are used in the characteristic equation. Moreover, all of this work is characterized by rather cumbersome algebra. However, having all of these cases available enabled us to make comparisons between these solutions and find expressions of rather startling generality. One expression in particular permits considerably easier and far more general application of our concepts than we had anticipated up to this point. I'll derive this relationship here for the binary panel case since the algebra is by far easier than for any other case. We'll need to refer to our auxiliary slide for some of the basic equations. In our next slide we start with equation A, our equation for the binary panel base curve. Differentiating this equation with respect to frequency yields equation B. The next steps depend on recognizing that this right hand side of the base curve equation contains many elements in common with the frequency polynomial  $G_2(\omega)$ , our denominator of the flutter solution



in Case A of the auxiliary slide. We must also recognize that the numerator of the right hand side of the differentiated base curve equation, equation B, is equal to the denominator of our approximate solution for  $\gamma_0$  in Case C. Now manipulating the base curve equation so that we can substitute directly the expression for  $G_2(\omega)$  leads to equation C. Compare the remaining terms on the right hand side of equation C to the numerator of equation B. The frequency polynomials differ only by an additive  $2\omega(a/2\bar{\mu}l)^2$ , which turns out to be always very small compared to the other terms. Combining equations B and C and solving for  $G_2(\omega)$  yields equation D. From our previous derivations, we note that the ratio of  $\gamma_0$  to  $g_R$  is given by equation E. Therefore, substituting  $G_2(\omega)$  from equation D and  $2\omega G_4(\omega)$  from equation B leads to the final form, equation F.

At this point, it should be stated that equation F may be general for all aeroelastic systems, insofar as we have been able to derive it from the basic equations of all of the systems we considered. These include the two binary systems, the binary panel, and the binary pitch-plunge wing and also the three ternary systems, the three degree of freedom panel, the pitch-plunge-plunge wing and the pitch-plunge-aileron wing. The big step forward here is that equation F finally allows us to ignore the system characteristic equation and also most system parameters in relating the flutter solution  $g_R$  to dynamic response  $\gamma$ . A numerical flutter solution, giving values of  $V$ ,  $g_R$ , and  $\omega$ , is all that is needed for input to equation F.

Two examples are shown here to demonstrate the validity of equation F. In the next slide a three-degree-of-freedom cantilever wing is treated. Points of exact numerical solutions obtained on an IBM 704 by dealing directly with the characteristic equation are shown as the symbols. The approximated values of  $\gamma_0$  obtained from a standard AMC type flutter analysis of the system being considered and then processed through equation F of the previous slide are shown as the lines. The correlation between the exact points and our corresponding approximate lines is seen to be very good.

In the next slide, a three-degree-of-freedom uniform wing with control surface is treated. Transforming the flutter data thru equation F yields approximate solutions for the dynamic response,  $\gamma_0$ , as shown by the lines. Exact numerical solutions obtained on an IBM 704 are shown as the points or symbols. Correlation between approximate and exact solutions again is quite good.

All of the previous derivations were performed for systems in high supersonic flow. In order to approximate a counterpart of equation F for incompressible flow, we performed a brief study in which we repeated some of our previous work substituting the Wagner indicial lift equation for our previous piston theory. We derived a relation between  $\gamma_0$  and  $g_R$  which is almost identical to the relation which we have shown to you in equation F for high supersonic flow.

This approximation is shown in the next slide. It is interesting to note that this is identically the relationship which we arrived at for low subsonic speeds by more or less ad hoc reasoning in AFOSR TR 60-182. We show two examples here to demonstrate the validity of this equation. In the next slide, an approximation to the dynamic response,  $\gamma$ , of the vertical tail of the B-58 Hustler bomber is compared to values of  $\gamma$  measured in flight and DAEAC solutions, all supplied to us through the AIA by Mr. Mahaffey of Convair, Fort Worth. Input data to the approximation were calculated flutter data, also furnished by Convair, Fort Worth. It is seen that the correlation is quite good. We emphasize that such correlation was obtained from the Convair flutter solution which, without correct interpretation, would imply that flutter is approached thru the second mode. Correct interpretation by our method and actual flight test both confirm that the flutter is, in fact, approached thru the first mode.

The next slide shows comparisons made using Lockheed 13 degree-of-freedom analytical data. These calculations were furnished to us through the AIA by Mr. J. Ford Johnston, of Lockheed, Burbank. Comparisons are shown here for the first two modes only, as data have been furnished by Lockheed for only these modes. In these comparisons, the solid curves are the approximations made by combining Lockheed furnished flutter data with the equations derived in this study. The corresponding points represent Lockheed digital dynamic response calculations. As in the previous cases, correlations between the direct calculations and our approximations are very good.

We presented additional practical examples in AFOSR Technical Report 60-182, but time does not permit showing these. Moreover, the report contains numerous derivations, supporting details and conclusions which we have not time to present here.

In summary, we have presented here a resume of the conception and early development of certain logical concepts germane to dynamic systems. We have introduced the "Base Curve", "High Damping Asymptotes", and "High Decay Asymptote" and we have shown how these particular concepts may be combined with existing dynamics technology to derive new aeroelastic system approximations. To demonstrate their validity we have compared these approximations to rather tedious numerical solutions and, where available, to experiment. Our future efforts will consist of generalization of these techniques plus exploration for additional approximate solutions which may be of further value.

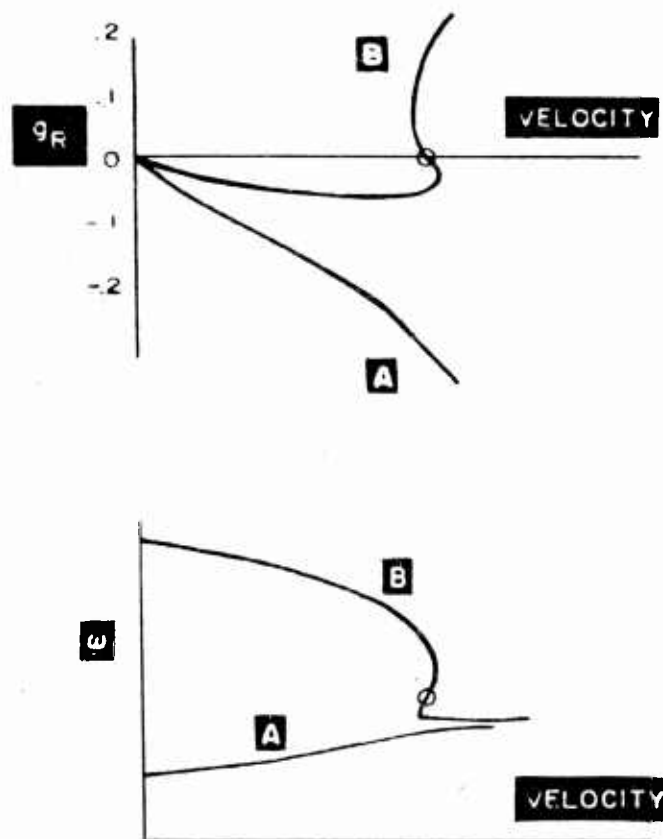


Figure 1

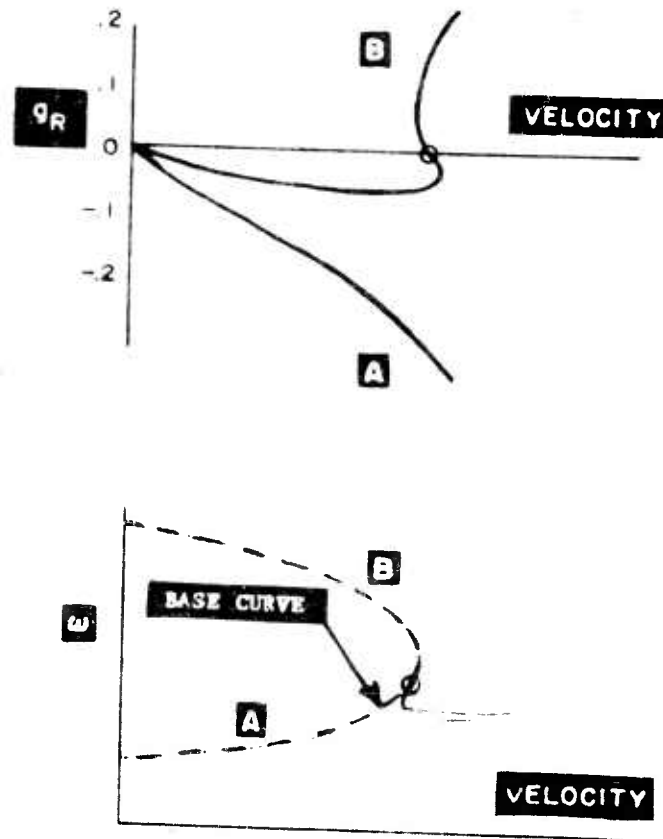


Figure 2

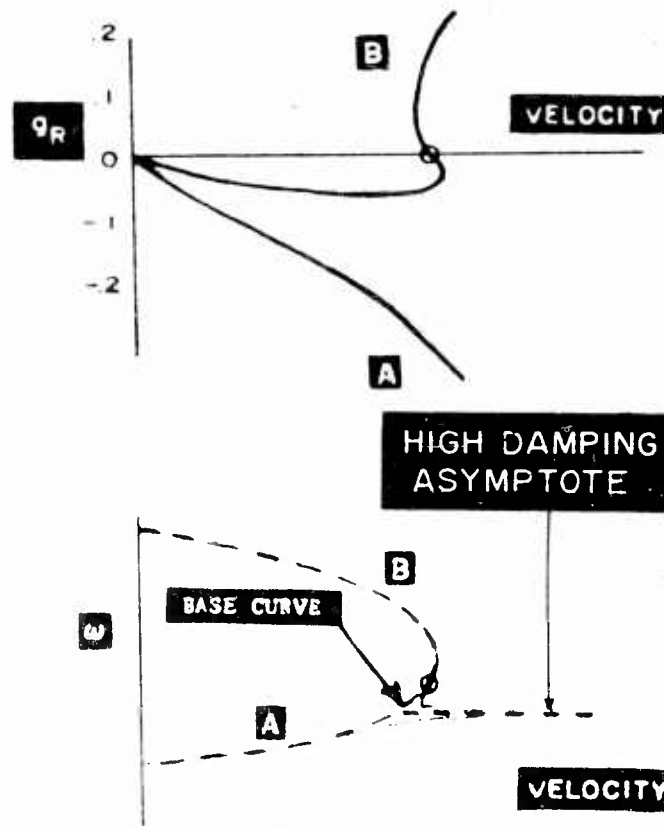


Figure 3

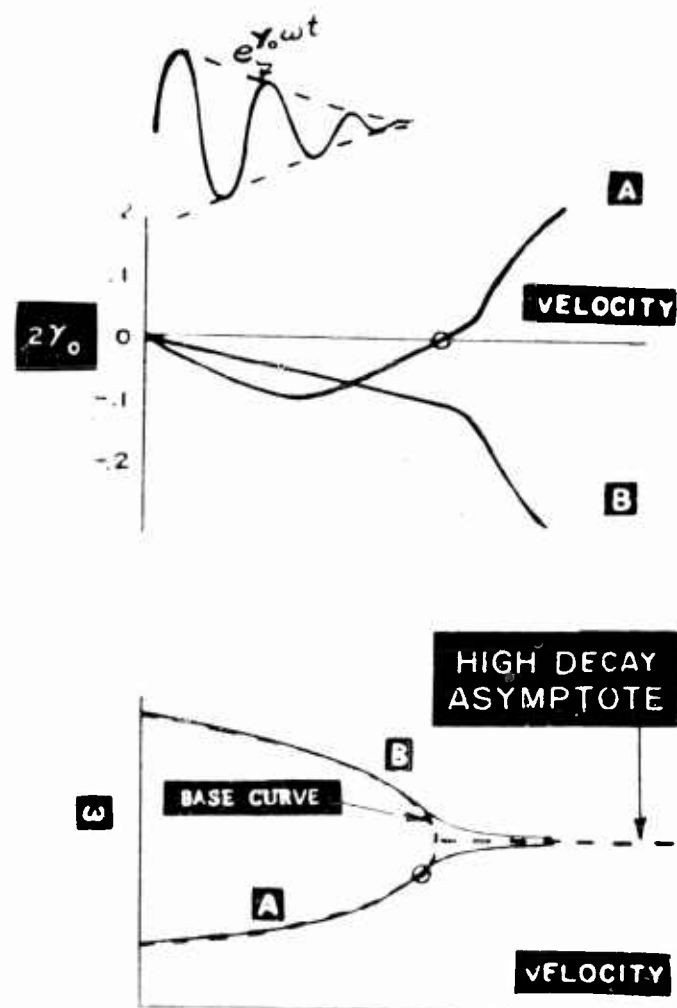


Figure 4

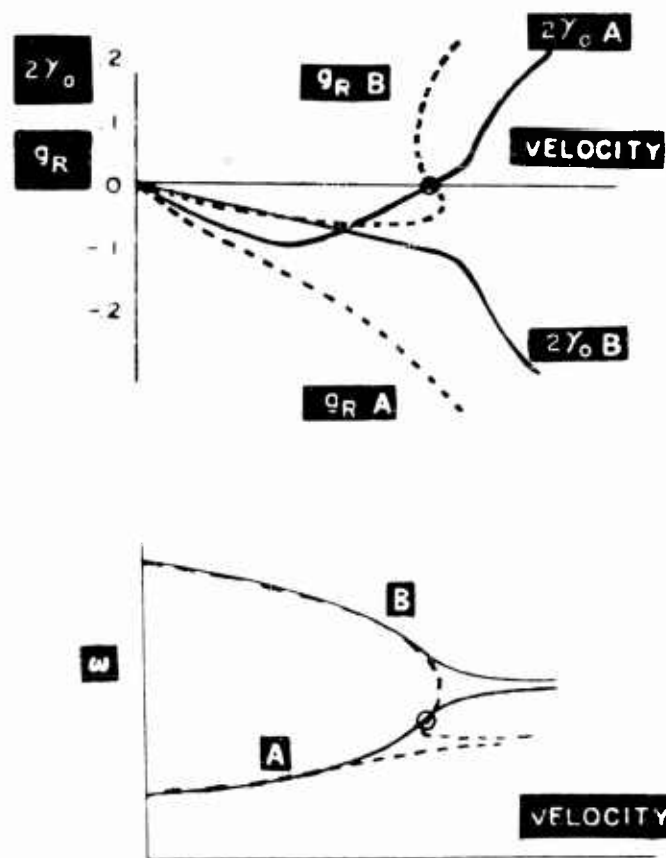
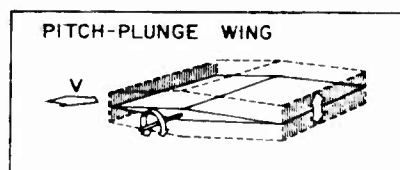


Figure 5



CHARACTERISTIC EQUATION:

$$\left(s^2 + 2\zeta_s \omega_h s + \frac{\omega_h^2 g_s s}{\omega} + \omega_h^2 + \frac{A_1 s}{\mu}\right) \left(s^2 + 2\zeta_s \omega_a s + \frac{\omega_a^2 g_s s}{\omega} + \omega_a^2 + \frac{A_3 s}{\mu r_a^2}\right) - \left(\frac{x_a}{r_a} s^2 + \frac{A_2 s}{\mu r_a}\right)^2 + V \left[ \frac{A_2}{\mu r_a^2} \left(s^2 + 2\zeta_s \omega_h s + \frac{\omega_h^2 g_s s}{\omega} + \omega_h^2\right) - \frac{A_1 x_a s^2}{\mu r_a^2} \right] = 0$$

CASE A  $\gamma = 0, \zeta_s = 0 \quad (x_a = 1 - 2x_0)$

$$g_R = \frac{-\omega \left[ \omega^2 \left( \frac{A_3}{\mu r_a^2} + \frac{A_1}{\mu} - \frac{2x_a A_2}{\mu r_a^2} \right) - \left( \frac{A_3}{\mu r_a^2} \omega_h^2 + \frac{A_1}{\mu} \omega_a^2 \right) \right]}{\left[ \omega^4 \left( 1 - \frac{x_a^2}{r_a^2} \right) + \frac{(A_2^2 - A_1 A_3) \omega^2}{\mu^2 r_a^2} - \omega_h^2 \omega_a^2 \right]} \equiv \frac{-\omega F_1(\omega)}{F_2(\omega)}$$

CASE B  $\gamma = 0, g_s = 0$

$$\zeta_R = \frac{-\omega_h F_1(\omega)}{\left[ \omega^4 \left( 1 - \frac{x_a^2}{r_a^2} \right) - \omega^2 \left( \omega_a^2 - \omega_h \omega_a + \frac{A_1 A_3 - A_2^2}{\mu^2 r_a^2} \right) - \omega_h^3 \omega_a \right]} \equiv \frac{-\omega_h F_1(\omega)}{F_3(\omega)}$$

CASE C  $\zeta_s = 0, g_s = 0$

$$\gamma_0 = \frac{-F_1(\omega)}{2\omega \left[ 2\omega^2 \left( 1 - \frac{x_a^2}{r_a^2} \right) + \frac{A_2^2 - A_1 A_3}{\mu^2 r_a^2} - (\omega_a^2 + \omega_h^2) \right]} \equiv \frac{-F_1(\omega)}{2\omega F_4(\omega)}$$

CASE D  $\zeta_s = 0$

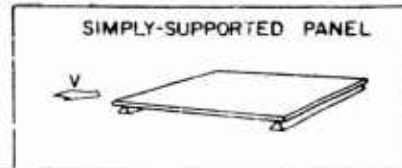
$$\gamma = \frac{-[F_1(\omega) + \frac{g_s}{\omega} F_2(\omega)]}{2\omega F_4(\omega)} \equiv \gamma_0 \left( 1 - \frac{g_s}{g_R} \right)$$

FOR  $\gamma = g_s = \zeta_s = 0$

$$V_0 = \frac{-\left[ \omega^4 \left( 1 - \frac{x_a^2}{r_a^2} \right) - (\omega_h^2 + \omega_a^2 + \frac{A_1 A_3 - A_2^2}{\mu^2 r_a^2}) \omega^2 + \omega_h^2 \omega_a^2 \right]}{\frac{A_2 \omega_h^2}{\mu r_a^2}}$$

Auxiliary Slide





CHARACTERISTIC EQUATION:

$$\left(s^2 + 2\zeta_s \omega_1 s + \frac{\omega_1^2 g_s s}{\omega} + \frac{as}{2\mu L} + \omega_1^2\right) \left(s^2 + 2\zeta_s \omega_2 s + \frac{\omega_2^2 g_s s}{\omega} + \frac{as}{2\mu L} + \omega_2^2\right) + \left(\frac{4V_0 a}{3\mu L^2}\right)^2 = 0$$

CASE A  $\gamma = 0, \zeta_s = 0$

$$g_R = \frac{-\left(\frac{a\omega}{\mu L}\right) \left[\omega^2 - \frac{\omega_1^2 + \omega_2^2}{2}\right]}{\left[(\omega_1^2 + \omega_2^2)\omega^2 - 2\omega_1^2 \omega_2^2\right]} = \frac{-\frac{a\omega}{\mu L} G_1(\omega)}{G_2(\omega)}$$

CASE B  $\gamma = 0, g_s = 0$

$$2\zeta_R = \frac{-\left(\frac{a\omega}{\mu L}\right) G_1(\omega)}{\left[(\omega_1 + \omega_2)(\omega^2 - \omega_1 \omega_2)\right]} = \frac{-\frac{a\omega}{\mu L} G_1(\omega)}{G_3(\omega)}$$

CASE C  $\zeta_s = 0, g_s = 0$

$$\gamma_0 = \frac{\left(\frac{a}{\mu L}\right) G_1(\omega)}{-2\omega \left[2\omega^2 - (\omega_1^2 + \omega_2^2 + \left(\frac{a}{2\mu L}\right)^2)\right]} = \frac{\left(\frac{a}{\mu L}\right) G_1(\omega)}{-2\omega G_4(\omega)}$$

CASE D  $\zeta_s = 0$

$$\gamma = \frac{\left(\frac{a\omega}{\mu L}\right) G_1(\omega) + g_s G_2(\omega)}{-2\omega^2 G_4(\omega)} = \gamma_0 \left(1 - \frac{g_s}{g_R}\right)$$

FOR  $\gamma = g_s = \zeta_s = 0$

$$\left(\frac{4V_0 a}{3\mu L^2}\right)^2 = -\left[\omega^4 - (\omega_1^2 + \omega_2^2 + \left(\frac{a}{2\mu L}\right)^2)\omega^2 + \omega_1^2 \omega_2^2\right]$$

Auxiliary Slide (Cont'd)

SIMPLY-SUPPORTED PANEL TERNARY APPROXIMATION	
<b>A</b>	$\gamma_0 = - \frac{\left(\frac{a}{\mu l}\right) H_x(\omega)}{2\omega H_y(\omega)}$
<b>B</b>	$\frac{dV_0}{d\omega} = \frac{-2\omega [2a_1\omega^6 - (a_1a_3 + 3a_2 + 3a_4\frac{\omega^2}{4})\omega^4 + 2a_2\omega^2(a_3 + 3\frac{\omega^2}{4}) - (a_2a_4 - a_1a_5 + a_2a_3\frac{\omega^2}{4})]}{2\frac{V_0}{l} (4\omega_A)^2 (a_1\omega^2 - a_2)^2}$
<b>C</b>	$H_4(\omega) = 2a_1\omega^6 - (a_1a_3 + 3a_2 + 3a_4\frac{\omega^2}{4})\omega^4 + 2a_2\omega^2(a_3 + 3\frac{\omega^2}{4}) - (a_2a_4 - a_1a_5 + a_2a_3\frac{\omega^2}{4})$
<b>D</b>	$\gamma_0 = \frac{-\left(\frac{a}{\mu l}\right) H_1(\omega)}{2\omega H_4(\omega)}$

Figure 6

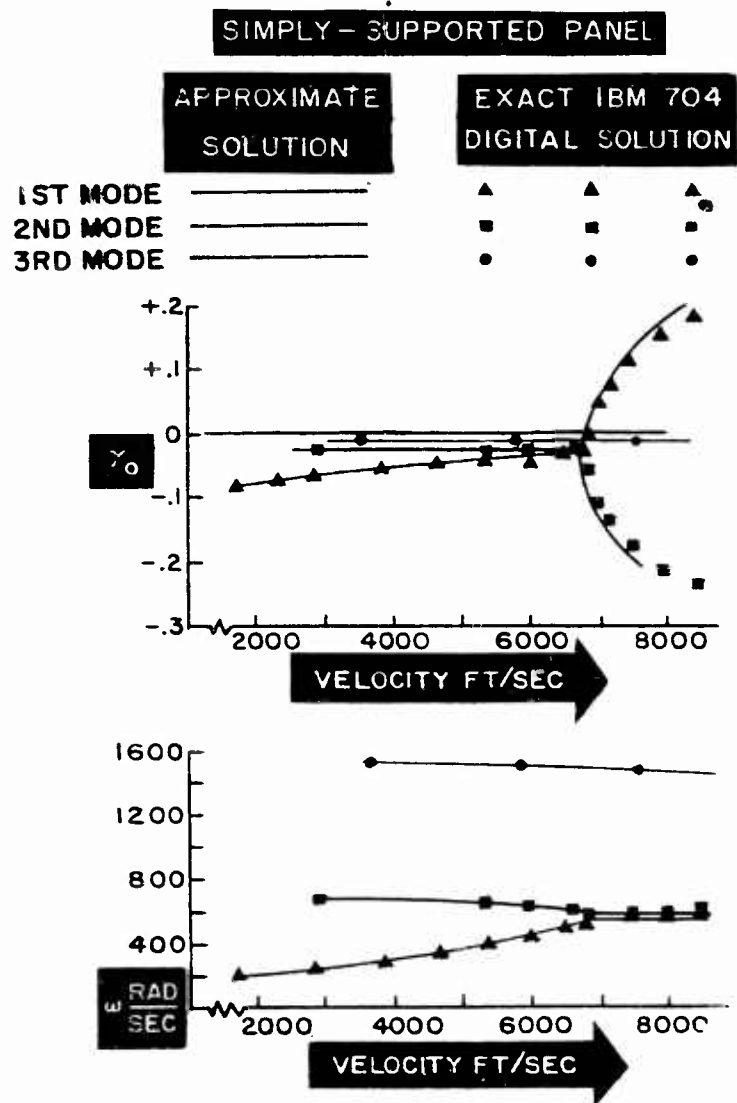


Figure 7

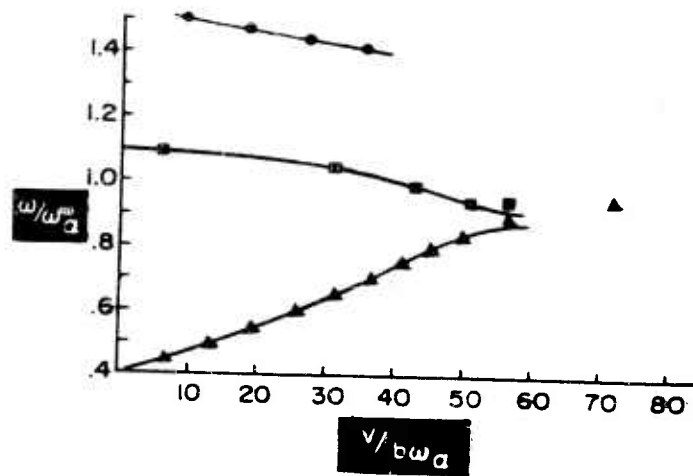
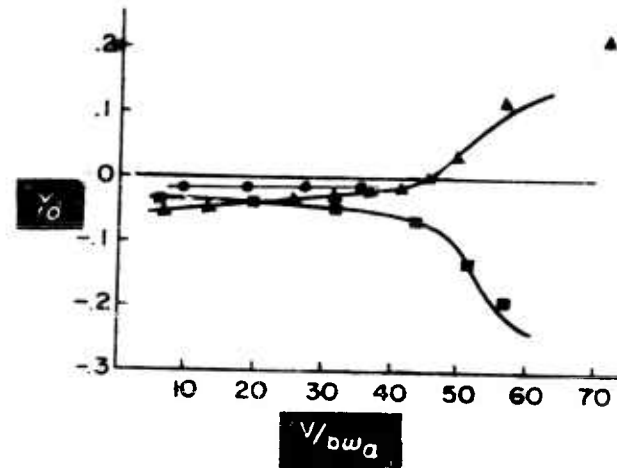
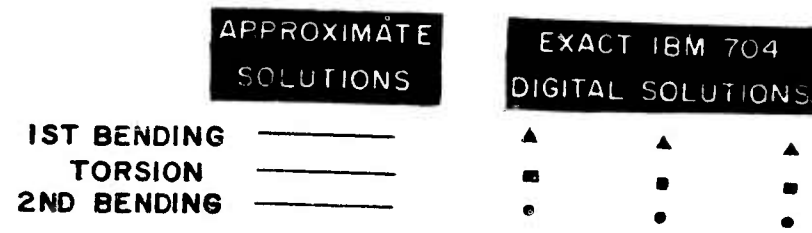


Figure 8

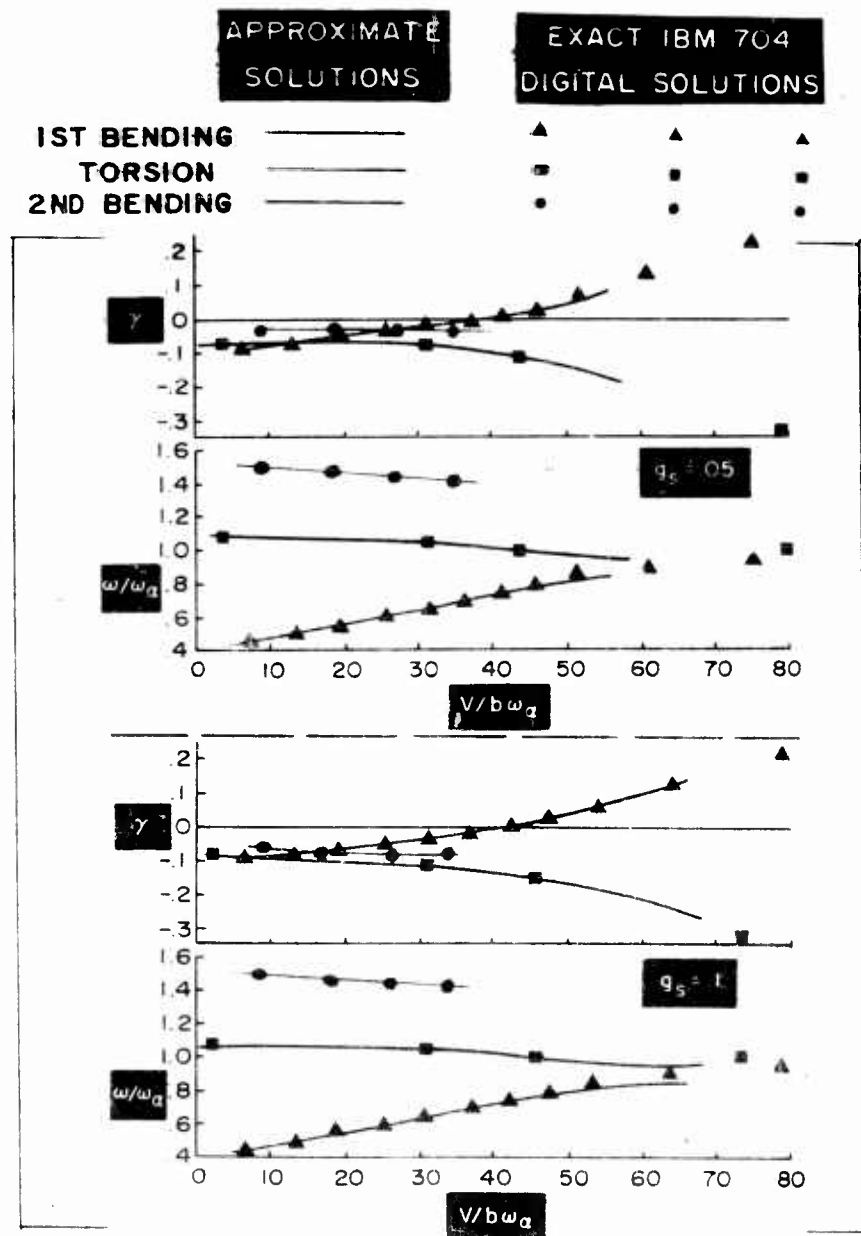


Figure 9

# DYNAMIC RESPONSE SOLUTION FROM FLUTTER SOLUTION

## STEPS IN DERIVATION

$$A \quad \left(\frac{4a}{3\bar{\mu}l^2}\right)^2 V_0^2 = \left\{ -\omega^4 + \left[ \omega_1^2 + \omega_2^2 + \left(\frac{a}{2\bar{\mu}l}\right)^2 \right] \omega^2 - \omega_1^2 \omega_2^2 \right\}$$

$$B \quad \frac{dV_0}{d\omega} = \frac{1}{\left(\frac{4a}{3\bar{\mu}l^2}\right)^2 2V_0} \left\{ -4\omega^3 + 2\omega \left[ \omega_1^2 + \omega_2^2 + \left(\frac{a}{2\bar{\mu}l}\right)^2 \right] \right\}$$

$$C \quad \left(\frac{4a}{3\bar{\mu}l^2}\right)^2 V_0^2 = \frac{G_2(\omega)}{2} + \frac{\omega}{4} \left\{ -4\omega^3 + 2\omega \left[ \omega_1^2 + \omega_2^2 + 2\left(\frac{a}{2\bar{\mu}l}\right)^2 \right] \right\}$$

$$D \quad G_2(\omega) \doteq -2V_0\omega \left(\frac{4a}{3\bar{\mu}l^2}\right)^2 \left\{ 1/2 \frac{dV_0}{d\omega} - \frac{V_0}{\omega} \right\}$$

$$E \quad \frac{\gamma_0}{g_R} \doteq \frac{G_2(\omega)}{2\omega G_4(\omega)}$$

$$F \quad \frac{\gamma_0}{g_R} \doteq \frac{\left[ 1/2 \frac{dV_0}{d\omega} - \frac{V_0}{\omega} \right]}{\frac{dV_0}{d\omega}}$$

Figure 10

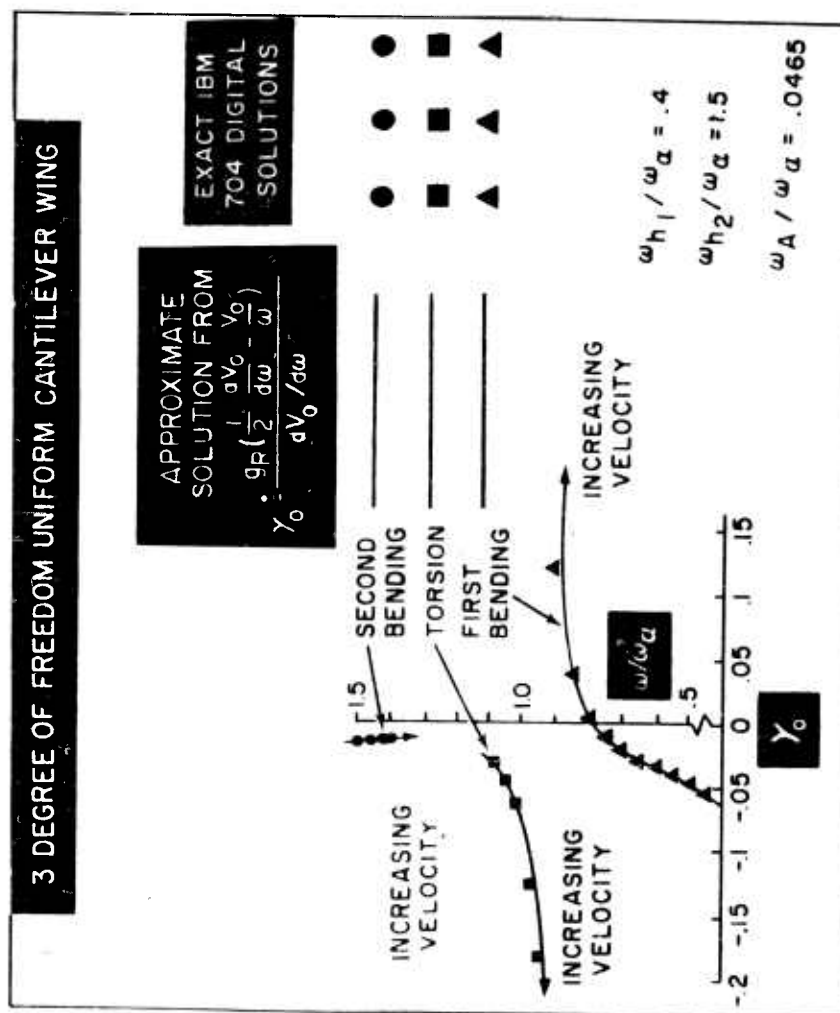


Figure 11

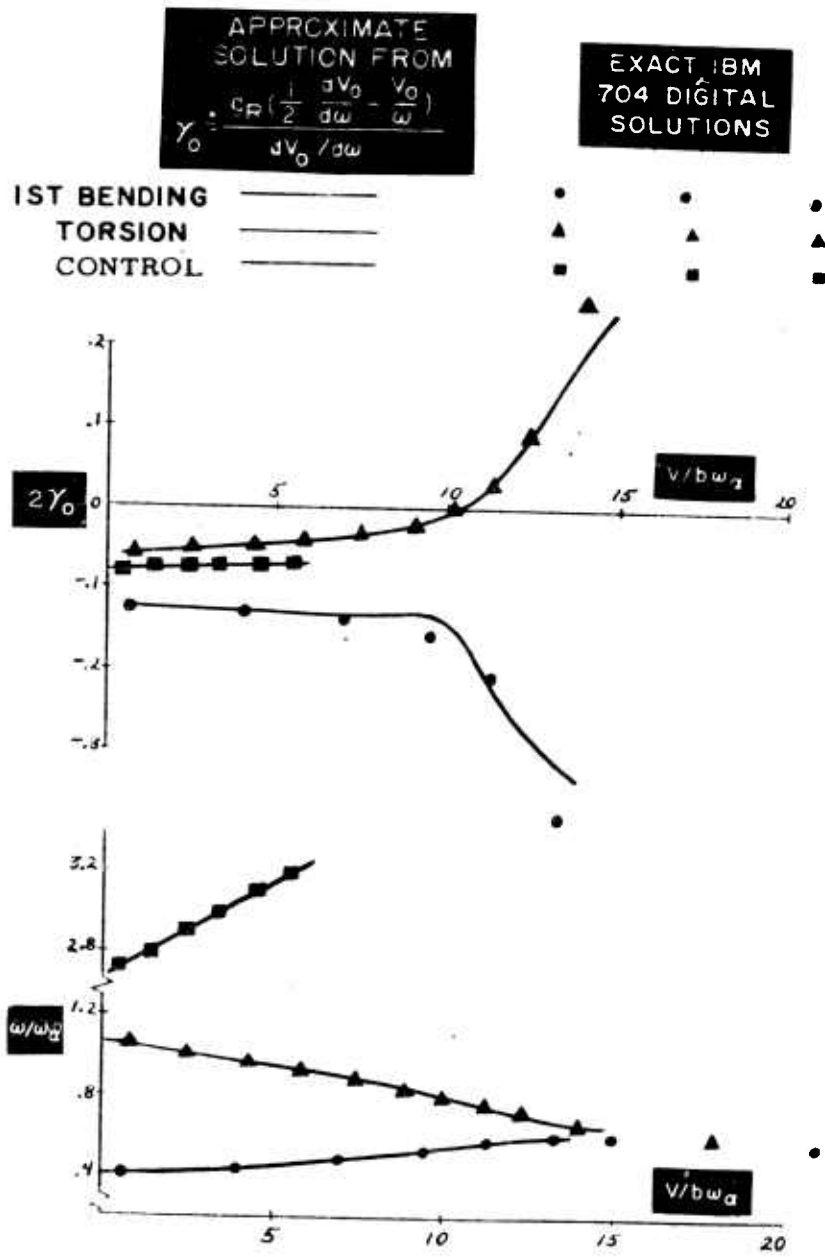


Figure 12



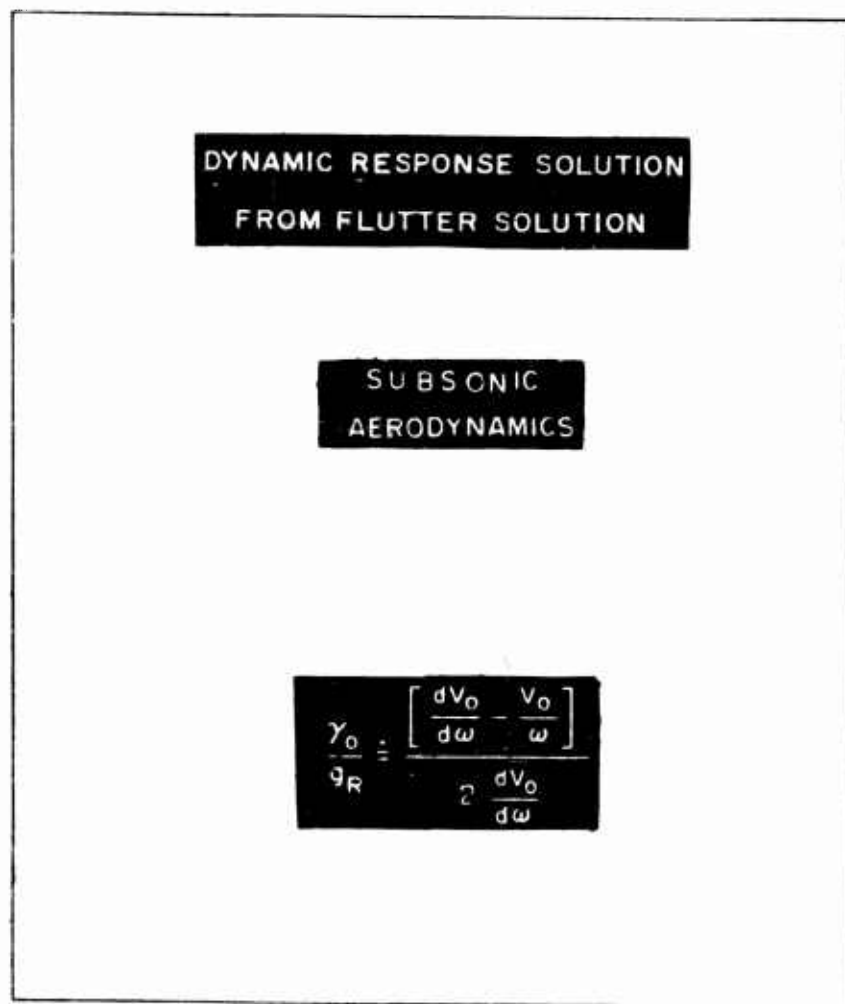


Figure 13

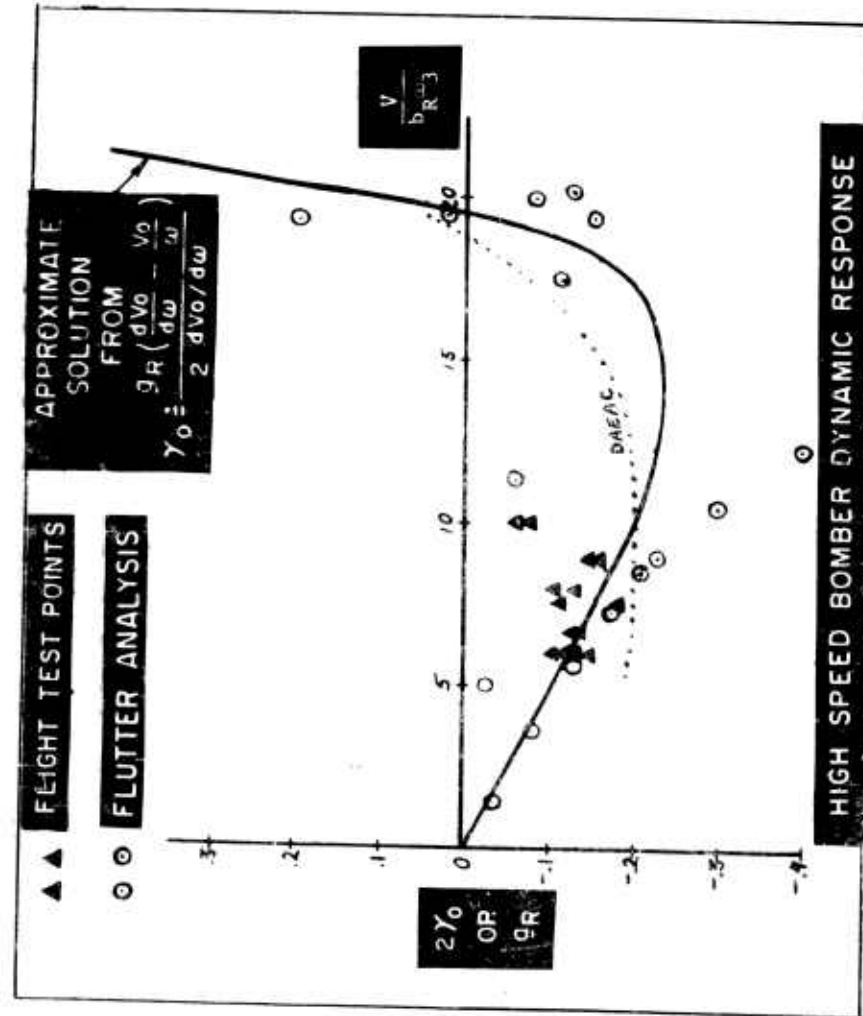


Figure 14

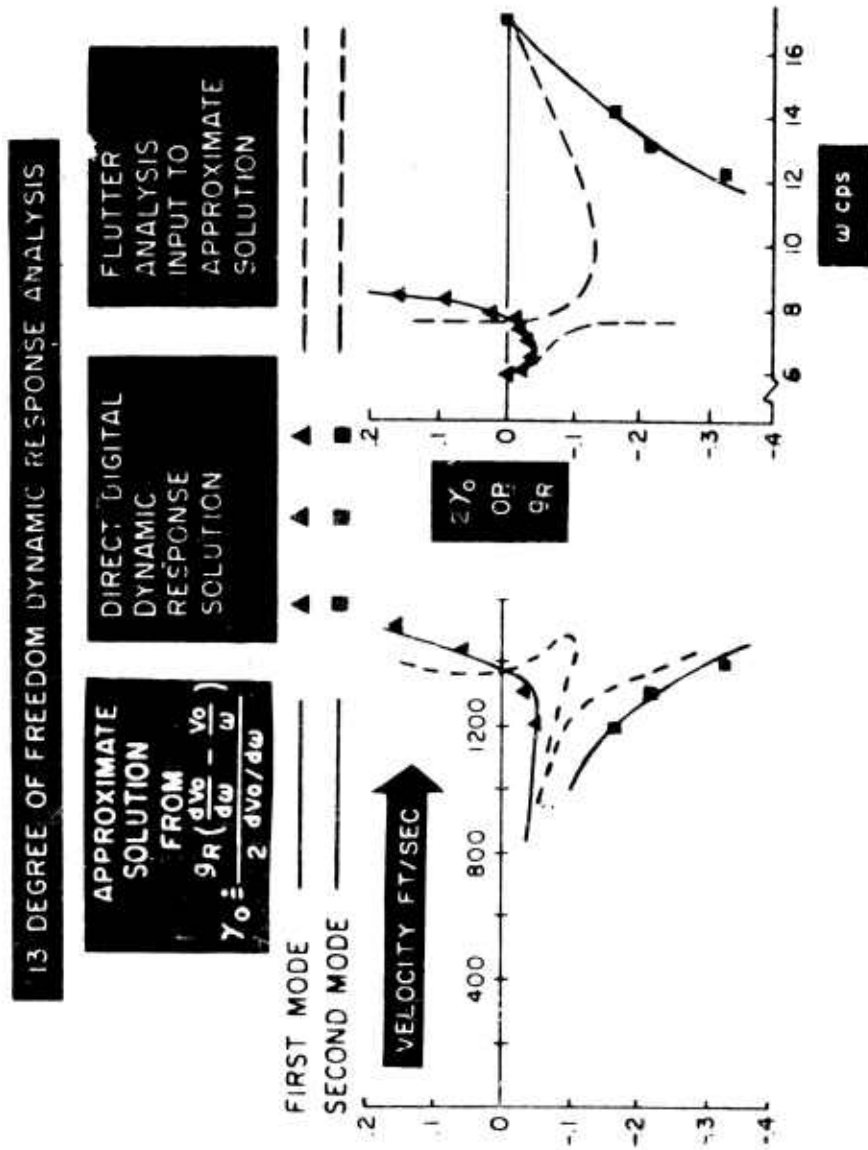


Figure 15

ELEMENTARY STATIC AERODYNAMICS ADDS SIGNIFICANCE  
AND SCOPE IN FLUTTER ANALYSES

Norman H. Zimmerman  
McDonnell Aircraft Corporation  
St. Louis, Missouri

Abstract

The feasibility of using simple approximate aerodynamics of the form  $C_L = C_{L\alpha} \alpha$  in flutter studies is investigated with a two-fold purpose in mind; (1) clear concise understanding of the basic flutter mechanism and (2) its practical application in flutter analyses.

It is shown that the lift component in phase with  $\alpha$  is capable of inducing large phase angles between it and the plunging motion, resulting in severe and sudden energy transfer from the ambient air to the airfoil. On the other hand, the quadrature lift component induces only slight phase angles with correspondingly modest energy exchange between ambient air and airfoil. Mechanics of this phasing is shown as airspeed is increased.

Equations for calculating flutter speed parameter and frequency are of simple closed form involving only three configuration parameters, A.C.-E.A. distance, E.A.-C.G. distance, and frequency ratio. A typical design chart from which the flutter speed parameter and flutter frequency can be read directly is shown. These equations and charts are equally applicable in the subsonic, transonic and supersonic regions. Straightforward relations are presented for determining sensitive configurations where slight uncertainties can result in enormous variation in computed flutter speed. These indicate areas where considerable disagreement may be expected between classical and approximate calculations. A relation is developed which indicates a safe practical method of flutter speed determination from flight tests at subcritical speeds. Finally flutter speed calculations based on approximate aerodynamics are compared to experiment with very good agreement, even down to aspect ratios as low as two.

Notation

Dimensional

$a$	exponential increase of motion
$b$	semi-chord
$d$	distance of elastic axis aft of aerodynamic center
$h$	plunging displacement of aerodynamic center, positive down
$I_o$	moment of inertia of airfoil about aerodynamic center, per unit span
$I_a$	moment of inertia of airfoil about elastic axis, per unit span
$k_h$	plunging spring constant, per unit span
$k_a$	pitching spring constant, per unit span
$L$	lift, per unit span (increment beyond static equilibrium lift)
$m$	airfoil mass, per unit span
$M_a$	aerodynamic moment about aerodynamic center, per unit span (increment beyond static equilibrium $M_a$ )
$p$	differential operator $d/dt$
$Q$	dynamic pressure
$r_a$	airfoil radius of gyration about elastic axis
$s$	root of characteristic equation
$t$	time
$U$	work done on airfoil by aerodynamic lift
$V$	airspeed
$X_a$	distance of center of gravity aft of elastic axis
$\alpha$	pitching displacement, positive nose up
$\rho$	air mass density
$\omega$	frequency
$\omega_h$	uncoupled plunging frequency
$\omega_a$	uncoupled pitching frequency
$\omega_1$	lowest coupled vibration frequency
$\omega_2$	highest coupled vibration frequency

Non-Dimensional

$C_L$	lift coefficient (increment beyond static equilibrium $C_L$ )
$CL_a$	$dC_L/d\alpha$ -- lift curve slope
$C_L^{as}$	steady flow lift curve slope
$C_M$	aerodynamic moment coefficient about aerodynamic center (increment beyond static equilibrium $C_M$ )
$C_{M_a}$	$dC_M/d\alpha$
$D$	flutter discriminant, see equation (57)
$g$	structural damping coefficient
$i$	the imaginary $\sqrt{-1}$
$K$	modulus of $q_h/q_a$
$M$	Mach number
$q_h$	$h/r_a$ -- non-dimensional plunging displacement
$q_a$	$\alpha$ -- non-dimensional pitching displacement
$R$	$\omega_h/\omega_a$ -- plunging/pitching frequency ratio

## Zimmerman

S	$s/\omega_a$ -- non-dimensional root of characteristic equation
W	parameter, see equation (17)
X	$X_a/r_a$ -- non-dimensional distance of center of gravity aft of elastic axis
Y	parameter, see equation (18)
Z	$2br_a (C_{L_a} Q)/k_a$ -- non-dimensional lift parameter
$Z_F$	$2br_a (C_{L_a} Q)_F/k_a$ -- flutter parameter
$\gamma$	$d/r_a$ -- non-dimensional distance of elastic axis aft of aerodynamic center
$\delta$	logarithmic decrement
$\eta$	$C_{L_a}/2\pi$ -- aerodynamic lift efficiency
$\eta_s$	steady flow lift efficiency component
$\eta_\omega$	oscillatory flow lift efficiency component, see Figure 13
$\mu$	$m/\pi \rho b^2$ -- non-dimensional mass
$\psi$	phase angle by which $q_h$ leads $q_a$

The subscripts F and D refer to flutter onset and divergence onset respectively.

## Introduction

Past effort in the flutter control of aircraft and missiles has predominantly stressed retention of considerable rigor in the mathematical idealization of the oscillatory aerodynamics used in the flutter analysis. This resulted in an unusually complex formulation of the flutter problem. As a corollary, emphasis was placed on calculation techniques with the subordination of basic physical insight into the flutter mechanism. A need exists, however, for parallel avenues of approach; one consists of the rigorous solution of the flutter problem which, for the most part, is already available; the other, a rational approximation stressing basic physical insight with adequate reliability. The state of the art in dynamic calculations has arrived at a point where it is possible and desirable to develop such a technique based on rational and simplified approaches by discarding secondary parameters in arriving at an adequate formulation of the flutter problem. This formulation emphasizes the rational retention of physical significance in the problem setup, solution and interpretation of results.

The ultimate development of such a rational approach consistent with adequate reliability over a wide range of problem parameters is a long range task. It is the author's belief that the long range effort should encompass the following objectives:

- (a) To search for and explain clearly and precisely the fundamental processes that lead to flutter.
- (b) To isolate essentials from secondaries in a sound rational theory.
- (c) To achieve a rational mathematical model logically suited to more direct physical interpretation.
- (d) To investigate the possible extent to which such a mathe-

mational model may be used in practical flutter control and to present methods for such use.

Except for isolated instances (Reference 1 and 2 for example), there had been no significant interest toward the overall development of a rational flutter approach until approximately three years ago at which time T. R. Beal of McDonnell (Reference 3) and S. Pines of Republic (Reference 4) further demonstrated the potential of the rational approach. The author is aware of four additional contributions (References 5 through 8) published within the past year. It appears that interest is increasing and progress in this area is being accelerated.

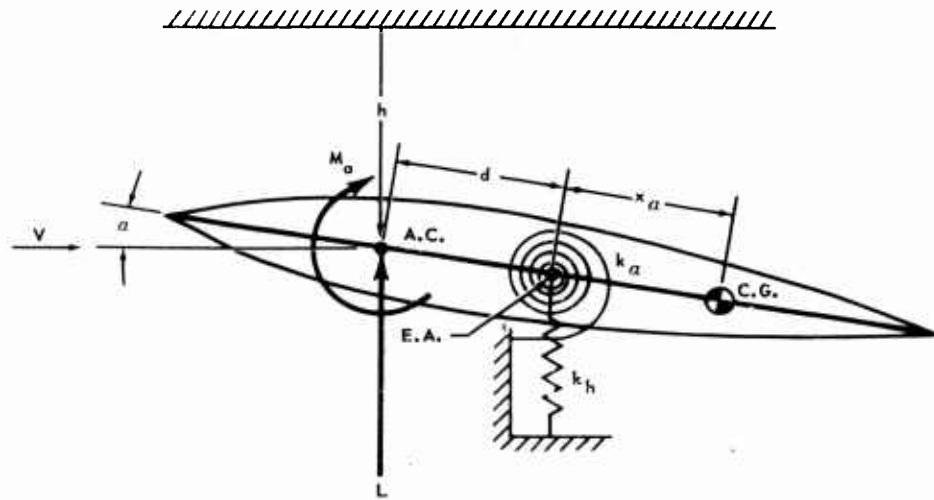
Because of the early state of the art, and in particular the unavailability of comprehensive comparisons between approximate formulations and experiment over a broad range of parameters, this technique is for the most part confined to advanced design studies at present with some initial probes in detail design to supplement the more rigorous approach. For example, the simplified formulation could be used to show trends in concise analytical form about the flutter speed calculated by more rigorous methods. There is a vast potential for the approximate formulation, even in detail design, but the extent of such use must be compatible with its adequacy in correlating with experimental results. Several simple aerodynamic formulations proposed to date, together with available comparisons with experiment, lead the author to believe that the satisfactory development of a rational approach, omitting non-essentials or secondary effects, is indeed feasible and should be pursued further.

The material covered in this paper contributes toward such overall development in both extending the work of previous authors and in presenting additional concepts and techniques. Except for an occasional digression, the scope of this paper is limited to the investigation of the two dimensional plunging-rotation problem. Extensive effort here is justified since it would be ridiculous to proceed with the more elaborate configurations without adequate proof of the validity of the aerodynamic approximations for the simpler configurations which do not require the introduction of additional uncertainties (such as assumed mode shapes, etc.).

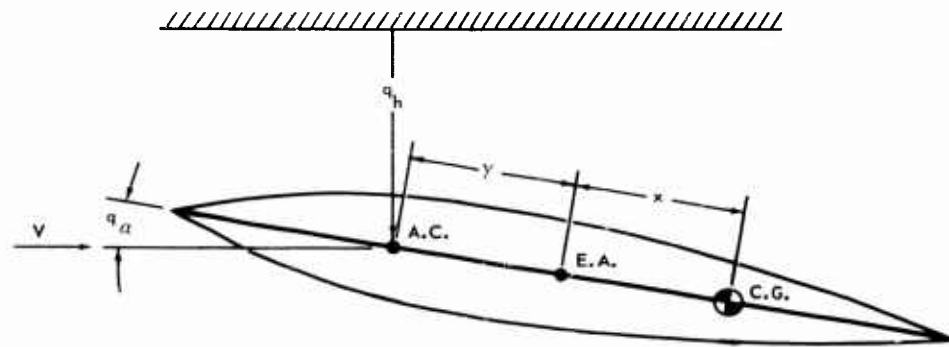
#### Basic Relations

The system shown in Figure 1 is allowed the degrees-of-freedom of plunging ( $h$ ) and rotation ( $\alpha$ ), each measured from the position of static equilibrium. The equations of motion, referred to the steady-state aerodynamic center, are

$$\left. \begin{aligned} m\ddot{h} + m(d + X_{\alpha})\ddot{\alpha} + k_h(h + d\alpha) &= -L \\ I_{\alpha}\ddot{\alpha} + m(d + X_{\alpha})\ddot{h} + k_h(h + d\alpha)d + k_{\alpha}\alpha &= M_{\alpha} \end{aligned} \right\} \quad (1)$$



(a) DIMENSIONAL GEOMETRY



(b) NON-DIMENSIONAL GEOMETRY

FIGURE 1. IDEALIZATION



Since  $L = Q(2b)C_L$  and  $M_a = Q(2b)^2C_M$ , the above equations may be rewritten

$$\left. \begin{aligned} m\ddot{h} + m(d + x_a)\ddot{a} + k_h h + (k_h d) a &= -(2bQ)C_L \\ I_a\ddot{a} + m(d + x_a)\ddot{h} + (k_h d)h + (k_a + k_h d^2) a &= (4b^2Q)C_M \end{aligned} \right\} \quad (2)$$

In order to arrive at a convenient non-dimensional formulation, the following relations are utilized:

$$\left. \begin{aligned} I_a &= I_a + m[(d + x_a)^2 - x_a^2] & R &= \omega_h/\omega_a \\ I_a &= m r_a^2 & \gamma &= d/r_a \\ k_h &= m \omega_h^2 & X &= x_a/r_a \\ k_a &= I_a \omega_a^2 & q_h &= h/r_a \\ & & q_a &= a \end{aligned} \right\} \quad (3)$$

Multiplying the first of equations (2) by  $r_a/k_a$ , the second by  $1/k_a$  and introducing equations (3)

$$\left. \begin{aligned} \frac{1}{\omega_a^2} \ddot{q}_h + \frac{1}{\omega_a^2} (\gamma + X) \ddot{q}_a + R^2 q_h + \gamma R^2 q_a &= -\left(\frac{2bQ}{k_a}\right) C_L \\ \frac{1}{\omega_a^2} [(\gamma + X)^2 + (1 - X^2)] \ddot{q}_a + \frac{1}{\omega_a^2} (\gamma + X) \ddot{q}_h + \gamma R^2 q_h + (1 + \gamma^2 R^2) q_a &= \left(\frac{4b^2Q}{k_a}\right) C_M \end{aligned} \right\} \quad (4)$$

Equations (4) allow a rather wide latitude on the specification of the aerodynamics to be considered. However, the aerodynamics employed here will be represented in a form compatible with the steady-state formulation, i.e.

$$C_L = C_{L_a} a = C_{L_a} q_a$$

$$C_M = C_{M_a} a = 0$$

Note that the representation of  $C_L$  is based on the geometric angle of attack and does not include the increment angle of attack due to plunging velocity. With this formulation of the aerodynamics then, equations (4) become

$$\left. \begin{aligned} \frac{1}{\omega_a^2} \ddot{q}_h + \frac{\gamma + X}{\omega_a^2} \ddot{q}_a + R^2 q_h + (\gamma R^2 + Z) q_a &= 0 \\ \frac{(\gamma + X)^2 + (1 - X^2)}{\omega_a^2} \ddot{q}_a + \frac{\gamma + X}{\omega_a^2} \ddot{q}_h + \gamma R^2 q_h + (1 + \gamma^2 R^2) q_a &= 0 \end{aligned} \right\} \quad (5)$$

where

$$Z = \frac{2b r_a}{k_a} (C_{L_a} Q) \quad (6)$$

The aerodynamics of the problem are embodied solely in the lift parameter  $Z$ . For a given configuration, the equations of motion above vary with  $Z$  as airspeed is changed. The advantageous occurrence of  $Z$  in just one term of the equations of motion stems directly from referring the motion to the aerodynamic center.

If  $p$  is used to denote the differential operator  $d/dt$ , equations (5) may be written in the operational form

$$\left. \begin{aligned} \left\{ \frac{p^2}{\omega_a^2} + R^2 \right\} q_h + \left\{ (\gamma + X) \frac{p^2}{\omega_a^2} + (\gamma R^2 + Z) \right\} q_a &= 0 \\ \left\{ (\gamma + X) \frac{p^2}{\omega_a^2} + \gamma R^2 \right\} q_h + \left\{ [(\gamma + X)^2 + (1 - X^2)] \frac{p^2}{\omega_a^2} + (1 + \gamma^2 R^2) \right\} q_a &= 0 \end{aligned} \right\} \quad (7)$$

From the first of equations (7)

$$q_h = - \left\{ \frac{(\gamma + X) \frac{p^2}{\omega_a^2} + (\gamma R^2 + Z)}{\frac{p^2}{\omega_a^2} + R^2} \right\} q_a \quad (8)$$

Substituting this into the second of equations (7),

$$\left\{ \frac{1-x^2}{\omega_a^4} p^4 + \frac{(1+R^2) - (\gamma+X)Z}{\omega_a^2} p^2 + R^2(1-\gamma Z) \right\} q_a = 0 \quad (9)$$

The solution to equation (9) is

$$\left. \begin{aligned} q_a &= \sum_{j=1}^{j=4} A_j e^{s_j t} \\ s_j &= \sigma_j + i\omega_j \end{aligned} \right\} \quad (10)$$

where the  $A_j$  are arbitrary integration constants and the  $s_j$  are the roots of the characteristic equation

$$(1-x^2) \left( \frac{s}{\omega_a} \right)^4 + [(1+R^2) - (\gamma+X)Z] \left( \frac{s}{\omega_a} \right)^2 + R^2(1-\gamma Z) = 0 \quad (11)$$

Equation (11) is quadratic in  $(s/\omega_a)^2$ . Thus

$$\left( \frac{s}{\omega_a} \right)^2 = - \left\{ \frac{(1+R^2) - (\gamma+X)Z}{2(1-x^2)} \right\} \pm \sqrt{\left\{ \frac{(1+R^2) - (\gamma+X)Z}{2(1-x^2)} \right\}^2 - \left\{ \frac{R^2(1-\gamma Z)}{(1-x^2)} \right\}} \quad (12)$$

For compactness it is desirable to denote

$$S = \frac{s}{\omega_a} \quad (13)$$

Thus equation (12) becomes

$$S^2 = - \left\{ \frac{(1+R^2) - (\gamma+X)Z}{2(1-x^2)} \right\} \pm \sqrt{\left\{ \frac{(1+R^2) - (\gamma+X)Z}{2(1-x^2)} \right\}^2 - \left\{ \frac{R^2(1-\gamma Z)}{(1-x^2)} \right\}} \quad (14)$$

The solution for  $q_h$  is similarly

$$q_h = \sum_{j=1}^{j=4} B_j e^{s_j t} \quad (15)$$

where the  $B_j$  integration constants are obtained by substituting equations (10) and (15) into equation (8), i.e.

$$B_j = - \left\{ \frac{(\gamma + X)S_j^2 + (\gamma R^2 + Z)}{S_j^2 + R^2} \right\} A_j \quad (16)$$

The stability characteristics of a configuration at any particular airspeed (embodied in  $Z$ ) may be examined via equation (14). It is to be noted that only two groupings of parameters are needed to fully define  $S^2$ . Let these be denoted by

$$W = \frac{(1 + R^2) - (\gamma + X)Z}{2(1 - X^2)} = \left[ \frac{1 + R^2}{2(1 - X^2)} \right] - \left[ \frac{\gamma + X}{2(1 - X^2)} \right] Z \quad (17)$$

$$Y = \frac{R^2(1 - \gamma Z)}{(1 - X^2)} = \left[ \frac{R^2}{1 - X^2} \right] - \left[ \frac{\gamma R^2}{1 - X^2} \right] Z \quad (18)$$

Both  $W$  and  $Y$  are linear in  $Z$  and depend upon airspeed as well as configuration parameters. It might be well to mention at this point that physical considerations limit  $X$  to values between plus and minus unity. (This results since  $X = X_a / r_a$  and  $r_a^2 = r_c^2 + x_a^2$  where  $r_c$  is the radius of gyration about the c.g.) Furthermore physical considerations limit  $R$  and  $Z$  to positive real values while  $\gamma$  may assume any positive or negative real value. With the above definitions of  $W$  and  $Y$ ,

$$S^2 = -W \pm \sqrt{W^2 - Y} \quad (19)$$

It is physically possible for  $W$  and  $Y$  to be positive, negative or zero. Depending on configuration and airspeed, various possible stability conditions can exist. These are covered in Table I and in Figure 2. (Recall that  $s = \omega_a S$  where  $\omega_a$  is real and positive.) In Table I and Figure 2,  $\phi$ ,  $\phi_1$ ,  $\phi_2$ , and  $A_1$  through  $A_4$  are arbitrary integration constants. Although mathematically Case 1 is referred to as an undamped vibration, in a practical sense it is a stable configuration since even minute amounts of inherent damping in the structure would render it stable. All the other conditions exhibit definite instabilities of various forms.

The transition from Case 1 to an unstable condition is considered next, for example as speed (or  $Z$ ) is increased. Two distinct transition paths are possible, both starting from the condi-

TABLE I. POSSIBLE STABILITY CONDITIONS

CASE	ROOTS OF $s^2$	REQUIREMENTS*	RESULTING MOTION ( $s = a + i\omega$ )	FIG.
1	BOTH ROOTS REAL AND NEGATIVE.	a) POSITIVE ( $W^2 - Y$ ) b) POSITIVE $W$ c) POSITIVE $Y$	$q = A_1 \cos(\omega_1 t - \phi_1) + A_2 \cos(\omega_2 t - \phi_2)$ TWO UNDAMPED VIBRATION MODES.	2a
2	ONE NEGATIVE REAL ROOT AND ONE POSITIVE REAL ROOT.	a) NEGATIVE $Y$	$q = A_1 e^{a_1 t} + A_2 e^{-a_1 t} + A_3 \cos(\omega t - \phi)$ ONE NON-OSC. DIVERGENT MODE, ONE NON-OSC. CONVERGENT MODE AND ONE UNDAMPED VIBRATION MODE.	2b
3	BOTH ROOTS POSITIVE AND REAL	a) POSITIVE ( $W^2 - Y$ ) b) NEGATIVE $W$ c) POSITIVE $Y$	$q = A_1 e^{a_1 t} + A_2 e^{a_2 t} + A_3 e^{-a_1 t} + A_4 e^{-a_2 t}$ TWO DIVERGENT AND TWO CONVERGENT NON-OSC. MODES.	2c
4	CONJUGATE COMPLEX ROOTS.	a) NEGATIVE ( $W^2 - Y$ )	$q = A_1 e^{a_1 t} \cos(\omega_1 t - \phi_1) + A_2 e^{-a_1 t} \cos(\omega_1 t - \phi_2)$ ONE OSC. DIVERGENT MODE (FLUTTER) AND ONE OSC. CONVERGENT MODE.	2d
5	CONJUGATE IMAGINARY ROOTS.	a) $W = 0$ b) POSITIVE $Y$	$q = A_1 e^{a_1 t} (\cos(\omega_1 t - \phi_1) + A_2 e^{-a_1 t} \cos(\omega_1 t - \phi_2))$ ( $a = \omega$ ) ONE OSC. DIVERGENT MODE (FLUTTER) AND ONE OSC. CONVERGENT MODE.	2e
* ALL REQUIREMENTS SHOWN MUST BE SATISFIED.				

TABLE II. CONDITIONS FOR INSTABILITY ONSET

CASE	ROOTS OF $s^2$	REQUIREMENTS*	RESULTING MOTION ( $s = a + i\omega$ )	FIG.
6	ONE NEGATIVE REAL ROOT AND ONE ZERO ROOT.	a) POSITIVE $W$ b) $Y = 0$	$q = A_1 t + A_2 + A_3 \cos(\omega t - \phi)$ ONSET OF NON-OSC. INSTABILITY, DIVERGENCE	3a
7	MULTIPLE NEGATIVE REAL ROOTS.	a) POSITIVE $W$ b) ( $W^2 - Y$ ) = 0	$q = A_1 t \cos(\omega t - \phi_1) + A_2 \cos(\omega t - \phi_2)$ ONSET OF OSC. INSTABILITY, FLUTTER.	3b
* ALL REQUIREMENTS SHOWN MUST BE SATISFIED.				

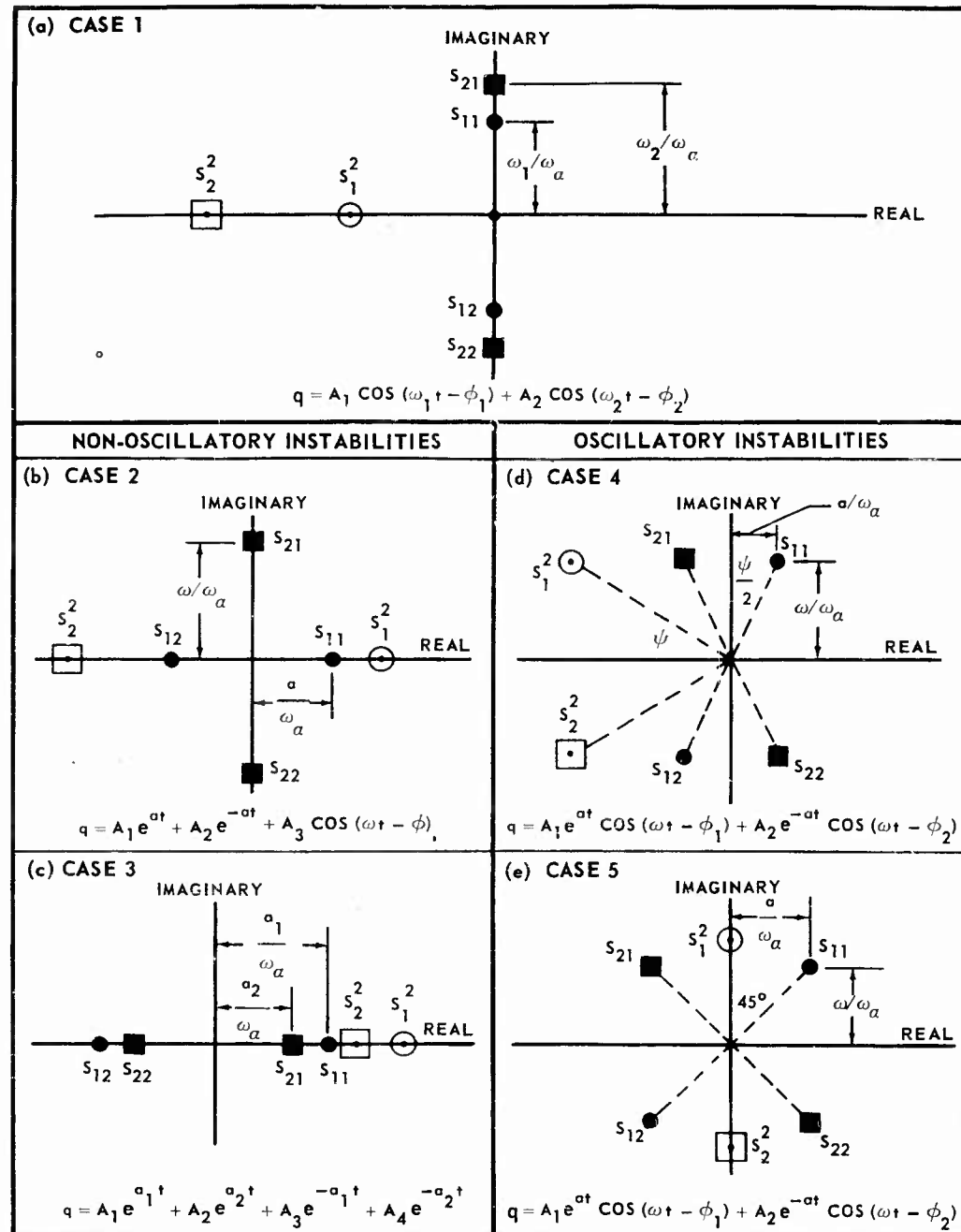


FIGURE 2. SIGNIFICANCE OF THE ROOTS  $s^2$

tions of Case 1, Figure 2; one tends toward the non-oscillatory instabilities on the left while the other tends toward the oscillatory instabilities on the right. These are covered in Table II and in Figure 3. A descriptive phrase for these transition cases would seem to be "instability onset," and this will be used in subsequent discussion when referring to Case 6 or 7.

The speed at which a given configuration reaches its instability onset is easily obtained from the requirements specified in Table II. For divergence onset,  $Y = 0$ . Satisfying this condition in equation (18) yields

$$Z_D = \frac{1}{\gamma} \quad (20)$$

and from equation (6)

$$(C_{L\alpha} Q)_D = \frac{k_\alpha}{2br_\alpha} Z_D = \frac{k_\alpha}{2br_\alpha} \frac{1}{\gamma} = \frac{k_\alpha}{2bd} \quad (21)$$

Flutter onset requires

$$w^2 - Y = 0$$

Introducing equations (17) and (18) above and solving for Z

$$Z_F = \left\{ \frac{1}{\gamma + X} \right\} + \left\{ \frac{(\gamma + X) - 2\gamma(1 - X^2)}{(\gamma + X)^2} \right\} R^2 \pm \left\{ \frac{2R}{(\gamma + X)^2} \right\} \sqrt{X(1 - X^2) [(\gamma + X) - \gamma(1 + \gamma X) R^2]} \quad (22)$$

and from equation (6)

$$(C_{L\alpha} Q)_F = \frac{k_\alpha}{2br_\alpha} Z_F \quad (23)$$

Equation (21) corresponds to the well known formula for static divergence. Equation (22) indicates that there exist two speeds at which the configuration is poised on the threshold of a flutter instability, flutter existing between these two speeds. Obviously the minus sign in equation (22) is the more significant and corresponds to flutter onset, but the plus sign will not be discarded since it has a significance of its own which will be discussed later. The subscripts D and F in equations (21) and (23) are specifically meant to apply to  $C_{L\alpha}$  as well as to Q, i.e.  $C_{L\alpha}$  must be compatible with the aerodynamic environment corresponding to Q. Although

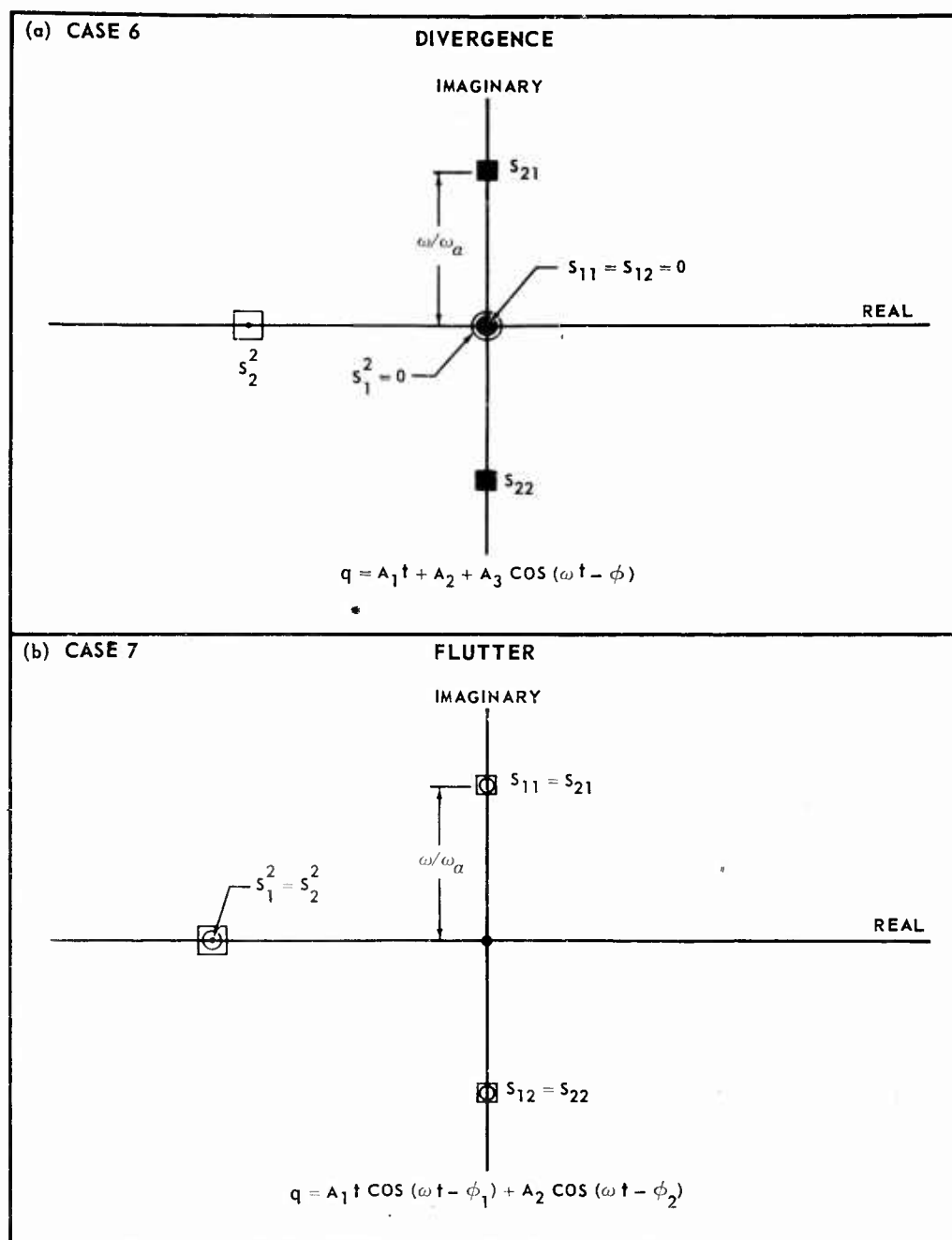


FIGURE 3. ROOTS OF  $s^2$  AT INSTABILITY ONSET.



apparently trivial, it is important to emphasize this in correlating airspeed with  $Z$ . Thus in general

$$V_j = \sqrt{\left(\frac{k_a}{\rho b r_a}\right) \left(\frac{Z_j}{C_{L_{a_j}}}\right)} \quad (24)$$

and in particular

$$V_D = \sqrt{\left(\frac{k_a}{\rho b r_a}\right) \left(\frac{Z_D}{C_{L_{a_D}}}\right)} \quad (25)$$

$$V_F = \sqrt{\left(\frac{k_a}{\rho b r_a}\right) \left(\frac{Z_F}{C_{L_{a_F}}}\right)} \quad (26)$$

It is particularly important to recognize that the problem formulation herein presented imposes no limitations on flight environment, and the equations are equally applicable throughout the complete flight envelope -- subsonic, transonic, supersonic. The compressibility effects are accounted for by introducing values of  $C_{L_a}$  and  $\gamma$  (location of aerodynamic center) appropriate to the flight environment. Thus the BASIC MECHANISM of the aeroelastic behavior is one-and-the-same regardless of flight regime, and if adequate agreement can be achieved between the above formulation and experiment in the low subsonic regime, there is good reason to expect adequate agreement in other flight regimes provided that  $C_{L_a}$  and  $\gamma$  reflect the appropriate environment. Furthermore  $C_{L_a}$  and  $\gamma$  are the direct ingredients in the present formulation and not Mach number (which is like a second cousin twice removed). If this is borne in mind, the salient characteristics of the aeroelastic behavior will be more easily recognizable.

It may have been noted that no consideration was given to the possibility of transition from Case 1 to the physically possible instabilities of either Case 3 or 5. Examination of Table I will reveal that these instabilities are never approached directly from the stable condition of Case 1; these will always be preceded by the instabilities of Case 6 or Case 7.

One further basic relation is useful, namely an alternate relation between  $V$  and  $Z$ . If the definition

$$C_{L_a} = 2\pi \eta \quad (27)$$

is introduced into equation (24) together with  $k_a = m r_a^2 \omega_a^2$  and  $\mu = m / \pi \rho b^2$ , there results

$$V_j = b \omega_a \sqrt{\frac{\mu r_a}{2b} \left( \frac{Z_j}{\eta_j} \right)} \quad (28)$$

The quantity  $\eta$  may be thought of as the aerodynamic lift efficiency.

#### Exploratory Example

Inclusion of an exploratory example at this point is considered advisable as background for further developments to be presented. Specifically, it is desirable to take a broad look at the dynamic characteristics of a given configuration as airspeed increases from zero to a value considerably in excess of its onset instability. This example assumes incompressible two-dimensional aerodynamics and a two degree of freedom plunging-rotation configuration. Configuration parameters for this example are given in Figure 4 and correspond to those of Figure 17, Reference 9. These configuration parameters represent a tested flutter model of large aspect ratio (14.5/1) which fluttered at a low subsonic speed. In this example  $C_{L\alpha}$  was taken as  $2\pi$ . Starting with  $Z = 0$  (zero airspeed), successively larger values of  $Z$  were introduced into equation (14) yielding the dual branch paths for the  $S^2$  shown in Figure 4. Note the following points:

- (a) Both values of  $S^2$  are real and negative at zero airspeed (corresponding to Case 1 Figure 2).
- (b) As speed is increased, both branches of  $S^2$  remain real and negative, approach each other and then become coincident at  $V = 307$  ft/sec. This corresponds to flutter onset shown in Figure 3.
- (c) With further increase in speed, each pair of  $S^2$  become complex conjugate (corresponding to Case 4 Figure 2), pass through conjugate imaginaries (Case 5 Figure 2) and once again become coincident, real and positive at  $V = 416$  ft/sec. The region between  $V = 307$  ft/sec. and  $V = 416$  ft/sec. is characterized by flutter instability.
- (d) With further increase in speed, corresponding pairs of  $S^2$  separate from each other, each being real and positive (corresponding to Case 3 Figure 2). This region is characterized by non-oscillatory instability.
- (e) Although not shown, the values of  $S^2$  never again become complex regardless of subsequent speed increases.

Plots such as those in Figure 4 are somewhat related to the Root Locus Method developed by Evans (Reference 10) and used quite frequently in stability analyses of servo systems.

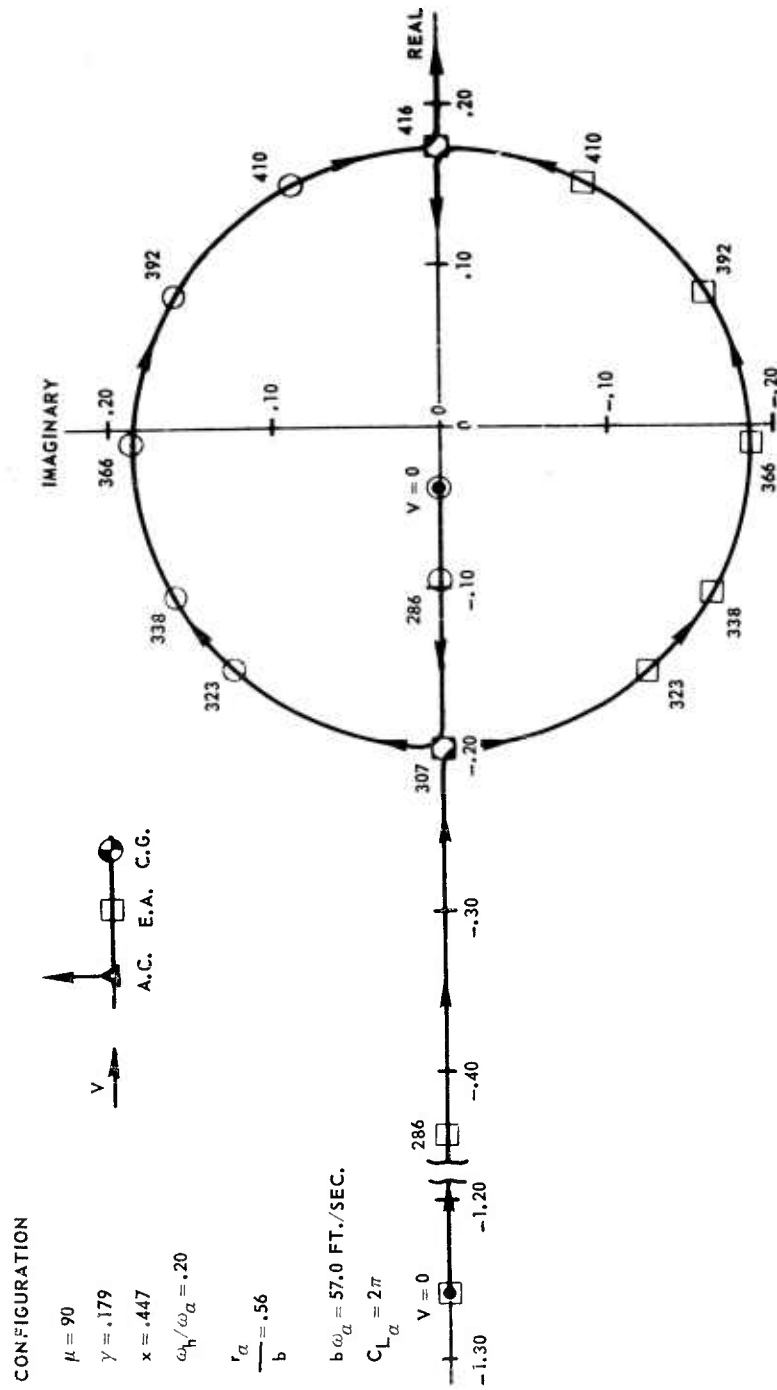


FIGURE 4. VARIATION OF CHARACTERISTIC  $s^2$  WITH SPEED.

Variation of the configuration dynamics with increasing speed is shown in somewhat different form in Figure 5. The two undamped coupled frequencies  $\omega_1$  and  $\omega_2$  approach each other with increasing speed becoming coincident at flutter onset. Continuing into the flutter region, the motion is the superposition of a divergent and convergent oscillatory mode, each of the same frequency  $\omega$ ; the rapidity of the divergence (and convergence) increases with speed while the common frequency  $\omega$  decreases and becomes zero at  $V = 416$  ft/sec. At this speed the type of instability changes from flutter to a non-oscillatory instability which continues indefinitely with further speed increase. The circular data point at 680 ft/sec. would correspond to the static divergence speed calculated by classical methods. Also shown for completeness is the logarithmic decrement which remains zero until the flutter onset speed is reached.

The flutter onset speed can be calculated directly from equations (22) and (26). The minus sign in equation (22) would result in a speed of 307 ft/sec., corresponding to flutter onset, while the plus sign would result in 416 ft/sec., corresponding to the transition from flutter instability to non-oscillatory instability.

#### Change of Dynamic Characteristics With Increase in Speed -- General

In the previous section the variation in the dynamic characteristics of a specific configuration was investigated as speed was increased. In this section the variation in dynamic characteristics with speed is presented for a wide range of typical configurations, the idea being to broaden basic concepts. Only the salient features are considered here. Important details, as applicable, are considered in later sections.

Figure 6 presents such dynamic characteristics for a variety of configurations. The arrows on the dual branch trajectories of  $S^2$  indicate increasing airspeed starting from zero, represented by 0 on the sketches. Pertinent remarks concerning the various cases are given below:

- Case (A) This was treated in the previous example in greater detail.
- Case (B) Two coupled vibration modes from 0 to A; flutter from A to B followed by another stable region of two coupled vibration modes; with further speed increases the lower frequency mode transforms into classical divergence instability beginning at C. The difference in behavior between Cases (A) and (B) is that the latter is representative of near-critical frequency ratios, i.e. frequency ratios where flutter solutions vanish.
- Case (C) Two coupled vibration modes from 0 to A; flutter from A to B; two coupled vibration modes thereafter.

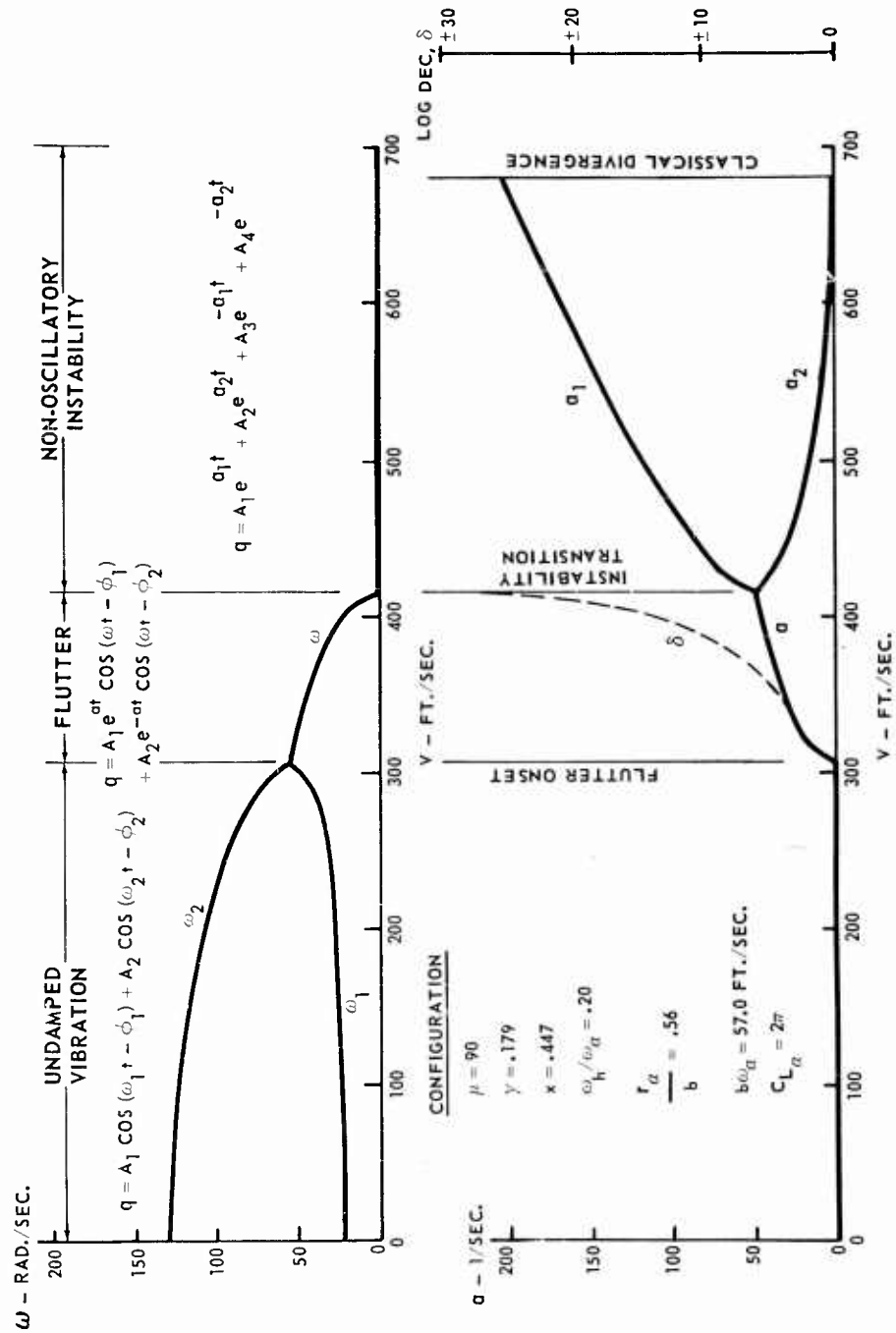


FIGURE 5. CHANGE OF DYNAMIC CHARACTERISTICS WITH SPEED

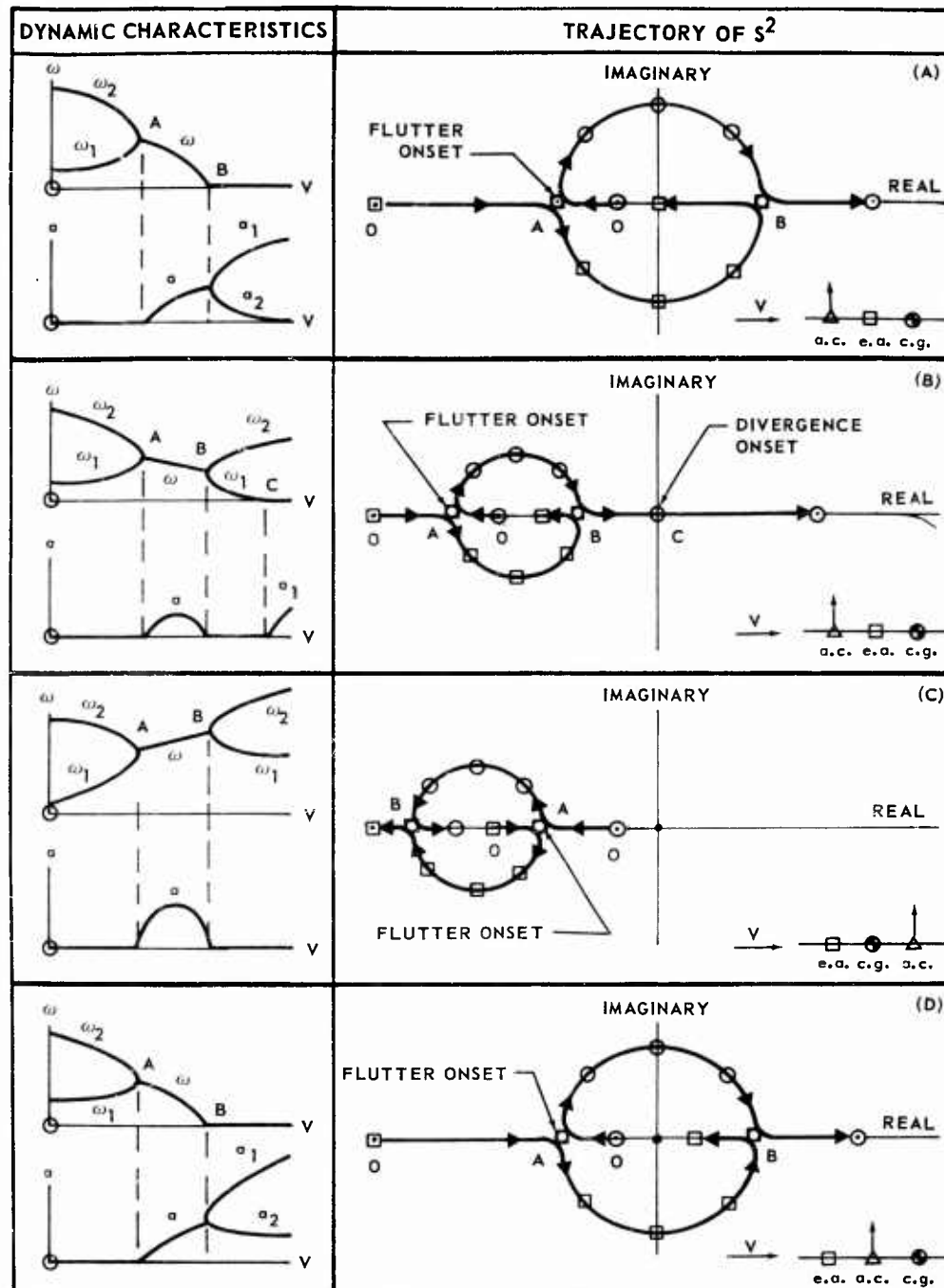


FIGURE 6. CHANGE OF DYNAMIC CHARACTERISTICS WITH SPEED-GENERAL

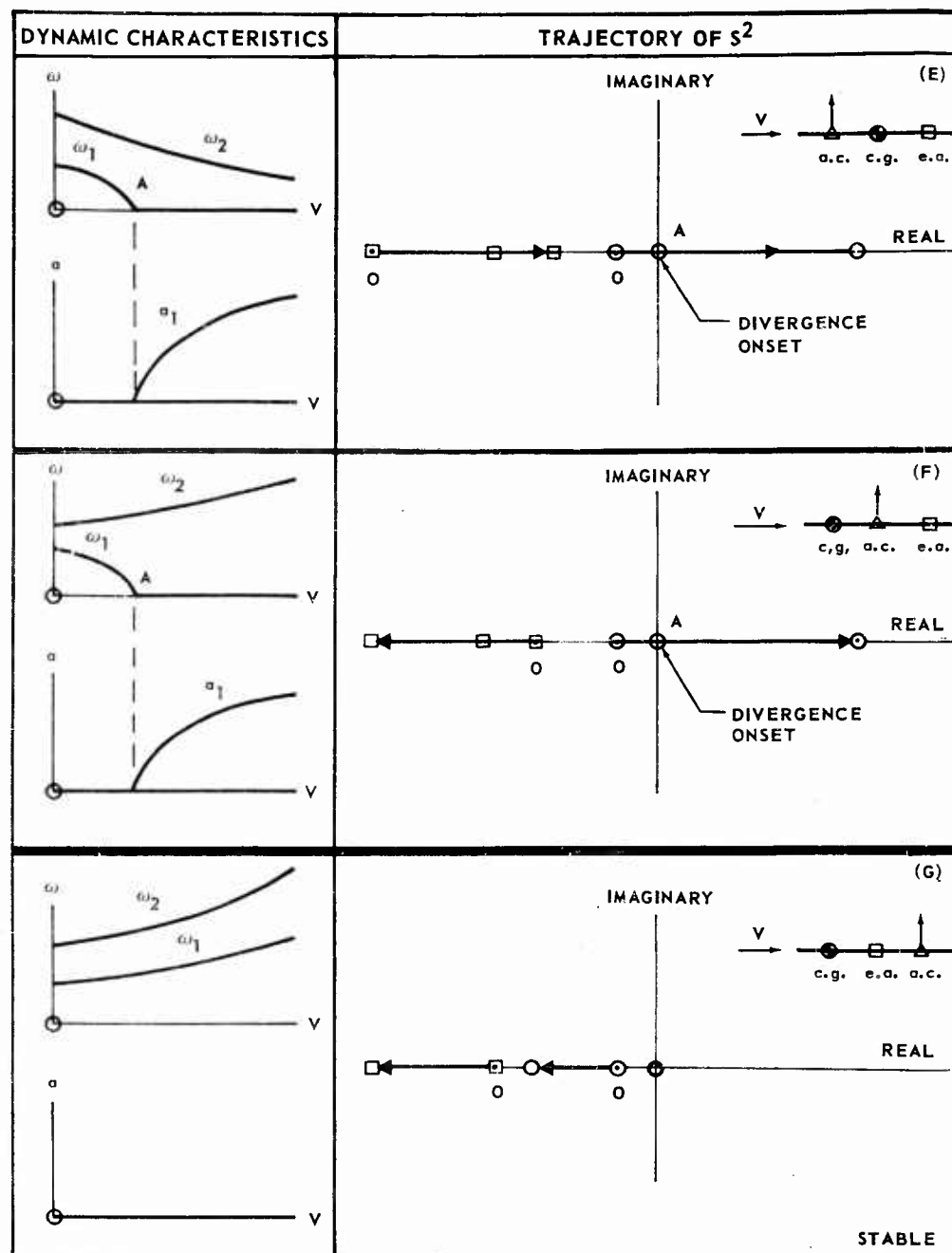


FIGURE 6. (CONCLUDED)

- Case (D) Two coupled vibration modes from 0 to A; flutter from A to B followed by non-oscillatory instability thereafter.
- Case (E) Two coupled vibration modes from 0 up to speed where the lower frequency mode transforms into classical divergence at A; the remaining vibration mode ( $\omega_2$ ) will continue to decrease in frequency with further speed increase but will never transform into instability.
- Case (F) Two coupled vibration modes from 0 up to speed where the lower frequency mode transforms into classical divergence. In contrast to Case (E), the remaining vibration mode ( $\omega_2$ ) will continue to increase in frequency with subsequent speed increases.
- Case (G) Two coupled vibration modes for all speeds.

In passing, it is interesting to note that configurations (B) and (C) regain stability at speed beyond the flutter region. Configuration (C) will thereafter remain stable while (B) will eventually exhibit classical divergence at some higher speed.

Below the initial instability onset speed all configurations are characterized by two undamped coupled vibration modes, which for all practical purposes are indicative of stability. These coupled vibration modes are similar to the usual still air coupled vibrations with the exception that aerodynamic as well as inertia coupling is present. The two coupled frequencies  $\omega_1$  and  $\omega_2$  can be obtained explicitly from equations (10) and (12) by setting  $s$  equal to  $i\omega$  resulting in

$$\left(\frac{\omega}{\omega_a}\right)^2 = \left\{ \frac{(1 + R^2) - (\gamma + X)Z}{2(1 - X^2)} \right\} \mp \sqrt{\left\{ \frac{(1 + R^2) - (\gamma + X)Z}{2(1 - X^2)} \right\}^2 - \left\{ \frac{R^2(1 - \gamma Z)}{(1 - X^2)} \right\}} \quad (29)$$

or with the aid of equations (17) and (18)

$$\left(\frac{\omega}{\omega_a}\right)^2 = W \mp \sqrt{W^2 - Y} \quad (30)$$

At flutter onset,  $W^2 - Y = 0$  as previously shown. Thus the square root term becomes zero and the two frequencies  $\omega_1$  and  $\omega_2$  coalesce into the single frequency  $\omega_F$  which may be calculated from

$$\left(\frac{\omega_F}{\omega_a}\right)^2 = \frac{(1 + R^2) - (\gamma + X)Z_F}{2(1 - X^2)} \quad (31)$$



The flutter frequency can be calculated explicitly in terms of the configuration parameters by introducing equation (22) for  $Z_F$  above. Thus,

$$\left(\frac{\omega_F}{\omega_a}\right)^2 = \frac{R}{\gamma + X} \left\{ \gamma R + \sqrt{\frac{X(\gamma + X)}{1 - X^2} \left[ 1 - \frac{\gamma(1 + \gamma X)}{\gamma + X} R^2 \right]} \right\} \quad (32)$$

Inspection of equation (32) shows that the flutter frequency  $\omega_F$  may lie beyond  $\omega_h$  or  $\omega_a$  and further indicates such configurations, for example  $(\gamma + X)$  near zero. The reduced frequency  $(b\omega_F/V_F)$  at flutter onset is obtained from the relation

$$\left(\frac{b\omega_F}{V_F}\right)^2 = \left(\frac{\omega_F}{\omega_a}\right)^2 \left(\frac{b\omega_a}{V_F}\right)^2$$

If  $V_F$  is used in the form presented in equation (28), this becomes

$$\left(\frac{b\omega_F}{V_F}\right)^2 = \left(\frac{2b}{\mu r_a}\right) \left(\frac{\omega_F}{\omega_a}\right)^2 \left(\frac{\eta_F}{Z_F}\right) \quad (33)$$

In the flutter region itself the characteristic eigenvalues are of the form  $s = a + i\omega$ . Thus

$$s = \frac{s}{\omega_a} = \left(\frac{a}{\omega_a}\right) + i \left(\frac{\omega}{\omega_a}\right)$$

$$s^2 = \left[ \left(\frac{a}{\omega_a}\right)^2 - \left(\frac{\omega}{\omega_a}\right)^2 \right] + i \left[ 2 \left(\frac{a}{\omega_a}\right) \left(\frac{\omega}{\omega_a}\right) \right]$$

In this region  $w^2 - Y$  is negative, and equation (19) is used in the form

$$s^2 = -w \pm i \sqrt{Y - w^2}$$

Simultaneous solution of the above equations results in

$$\left. \begin{aligned} \left( \frac{\omega}{\omega_a} \right)^2 &= \frac{W + \sqrt{Y}}{2} \\ \left( \frac{\alpha}{\omega_a} \right)^2 &= \frac{\sqrt{Y} - W}{2} \end{aligned} \right\} \quad (34)$$

Introducing equations (17) and (18) for W and Y,

$$\left( \frac{\omega}{\omega_a} \right)^2 = \frac{R \sqrt{(1 - X^2)(1 - \gamma Z)} + \frac{1}{2} [(1 + R^2) - (\gamma + X) Z]}{2(1 - X^2)} \quad (35)$$

$$\left( \frac{\alpha}{\omega_a} \right)^2 = \frac{R \sqrt{(1 - X^2)(1 - \gamma Z)} - \frac{1}{2} [(1 + R^2) - (\gamma + X) Z]}{2(1 - X^2)} \quad (36)$$

The logarithmic decrement during flutter is obtained from

$$\delta = -2\pi \left( \frac{\alpha}{\omega} \right)$$

or with the help of equations (35) and (36)

$$\delta = -2\pi \left\{ \frac{R \sqrt{(1 - X^2)(1 - \gamma Z)} - \frac{1}{2} [(1 + R^2) - (\gamma + X) Z]}{R \sqrt{(1 - X^2)(1 - \gamma Z)} + \frac{1}{2} [(1 + R^2) - (\gamma + X) Z]} \right\}^{\frac{1}{2}} \quad (37)$$

Further discussion pertaining to the relations developed herein will be covered later as appropriate.

#### Vibration and Flutter Modes

This section and the section following probes into the very heart of the flutter mechanism. The basic process which leads to flutter is easily seen in its obvious simplicity.

# Zimmerman

Clarity in presenting pertinent relations for the vibration and flutter modes is enhanced if complex symbology is used for the pitching and plunging motion, i.e.

$$q_a = A_1 e^{s_1 t} + A_2 e^{s_2 t}$$

$$q_h = B_1 e^{s_1 t} + B_2 e^{s_2 t}$$

Below the instability speed the eigenvalues are of the form

$$s_1 = i\omega_1 ; s_1 = i(\omega_1/\omega_a)$$

$$s_2 = i\omega_2 ; s_2 = i(\omega_2/\omega_a)$$

while in the flutter region these are of the form

$$s_1 = \sigma + i\omega ; s_1 = (\sigma/\omega_a) + i(\omega/\omega_a)$$

$$s_2 = -\sigma + i\omega ; s_2 = -(\sigma/\omega_a) + i(\omega/\omega_a)$$

The constants  $B_1$  and  $B_2$  are not arbitrary; they are related to  $A_1$  and  $A_2$  as shown in equation (16), specifically

$$\left. \begin{aligned} \frac{B_1}{A_1} &= - \frac{(\gamma + X) s_1^2 + (\gamma R^2 + Z)}{s_1^2 + R^2} \\ \frac{B_2}{A_2} &= - \frac{(\gamma + X) s_2^2 + (\gamma R^2 + Z)}{s_2^2 + R^2} \end{aligned} \right\} \quad (38)$$

As shown previously both characteristic  $s^2$  are real and negative below the instability speed; during flutter they are complex conjugate. Consequently for each mode  $(q_h/q_a)_1$ , the phase angle between plunging and pitching degrees of freedom must be zero (or  $180^\circ$ ) below instability, while during flutter phase angles other than zero (or  $180^\circ$ ) are possible.

Below the instability speed the motion is represented by

$$\left. \begin{aligned} q_a &= A_1 e^{i\omega_1 t} + A_2 e^{i\omega_2 t} \\ q_h &= B_1 e^{i\omega_1 t} + B_2 e^{i\omega_2 t} \end{aligned} \right\} \quad (39)$$

which is the superposition of the two coupled vibration modes given by

<u>Low Frequency Mode</u>	<u>High Frequency Mode</u>	
$q_{a1} = A_1 e^{i\omega_1 t}$	$q_{a2} = A_2 e^{i\omega_2 t}$	
$q_{h1} = B_1 e^{i\omega_1 t}$	$q_{h2} = B_2 e^{i\omega_2 t}$	
$\left( \frac{q_h}{q_a} \right)_1 = \frac{B_1}{A_1}$	$\left( \frac{q_h}{q_a} \right)_2 = \frac{B_2}{A_2}$	} (40)

where

$$\left. \begin{aligned} \left( \frac{q_h}{q_a} \right)_1 &= \frac{B_1}{A_1} = \frac{(\gamma + X)(\omega_1/\omega_a)^2 - (\gamma R^2 + Z)}{R^2 - (\omega_1/\omega_a)^2} \\ \left( \frac{q_h}{q_a} \right)_2 &= \frac{B_2}{A_2} = \frac{(\gamma + X)(\omega_2/\omega_a)^2 - (\gamma R^2 + Z)}{R^2 - (\omega_2/\omega_a)^2} \end{aligned} \right\} \quad (41)$$

The coupled frequency ratios  $(\omega_1/\omega_a)$  and  $(\omega_2/\omega_a)$  can be calculated from equation (29) for any speed below instability.

During flutter the motion is represented by

$$\left. \begin{aligned} q_a &= A_1 e^{(\sigma + i\omega)t} + A_2 e^{(-\sigma + i\omega)t} \\ q_h &= B_1 e^{(\sigma + i\omega)t} + B_2 e^{(-\sigma + i\omega)t} \end{aligned} \right\} \quad (42)$$

which is the superposition of two oscillatory modes, one stable and the other unstable, i.e.

Unstable Mode

$$q_{a1} = A_1 e^{(\alpha + i\omega)t}$$

$$q_{h1} = B_1 e^{(\alpha + i\omega)t}$$

$$\left(\frac{q_h}{q_a}\right)_1 = \frac{B_1}{A_1}$$

Stable Mode

$$q_{a2} = A_2 e^{(-\alpha + i\omega)t}$$

$$q_{h2} = B_2 e^{(-\alpha + i\omega)t}$$

$$\left(\frac{q_h}{q_a}\right)_2 = \frac{B_2}{A_2}$$

(43)

The modal deflections  $(q_h/q_a)_1$  and  $(q_h/q_a)_2$ , obtained by introducing  $S_1 = (\alpha/\omega_a) + i(\omega/\omega_a)$  and  $S_2 = -(\alpha/\omega_a) + i(\omega/\omega_a)$  into equations (38), are

$$\left(\frac{q_h}{q_a}\right)_1 = \frac{B_1}{A_1} = - \frac{\left[ (\gamma + X) \left( \frac{\alpha^2 - \omega^2}{\omega_a^2} \right) + (\gamma R^2 + Z) \right] + i \left[ 2(\gamma + X) \left( \frac{\alpha\omega}{\omega_a^2} \right) \right]}{\left[ \left( \frac{\alpha^2 - \omega^2}{\omega_a^2} \right) + R^2 \right] + i \left[ 2 \left( \frac{\alpha\omega}{\omega_a^2} \right) \right]}$$

$$\left(\frac{q_h}{q_a}\right)_2 = \frac{B_2}{A_2} = - \frac{\left[ (\gamma + X) \left( \frac{\alpha^2 - \omega^2}{\omega_a^2} \right) + (\gamma R^2 + Z) \right] - i \left[ 2(\gamma + X) \left( \frac{\alpha\omega}{\omega_a^2} \right) \right]}{\left[ \left( \frac{\alpha^2 - \omega^2}{\omega_a^2} \right) + R^2 \right] - i \left[ 2 \left( \frac{\alpha\omega}{\omega_a^2} \right) \right]}$$

(44)

where the ratios  $(\alpha/\omega_a)$  and  $(\omega/\omega_a)$  can be calculated from equations (35) and (36) in the flutter region. Since equations (44) are of the form

$$\frac{B_1}{A_1} = - \frac{u + iv}{\gamma + iz}$$

$$\frac{B_2}{A_2} = - \frac{u - iv}{\gamma - iz}$$

it is easily shown that  $B_2/A_2$  is the complex conjugate of  $B_1/A_1$ . Thus

$$\frac{B_1}{A_1} = K e^{i\psi}$$

$$\frac{B_2}{A_2} = K e^{-i\psi} \quad (45)$$

where  $K$  is the modulus and  $\psi$  is the phase angle relating the respective  $q_h$  and  $q_a$  motions. The motion during flutter is then characterized by

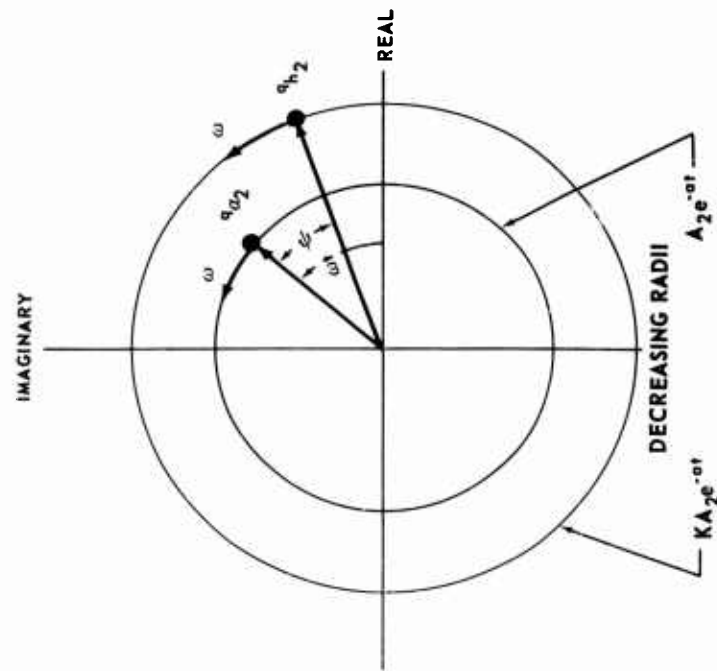
<u>Unstable Mode</u>	<u>Stable Mode</u>
$q_{a1} = (A_1 e^{\alpha t}) e^{i\omega t}$	$q_{a2} = (A_2 e^{-\alpha t}) e^{i\omega t}$
$q_{h1} = K(A_1 e^{\alpha t}) e^{i(\omega t + \psi)}$	$q_{h2} = K(A_2 e^{-\alpha t}) e^{i(\omega t - \psi)}$
$\left(\frac{q_h}{q_a}\right)_1 = K e^{i\psi}$	$\left(\frac{q_h}{q_a}\right)_2 = K e^{-i\psi}$

$\left. \vphantom{\begin{matrix} q_{a1} \\ q_{a2} \\ q_{h1} \\ q_{h2} \end{matrix}} \right\} \quad (46)$

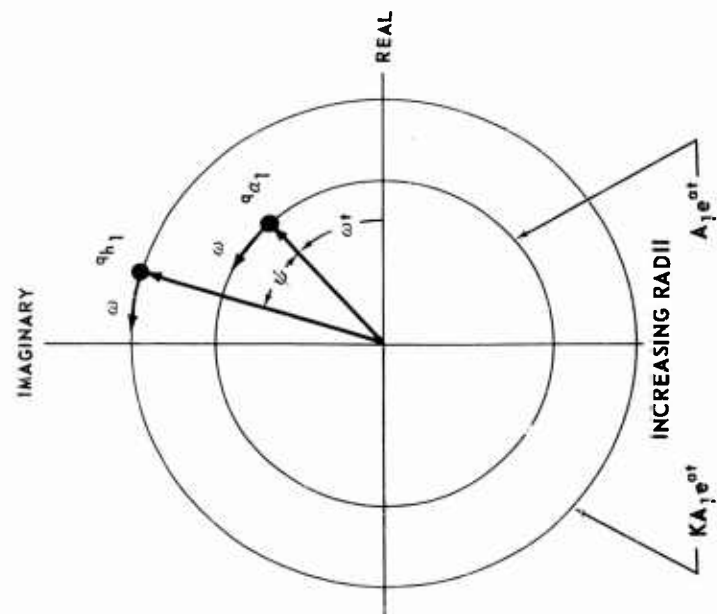
and is represented by the rotating vector scheme shown in Figure 7. This is similar to the usual vector representation of vibrations except for the idea of the increasing or decreasing vector radii.

Equations (41) and (44) have been used to calculate the variation in the modal deflections,  $q_h/q_a$ , with increasing airspeed for the configuration of the previous example and for two other configurations differing only in frequency ratio,  $\omega_h/\omega_a$ . These are shown in the complex plane plot of Figure 8 with velocity as a parameter. Modulus and phase of  $q_h/q_a$  during flutter is shown in Figure 9. The transition from real to complex values of  $q_h/q_a$  coincides with a similar transition of  $S^2$  occurring when  $W^2 - Y = 0$ . This further coincides with coalescence of the two coupled frequencies  $\omega_1$  and  $\omega_2$ . Thus, it is not strange that flutter should be associated with frequency coalescence, for it is at this point that the "phasing" between the pitching and plunging motions begins to develop allowing work to be done on the system by the large lift force which is in phase with the pitching displacement  $q_a$ .

If the magnitude of the lift  $L$  and the displacement  $q_h$  of its point of application are considered constant, maximum energy input would result when  $L$  lags  $q_h$  by  $90^\circ$ . Since it has been assumed in this example that the lift is in phase with the pitching displacement ( $C_L = C_{L_a} q_a$ ), this would correspond to  $q_h$  leading  $q_a$  by  $90^\circ$ , the input diminishing as the phase angle tends toward either zero or  $180^\circ$ . For a frequency ratio  $\omega_h/\omega_a = .2$  the phase angle  $\psi$  rapidly builds up to significant values with only slight increase in speed beyond flutter onset. Thus the large lift force in phase with  $q_a$  is capable of imparting considerable energy to the system in a short time-explosive flutter. In such cases only the "in phase" (with  $q_a$ ) component of the lift is significant; the quadrature lift components such as those embodied in classical oscillatory aerodynamics are of secondary importance and may be disregarded. On the other hand, the situation is somewhat different for the frequency ratio  $\omega_h/\omega_a = 1.60$  (which is near the critical frequency ratio of  $1.8$  where the



STABLE MODE



UNSTABLE MODE

FIGURE 7. COMPLEX REPRESENTATION OF FLUTTER MODES.

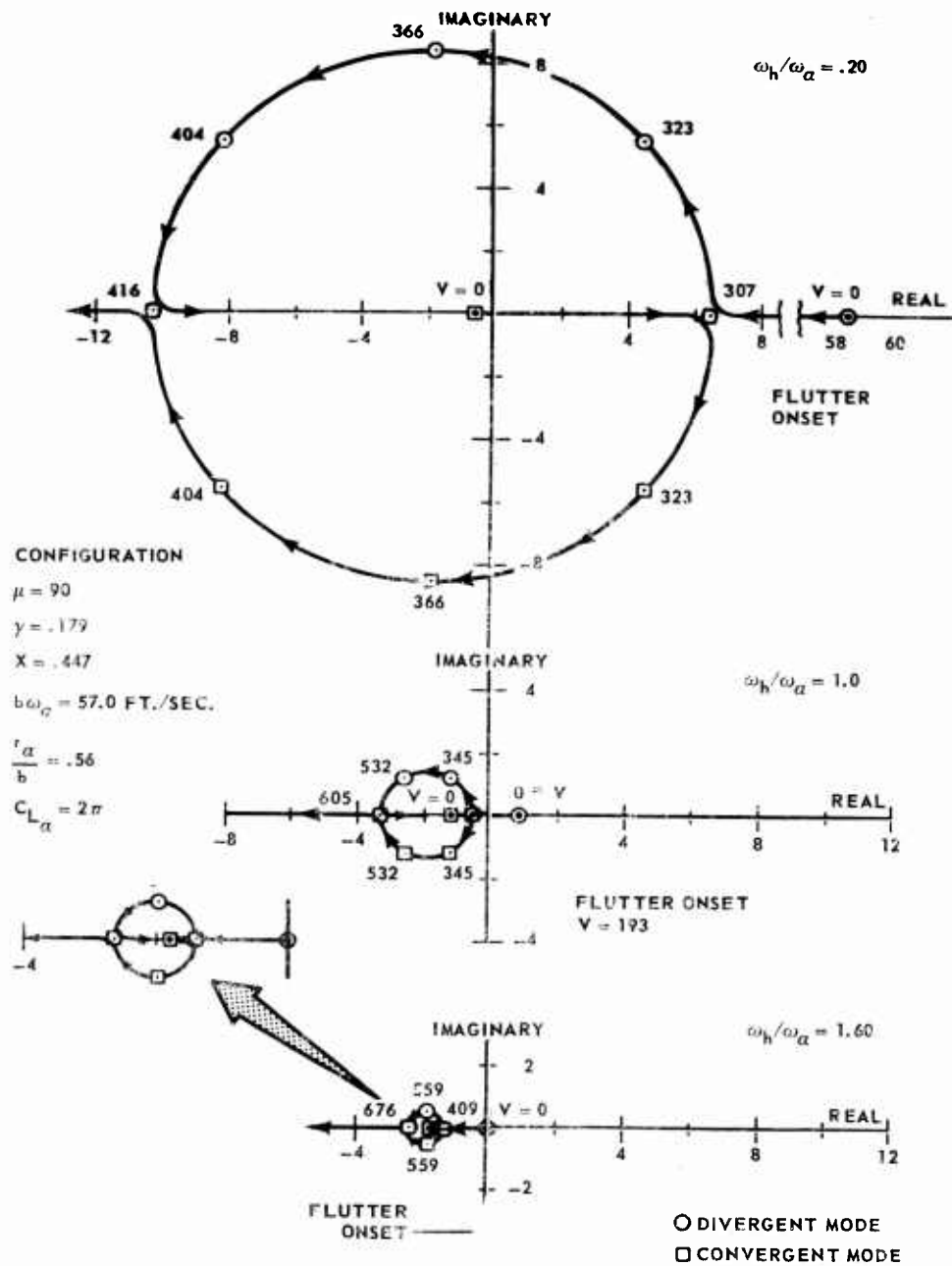


FIGURE 8  $q_h / q_\alpha$  vs. VELOCITY



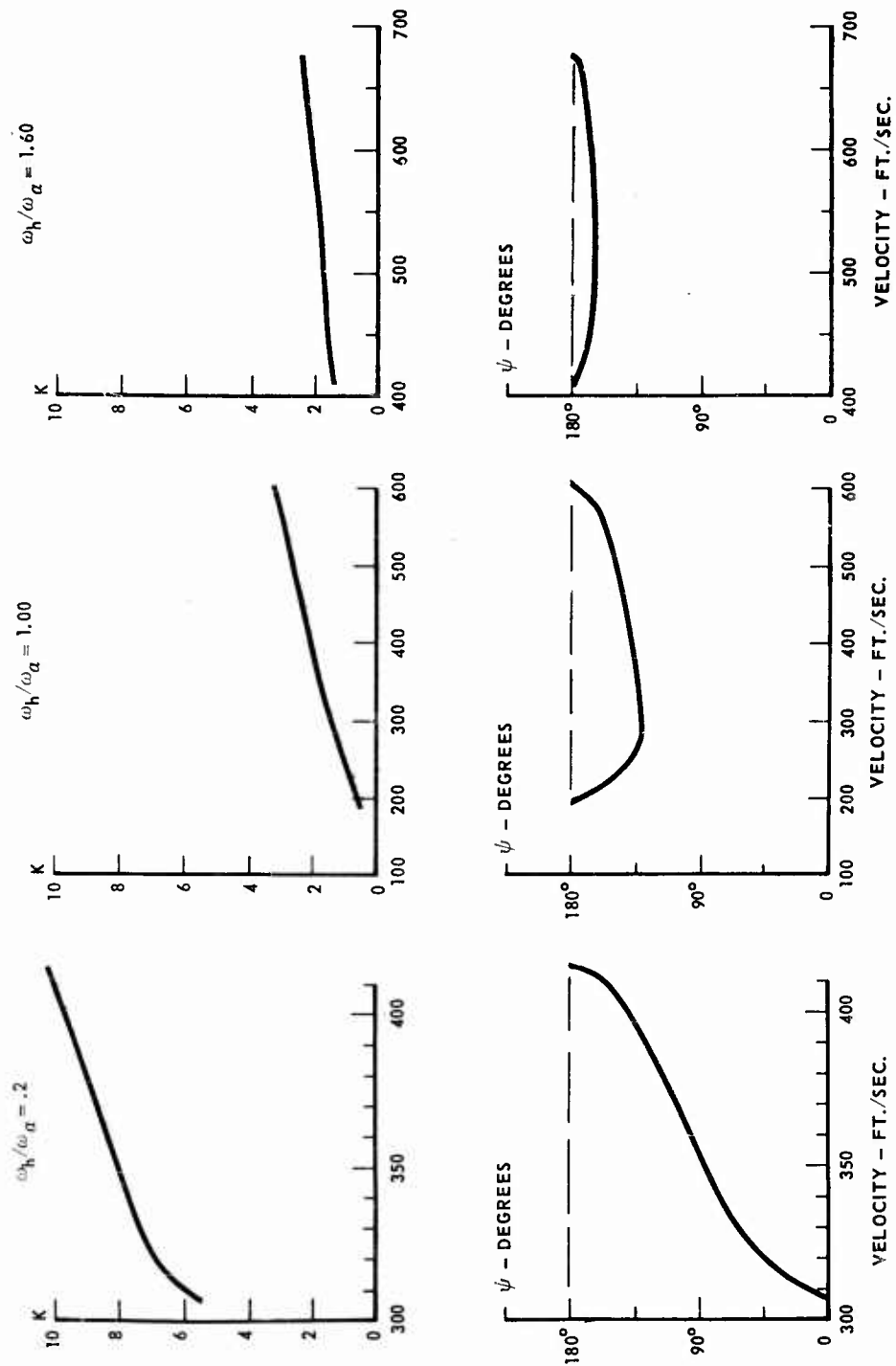
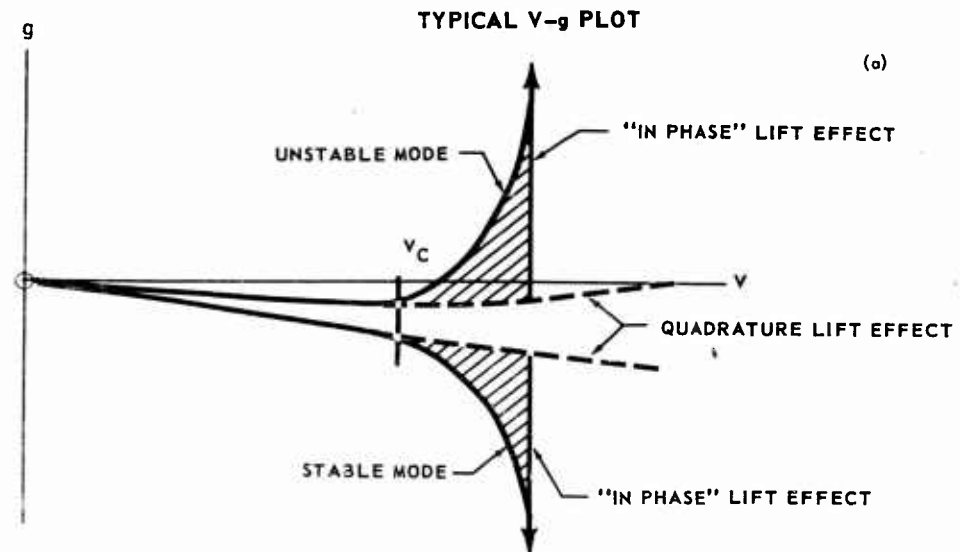


FIGURE 9. MODULUS AND PHASE OF  $q_h/q_\alpha$  DURING FLUTTER.

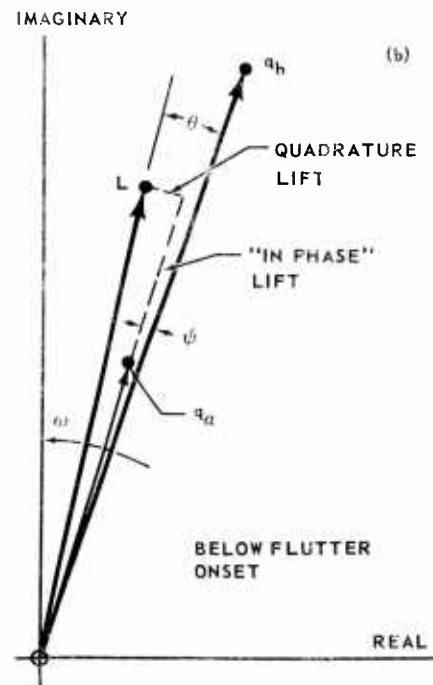
flutter solution disappears). Although the "in phase" lift force is large, the phase angle between it and  $q_h$  does not appear to be significant enough to overwhelm the quadrature lift components of classical oscillatory aerodynamics. In this case the flutter speed calculated with simplified aerodynamics may show considerable disagreement with that calculated using classical oscillatory aerodynamics. The type of flutter encountered here should not be of the explosive type. The other case shown in Figure 9 for a frequency ratio of 1.0 lies between the two extremes previously discussed. Even here, however, simplified "in phase" aerodynamics should yield good results since significant phasing is reached with only slight speed increase beyond flutter onset.

On the basis of the above discussion, the following inferences have been drawn:

- (1) Fortuitously, the accuracy of simplified "in phase" aerodynamics for flutter calculations is good when it counts most (violent flutter with no warning) and in doubt when flutter is mild and preceded by sufficient warning of damping degradation.
- (2) The peculiar behavior of the usual V-g flutter plots such as shown in Figure 10 (a) now appears evident. Beginning with zero airspeed, the damping in each mode gently changes with speed until some speed  $V_c$  is reached. At this point, one mode abruptly reverses and becomes unstable while concurrently the other mode abruptly increases its stability. It is inferred that the gentle variations or base curves in the V-g plot are due principally to the quadrature components of the oscillatory aerodynamics and that the "in phase" component supplies little energy until  $V_c$  is reached when the flutter mechanism previously described herein begins to take effect.
- (3) The general behavior in Figure 10 (a) is brought into sharper focus in Figures 10 (b) and 10 (c) where the phase angle relations between  $q_h$ ,  $q_a$  and  $L$  are shown for the unstable mode. Below flutter onset the quadrature lift, which is only a small fraction of the "in phase" lift, induces only a slight phase angle  $\psi$  between  $q_h$  and  $q_a$  (and also between  $q_h$  and "in phase" lift). This, together with the small phase increment of the quadrature lift itself, results in only a modest net phase angle  $\Theta$  between resultant lift  $L$  and  $q_h$ . Consequently, only moderate energy exchange is involved here. During flutter, however, it was shown that the "in phase" lift can induce a very large phase angle  $\psi$ , such as shown in Figure 10 (c), and correspondingly large net phase angle  $\Theta$ . Obviously, the aerodynamic energy input here is considerable and due



**PHASE ANGLE BELOW FLUTTER**



**PHASE ANGLE DURING FLUTTER**

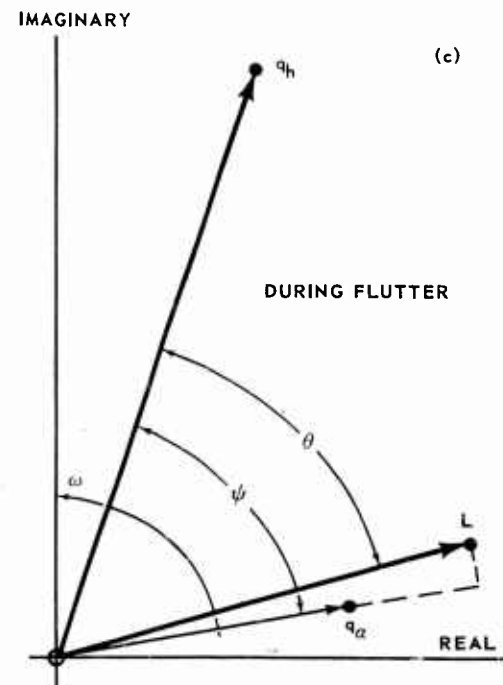


**FIGURE 10 INFERENCES FROM PHASE ANGLE RELATIONS**

almost entirely to the "in phase" lift component.

- (4) Based on (2) above, frequencies should be carefully monitored during flight test since frequency approach is a good indication that reversal in damping is imminent. A basis for predicting the frequency approach from sub-critical flight flutter testing is covered in a later section.

A more exact treatment of the energy exchange in a fluttering system is presented in the next section.

#### Mechanism of the Energy Exchange

At airspeeds below instability, the aerodynamic idealization used herein would indicate that the system would extract energy from the air during part of the vibration cycle and return it during the other part for a zero net energy exchange. Practically, however, there is a small net energy exchange from the vibrating system to the ambient air. This point will not be belabored further since it is more significant to investigate the energy exchange during flutter instability.

From Figure 1 it is seen that the work done on the system by the aerodynamic force is

$$\begin{aligned} dU &= -Ldh = -(2bQC_{L_\alpha})dh \\ &= -(2br_\alpha QC_{L_\alpha})q_\alpha dq_h \\ dU &= -k_\alpha Z q_\alpha dq_h \end{aligned}$$

and the rate at which the aerodynamic force transfers energy to the system is

$$\frac{dU}{dt} = -k_\alpha Z q_\alpha \frac{dq_h}{dt} \quad (47)$$

In classical symbology, the unstable mode is characterized by the motions

$$\left. \begin{aligned} q_{\alpha_1} &= A_1 e^{\sigma t} \cos \omega t \\ q_{h_1} &= K A_1 e^{\sigma t} \cos (\omega t + \psi) \end{aligned} \right\} \quad (48)$$

Substituting equations (48) into (47)

$$\frac{dU_1}{dt} = -k_a Z (KA_1^2 e^{2\alpha t}) \left\{ a \cos \omega t \cos (\omega t + \psi) - \omega \cos \omega t \sin (\omega t + \psi) \right\} \quad (49)$$

Upon introducing the trigonometric identities

$$\cos (\omega t + \psi) = \cos \psi \cos \omega t - \sin \psi \sin \omega t$$

$$\sin (\omega t + \psi) = \cos \psi \sin \omega t + \sin \psi \cos \omega t$$

$$\cos^2 \omega t = \frac{1}{2}(1 + \cos 2\omega t)$$

$$\sin \omega t \cos \omega t = \frac{1}{2} \sin 2\omega t$$

equation (49) becomes

$$\frac{dU_1}{dt} = \frac{1}{2} k_a Z (KA_1^2 e^{2\alpha t}) \left\{ (\omega \sin \psi - a \cos \psi) + (\omega \sin \psi - a \cos \psi) \cos 2\omega t + (\omega \cos \psi + a \sin \psi) \sin 2\omega t \right\} \quad (50)$$

Similarly for the stable mode characterized by the motions

$$\left. \begin{aligned} q_{\alpha 2} &= A_2 e^{-\alpha t} \cos \omega t \\ q_{h 2} &= KA_2 e^{-\alpha t} \cos (\omega t - \psi) \end{aligned} \right\} \quad (51)$$

the rate of transfer of aerodynamic energy to the system is

$$\frac{dU_2}{dt} = -\frac{1}{2} k_a Z (KA_2^2 e^{-2\alpha t}) \left\{ (\omega \sin \psi - a \cos \psi) + (\omega \sin \psi - a \cos \psi) \cos 2\omega t - (\omega \cos \psi + a \sin \psi) \sin 2\omega t \right\} \quad (52)$$

In both equations (50) and (52), the aerodynamic energy transfer rate is seen to consist of a "steady-state transfer" and a "harmonic transfer," the latter alternately absorbing energy during parts of the cycle and returning energy during other parts. If the

harmonic transfer is discarded, the net energy transfer rates are

$$\frac{dU_1}{dt} = \frac{1}{2} k_a Z \omega K A_1^2 e^{2\alpha t} (\sin \psi - \frac{\alpha}{\omega} \cos \psi) \quad (53)$$

$$\frac{dU_2}{dt} = -\frac{1}{2} k_a Z \omega K A_2^2 e^{-2\alpha t} (\sin \psi - \frac{\alpha}{\omega} \cos \psi). \quad (54)$$

As will later be seen, the quantity  $(\sin \psi - \alpha/\omega \cos \psi)$  is positive. Consequently, aerodynamic energy is transferred into the unstable mode at an ever increasing rate, while the stable mode transfers its mechanical energy to the ambient air at an ever diminishing rate until it ceases to exist. Thus, the author does not agree with Pines (Reference 4) in his belief that flutter arises "from the condition where one degree of freedom is driven at resonance by a second degree of freedom, both oscillating at the same frequency." Instead, the ambient air itself is either the source of the energy which drives the unstable mode or the depository for the mechanical energy given up by the stable mode.

The quantity  $(\sin \psi - \alpha/\omega \cos \psi)$  in a manner of speaking represents an effective phase angle between  $L$  and  $q_h$ , accounting for their exponential increases with time. This is plotted in Figure 11 for the configurations treated in the previous section. Note that the quantity is positive in the flutter region.

#### Comparison With Experiment

Up to this point no evidence has been presented substantiating the validity of the "in phase" aerodynamics approximation. The data presented herein supports this validity only in part since analytical-to-experimental comparisons made to date do not cover a sufficiently wide range of configurations to be considered conclusive. However, all the comparisons to date have been more than gratifying and indicate that the ultimate development of a rational flutter theory based on simple approximate aerodynamics is quite feasible.

Figure 12 shows a comparison between flutter speeds calculated on the basis of classical two dimensional incompressible flow theory and those calculated using only the "in phase" aerodynamic lift. The flutter speeds based on classical theory (shown as the dashed curve) as well as the flutter model test points were taken from Figure 17 of NACA TR 685 (Reference 9), i.e. the configuration treated here is the same as that used in the previous examples. The complete flutter region is shown by the circles for the approximate aerodynamics with  $C_{L\alpha}$  set equal to  $2\pi$  (steady flow two dimensional

$$\sin \psi - \frac{\alpha}{\omega} \cos \psi$$

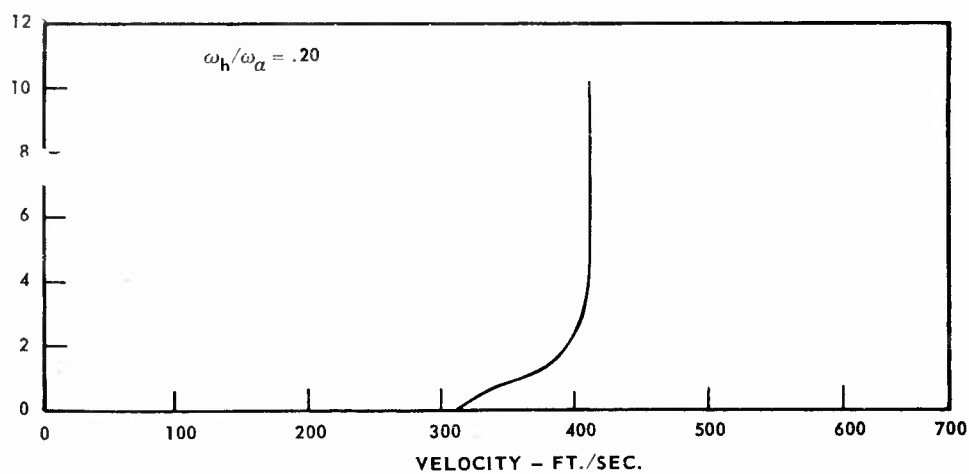
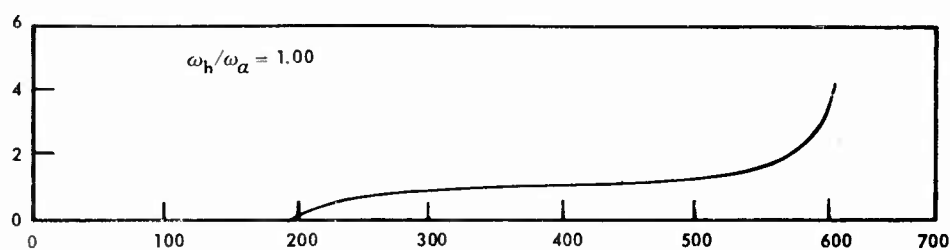
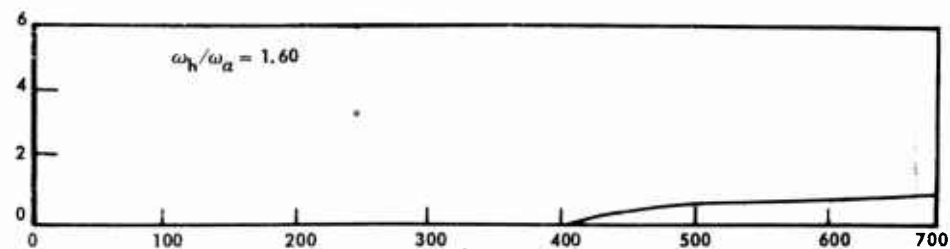


FIGURE 11.  $(\sin \psi - \alpha / \omega \cos \psi)$  VS VELOCITY.

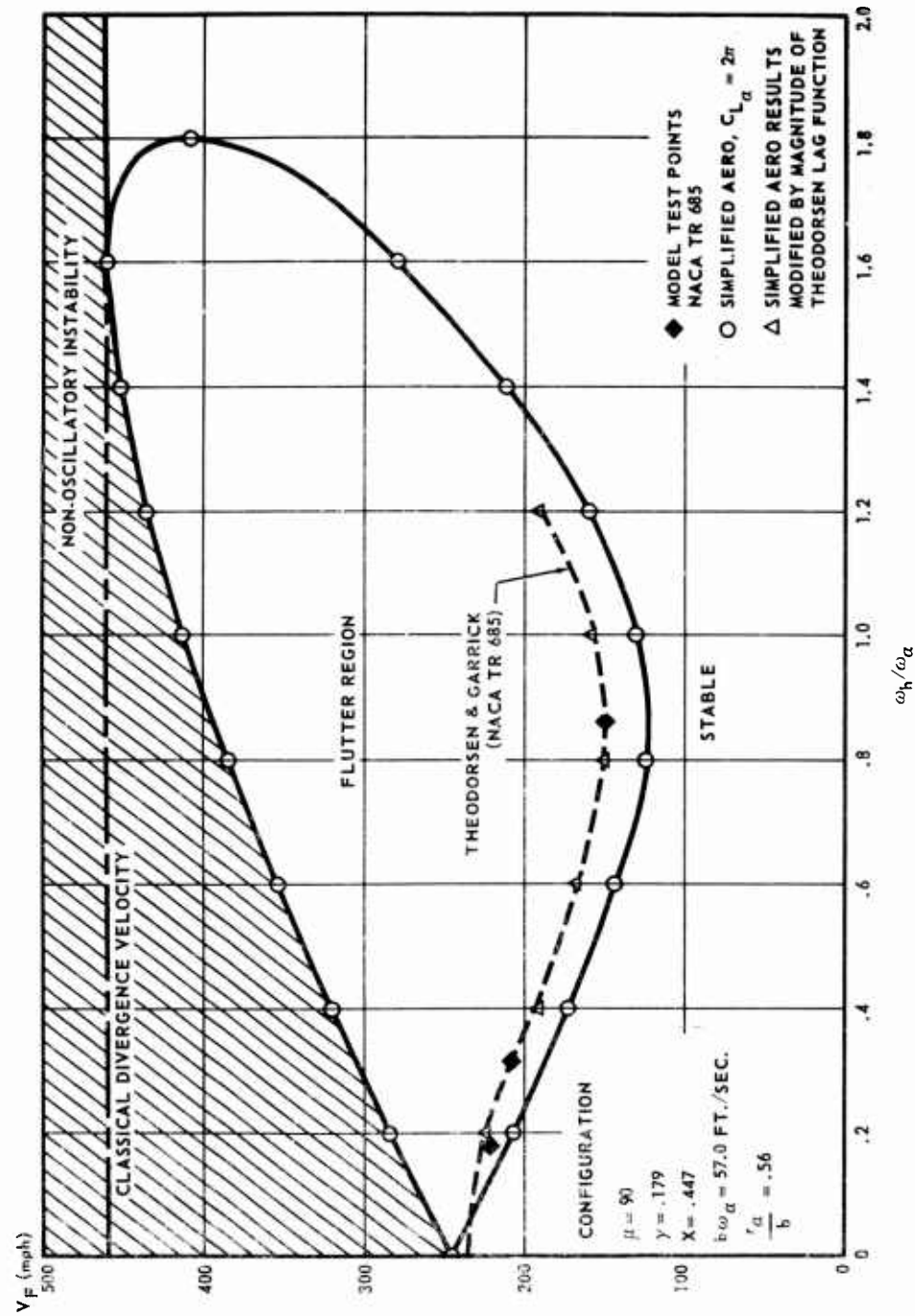


FIGURE 12. FLUTTER VELOCITY COMPARISON



aerodynamics). The triangles represent the steady flow  $C_{L\alpha}$  modified by the magnitude of the Theodorsen lag function as suggested by Pines (Reference 4), i.e.

$$C_{L\alpha} = 2\pi\eta_\omega \quad (55)$$

where  $\eta_\omega$  is shown in Figure 13. These calculations show excellent agreement.

Extending this idea further it appears quite logical that the central idea in successfully developing a simple incompressible flow flutter approach depends on a straightforward yet adequate specification of  $C_{L\alpha}$ . It further appears logical that such specification of  $C_{L\alpha}$  consist fundamentally of the steady flow  $C_{L\alpha}$  (obtained either from theory or experiment) and that this be modified by an oscillatory flow correction in the form

$$C_{L\alpha} = C_{L\alpha_s} \eta_\omega \quad (56)$$

where  $C_{L\alpha_s}$  is the steady flow lift slope. The oscillatory flow correction  $\eta_\omega$  need not take the form suggested by Pines, but analytical-experimental comparisons to date indicate that it is satisfactory.

Since the central theme here is the ultimate development of an adequate aerodynamic approximation in the formulation of a rational flutter theory, a search was made for flutter model test configurations which lend themselves to mathematical idealizations exact in every respect except for the assumption of aerodynamics. Test results for such ideal configurations are covered in Reference 11. Briefly, Reference 11 presents low subsonic flutter test results for rigid planform airfoils (of aspect ratios between two and six) possessing root pitch and root roll degrees of freedom. Sketches of these models are shown in Figures 14 through 16. Complete configuration data are contained in Reference 11, but within each of the general configurations the inertia properties and aspect ratio were varied while the pitch and roll frequencies were held constant. These configurations are mathematically idealized by the equations

$$I_r \ddot{\beta} + I_r \omega_r^2 \beta - I_{rp} \ddot{\alpha} = -\frac{1}{2} \bar{y} L$$

$$-I_{rp} \ddot{\beta} + I_p \ddot{\alpha} + I_p \omega_p^2 \alpha = \frac{1}{2} \bar{b} L$$

$$L = \frac{1}{2} \rho V^2 C_{L\alpha} a$$

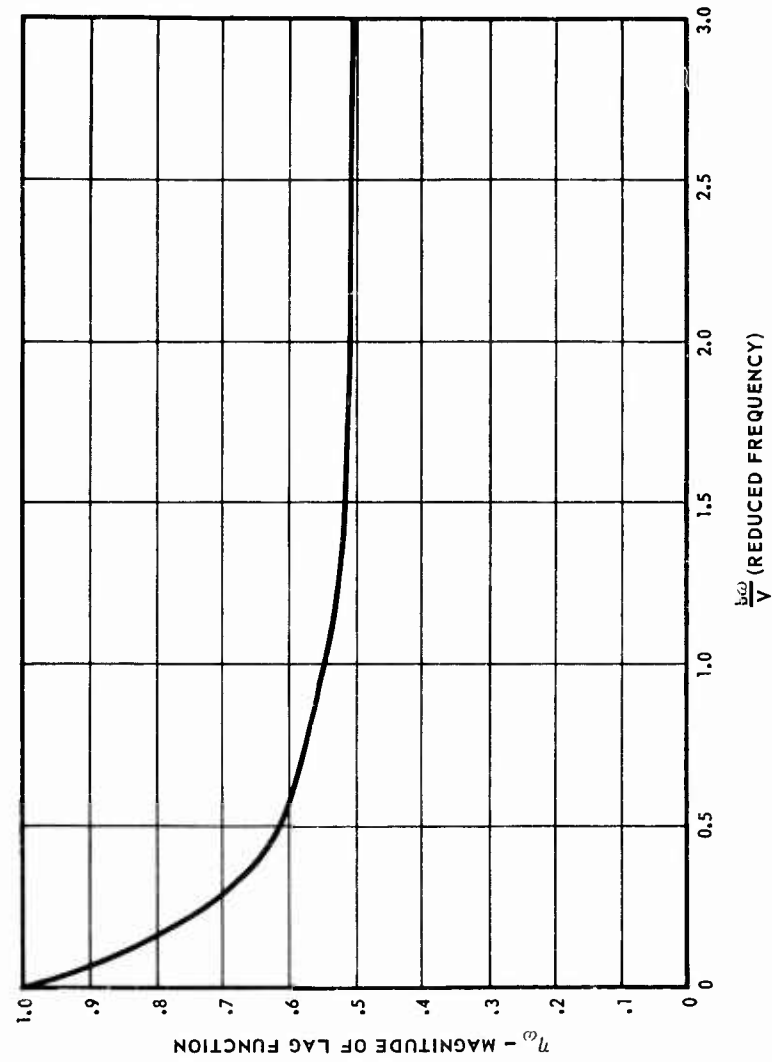


FIGURE 13. MAGNITUDE OF THEODORSEN LAG FUNCTION  
VS. REDUCED FREQUENCY.

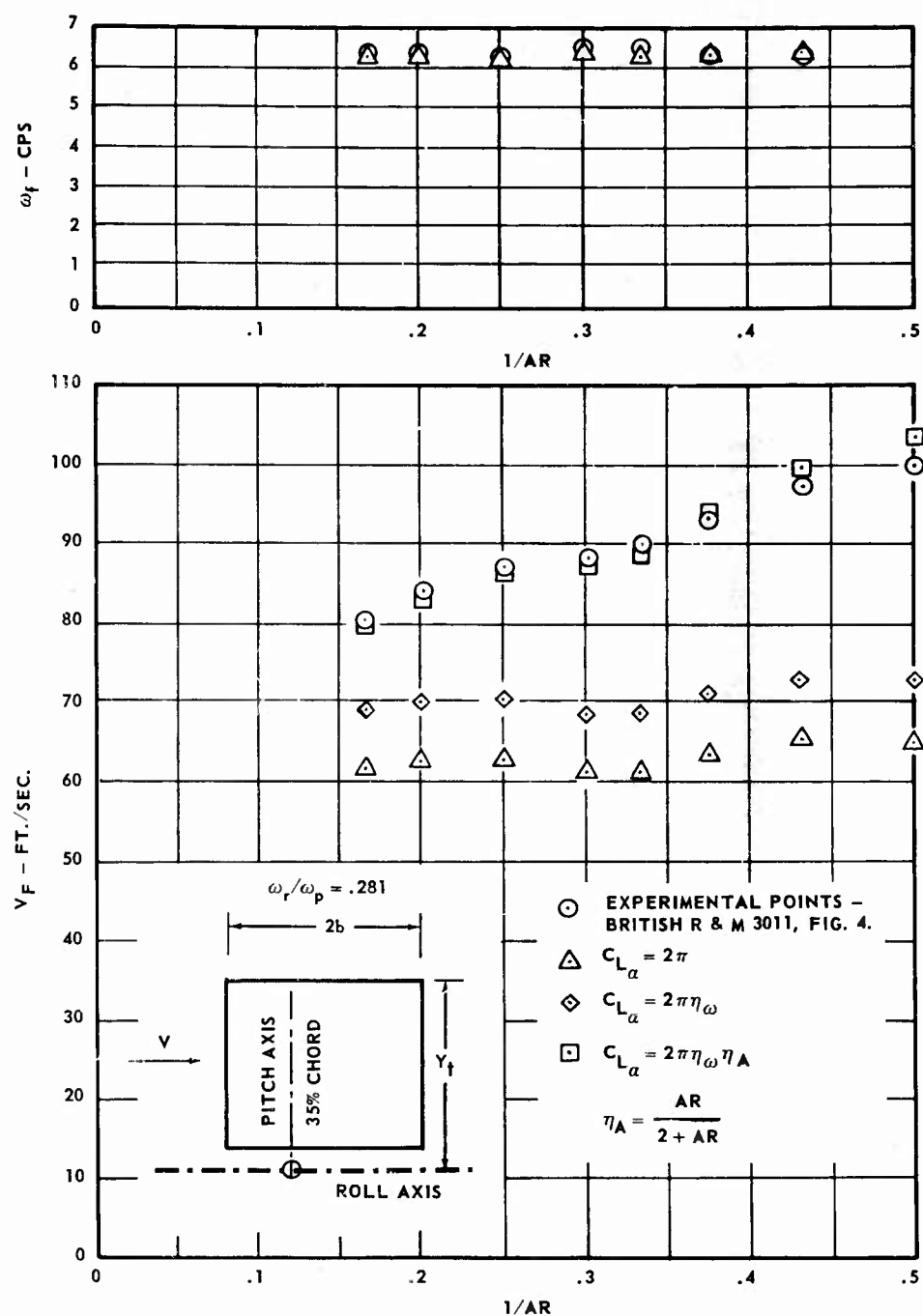


FIGURE 14. COMPARISON WITH FLUTTER TEST, RECTANGULAR PLAN FORM.

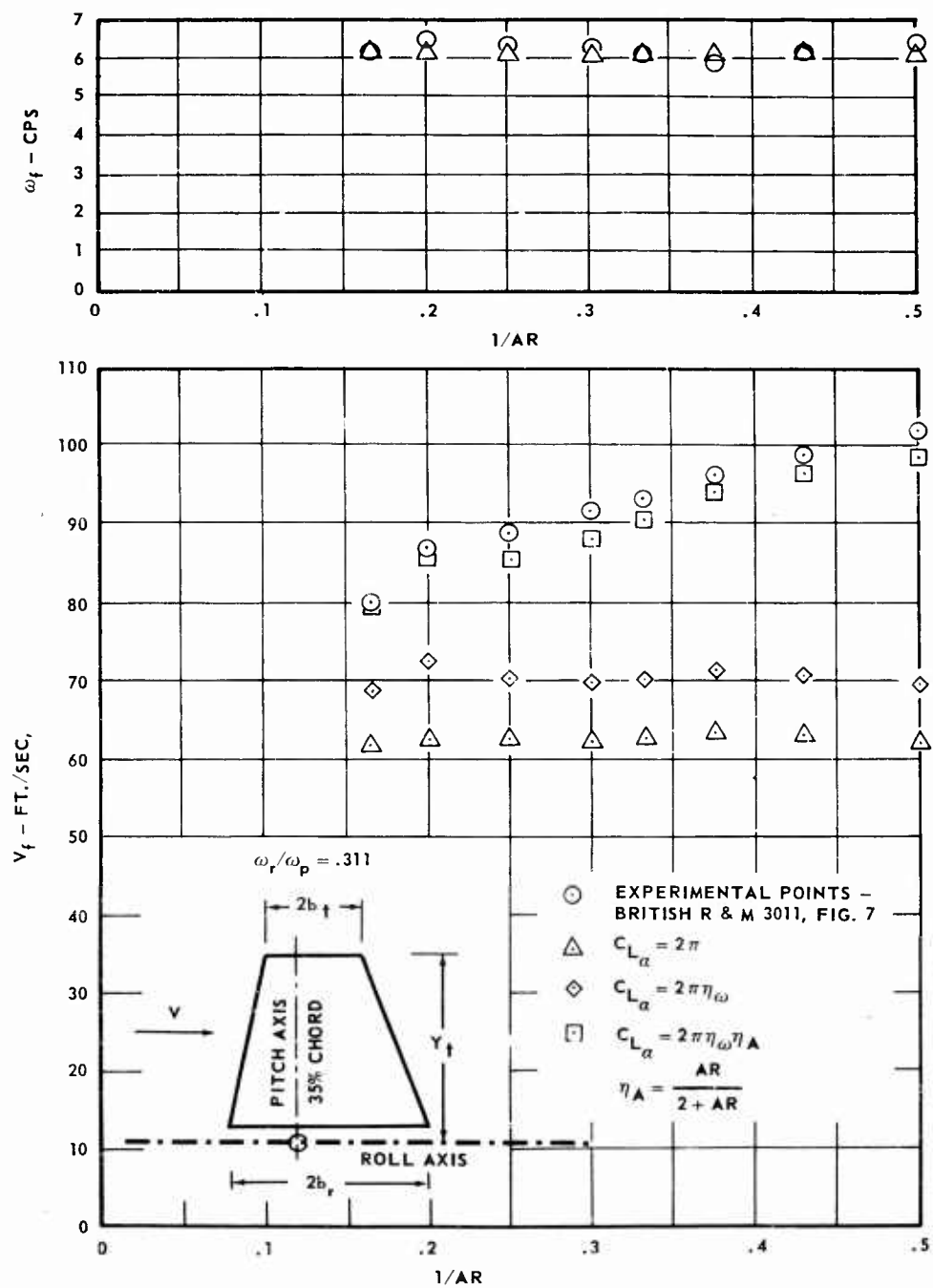


FIGURE 15. COMPARISON WITH FLUTTER TEST.  
TAPERED PLANFORM

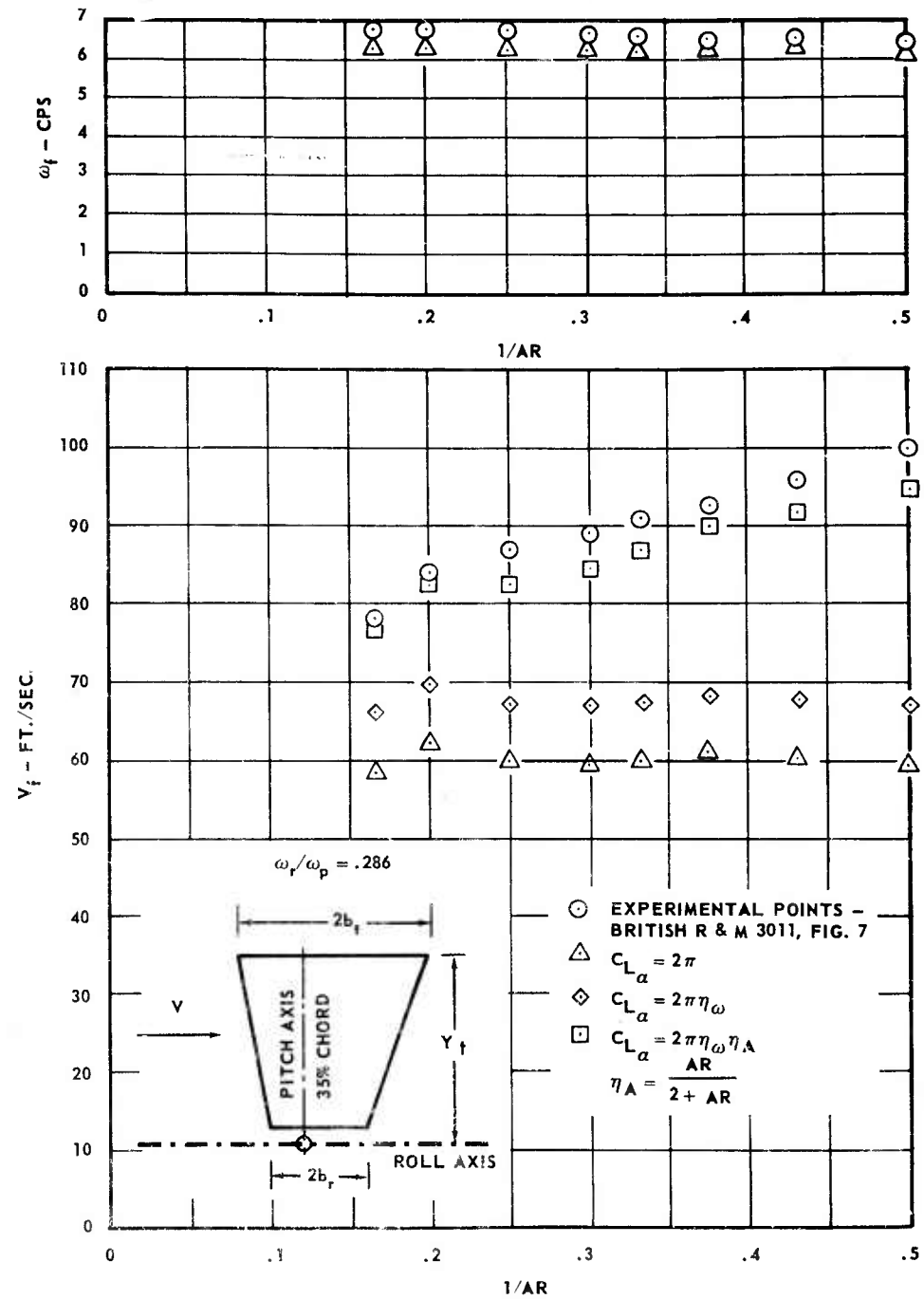


FIGURE 16. COMPARISON WITH FLUTTER TEST.  
INVERSE TAPER.

$$C_{L\alpha} = C_{L\alpha_s} \eta_\omega = 2\pi \eta_A \eta_\omega$$

$$\eta_A = \frac{AR}{2 + AR}$$

In the above equations  $\alpha$  is the pitch angle,  $\beta$  is the roll angle,  $\bar{y}$  is the spanwise coordinate of the planform centroid,  $\bar{b}$  is the mean aerodynamic semi-chord and  $\eta_A$  is the aerodynamic efficiency due to aspect ratio. All other terminology is standard. It is seen from these equations that the only uncertainty in the mathematical model is in the aerodynamic assumption equivalent to equation (56). Correlation of the theoretical results based on this assumption are more than gratifying down to aspect ratios as low as 2.0 even for the inverse taper planform of Figure 16. Also shown for comparison are the theoretical results from  $C_{L\alpha} = 2\pi$  and  $C_{L\alpha} = 2\pi\eta_\omega$ .

In further developing the approximate aerodynamic formulation to be applicable in the transonic and supersonic region,  $C_{L\alpha_s}$  in equation (56) must now also include the effects of compressibility obtained from steady flow aerodynamic theory or experiment. Further the shift of the aerodynamic center with Mach number (which enters the flutter formulation through the parameter  $\gamma$ ) must also be accounted for. Logically it should be sufficient to obtain this from steady flow theory or experiment. Ideal flutter model tests such as those of Reference 11 for checking the adequacy of the aerodynamic approximations in the transonic and supersonic region are not available to the author's knowledge. On the few occasions when the approximate formulation has been used by the author in the supersonic region, it had shown adequate correlation with classical theory.

#### Configuration Stability Criteria

The quantity under the square root sign in equations (14) or (19) will be referred to as the "flutter discriminant,"  $D$ . Specifically,

$$D = W^2 - Y = \left\{ \frac{(1 + R^2) - (\gamma + X) Z}{2(1 - X^2)} \right\}^2 - \left\{ \frac{R^2(1 - \gamma Z)}{(1 - X^2)} \right\} \quad (57)$$

Since the flutter characteristics of a given configuration depend on the variation of  $D$  with airspeed, the properties of  $D$  merit further study.

One approach suggested by the form of equation (57) is to plot  $W^2$  and  $Y$  versus  $Z$  such as shown for several configurations in Figure 17. Except for minor differences this is essentially the same as that proposed by Mac Neal (Reference 6). By the additional consideration that

$$S^2 = -W \pm \sqrt{D} \quad (58)$$

together with the significance of the roots  $S^2$  (Figures 2 and 3), the versatility of these plots can be extended beyond flutter considerations alone and shed light on the general dynamic behavior of a system without quantitative configuration data. As a matter of fact the sketches shown in Figure 6 were prepared without the aid of any numerical data, relying in part on this approach (and other concepts subsequently presented).

The other approach is based on the expansion of equation (57) in the form  $D = AZ^2 + BZ + C$ ,

$$D = \left\{ \frac{\gamma + X}{2(1 - X^2)} \right\}^2 Z^2 - 2 \left\{ \frac{(\gamma + X)(1 + R^2) - 2\gamma(1 - X^2)R^2}{[2(1 - X^2)]^2} \right\} Z + \left\{ \frac{(1 - R^2)^2 + 4X^2R^2}{[2(1 - X^2)]^2} \right\} \quad (59)$$

From inspection above it is seen that the constant term and the coefficient of  $Z^2$  are positive for all configurations. Thus all "characteristic flutter parabolas" are concave upward and have a positive intercept at zero airspeed as shown in Figure 18. The value of  $Z$  for which  $D$  is minimum is designated by  $\bar{Z}$  and the depth of this minimum below the abscissa is designated by  $\bar{D}$ . Note from Figure 18 (a) that  $\bar{D}$  is positive if the parabola dips below the abscissa. Also shown is flutter onset  $Z_F$  occurring when  $D$  is zero. The parabola in Figure 18 (a) can be written

$$\left. \begin{aligned} D &= A(Z - \bar{Z})^2 - \bar{D} \\ D &= AZ^2 - 2(A\bar{Z})Z + (A\bar{Z}^2 - \bar{D}) \end{aligned} \right\} \quad (60)$$

Comparing equations (59) and (60) yields for  $\bar{D}$ ,  $\bar{Z}$  and  $A$ ,

$$\bar{Z} = \left\{ \frac{1}{\gamma + X} \right\}^2 \left\{ (\gamma + X) + [(\gamma + X) - 2\gamma(1 - X^2)]R^2 \right\} \quad (61)$$

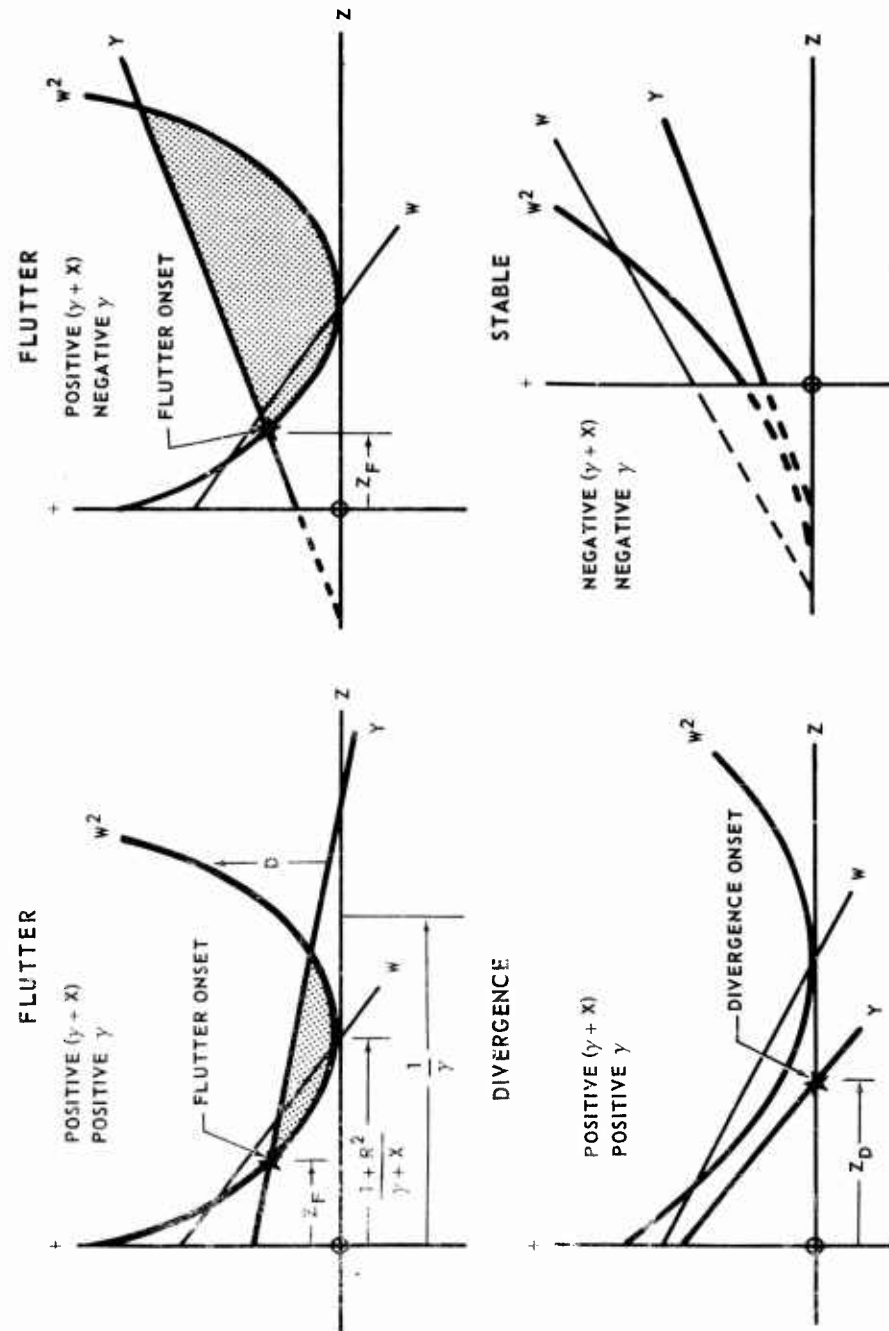


FIGURE 17. SYSTEM DYNAMIC CHARACTERISTICS.



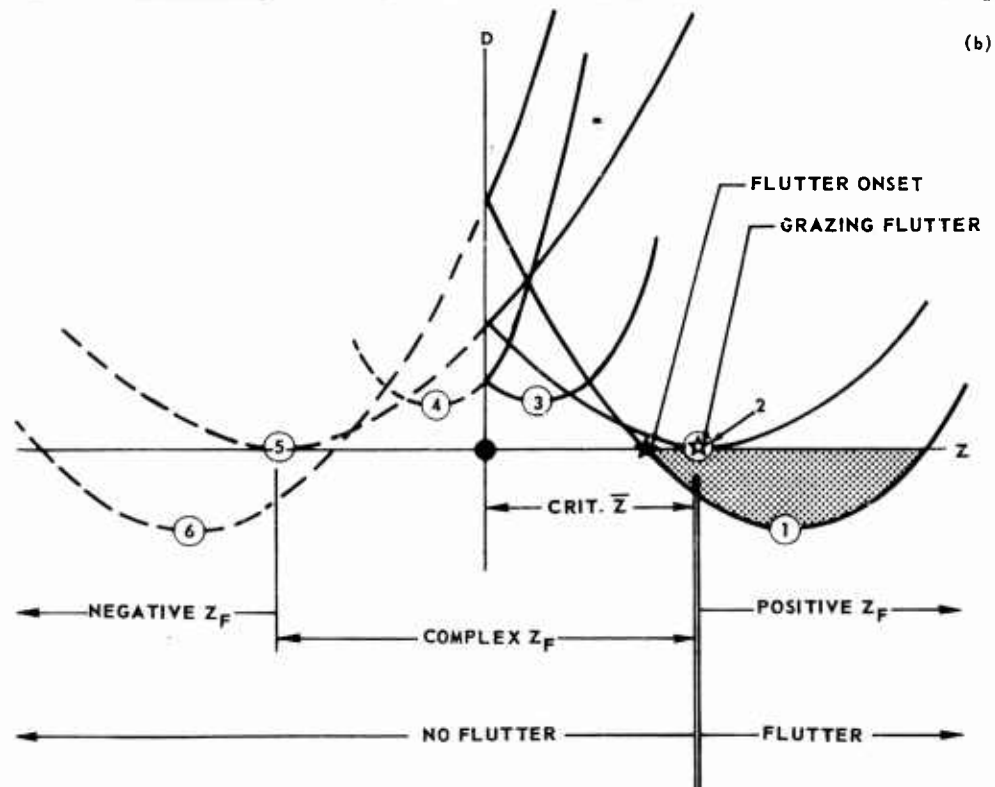
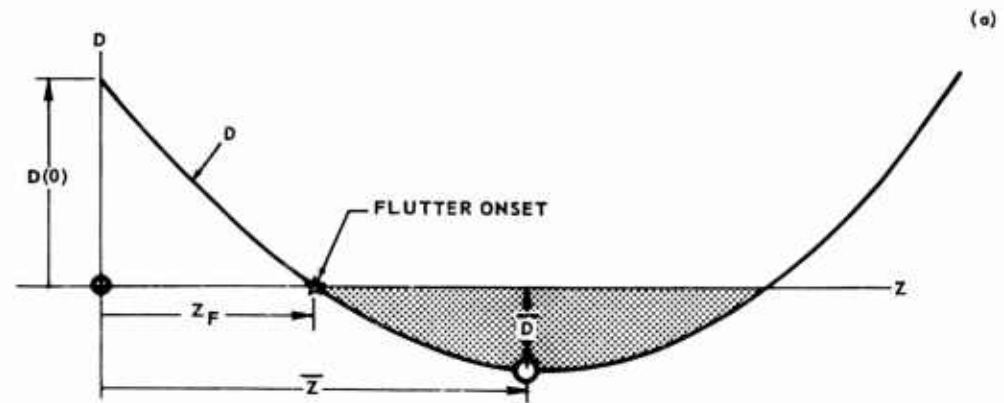


FIGURE 18. CHARACTERISTIC FLUTTER PARABOLAS.

$$\bar{D} = \left\{ \frac{R^2}{(\gamma + X)^2 (1 - X^2)} \right\} \left\{ X [(\gamma + X) - \gamma(1 + \gamma X) R^2] \right\} \quad (62)$$

$$A = \left\{ \frac{\gamma + X}{2(1 - X^2)} \right\}^2 \quad (63)$$

Depending on the values of  $\gamma$ ,  $X$  and  $R$  it is seen that  $\bar{Z}$  and  $\bar{D}$  may be positive or negative. In Figure 18 (b) a number of characteristic flutter parabolas are shown. The numbers identifying each parabola are indicative of the configuration susceptibility to flutter. If a configuration capable of fluttering is gradually modified toward increasing stability, its characteristic parabolas would follow the sequence 1 to 6. The configuration corresponding to parabola number 2 would be marginally stable. It would be characterized by a "grazing flutter," i.e. it would exhibit flutter onset at some speed, being stable above as well as below that speed. Subsequent configuration modifications would follow the sequence from parabola number 3 to 6, etc.

Since flutter onset  $Z_F$  is obtained by setting  $D$  equal to zero, flutter computations would result in complex  $Z_F$  for configurations 3 or 4 and negative real  $Z_F$  for configuration 6. Thus the degree of flutter stability can be inferred directly from the results of flutter speed calculations, negative real  $Z_F$  indicating the most stable configurations.

Configuration stability criteria are obtained quite easily from Figure 18 (a). A configuration will be susceptible to flutter at some speed only if  $\bar{D}$  and  $\bar{Z}$  are both positive. Conversely, a configuration will be stable flutterwise if either  $\bar{D}$  or  $\bar{Z}$  is negative. If it is recalled that physical considerations limit  $X$  to values between plus and minus unity, a stable configuration is indicated if either of the following conditions is fulfilled:

$$\bar{D} < 0; \quad X[(\gamma + X) - \gamma(1 + \gamma X) R^2] < 0 \quad (64)$$

$$\bar{Z} < 0; \quad (\gamma + X) + [(\gamma + X) - 2\gamma(1 - X^2)] R^2 < 0. \quad (65)$$

Since  $\bar{D}$  and  $\bar{Z}$  must both be positive for a configuration prone to flutter, subsequent modifications toward a stable configuration will be occasioned by a change to negative  $\bar{D}$  before a similar change in  $\bar{Z}$ ; this can be seen by inspection of the constant term in equation (60) which was previously shown to be positive for all configurations.

The transition is so shown in Figure 18 (b) (grazing flutter). Thus a flutter prone configuration can be made stable with minimum modification if the criterion of equation (64) is employed as a guide.

Grazing flutter configurations are easily found by setting  $\bar{D}$  equal to zero in equation (62) and the corresponding  $Z_F$  from setting this requirement into equation (22). These are shown in Table III.

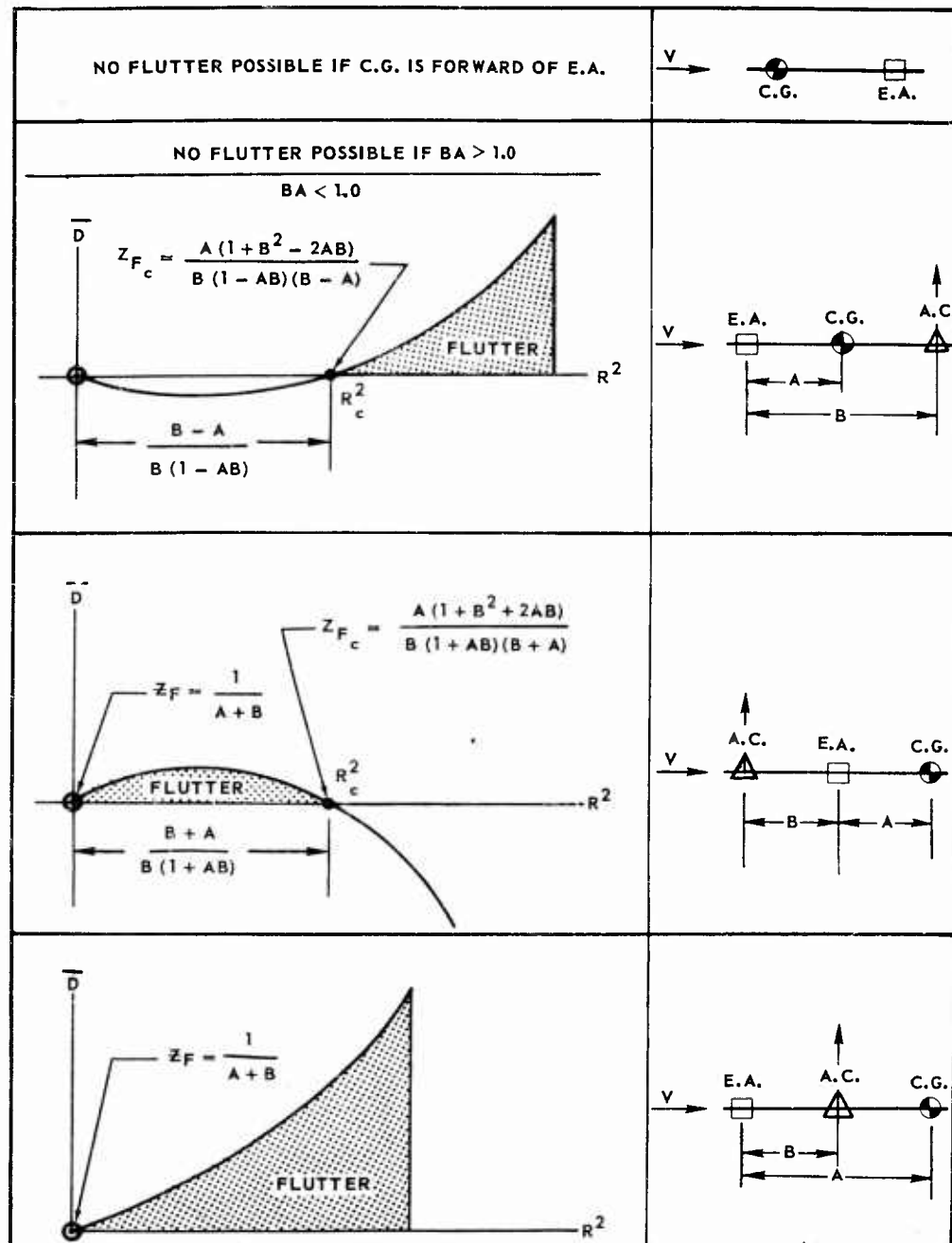
TABLE III. GRAZING FLUTTER

<u>Critical Configuration</u>	<u>Grazing <math>Z_F</math></u>
$R_C = 0$	$Z_{FC} = \frac{1}{\gamma + X}$
$R_C = \sqrt{\frac{\gamma + X}{\gamma(1 + \gamma X)}}$	$Z_{FC} = \frac{X(1 + \gamma^2 + 2\gamma X)}{\gamma(\gamma + X)(1 + \gamma X)}$
$X_C = 0$	$Z_{FC} = \frac{1 - R^2}{\gamma}$

Only the latter two, however, represent marginal situations separating flutter prone from stable configurations since  $\bar{D}$  does not change sign at  $R = 0$ . Although marginal configuration requirements are indicated in Table III nothing is said about which direction one must move to obtain a stable configuration and vice versa. This is covered in the following paragraph.

Configuration stabilities based on equations (64) and (65) are shown in Figure 19 and agree with Pines (Reference 4). In addition, the degree of stability (or instability) is qualitatively indicated by  $\bar{D}$  along with grazing flutter  $Z_F$ . Special cases for E.A.-G.C. coincidence and E.A.-A.C. coincidence are shown in Figure 20. For the special case of A.C.-C.G. coincidence,  $(\gamma + X)$  equals zero and the flutter discriminant  $D$  degenerates into a linear variation with  $Z$ , the corresponding  $Z_F$  given by

$$Z_F = \left\{ \frac{(1 - R^2)^2 + 4X^2R^2}{4XR^2(1 - X^2)} \right\} \quad \text{Provided } (\gamma + X) = 0 \quad (66)$$



NOTE: A IS MAGNITUDE OF X AND B IS MAGNITUDE OF Y

FIGURE 19. CONFIGURATION STABILITIES

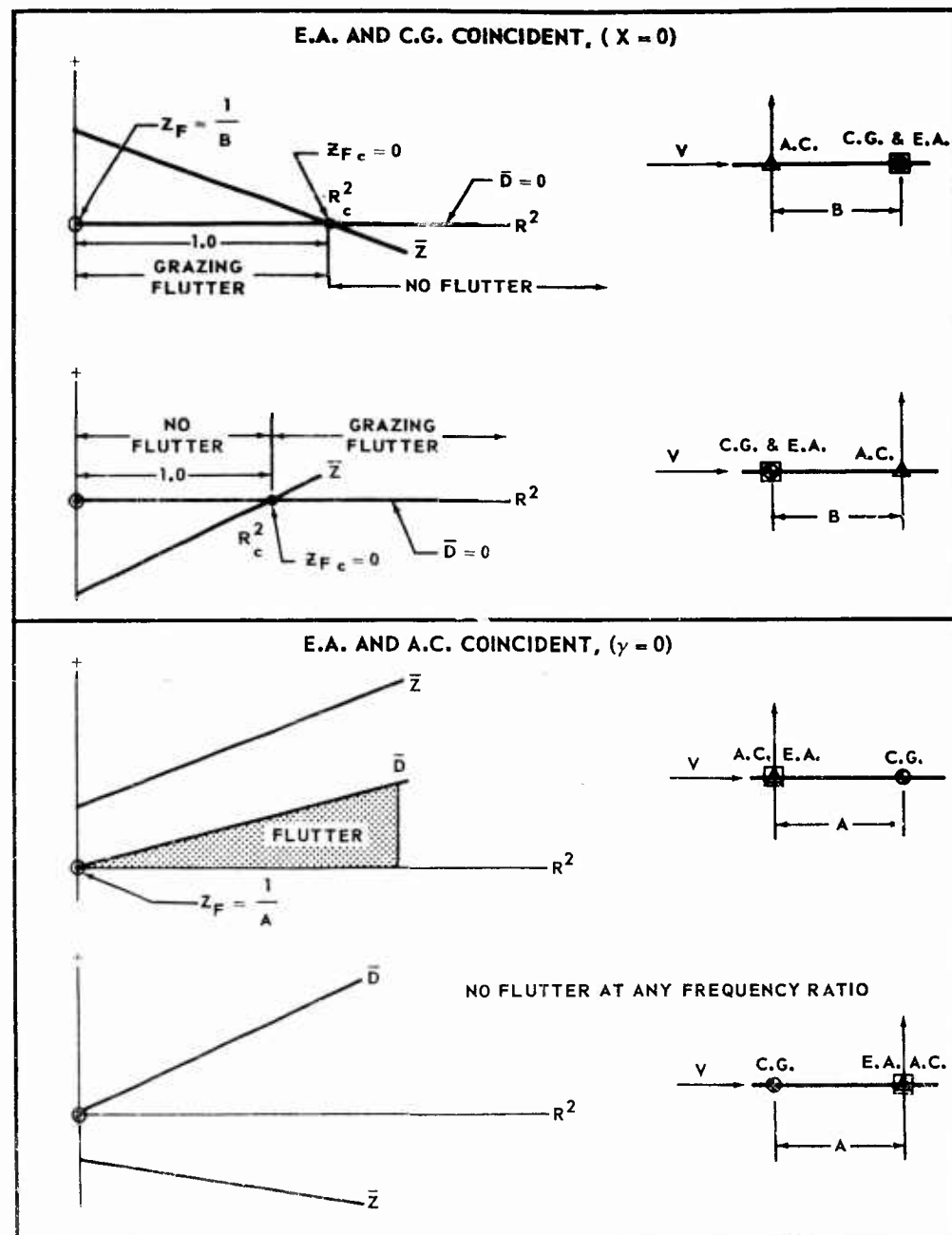


**FIGURE 20. CONFIGURATION STABILITIES-SPECIAL CASES**

### Frequency Approach Technique in Flight Testing

It was inferred in discussing Figure 10 that the catastrophic sudden reversal of damping was intimately associated with the approach of the two coupled frequencies  $\omega_1$  and  $\omega_2$ . A technique for predicting this sudden reversal (as well as an indication of the progress toward flutter) from sub-critical flight test is covered in this section.

Below instability the two coupled vibration frequencies  $\omega_2$  and  $\omega_1$  can be obtained from equation (30),

$$\left(\frac{\omega}{\omega_a}\right)^2 = W \pm \sqrt{W^2 - Y} = W \pm \sqrt{D}$$

$$\left(\frac{\omega_2}{\omega_a}\right)^2 = W + \sqrt{D} \quad (67)$$

$$\left(\frac{\omega_1}{\omega_a}\right)^2 = W - \sqrt{D}. \quad (68)$$

Subtracting equation (68) from (67) and squaring

$$\left[ \left(\frac{\omega_2}{\omega_a}\right)^2 - \left(\frac{\omega_1}{\omega_a}\right)^2 \right]^2 = D. \quad (69)$$

From equation (59) it is seen that D varies parabolically with Z in the form  $D = AZ^2 + BZ + C$ . Thus

$$D = \left[ \left(\frac{\omega_2}{\omega_a}\right)^2 - \left(\frac{\omega_1}{\omega_a}\right)^2 \right]^2 = AZ^2 + BZ + C. \quad (70)$$

This may be related in some way to the frequency-velocity curves of Zisfein and Frueh (Reference 7) but the relation is not directly evident. Continuing further, it is seen from the above equation that the characteristic parabolas in Figure 18 are also applicable to the frequency difference above. Therefore the parabolas of Figure 18 can be reconstructed solely from flight test measurements of the two coupled frequencies  $\omega_2$  and  $\omega_1$  as airspeed is increased, without any knowledge whatsoever of the configuration parameters (except for  $\omega_a$ , which is nothing more than a scale factor for D anyhow). Of utmost significance, however, is the fact that the shape of this curve is

known to be a parabola of the form  $AZ^2 + BZ + C$  (in contrast to the usual V-g curves). This allows a rational extrapolation of the characteristic parabola out to flutter onset from sub-critical flight flutter test.

This approach can be brought closer to physical reality by noting in equation (6) that the first factor in

$$Z = \left( \frac{2br_a}{k_a} \right) (C_{L_a} Q)$$

is independent of flight conditions. If this factor (as well as  $\omega_a$ ) is lumped in with the constants A, B and C in equation (70), there results

$$\omega_a^4 D = (\omega_2^2 - \omega_1^2)^2 = A_1 (C_{L_a} Q)^2 + B_1 (C_{L_a} Q) + C_1 \quad (71)$$

where  $A_1$ ,  $B_1$  and  $C_1$  are configuration constants. These can be obtained from in-flight resonance testing at sub-critical speeds by plotting  $(\omega_2^2 - \omega_1^2)^2$  vs  $(C_{L_a} Q)$ . Once these constants have been evaluated, a rational extrapolation of the characteristic parabola is possible.

In applying this technique to flight testing it is well to note from equation (71) that  $(\omega_2^2 - \omega_1^2)^2$  varies parabolically with  $C_{L_a} Q$  and not with  $Q$  alone. If a resonance test with sinusoidal excitation is conducted at a particular  $Q$ , the higher frequency  $\omega_2$  would correspond to a somewhat different  $C_{L_a} Q$  than that applicable for the lower frequency. This results since

$$\left. \begin{aligned} C_{L_{a_2}} &= C_{L_{a_s}} \eta_{\omega_2} \quad (\text{For } \omega_2) \\ C_{L_{a_1}} &= C_{L_{a_s}} \eta_{\omega_1} \quad (\text{For } \omega_1) \end{aligned} \right\} \quad (72)$$

where the oscillatory flow corrections  $\eta_{\omega_2}$  and  $\eta_{\omega_1}$  would be somewhat different due to the two different frequencies. This may be accounted for by plotting  $\omega_2$  and  $\omega_1$  separately against their respective  $C_{L_a} Q$  as shown in Figure 21 (a) and then form the quantity  $(\omega_2^2 - \omega_1^2)^2$  for comparable  $C_{L_a} Q$  as shown in Figure 21 (b). Steady flow effects of aspect ratio, compressibility, etc. may be lumped into  $C_{L_{a_s}}$ .

The method outlined above is subject to certain limitations at this time. First of all it was based on two degree of freedom considerations. Thus it should be used only if flutter is expected to be predominantly two degrees of freedom. Secondly, D is

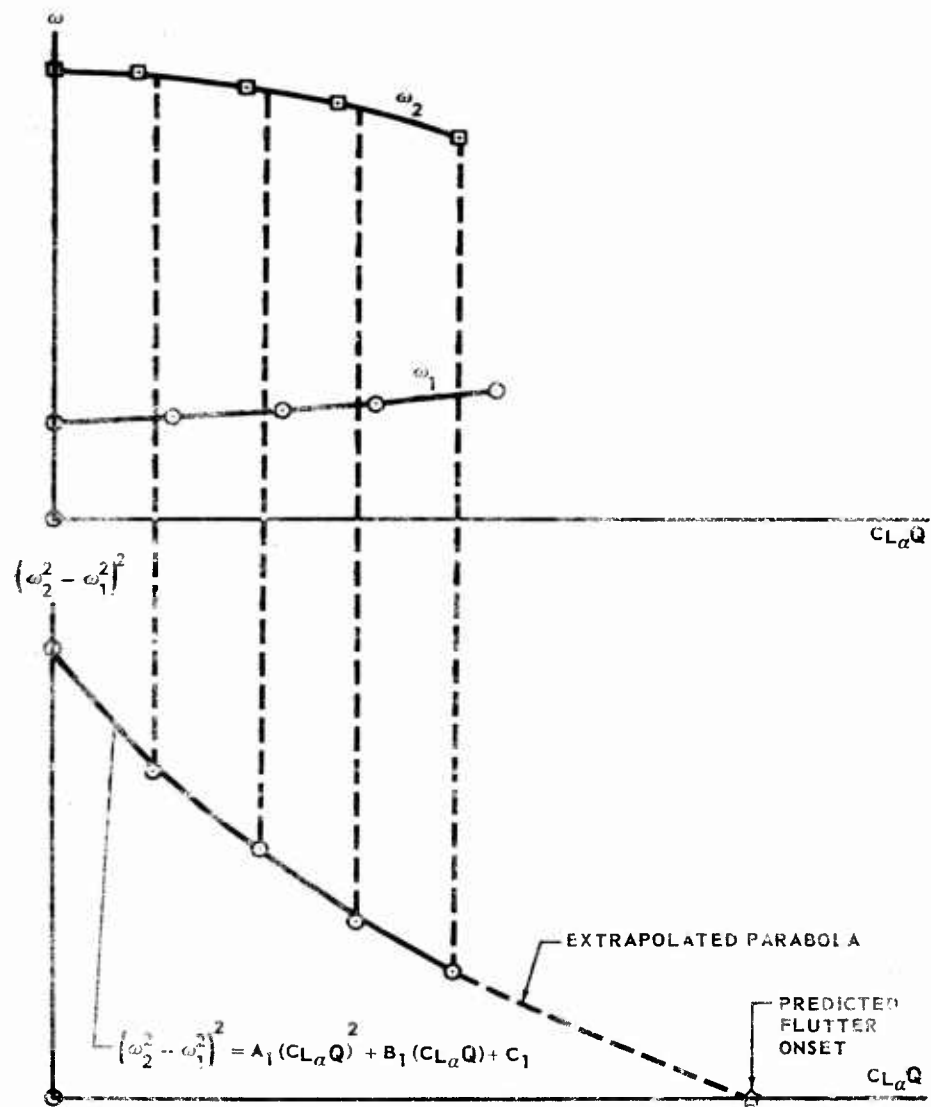


FIGURE 21. FREQUENCY APPROACH TECHNIQUE



parabolic with  $Z$  only so long as  $A$ ,  $B$  and  $C$  are constants; however, these coefficients depend on  $\gamma$  which in turn is affected by a shift in aerodynamic center. Unfortunately, the technique in its present form cannot be used in the transonic range where this shift is large with small changes in airspeed.

Only cursory checks have been made to date with subsonic wind tunnel tests and indicate that the technique has merit.

### Design Charts

As a direct result of normalizing linear geometry with respect to  $r_a$  it becomes possible to compute the flutter parameter  $Z_F$  and  $\omega_F/\omega_a$  with only the three parameters  $\gamma$ ,  $X$  and  $R$ . This makes it practical to construct design charts from which  $Z_F$  and  $\omega_F/\omega_a$  may be read off directly. Construction of these charts is based on equations (22) and (32). One such chart is shown in Figure 22 for  $\gamma = 0.2$ . The diamond symbols indicate critical frequency ratios beyond which the flutter solution vanishes, namely  $R_C = \sqrt{(\gamma + x)/\gamma(1 + \gamma X)}$ . Also it will be recalled that flutter solutions vanish for negative  $X$ . In the vicinity of  $R_C$  or  $X$  equal to zero, then, it would be expected that flutter speed calculations would be extremely sensitive and of doubtful accuracy (such as divergence calculations when the elastic axis and aerodynamic center approach each other). These sensitive areas are indicated by dashed lines.

Such charts are ideal for preliminary design work where speed and fluidity of design are the rule rather than the exception. These are applicable for transonic and supersonic as well as subsonic Mach numbers by entering the charts at the  $\gamma$  appropriate to the Mach number (since  $\gamma$  depends upon the location of the aerodynamic center). Determination of the flutter parameter  $Z_F$  does not depend on  $C_{L_a}$ .

Flutter onset velocity  $V_F$  is obtained from  $Z_F$  by a simple iteration process which converges so rapidly that it has never been necessary to repeat the iteration more than once. It is based on the following equations:

$$\left. \begin{aligned} V_F &= b \omega_a \sqrt{\left(\frac{\mu r_a}{2b}\right) \left(\frac{Z}{\eta}\right)_F} \\ \left(\frac{b \omega}{V}\right)_F &= \left(\frac{\omega_F}{\omega_a}\right) \left(\frac{b \omega_a}{V_F}\right) \\ \eta_F &= \eta_s \eta_{\omega_F} \end{aligned} \right\} (73)$$

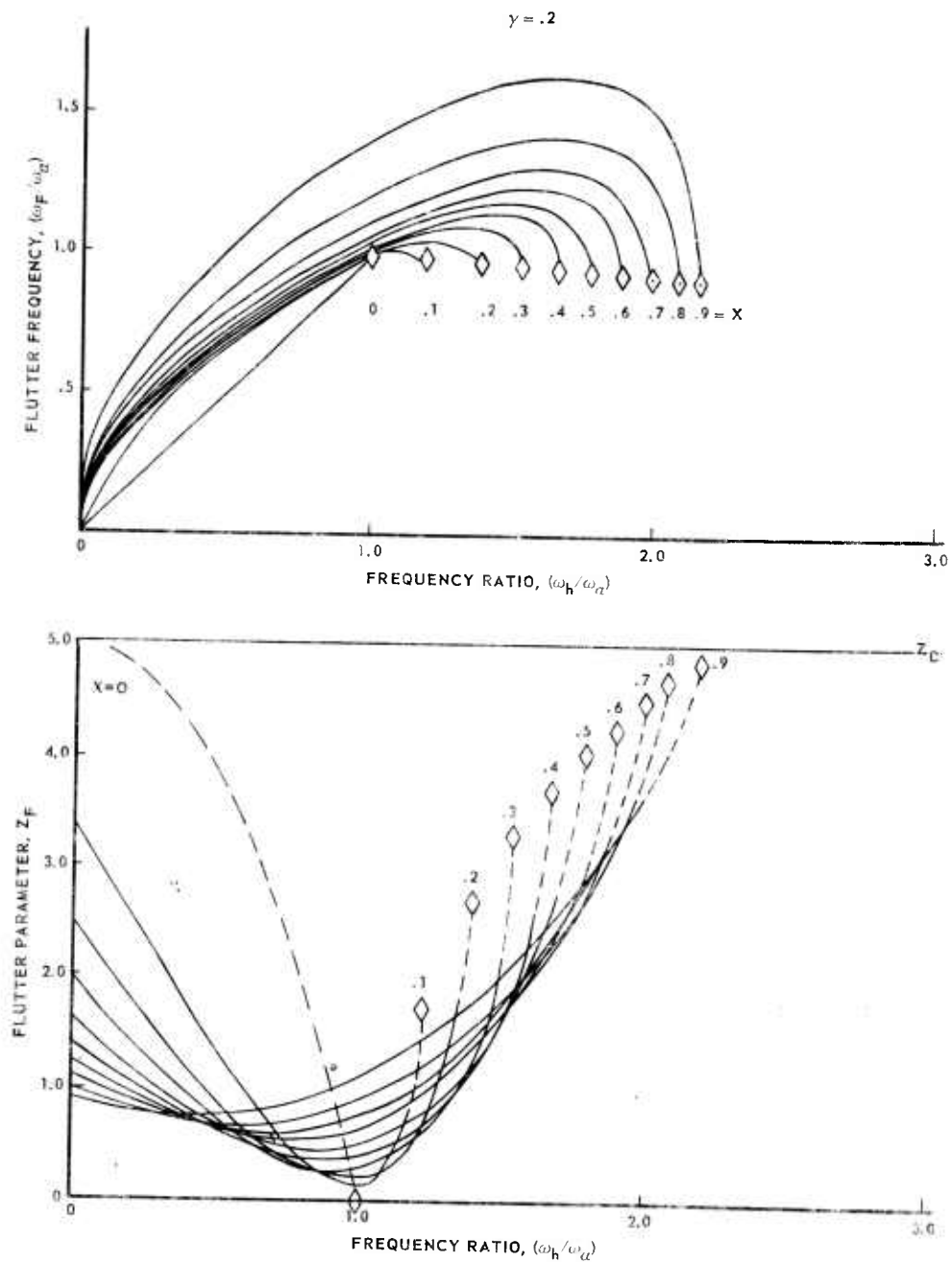


FIGURE 22 DESIGN CHART

The last equation above basically states that the overall aerodynamic efficiency is the product of steady flow and oscillatory flow efficiencies, the former including steady flow effects such as aspect ratio and Mach number and the latter including some form of oscillatory flow correction such as shown in Figure 13. Once  $Z_F$  has been determined from the chart, an approximate value of flutter speed  $V_F$  can be calculated by introducing the starting assumption  $\eta_F = \eta_s$  into the top equation. The approximate  $V_F$  is then introduced into the right side of the middle equation to obtain a first approximation of the reduced flutter frequency which in turn is used to obtain an approximate value of  $\eta_F$  from Figure 13. The first approximation of  $\eta_F$  evaluated from the bottom equation is introduced back into the top equation for a second try at  $V_F$ . Based on past experience this approximation of  $V_F$  should have converged for all practical purposes.

#### Concluding Remarks

It has been shown that good agreement exists between flutter speed calculations based on approximate "in phase" aerodynamics and those obtained from subsonic wind tunnel tests for a number of configurations covering a wide range of aspect ratio. Analysis of the basic processes leading to flutter, such as the concepts discussed in connection with Figure 10, further indicate that such correlation is not just accidental, and in fact demonstrates the ability of the "in phase" lift to induce severe and sudden changes in phase angle. Additional theoretical-experimental comparisons are desirable for assessing the adequacy of the "in phase" approximation over a broader range of problem variables, particularly including compressibility effects and near-critical configurations, i.e.  $R$  approaching  $R_c$  and  $X$  approaching zero and becoming negative.

Formulation of the flutter problem by non-dimensionalizing with respect to  $r_a$ , i.e.  $Z_F = f(\gamma, X, R)$  was shown to possess obvious advantages in reducing the number of variables necessary to specify  $Z_F$ . Such non-dimensionalizing is recommended for presenting flutter trends even for the more rigorous aerodynamic idealizations.

The full potential of the rational flutter approach using such approximate aerodynamics is far from being realized. In addition to further follow-up effort on the two degree of freedom system considered here, initiation of studies for extending this approach to more practical configurations seems justified in the near future. A logical evolution would seem to be:

- (a) Two dimensional plunging-rotation-control surface
- (b) Three dimensional rigid planform with sweepback possessing root roll and root pitch, followed by the addition of control surface
- (c) Uniform cantilever wing bending-torsion, followed by the addition of control surface. Sweepback effects would

follow no-sweepback studies.

- (d) Non-uniform wing following the sequence in (c) above.
- (e) Other miscellaneous studies including control surface tabs, rigid and flexible body degrees of freedom, etc.

#### References

1. von Kármán, T. and Biot, M. A., "Mathematical Methods in Engineering," McGraw-Hill, 1940
2. Rocard, Y., "Dynamic Instability," (Translated from "L'Instabilité en Mécanique; Automobiles, Avions, Ponts Suspendus"), Frederick Ungar Publishing Co., 1957.
3. Mirowitz, L. I., "NACA Subcommittee on Vibration and Flutter, Status Report," 17-18 October 1957.
4. Pines, S., "An Elementary Explanation of the Flutter Mechanism," Proceedings of the National Specialists Meeting on Dynamics and Aeroelasticity, Fort Worth, Texas, 6-7 November 1958.
5. Bryce, W. W., Cooper, R. E., and Gravitz, S. I., "Development of a Quasi-Steady Flutter Approach and Correlation of Quasi-Steady, Quasi-Unsteady, and Kernal Function Flutter Analyses with Experimental Data," USAF WADD TR 60-367, May 1960.
6. MacNeal, R. H., "Simple Analytical Solutions of the Binary Flutter Problem," USAF WADD TN 60-130, March 1960.
7. Zisfein, M. B., and Frueh, F. J., "A Study of Velocity-Frequency-Damping Relationships for Wing and Panel Binary Systems in High Supersonic Flow," AFOSR TN 59-969, October 1959.
8. Zisfein, M. B. and Frueh, F. J., "Approximate Methods for Aeroelastic Systems in High Supersonic Flow," AFOSR TR 60-182, October 1960.
9. Theodorsen, T. and Garrick, I. E., "Mechanism of Flutter - A Theoretical and Experimental Investigation of the Flutter Problem," NACA Report 685, 1940.
10. Evans, W. R., "Servo Analysis By the Root-Locus Method," North American Aviation Report EM-138, 1 June 1953.
11. Molyneux, W. G. and Hall, H., "The Aerodynamic Effects of Aspect Ratio and Sweepback on Wing Flutter," (British) R & M No. 3011, 1957.

## NEW TECHNIQUES IN FLUTTER AT HIGH MACH NUMBERS

J. Stuart Keith\*  
Chance Vought Corporation  
Vought Aeronautics Division  
Dallas, Texas

The prospect of flutter of low-aspect ratio surfaces at very high Mach numbers has focused attention on replacing flat plate aerodynamic theories by new theories which account for the non-linear effects of wing thickness. Surfaces on present missiles and aircraft designed for high Mach numbers are typically low-aspect ratio, thin structures. Conventional methods have fallen short, and attempts to modify the older methods have possibly overlooked simplifications that are present in the aeroelastic problems at high Mach numbers.

In this paper use has been made of numerous current publications which have indicated the advantage and simplification of a 'quasi-steady' aerodynamic approach. It appears that the quasi-steady relation is the same form as the truly unsteady aerodynamic theories at high supersonic and hypersonic speeds. There is very little additional contribution to be made to the development of the quasi-steady concept, but a review of the methods in the most general form will possibly reveal some new techniques that may be employed to advantage.

Briefly, the discussion below is divided into three parts. The first part reviews the form of the governing equations of an aeroelastic system, and indicates the advantage of using Hamilton's system of first order equations. The second part is a review of high Mach number aerodynamic theories in an effort to show that they are of the correct form for analysis by the Hamiltonian approach. The final part is concerned with a generalized approach for dealing with the numerical problem of passing from a continuous system to a discrete system of a finite number-of-degrees-of-freedom.

---

\* Engineer - Structures Dynamics Group

A List of the Symbols and Definitions  
Used in the Text

$[A], a_{ij}$	inertia matrix referred to "panel point" coordinates
$[K], k_{ij}$	stiffness matrix referred to "panel point" coordinates
$[\Lambda]$	aerodynamic influence coefficients
$\{p(t)\}, p_i(t)$	"panel point" displacements
$\{P(t)\}, P_i(t)$	"panel point" loads, the generalized forces associated with $p_i(t)$
$\{\alpha(t)\}, \alpha_i(t)$	"panel point" angles of attack
$\{w(t)\}, w_i(t)$	downwash at the panel points
$[\Delta]$	slope matrix, transforms panel point displacements into slopes
$[\varphi]$	matrix of panel point displacements in the modes
$\{q(t)\}, q_i(t)$	modal coordinates
$\{Q(t)\}, Q_i(t)$	generalized forces associated with $q_i(t)$
$[M]$	mass matrix referred to modal coordinates
$[F]$	stiffness matrix referred to modal coordinates
$[C_R], [C_I], [C_M]$	aerodynamic matrices referred to modal coordinates
$[C(\frac{\omega}{v}, M)]$	the complex airforce matrix referred to modal coordinates
$\{\pi(t)\}, \pi_i(t)$	generalized velocities or the generalized momenta
$[N(\rho, v, M)]$	the aeroelastic "dynamical matrix"

$p(x, y, t)$	pressure at the point $(x, y)$
$\Delta p(x, y, t)$	pressure difference between upper and lower surfaces
$C_L(x, y, t) = \frac{\Delta p}{\frac{1}{2} \rho v^2}$	aerodynamic lift coefficient
$p_z(x, y, t)$	continuous displacement of surface in z-direction
$w(x, y, t)$	continuous downwash
$\alpha(x, y, t)$	non-dimensional downwash, the "effective" angle of attack
$\tau(x, y)$	total thickness
$[T]$	matrix of interpolation coefficients
$\{f(x, y)\}', f_j(x, y)$	assumed interpolation functions
$\bar{w}(x, y, \omega)$	Fourier transform of downwash
$\bar{\Delta p}(x, y, \omega)$	Fourier transform of lift
$K(x, y, \xi, \eta)$	the kernel function of the three-dimensional flat plate problem
$\{a(t)\}', a_i(t)$	"undetermined" amplitudes of assumed lifts
$\{\bar{a}(\omega)\}', \bar{a}(\omega)$	Fourier transform of $Q_i(t)$
$[R]$	matrix of coefficients associated with the kernel function problem
$[L]$	collocation of assumed lifts to panel points
$[L_1] \quad [L_5]$	Aerodynamic matrices arising in the Newtonian flow problem
$\{\bar{P}(\omega)\}$	Fourier transform of panel point loads
$[-\Lambda(\frac{\omega}{v}, M)]$	unsteady aerodynamic influence coefficients
$w_p(x, y, t)$	velocity of piston in the piston analogy to high speed flow
$\theta = \tan^{-1} \frac{\partial z}{\partial x}$	slope associated with surface, $z(x, y, t)$

$Z(x, y, t)$	equation of the surface used in the Newtonian flow analysis
$\rho$	air density
$v$	air speed
$a$	speed of sound
$\omega$	frequency variable
$S = \nabla + i\omega$	transform variable
$M$	Mach number
$S, S_i$	regions of integration
$\gamma$	adiabatic constant
$F_1(x, y)$ $F_4(x, y)$	functions arising in Newtonian flow problem



# I. The Equations Governing an Aeroelastic System

It will be assumed that the configuration of any aeroelastic system can be defined by a number of generalized coordinates,  $p_i(t)$   $i = 1 \dots N$ , which are considered to be displacements or rotations at a number of discrete points in the structure. If these displacements are assumed small, the kinetic and strain energies of the aeroelastic system are quadratic in the coordinates,  $p_i(t)$ .

$$(1) \quad T = \frac{1}{2} \sum_{i,j} a_{ij} \dot{p}_i(t) \dot{p}_j(t)$$

$$(2) \quad U = \frac{1}{2} \sum_{i,j} k_{ij} p_i(t) p_j(t)$$

By the definitions of matrix algebra, these may also be expressed concisely as,

$$(3) \quad T = \frac{1}{2} \{\dot{p}\}' [A] \{\dot{p}\}$$

$$U = \frac{1}{2} \{p\}' [K] \{p\}$$

The approximations involved depend upon how adequately the continuous system has been described in terms of the discrete displacements,  $p_i(t)$ . This is the subject of the third part of this discussion.

If the quasi-steady\* description of aerodynamic forces is used, it is possible to write the virtual work of these forces

---

\* For the purposes of this discussion, quasi-steady implies that time-dependency only occurs in the downwash.

in the following form:

(4)

$$\delta W = -\frac{1}{2}\rho v^2 \{\delta p\}' [\Lambda] \{\alpha\}$$

where  $\{\alpha\} = \frac{1}{v} \{w\}$ , the downwash induced by the motion of the structure against the fluid. If the  $p_i(t)$  are all displacements normal to the free stream direction then expression (4) describes the normal aerodynamic loads (the generalized forces associated with the normal displacements,  $p_i(t)$ ).

(5) 
$$\{\dot{P}(t)\} = -\frac{1}{2}\rho v^2 [\Lambda] \{\alpha(t)\}$$

The matrix of aerodynamic influence coefficients is a real matrix which is at most a function of Mach number and temperature.

The downwash can be related to the displacements,  $p_i(t)$ , by the tangency condition:

(6) 
$$\{\alpha(t)\} = \frac{1}{v} \{w(t)\} = \{\delta p_X\} + \frac{1}{v} \{\delta \dot{p}_X\}$$

or

(7) 
$$\{\alpha\} = [\Delta] \{p\} + \frac{1}{v} \{\dot{p}\}$$

In this expression,  $[\Delta]$  is a matrix which transforms displacements at discrete points into slopes at those points.

In summary, when the quasi-steady assumption is made the aeroelastic system can be described by three real matrices:

$$(8) \quad T = \frac{1}{2} \{\dot{p}\}' [A] \{\dot{p}\}$$

$$(9) \quad U = \frac{1}{2} \{p\}' [K] \{p\}$$

$$(10) \quad \delta W = -\frac{1}{2} \rho v^2 \{\delta p\}' [\Delta] \left( [\Delta] \{p\} + \frac{1}{v} \{\dot{p}\} \right)$$

It is almost always expedient in aeroelastic analyses to reduce the number of degrees-of-freedom by constraining the higher modes of deformation. This we do by transforming to modal coordinates.

$$(11) \quad \{p(t)\} = [\psi] \{q(t)\}$$

In this expression,  $\psi_{ij}$  is the displacement of the  $i^{\text{th}}$  point in the structure in the  $j^{\text{th}}$  mode. Making this transformation on (8), (9), and (10) yields

$$(12) \quad T = \frac{1}{2} \{\dot{q}\}' [M] \{\dot{q}\}$$

$$(13) \quad U = \frac{1}{2} \{q\}' [F] \{q\}$$

$$(14) \quad \delta W = -\frac{1}{2} \rho v^2 \{\delta q\}' \left( [C_R] \{q\} + \frac{1}{v} [C_L] \{\dot{q}\} \right)$$

In the above expressions, the following definitions have been made.

$$(15) \quad [M] = [\varphi]'[A][\varphi]$$

$$(16) \quad [F] = [\varphi]'[K][\varphi]$$

$$(17) \quad [C_R] = [\varphi]'[\Lambda][\Delta][\varphi]$$

$$(18) \quad [C_I] = [\varphi]'[\Lambda][\varphi]$$

In some cases, where it appears important, virtual mass aerodynamic forces may be added to the quasi-steady forces; these forces are linearly related to the accelerations of the system and appear as additional terms of the form:

$$(19) \quad \frac{1}{\sigma^2} [C_M] \{\ddot{q}\}$$

This system would be governed by the following relations:

$$(20) \quad T = \frac{1}{2} \{\dot{q}\}' [M] \{\dot{q}\}$$

$$(21) \quad U = \frac{1}{2} \{q\}' [F] \{q\}$$

$$(22) \quad \delta W = -\frac{1}{2} \rho \sigma^4 \{ \delta q \}' \left( [C_R] \{q\} + \frac{1}{\sigma} [C_I] \{\dot{q}\} + \frac{1}{\sigma^2} [C_M] \{\ddot{q}\} \right)$$

Conventional approaches to flutter analysis would use Lagrange's equations and the assumption of "harmonic motion" to arrive at the governing equations expressed in the frequency domain:

$$(23) \quad \left( -\omega^2 [M] + [F] + \frac{1}{2} \rho v^2 [C(\frac{\omega}{v}, M)] \right) \{ \bar{q}(\omega) \} = \{ 0 \}$$

where, for the quasi-steady case,

$$(24) \quad [C(\frac{\omega}{v}, M)] = [C_R] + i \left( \frac{\omega}{v} \right) [C_I] - \left( \frac{\omega}{v} \right)^2 [C_M]$$

Note that for the unsteady theories in the subsonic and low supersonic region, equation (23) is the only possible description because the aerodynamic forces can only be described in the frequency domain; and the dependency on  $\frac{\omega}{v}$  is far more complicated than that indicated by equation (24). For example, the kernel function approach can be used to derive unsteady three-dimensional aerodynamic influence coefficients for which a quasi-steady approximation may be made (see Part II).

Returning again to equations (20), (21), and (22) we will employ Hamilton's system of first order equations. These are (see, for example, Theoretical Mechanics, Ames, Murnaghan, pp. 264):

$$(25) \quad \pi_i = \frac{\partial T}{\partial \dot{q}_i}$$

$$(26) \quad \dot{\pi}_i = \frac{\partial T}{\partial q_i} - \frac{\partial U}{\partial q_i} + Q_i$$

with  $Q_i$  determined from

$$(27) \quad \delta W = \sum_i Q_i \delta q_i$$

In the present case this yields

$$(28) \quad \{\dot{\pi}\} = [M]\{\dot{q}\}$$

$$(29) \quad \{\ddot{\pi}\} = -[F]\{q\} - \frac{1}{2}\rho v^2 \left( [C_R]\{q\} + \frac{1}{v} [C_I]\{\dot{q}\} + \frac{1}{v^2} [C_M]\{\ddot{q}\} \right)$$

This can be arranged as

$$(30) \quad \{\ddot{\pi}\} = -[M] \left( [M] + \frac{1}{2}\rho [C_M] \right)^{-1} \left( [F] + \frac{1}{2}\rho v^2 [C_R] \right) \{q\} - \frac{1}{2}\rho v [M] \left( [M] + \frac{1}{2}\rho [C_M] \right)^{-1} [C_I] [M]^{-1} \{\dot{\pi}\}$$

$$(31) \quad \{\dot{q}\} = [M]^{-1} \{\dot{\pi}\}$$

Equations (30) and (31) are in a desired form, but a simplification will result if the generalized velocities,  $\dot{q}_i$ , are introduced as coordinates instead of the generalized momenta.

If  $\pi_i$  is used to denote the generalized velocities one obtains

$$(32) \quad \{\ddot{\pi}\} = - \left( [M] + \frac{1}{2}\rho [C_M] \right)^{-1} \left( [F] + \frac{1}{2}\rho v^2 [C_R] \right) \{q\}$$

$$(33) \quad - \frac{1}{2}\rho v \left( [M] + \frac{1}{2}\rho [C_M] \right)^{-1} [C_I] \{\pi\}$$

$$\{\dot{q}\} = \{\pi\}$$

More concisely,

$$(34) \quad \begin{bmatrix} \{\ddot{\eta}\} \\ \{\dot{q}\} \end{bmatrix} = [N(\rho, v, M)] \begin{bmatrix} \{\eta\} \\ \{q\} \end{bmatrix}$$

where  $[N(\rho, v, M)]$

$$= \begin{bmatrix} -\frac{\rho v}{2} [M] + \frac{\rho}{2} [C_M]^{-1} [C_I] & -([M] + \frac{\rho}{2} [C_M])^{-1} [F] + \frac{v}{2} [C_R] \\ [1] & [0] \end{bmatrix}$$

The matrix,  $[N(\rho, v, M)]$ , is the "dynamical matrix" for the aeroelastic system. It is a  $2n$  by  $2n$  real matrix, where  $n$  is the number-of-degrees-of-freedom; and it is a function of altitude, airspeed, and temperature. These three independent variables are those same variables that define the flight profile. At constant temperature only two are independent and these may

be taken as:

Dynamic pressure - Mach number, or  
 Equivalent airspeed - Mach number, or  
 Air density - Mach number, or  
 Altitude - Mach number

$$\text{where } \frac{1}{2} \rho v^2 = \frac{\rho a^2}{2} M^2, \quad v_{EAS} = \sqrt{\frac{\rho}{\rho_0}} a M$$

$a$  = speed of sound

For investigating the stability of a system, the LaPlace transform is a recognized tool. Application to the particular problem at hand gives

$$(36) \quad \left( S [1] - [N(\rho, M)] \right) \begin{bmatrix} \{ \bar{u}(s) \} \\ \{ \bar{q}(s) \} \end{bmatrix} = \begin{bmatrix} \{ 0 \} \\ \{ 0 \} \end{bmatrix}$$

The flutter roots are determined by the condition

$$(37) \quad | S [1] - [N] | = 0$$

which is a  $2n^{\text{th}}$  order polynomial in  $S$  with real coefficients, having complex roots occurring in conjugate pairs. Any flight-mission profile can be chosen along which

$\rho$  and  $M$  are compatible, and the stability roots may be plotted with either variable as a parameter; for example, Mach number. Let  $\sqrt{\phantom{x}}, \omega$

be the real and imaginary parts of the root.

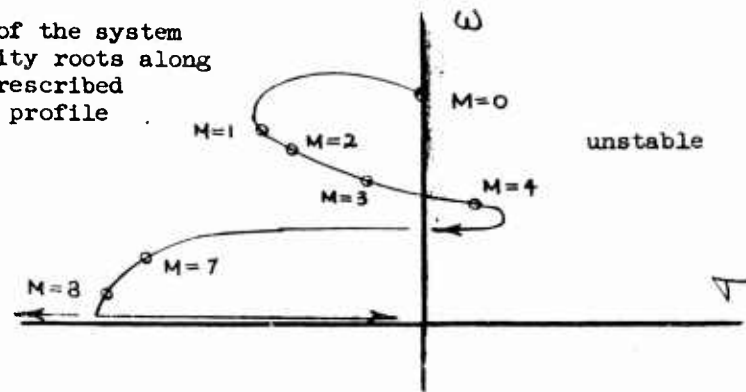
$$(38) \quad S = \sqrt{\phantom{x}} + i \omega$$



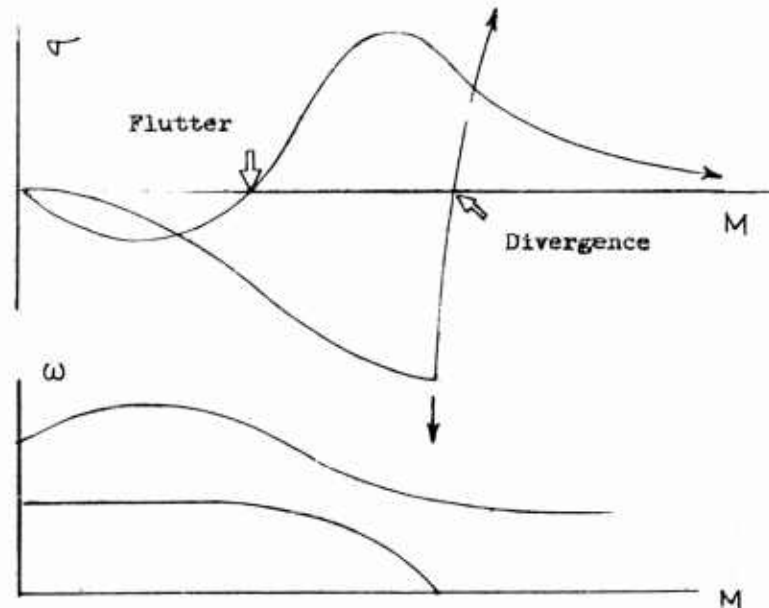
From general transform theory it is known that unstable systems are characterized by roots in the right-hand half-plane where

$\zeta > 0$ . Flutter is therefore indicated when the locus of the root crosses the line  $\zeta = 0$ . Typical plots of the locus of the roots determined by condition (37) are shown below.

Locus of the system stability roots along some prescribed flight profile



Plots may also be made of the real and imaginary parts of the root which are analogous to the plots of the aerodynamic damping parameter, "g".



## II. Aerodynamic Theories at High Mach Numbers

The piston theory analogy suggests that a point relationship exists between the lift and downwash on bodies and surfaces at high Mach numbers. This simplification along with the quasi-steady assumption leads to a lift expressed in the following form:

$$(39) \quad \Delta p(x, y, t) = \frac{1}{2} \rho v^2 \frac{\partial C_L}{\partial \alpha}(x, y) \alpha(x, y, t)$$

with

$$(40) \quad \alpha(x, y, t) = \frac{w(x, y, t)}{v} = \frac{\partial p_z}{\partial x} + \frac{1}{v} \frac{\partial p_z}{\partial t}$$

In this expression  $\Delta p$  is the pressure difference between upper and lower surfaces and  $p_z(x, y, t)$  is the displacement function of the body or surface. Although the above two assumptions are not valid at all Mach numbers, the convenience of such a form makes it worthwhile to consider the otherwise general form without dictating the theory used to derive the  $\frac{\partial C_L}{\partial \alpha}(x, y)$  term (which depends upon the thickness of the wing). It will be shown below that the piston analogy yields

$$(41) \quad \frac{\partial C_L}{\partial \alpha}(x, y) = \frac{4}{M} \left( 1 + \frac{\gamma-1}{4} M \frac{\partial \tau}{\partial x}(x, y) \right)^{\frac{\gamma+1}{\gamma-1}}$$

or a second order expansion gives

$$(42) \quad \frac{\partial C_L}{\partial \alpha}(x, y) = \frac{4}{M} \left( 1 + \frac{\gamma-1}{2} M \frac{\partial \tau}{\partial x}(x, y) + \dots \right)$$

$\tau(x, y)$  is the total thickness of the surface. The simplicity of the piston analogy and its proven use at moderate values of  $M \frac{\partial \tau}{\partial x}$

has given it popularity as an aeroelastic tool. There appears to be no reason, however, why more accurate results cannot be obtained by using other steady aerodynamic theories while still complying with the assumption of

- (1) point relation between lift and angle of attack, and
- (2) assuming only time dependency occurs in downwash.

Following this approach, shock expansion or experimental distributions of

$\frac{\partial \mathcal{L}}{\partial x}(x, y)$  could be used in place of the piston analogy. This would go part way in accounting for edge effects, thickness geometry, and finite shocks. The approach is also applicable to bodies in flows at high Mach numbers. In any case, the problem we want to consider is one of showing the form of the aerodynamic matrices which follow from the expressions (39) and (40). The aerodynamic influence matrices are derived from the virtual work:

$$(43) \quad \delta W = - \iint_S \Delta p(x, y, t) \delta p_z(x, y, t) dx dy$$

Some suitable interpolation must be used to relate the continuous system to one of a finite number-of-degrees-of-freedom. This relation is of the form (see Part III):

$$(44) \quad p_z(x, y, t) = \{f(x, y)\}' [\gamma]_i \{p(t)\}$$

valid for  $x, y$  on the region  $S_1$

It follows from (44) that

$$(45) \quad \delta p_z = \{f(x, y)\}' [\gamma]_i \delta p$$

$$(46) \quad \frac{\partial p_z}{\partial x} = \left\{ \frac{\partial f}{\partial x}(x, y) \right\}' [\gamma]_i \{p\}$$

$$(47) \quad \frac{\partial p_z}{\partial t} = \{f(x, y)\}' [\gamma]_i \dot{p}$$

Equations (46) and (47) may be used to define the downwash, or alternatively, the expression

$$(48) \quad \alpha(x, y, t) = \{f(x, y)\}' [\gamma]_i \{ \alpha(t) \}$$

may be used.

When relation (48) is used, equation (46) may be used to derive the matrix,  $[\Delta]$ , previously defined. In employing the second alternative, equation (43) is broken into a sum of integrals over the regions where equation (44) is valid.

$$(49) \quad \overline{W} = - \sum_i \iint_{S_i} \Delta p(x, y, t) \overline{p}_z(x, y, t) dx dy$$

Substitution of (45) into (49) gives

$$(50) \quad \overline{W} = - \frac{1}{2} \rho v^2 \{ \overline{p} \}' \sum_i [\gamma]_i' \iint_{S_i} \{f(x, y)\} \frac{\partial}{\partial x} \alpha dx dy$$

Substitution of (48) yields

$$(51) \quad \overline{W} = - \frac{1}{2} \rho v^2 \{ \overline{p} \}' \sum_i \left( [\gamma]_i' \iint_{S_i} \{f\} \{f\}' \frac{\partial}{\partial x} dx dy [\gamma]_i \right) \{ \alpha \}$$

By our previous definitions the aerodynamic influence matrix is

$$(52) \quad [A] = \sum_i [\gamma]_i' \iint_{S_i} \{f(x, y)\} \{f(x, y)\}' \frac{\partial}{\partial x} (x, y) dx dy [\gamma]_i$$

Use of equation (46) to calculate the slopes gives

$$\left\{ \frac{\partial p}{\partial x} \right\} = \begin{bmatrix} \frac{\partial p_z}{\partial x}(x_1, y_1, t) \\ \vdots \\ \frac{\partial p_z}{\partial x}(x_i, y_i, t) \\ \vdots \\ \frac{\partial p_z}{\partial x}(x_N, y_N, t) \end{bmatrix} = \begin{bmatrix} \left\{ \frac{\partial f}{\partial x}(x_i, y_i) \right\}' [\zeta] \\ \vdots \\ \left\{ \frac{\partial f}{\partial x}(x_N, y_N) \right\}' [\zeta] \end{bmatrix} \{p\}$$

or

$$(53) \quad \left\{ \frac{\partial p}{\partial x} \right\} = [\Delta] \{p\}$$

As previously described, (52) and (53) give the aerodynamic loads through the relation

$$(54) \quad \{P\} = -\frac{1}{2} \rho v^2 [\Lambda] \left( [\Delta] \{p\} + \frac{1}{v} \{\dot{p}\} \right)$$

While equation (54) was derived on the assumptions implied by equation (39), it remains unchanged in form when three-dimensional subsonic and supersonic aerodynamics are used in a quasi-steady fashion. To illustrate, the integral equation of subsonic or supersonic flow is of the form

$$(55) \quad \frac{\bar{w}(x, y, \omega)}{v} = \iint_S K(x, y, \xi, \eta) \frac{\bar{\Delta p}(\xi, \eta, \omega)}{\frac{1}{2} \rho v^2} d\xi d\eta$$

which is necessarily expressed in the frequency domain by the relations

$$(56) \quad w(x, y, t) = \int_{-\infty}^{\infty} \bar{w}(x, y, \omega) e^{i\omega t} d\omega$$

$$(57) \quad \Delta p(x, y, t) = \int_{-\infty}^{\infty} \Delta \bar{p}(x, y, \omega) e^{i\omega t} d\omega$$

The usual assumption of a superposition of assumed lift functions is expressed as

$$(58) \quad C_L(x, y, t) = \frac{\Delta p(x, y, t)}{\frac{1}{2}\rho v^2} = \{L(x, y)\}' \{a(t)\}$$

which can be used to reduce (55) to a set of simultaneous equations

$$(59) \quad \{\bar{w}(\omega)\}' = [R] \{\bar{a}(\omega)\}$$

The rather complex details of the three-dimensional problem can be formally relegated to the integrations indicated by

$$(60) \quad [R] = \iint_S \{K(x_i, y_i, \xi, \eta)\}' \{L(\xi, \eta)\}' d\xi d\eta$$

Collocation of the assumed lift functions can be accomplished by use of the virtual work principle and a relation of the form expressed in equation (44).

$$\begin{aligned}
 \delta W &= -\frac{1}{2}\rho v^2 \iint_S C_L(x,y,t) \delta p_z(x,y,t) dx dy \\
 &= -\frac{1}{2}\rho v^2 \{\delta p\}' \sum_i [\gamma]_i' \iint_{S_i} \{f(x,y)\} \{L(x,y)\}' dx dy \{a(t)\} \\
 &= -\frac{1}{2}\rho v^2 \{\delta p\}' [L] \{a(t)\}
 \end{aligned}$$

where

$$(61) \quad [L] = \sum_i [\gamma]_i' \iint_{S_i} \{f(x,y)\} \{L(x,y)\}' dx dy$$

or

$$\{P(t)\} = -\frac{1}{2}\rho v^2 [L] \{a(t)\}$$

Use of (61) in conjunction with a least squares solution to equation (59) results in

$$(62) \{ \bar{P}(\omega) \} = -\frac{1}{2} \rho v^2 [L] ([R]' [R])^{-1} [R]' \{ \frac{\bar{w}(\omega)}{v} \}$$

The unsteady aerodynamic influence coefficients are then

$$[\Lambda(\frac{\omega}{v}, M)] = [L] ([R]' [R])^{-1} [R]'$$

giving the relation

$$(63) \{ \bar{P}(\omega) \} = -\frac{1}{2} \rho v^2 [\Lambda(\frac{\omega}{v}, M)] \{ \frac{\bar{w}(\omega)}{v} \}$$

According to the quasi-steady assumption

$$(64) \{ P(t) \} = -\frac{1}{2} \rho v^2 [\Lambda(0, M)] \{ \frac{w(t)}{v} \}$$

Equation (64) is identical in form to equation (54); however, the assumption of the pressure-downwash point relationship is not present in the derivation of equation (64); this is evidenced by a full matrix of aerodynamic influence coefficients as contrasted to a nearly diagonal matrix in the former case.

#### Piston Theory

The piston analogy uses the expression

$$(65) \frac{p}{p_\infty} = \left( 1 + \frac{\gamma-1}{2} \frac{w_p}{a_\infty} \right)^{\frac{2\gamma}{\gamma-1}}$$



for the pressure on upper and lower surfaces where

$$(66) \quad w_p = \frac{\partial p_z}{\partial x} v + \frac{\partial p_z}{\partial t} + \frac{1}{2} \frac{\partial \tau}{\partial x} v$$

on lower surface, and

$$(67) \quad w_p = -\frac{\partial p_z}{\partial x} v - \frac{\partial p_z}{\partial t} v + \frac{1}{2} \frac{\partial \tau}{\partial x} v$$

on upper surface.

Expression (65) is valid only to second order in compression, but should be valid for expansion up to speeds where the pressure goes to zero (in regions where  $\frac{\partial \tau}{\partial x} < 0$ ).

In terms of previous definitions

$$(68) \quad \alpha(x, y, t) = \frac{w(x, y, t)}{v} = \frac{\partial p_z}{\partial x} + \frac{1}{v} \frac{\partial p_z}{\partial t}$$

so that (66) and (67) can be written as

$$(69) \quad \frac{w_p}{v} = \frac{w}{v} + \frac{1}{2} \frac{\partial \tau}{\partial x} \quad \text{on lower surface.}$$

$$(70) \quad \frac{w_p}{v} = -\frac{w}{v} + \frac{1}{2} \frac{\partial \tau}{\partial x} \quad \text{on upper surface.}$$

The state equation

$$(71) \quad p_w = p_{\infty} \frac{a_{\infty}^2}{\gamma} \quad \text{is used along with}$$

the definition of Mach number

$$(72) \quad M_{\infty} = \frac{v_{\infty}}{a_{\infty}} \quad \text{to express (65) as}$$

$$(73) \quad \frac{p(x,y,t)}{\frac{1}{2}\rho\infty v_\infty^2} = \frac{2}{\gamma M_\infty^2} \left( 1 + \frac{\gamma-1}{2} M_\infty \frac{w_F}{a_\infty} \right)^{\frac{2\gamma}{\gamma-1}}$$

Since no confusion can result the subscripts  $( )_\infty$  are omitted and (69) and (70) are used in (73) to obtain the lift coefficient.

(74)

$$\begin{aligned} C_L(x,y,t) &= \frac{\Delta p}{\frac{1}{2}\rho v^2} \\ &= \frac{\left( 1 - \frac{\gamma-1}{2} M \frac{w}{v} + \frac{\gamma-1}{4} M \frac{\partial \tau}{\partial x} \right)^{\frac{2\gamma}{\gamma-1}} - \left( 1 + \frac{\gamma-1}{2} M \frac{w}{v} + \frac{\gamma-1}{4} M \frac{\partial \tau}{\partial x} \right)^{\frac{2\gamma}{\gamma-1}}}{\frac{\gamma}{2} M^2} \end{aligned}$$

Expansion in powers of  $\frac{w}{v}$  yields

(75)

$$C_L(x,y,t) = \frac{4}{M} \left( 1 + \frac{\gamma-1}{4} M \frac{\partial \tau}{\partial x}(x,y) \right)^{\frac{\gamma+1}{\gamma-1}} \left( \frac{w}{v} \right) + \dots O\left(\frac{w}{v}\right)^2$$

terms of order of  $\left(\frac{w}{v}\right)^2$

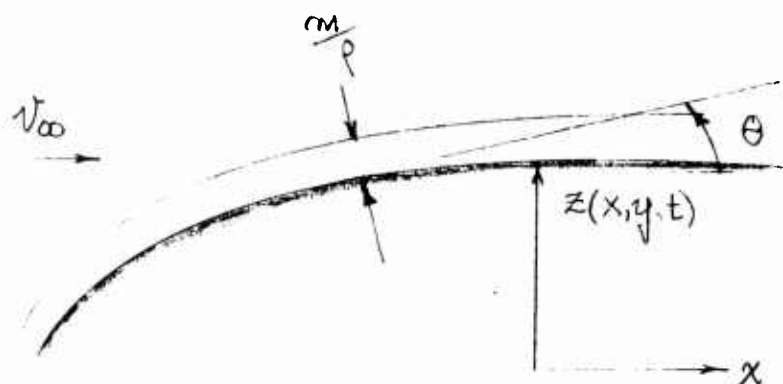
Equation (75) is an expression that is linear in the downwash, but "exact" in thickness. By comparison with equation (39)

(76)

$$\frac{\partial C_L}{\partial \alpha}(x,y) = \frac{4}{M} \left( 1 + \frac{\gamma-1}{4} M \frac{\partial \tau}{\partial x}(x,y) \right)^{\frac{\gamma+1}{\gamma-1}}$$

It is felt that equation (76) would describe pressures in regions where  $\frac{\partial \tau}{\partial x} < 0$  better than the corresponding second or third order expansions, and in practical cases it would introduce little additional complication. Viewed as a quasi-steady theory this "exact" piston theory can be rationalized as an approximation to steady shock expansion theory.

#### Unsteady Newtonian Flow



From results derived in the appendix, the pressure on a surface,  $z(x, y, t)$  in unsteady flow at very high Mach numbers is

$$(77) \quad p - p_\infty = \frac{mv^2}{R} + \rho_\infty v_\infty^2 \left( \tan \theta + \frac{1}{v_\infty} \frac{\partial z}{\partial t} \right)^2 \cos^2 \theta + m \frac{\partial^2 z}{\partial t^2}$$

with use of the continuity relation and momentum tangent to the surface one obtains

$$(78) \quad m = \frac{\rho_\infty \tau}{\cos \theta} \quad , \quad v = v_\infty \cos \theta$$

So that

(79)

$$\begin{aligned}
 \frac{p-p_\infty}{\frac{1}{2}\rho_\infty u_\infty^2} &= \frac{\tau \cos \theta}{R} + 2 \cos^2 \theta \left( \tan \theta + \frac{1}{u_\infty} \frac{\partial Z}{\partial t} \right)^2 + \frac{\tau}{u_\infty^2 \cos^2 \theta} \frac{\partial^2 Z}{\partial t^2} \\
 &= \frac{\tau \frac{\partial^2 Z}{\partial x^2}}{\left( 1 + \left( \frac{\partial Z}{\partial x} \right)^2 \right)^3} + \frac{2 \left( \frac{\partial Z}{\partial x} + \frac{1}{u_\infty} \frac{\partial Z}{\partial t} \right)^2}{1 + \left( \frac{\partial Z}{\partial x} \right)^2} \\
 &\quad + \frac{\tau \sqrt{1 + \left( \frac{\partial Z}{\partial x} \right)^2}}{u_\infty^2} \frac{\partial^2 Z}{\partial t^2}
 \end{aligned}$$

For symmetrical airfoils at zero mean angle of attack:

(80)

$$\begin{aligned}
 z(x, y, t) &= p_z(x, y, t) + \frac{\tau(x, y)}{2} \\
 &\quad \text{on lower surface} \\
 &= -p_z(x, y, t) + \frac{\tau(x, y)}{2} \\
 &\quad \text{on upper surface}
 \end{aligned}$$

The pressure difference is computed by substituting equation (80) into (79) and forming

$$(81) \quad C_L(x, y, t) = \frac{p - p_\infty}{\frac{1}{2} \rho_\infty u_\infty^2} \bigg|_{z = p_z + \frac{\tau}{2}} - \frac{p - p_\infty}{\frac{1}{2} \rho_\infty u_\infty^2} \bigg|_{z = -p_z + \frac{\tau}{2}}$$

For aeroelastic applications it is necessary to linearize equation (79). For this purpose consider

as a function of

$$\frac{\partial^2 z}{\partial x^2}, \frac{\partial z}{\partial x}, \frac{\partial z}{\partial x} + \frac{\partial z}{u_\infty \partial t}, \frac{1}{u_\infty^2} \frac{\partial^2 z}{\partial t^2}$$

$$\frac{p - p_\infty}{\frac{1}{2} \rho_\infty u_\infty^2}$$

$$(82) \quad \frac{p - p_\infty}{\frac{1}{2} \rho_\infty u_\infty^2} = C_p = C_p \left( \frac{\partial^2 z}{\partial x^2}, \frac{\partial z}{\partial x}, \frac{\partial z}{\partial x} + \frac{\partial z}{u_\infty \partial t}, \frac{1}{u_\infty^2} \frac{\partial^2 z}{\partial t^2} \right)$$

Expand this in a Taylor's series about the point:

$$(83) \quad \frac{\partial^2 z}{\partial x^2} = \frac{1}{2} \frac{\partial^2 \tau}{\partial x^2}$$

$$\frac{\partial z}{\partial x} = \frac{1}{2} \frac{\partial \tau}{\partial x}$$

$$\frac{\partial z}{\partial x} + \frac{1}{u_\infty} \frac{\partial z}{\partial t} = \frac{1}{2} \frac{\partial \tau}{\partial x}$$

$$\frac{1}{u_\infty^2} \frac{\partial^2 z}{\partial t^2} = 0$$

Retaining only the first order terms we have

(84)

$$\begin{aligned}
 \frac{p - p_\infty}{\frac{1}{2} \rho_\infty v_\infty^2} &= C_p \left( \frac{1}{2} \frac{\partial^2 \tau}{\partial x^2}, \frac{1}{2} \frac{\partial \tau}{\partial x}, \frac{1}{2} \frac{\partial \tau}{\partial x}, 0 \right) \\
 &+ \frac{\partial C_p}{\partial \left( \frac{\partial^2 z}{\partial x^2} \right)} \left( \frac{1}{2} \frac{\partial^2 \tau}{\partial x^2}, \frac{1}{2} \frac{\partial \tau}{\partial x}, \frac{1}{2} \frac{\partial \tau}{\partial x}, 0 \right) \left( \frac{\partial^2 z}{\partial x^2} - \frac{1}{2} \frac{\partial^2 \tau}{\partial x^2} \right) \\
 &+ \frac{\partial C_p}{\partial \left( \frac{\partial z}{\partial x} \right)} \left( \frac{1}{2} \frac{\partial^2 \tau}{\partial x^2}, \frac{1}{2} \frac{\partial \tau}{\partial x}, \frac{1}{2} \frac{\partial \tau}{\partial x}, 0 \right) \left( \frac{\partial z}{\partial x} - \frac{1}{2} \frac{\partial \tau}{\partial x} \right) \\
 &+ \frac{\partial C_p}{\partial \left( \frac{\partial z}{\partial x} + \frac{1}{v_\infty} \frac{\partial z}{\partial t} \right)} \left( \frac{1}{2} \frac{\partial^2 \tau}{\partial x^2}, \frac{1}{2} \frac{\partial \tau}{\partial x}, \frac{1}{2} \frac{\partial \tau}{\partial x}, 0 \right) \left( \frac{\partial z}{\partial x} + \frac{1}{v_\infty} \frac{\partial z}{\partial t} - \frac{1}{2} \frac{\partial \tau}{\partial x} \right) \\
 &+ \frac{\partial C_p}{\partial \left( \frac{1}{v_\infty^2} \frac{\partial^2 z}{\partial t^2} \right)} \left( \frac{1}{2} \frac{\partial^2 \tau}{\partial x^2}, \frac{1}{2} \frac{\partial \tau}{\partial x}, \frac{1}{2} \frac{\partial \tau}{\partial x}, 0 \right) \left( \frac{1}{v_\infty^2} \frac{\partial^2 z}{\partial t^2} \right) \\
 &+ \dots
 \end{aligned}$$

Carrying out the indicated operations and substituting into equation (81) results in the following expression for the lift coefficient

$$\begin{aligned}
 (85) \quad C_L(x, y, t) &= \frac{2\tau}{\left(1 + \frac{1}{4} \left(\frac{\partial \tau}{\partial x}\right)^2\right)^3} \frac{\partial^2 p_z}{\partial x^2} - \frac{3\tau \frac{\partial^2 \tau}{\partial x^2} \frac{\partial \tau}{\partial x}}{\left(1 + \frac{1}{4} \left(\frac{\partial \tau}{\partial x}\right)^2\right)^4} \frac{\partial p_z}{\partial x} \\
 &+ \frac{4 \frac{\partial \tau}{\partial x}}{1 + \frac{1}{4} \left(\frac{\partial \tau}{\partial x}\right)^2} \left( \frac{\partial p_z}{\partial x} + \frac{1}{v} \frac{\partial p_z}{\partial t} \right) + \frac{2\tau \sqrt{1 + \frac{1}{4} \left(\frac{\partial \tau}{\partial x}\right)^2}}{v^2} \frac{\partial^2 p_z}{\partial t^2}
 \end{aligned}$$

The virtual work corresponding to this lift is

$$(86) \quad \delta W = -\frac{1}{2}\rho v^2 \iint_S C_L(x, y, t) \delta p_z(x, y, t) dx dy$$

For brevity, the following definitions are introduced

$$(87) \quad F_1(x, y) = \frac{2\tau}{\left(1 + \frac{1}{4}\left(\frac{\partial \tau}{\partial x}\right)^2\right)^3}$$

$$(88) \quad F_2(x, y) = \frac{3\tau \frac{\partial^2 \tau}{\partial x^2} \frac{\partial \tau}{\partial x}}{\left(1 + \frac{1}{4}\left(\frac{\partial \tau}{\partial x}\right)^2\right)^4}$$

$$(89) \quad F_3(x, y) = \frac{4 \frac{\partial \tau}{\partial x}}{1 + \frac{1}{4}\left(\frac{\partial \tau}{\partial x}\right)^2}$$

$$(90) \quad F_4(x, y) = 2\tau \sqrt{1 + \frac{1}{4}\left(\frac{\partial \tau}{\partial x}\right)^2}$$

Then

$$(91) \quad \delta W = -\frac{1}{2}\rho v^2 \left( \iint_S F_1(x, y) \frac{\partial^2 p_z}{\partial x^2} \delta p_z dx dy \right. \\ \left. - \iint_S F_2(x, y) \frac{\partial p_z}{\partial x} \delta p_z dx dy + \iint_S F_3(x, y) \left( \frac{\partial p_z}{\partial x} + \frac{1}{v} \frac{\partial p_z}{\partial t} \right) \delta p_z dx dy \right. \\ \left. + \frac{1}{v^2} \iint_S F_4(x, y) \frac{\partial^2 p_z}{\partial t^2} \delta p_z dx dy \right)$$

The approach used previously to pass to the discrete system can be used here also; there are, however, additional terms of the form

$$(92) \quad \frac{\partial^2 p_z}{\partial x^2} = \left\{ \frac{\partial^2 f}{\partial x^2}(x, y) \right\}' [\gamma]_i \{p\}$$

Interpolation schemes that describe the displacement and slope adequately do not necessarily give a good description of the "curvature",  $\frac{\partial^2 p_z}{\partial x^2}$

Part III gives some discussion to a formula which has been employed with success in a stiffness-strain energy approach to using plate theory in structural analyses. The description of the curvature is required in this approach to structural analysis; hence, application of this formula to the term, (92), appearing in the Newtonian aerodynamics can be made with some confidence.

Making use of equation (92), and similar expressions considered previously we obtain equation (91) in the form

$$(93) \quad \begin{aligned} \delta W = & -\frac{1}{2} \rho v^2 \{ \delta p \}' \left( \sum_i [\gamma]_i' \iint_{S_i} F_1(x, y) \{f\} \left\{ \frac{\partial^2 f}{\partial x^2} \right\}' dx dy [\gamma]_i \{p\} \right. \\ & + \sum_i [\gamma]_i' \iint_{S_i} F_2(x, y) \{f\} \left\{ \frac{\partial f}{\partial x} \right\}' dx dy [\gamma]_i \{p\} \\ & + \sum_i [\gamma]_i' \iint_{S_i} F_3(x, y) \{f\} \left\{ \frac{\partial f}{\partial y} \right\}' dx dy [\gamma]_i \{p\} \\ & + \frac{1}{\sigma} \sum_i [\gamma]_i' \iint_{S_i} F_3(x, y) \{f\} \{f\}' dx dy [\gamma]_i \{\dot{p}\} \\ & \left. + \frac{1}{v^2} \sum_i [\gamma]_i' \iint_{S_i} F_4(x, y) \{f\} \{f\}' dx dy [\gamma]_i \{\ddot{p}\} \right) \end{aligned}$$



With evident definition of terms, (93) can be written more concisely as

$$(94) \quad \mathcal{W} = -\frac{1}{2}\rho v^2 \{ \mathcal{P} \}' \left( [L_1] \{ p \} + [L_2] \{ \dot{p} \} + [L_3] \{ p \} + \frac{1}{v} [L_4] \{ \dot{p} \} + \frac{1}{v^2} [L_5] \{ \ddot{p} \} \right)$$

If the transformation is made to modal coordinates we obtain

$$(95) \quad \mathcal{W} = -\frac{1}{2}\rho v^2 \{ \mathcal{Q} \}' \left( [C_R] \{ q \} + \frac{1}{v} [C_I] \{ \dot{q} \} + \frac{1}{v^2} [C_M] \{ \ddot{q} \} \right)$$

where

$$(96) \quad [C_R] = [\varphi]' ([L_1] + [L_2] + [L_3]) [\varphi]$$

$$(97) \quad [C_I] = [\varphi]' [L_4] [\varphi]$$

$$(98) \quad [C_M] = [\varphi]' [L_5] [\varphi]$$

Keith

Equation (95) is identical to equation (22) and all the statements made earlier concerning the applicability of the Hamiltonian approach will apply to equation (95). It is interesting to note that the quasi-steady assumption for Newtonian flow would give the aerodynamic influence coefficients as

$$(99) \quad [\Lambda] \equiv [L_2] + [L_3] \quad \text{which should be}$$

the limiting form of any quasi-steady theory as  $M \rightarrow \infty$ .

### III. Numerical Methods Applicable to Bodies and Low-Aspect Ratio Surfaces

In the "discrete" approach to aeroelasticity, the governing equations are satisfied at a finite number of points (panel points or collocation points). The approximation of a finite number-of-degrees-of-freedom requires some assumptions about the shape of the deformed body or surface in the region between points where discrete displacements are given. The problem is one of relating a continuous displacement function to a matrix of discrete displacements,  $p_i(t)$ . For a surface, the

general relation is one like

$$(100) \quad p_z(x, y, t) = \{f_1(x, y), f_2(x, y), \dots\} [\gamma]_i \{p(t)\}$$

valid for  $(x, y)$  on the region,  $S_i$

In this expression

$p_z(x, y, t)$

is the continuous displacement of the surface

$f_1(x, y), f_2(x, y)$

..... are some appropriate assumed functions

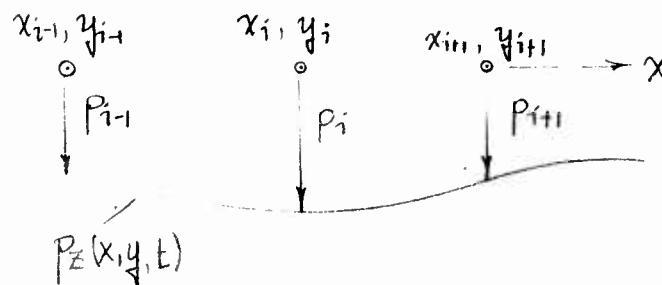
$[\gamma]_i$

is a matrix of interpolation coefficients associated with the assumed functions,  $f_j(x, y)$  which is, in general, different for different regions,  $S_i$ , of the surface

$\{p(t)\}$

is a matrix of displacements at discrete points, for example

$$p_i(t) = p_z(x_i, y_i, t)$$



To fix ideas, consider the trapezoidal interpolation in one dimension; it may be put in the form, (100):

$$(101) \quad p_z(x, t) = \{1, x\} [\gamma]_i \begin{bmatrix} p_{i-1} \\ p_i \end{bmatrix}$$

valid for  $x_{i-1} \leq x \leq x_i$

$$\text{where } [\gamma]_i = \begin{bmatrix} \frac{x_i}{x_i - x_{i-1}} & -\frac{x_{i-1}}{x_i - x_{i-1}} \\ -\frac{1}{x_i - x_{i-1}} & \frac{1}{x_i - x_{i-1}} \end{bmatrix}$$

In expanded form, (101) is

$$(102) \quad p_z(x, t) = p_{i-1}(t) + \frac{x - x_{i-1}}{x_i - x_{i-1}} (p_i(t) - p_{i-1}(t))$$

$$x_{i-1} \leq x \leq x_i$$

For application to surfaces where chordwise flexibility is important, it seems desirable to have an interpolation formula which may be used for

- (1) structural analyses, and
- (2) mass distributions, and
- (3) collocation of aerodynamic forces.

The "bilinear" formula, which is of the form

$$(103) \quad p_z(x, y, t) = \{1, x, y, xy\} [\gamma]_i \{p\}$$

has proven

to be adequate for distributing mass, but it gives a poor description of the angle of attack, and it cannot describe the curvature at all. Experience has shown that higher order interpolations give poor results for mass distributions. A fair amount of success is achieved by "assumed mode" methods which are interpolations, so to speak, that are valid over the entire surface.

$$(104) \quad p_z(x, y, t) = \{\varphi_1(x, y), \varphi_2(x, y) \dots\} [\zeta] \{p(t)\}$$

valid for  $(x, y)$  on the region,  $S_i$

This approach is difficult to generalize for production use, but has always given quick results for "hand" calculations.

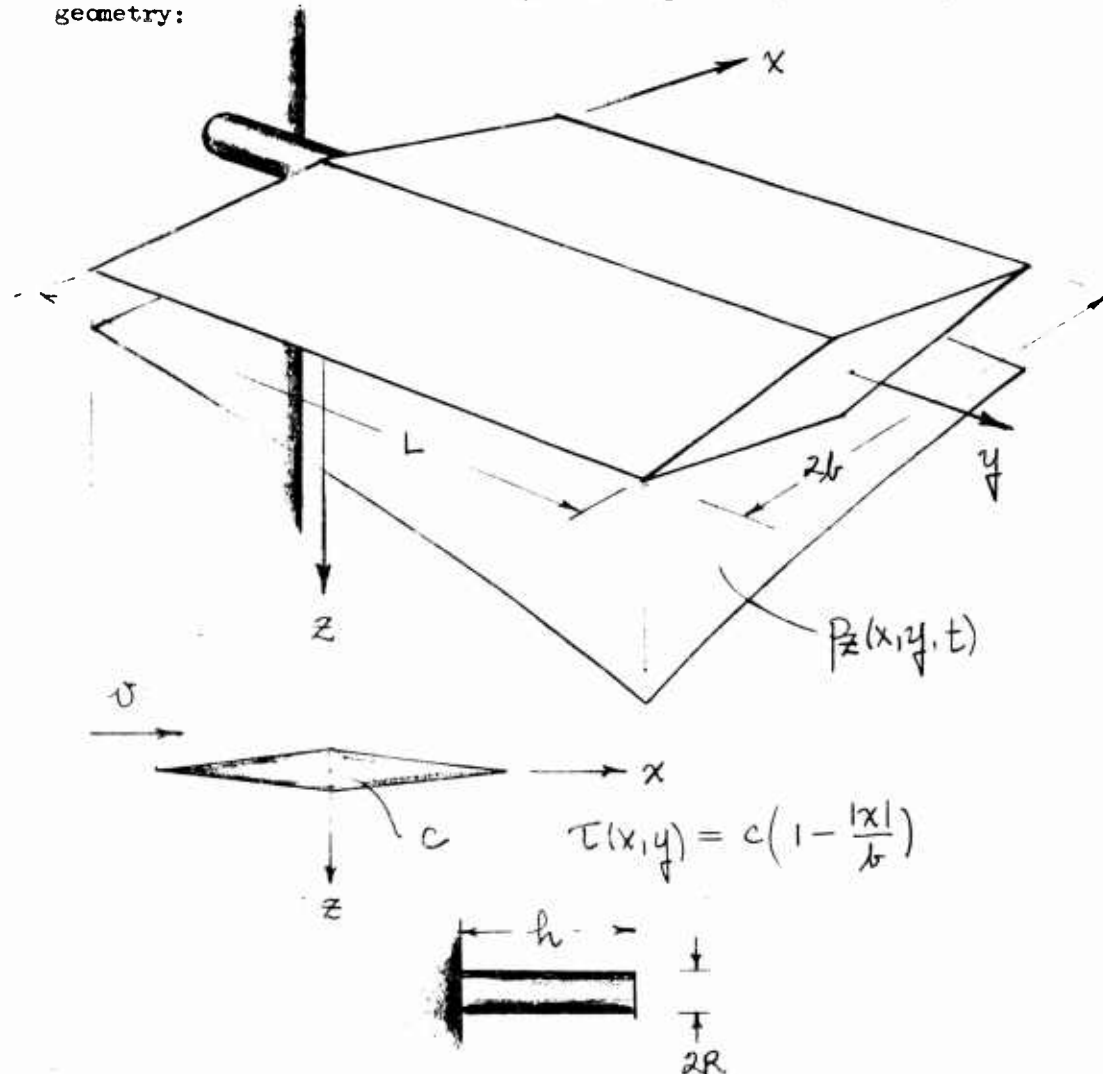
What has been sought is one, common interpolation formula that describes the displacement, slope, and curvature for use to distribute mass, define angle of attack, collocate arbitrary load distributions, and define the curvature accurately enough to be used in plate theory approaches to low-aspect ratio surfaces. A formula with the desired properties has been developed by J. A. Griffin, Jr. The interpolation, which he calls "diparabolic", is a cubic-four point (16-point in two dimensions) formula that is constrained in such a manner that the slope at the boundaries of adjacent regions is the same when described by the formula valid for either region. The formula then describes a surface with continuous displacement and continuous slope over the entire area of the surface. In one dimension, for equal intervals, the formula is

$$(105) \quad p_z(x, t) = p_z(\xi l + x_{i-1}, t) \\ = \{1 \quad \xi \quad \xi^2 \quad \xi^3\} \begin{bmatrix} 0 & 1 & 0 & 0 \\ -\frac{1}{2} & 0 & \frac{1}{2} & 0 \\ 1 & -2\xi & 2 & -\frac{1}{2} \\ -\frac{1}{2} & \frac{1}{2} & -\frac{1}{2} & \frac{1}{2} \end{bmatrix} \begin{bmatrix} p_{i-2}(t) \\ p_{i-1}(t) \\ p_i(t) \\ p_{i+1}(t) \end{bmatrix} \\ \xi = \frac{x - x_{i-1}}{x_i - x_{i-1}} = \frac{x - x_{i-1}}{l}$$

A generalization of this formula to two dimensions has been used in the illustrative example given in this paper. In this example, an equal interval grid was used for simplicity; however, a formula for oblique regions has been developed for use on swept surfaces with arbitrary leading and trailing edges.

#### IV. Illustration of the Methods Applied to the Aeroelastic Analysis of an All-movable Rectangular Wing

The methods indicated in parts I, II, and III will be illustrated in the analysis of a homogenous wing with the following geometry:



Keith

Flutter analyses using the Hamiltonian approach were performed for the rigid surface (three degrees-of-freedom) and for the elastic surface (five degrees-of-freedom). In the latter case plate theory was used to derive influence coefficients for the cantilevered surface. Ten cantilevered modes were coupled with the three modes of the rigid surface, and five coupled modes were retained for the analysis. See figures 1 through 6.

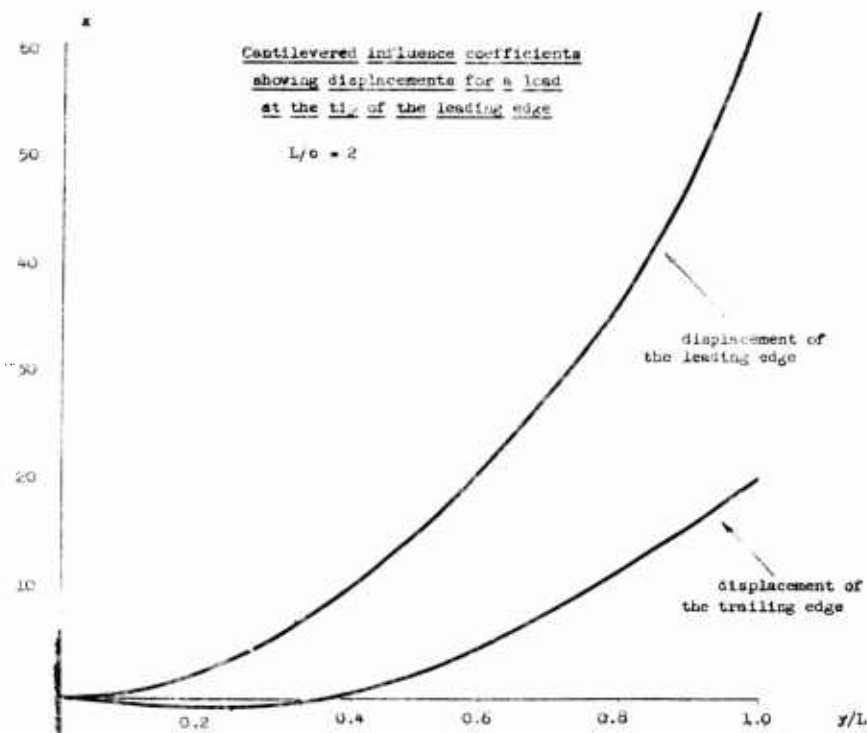
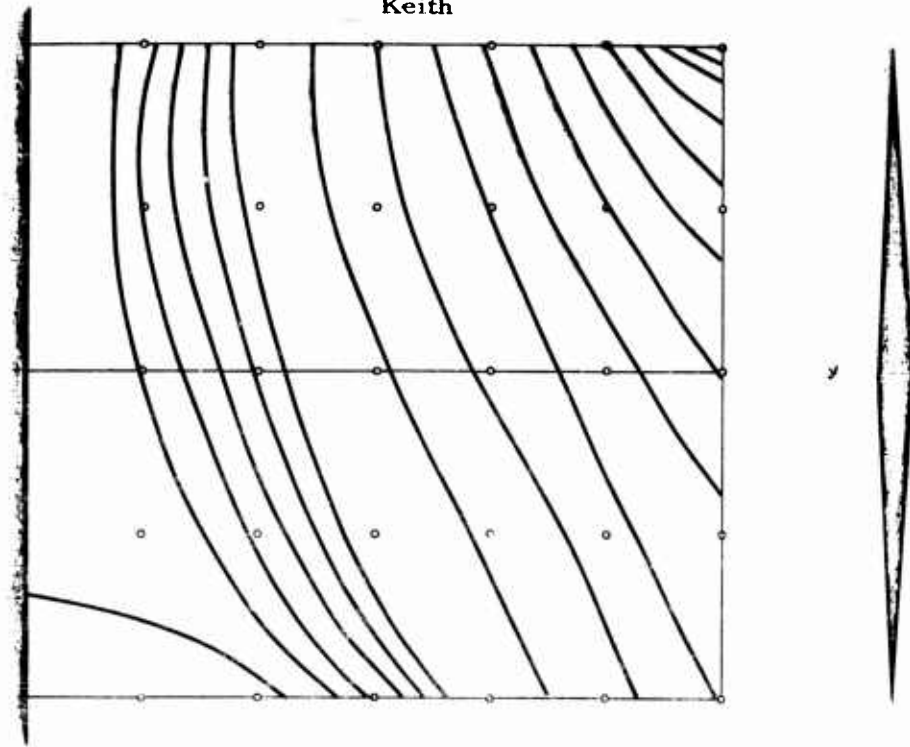
The diparabolic formula described in Part III was used in the elastic surface analysis to distribute the mass, stiffness and aerodynamic lift. Mass, stiffness, and aerodynamic influence coefficients were calculated referred to 40 panel point displacements. In the calculation of the flutter mode, illustrated in figures 7 and 8, use was made of a method to obtain eigen-vectors for the asymmetric eigen-value problem.

In both flutter analyses, the flight profile considered was one at constant altitude (sea level) and varying Mach number. The surface was considered to be solid aluminum. The aspect ratio,  $L/b$ , was 2.0 and the thickness gradient,  $c/b$ , was 0.1 (5% thick).

Airforces in the subsonic and supersonic range were calculated in the steady case for comparison. Three-dimensional methods were employed: kernel function in subsonic cases, and velocity potential method in supersonic case.

Figure 10 illustrates the application of the Hamiltonian method to the aeroelastic stability of a slender missile. Two rigid-body and two elastic modes of the elastic body were used. The plot shows the locus of the short period mode as airspeed is increased along a flight at constant altitude. At a very high dynamic pressure elastic body "buckling" divergence is indicated.

Keith





Keith

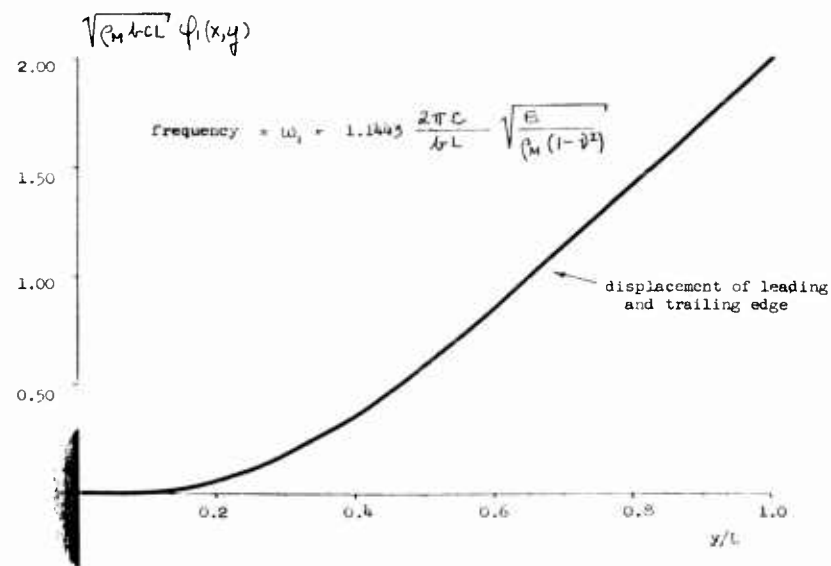
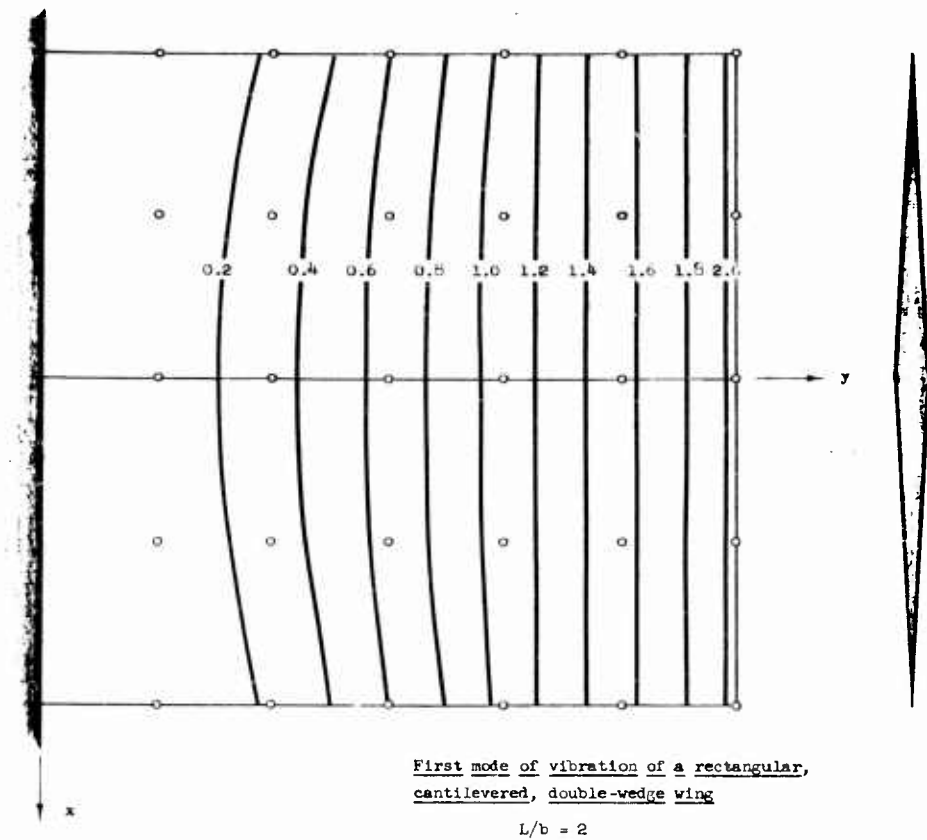
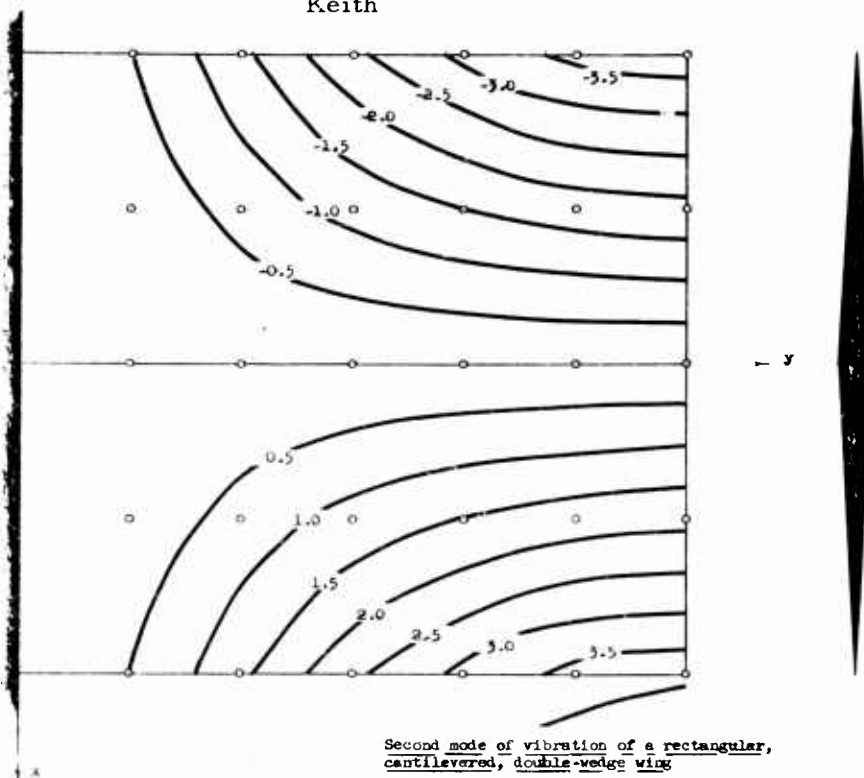
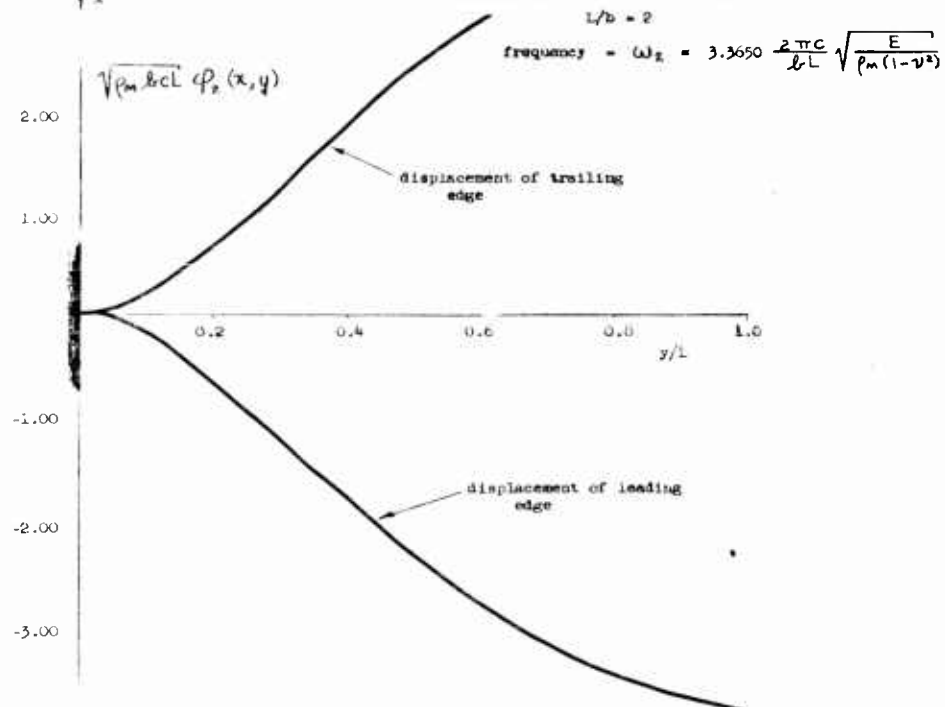


Fig. 2

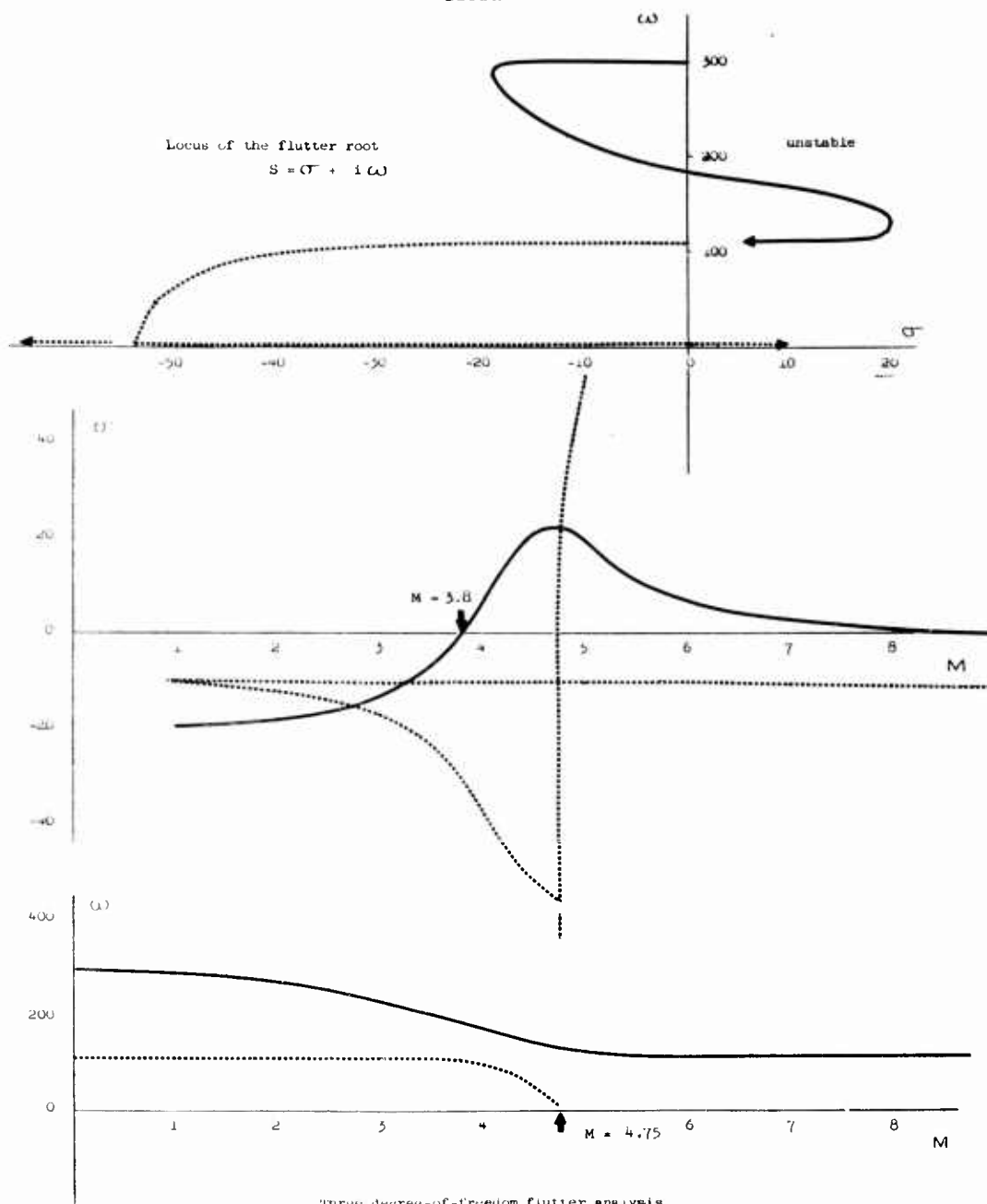
Keith



Second mode of vibration of a rectangular, cantilevered, double-wedge wing



Keith



Three degree-of-freedom flutter analysis  
of air-movable rectangular wing

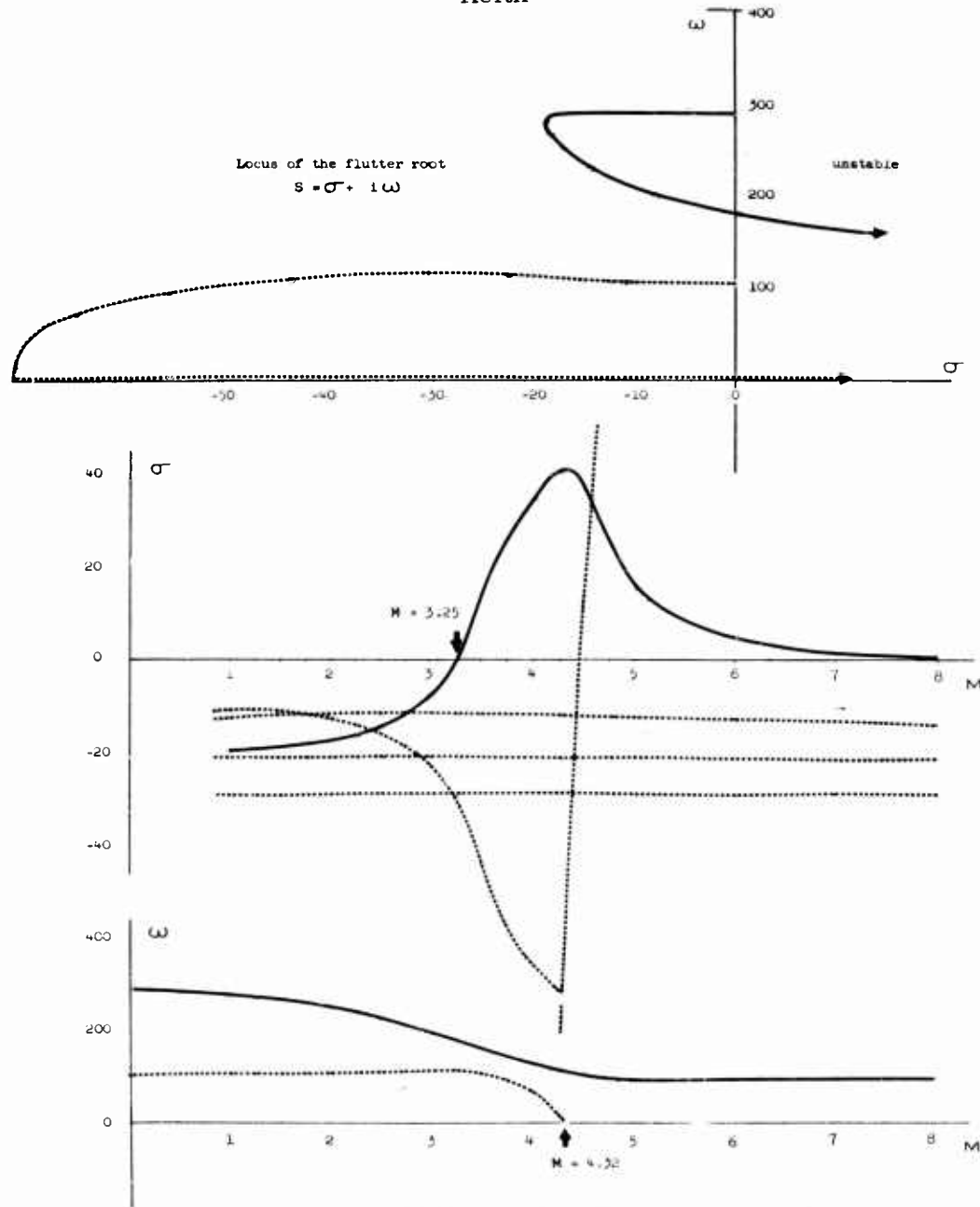
Flight profile is at  
constant altitude -  
constant temperature

$$\rho = 4.428 \times 10^{-5} \text{ lb}_m/\text{in}^3$$

Still air frequencies:

$$\begin{aligned} \omega_1 &= 112 \text{ sec.}^{-1} & (17.85 \text{ c.p.s.}) \\ \omega_2 &= 299 \text{ sec.}^{-1} & (47.60 \text{ c.p.s.}) \\ \omega_3 &= 5400 \text{ sec.}^{-1} & (860.0 \text{ c.p.s.}) \end{aligned}$$

Keith



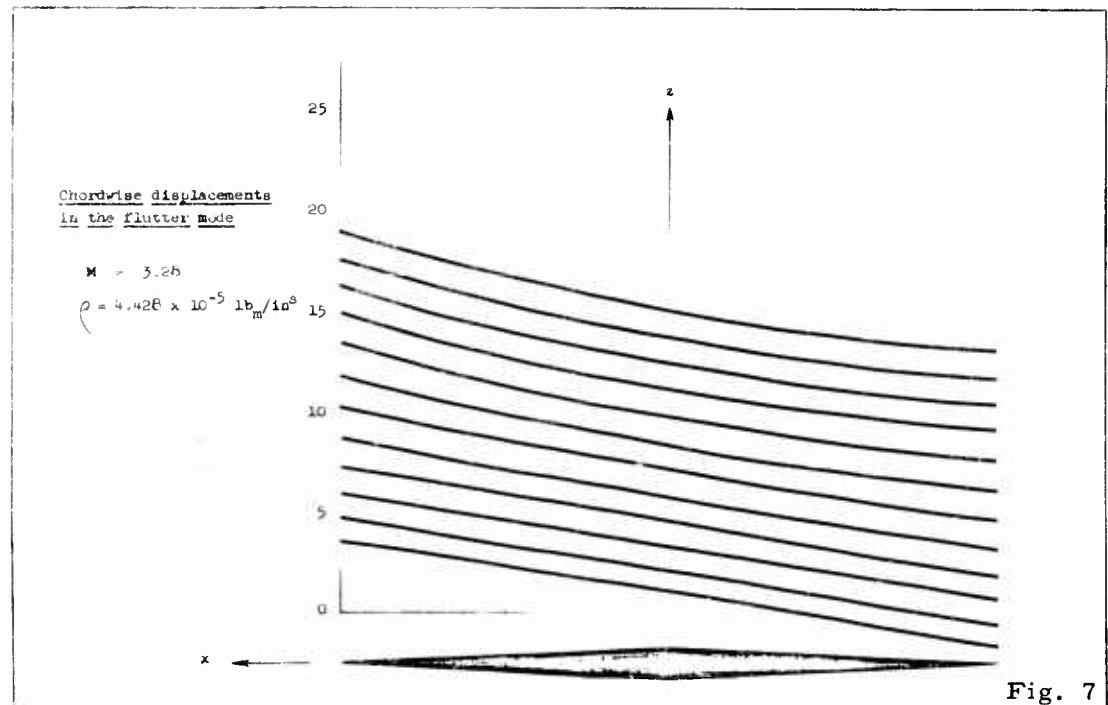
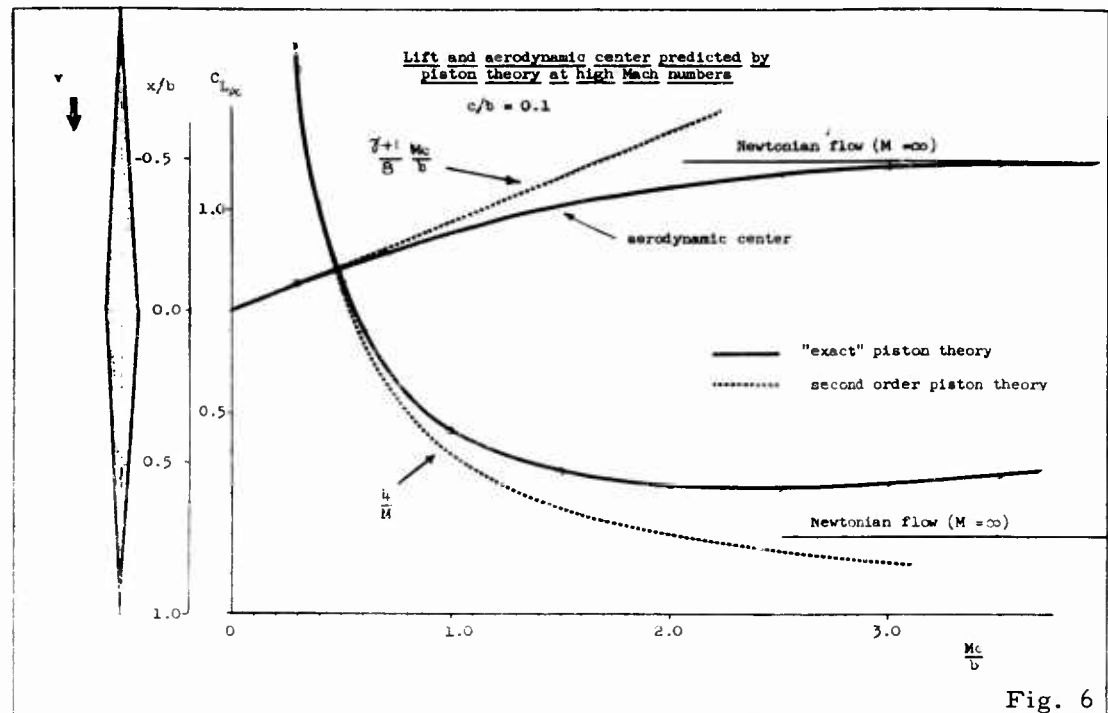
Five degree-of-freedom flutter analysis  
of all-movable rectangular wing

Flight profile is at  
constant altitude (sea level),  
constant temperature

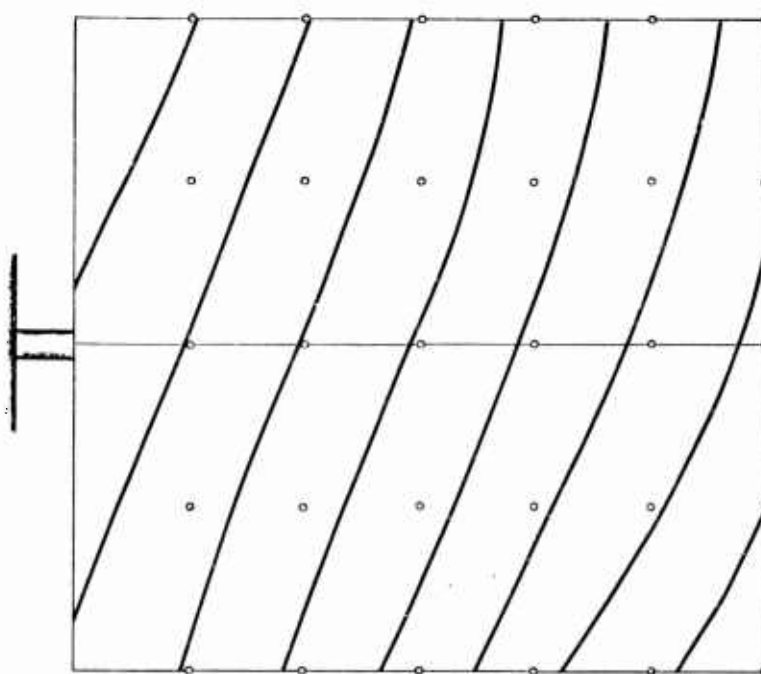
$$\rho = 4.428 \times 10^{-5} \text{ lb}_m/\text{in}^3$$

Still air frequencies:

$\omega_1 =$	$105.9 \text{ sec.}^{-1}$	(16.9 c.p.s.)
$\omega_2 =$	$288.1 \text{ sec.}^{-1}$	(45.9 c.p.s.)
$\omega_3 =$	$1225 \text{ sec.}^{-1}$	(195.1 c.p.s.)
$\omega_4 =$	$1711 \text{ sec.}^{-1}$	(272.4 c.p.s.)
$\omega_5 =$	$3238 \text{ sec.}^{-1}$	(513.6 c.p.s.)



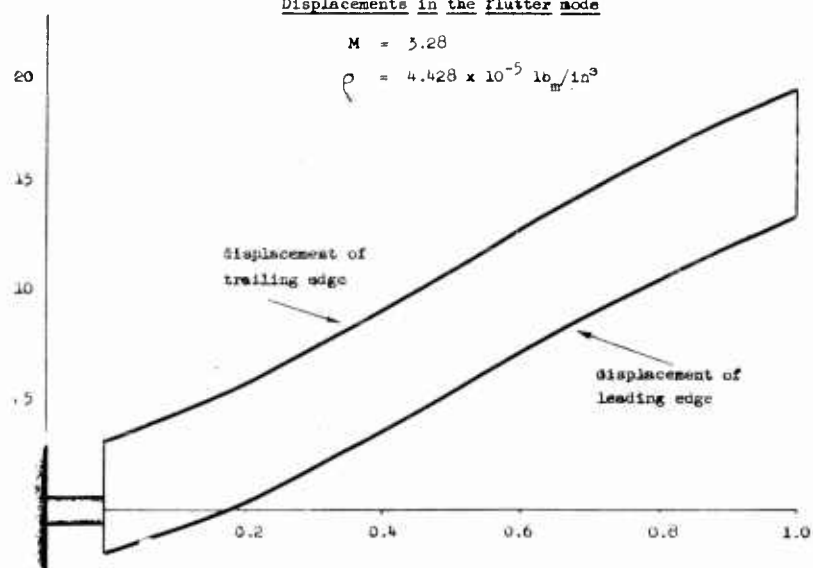
Keith

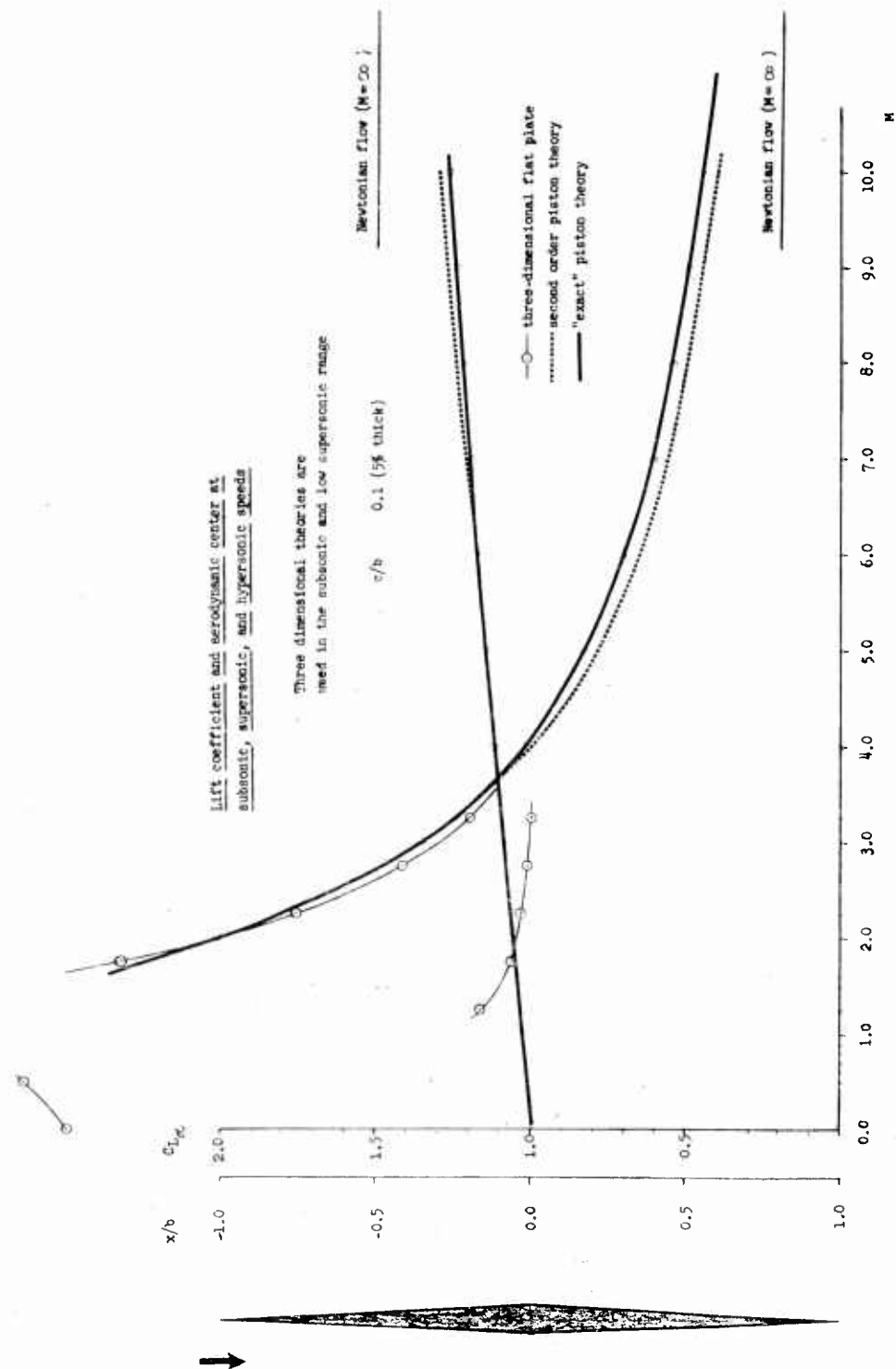


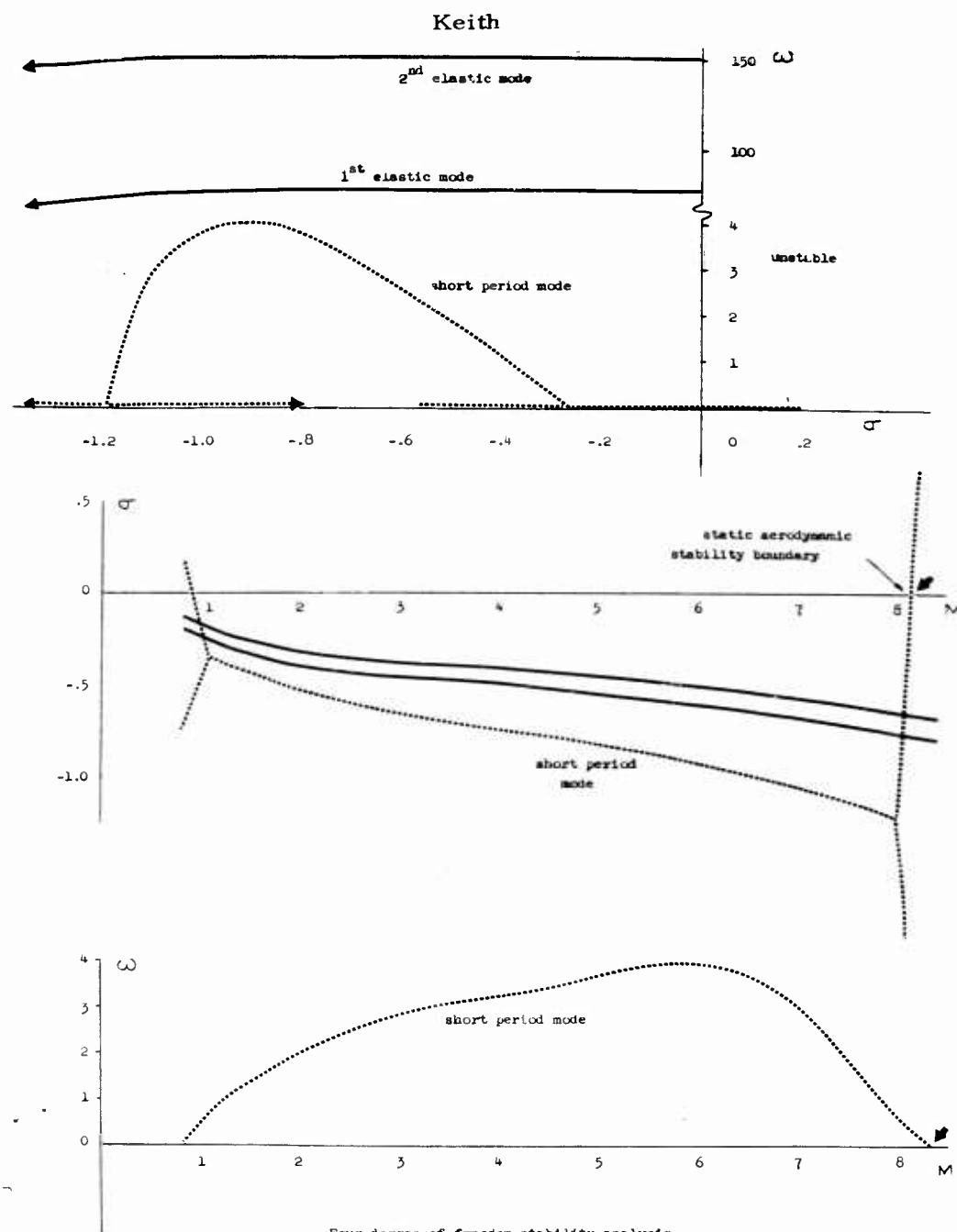
Displacements in the flutter mode

$$M = 5.28$$

$$\rho = 4.428 \times 10^{-5} \text{ lb}_m/\text{in}^3$$







Four degree-of-freedom stability analysis  
of a slender elastic body

Flight profile at  
constant altitude

$$\rho = 4.488 \times 10^{-5} \text{ lb}_m/\text{in}^3$$

(sea level)

$$\omega_1 = 0$$

$$\omega_2 = 0$$

$$\omega_3 = 12.646 \text{ c.p.s.}$$

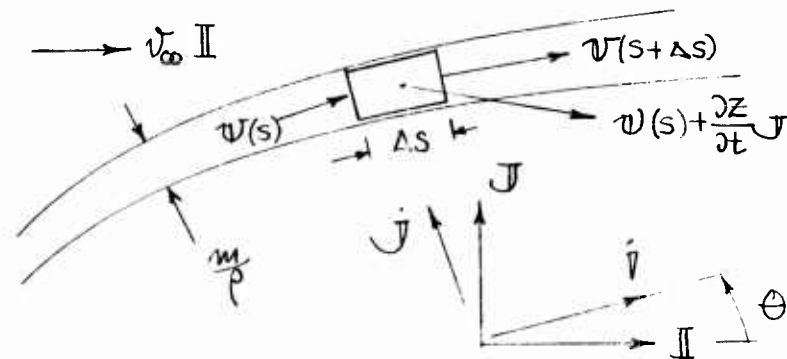
$$\omega_4 = 24.063 \text{ c.p.s.}$$



References

1. Ames, Joseph, and Murnaghan, Francis: Theoretical Mechanics, Dover, 1957.
2. Ashley, H., and Zartarian G.: Supersonic Flutter Trends as Revealed by Piston Theory Calculations, WADC TR-58-74m, May, 1958.
3. Bisplinghoff et al: M.I.T., Department of Aeronautical Engineering, Aeroelasticity, June, 1958, Summer Lecture Courses.
4. Foss, K. A.: Coordinates Which Uncouple the Equations of Motion of Damped Linear Dynamic Systems, Journal of Applied Mechanics, September, 1958.
5. Frazer, R. A., Duncan, W. J., and Collar, A. R.: Elementary Matrices, Cambridge University Press, 1950.
6. Griffin, J. A.: A Diparabolic Method of Four-Point Interpolation, Journal of the Aeronautical Sciences, Vol. 28 No. 2, Reader's Forum, February, 1961.
7. Harder, R. L., et al: Supersonic Flutter Analyses Including Aerodynamic Heating Effects, WADC TR-59-559, February, 1960.
8. Hayes, W. D., and Probstein, R. F.: Hypersonic Flow Theory, Academic Press, New York, 1959.
9. Kaufman, L. G., II, and Scheuing, R. A.: An Introduction to Hypersonics, Grumman Aircraft Engineering Corporation Research Department Report RE-82, October, 1956, (Confidential)
10. Keith, J. S.: Notes on Dynamics and Aeroelasticity, Chance Vought Report EOR-13103, August 1960.
11. Keith J. S.: IBM Program for Integration Of Subsonic Integral Equation, Chance Vought Report AER-EI-TM-1, January, 1961.
12. Landahl, M. T.: Unsteady Flow Around Thin Wings at High Mach Numbers, Journal of the Aeronautical Sciences, Vol. 24, No. 1, January, 1957.
13. Lighthill, M. J.: Oscillating Airfoils at High Mach Number, Journal of the Aeronautical Sciences, Vol. 20, No. 6, June, 1953.

14. Morgan, H. G., Runyan, H. L., and Huckel, V.: Theoretical Considerations of Flutter at High Mach Number, Journal of the Aeronautical Sciences, June, 1958.
15. Van Dyke, M. D.: Supersonic Flow Past Oscillating Airfoils Including Non-linear Thickness Effects, NACA Report 1183, 1954.
16. Watkins, C., Runyan, H., and Woolston, D.: Kernal Function of the Integral Equation Relating the Lift and Downwash Distributions of Oscillating Finite Wings in Subsonic Flow, NACA Report 1234, 1955.
17. Zartarian, G.: Unsteady Airloads on Pointed Airfoils and Slender Bodies at High Mach Numbers, WADC TR-59-583, December, 1959.
18. Zartarian G., Hsu, P. T., and Ashley, H.: Dynamic Airloads and Aeroelastic Problems at Entry Mach Numbers, Journal of the Aeronautical Sciences, preprint paper number 60-32.

AppendixThe equations of unsteady Newtonian flow

Assume that the fluid has the velocity  $U_{\infty} \mathbf{I}$  everywhere except in the thin layer on the positive side of the surface  $Z(x, y, t)$

(1A)

$$\begin{aligned} U &= U_{\infty} \mathbf{I}, & z > Z(x, y, t) \\ &= U(s) + \frac{\partial Z}{\partial t} \mathbf{J}, & z = Z(x, y, t) \\ &= 0, & z < Z(x, y, t) \end{aligned}$$

where

$$U(s) = U(s) \dot{\mathbf{I}}$$

The pressures corresponding to this velocity field can be found from the inviscid equations for momentum and continuity

$$(2A) \quad \frac{\partial p}{\partial t} + \nabla \cdot (p \mathbf{U}) = 0$$

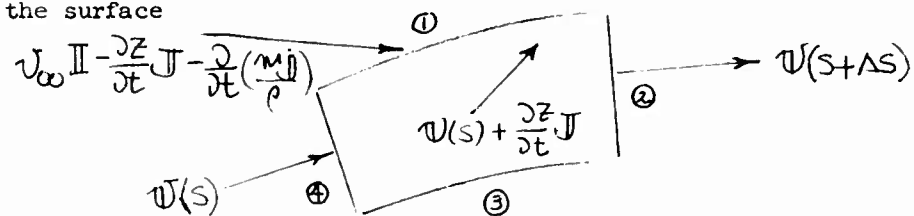
$$(3A) \quad \nabla p + \rho \frac{d\mathbf{U}}{dt} = 0$$

By the use of the divergence theorem these may also be expressed in the integral form:

$$(4A) \text{ continuity} \quad \int_V \frac{\partial \rho}{\partial t} dv + \oint_S \rho \mathbf{v} \cdot d\mathbf{S} = 0$$

$$(5A) \text{ momentum} \quad \int_V \frac{\partial}{\partial t} (\rho \mathbf{v}) dv + \oint_S (p \mathbf{\hat{I}} + \rho \mathbf{v} \mathbf{v}) \cdot d\mathbf{S} = 0$$

These are to be applied to a control volume moving with the surface



The velocity of the volume is

$$\mathbf{V}(S) + \frac{\partial Z}{\partial t} \mathbf{J}$$

The velocities relative to the faces of the volume are

$$(6A) \quad \begin{aligned} \mathbf{V}_1 &= \mathbf{V}_\infty \mathbf{II} - \frac{\partial Z}{\partial t} \mathbf{J} - \frac{\partial}{\partial t} \left( \frac{m}{\rho} \mathbf{j} \right) \\ \mathbf{V}_2 &= \mathbf{V}(S + \Delta S) \\ \mathbf{V}_3 &= 0 \\ \mathbf{V}_4 &= \mathbf{V}(S) \end{aligned}$$

Application of relations (6A) to the control volume using the integral relations (4A) and (5A) and letting  $\Delta S \rightarrow 0$  yields

$$(7A) \text{ continuity} \quad \frac{\partial}{\partial S} (m \mathbf{V}) + \rho_\infty \mathbf{V}_\infty \left( \mathbf{II} \cdot \mathbf{j} - \frac{1}{V_\infty} \frac{\partial Z}{\partial t} \mathbf{J} \cdot \mathbf{j} - \frac{1}{V_\infty} \frac{\partial}{\partial t} \left( \frac{m}{\rho} \right) \right) + \frac{m}{\rho} \frac{\partial \rho}{\partial t} = 0$$

(8A) momentum

$$\begin{aligned} \frac{\partial}{\partial s} \left( \frac{m}{\rho} p + m v^2 \right) \dot{i} + \left( \frac{m}{\rho} p + m v^2 \right) \frac{1}{R} \dot{j} - (p - p_\infty) \dot{j} \\ + \rho_\infty v_\infty^2 \left( 1 - \frac{1}{v_\infty} \frac{\partial z}{\partial t} \mathcal{J} - \frac{1}{v_\infty} \frac{\partial}{\partial t} \left( \frac{m}{\rho} \mathcal{J} \right) \right)^2 \dot{j} \\ + \frac{m}{\rho} \frac{\partial}{\partial t} \left( \rho w + \rho \frac{\partial z}{\partial t} \mathcal{J} \right) = 0 \end{aligned}$$

where

$$v = v \dot{i}, \quad \frac{1}{R} = \frac{\partial \theta}{\partial s}$$

If the assumption is made that

$$\frac{\theta}{R} \sim 0, \quad \frac{m}{\rho} \sim 0, \quad \frac{\partial}{\partial t} \left( \frac{m}{\rho} \right) \sim 0$$

the above equations reduce to

$$(9A) \quad p - p_\infty = \frac{m v^2}{R} + \rho_\infty v_\infty^2 \left( \tan \theta + \frac{1}{v_\infty} \frac{\partial z}{\partial t} \right)^2 \cos^2 \theta + m \frac{\partial^2 z}{\partial t^2}$$

$$(10A) \quad \frac{\partial}{\partial x} (m v) = \rho_\infty v_\infty \left( \tan \theta + \frac{1}{v_\infty} \frac{\partial z}{\partial t} \right)$$

$$(11A) \quad \frac{\partial}{\partial x} (m v^2) = \rho_\infty v_\infty^2 \left( \cos \theta - \frac{1}{v_\infty} \sin \theta \frac{\partial z}{\partial t} \right) \left( \tan \theta + \frac{1}{v_\infty} \frac{\partial z}{\partial t} \right)^2 + m \frac{\partial^2 z}{\partial t^2} \tan \theta$$

Integration of (10A) over top and bottom surfaces gives

$$(12A) \quad m = \frac{\rho_\infty \tau}{2 \cos \theta}$$

Neglect of the term, 
$$\frac{\sin \theta \frac{\partial^2 Z}{\partial t^2} \left( \tan \theta + \frac{1}{v_\omega} \frac{\partial \xi}{\partial t} \right)}{v_\omega}$$

results in

$$(13A) \quad v = v_\omega \cos \theta$$

In Summary

$$(14A) \quad p - p_\omega = \frac{mv^2}{R} + \rho_\omega v_\omega^2 \left( \tan \theta + \frac{1}{v_\omega} \frac{\partial \xi}{\partial t} \right)^2 \cos^2 \theta + m \frac{\partial^2 Z}{\partial t^2}$$

where  $m = \frac{\rho_\omega \tau}{2 \cos \theta}$  and  $v = v_\omega \cos \theta$

AN INDICIAL FLUTTER ANALYSIS PROCEDURE FOR HYPERSONIC DELTA WINGS

Bernard Mazelsky, Consultant  
and  
Harry B. Amey, Jr.

Aerojet-General Corporation

ACKNOWLEDGEMENT:

This work was supported by the United States Air Force under Contract No. AF 33(616)-7420, for the Dynamics Branch, Wright Air Development Division under the technical cognizance of Lt. Thor Snaring.

SUMMARY

A proposed method of flutter analysis which utilizes indicial functions to represent the unsteady aerodynamics is described. The basic concepts are illustrated in detail for a two dimensional wing section free to pitch and plunge; the extension to a spanwise distorting wing is then briefly discussed. A review follows of the significant aerodynamic parameters which are pertinent to a highly swept hypersonic delta wing. The conclusion is reached that the principle factor required for adequate prediction of flutter (other than detailed knowledge of the chordwise and spanwise modes of distortions) is knowledge of the steady and quasi-steady aerodynamic influence coefficients. The unsteady contributions, on the other hand, are shown to have a negligible effect on the flutter characteristics. The powerful influence of chordwise distortions is illustrated by a comparison of the flutter dynamic pressure for a wing experiencing semi-rigid degrees of freedom (pitch and roll) and a uniform elastic wing cantilevered at the root.

Finally a unique force test model technique is proposed to determine the steady state influence coefficients for arbitrary chordwise and spanwise distortions. The procedure allows the analyst to determine experimentally a complete  $9 \times 9$  aerodynamic influence coefficient matrix.



TABLE OF SYMBOLS

$h, \theta$	=	structural coordinates of wing
$\alpha$	=	angle of attack
$q$	=	pitching velocity
$V$	=	velocity
$t$	=	time
$s$	=	non dimensional time $Vt/\bar{c}$
$c(\eta)$	=	local chord of wing
$\bar{c}$	=	mean aerodynamic chord
$L_{\alpha}, L_q$	=	total and spanwise lift on wing, respectively
$M_{ra}, M_{ra}$	=	total and spanwise moment on wing, respectively, about reference axis
$\rho$	=	density of air
$C_{L_{\alpha}}$	=	lift curve slope due to angle of attack
$C_{L_q}$	=	lift curve slope due to pitching velocity
$C_{M_{\alpha}}$	=	moment curve slope due to angle of attack
$C_{M_q}$	=	moment curve slope due to pitching velocity
$ra$	=	reference axis
$x_o$	=	aerodynamic moment center
$x_l$	=	aerodynamic rotation center
$k$	=	reduced frequency $\omega c/V$
$z_c$	=	height of cambered surface
$p$	=	$d/ds$

TABLE OF SYMBOLS - CONTINUED

$Q_{L\alpha}$	= influence matrix of $C_{L\alpha}$
$Q_{m q_{x_0} x_1}$	= influence of matrix $C_{M q_{x_0} x_1}$
$\omega_1$	= first fundamental frequency of wing
$\omega_2$	= second fundamental frequency of wing
$\omega_f$	= flutter frequency
$\lambda$	= dynamic pressure parameter
$m$	= local mass of wing
$x^i$	= mode shape corresponding to i th mode
$S$	= wing area
$\ell$	= rolling moment

### INTRODUCTION

The problem of predicting the unsteady aerodynamic forces on deforming wings has been the subject of many investigations. Even the most developed of these methods such as the NASA Kernel Function require considerable calculations, all of which must be repeated each time a planform parameter, Mach number or reduced frequency is changed. The most significant drawback, however, is that any method of prediction based on theory alone is always open to question. In the past the principal technique of correlating theory with experiment has been the use of flutter models tested over a wide range of configurations, Mach numbers, and other pertinent parameters such as center-of-gravity location. The experimental results obtained from these tests are then compared with various theoretical predictions from which an estimate is made concerning the applicability of each of the theories. Unless the difference between experimental and theoretical predictions are carefully scrutinized in an effort to understand the nature of the discrepancies, the principal result obtained is limited to the determination of the degree of conservatism or unconservatism of the particular aerodynamic theory used. This knowledge is further limited or restricted to the particular configuration and/or mode of flutter under consideration. If, however, the unsteady aerodynamic influence matrix is studied to determine the most pertinent properties, insight may be obtained to determine how the theoretical aerodynamics can best be amended or altered to yield better flutter correlation. The procedure which the authors selected was to isolate the steady state properties from the unsteady and the important from the unimportant by utilizing an indicial function approach and compatible axes transformations.

This procedure has several additional advantages in that the representation of the unsteady aerodynamic forces on analog computers is easily accomplished with simple circuits. For practical configurations of hypersonic flight, where the aspect ratio is very low ( $A < 1.5$ ), the most significant aerodynamic properties are those associated with steady and quasi-steady flow. Fortunately, the "indicial function" procedure also allows the analyst to utilize experimental measurements obtained from specially designed rigid force models in such a manner that the complete unsteady aerodynamic influence coefficient matrix is obtained for arbitrary chordwise and spanwise distortions.

The purpose of this paper is to provide a brief yet comprehensive dissertation of the basic principles involved together with a new experimental technique of measuring the steady and quasi-steady aerodynamic influence coefficient matrix for hypersonic low aspect ratio wings.

## BASIC CONCEPTS ON THE INDICIAL FUNCTION PROCEDURE

For simplicity, consider first the case of a rigid wing having two degrees of freedom. Although structural or space coordinates are more often used in flutter analysis, the aerodynamics are more naturally expressed with stability coordinates. The use of the stability coordinates facilitates both the indicial representation of the unsteady problem and the replacement of theoretical stability derivatives with experimentally determined values from wind tunnel tests. The relationship between the structural and stability coordinates (which are defined in Figure 1) is as follows:

$$\alpha = \theta - \frac{1}{V} \frac{dh}{dt} = \theta - \frac{d}{ds}(h/\bar{c}) \quad (1)$$

$$q = \frac{d\theta}{ds} \quad (2)$$

where  $V$  is the forward velocity and  $s$  is the distance travelled in chord lengths ( $s = \frac{Vt}{\bar{c}}$ ).

In addition to steady and quasi-steady motions one must idealize the description of the transient motions such that arbitrary transient behavior can be simulated accurately. Of the two representations usually available, the indicial and the oscillatory, the former is selected because it is more easily adapted to the general unsteady problem and unlike the oscillatory representation is accurate even when the lifting surface is not in pure harmonic motion. This accuracy may be important when the lifting surface is lightly damped and appreciable variations in structural damping are present in the system.

The generalization of the indicial representation requires convolution integrals of the type

$$\int_0^t C(t-\tau) \frac{dw(\tau)}{d\tau} d\tau$$

which can be abbreviated using the notation  $C(t) * \frac{dw(t)}{dt}$ ; this allows the analyst to write a complete set of equations for the lift and moment defined in Figure 1 as follows:

$$L = \frac{1}{2} \rho V^2 S \left\{ C_{L_\alpha}(s) * \frac{d\alpha(s)}{ds} + C_{L_{q_{ra}}}(s) * \frac{dq(s)}{ds} \right\} \quad (3)$$

$$M_{ra} = \frac{1}{2} \rho V^2 S \bar{c} \left\{ C_{M_\alpha}(s) * \frac{d\alpha(s)}{ds} + C_{M_{q_{ra}}}(s) * \frac{dq(s)}{ds} \right\} \quad (4)$$

where  $L$ ,  $M$ ,  $\alpha$ , and  $q$  are the lift, moment, angle of attack, and pitching velocity all relative to the reference axis,  $ra$ .

Equations (3) and (4), if left in their present form, are difficult to work with, especially if an analog computer is utilized. First, a large number of transient terms are required which for analog simulation involves complexity; second, since many of these terms are equally important, their resulting effect when opposing each other would be inaccurately represented due to the analog's inherent limitation to measure the small differences of large numbers. Finally, the retention of physical concepts, which is one of the analog's chief virtues, is difficult to achieve.

In order to circumvent these disadvantages, moments will be referred to the moment center defined as:

$$x_o/\bar{c} = -C_{M_\alpha} / C_{L_\alpha} - c_o/\bar{c} \quad (5)$$

and pitching effects to a rotation center defined as

$$x_l/\bar{c} = C_{L_{q_{apex}}} / C_{L_\alpha} - c_o/\bar{c} \quad (6)$$

where the subscript *apex* refers to the apex of the wing and  $c_o$  is the leading edge location. Using these two centers the following lift and pitching moment equations result:

$$\begin{pmatrix} M_{\alpha_{ra}} \\ M_{q_{ra}} \end{pmatrix} = \begin{pmatrix} M_{\alpha_{x_o}} \\ M_{q_{x_o}} \end{pmatrix} + (ra - x_o) \begin{pmatrix} L_\alpha \\ L_{q_{ra}} \end{pmatrix} \quad (7)$$

$$\begin{pmatrix} L_{q_{ra}} \\ M_{q_{ra}} \end{pmatrix} = \begin{pmatrix} L_{q_{x_l}} \\ M_{q_{x_l}} \end{pmatrix} + \begin{pmatrix} L_\alpha \\ M_{\alpha_{ra}} \end{pmatrix} \left( \frac{x_l - ra}{\bar{c}} \right) \quad (8)$$

This choice of axes has the advantage of making all important contributions derivable from two basic transients,  $L_{\alpha}(s)$  and  $M_{\alpha x_0}(s)$ ; the remaining transients,  $L_{\alpha x_1}(s)$  and  $M_{\alpha x_1}(s) - M_{\alpha x_0}(\infty)$ , both of which vanish in steady flow, are generally small.

Substituting of equations (7) and (8) into (3) and (4) and collecting similar transient terms results in the following expressions:

$$L = \frac{1}{2} \rho V^2 S \left\{ C_{L_{\alpha}}(\infty) \frac{C_{L_{\alpha}}(s)}{C_{L_{\alpha}}(\infty)} * \left( \frac{d\alpha(s)}{ds}_{ra} + \frac{x_1 - ra}{\bar{c}} \frac{dq(s)}{ds} \right) + \epsilon(s) \right\} \quad (9)$$

$$M_{ra} = \bar{c} \left( \frac{ra - x_0}{\bar{c}} \right) L + \frac{1}{2} \rho V^2 S \bar{c} \left\{ C_{M_{q_{x_0 x_1}}}(\infty) q(s) + C_{M_{\alpha_{x_0 x_1}}}(s) * \right. \quad (10)$$

$$\left. \left( \frac{d\alpha(s)}{ds}_{ra} + \frac{x_1 - ra}{\bar{c}} \frac{dq(s)}{ds} \right) + \delta(s) \right\}$$

where

$$\epsilon(s) = C_{L_{q_{x_1}}}(s) * \frac{dq}{ds}$$

$$\delta(s) = (C_{M_{q_{x_0 x_1}}}(s) - C_{M_{q_{x_0 x_1}}}(\infty)) * \frac{dq}{ds}$$

The equations consist of 8 basic aerodynamic quantities of which 4 are steady or quasi-steady and 4 are unsteady; two of the four unsteady terms have been made insignificantly small for engineering purposes. On the basis of continued use of these aerodynamic equations the authors have found that of the remaining 6 significant parameters, two have shown to be the most important in predicting the stability, namely the lift curve slope,  $C_{L_{\alpha}}$ , and the aerodynamic center  $x_0/\bar{c}$ .

#### STEADY AND QUASI-STEADY PARAMETERS

It should be noted that all of the steady and quasi-steady quantities can be determined experimentally through the proper use of wind tunnel models. The commonly measured quantity is  $C_{L_{\alpha}}$ , the lift curve slope; this quantity determines the order or level of

the aerodynamic forces with respect to the inertial or mechanical forces acting in the system. The coefficient  $C_{M \dot{x}_1}$  is not in general

measured directly in wind tunnel tests since it is usually difficult to separate out from other aerodynamic parameters, especially if a "damping-in-pitch" test technique is used. Although  $C_{M \dot{x}_1}$  is a

quasi-steady coefficient, it can be measured directly from a steady state test quite accurately using a parabolically cambered wing section. If  $z_c$  is the maximum parabolic camber height, then the rate of downwash change in the stream wise direction corresponds to the pitch rate as follows:

$$\partial z_c / \partial t = k \dot{\theta} \quad (11)$$

where  $k$  is the reduced frequency of oscillation, ( $k = \frac{\omega c}{V}$ ). As indicated by the subscript the corresponding pitching moment must be measured at (1) either the aerodynamic center corresponding to the flat wing or (2) at an angle of attack corresponding to no lift on the wing. In other words the  $C_{M \dot{x}_1}$  parameter represents a pure

aerodynamic couple acting on the wing.

The quantities  $x_{o/c}$  and  $x_{l/c}$  are respectively the optimum moment and rotation centers. The former is probably the most important quantity affecting the flutter stability. The latter on the other hand has been found in practically all known instances to be relatively unimportant. Wind tunnel measurements of  $C_{L\alpha}$  and  $C_{M\alpha}$

are used to obtain  $x_{o/c}$  in the usual way. The parameter  $x_{l/c}$  can be obtained from the parabolically cambered wing by rotating the wing until the lift vanishes and measuring the point on the mean aerodynamic chord at which the angle of attack is zero; this distance when measured from the leading edge is  $x_{l/c}$ .

#### UNSTEADY PARAMETERS

Prior to a discussion of the significance or importance of the unsteady quantities, it is first convenient to explore the various methods available to represent the indicial functions. For generality consider any aerodynamic coefficient,  $C$ , on a surface due to an

arbitrary downwash,  $w$ . If the response due to a unit change in downwash (herein after denoted as the indicial response) is  $C_w(s)$ , the coefficient for any arbitrary form of  $w(s)$  is

$$C(s) = C_w(s)w(0) + \int_0^s C_w(s-\tau) \frac{dw(\tau)}{d\tau} d\tau \quad (12)$$

The coefficient  $C(s)$  can be written (under certain limitations which will be defined later) using a series of aerodynamic derivatives as follows:

$$C(s) = C_w w(s) + C_{\dot{w}} \dot{w}(s) + C_{\ddot{w}} \ddot{w}(s) + \dots \quad (13)$$

Taking the Laplace transform of both (12) and (13) and equating the results gives:

$$p C_w(p) w(p) = (C_w + p C_{\dot{w}} + p^2 C_{\ddot{w}} + \dots) w(p) \quad (14)$$

where  $p = \frac{d}{ds}$ . The coefficients of the powers of  $p$ , namely  $C_w$ ,  $C_{\dot{w}}$ ,  $C_{\ddot{w}}$ , ...etc., can be substituted directly into the flutter determinant provided the series converges rapidly. If terms up to and including the second derivative are included, closed form solutions for the flutter dynamic pressure and frequency are available, which in turn can lead to the development of rational flutter index parameters. If the series given by equation (14) does not converge rapidly, alternate procedures must be used which unfortunately may or may not provide clear physical insight to the problem. In order to study convergence of the series, assume that the indicial function  $C_w(s)$  approaches  $C_w(\infty)$  asymptotically using the following exponential form:

$$C_w(s) = C_w(\infty) (1 - a e^{-bs}) \quad (15)$$

From equation (14)

$$p \int_0^\infty e^{-ps} [C_w - C_w(s)] ds = -p C_{\dot{w}} - p^2 C_{\ddot{w}} - \dots - p^n C_{w^{(n)}} \quad (16)$$

or expanding in powers of  $p$

$$\frac{(-)^{n-1}}{(n-1)!} \int_0^\infty s^{n-1} [C_w - C_w(s)] ds = -C_{w^{(n)}} \quad (17)$$

since  $C_w(s) = C_w(\infty) (1 - a e^{-bs})$ , then

$$C_{w^{(n)}} = -\frac{(-)^n a}{(n-1)!} C_w(\infty) \int_0^\infty s^{n-1} e^{-bs} ds = \frac{(-)^n a C_w(\infty)}{b^n} \quad (18)$$



consequently

$$pC_w(p) = C_w \left[ 1 - a \frac{p}{b} + a \left( \frac{p}{b} \right)^2 - a \left( \frac{p}{b} \right)^3 + \dots \right] \quad (19)$$

Examination of Eq. (19) indicates that as long as  $p$  (which for oscillatory motion corresponds to  $p = ik$ ) is less than  $b$ , the series converges. Consequently one can obtain reasonably good closed form solutions provided the flutter reduced frequency is somewhat less than the indicial response decay rate,  $b$ . The most critical decay rates occur at very large aspect ratios near the speed of sound. Fortunately such wings are highly impractical from a performance standpoint. In addition flight at hypersonic speeds where the heating problem requires prime consideration necessitates the use of very high sweep angles which result in extremely low aspect ratios. This trend substantiates the use of the power series representation in that such configurations result in high decay rates for the indicial functions.

The preceding discussion although qualitative can be made more quantitative by examination of the aerodynamic indicial function properties which exist in the literature. Consider first the infinite aspect ratio wing which, for unsteady aerodynamic effects, represents the most critical case. In Fig. 2 plots are given for the four indicial functions for a range of Mach numbers. From an analysis of this figure the following trends can be observed:

1. The lowest decay rate ( $b$  is smallest) occurs near  $M = 1.0$ .
2. As a result of the optimum axes ( $x_0/\bar{c}$  and  $x_1/\bar{c}$ ) the most important indicial function is the normalized lift due to the angle of attack.

3. The indicial functions  $C_{M_{\alpha x_0}}(s) = C_{L_{q x_1}}(s)$  are identical. This is true not only for infinite aspect ratio but also for any wing whose mid-chord line is unswept (and where the principles of linearized flow are applicable).

4. For the power series expansion form the first term in the series for the  $C_{L_{q x_1}}(s)$  indicial function is an "apparent inertia" term (a  $\bar{\theta}$  results since the term  $C_{L_{q x_1}}(\infty) = 0$  and  $pq = \bar{\theta}$ ).

5. The same is true for  $C_{M_{\alpha x_0}}(s)$  when considered in the form  $C_{M_{\alpha x_0}}(s) - C_{M_{\alpha x_0}}(\infty)$ .

6. If the decay rate for the normalized indicial lift function,  $C_{L\alpha}(s)/C_{L\alpha}(\infty)$  satisfies the convergence requirements, then the requirements for the remaining three indicial functions will be satisfied.

On the basis of the preceding observations, the reciprocal of the decay rate,  $1/b$ , for the indicial lift due to angle of attack was plotted as a function of Mach number and aspect ratio in Fig. 3. The solid line represents information obtained from available theoretical sources. The dashed line represents information obtained from either limited experimentally deduced flutter data and/or estimates from approximate aerodynamic theories. The significance of the decay rate parameter,  $b$ , depends of course on the value of the reduced frequency,  $k$ , where a possible instability can occur. In general, if  $k = \frac{\omega \bar{c}}{V}$  is never greater than 1.0, then for low aspect ratio wings (say  $A < 1.5$ ) the power series representation has an excellent chance of applying throughout the complete Mach number regime. It is also obvious that for large aspect ratio wings operating at high subsonic Mach numbers the series will not converge in the expected range of reduced frequencies; thus an alternate form for the indicial functions is required (such as a series of exponentials). Fortunately for hypersonic flight the wing aspect ratio will be of the order of  $A = 1.5$  or lower thus the power series representation can be expected to be extremely useful.

In concluding the discussion on unsteady parameters it is worthy to note that based on the power series expansion representation the only two parameters required for analysis are the  $C_{L\alpha}(s)/C_{L\alpha}(\infty)$  and  $C_{M\alpha}(s)$  indicial functions. These two functions when written in power series form; e.g.

$$p \frac{C_{L\alpha}(p)}{C_{L\alpha}(0)} = 1 + p \frac{C_{L\dot{\alpha}}}{C_{L\alpha}} + p^2 \frac{C_{L\ddot{\alpha}}}{C_{L\alpha}} + \dots \quad (20)$$

$$p C_{M\alpha}(p) = p C_{M\dot{\alpha}} + p^2 C_{M\ddot{\alpha}} + \dots \quad (21)$$

provide the analyst with direct identification of the contributions of the aerodynamic damping due to the unsteady aerodynamic terms. For instance, the  $C_{L\dot{\alpha}}/C_{L\alpha}$  and  $C_{M\dot{\alpha}}$  terms represent the major portions of the damping when the series converges rapidly; for slow convergence they represent at least a major portion of the aerodynamic damping. These two quantities (as well as other terms of the series) can be plotted as a function of Mach number and aspect

ratio in a systematic manner. Typical trends are shown in Fig. 4 for  $C_{L\dot{\alpha}}/C_{L\alpha}$  and  $C_{M\dot{\alpha}x_0}$ . Also shown is the trend for  $C_{M\dot{\alpha}x_1}$  which

is directly comparable with the values obtained for  $C_{M\dot{\alpha}x_0}$ . It

should be noted that the curves shown in Fig. 4 for  $A > 1.5$  are given only to indicate trends; their applicability would obviously be contingent on the reduced frequency of oscillation. The results of Fig. 4 do, however, emphasize that the importance of the unsteady effects is primarily limited to the transonic regime where methods of prediction based on the theory above appear least likely to succeed. For  $A \leq 1.5$  the  $C_{M\dot{\alpha}x_0}$  values are extremely small even for

transonic speeds (since the values apparently are changing sign through  $M = 1.0$ ) thus the quasi-steady parameter  $C_{M\dot{\alpha}x_0}$  dominates for

$A < 1.5$ . Apparently for wings with  $A \leq 1.5$ , the only unsteady parameter required for flutter analysis is the quantity  $C_{L\dot{\alpha}}/C_{L\alpha}$

and the values of this parameter probably have little effect on the flutter stability since they are inherently small to begin with. Thus for wings designed for hypersonic flight the unsteady parameters have little or no effect throughout the Mach number regime. On this basis primary emphasis should be given to the accurate determination of the steady and quasi-steady aerodynamic parameters and their use in the calculation of the flutter stability.

#### APPLICATION OF BASIC CONCEPTS TO SPANWISE DISTORTIONS \*

Prior to treating the arbitrarily distorted wing, application of the principles previously described for the case of spanwise distortions appears desirable. The extension is straightforward; one need only replace each of the properties encountered on the rigid wing by a matrix of such properties distributed along the span of the wing. The lifts, moments, angles of attack, and pitching rates are represented by column matrices; the aerodynamics on the other hand are square matrices of influence coefficients.

The analogous equations for the lift and moment distributions can be written as follows:

\* The analysis has been presented in much more detail in Ref. 1.

$$\{l(\eta_i, s)\}_{ra} = \frac{1}{2} \rho V^2 \bar{c} \left\{ C_{l\alpha}^{(\infty)} \left[ \frac{C(\eta_i) C_{l\alpha}(\eta_i, \eta_j, s)}{\bar{c} C_{l\alpha}^{(\infty)}} \right] * \left\{ \left\{ \frac{d\alpha(\eta_j, s)}{ds} \right\}_{ra} + \left[ \frac{x_i(\eta_j) - r_a}{\bar{c}} \right] \left\{ \frac{dq(\eta_j, s)}{ds} \right\} \right\} + \epsilon(s) \right\} \quad (22)$$

$$\begin{aligned} \{m(\eta_i, s)\}_{ra} = & \bar{c} \left[ \frac{r_a - x_i(\eta_j)}{\bar{c}} \right] \{l(\eta_j, s)\} + \frac{1}{2} \rho V^2 \bar{c}^2 \left\{ C_{mq}^{(\infty)} \left[ \frac{C^2(\eta_i) C_{mq}(\eta_i, \eta_j, s)}{\bar{c}^2 C_{mq}^{(\infty)}} \right] \left[ \frac{C(\eta_j)}{\bar{c}} \right] \left\{ q(\eta_j, s) \right\} \right. \\ & \left. + \left[ \frac{C^2(\eta_i) C_{mq}(\eta_i, \eta_j, s)}{\bar{c}^2} \right] * \left\{ \left\{ \frac{d\alpha(\eta_j, s)}{ds} \right\}_{ra} + \left[ \frac{x_i(\eta_j) - r_a}{\bar{c}} \right] \left\{ \frac{dq(\eta_j, s)}{ds} \right\} \right\} + \delta(s) \right\} \quad (23) \end{aligned}$$

where

$$\epsilon(s) = \left[ \frac{C(\eta_i) C_{l\alpha}(\eta_i, \eta_j, s)}{\bar{c}} \right] \left[ \frac{C(\eta_j)}{\bar{c}} \right] * \left\{ \frac{dq(\eta_j, s)}{ds} \right\}$$

and

$$\delta(s) = C_{mq}^{(\infty)} \left[ \frac{C^2(\eta_i) [C_{mq}(\eta_i, \eta_j, s) - C_{mq}(\eta_i, \eta_j, \infty)]}{\bar{c}^2 C_{mq}^{(\infty)}} \right] \left[ \frac{C(\eta_j)}{\bar{c}} \right] * \left\{ \frac{dq(\eta_j, s)}{ds} \right\}$$

and also

$$\lim_{s \rightarrow \infty} C_{mq}(\eta_i, \eta_j, s) * \frac{dq(\eta_j, s)}{ds} = C_{mq}(\eta_i, \eta_j, s) * q(\eta_j, s)$$

where  $l$ ,  $m$ ,  $\alpha$ , and  $q$  are running lifts, moments, angles of attack, and pitching velocities all relative to the reference axis,  $r_a$ , and the influence coefficients  $C_{l\alpha}$ ,  $C_{m\alpha}$ ,  $C_{lq}$ , and  $C_{mq}$  are defined

as the running lift or moment coefficients at  $\eta_i$  due to the integrated effect of  $\alpha$  or  $q$  in the neighborhood of  $\eta_j$ . The diagonal matrix  $c(\eta_j)/\bar{c}$  arises because  $q$  is defined with respect to the

mean chord  $\bar{c}$  rather than  $c(\eta_j)$ .

The axes transformations must now be made with respect to the local moment and rotation centers, i.e.

$$x_o(\eta)/c(\eta) = -C_{m\alpha}(\eta)/C_{l\alpha}(\eta) - c_o(\eta)/c(\eta)$$

$$x_l(\eta)/c(\eta) = C_{lq}(\eta)/C_{l\alpha}(\eta) - c_o(\eta)/c(\eta)$$

If the term  $C_{l\alpha}(\eta_i, \eta_j, s)/C_{l\alpha}^{(\infty)}$  is rewritten as a product of  $C_{l\alpha}(\eta_i, \eta_j, s)/C_{l\alpha}(\eta_i, \eta_j, \infty)$  and  $C_{l\alpha}(\eta_i, \eta_j, \infty)/C_{l\alpha}^{(\infty)}$  then the equations are seen to consist of ten basic quantities which are listed below:

1.  $C_{L\alpha}(\infty)$
2.  $x_o(\eta)/c(\eta)$
3.  $c(\eta_i)c_{l\alpha}(\eta_i, \eta_j, \infty)/\bar{c}C_{L\alpha}(\infty) = Q_{l\alpha}(\eta_i, \eta_j, \infty)$
4.  $C_{M_{q_{x_o} x_1}}(\infty)$
5.  $x_1(\eta)/c(\eta)$
6.  $c^2(\eta_i)c(\eta_j)C_{m_{q_{x_o} x_1}}(\eta_i, \eta_j, \infty)/\bar{c}^3C_{M_{q_{x_o} x_1}}(\infty) = Q_{M_{q_{x_o} x_1}}(\eta_i, \eta_j, \infty)$
7.  $c_{l\alpha}(\eta_i, \eta_j, s)/c_{l\alpha}(\eta_i, \eta_j, \infty)$
8.  $c^2(\eta_i)c_{m_{q_{x_o} x_1}}(\eta_i, \eta_j, s)/\bar{c}^2$
9.  $c(\eta_i)c(\eta_j)C_{l_{q_{x_1}}}(\eta_i, \eta_j, s)/\bar{c}^2$
10.  $c^2(\eta_i)c(\eta_j)[C_{m_{q_{x_o} x_1}}(\eta_i, \eta_j, s) - C_{m_{q_{x_o} x_1}}(\eta_i, \eta_j, \infty)]/\bar{c}^3C_{M_{q_{x_o} x_1}}(\infty)$

# STEADY AND QUASI-STEADY PARAMETERS

The parameter  $C_{L\alpha}$  has been discussed previously for the rigid wing. The parameter  $C_{M_{q_{x_o} x_1}}(\infty)$ , although a total coefficient, must be understood to be defined as the integral of the spanwise distribution of  $c^3(\eta)C_{m_{q_{x_o} x_1}}(\eta)/\bar{c}^3$  for the planar case where  $C_{m_{q_{x_o} x_1}}(\eta)$  is the local coefficient about the local moment center,  $x_o^o(\eta)/c(\eta)$ , due to pitching about the local rotation center,  $x_1^o(\eta)/c(\eta)$ , (where the zero superscripts refer to the constant spanwise mode). This is not the same as the total moment coefficient about the mean

aerodynamic moment center,  $x_o^0/\bar{c}$ , due to pitching about the mean aerodynamic rotation center,  $x_1^0/\bar{c}$ , which is denoted as  $C_{M_q}^*(\infty)$ , or equivalently  $C_{M_q}' - C_{M_q}' C_{L_q}' / C_{L_\alpha}'$ , in Ref. (2) While  $C_{M_q}^*(\infty)$  is important for stability considerations,  $C_{M_q}(\infty)$  is more closely associated, in

view of our choice of local axis,  $x_o(\eta)/c(\eta)$ , to the spanwise moment distribution affecting the aeroelastic behavior.

The quantities  $x_o(\eta)/c(\eta)$  and  $x_1(\eta)/c(\eta)$  are the local moment and rotation centers for the particular spanwise deformation which the wing is undergoing. They must not be confused with  $x_o^0(\eta)/c(\eta)$  and  $x_1^0(\eta)/c(\eta)$ , the moment and rotation centers for the constant spanwise mode which are used to determine  $C_{M_q}(\infty)$ .

The quantities  $c(\eta_i)c_{l_\alpha}(\eta_i, \eta_j, \infty)/\bar{c}C_{L_\alpha}$  and  $c^2(\eta_i)c(\eta_j)c_{m_q}(\eta_i, \eta_j, \infty)/\bar{c}^3C_{M_q}(\infty)$

are more familiarly abbreviated by  $Q_{l_\alpha}(\eta_i, \eta_j, \infty)$  and  $Q_{m_q}(\eta_i, \eta_j, \infty)$ ,

the aerodynamic influence coefficients corresponding to  $C_{L_\alpha}$  and  $C_{M_q}$ .

In the absence of pressure measurements it is very difficult to experimentally determine either  $Q_{l_\alpha}$  or  $Q_{m_q}$ . They can, however, be

determined analytically by either the subsonic or supersonic kernel function procedure.

#### UNSTEADY PARAMETERS

The quantity  $c_{l_\alpha}(\eta_i, \eta_j, s)/c_{l_\alpha}(\eta_i, \eta_j, \infty)$  is the normalized indicial response of the lift at  $\eta_i$  due to the integrated effect of  $\alpha$  at  $\eta_j$ . A sketch of the expected indicial response distribution throughout the matrix is shown in Fig. 5. The response of diagonal elements in this figure have starting values greater than one since piston theory lift is greater than the self induced component of the

steady-state lift. Only for high aspect ratios is the piston theory value less. The responses of off-diagonal elements involve time delays, the extent of which depends on the distance between the individual stations. Calculations of the above transients, however, would be exceedingly cumbersome and, furthermore, their simulation on an analog computer would be next to impossible. Fortunately, such an approach is neither necessary nor logical. First, these transients do not have to be known with great accuracy since they play only a secondary role in most aeroelastic problems and second it would be inconsistent to determine them accurately when the influence coefficients they modify,  $(c(\eta_i)c(\eta_i, \eta_j, \infty)/\bar{c}C_{L\alpha}(\infty))$ , have no real physical significance. When using such an influence coefficient approach only the integrated effects, namely,  $\{l(\eta_i, s)\} = [Q_{L\alpha}(\eta_i, \eta_j, s)]\{\alpha(\eta_j)\}$  or

$[L(\eta_i, s)] = [I_i] [Q_{L\alpha}(\eta_i, \eta_j, s)]$ , have any meaning. Consequently, diagonal transient matrices relating the steady to the unsteady lift matrices should be sufficient to treat the unsteady problem, i.e.:

$$\{l(\eta_i, s)\} = [T_i(s)] \{l(\eta_i, \infty)\} \quad (26)$$

$$\text{or} \quad [L(\eta_i, s)] = [L(\eta_i, \infty)] [T_j^*(s)] \quad (27)$$

The transient matrix  $T_i(s)$  relates the steady state spanwise lift distribution to its unsteady counterpart while the matrix  $T_j^*(s)$

relates the total steady state lift per angle of attack at each station to its unsteady counterpart. To determine  $C_{L\alpha}(s)$  one

should use some combination of the above transient representations. From a study of reverse flow requirements and for moderate sweep the following approximation has been found to be extremely useful:

$$[Q_{L\alpha}(\eta_i, \eta_j, s)] = [\sqrt{T_{O_i}(s)}] [Q_{L\alpha}(\eta_i, \eta_j, \infty)] [\sqrt{T_{O_j}(s)}] \quad (28)$$

where  $T_{O_i}$  is the transient matrix for an unswept wing. When the sweep is very large the error of the above approximation is difficult to evaluate, for, at present, very little information on the transient behavior of highly swept wings is available. The transient effects of narrow delta wings, however, appear to be quite small.

Most of the effort at present has been concentrated on evaluating  $T_{O_i}(s)$  for rectangular wings. This is sufficient to treat

a very wide class of wings experiencing spanwise distortions only; however, comparisons with results obtained from more sophisticated material, such as the NASA Kernel Function method, may be necessary to evaluate the soundness of the approximations. Complete knowledge of the total transient  $T_{O_i}(s)$  which relates  $C_{L\alpha}(s)$  and  $C_{L\alpha}(\infty)$  for a

range of aspect ratios is available; however only scant knowledge of

the transient  $T_{o_i}(s)$  (which relates the steady and unsteady lift distributions) is available. From an analysis of the trend of the total transients with aspect ratio for the rigid wing, one could conclude that the spanwise transients behave similarly, with the more outboard transients behaving like the total transients of the lower aspect ratio wings since in both cases three dimensional effects are becoming more important resulting in an increasing percent of spanwise flow. An excellent measurement of the spanwise flow distribution is the local aerodynamic center which can be determined experimentally. Knowledge of this parameter together with a simple correlation of the growth of lift variation with aspect ratio can be used to develop the transient  $T_{o_i}(s)$ .

The foregoing analysis is intended primarily as a guide and is by no means a unique approach to the transient problem; however, the accuracy of the above approximations is attested by a comparison with the results of Nelson, Rainey, and Watkins. (See Ref. 1).

The same approach is also applicable to the less important transient

$$c^2 c_{m_{\alpha x_0}}(\eta_i, \eta_j, s) / \bar{c}^2. \text{ The two remaining transients } c^2 c_{\eta_q}(\eta_i, \eta_j, s) / \bar{c}^2$$

$$\text{and } c^3 [c_{m_{\alpha x_0 x_1}}(\eta_i, \eta_j, s) - c_{m_{\alpha x_0 x_1}}(\eta_i, \eta_j, \infty)] \text{ need not be considered at all}$$

since they have been shown to be unimportant for all practical cases.

#### APPLICATION OF BASIC PRINCIPLES TO HYPERSONIC VEHICLES

The uncertainties regarding aeroelastic instability at hypersonic speeds have provided the motive for a variety of investigations. Since a hypersonic winged vehicle must be flutter free at constant equivalent airspeed over its complete Mach number regime, its aeroelastic characteristics must be examined at transonic and supersonic speeds as well as hypersonic speeds. Certain configuration and flight characteristics are identified with the hypersonic vehicle which heretofore have not required detailed consideration in flutter analysis. For instance the hypersonic vehicle usually

1. is a very low aspect ratio configuration ( $A < 1.5$ )
2. has large leading edge sweepback angles,  $70^\circ$  to  $80^\circ$ .
3. has thick wing profiles ( $t/c = 6\%$  to  $15\%$ )
4. has blunt leading edges
5. must operate over a broad range of angle of attack ( $0^\circ \leq \alpha < 90^\circ$ )

#### EVALUATION OF AERODYNAMIC PARAMETERS ON FLUTTER CHARACTERISTICS

As a direct result of the very low aspect ratio characteristic of hypersonic vehicles it is first necessary to show the



importance of the chordwise degrees of freedom in predicting flutter. A simple example which illustrates this point is shown in Fig. 6 where a flutter boundary is plotted for a  $70^\circ$  swept constant thickness delta wing utilizing the semi-rigid degrees of freedom of pitch and roll. The roll axis is held at the root while the pitch axis is variable to simulate various possible torsion axis locations. Also shown is the flutter point obtained for a cantilevered wing having uniform stiffness and mass with corresponding torsion axis located approximately at the 89% root chord. The roll and pitch frequencies for the flutter boundary correspond identically to those determined for the cantilevered wing. It is noted that wide differences exist between the two cases. These differences exist primarily from the camber modes of the elastic wing. If the root compliance for the cantilevered case were changed to simulate the actual attachment representative of fuselage bending, then a considerable increase in wing camber would exist resulting in an appreciable decrease in flutter dynamic pressure thus resulting in further differences with the semi-rigid wing. It is clear then that the camber or chordwise bending modes represent a first order effect on the flutter characteristics of hypersonic vehicles. In addition the aerodynamic forces produced by the arbitrary distortions must also take into account the effects of sweepback, wing thickness, blunt leading edge, and angle of attack variations.

Rather than explore each of these effects separately by comparing experimental flutter results with those determined analytically using a particular aerodynamic theory which accounts for each or possibly several of these effects to some extent, an alternate analytical approach was undertaken whereby an evaluation of the steady and unsteady aerodynamic effects on a particular hypersonic configuration was made. In order to retain maximum insight only two fundamental modes were assumed to dominate the flutter characteristics. The following simple equation for flutter equilibrium is obtained:

$$\left\{ \left( \frac{\omega}{\omega_1} \right)^2 - \left( \frac{\omega}{\omega_2} \right)^2 + \lambda (\bar{A}_1 + i k \bar{B}_1) \right\} \left\{ 1 - \left( \frac{\omega}{\omega_2} \right)^2 + \lambda (\bar{A}_2 + i k \bar{B}_2) \right\} - \lambda^2 (\bar{A}_1 + i k \bar{B}_1) (\bar{A}_2 + i k \bar{B}_2) = 0 \quad (29)$$

where

$\omega_f$  is the flutter frequency (the subscripts 1 and 2 denote respectively the first and second natural free vibration frequencies)

$$k = \text{reduced frequency, } \frac{\omega^c}{V}$$

$$\lambda = \frac{q S C_{L\alpha}}{M c_r \omega_2^2}$$

In the equation for  $\lambda$

$q$  = dynamic pressure for flutter  
 $S$  = wing area  
 $M$  = total mass of wing

$c_r$  = root chord

The aerodynamic coefficients  $\bar{A}_{mn}$  and  $\bar{B}_{mn}$  are modalized aerodynamic coefficients corresponding to natural modes  $\gamma_1$  and  $\gamma_2$  and are defined as

$$\begin{bmatrix} \bar{A}_{11} & \bar{A}_{12} \\ \bar{A}_{21} & \bar{A}_{22} \end{bmatrix} = \begin{bmatrix} m_1 & \\ & m_2 \end{bmatrix}^{-1} \begin{bmatrix} \gamma^T \\ \gamma \end{bmatrix} \left[ \frac{C_{l_\alpha}(k)}{C_{L_\alpha}} \right] \begin{bmatrix} \frac{\partial \gamma}{\partial x} \end{bmatrix} \quad (30)$$

$$\begin{bmatrix} \bar{B}_{11} & \bar{B}_{12} \\ \bar{B}_{21} & \bar{B}_{22} \end{bmatrix} = \begin{bmatrix} m_1 & \\ & m_2 \end{bmatrix}^{-1} \begin{bmatrix} \gamma^T \\ \gamma \end{bmatrix} \left[ \frac{C_{l_\alpha}(k)}{C_{L_\alpha}} \right] \begin{bmatrix} \gamma \end{bmatrix} \quad (31)$$

In equations (30) and (31)  $c_{l_\alpha}(k)/C_{L_\alpha}$  is the unsteady normalized lift influence coefficient matrix due to arbitrary angle of attack over the complete wing surface, whereas the diagonal matrix  $\begin{bmatrix} m_1 & \\ & m_2 \end{bmatrix}$  represents the modalized mass corresponding to modes  $\gamma_1$  and  $\gamma_2$  as follows:

$$\begin{bmatrix} m_1 & \\ & m_2 \end{bmatrix} = \begin{bmatrix} \gamma^T \\ \gamma \end{bmatrix} \begin{bmatrix} m/M \end{bmatrix} \begin{bmatrix} \gamma \end{bmatrix} \quad (32)$$

where  $M$  is the total mass of the wing.

Once the modes  $[\gamma]$  and their natural frequencies are well defined from shake tests, the main problem left for the adequate prediction of flutter is knowledge of the aerodynamic time-dependent matrix  $c_{l_\alpha}(k)/C_{L_\alpha}$ . For the purpose of evaluating the effects due

to the influence coefficients along the lifting surface as well as their frequency or time dependence, just consider the simplest form of aerodynamics, which fortunately for hypersonic flow is the most applicable representation - steady state localized aerodynamics. For further simplicity consider the wing to be a constant density plate where the mass and local aerodynamic forces are proportional to the area of the stations (simple Piston theory). On this basis the matrix given by equation (31) becomes

$$[\bar{B}_{mn}] = [1] \quad (33)$$

and the non dimensional dynamic pressure parameter becomes

$$\lambda = \frac{1 - (\omega/\omega_2)^2}{2 \sqrt{-\bar{A}_{12}\bar{A}_{21} + \bar{A}_{11} - \bar{A}_{22}}} \quad (34)$$

the corresponding expression for the flutter frequency is:

$$\omega^2 = \frac{[1 + (\frac{\omega_1}{\omega_2})^2] \sqrt{-\bar{A}_{12}\bar{A}_{21}} + \bar{A}_{11} - \bar{A}_{22}(\frac{\omega_1}{\omega_2})^2}{2 \sqrt{-\bar{A}_{12}\bar{A}_{21}} + \bar{A}_{11} - \bar{A}_{22}} \quad (35)$$

Thus the flutter speed is contingent primarily upon the knowledge of the aerodynamic coefficients  $\bar{A}_{mn}$  and to a minor extent on the natural frequency ratio,  $(\omega_1/\omega_2)$  (unless the two natural modes are very close together). The flutter frequency on the other hand does not appear to be very sensitive to the aerodynamic coupling or the frequency separation; regardless of the values of  $\omega_1$  and  $\omega_2$  the flutter frequency should lie near, yet below the value for  $\omega_2$ . It should be noted that the effects of camber dominate the  $\bar{A}_{mn}$  matrix as a direct result of the matrix  $\partial \bar{x}/\partial x$  (See Eq. 30). When appreciable camber exists as would be true in the second, or torsion mode, of the wing, the coupling terms  $\bar{A}_{12}$  and  $\bar{A}_{21}$  can not only change over wide values but also experience sign changes. Thus both the aerodynamic influence coefficient matrix  $c_{l\alpha}(k)/C_{L\alpha}$  and the mode  $[\bar{x}']$  can have a predominant effect in the calculation of the  $\bar{A}_{mn}$  matrix.

In order to examine the effects of the aerodynamic influence coefficients on the flutter characteristics, equation (29) must be solved in its general form. However, it can be shown that for a reasonable distribution of the aerodynamic influence coefficients, under steady state conditions, the expressions for the flutter dynamic pressure and frequency, as given by equations (34) and (35), are still valid provided the coefficients  $\bar{A}_{mn}$  are computed properly according to equation (30). To establish this conclusion assume that in equation (31) the following relation exists:

$$\begin{bmatrix} m_1 \\ m_2 \end{bmatrix} \begin{bmatrix} \gamma \end{bmatrix}^T \begin{bmatrix} c_{l\alpha}/C_{L\alpha} \end{bmatrix} \begin{bmatrix} \gamma \end{bmatrix} = \begin{bmatrix} B + \epsilon & \mu_1 \epsilon \\ \mu_2 \epsilon & B - \epsilon \end{bmatrix} \quad (36)$$

where the terms in  $\epsilon$  will be assumed to be no larger than  $B/2$  such that higher order terms in  $\epsilon$  can be ignored. On this basis the equivalent expression for  $\lambda$  becomes

$$\lambda = \frac{[1 - (\frac{\omega_1}{\omega_2})^2](1 + \delta)}{2 \sqrt{-\bar{A}_{12}\bar{A}_{21}} + \bar{A}_{11} - \bar{A}_{22}}$$

where

$$\delta = -\frac{1}{4} \left( \frac{\epsilon}{B} \right)^2 \left\{ \frac{2\sqrt{-\bar{A}_{12}\bar{A}_{21}} - \mu_1 \bar{A}_{21} - \mu_2 \bar{A}_{12}}{\sqrt{-\bar{A}_{12}\bar{A}_{21}} (2 \sqrt{-\bar{A}_{12}\bar{A}_{21}} + \bar{A}_{11} - \bar{A}_{22})} \right\} \quad (37)$$

In practice the quantity  $\delta$  is quite small - of the order of a few percent; consequently the relationship between the flutter dynamic pressure and the generalized aerodynamic forces given by equation (34) is applicable for "influence" type aerodynamic coefficients provided they are calculated by equation (30).

Next one can examine the role of the unsteady aerodynamic properties on the dynamic pressure for flutter. If the power series expansion for  $c_{l\alpha}(p)/C_{L\alpha}$  is used

$$\frac{c_{l\alpha}(p)}{C_{L\alpha}} = \frac{c_{l\alpha}}{C_{L\alpha}} + \frac{c_{l\dot{\alpha}}}{C_{L\alpha}} p + \frac{c_{l\ddot{\alpha}}}{C_{L\alpha}} p^2 + \dots$$

then the expression for  $\lambda$  becomes

$$\lambda = \frac{[1 - (\frac{\omega_1}{\omega_2})^2] (1 - \delta_1)}{2 \sqrt{-\bar{A}_{12}\bar{A}_{21}} + \bar{A}_{11} - \bar{A}_{22}}$$

where

$$\delta_1 = \frac{k^2}{4 \sqrt{-\bar{A}_{12}\bar{A}_{21}}} \left( \frac{\omega_1}{\omega_2} \right)^2 \left[ (\bar{F}_{11} - \bar{F}_{22}) \left( 1 + \left( \frac{\omega_1}{\omega_2} \right)^2 \right) - 2 \frac{(\bar{A}_{11}\bar{A}_{22} + \bar{A}_{22}\bar{F}_{11}) \left( \frac{\omega_1}{\omega_2} \right)^2}{\sqrt{-\bar{A}_{12}\bar{A}_{21}}} \right] \quad (38)$$

where

$$\begin{bmatrix} F \end{bmatrix} = \begin{bmatrix} \gamma \end{bmatrix}^T \left[ \begin{bmatrix} \frac{c_{l\alpha}}{C_{L\alpha}} \end{bmatrix} \begin{bmatrix} \frac{\partial \gamma}{\partial x} \end{bmatrix} + \begin{bmatrix} \frac{c_{l\dot{\alpha}}}{C_{L\alpha}} \end{bmatrix} \begin{bmatrix} \gamma \end{bmatrix} \right] \quad (39)$$

In practice the quantity  $\delta_1$  has been calculated to be extremely small. Results on practical configurations to date have indicated that  $\delta_1$  at transonic speeds is of the order of 1%. It should be noted that for low aspect ratio hypersonic wings the  $F$  matrix is inherently very small and could only produce an effect, if at all, at transonic Mach numbers. Thus one can conclude that for hypersonic configurations the expression for the flutter dynamic pressure given by equation (34) represents an excellent approximation for the general problem even when unsteady effects are present. Thus the familiar conclusion is reached: the steady state aerodynamic influence coefficient matrix dominates the flutter characteristics of the hypersonic vehicle in comparison to the effects produced by the transient or unsteady aerodynamic characteristics.

It is significant, therefore, to discuss the characteristics of the generalized aerodynamic matrix  $\bar{A}_{mn}$  defined by equation (30). For the highly swept delta wing, in particular, the term  $\bar{A}_{21}$  - that is the energy put into the second or torsion mode by the first or bending mode - is the most significant. Although the  $\bar{A}_{12}$  term is equally important, it is not nearly as sensitive to variations in

structural and aerodynamic properties. Based on local aerodynamic or piston theory  $\bar{A}_{21}$  is a small negative value. If the pressure is high at the leading edge, however, as is the case near Mach 1 the coefficient  $\bar{A}_{21}$  can achieve very high negative values which in turn reduces the flutter dynamic pressure considerably. This result indicates the important effect which the aerodynamic center (particularly on the outboard portions of the wing) has upon the flutter characteristics. Furthermore the effects of sweepback angle, wing thickness profiles, leading edge bluntness and wing angle-of-attack on the  $\bar{A}_{12}$  and  $\bar{A}_{21}$  terms must be studied. Although existing aerodynamic theories provide some insight as to how each of these conditions will affect the  $\bar{A}_{nn}$  matrix, it appears that an experimental approach which can determine the steady state generalized aerodynamic matrix over a broad range of Mach numbers and Reynolds numbers is highly desirable. Such an approach will be described in the next section.

#### EXPERIMENTAL DETERMINATION OF AERODYNAMIC INFLUENCE COEFFICIENTS

Invariably, the first decision to be made when analyzing dynamic problems is to select the nature and number of degrees of freedom. With problems involving motion of discrete particles or point masses, the theoretical calculation of the corresponding aerodynamic forces leads to a set of integral equations involving surface integrals of the system variables. The extreme complexity of such an approach requires replacement of the integral equations by a matrix representation utilizing a finite number of degrees of freedom. The critical decision lies in judiciously selecting the degrees of freedom - the criteria being whether the system is compatible with representing both the structural and aerodynamic properties. For instance one set of degrees of freedom may be optimum for the natural modes of vibration; a completely different set may be required for optimum representation of the aerodynamics, which in turn may vary as a function of Mach number. Historically, analysts have used either the modal or station representation. Whereas the former enjoys a simplicity in mathematical operations, the latter provides clearer physical insight especially when trend studies are obtained utilizing the passive or direct analog computer. However once a clear understanding of the physical problem is attained conversion of the equations of motion from discrete to modal or generalized coordinates is achieved by a simple matrix operation. Although the modes to be used can be determined readily from the free vibrations of the structure, the optimum choice of stations is not so clear. For large aspect ratio lifting surfaces the "station" method does not require detailed consideration of the degrees of freedom; usually five or six spanwise stations are selected, each of which have degrees of freedom in pitch and plunge. For very low aspect ratio delta type wings the problem of station representation becomes complicated, especially if correlation of aerodynamic theory with corresponding experimental measurements is desired. Three typical representations for the

station method are shown in Fig. 7. Considerable effort has been spent in the calculation of the theoretical aerodynamic forces utilizing a mesh of rectangular boxes (see Fig. 7-A) each of which represents a single degree of freedom having uniform downwash over the rectangular area. This technique has also been used extensively in representing the complete equations of motion of the wing (as well as the aerodynamic forces) on the direct analog computer. Regardless of the computing technique or device used this representation requires a large number of boxes to adequately describe the rapidly varying downwashes in both the chordwise and spanwise directions. As a result the calculation of the aerodynamic coefficients by theory is complicated, requiring inversion of large matrices for each environmental condition, such as Mach number, etc. Furthermore effects of angle of attack, wing thickness, Reynold's number, large sweepback angles, etc., can not be readily accounted for by existing linearized theories. Experimental verification of influence coefficients appears prohibitive thus introducing one more disadvantage to this method of station representation.

A second well exploited method is the control point technique; an excellent application is the development of the aerodynamic influence coefficients by the NASA Kernel Function procedure. This method determines the load distribution for downwashes located at a network of control points. This method, however, requires a reasonably uniform distribution of the control points. For the highly swept delta wing rapid downwash variations occur for the second, or so-called torsion mode, of the wing outboard of the 70% span. For a 70° delta wing this means that the principal downwash variations occur over only 9% of the wing area. Since aerodynamic coupling between the first two fundamental modes is often very sensitive, (see equations for  $\bar{A}_{21}$  and  $\bar{A}_{12}$ ) failure to accurately describe this portion of the wing will lead to spurious results. The concentration of many control points in a small area, however, has produced numerical difficulties due to near-singular matrices. Although this problem may be overcome, or at least alleviated, by invoking double precision accuracy on the digital computer, the impracticality of experimental correlation still exists as previously discussed for the box method.

In order to alleviate these restrictions the authors have proposed to utilize a wing made up of articulated panels having simple prescribed modes of distortion where the force and center-of-pressure (both chordwise and spanwise) can be easily and accurately measured experimentally using conventional three-component balances. For the case of a delta wing these panels consist of a rectangular main panel and two triangular panels located in front and along the side of the rectangular panel. A sketch of this arrangement is shown in Fig. 7c. Through a special arrangement of three-component balances, the force and its chordwise and spanwise center of pressure location can be interpreted as three uniform loadings for each section. This loading distribution is represented by the dashed

lines in Fig. 7c. By articulating each flap with respect to the main wing (which itself can be rotated to provide an angle of attack) three degrees of freedom can be obtained if only planar surfaces are used. By providing each of these panels with two additional prescribed downwashes, namely parabolic camber and linear twist, each panel will have three independent downwashes with a corresponding number of loadings. Thus a complete  $9 \times 9$  matrix of aerodynamic influence coefficients can be measured experimentally throughout the Mach number and Reynold's number regime. Through such an arrangement an optimum distribution of the boxes can be determined beforehand to match the free-vibration modes of the wing without compromising the accuracy of the aerodynamic forces.

By locating the break line of the flaps at the 50% root chord and span locations, the three wing segments can be generated from one rectangular section. For example, see Fig. 8 where three parabolically cambered segments are generated from a single cambered rectangular section. This arrangement is likewise applicable for the linearly twisted wings. Thus the generation of the three panel downwashes is relatively simple, and more important, interchangeability of the flat, twisted, and cambered sections enables the complete aerolastic matrix to be generated experimentally for a complete range of Mach numbers. By using two values or levels of camber and twist, the effects of amplitude can be evaluated experimentally. This capability is extremely desirable at hypersonic speeds where wide ranges of angles of attack and distortions due to aerodynamic heating and boundary layer thickness are possible. By utilizing flat, parabolic camber, and linear twist modes, the complete aerodynamic loading matrix is obtained directly for the case of pitch-roll coupling flutter. This mode although not applicable for the elastic modes is directly applicable for the control surface modes; for instance the actuator stiffness requirements and optimum rotation axis can be determined for all-moveable canard or tail surface.

Measurements of the lift, pitching moment, and rolling moment coefficients on each of the three surfaces,  $C_{L1}$ ,  $C_{M1}$ ,  $C_{L2}$ ,  $C_{M2}$ ,  $C_{L3}$ ,  $C_{M3}$ , and  $C_{L3}$ , due to angle of attack, camber and twist of each surface,  $\alpha_1$ ,  $\alpha_2$ ,  $\alpha_3$ ,  $c_1$ ,  $c_2$ ,  $c_3$ ,  $t_1$ ,  $t_2$ , and  $t_3$ , results in the following  $9 \times 9$  aerodynamic influence coefficient matrix:

$$C_{exp} = \begin{bmatrix} C_{L1} & C_{L1} & C_{L1} & C_{L1} \\ \alpha_1 & \alpha_2 & \alpha_3 & c_1 \\ C_{L2} & \dots & \dots & \dots \\ \alpha_1 & & & \\ C_{L3} & \dots & \dots & \dots \\ \alpha_1 & & & \\ C_{M1} & \dots & \dots & \dots \\ \alpha_1 & & & \\ \vdots & & & \end{bmatrix} \quad (40)$$

For each vibration mode of the wing, the normalized deflection  $\delta(x,y)$  can be approximated by a least squares plane through each wing panel,  $m$  ( $m = 1,2,3$ ); for instance for the  $i^{\text{th}}$  mode

$$\delta_m^i = d_m^i + e_m^i x + f_m^i \quad (41)$$

In addition the mode can be approximated by a surface one degree higher in  $x$  and  $y$  such that the steady state downwash will be planar, i.e.

$$\delta_m^i(x,y) = a_m^i + b_m^i y + c_m^i y^2 + g_m^i x + \frac{h_m^i}{2} x^2 + l_m^i xy \quad (42)$$

or

$$\frac{\partial \delta_m^i}{\partial x}(x,y) = g_m^i + h_m^i x + l_m^i y \quad (43)$$

Pre- and post-multiplying the experimental aerodynamic matrix  $[C_{\text{exp}}]$  by the modal coefficients  $[T_1]$  and  $[T_2]^T$  results in the generalized aerodynamic force matrix.

$$[Q_{ij}] = [T_1][C_{\text{exp}}][T_2^T] \quad (44)$$

where  $[T_1]$  and  $[T_2]$  are defined as follows:

$$[T_1] = \begin{bmatrix} d_1^1 & d_2^1 & d_3^1 & e_1^1 & e_2^1 & e_3^1 & f_1^1 & f_2^1 & f_3^1 \\ d_1^2 \\ \vdots \\ d_1^i & d_2^i & d_3^i & e_1^i & \dots & \dots & \dots & \dots & f_3^i \end{bmatrix} \quad (45)$$

$$[T_2] = \begin{bmatrix} g_1^1 & g_2^1 & g_3^1 & h_1^1 & h_2^1 & h_3^1 & l_1^1 & l_2^1 & l_3^1 \\ g_1^2 \\ \vdots \\ g_1^i & g_2^i & g_3^i & h_1^i & \dots & \dots & \dots & \dots & l_3^i \end{bmatrix} \quad (46)$$



The quasi-steady contribution to the generalized force can be determined from the  $[C_{\text{exp}}]$  matrix as follows:

$$[Q_{ij}]_{\text{quasi-steady}} = ik [T_1] [C_{\text{exp}}] [T_1]^T \quad (47)$$

The unsteady form of the  $[Q_{ij}]$  matrix can not be obtained experimentally; however from the results previously presented, the unsteady effect on the flutter characteristics is negligible. Thus the ability to predict the flutter characteristics will depend more on the accuracy of the steady and quasi-steady measurements than on the theoretical estimates of the unsteady contributions.

REFERENCES

1. Amey, Harry B. Jr., Lundgren, Stig, and Mazelsky, Bernard, "Steady and Quasi-Steady Aerodynamic Properties of Wings Having Arbitrary Spanwise Deformations in a Supersonic Flow -- With Particular Emphasis on Their Application to Aeroelastic Phenomena." Lockheed Report 12761 - March 7, 1958.
2. Martin, John C.; Margolis, Kenneth; and Jeffreys, Isabella - "Calculation of Lift and Pitching Moments Due to Angle of Attack and Steady Pitching Velocity at Supersonic Speeds for Thin Sweptback Tapered Wings with Streamwise Tips and Supersonic Leading and Trailing Edges" NACA TN 2699, June 1952.

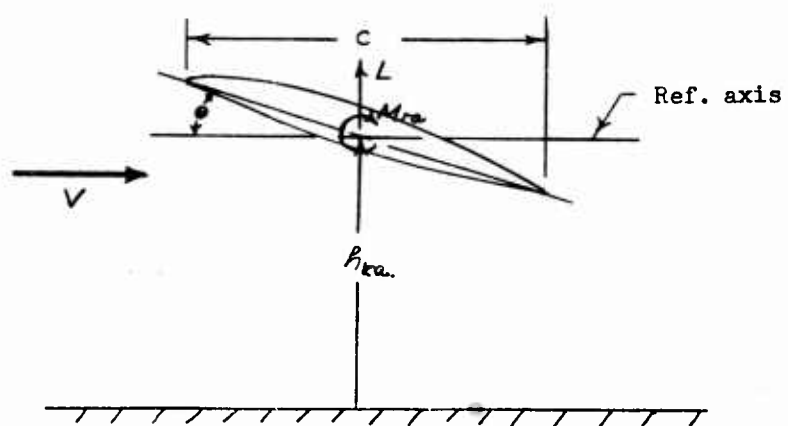


Figure 1 - DEFINITION OF COORDINATES AND FORCES FOR RIGID WING

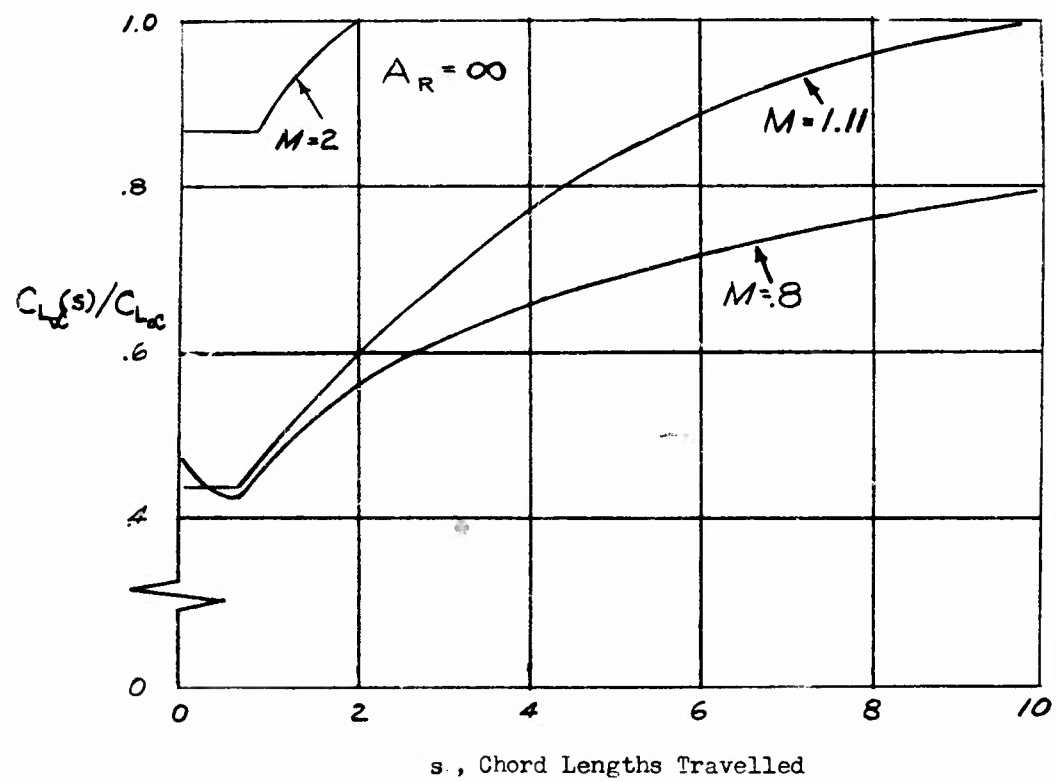


Figure 2 - AERODYNAMIC INDICIAL FUNCTIONS FOR INFINITE ASPECT RATIO WING  
(a) Normalized Lift Due to Angle of Attack

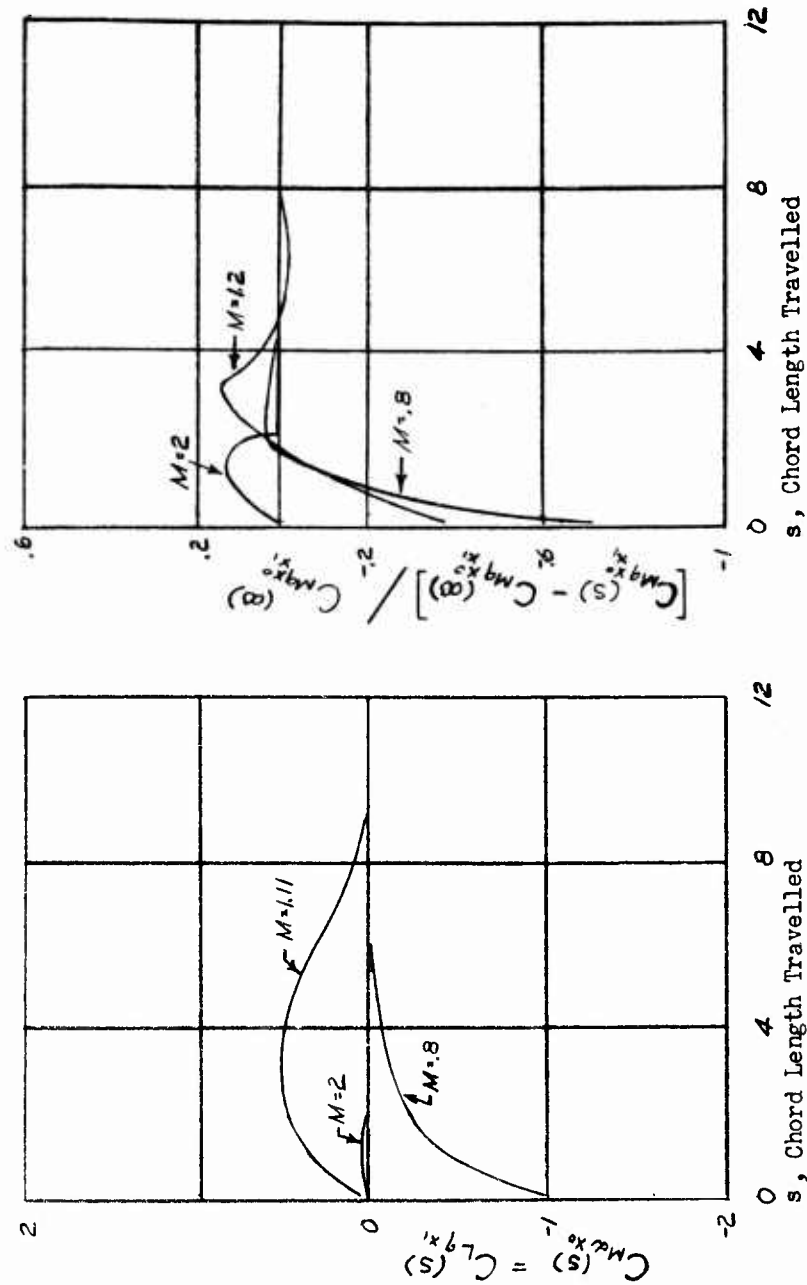


Figure 2 - AERODYNAMIC INDICIAL FUNCTIONS FOR INFINITE ASPECT RATIO WING  
 (b) Pitching Moment Due to Angle of Attack (Lift Due to Pitching Velocity)  
 (c) Normalized Pitching Moment Due to Pitching Velocity

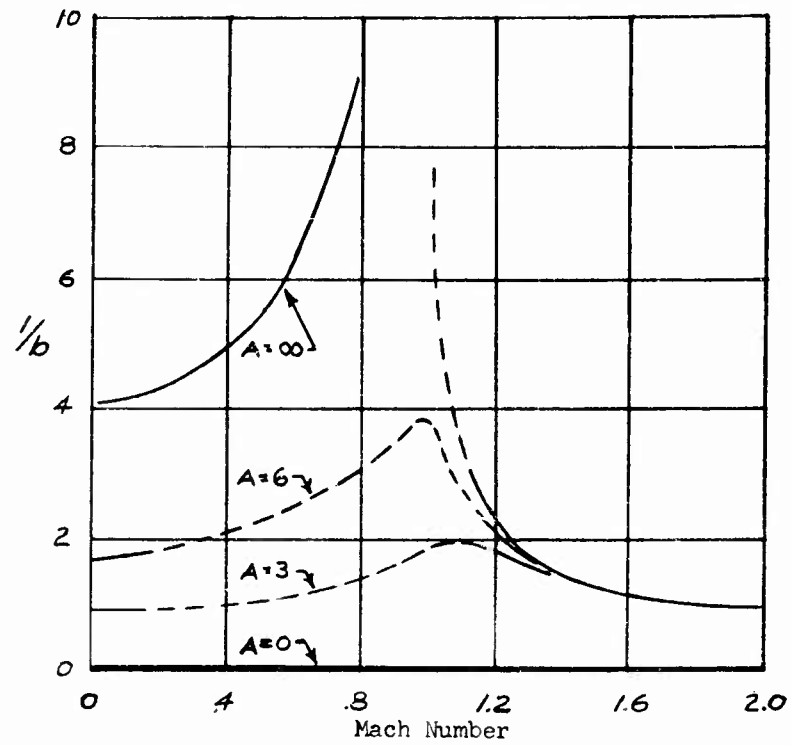


Figure 3 - RECIPROCAL OF DECAY RATE FOR INDICIAL LIFT  
DUE TO ANGLE OF ATTACK

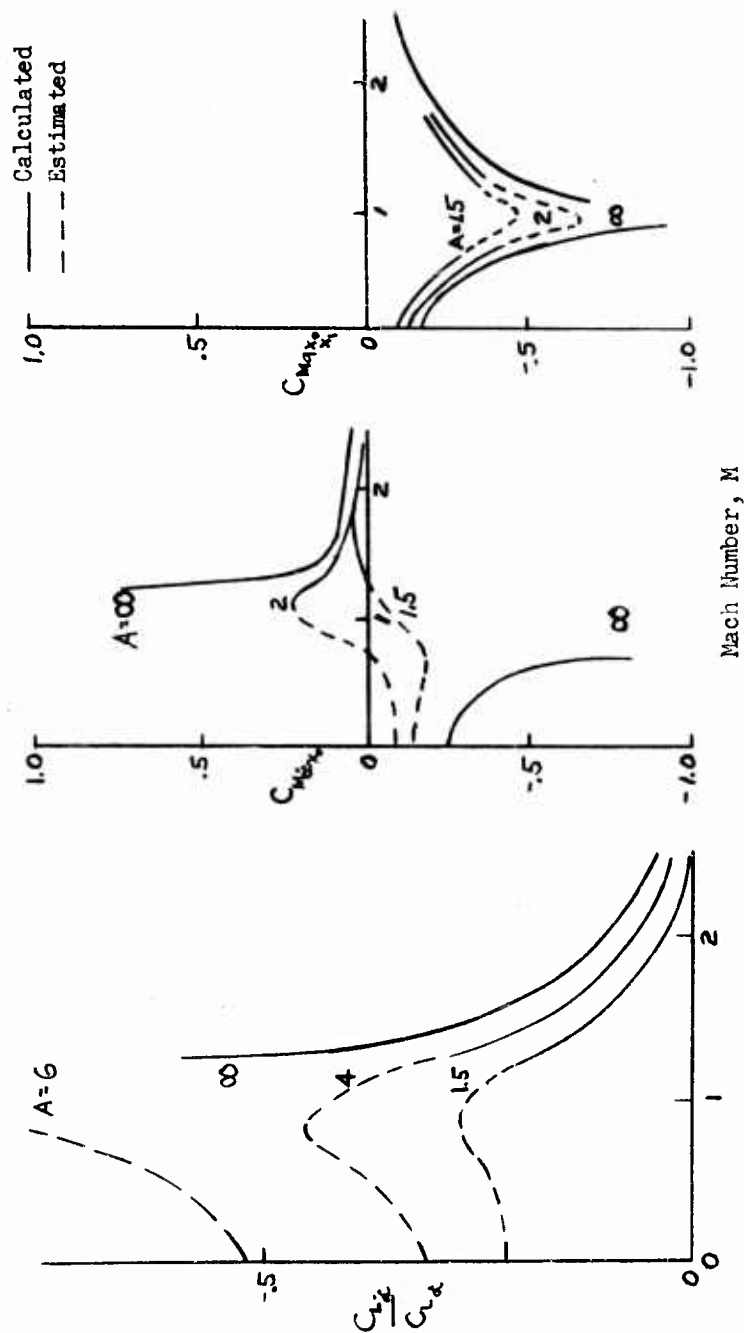


Figure 4 - VALUES OF AERODYNAMIC DAMPING TERMS

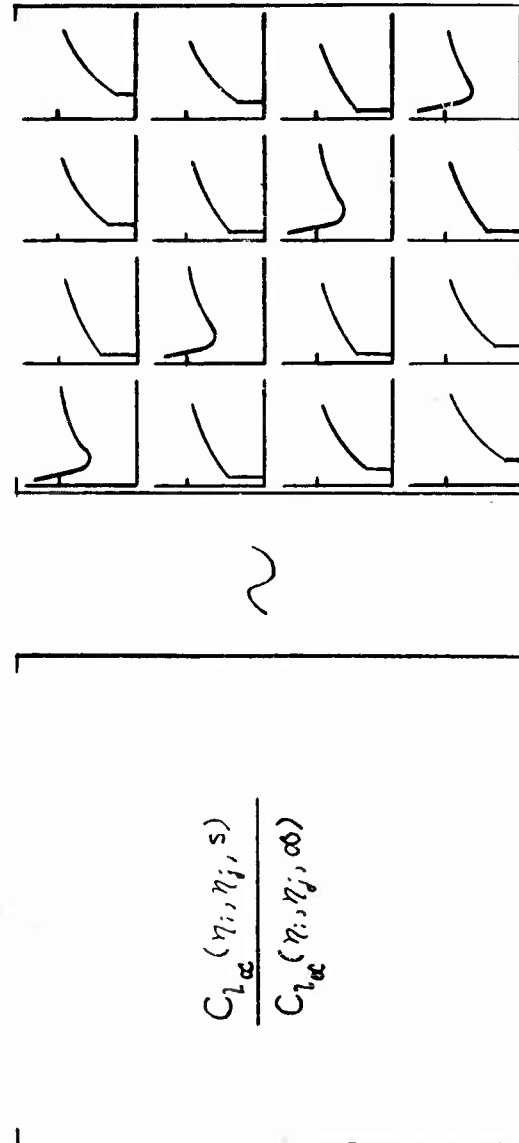


Figure 5 - SKETCH OF NORMALIZED INDICIAL LIFT MATRIX DISTRIBUTION FOR SPANWISE DISTORTIONS



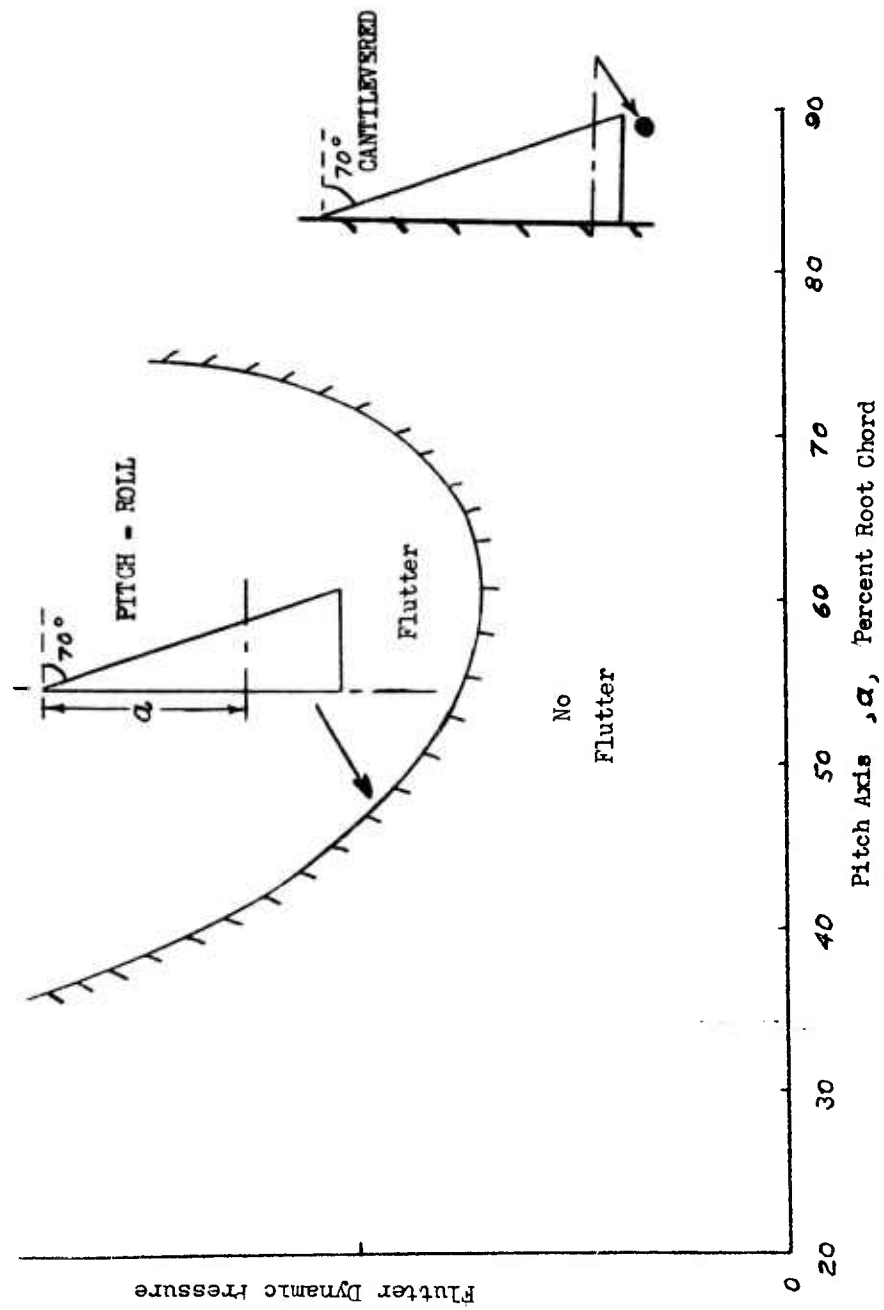


Figure 6 - COMPARISON OF FLUTTER FOR SEMI-RIGID (PITCH-ROLL) AND CANTILEVERED ELASTIC WING

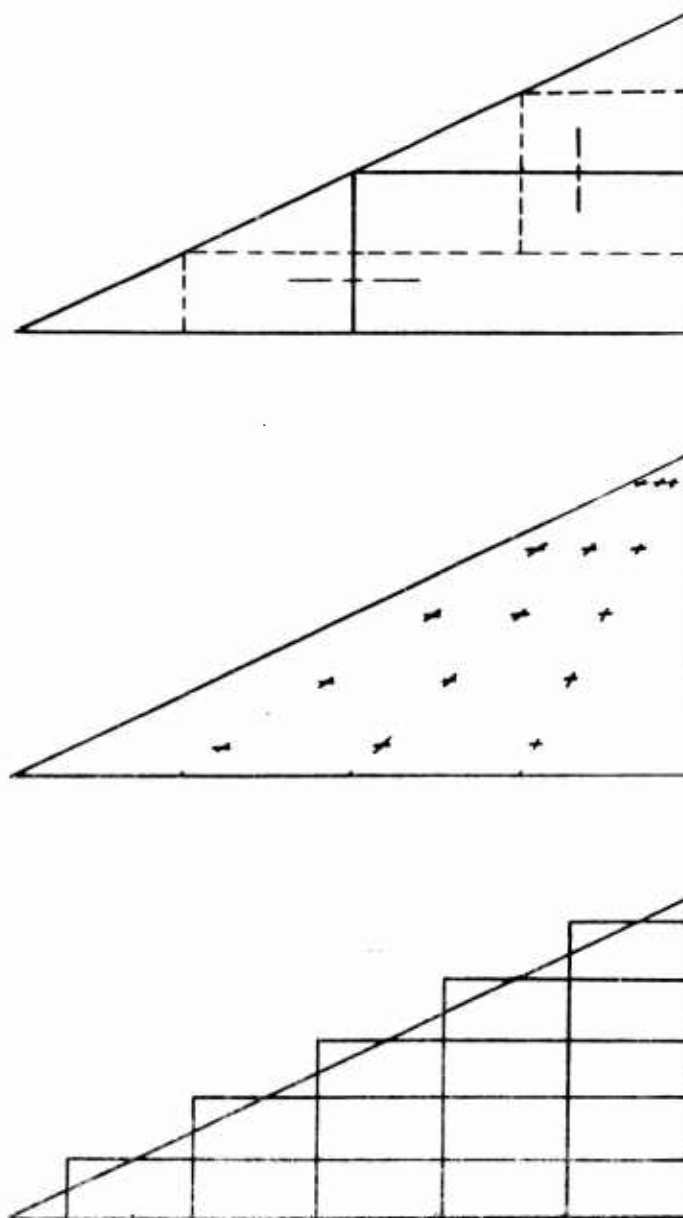


Figure 7 - THREE TYPICAL STATION METHOD TECHNIQUES

(a) Boxes

(b) Control Points

(c) Articulated-Distorted Panels

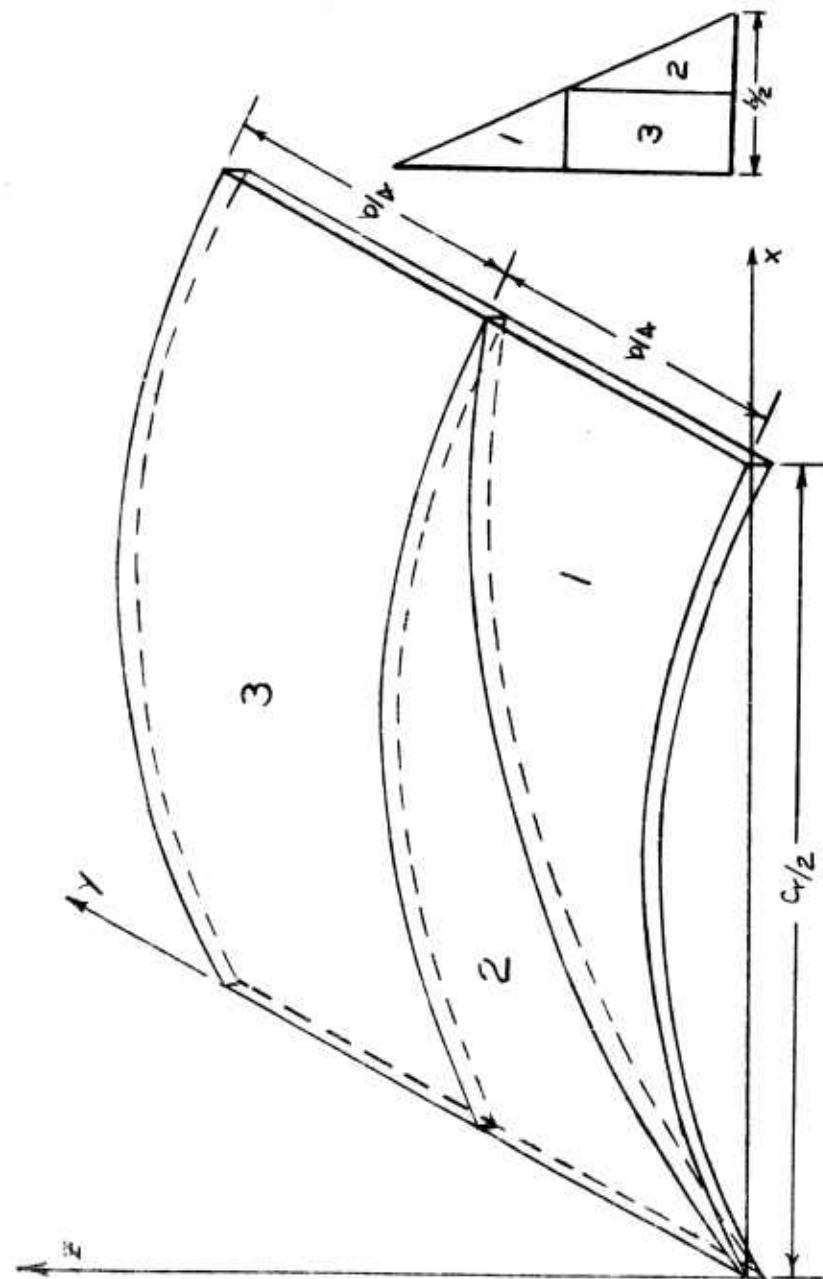


Figure 8 - CAMBERED DELTA WING GENERATED FROM TWO-DIMENSIONAL RECTANGULAR SECTION

## SESSION II | FLUTTER AND VIBRATION

Chairman: Professor John W. Miles  
University of California

APPLICATION OF A MODIFIED LOW-ASPECT RATIO THEORY TO  
AEROELASTIC STUDIES OF FLEXIBLE DELTA LIFTING SURFACES

D. O. Neilson\* and I. Jaszlics\*\*  
Boeing Airplane Company, Transport Division  
Renton, Washington

SUMMARY

The present paper presents a simple modification to existing subsonic low-aspect-ratio theory which renders it suitable for useful application to delta-type wings. The proposed method retains the inherent simplicity of very low-aspect-ratio theory, extends the applicable range to include higher aspect ratio surfaces, and incorporates the effects of compressibility. Specifically, delta wings of aspect ratios up to 4.0 are investigated for various Mach numbers up to  $M = 1.0$ .

Following the derivation of the correction factor which is based on known steady-state parameters, the modified theory is applied to both rigid and flexible delta wings. The rigid wing results, which cover both steady-state conditions and rigid-body motion, are compared with other theoretical values as well as with experimental data. Finally, two methods of applying the modified theory to the aeroelastic investigation of flexible delta surfaces are indicated. Again, comparisons with other theoretical results are made and, in all cases, experimental flutter data are utilized to help determine the validity of the present theory.

In view of its simplicity, the ensuing rapidity of application and the degree of accuracy obtained, it is concluded that this modified theory can be a useful tool for the preliminary design engineer.

---

\* Research Specialist - Structural Dynamics Research Unit

\*\* Associate Research Engineer - Structural Dynamics Research Unit

SYMBOLS

$A_{j, k}$	Power series coefficients
$a_n$	Fourier series coefficients
AR	Aspect ratio
$b_o$	Root semichord
$b_o s_o$	Wing semispan
$c$	Root chord
cp	Center of pressure
$C_L$	Lift coefficient
$C_{L\alpha}$	Lift curve slope
$C_M$	Moment coefficient
$C_{pr}$	Damping-in-roll coefficient
$C_p$	Pressure coefficient
F	Chordwise correction factor constant
j, J, k, K	Summation indices. Also k = reduced frequency.
M	Mach number
n	Chordwise correction factor exponent
$\Delta P$	Pressure difference
q	Dynamic pressure
{q}	Generalized coordinates
S	Wing area
U	Air speed
w	Downwash velocity
x	Chordwise coordinate
$x_o$	Pitch axis location
y	Spanwise coordinate
z	Vertical translation displacement
$\alpha$	Angle of attack
$\frac{\beta(x)}{b_o}$	Local semispan
$\delta$	Amplitude of motion ( $z/b_o$ for vertical translation, for pitching)
$\eta$	Fraction of semispan

$\theta$	Polar coordinate = $\cos^{-1} \frac{y(x)}{\beta(x)}$
$\rho$	Air density
$\Delta\phi$	Disturbance velocity potential
$\Phi$	Natural vibration mode shape
$\omega$	Circular frequency of simple harmonic motion.

# INTRODUCTION

The appeal of very low aspect ratio theory as an aerodynamic tool has long been recognized, but almost all attempts at useful application have been thwarted by its inability to give reliable results for other than extremely low aspect ratio surfaces. Nevertheless, its utter simplicity and ease of application is a continual temptation, particularly to the preliminary design engineer who frequently, in the eyes of the purist, resorts to brutal approximations in early stages of design.

The purpose of the present paper is to indicate a correction factor injection which can give the old theory new life and, in fact, allow extension of very-low-aspect ratio theory to permit aeroelastic investigation of delta-type surfaces of aspect ratios up to 4.0. In the application of this modified theory Mach-number effects are accounted for either by introducing a compressibility factor such as Prandtl-Glauert or, alternately, by letting these effects be inherently contained within the proposed correction factor.

# DERIVATION OF THE CHORDWISE CORRECTION FACTOR

The mathematical representation of a low-aspect-ratio lifting surface is given in Fig. 1 where the coordinate transformation between  $y$  and  $\beta$  is also indicated. Although the theory is not restricted to triangular wings, this is the only type which is considered in this development.

Before proceeding with the modified theory, we will review the basic steady-state theory of R. T. Jones<sup>1</sup>. A low-aspect-ratio triangular wing is shown in Fig. 2 together with the familiar Jones' pressure distribution associated with this type of wing. The corresponding chordwise lift distribution obtained as a result of integrating the pressure distribution of Fig. 2 is subsequently shown in Fig. 3. While the simplicity of this particular theory is apparent, so is the glaring violation of the Kutta condition which allows no pressure difference at the wing trailing edge. Another contradiction is evident in that the lift distribution and, hence, the center of pressure is fixed regardless of wing aspect ratio.

One method of partially overcoming the above objections to Jones'

theory was proposed in 1955 by Laidlaw and Halfman<sup>2</sup> who suggested a chordwise multiplier of the form  $\sqrt{1 - (x/c)^2}$ . Applying this factor changed both the lift magnitude and the center of pressure location, and at the same time satisfied the Kutta condition as indicated in Fig. 3. This correction provided marked improvements both in the prediction of pressure distributions and in the results of a particular flutter example. The shortcomings of this correction factor are shown in Fig. 4 where it is seen that while more realistic values of  $C_L \alpha$ <sup>3</sup> and center of pressure location  $x_{cp}$ <sup>3, 4</sup> are attained, the aspect ratio range of applicability is quite restricted. The band on the center of pressure graph indicates a typical variation of data in the literature.

Now a simple variable factor can be derived which will simultaneously give the correct lift curve slope ( $C_L \alpha$ ) and the proper center of pressure location ( $x_{cp}$ ) for a triangular wing of any given aspect ratio. This proposed factor is of the form  $F(1-x/c)^n$  where F is a constant multiplier which adjusts the lift amplitude to give the correct  $C_L \alpha$  and the exponent n prescribes the chordwise lift distribution in such a manner as to produce the desired  $x_{cp}$ . Fig. 5 indicates how the foreknowledge of both  $C_L \alpha$  and  $x_{cp}$ , as just indicated in Fig. 4, may be used in conjunction with the simple lift and moment equations to determine the factors F and n. Sample results of application of this factor are shown in Fig. 6 where the modified chordwise lift distribution for wings of various aspect ratios (AR = 1.6, 2.4, 3.7, and 4.0) are indicated. Jones' unmodified theory and the Laidlaw  $\sqrt{1-(x/c)^2}$  modification are included for comparison.

#### STEADY-STATE PRESSURE DISTRIBUTIONS

Since the  $F(1-x/c)^n$  correction modifies only the chordwise lift distribution, the question of how it affects the pressure distributions across the surface is of interest. Returning to the work of R. T. Jones<sup>1</sup> the application of the correction factor gives the modified pressure distribution as,

$$C_p = \frac{ARF (1-x/c)^n \alpha}{\sqrt{1-(y/b)^2}}$$

To obtain an experimental check on the present theory, pressure data was taken from the results of wind tunnel tests of two delta wing models<sup>5, 6</sup>. For comparison with other theory the pressure distribution has been calculated for these two wings using a Boeing digital program<sup>7</sup> which is based on the lifting surface theory of Kuchemann. Fig. 7 shows both the theoretical and experimental chordwise pressure distributions for various span stations of a delta wing of AR = 2.0. This particular data indicate that the effect of the proposed modification is most pronounced near the wing tip where the total local chord is near the wing trailing edge. Another delta wing of AR = 1.0



is presented in Fig. 8 where this time the pressure distributions are plotted spanwise at various positions along the root chord. Except near the trailing edge the modified theory provides very good correlation with experimental values. It should be noted that the modified-low-aspect-ratio values shown here can be hand calculated for both wings in about an hour. The other theoretical points were obtained from about 5 minutes of machine time on an IBM 704 digital computer.

#### DEVELOPMENT OF THE PRESSURE EQUATION

This development follows that given in Ref. 8 (p. 403) from which the key equations have been reproduced in Fig. 9. Here it can be seen that if the disturbance velocity potential,  $\Delta\phi$ , is known, the pressure difference,  $\Delta p$ , can be determined. Assuming that the spanwise downwash distribution,  $w(x,y,t)$ , can be expressed as a Fourier series, the corresponding disturbance velocity potential which is required to solve for the pressure difference is likewise representable in series form. Ribner<sup>9</sup> has previously indicated a similar series representation for the velocity potential.

From this point, then, the present extension retains the first four terms in the downwash series and develops the resulting expression for the pressure difference. In order to transmit some understanding of the physical meaning of the terms in the downwash series, let us examine the first or constant term  $a_0$ . Starting then, with the known spanwise downwash distribution (a constant) and methodically following through the equations in Fig. 10 leads ultimately to the pressure equation which proves to be the previous result of R. T. Jones<sup>1</sup>.

Without repeating the mathematical development, the next three downwash terms are taken separately. For each term the resulting downwash shape, together with the associated pressure distribution, is illustrated in Fig. 11. The second or linear term is associated with rolling motion and again produces a familiar pressure distribution.

#### RIGID BODY DERIVATIVES

##### A. Pitching and Vertical Translation Motions

In the consideration of both pitching and vertical translation motions the angle of attack across any rigid spanwise strip is constant and, therefore, only the first downwash term need be considered. With the wing in motion the unsteady part of the disturbance velocity potential,  $\partial\phi/\partial t$ , must be included. The unsteady downwash associated with any wing motion can be divided into slope and velocity components,  $w = U \partial z/\partial x + \partial z/\partial t$ . With this downwash term inserted into the pressure equation, an integration on the spanwise direction produces the chordwise lift distribution. A second appropriate integration chordwise with the  $F(1-x/c)^n$  factor will provide either the complex lift or the complex moment about some specified axis. These in turn

can be described in coefficient form as:

$$C_L = l_{\delta} + ikl_{\dot{\delta}}$$

$$C_M = m_{\delta} + ikm_{\dot{\delta}}$$

where  $\delta = z/b_0$  for vertical translation  
 $\delta = \alpha$  for pitch

The delta-wing derivatives for specific values of lift curve slope,  $C_{L\alpha}$ , center of pressure location  $x_{cp}$ , and reference axis  $x_0$  are listed in Fig. 12. The total lift and moment coefficients can be alternately expressed in amplitude/phase-angle form for comparison with previously published data<sup>10</sup>. Such comparisons of various theories with experimental wind tunnel results for delta wings of  $AR = 2.31$  and  $AR = 1.07$  are shown in Figs. 13 through 16 respectively. The lift curve slope and the center of pressure location used in calculating the modified-theory derivatives were taken from Fig. 4.

#### B. Damping in Roll

Pure rolling motion produces an anti-symmetric linear downwash distribution  $w = py$ , with "p" being the angular rolling velocity. Integration of the corresponding pressure equation with no correction factor yields the unmodified damping-in-roll derivative of Ribner<sup>9</sup>,  $C_{pr} = \pi AR/32$ . This curve is shown in Fig. 17 which is taken directly from Ref. 3 (p. 688). The results of the present modified theory,

$$C_{pr} = \frac{3}{8} C_{L\alpha} \frac{(x_{cp}/c)^2}{2 + x_{cp}/c}$$

are also plotted here for comparison with Lawrence's theory and the three experimental values. The band corresponds to the center of pressure band as previously presented in Fig. 4. The fact that the modified theory gives lower values than that of Lawrence for wings with the same lift curve slope and center of pressure location is probably the result of the pressure reduction induced at the wing tips by the  $(1-x/c)^n$  correction factor.

#### SURFACES DEFORMING IN ARBITRARY DEFLECTION SHAPES

The procedure for calculating the pressure (and lift) distributions on the flexible wing follows along the lines previously outlined for the rigid wing but incorporates the first four terms in the spanwise downwash representation. Although the retention of these extra terms leads to more lengthy mathematical expressions than have thus far been indicated, the complexity is still restricted to a composite of simple trigonometric functions. In addition, as a result of

subdividing the wing into grid sections in order to account for both spanwise and chordwise flexibility, the required mathematical manipulation is most easily handled by matrix techniques. Two separate methods of applying the present modified low-aspect-ratio theory to flexible wings have been developed. For discussion purposes these methods will be denoted as the cell method and the power series method.

#### A. The Cell Method

This method was originally developed for application to a direct analogy electric analog computer which would provide the deflections and slopes needed for the lift equations at specified points on the wing surface. However, the examples in this paper which utilize the cell method have all been solved on high speed digital equipment. Furthermore, while the selection of both grid size and number is arbitrary, all integrations presented herein were carried out on a half-wing rectangular grid of six equal divisions in both spanwise and chordwise directions. In Fig. 18 this rectangular grid is compared with the radial grid which is discussed later in the power series method. In solving for the pressure difference spanwise integrations are made across the cells in a given spanwise strip of width  $\Delta x$  with the assumption that the downwash and all of its derivatives maintain a constant value across any individual grid section. The form of the lift equation which results are shown in Fig. 19, where the lift is seen to depend on wing deflection and its derivatives in both spanwise and chordwise directions. Finally, the expression for the generalized force in its conventional form employing vibration mode shapes as generalized coordinates is also shown here.

Regardless of the aerodynamic theory used, the mode shapes are assumed to be given in terms of the vertical deflections at discrete points on the wing surface. In order to define the deflection and all its necessary derivatives at specific locations as required by a particular aerodynamic theory, it is further assumed that the actual shape can be approximated by a power series of the form,

$$z(x,y) = \sum_{j=0}^J \sum_{k=0}^K A_{j,k} x^j y^k$$

This can be written in matrix form as:

$$\{z\} = [B] [A]$$

Where  $[B]$  is a matrix of all the desired powers of  $x$  and  $y$  for each point and  $[A]$  is the matrix of power series coefficient as determined by a least-squares procedure.

Multiplication by operator matrices will then produce any required derivatives ( $dz/dx$  for example).

#### B. The Power Series Method

This method utilizes known deflection shapes over a wing surface in order to generate generalized airforces, and is presented here in condensed form. Fig. 20 presents a general review of the mathematical procedure of this method. Assuming that the wing deformation can be expressed in terms of its natural vibration mode shapes the downwash can be written as shown here for the case of simple harmonic motion. These mode shapes can, in turn, be represented by a two-dimensional power series as selected by a least-squares fit of the input mode shapes over the wing surface. With the deformed shape of the wing thus described, it now remains to determine the associated pressure distribution. To accomplish this the spanwise variation of downwash is again allowed to assume the form of a Fourier series as in Ref. 8. Thus, with the given deflections expressed in terms of a power series, the corresponding Fourier coefficients,  $a_n$ , which are required for the determination of the pressure, can be written as a function of wing geometry and the power series coefficients,  $A_{j,k}$ . Having determined the  $a_n$  coefficients the disturbance velocity potential, in conjunction with the chordwise correction factor, results in the pressure difference equation shown in Fig. 20. This pressure equation can, in turn, be extended to form the generalized forces for the flutter equations of motion. In the present application of this method the radial grid of Fig. 18 was selected for integration purposes, and the first four terms in the Fourier downwash representation were again retained.

#### MACH NUMBER CORRECTIONS

The principal effects of Mach number on a lifting surface are to alter its lift curve slope and to shift the center of pressure. If these variations with Mach number are known for a typical wing as shown in Fig. 21, the  $F$  and  $n$  factors can then be calculated and the  $F(1-x/c)^n$  correction factor provides an extremely easy method of incorporating Mach number effects. An alternate method of accounting for Mach number changes is to introduce a compressibility factor such as Prandtl-Glauert to the airforces after they have been calculated.

#### RESULTS AND DISCUSSION

A variety of delta wings which had been flutter tested were selected for trial application of the modified theory. Some of the flutter tests included a sweep of Mach number, while others provided only one flutter point. Fig. 22 shows the results of applying the modified theory to a  $45^\circ$  delta wing ( $AR = 4.0$ ) previously considered by Hsu and Weatherill<sup>10</sup>. In the present study the first three vibration modes employed were calculated from given mass and stiffness data<sup>11</sup>.

Mach number effects were introduced by assuming the variation of lift curve slope and center of pressure indicated in Fig. 22. In this example all flutter velocities are predicted within 10% of experimental values and except for the highest Mach number the frequency correlation is within 20%. Also shown here is the marked improvement in the Hsu method flutter results which accompanies the use of calculated mode shapes rather than assumed modes as was done with reservation in Ref. 10.

The time advantage of the modified low-aspect-ratio theory over an unsteady lifting surface theory becomes evident when airforce calculations for comparative studies are made. To obtain Mach number convergence for one condition with the Hsu program three different Mach numbers, which required a total of four hours of high speed digital computer time, were considered. In contrast, the modified-theory airforces for a specific flutter condition are machine calculated in five minutes.

Fig. 23 presents a comparison of theoretical and experimental flutter results<sup>12</sup> for a  $70^\circ$  flat plate delta wing ( $AR = 1.46$ ) as Mach number is varied. One Hsu solution and one power-series solution are included for comparison, and all methods used the four deflection mode shapes as given in the report. Here the modified-theory flutter speeds obtained with assumed lift curve slope and center of pressure variations overestimate at low Mach number and underestimate at the higher values. Accuracy in velocity prediction for this wing is within 10% while flutter frequencies fall within 12% of experimental values.

Finally, Fig. 24 summarizes the results from three other delta wings<sup>13</sup>. The power series method is applied to all three wings in conjunction with the admittedly severe Prandtl-Glauert Mach number correction. Here the calculated flutter velocities correlate well with experiment but the corresponding flutter frequencies are too high. Application of the cell method to one of the wings with different values of lift curve slope and center of pressure provides some improvement.

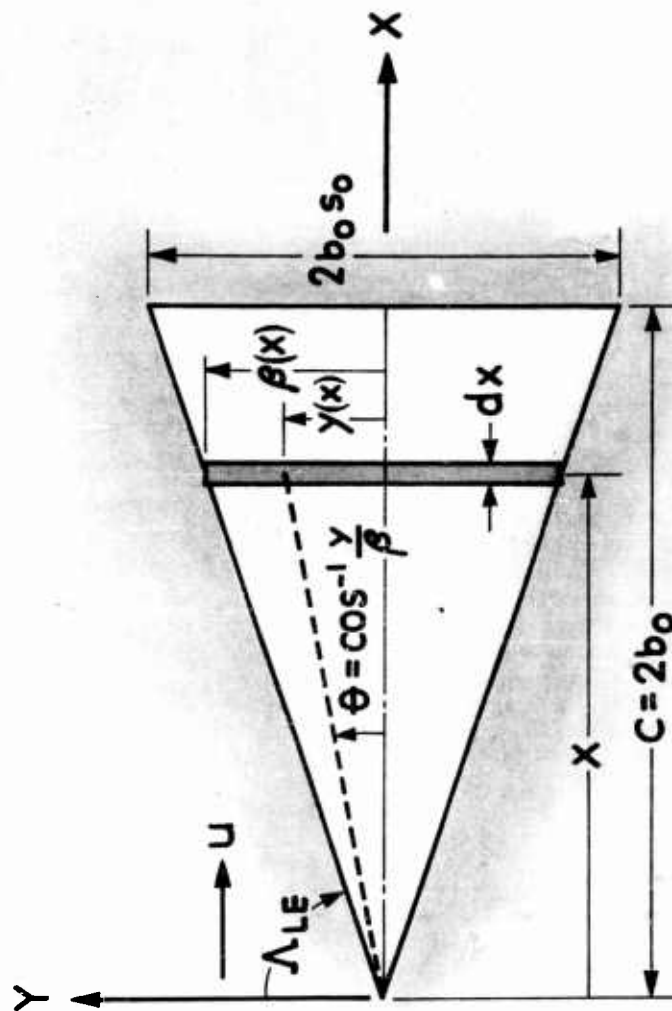
#### CONCLUDING REMARKS

It is felt that while values of lift curve slope and center of pressure can be judiciously assumed, greater accuracy can be attained by using experimental static values from a rigid test article.

While the proposed modification to low-aspect-ratio theory was originally developed in an attempt to provide a rapid means of making qualitative trend studies, results obtained to date give acceptable quantitative information as well. Considering the accuracy obtained and noting the time savings effected, it is concluded that the modified theory can be a useful tool in the preliminary design of flexible delta-type surfaces.

REFERENCES

1. Jones, R. T., Properties of Low-Aspect-Ratio Pointed Wings at Speeds Below and Above the Speed of Sound, NACA Report 835, 1946.
2. Laidlaw, W. R., and Halfman, R. L., Experimental Pressure Distributions on Oscillating Low-Aspect-Ratio Wings, IAS Preprint No. 499, January 1955.
3. Lawrence, H. R., The Lift Distribution on Low-Aspect-Ratio Wings at Subsonic Speeds, Journal of the Aeronautical Sciences, Vol. 18, No. 10, October 1951.
4. Holmboe, V., The Center of Pressure Position at Low Speeds and Small Angles of Attack for a Certain Type of Delta Wings, SAAB TN13, 1952.
5. Graham, D., Chordwise and Spanwise Loadings Measured at Low Speeds on a Large Triangular Wing Having an Aspect Ratio of 2.0 and a Thin, Subsonic-Type Airfoil Section, NACA RM A50A04a.
6. Peckham, D.H., Low-Speed Wind-Tunnel Tests on a Series of Uncambered Slender Pointed Wings with Sharp Edges, RAE Report Aero 2613.
7. Hahn, E. J., and Rogers, J. T., The Development and Digital Programming of a Subsonic and Supersonic Elastic Airload Solution, BAC Document D6-3393, Vol. II, 1960.
8. Bisplinghoff, R. L., Ashley, H., and Halfman, R. L., Aeroelasticity, Addison-Wesley Publishing Company, Reading, Mass., 1955.
9. Ribner, H. S., The Stability Derivatives of Low-Aspect-Ratio Triangular Wings at Subsonic and Supersonic Speed, NACA TN 1423, 1947.
10. Hsu, P. T., and Weatherill, W.H., Pressure Distribution and Flutter Analysis of Low-Aspect-Ratio Wings in Subsonic Flow, M.I.T. Aeroelastic and Structures Research Laboratory Report 64-3, 1959.
11. Herr, R. W., A Preliminary Wind-Tunnel Investigation of Flutter Characteristics of Delta Wings, NACA RM L52B14a, 1952.
12. Hansen, P.W., and Levey, G.M., Experimental and Calculated Results of a Flutter Investigation of Some Very Low Aspect-Ratio Flat-Plate Surfaces at Mach Numbers from 0.62 to 3.00, NASA TM X-53, 1959.
13. Lauten, W. T., Jr., and Burgess, M. F., Flutter Investigation in the High Subsonic and Transonic Speed Range on Cantilever Delta-Wing Planforms with Leading-Edge Sweepback of 60°, 53.8°, and 45°. NACA RM L56K26, 1957.



FOR A TRIANGULAR WING :

$$\beta(x) = \frac{s_0}{2} x$$

$$s_0 = \frac{AR}{2}$$

$$\text{AREA } S = 2b_0^2 s_0$$

Figure 1 - Low-Aspect-Ratio Planform

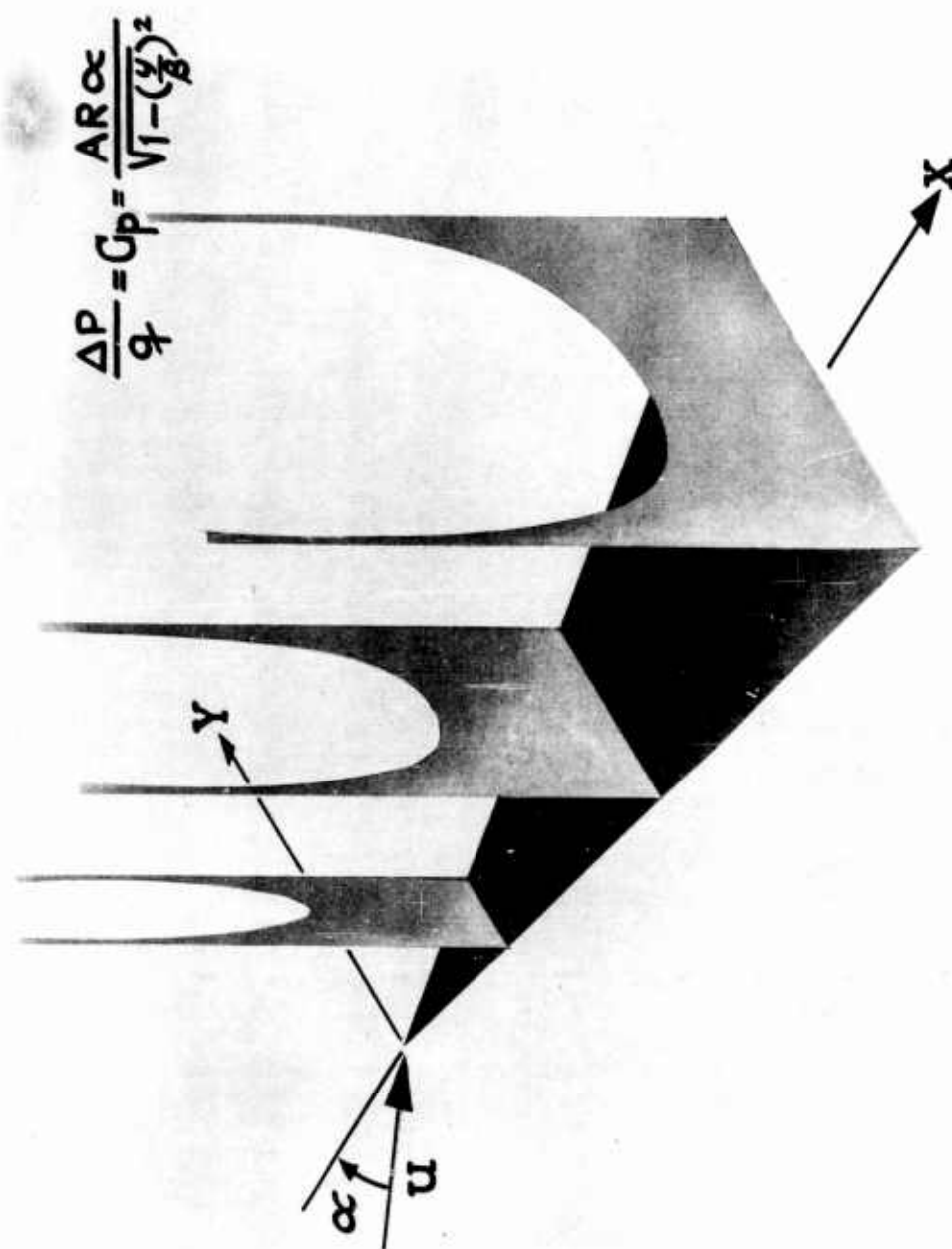


Figure 2 - Pressure Distribution From Jones' Low-Aspect-Ratio Theory



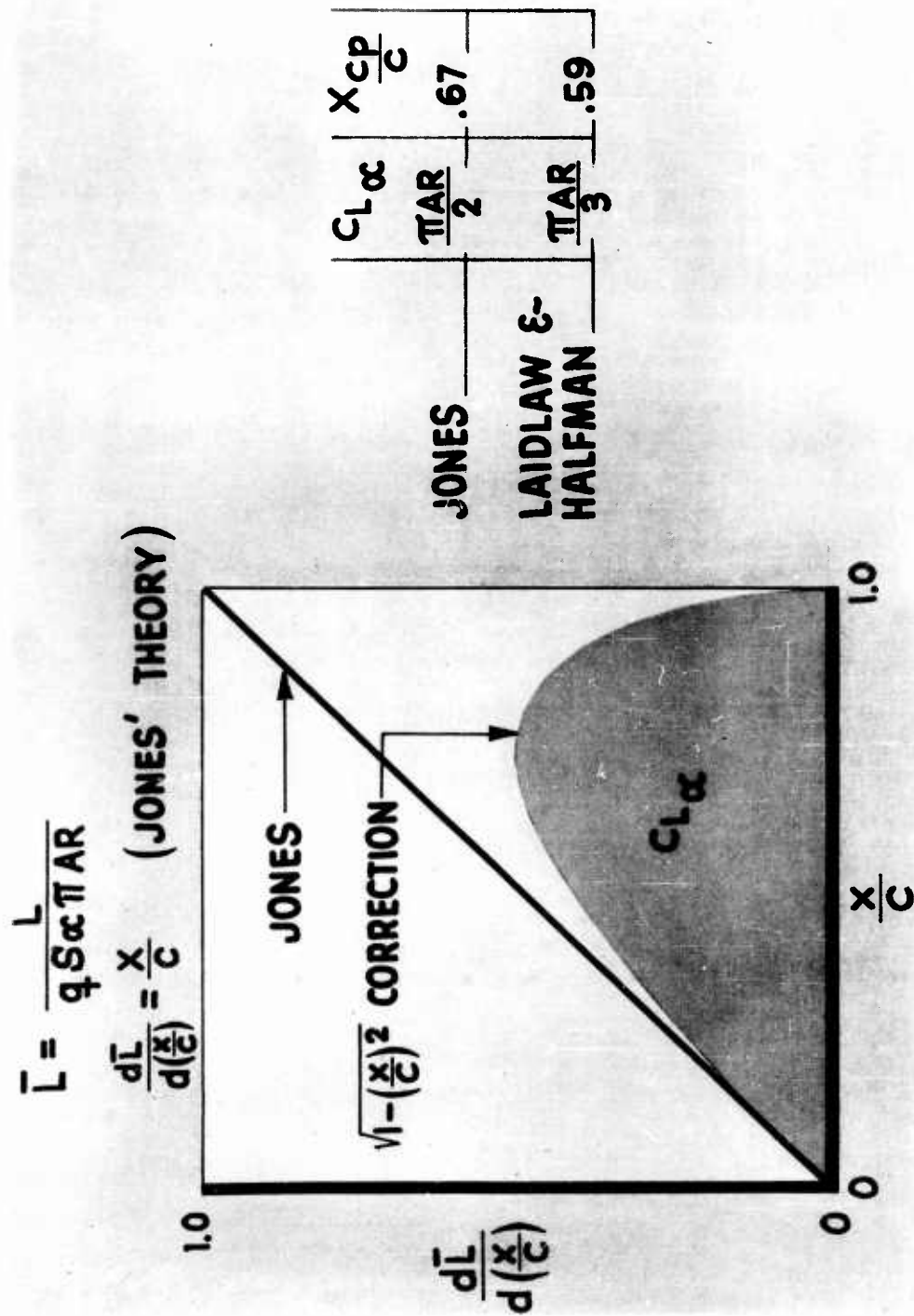


Figure 3 - Chordwise Lift Distributions

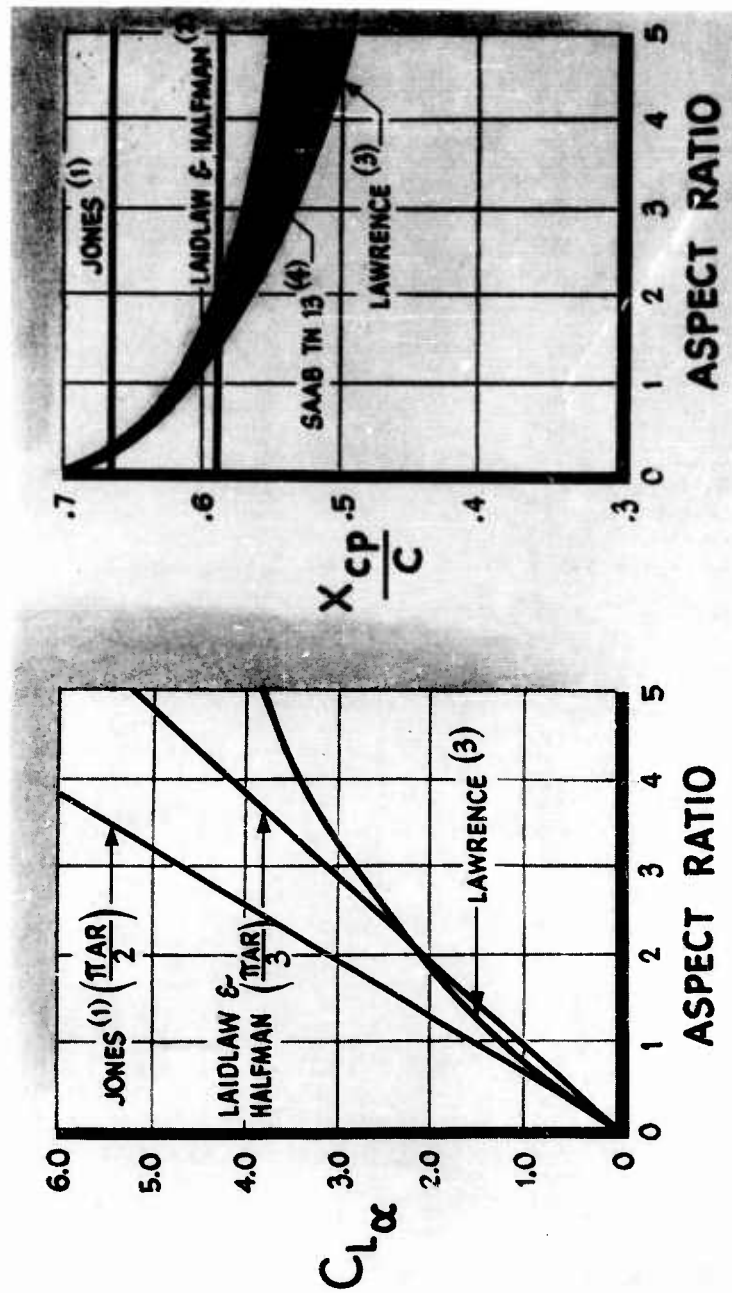


Figure 4 - Variations of  $C_L$  and  $x_{cp}$  With Aspect Ratio

$$\begin{aligned}
 \text{UNMODIFIED } \bar{L} &= \frac{L}{qS\alpha\pi AR} = \int_0^{1.0} \left(\frac{x}{c}\right) d\left(\frac{x}{c}\right) \\
 \text{INTRODUCE } F \left(1 - \frac{x}{c}\right)^n &\text{ and then} \\
 \text{MODIFIED } \bar{L} &= F \int_0^1 \left(\frac{x}{c}\right) \left(1 - \frac{x}{c}\right)^n d\left(\frac{x}{c}\right) = \frac{F}{(n+1)(n+2)} \\
 &\text{a/s/o} \\
 \text{MODIFIED } \bar{M}_{\text{APEX}} &= CF \int_0^1 \left(\frac{x}{c}\right)^2 \left(1 - \frac{x}{c}\right)^n d\left(\frac{x}{c}\right) = C \left(\frac{2}{n+3}\right) \frac{F}{(n+1)(n+2)}
 \end{aligned}$$

# SOLVING FOR CENTER OF PRESSURE LOCATION

$$\frac{x_{cp}}{c} = \frac{2}{n+3} \quad \text{or} \quad n = \frac{2}{\frac{x_{cp}}{c}} - 3$$

$$\text{DEFINE } C_{L\alpha} = \frac{L}{qS\alpha} = \frac{\pi ARF}{(n+1)(n+2)}$$

$$\text{WHENCE } F = \frac{(n+1)(n+2)}{\pi AR} C_{L\alpha}$$

Figure 5 - Derivation of n and F Factors

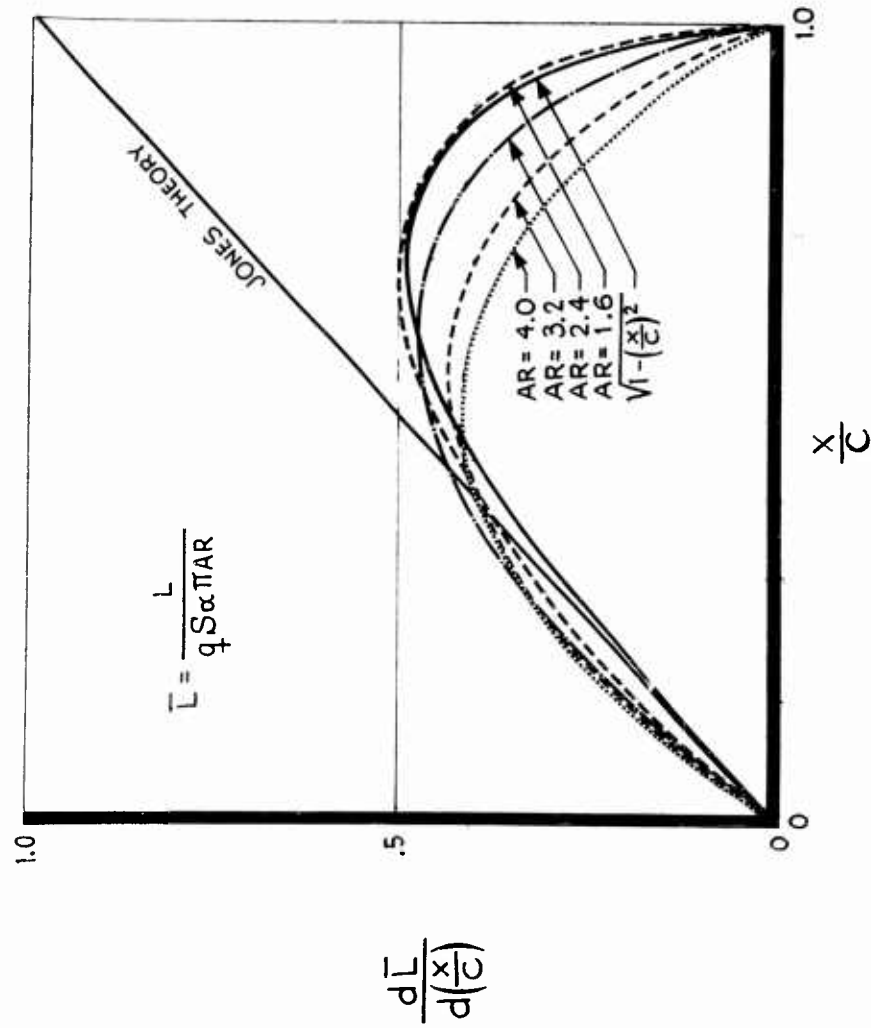


Figure 6 - Modified Chordwise Lift Distributions

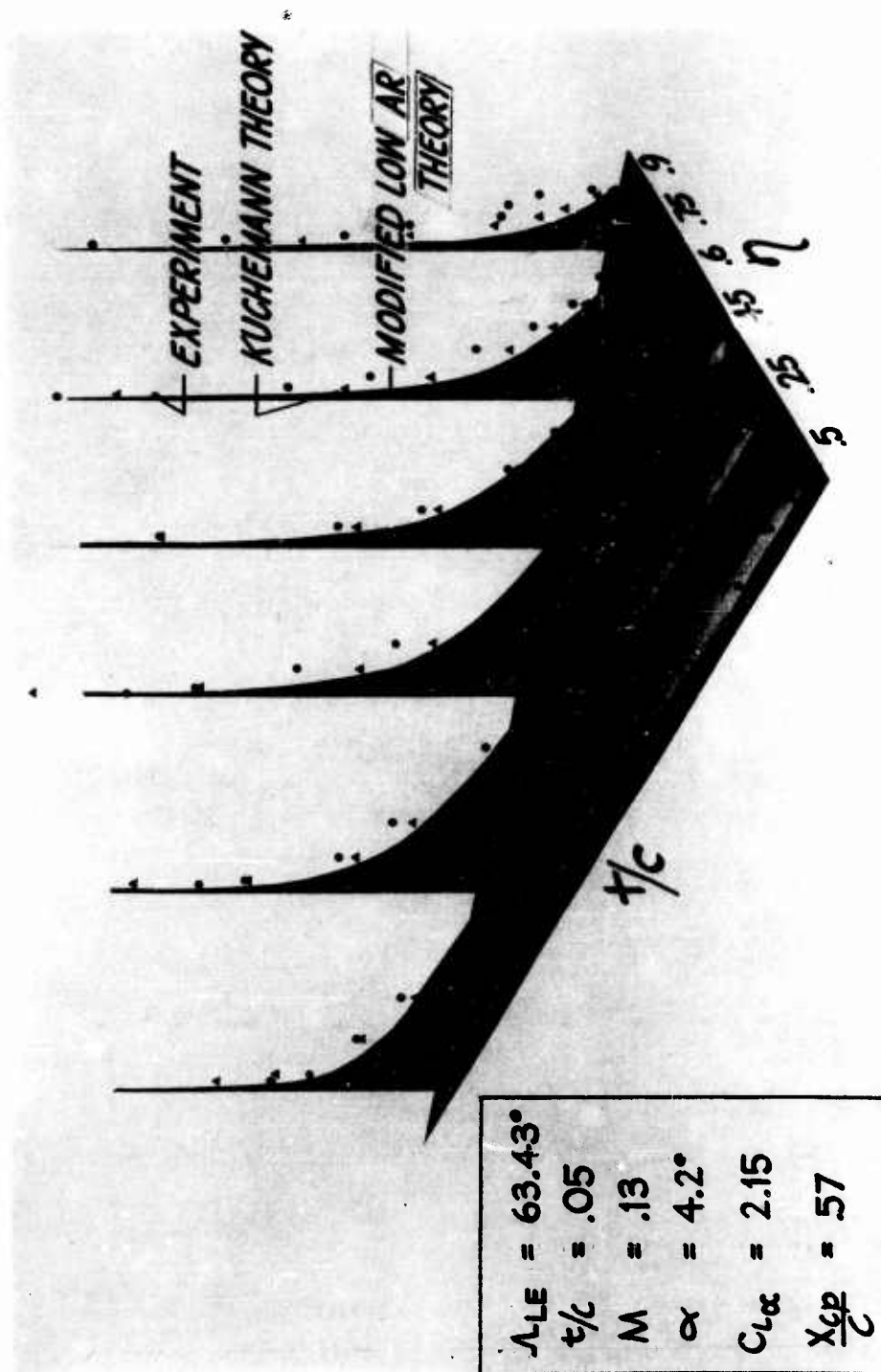


Figure 7 - Chordwise Pressure Distribution on an AR = 2.0 Delta Wing

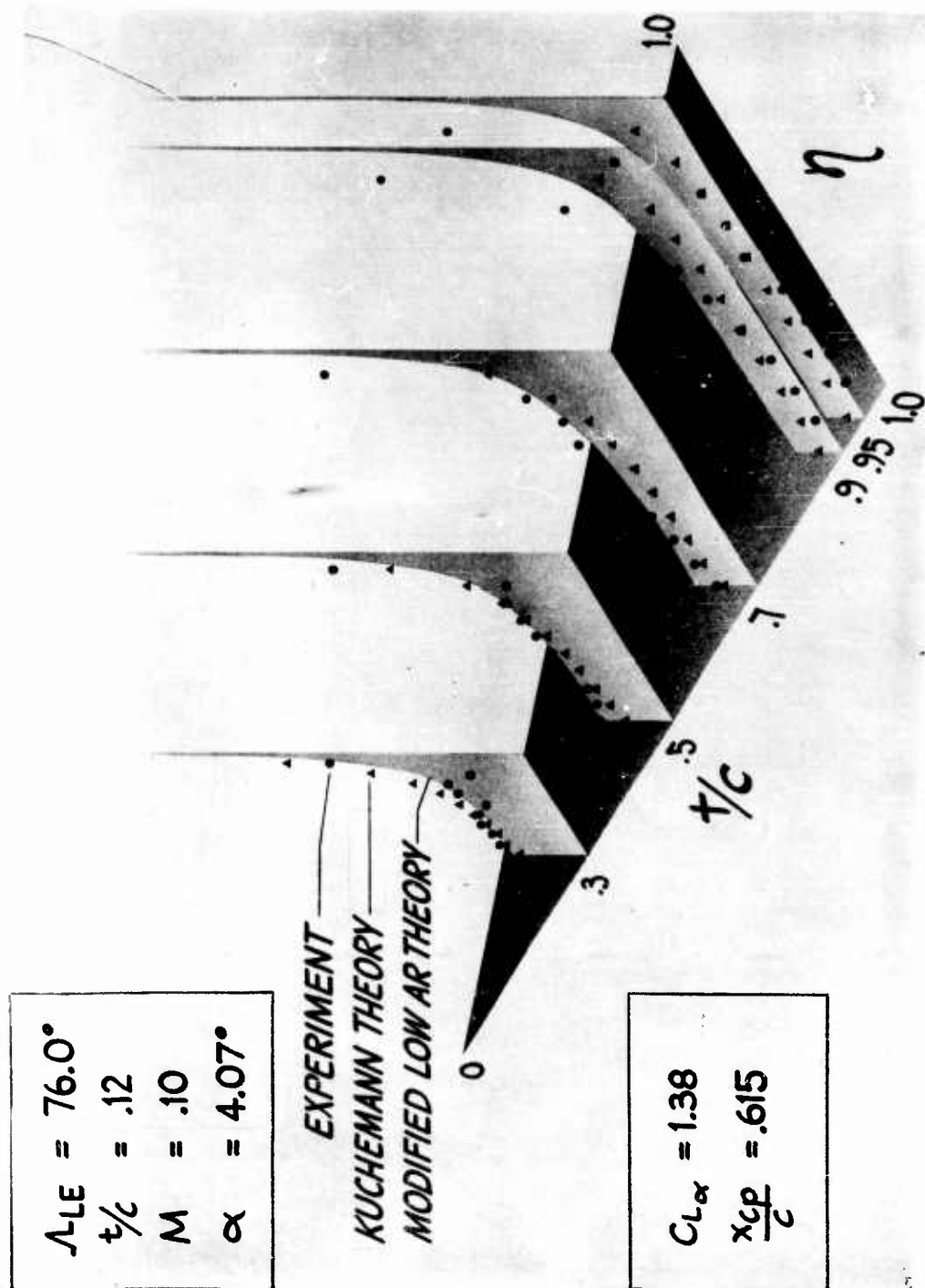


Figure 8 - Spanwise Pressure Distribution on an AR = 1.0 Delta Wing

# **PRESSURE DIFFERENTIAL**

$$\Delta p = \rho \left[ \frac{\partial(\Delta\phi)}{\partial t} + u \frac{\partial(\Delta\phi)}{\partial x} \right]$$

**WHERE  $(\Delta\phi) = \text{DISTURBANCE VELOCITY POTENTIAL}$**

**ASSUME DOWNWASH VELOCITY AS A FOURIER SERIES**

$$w(x, y, t) = f(x, t) \sum_{n=0}^N a_n \cos n\theta$$

**AND  $\Delta\phi$  BECOMES ANOTHER SERIES**

$$\Delta\phi(x, y, t) = f(x, t) \beta(x) \left\{ 2a_0 \sin\theta + a_1 \sin\theta \cos\theta \right. \\ \left. + 2 \sum_{n=2}^N \frac{a_n}{n^2-1} [n \sin\theta \cos n\theta - \cos\theta \sin n\theta] \right\}$$

Figure 9 - Basic Equations

# RETAINING FIRST DOWNWASH TERM

$$w = fa_o = \text{constant}$$

WHICH GIVES

$$\Delta\phi = 2w\beta\sin\theta$$

DIFFERENTIATING  $\epsilon$ - SUBSTITUTING INTO  $\Delta p$  EQUATION

$$\Delta p = \frac{2\rho U w \beta'}{\sin\theta}$$

WHICH LEADS TO

$$\frac{\Delta p}{q} = \frac{AR}{\sin\theta} \propto \frac{AR}{\sqrt{1-(\frac{\gamma}{\beta})^2}} \xrightarrow{\text{R.T. JONES}} \text{RESULT}$$

Figure 10 - Illustration of First Downwash Term



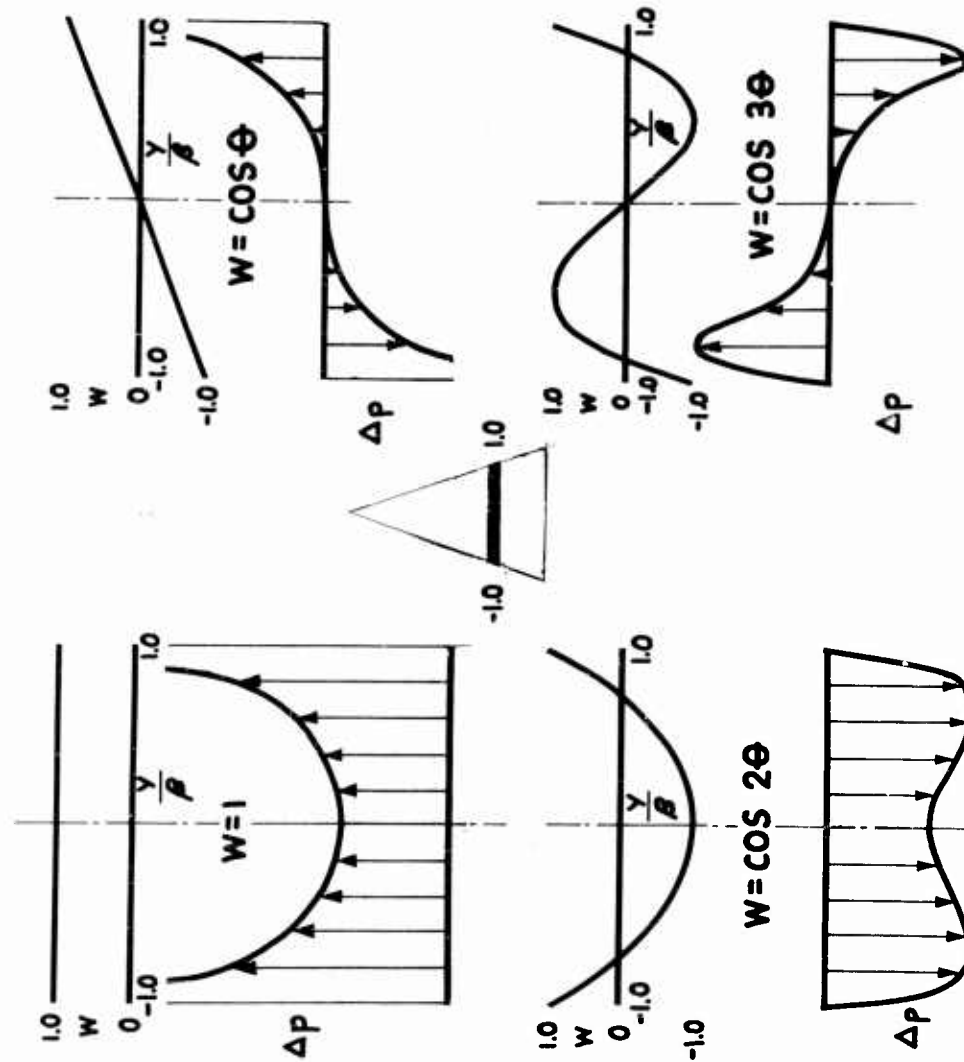


Figure 11 - Downwash-Pressure Distribution Relationships

$$C_L = \frac{L}{qS} = l_\gamma + ik l_\gamma'$$

$$C_M = \frac{M}{qSc} = m_\gamma + ik m_\gamma'$$

# VERTICAL TRANSLATION

## PITCHING ABOUT $\bar{x}_O$ AXIS

( $\gamma = \alpha$ )

$$l_z = -k^2 \bar{x}_{cp} C_{L\alpha}$$

$$l_z' = C_{L\alpha}$$

$$m_{\bar{z}x_O} = -k^2 \bar{x}_{cp} C_{L\alpha} \left( \frac{3}{n+4} - \bar{x}_O \right)$$

$$m_{\bar{z}x_O}' = C_{L\alpha} (\bar{x}_{cp} - \bar{x}_O)$$

$$\text{WHERE } \bar{x} = \frac{x}{c}$$

$$l_\alpha = 2C_{L\alpha} \left[ -k^2 \bar{x}_{cp} \left( \frac{3}{n+4} - \bar{x}_O \right) + \frac{1}{2} \right]$$

$$l_\alpha' = 2C_{L\alpha} (2\bar{x}_{cp} - \bar{x}_O)$$

$$m_{\alpha x_O} = 2C_{L\alpha} \left\{ \bar{x}_{cp} \left[ \left( \frac{6}{n+4} \right) \left( -\frac{2}{n+5} + \bar{x}_O \right) - \bar{x}_O^2 \right] k^2 \right.$$

$$\left. + \frac{1}{2} (\bar{x}_{cp} - \bar{x}_O) \right\}$$

$$m_{\alpha x_O}' = 2C_{L\alpha} \left[ \frac{6\bar{x}_{cp}^2}{\bar{x}_{cp} + 2} - 3\bar{x}_{cp} \bar{x}_O + \bar{x}_O^2 \right]$$

Figure 12 - Vertical Translation and Pitching Motion Derivatives

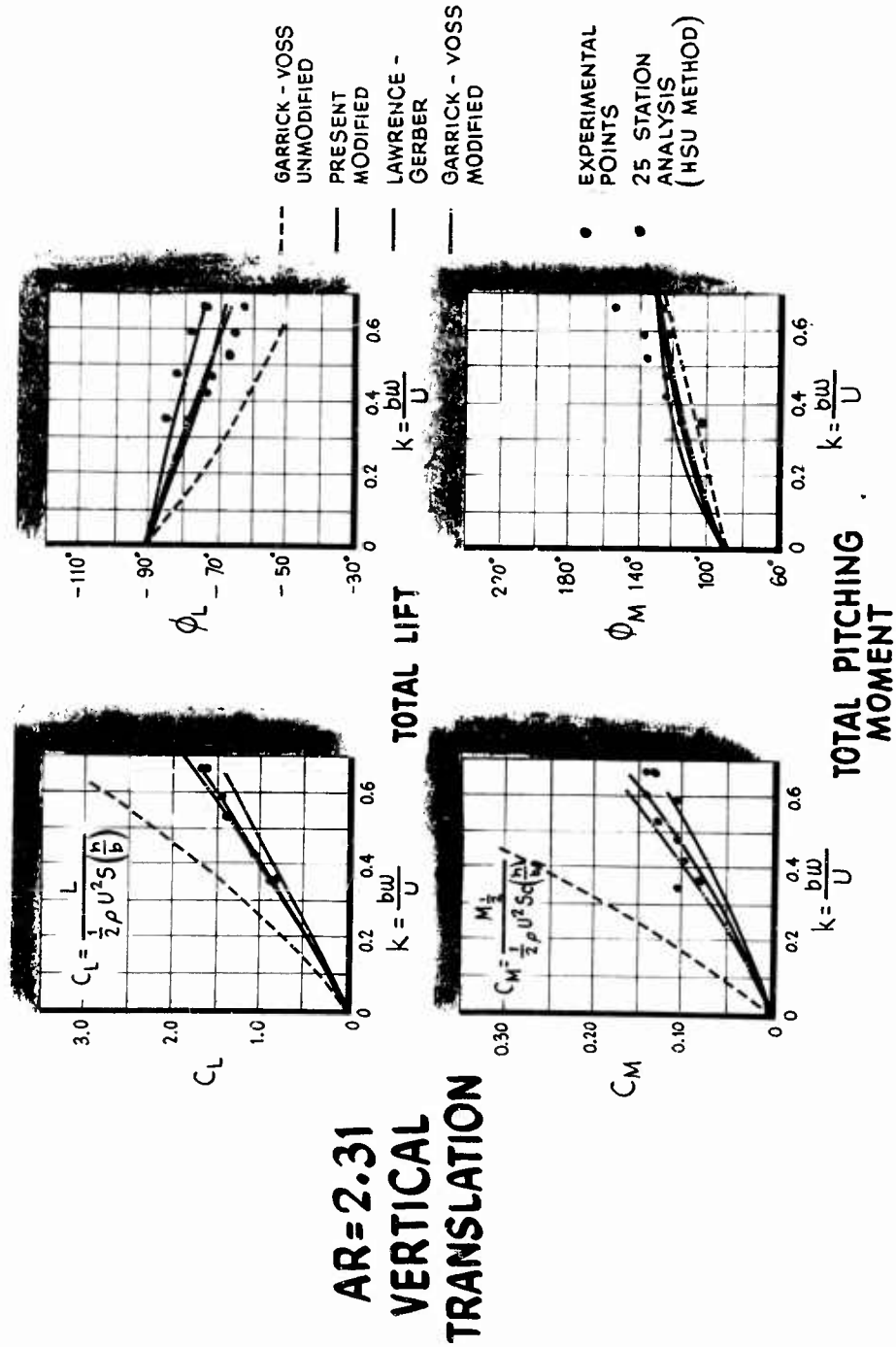


Figure 13 - Lift and Pitching Moment Amplitudes and Phase Angles for Vertical Translation Motion. Delta Wing, Aspect Ratio = 2.31

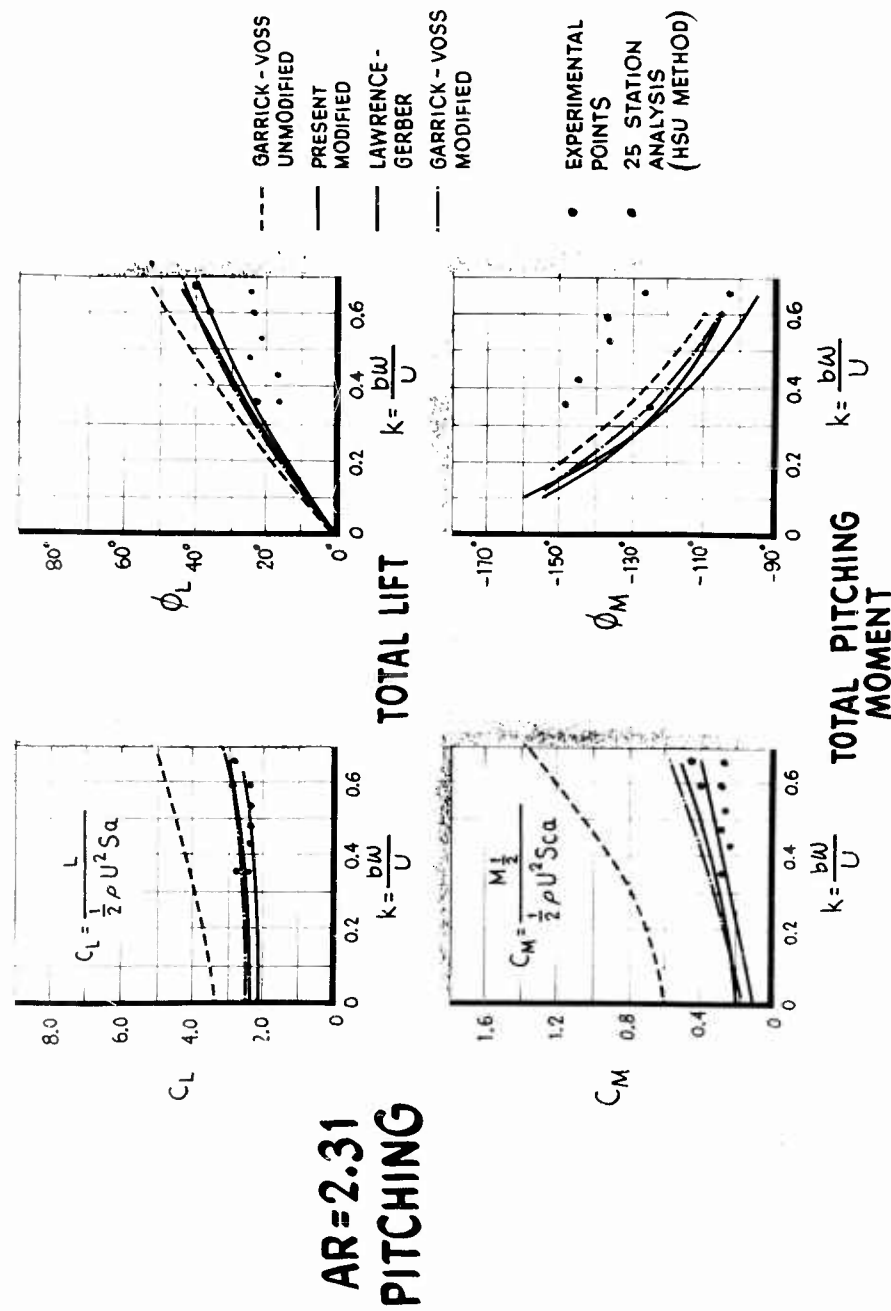


Figure 14 - Lift and Pitching Moment Amplitudes and Phase Angles for Pitching Motion. Delta Wing, Aspect Ratio = 2.31

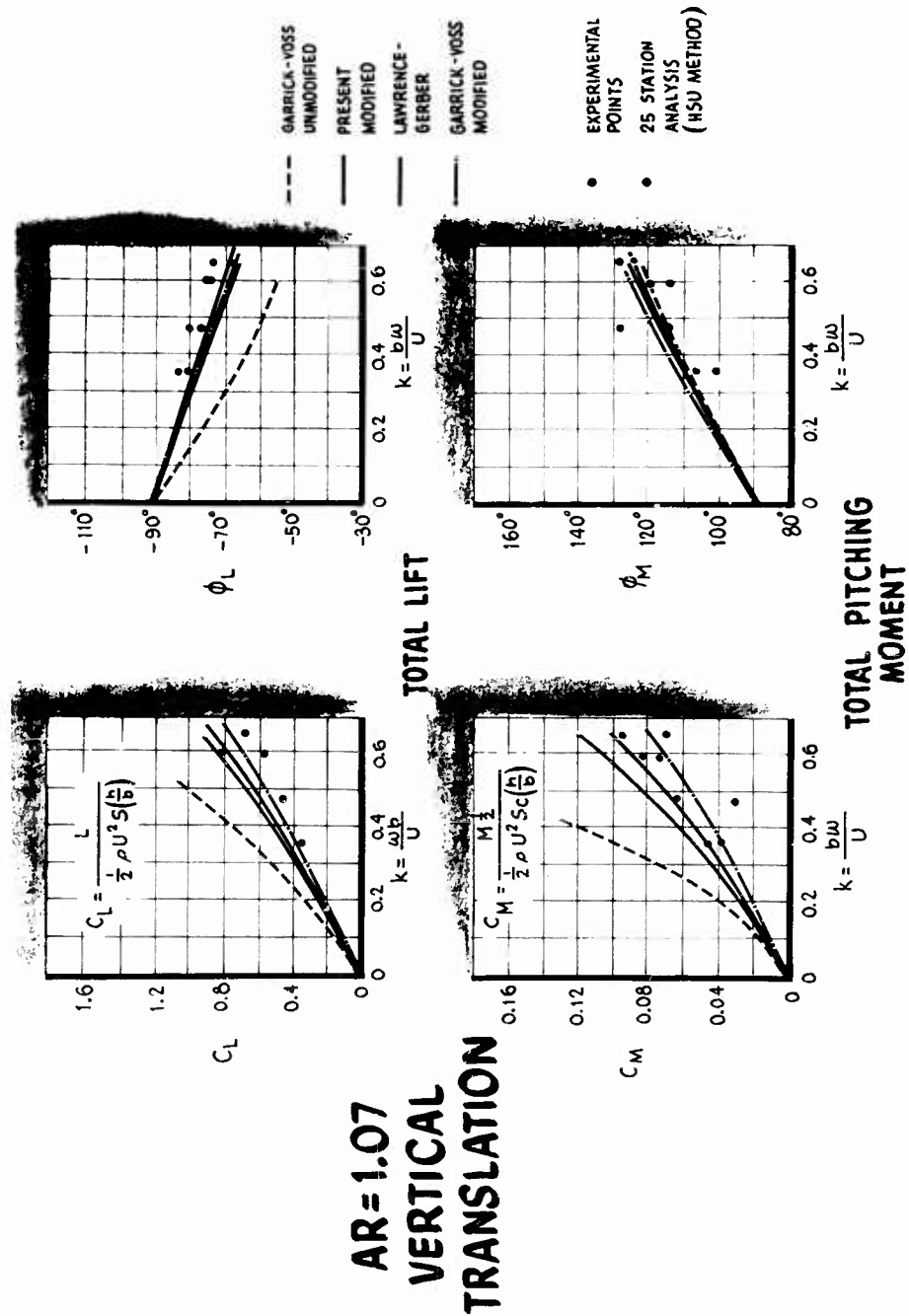


Figure 15 - Lift and Pitching Moment Amplitudes and Phase Angles for Vertical Translation Motion. Delta Wing, Aspect Ratio = 1.07

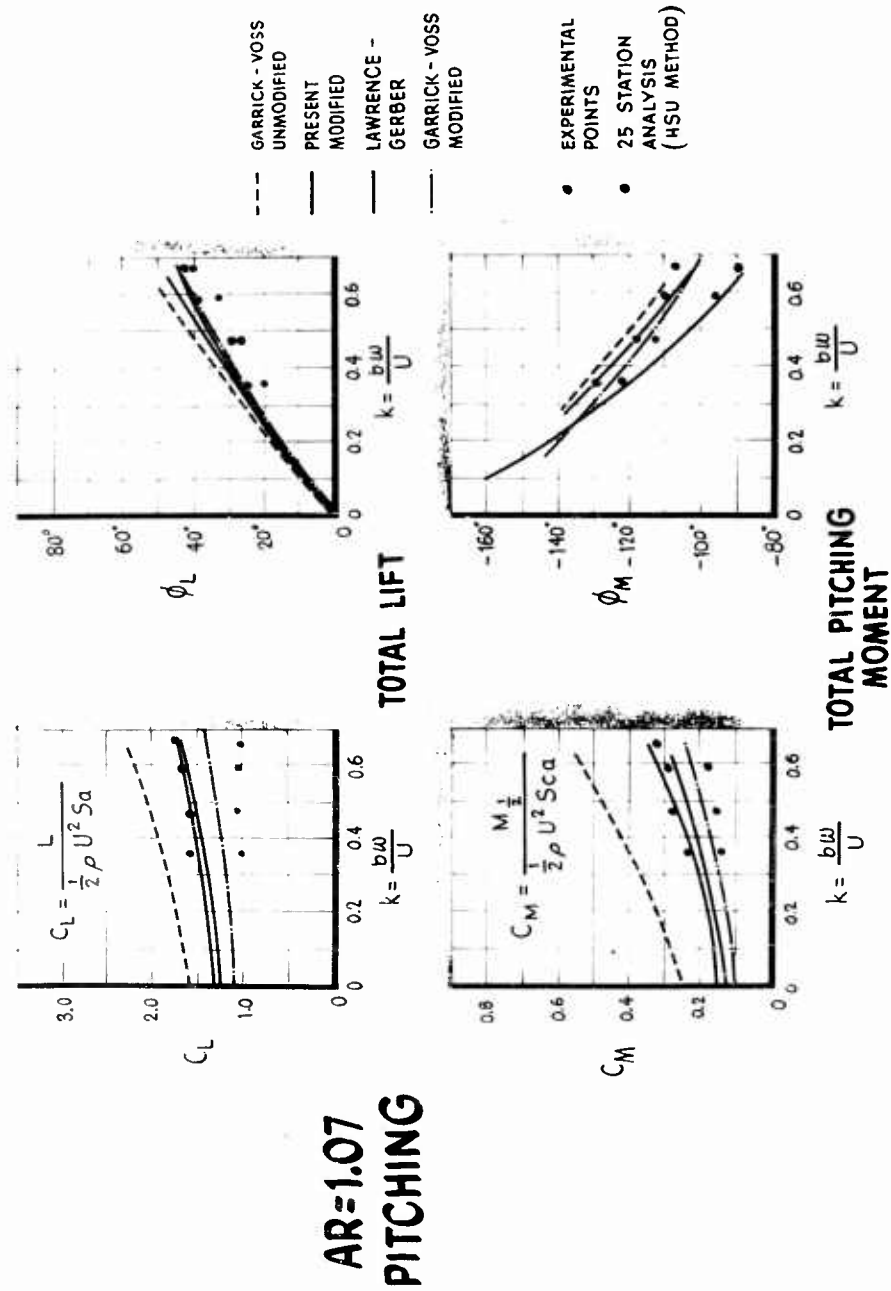


Figure 16 - Lift and Pitching Moment Amplitudes and Phase Angles for Pitching Motion. Delta Wing, Aspect Ratio = 1.07

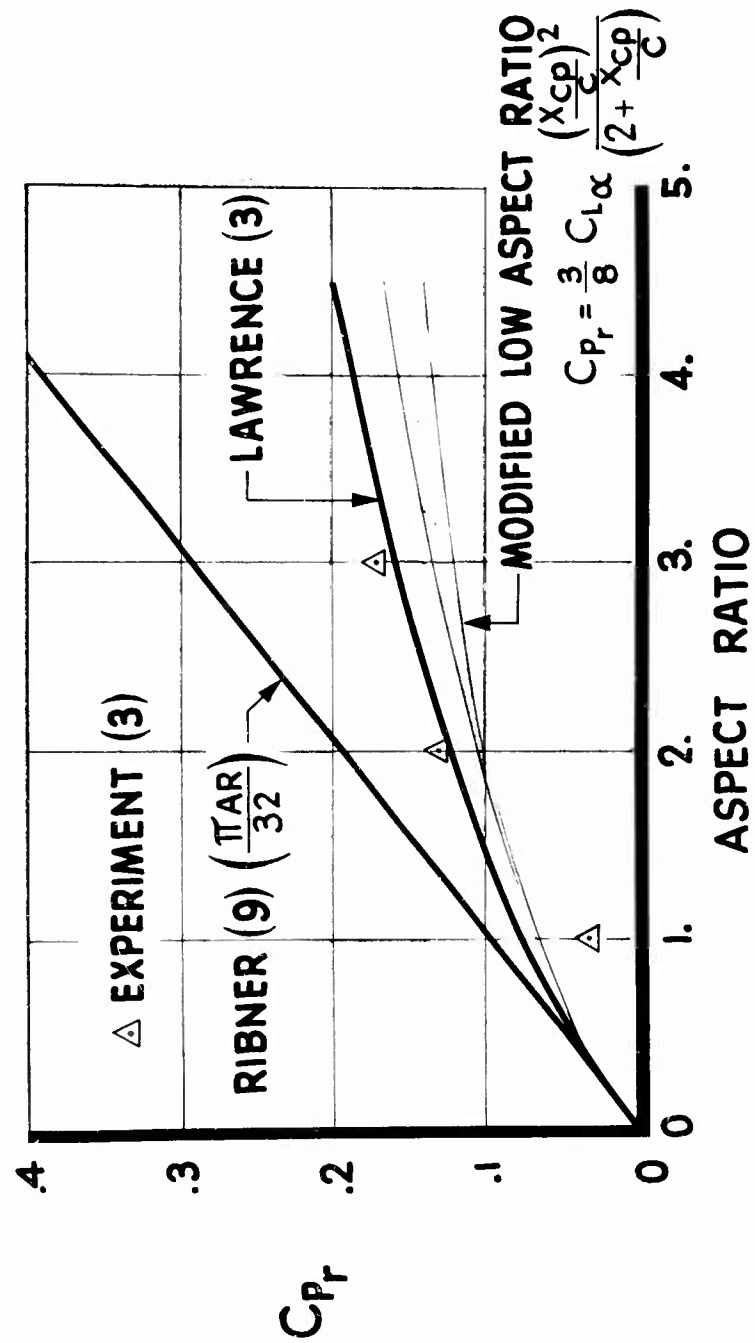


Figure 17 - Comparison of Damping-in-Roll Coefficients

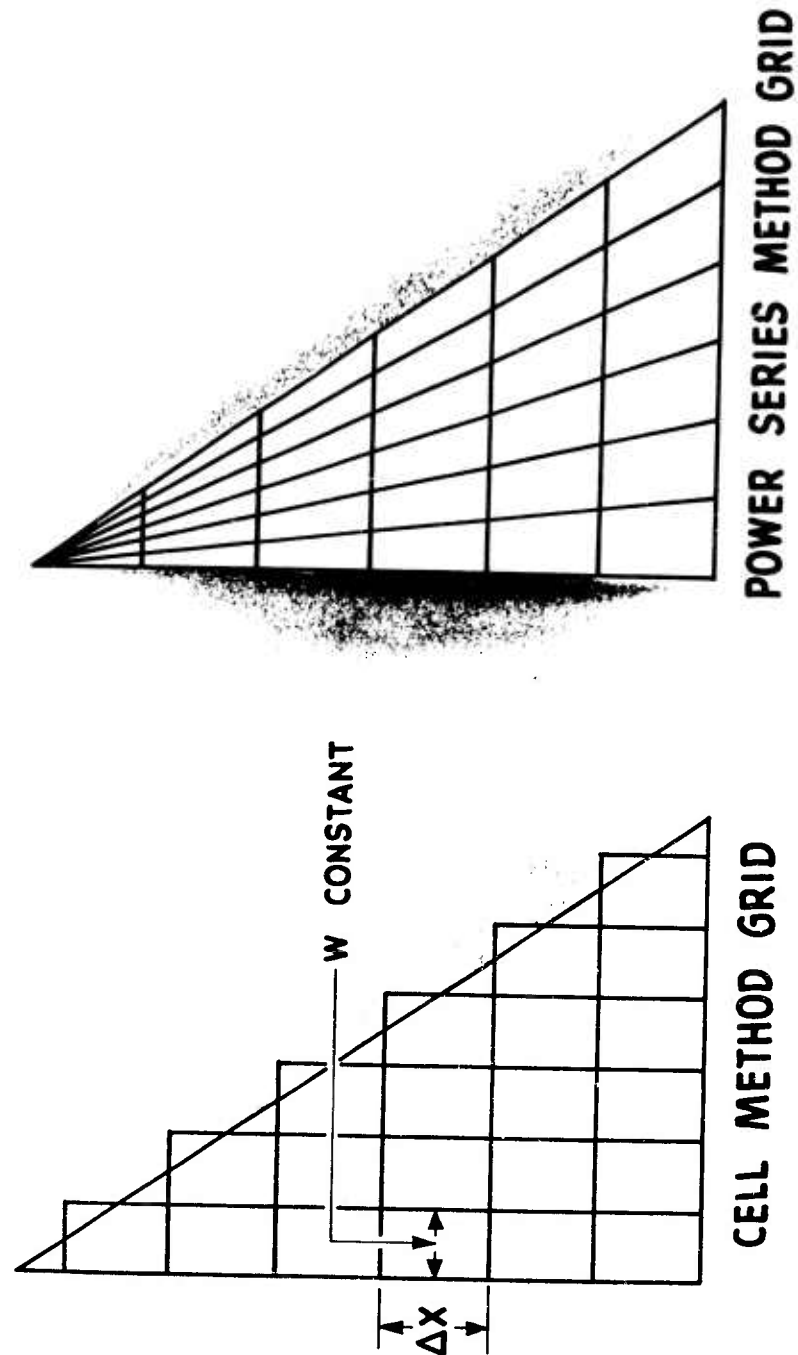


Figure 18 - Typical Aerodynamic Grid for a Flexible Wing



THE LIFT EQUATION FOR A SPANWISE STRIP IS:

$$\{dL\} = \frac{\rho}{2} \frac{ARF}{\pi} S \Delta X \left(1 - \frac{x}{c}\right)^n \left\{ [A_1] \{\ddot{z}\} + U [A_2] \{\dot{z}\} + [A_3] \{\dot{\alpha}\} + [A_4] \left\{ \frac{d\dot{z}}{dy} \right\} \right. \\ \left. + U^2 [A_5] \{\alpha\} + [A_6] \left\{ \frac{d\alpha}{dx} \right\} + [A_7] \left\{ \frac{d\alpha}{dy} \right\} \right\}$$

WHERE THE  $[A_n]$  ARE SPANWISE INTEGRATION MATRICES.  
IN TERMS OF VIBRATION MODE SHAPES

$$\begin{Bmatrix} \{z\} \\ \{\alpha\} \end{Bmatrix} = \begin{Bmatrix} [\phi_z] \\ [\phi_\alpha] \end{Bmatrix} \{q\}$$

AND THE INTEGRATED GENERALIZED AERODYNAMIC FORCE  
ASSUMES THE FORM

$$Q = \underbrace{[\lambda_1]}_{\text{INERTIA}} \{\ddot{q}\} + U \underbrace{[\lambda_2]}_{\text{DAMPING}} \{\dot{q}\} + U^2 \underbrace{[\lambda_3]}_{\text{STIFFNESS}} q$$

Figure 19 - Form of the Cell Method Equations

WITH  $z = \bar{\Phi}q$ , THE DOWNWASH IS

$$w(x,y) = \sum_k \left( i\omega z(x,y) + u \frac{\partial \bar{\Phi}(x,y)}{\partial x} \right) = \left( i\omega \bar{\Phi}(x,y) + u \frac{\partial \bar{\Phi}(x,y)}{\partial x} \right) q$$

LET  $\bar{\Phi}(x,y) = \sum_{j=0}^{\infty} \sum_{k=0}^{\infty} A_{j,k} x^j y^k$  WHERE  $y = \frac{AR}{4} \times \cos \Theta$

AND SUBSTITUTE BACK TO OBTAIN

$$w(x,y) = f(x, AR, \Theta, A_{j,k})$$

NOW TO FIND PRESSURE DIFFERENCE ASSUME

$$w(x,y) = \sum_{n=0}^N a_n \cos n\Theta$$

EQUATING THE TWO  $w(x,y)$  FORMS GIVES

$$a_n = f(x, AR, \Theta, A_{j,k})$$

AS BEFORE

$$\begin{array}{ccc} a_n & \xrightarrow{\Delta \Phi} & \Delta p \\ \text{FOURIER COEFFICIENTS} & \text{VELOCITY POTENTIAL} & \text{PRESSURE DIFFERENCE} \end{array}$$

FINALLY

$$\{\Delta p\} = \frac{\rho}{2} U^2 \left[ \underbrace{F(AR, x)}_{\text{CHORDWISE CORRECTION}} \right] \left[ \underbrace{P(x, \Theta)}_{\text{COMPLEX PRESSURE FUNCTIONS}} \right] \left[ \underbrace{AR^m}_{\text{ASPECT RATIO EFFECT}} \right] \left[ \underbrace{A}_{\text{POWER SERIES COEFFICIENTS}} \right] \{q\}$$

Figure 20 - Form of the Power-Series Method Equations

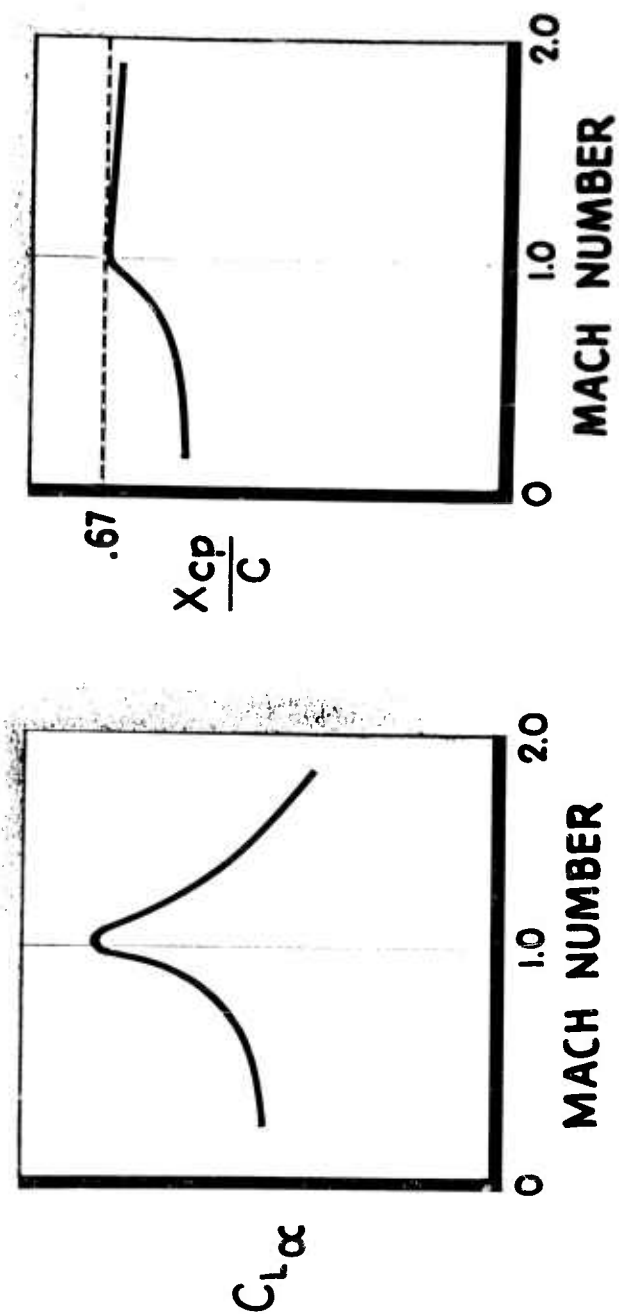


Figure 21 - Typical Variations of  $C_L$  and  $x_{cp}$  With Mach Number

# 45° DELTA WING

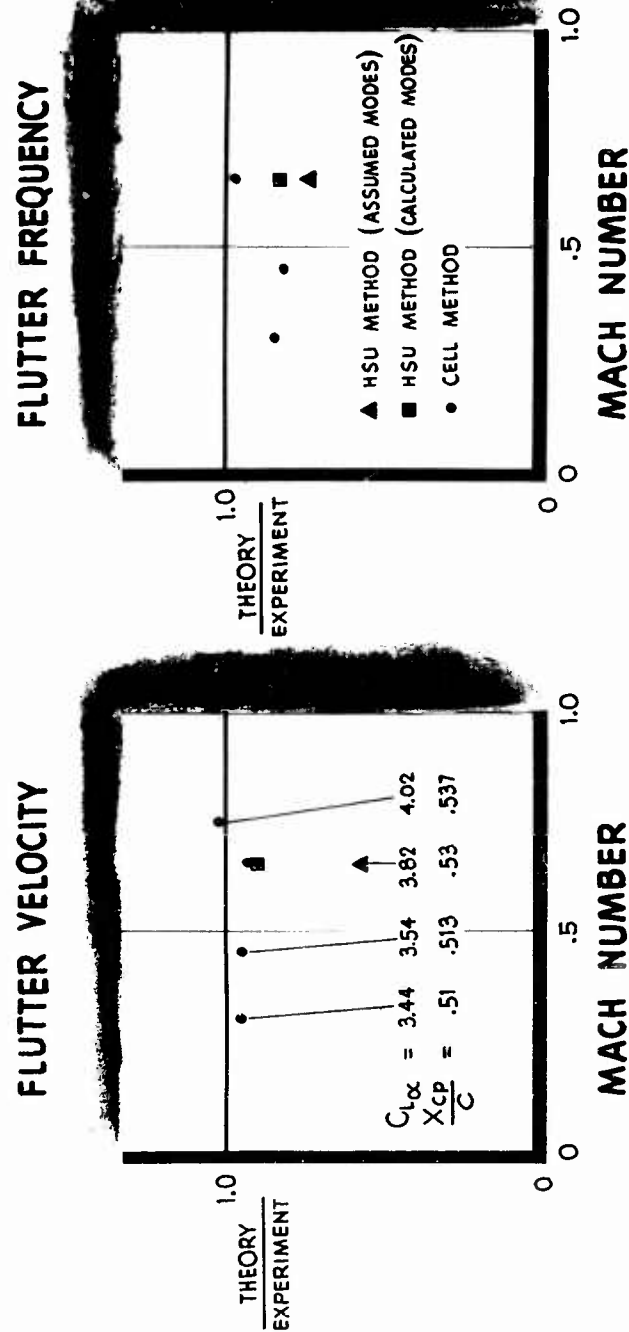


Figure 22 - Comparison of Experimental and Theoretical Flutter Results for a 45° Delta Wing

# 70° FLAT PLATE DELTA WING

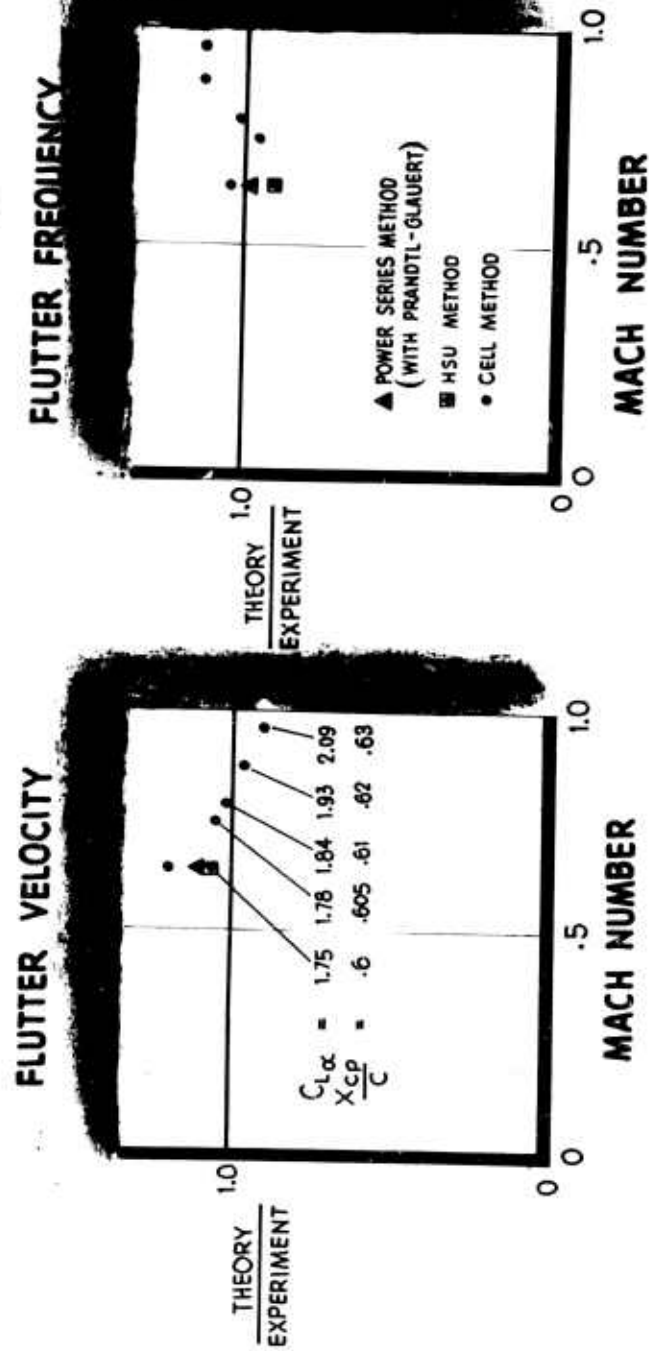


Figure 23 - Comparison of Experimental and Theoretical Flutter Results for a 70° Flat Plate Delta Wing

**ADDITIONAL DELTA WINGS**

L.E. SWEEP ANGLE	WING NO. <sup>(13)</sup>	METHOD	MACH NO.	$\frac{V_f}{V_{fex}}$	$\frac{f_f}{f_{fex}}$
45°	12	POWER SERIES WITH PRANDTL-GLAUERT	.849	.905	1.4
53° 8'	15		.858	.975	2.25
60°	8		.909	.83	1.31
45°	12	CELL $C_{L\alpha} = 4.6$ $X_{cp} = .52$	.849	1.08	1.25

Figure 24 - Summary of Comparison of Flutter Results for Three Delta Wings

A COMPARATIVE EXPERIMENTAL AND THEORETICAL  
STUDY OF THE FLUTTER OF FLAT PANELS IN A LOW  
SUPERSONIC FLOW \*

M. H. Lock and Y. C. Fung  
California Institute of Technology  
Pasadena, California

Abstract

A series of panel flutter experiments were performed in the GALCIT transonic wind tunnel. The preflutter panel motion and the motion during flutter were studied in detail. Flutter boundaries were obtained between Mach numbers 1.15 and 1.5. Three analytical studies of the flutter phenomenon, based upon conventional assumptions, are presented which facilitate comparison between theory and experiment. A detailed comparison between the theoretical and experimental results reveals considerable disagreement in the flutter boundaries at supersonic Mach numbers less than 1.4. The agreement between theory and experiment improves at the higher Mach numbers. The theory appears to be overconservative for the prediction of flutter boundaries at the lower supersonic Mach numbers. A possible cause of this inadequacy of the theory is discussed.

\*This research was supported by the United States Air Force, through the Office of Scientific Research of the Air Research and Development Command.

LIST OF SYMBOLS

$b$	Plate semi-chord
$B_1$	Amplitude of the static deflection of the plate (see Section 2.2.)
$f(\omega)$	Power spectrum of the response of the plate
$g$	Structural damping coefficient
$h$	Plate thickness
$k$	$= \frac{\omega b}{U}$ , reduced frequency of flutter
$k_0$	$= \frac{2\omega_0 b}{U}$ , stiffness parameter
$M$	Mach number of the flow
$p(x, y, t)$	Aerodynamic pressure induced by the deflection
	$Z_a$ acting upon the upper surface of the plate
$R_I$	Energy contribution per cycle at flutter arising from the integral term in equation 1
$R_x$	Energy contribution per cycle at flutter arising from the $\partial Z_a / \partial x$ term in equation 1
$R_T$	Energy contribution per cycle at flutter arising from the $\partial Z_a / \partial t$ term in equation 1
$t$	Time



$U$	Velocity of the undisturbed flow
$w_a(x)$	Downwash (see equation 11)
$\bar{x}$	Streamwise co-ordinate
$x$	$= \bar{x}/b$ , dimensionless streamwise co-ordinate
$Y(x)$	Plate mode shape
$Y_1(x)$	Static deflection surface of the panel
$z$	Spatial co-ordinate
$Z_a(x, t)$	Vertical deflection of the plate, positive upwards
$\mu$	$= \frac{\rho_s h}{2b \rho_0}$ , mass ratio of the panel to air
$\rho_0$	Density of the undisturbed air
$\rho_s$	Density of the plate material
$\omega$	Flutter frequency, radians per second
$\omega_0$	Fundamental frequency of free vibration, radians per second
$\bar{\omega}$	$= \frac{2kM^2}{(M^2-1)}$ , the supersonic reduced frequency
$\bar{\delta}$	Ratio of the amplitude of vibration of the plate to the plate chord

# Introduction

The flutter of flat or curved panels in a flow has been the subject of numerous theoretical and experimental studies. In Reference 1, a critical survey of the methods of analysis and the results thereof is given: the results are usually presented in the form of minimum panel thickness required for prevention of flutter at various geometric and flow conditions. This form seems to be the most useful for assessing the engineering significance of the theoretical or experimental results. From such a review it is clear that the understanding of panel flutter as a mathematical problem has progressed a long way, but a detailed comparison between theoretical and experimental results is lacking.

Considerable experimental work has been performed at the NACA-NASA, Caltech, M.I.T. and at various aircraft firms. The earliest experiments were reported upon by Jordan (Ref. 2), Sylvester and Baker (Ref. 3) and Sylvester (Ref. 4). Eisley (Ref. 5) described some experimental studies on the flutter of buckled panels at Mach number 2.18 and showed reasonable agreement with the theoretical flutter boundaries, however, there were some aspects of his experimental observations that still remain to be explained (see Ref. 6). Jordan, Greenspan and Goldman (Ref. 7) have reported upon panel flutter experiments at subsonic and supersonic speeds. Stearman (Ref. 8) gave a detailed experimental study of the flutter of a narrow membrane in a subsonic flow and found the puzzling fact that no agreement could be obtained at all with a theory based upon slender body aerodynamics. Tuovila and Hess (Ref. 9) Kordes, Tuovila and Guy (Ref. 10) gave a wealth of experimental data, but a very broad range of panel forms, structural construction, flow conditions, mid-plane stress and

heat input was covered. These parameters were accounted for in an overall fashion; they were not separated and no detailed comparison with theory was made.

Because of the complexity in quantitative analysis, only the theory of linearized two-dimensional supersonic flutter of unbuckled panels has reached a reasonable degree of completeness. Hence if an experimental evaluation of the theory is attempted this should be the first case to be investigated. However a critical comparison in this case has yet to be made.

One reason for this lack of definitive comparison between theory and experiment is because of the experimental difficulty in assuming the linear condition of the phenomenon. Unlike the buckled panel or the narrow membrane, for which the flutter amplitude is large and the onset of flutter is sudden and unmistakable, the plate motion will be linear only for small amplitude oscillations and, in the presence of disturbances in a wind tunnel, the experimental definition of flutter requires clarification. It seems evident that one must not only take steps to ensure that the panel conditions remain linear, but also must carefully examine the panel response at all times to detect if flutter occurs.

Under the auspices of the Office of Scientific Research, U.S. Air Force, research has been carried on at the California Institute of Technology on the subject of panel flutter, with major emphasis on the critical comparison between theory and experiment. The first topic that was completed concerns the flutter of linear flat panels in lower supersonic flows. A brief report on this subject will be given below; a more detailed presentation can be found in Ref. 24. Other aspects under investigation at Caltech include a similar study of the flutter of linear flat panels at a higher supersonic Mach number (2.8), and of the flutter of slightly curved panels, curved in the streamwise direction, but straight in the spanwise direction. Experiments on this second subject have been completed, but a theoretical comparison requires more calculations. The most ambitious part of the current Caltech-OSR project concerns the flutter of unstiffened circular cylinders, with flow parallel to the cylinder axis. The experiments on this last topic are to be carried out shortly at the Unitary Wind Tunnel of the NASA Ames Laboratory. The associated theoretical investigations are being pursued.

The following presentation is therefore directed towards an experimental evaluation of the theory in the linear two-dimensional supersonic case. A series of panel flutter experiments carried out in the GALCIT transonic wind tunnel at Mach numbers up to 1.5 are described. A detailed comparison between the theoretical and experimental results reveals considerable disagreement in the flutter boundaries at Mach numbers less than about 1.4. The agreement between theory and experiment improves at higher Mach

numbers. The conventional theory appears inadequate for the prediction of flutter boundaries at the lower supersonic Mach numbers. A possible cause of this inadequacy of the theory is discussed.

## 1. EXPERIMENTAL STUDIES

A series of panel flutter experiments were carried out in the GALCIT 4' x 10' transonic wind tunnel at Mach numbers up to 1.5. The wind tunnel installation was designed to represent two-dimensional conditions without mid-plane stress. The panels were installed in the ceiling block of the wind tunnel such that the panel surface would lay flush with the ceiling surface (Figure 1). Each test panel was soldered rigidly to a mounting frame at its leading edge, and attached to a flexure, which prevents vertical displacement but permits horizontal displacement, at the trailing edge. The streamwise edges of the panels were free. The space behind the test panel, the venting chamber, was vented to the free stream.

Measurements were made of the velocity profile of the boundary layer over the test panel. On the tunnel centerline, the thickness of the boundary layer, defined as the height above the solid surface where the flow velocity reached 99 per cent of the free stream velocity, was found to be of the order of 0.34" - 0.40". The velocity profiles were typical of a turbulent boundary layer (see Figure 2). Pressure fluctuations in the boundary layer served as a source of excitation of the panels in the non-flutter regime. The lateral motion of the plates was measured and analyzed at different flow Mach numbers. The flutter boundaries were estimated from these measurements. Harmonic analysis of the plate motion yielded certain of the natural frequencies of the test panels at the different Mach numbers. By this means the origin of the flutter mode was identified.

### 1.1 Test Panels and Equipment

The test panels were made from thin brass sheets (0.010" to 0.0155" thickness) and were attached to a brass mounting frame at their leading and trailing edges. The leading edges of the panels were soldered directly to the mounting frame. The trailing edges of the panels were mounted upon a flexure support (see details in Figure 1). A Z section flexure of 0.006" thick phosphor bronze sheet was employed. The horizontal deflection-load characteristics of the flexure were linear up to at least 0.026" deflection at the trailing edge. The flexure stiffness per unit width was found to be approximately 22 lbs. per inch per inch. The rotational stiffness of the flexure was approximately 0.92 lbs-inches per inch per radian.

This type of panel support was found necessary to reduce the development of mid-plane stresses in the test panels. Such stresses, which have an appreciable effect upon the flutter boundaries, could be easily developed by static pressure differentials

across the plates, by thermal effects and by mechanical distortion of the mounting frame when it is inserted in the wind tunnel. The flexure support conveniently circumvents these difficulties and has the added advantage of reducing the structural effect of any small initial panel curvature upon the flutter phenomenon. The experimental frequencies of flexural vibration of the various test panels are shown in Table 1 and they are seen to be intermediate to the corresponding theoretical frequencies of plates with clamped-clamped and clamped-simply supported boundary conditions.

The mounting frame, to which the test panels were attached, fitted into the ceiling block of the wind tunnel such that the surface of the test panel would lay flush with the ceiling surface. To reduce the effect of the sidewall boundary layers the streamwise edges of the plates were set approximately 0.22" from the tunnel walls. A gap of about 0.038" was left between these edges of the panel and the mounting frame. These gaps served to vent the chamber behind the panels to the free stream static pressure.

The wind tunnel was of the closed circuit type and had a test section that was 4" wide and approximately 10" deep. (Ref. 11). The Mach number of the flow was varied continuously by two screw jacks which controlled a flexible nozzle on the tunnel floor block. The supply pressure was kept at atmospheric pressure throughout the tests. The supply temperature was kept between 30 to 32° C. The test section Mach number was estimated from static pressure measurements taken upon the mounting frame and the ceiling liner under the assumption of isentropic flow. Ten static pressure taps were provided for these measurements. Three taps were located upstream of the model, three more taps were downstream of the model and four taps were located on the mounting frame itself. The pressure in the venting chamber behind the test panels was also measured. Pressure measurements taken from these taps during the experiments indicated that good flow conditions were obtained over the test panel installation. The estimated variation of Mach number over the panel chord was of the order of 0.5 - 1 per cent of the average estimated Mach number. The spanwise variation of the free stream Mach number was of the same order of magnitude.

When the wind tunnel was in operation the motion of the panel induced by the pressure fluctuations present in the turbulent boundary layer was measured by an inductance pickup. This pickup was located in the chamber behind the panel, on the tunnel centerline at 2.2" downstream of the test panel leading edge position. The pickup, which employed a 100 kilocycle carrier system, had the advantage of permitting simultaneous static and dynamic measurements of the plate motion. The signal from the pickup was relayed to a harmonic analyser (Technical Products TP 627 and TP 626), a Ballantine true root mean square meter and a Moseley automatic plotter. Precise determination of the plate frequencies was

accomplished with the use of a Hewlett Packard oscillator and a Berkeley type 5501 counter. An oscilloscope was also employed in the analysis of the plate response.

A number of panels with thickness ratios ( $h/2b$ ) varying from 0.00297 to 0.0046 were tested. See Table 1. The chord lengths were varied between 3.14" and 3.79". The majority of the tests were made with 0.0125" thick panels. The panel widths were kept at 3.56".

### 1.2 Still-air Vibration Tests

The flexural modes of vibration of the test panels may be divided into two classes, namely; (1) the "two-dimensional" modes, where the nodal lines are all essentially parallel to the fixed edges of the plate and, (2) the "three-dimensional" modes where nodal lines appear that are not parallel to the fixed edges. A few nodal line patterns for a typical test panel are shown in Figure 3, obtained by acoustic excitation. The two-dimensional modes that are shown are the modes labeled (2, 0), (3, 0) and (4, 0).

By tracing the continuous variations of the natural frequencies of the plates at different Mach numbers to their still air values, it is possible to identify the source of the flutter mode and to assess the importance of the three-dimensional plate modes in what is intended to be a two-dimensional experiment.

### 1.3 Wind Tunnel Tests

The wind tunnel test procedure consisted of measuring and analyzing the lateral motion of a given test panel at successive Mach numbers.

The following description of two types of motion serves as an experimental definition of flutter. In the non-flutter region the plate motion was of a highly irregular nature. The flutter motion on the other hand was very regular and was of appreciably greater amplitude. In Figure 4, the first oscilloscope trace shows a typical plate response in the non-flutter region; the second oscilloscope trace shows a typical plate response at flutter. Harmonic analysis of the plate response in non-flutter region revealed a series of spectral peaks at the natural frequencies of the panels (see Figure 5). The major contribution to the energy spectrum came from the lowest natural frequency. An example is shown in Figure 6, in which the upper trace shows the variation of the measured mean square response of a test panel in the non-flutter region; the lower trace shows the same after the signal passed through a filter of 50 cps band width centered about the fundamental natural frequency of the plate. The mean square values were obtained by averaging over about 5 seconds. On the average it is seen that the response in the frequency band around the fundamental frequency contributed

about 75 per cent of the total. The corresponding fundamental mode of vibration derived originally from the mode (2,0). The non-flutter response was found to be larger in the subsonic flows than at the supersonic Mach numbers; an effect believed to be due to disturbances from the wind tunnel diffuser being propagated upstream into the working section. For supersonic flow the root mean square amplitude of the measured plate motion in the non-flutter region would be of the order of  $0.0005'' - 0.0015''$ . During the flutter motion, root mean square amplitudes of the order of  $0.016''$  were recorded, corresponding to actual amplitudes of the order of twice the plate thickness.

The approach to the flutter boundary would be characterized by a rapid increase in the amplitude of the plate response. The variation of the mean square plate response with Mach number at the flutter boundary of a typical test panel is shown in Figure 7. The exact determination of the flutter Mach number from such measurements is not possible. However, the rapid increase of the mean square response with Mach number allows a close estimate to be made. The method employed was to choose, as the flutter Mach number, some value at which the mean square response had increased appreciably (by a factor of 20~30) from an average value for the non-flutter region. At such a Mach number the major contribution to the response was the regular harmonic motion characteristic of the flutter region. Such a method appears rather vague; however, the increase in the plate response as the flutter region is approached is so rapid that the method is practical. For example, for the case shown in Figure 7, computation of the boundary using an increase factor of 30 instead of 20 would change the flutter Mach number by less than 1 per cent.

A certain amount of irregularity was present in the plate response at flutter; however, this irregularity was very small compared to the steady component of the mean square response (see Figure 8). This irregularity in the response was due to the random pressure fluctuations acting upon the test panel. A power spectrum of the flutter motion of one of the test panels is shown in Figure 9. A different way of showing the character of the flutter motion is by means of the oscilloscope traces presented in Figure 10. The upper trace shows the total response. The second trace shows the response when it is filtered at the flutter frequency (a 2 cycle/sec bandwidth filter was employed) and the third trace shows the response in the frequency band around the second two-dimensional mode (i. e. the signal has been filtered at the plate natural frequency that originally derived from mode (3,0) in still air).

The variation of the frequency of the lower modes with Mach number is shown in Figure 11. The fundamental frequency of the test panels (mode 2,0) appeared to be more sensitive to the influence of the airstream: it decreased steadily in the subsonic range and increased steadily with increasing supersonic Mach number.

The frequency of the mode (3,0) changed little in the supersonic flow, but its value was somewhat different from that in still air. Frequencies of higher modes showed very little change from their still air values.

#### 1.4 Experimental Results

Panel flutter was observed only at the supersonic Mach numbers. The flutter boundaries obtained in the Mach number range 1.15 to 1.5 are shown in Figure 12. The maximum value of the minimum thickness ratio ( $h/2b$ ) required to prevent the flutter of "flat" panels at these Mach numbers was found to be slightly less than 0.0046. The thickness requirements for prevention of flutter were found to decrease with increasing Mach number at Mach numbers above  $M = 1.2$ .

The boundaries of the flutter region were quite distinct but proved to be rather sensitive to the test conditions. In particular, static deflection of the test panels was found to influence the flutter Mach number of the test panels. In Figure 12 the "flat" panel boundary was obtained for panels whose static deflection was less than a plate thickness, whereas those points marked with  $\Delta$  values are for panels which exhibited considerable static deflection when flutter occurred. The flutter Mach number for these latter points was taken as the average Mach number over the panel chord. The measured static deflections, and frequency ratios  $\omega/\omega_0$ , are also shown in the figure, where  $\omega_0$  denotes the frequency of the mode (2,0) in still air and  $\omega$  denotes the flutter frequency. The frequency ratios  $\omega/\omega_0$  of the "flat" panels were found to vary from about 0.83 to slightly above unity.

The flutter mode in all cases was found to derive from the mode (2,0) in still air. The maximum amplitude of displacement in the flutter mode appeared to be downstream of the mid-chord point of the panel. There was very little phase shift present in the flutter modes. The phase shift between the displacements at the 22 per cent and 65 per cent chord stations of the plate was estimated to be  $2.5^\circ$ ,  $1^\circ$ , and  $1^\circ$  at Mach numbers of 1.18, 1.31, and 1.34 respectively. Visual observation of the flutter response revealed no detectable spanwise variation of the plate motion. No "second mode" flutter (i.e. one originating from the mode (3,0) in still air) was observed throughout the test series. No frequency coalescence was observed. The higher natural frequencies of the test panels were found to vary only slightly from their still air values.

It was not possible to extend the flutter boundaries to Mach numbers less than about 1.15 due to shockwave interference in the working section.

Review of the experimental data indicated that good

two-dimensional conditions were obtained in the experiments. The flutter modes were all "two-dimensional" and the excitation of the "three-dimensional" plate modes was small.

The low stiffness of the flexure support ensures that the mid-plane stresses developed by the effects of thermal expansion and by the action of static pressure differentials will be small. For example, when considering a typical test panel that has deflected, under the action of a static pressure loading, into the form of a half sine wave with an amplitude of 0.020 inches, it is found that the mid-plane stress that is developed due to the flexure stiffness is only of the order of 3 psi. The development of mid-plane stresses by mechanical distortion of the mounting frame when it is installed in the wind tunnel would be revealed by the changes between the natural frequencies of the test panels measured in still air and measured after the panel was installed in the wind tunnel. The changes in the frequencies that were noted were small (of the order of 2-3 cycles/sec in the fundamental frequency), indicating that any stresses that were developed by this means were also negligible. A conservative limit upon the magnitude of mid-plane stresses that were developed in the panels during the experiments is that they would be less than 20 psi. Previous flutter analysis has indicated that mid-plane stresses of this order of magnitude would produce such small changes of the flutter boundaries from the results for zero stress conditions that the experimental flutter boundaries may be considered representative of the zero stress conditions.

## 2. THEORETICAL STUDIES

Although extensive analyses of two-dimensional panel flutter exist in the literature (Refs. 6, 13, 14, 15), three additional studies are made to facilitate the comparison between theory and experiment.

All of these analyses employ what may be called the ideal theory. This theory is based upon the following set of assumptions:

- (a) The fluid is homogeneous, isotropic, nonviscous, and non-heat conducting.
- (b) The flow is irrotational and all perturbation velocities and pressures are small compared to the free stream velocity and pressure respectively.
- (c) The plate material is homogeneous, isotropic and linearly elastic.
- (d) The amplitude of the plate motion is small compared to the plate thickness, and the Kirchhoff-Love theory of thin plates applies.



- (e) The characteristic flutter time is large compared with the time that it takes an elastic wave to travel the length of the plate.

## 2.1. Two-Dimensional Transonic Panel Flutter

Our first study deals with the question whether, for a flat plate, panel flutter is possible at  $M \approx 1$  according to the linearized transonic flow theory. The assumptions

$$k \gg \tilde{\delta}^{2/3}, \quad k = O(1), \quad \tilde{\delta} \ll 1$$

$$k \gg |M^2 - 1|, \quad M \geq 1$$

are used (Refs. 16, 17). Here  $k = \omega b / u$  is the reduced frequency and  $\tilde{\delta}$  is the ratio of the amplitude of lateral vibration to the plate chord. The pressure distribution due to arbitrary plate motion is given by an integral. The generalized aerodynamic force coefficient for a sequence of modes of motion are evaluated. Actual numerical calculations are made with two modes only. See details in Ref. 24. The conclusion is reached for a flat panel with simply supported edges and zero mid-plane stress, exposed to a sonic airstream ( $M \approx 1$ ), the flutter determinant yields no harmonic oscillations at reduced frequencies between 0.001 and 1.5, nor did it asymptotically at large values of the reduced frequency.

## 2.2. Supersonic Flutter Effect of Structural Damping and Initial Curvature.

The second study concerns with the effect of structural damping and plate curvature on supersonic panel flutter. The analysis of the effect of plate curvature is undertaken to show that the flexure support employed in the experiments renders this effect negligible.

The effect of structural damping on the supersonic flutter of clamped edge panels has been treated extensively in Reference 13. We therefore treat the flutter of simply supported panels. The results of this analysis, together with the results of Reference 13, provides flutter boundaries for two limiting cases against which the experimental results may be compared.

The damping is introduced in the conventional way by replacing the stiffness parameter  $k_0^2$  by  $k_0^2 (1 + i\eta)$ .

Numerical calculations were performed at Mach numbers 1.2, 1.3,  $\sqrt{2}$ , and 1.56. The results at Mach numbers 1.2 and 1.3 are shown in Figure 13. The analytical details are given in Ref. 24.

As to the effect of plate curvature, it has been shown by Yates and Zeijdel (Reference 19) that at higher Mach numbers

( $M \geq 1.5$ ) initial plate curvature is destabilizing up to some critical value of the curvature at which the first and second natural frequencies of the panel (in vacuum) coalesce. This result was confirmed by the present analysis when an initial plate deflection surface of the form

$$\gamma_1(x) = B_1 \sin \pi x/2 \quad (B_1 \ll 1)$$

was assumed for a panel that was simply supported. At Mach number 1.3 and with  $B_1$  equal to one plate thickness, however, it has been found that the initial curvature was stabilizing (see Fig. 14). The effect was therefore opposite to that at the higher Mach numbers.

The Yates and Zeijdel analysis of curved panels, as well as the above, are for edge conditions that are simply-supported with respect to bending, but fixed with respect to membrane stress; i.e. the edge conditions are zero bending moment and zero vertical and horizontal displacement. Now, in our experimental panel, a flexure support was used at the trailing edge, which permitted horizontal displacement and offered restraint against rotation. A different analysis is therefore necessary to estimate the effect of plate curvature upon flutter. Such an analysis was made (Ref. 24). Numerical results at  $M = 1.3$  for  $B_1$  equal to either zero or one plate thickness, or three plate thicknesses, and for experimentally determined values of the flexure influence coefficient, yield the flutter boundaries as shown in Figure 15.

For the case  $B_1$  equal to zero, the panel thickness ratio requirement to prevent flutter, for panels similar to the test panels, is found to be 0.0197. This result compares with the requirements at  $M = 1.3$  of

$$h/2b = 0.0214 \quad (\text{simply supported panels}),$$

$$h/2b = 0.011 \quad (\text{clamped edge panels}).$$

The requirement is therefore seen to be only slightly changed from the simply supported case and also is intermediate to the simply supported and clamped edge plate results.

The inclusion of plate curvature in the analysis produces very little effect on the flutter boundaries. When  $B_1$  equals one plate thickness the thickness ratio requirement becomes 0.0195, and when  $B_1$  equals three plate thicknesses the requirement is 0.0190. The effect of the specified plate curvature is therefore seen to be stabilizing; however, the magnitude of the effect is so small that the curvature terms may be safely neglected from the flutter analysis to be used in comparison with the experimental data.

### 2.3. Energy Transfer at Flutter

It is of interest to examine the energy transfer between the airstream and the plate to show the relative importance of various terms in the aerodynamic pressure expression and thus clarify the difference in flutter characteristics below and above Mach number  $\sqrt{2}$ .

The aerodynamic pressure expression for supersonic flows may be written

$$p(\bar{x}, 0^+, t) = \frac{\rho_0 U^2}{\sqrt{M^2 - 1}} \left[ \frac{\partial Z_a}{\partial \bar{x}} + \frac{(M^2 - 2)}{(M^2 - 1)} \frac{1}{U} \frac{\partial Z_a}{\partial t} + I \right] \quad (1)$$

where  $Z_a(\bar{x}, t)$  denotes the deflection surface of the plate and  $I$  denotes a complicated integral term (see Eq. 37 of Ref. 24). The rate at which work is done by the plate against the aerodynamic pressure is

$$\frac{dE}{dt} = - \int_0^{2b} p(\bar{x}, 0^+, t) \frac{\partial Z_a}{\partial t} d\bar{x} \quad (2)$$

For harmonic oscillations it is convenient to write the deflection surface as

$$Z_a(\bar{x}, t) = Y(\bar{x}) \cos(\omega t + \psi(\bar{x})) \quad (3)$$

On combining (1), (2), (3), integrating  $d/dt E$  over one period  $T$  of the flutter motion, we obtain the loss of energy by the plate per cycle,  $\Delta E$ . At the flutter boundary the net exchange of energy between the panel and the flow must vanish. Hence

$$\Delta E = 0 \quad \text{at flutter,} \quad (4)$$

The final form of  $\Delta E$  may be written as

$$\Delta E = R_I + R_x + R_T \quad (5)$$

Corresponding to Eq. (1)  $R_T$  represents the contribution from the damping term  $\partial Z_a / \partial t$ ,  $R_x$  is that from the static pressure  $\partial Z_a / \partial \bar{x}$ , and  $R_I$  that from the integral term. On employing the data from Reference 6 the following table may be constructed to evaluate the relative importance of these three terms insofar as the flutter process is concerned.

M	$R_t$	$R_x$	$R_I$	$\frac{R_I}{R_x}$
1.1	-1.56	0.3	1.26	4.24
1.2	-0.657	0.07	0.587	8.49
1.3	-0.214	0.027	0.187	6.84
1.4	-0.0062	0.0052	0.001	0.19

The values given in the above table clearly indicate the importance of the integral term  $I$  for the flutter process in the low supersonic region (see also Figure 16). It is seen that at Mach numbers 1.1, 1.2, and 1.3, the  $R_I$  term provides the major stabilizing factor to balance and overcome the influence of the  $\partial Z_a / \partial t$  term, which is destabilizing at Mach numbers less than  $\sqrt{2}$ . The small contribution of the  $\partial Z_a / \partial x$  term to the energy exchange lies in the fact that the phase shift along the chord,  $\partial \psi / \partial x$ , in the flutter mode at the low supersonic Mach numbers, is so small that relatively little net energy exchange is provided. Herein lies the reason for the failure at low supersonic Mach numbers of the approximate quasi-steady aerodynamic theory which neglects the integral term and retains the other two contributions. At the low supersonic Mach numbers the neglect of  $R_I$  term cannot be justified.

On the other hand, at higher Mach numbers, say at  $M > 1.6$ , the results of Reference 20 reveal that the flutter mode exhibits a considerable amount of phase shift across the chord (see Figure 16). The flutter boundary is obtained when the destabilizing contribution  $R_x$  balances the damping term  $R_t$ . (Note the difference in sign of these terms from those in the cases  $M < \sqrt{2}$ ). Here the  $R_I$  contribution is small. Unlike the phenomenon in the low supersonic region such a flutter mechanism is adequately described by the static or linear piston aerodynamic theories.

It is also instructive to examine the physical significance of the various terms in the aerodynamic pressure expression (1) now that their relative importance in the flutter process has been assessed. The first two terms represent the "local" influence, due to slope and deflection at the local point concerned; but the last term, the integral, represents the influence, at a given point along the chord and at a given time, of the disturbances produced at earlier times upstream of this point. These disturbances propagate as waves through the fluid and are convected with the supersonic stream over the panel. For an "almost in phase" mode shape exhibited in the low supersonic region it appears that the phase shifts between aerodynamic pressure and plate displacement introduced by such a convection process are of extreme importance in the flutter phenomenon at these Mach numbers.

### 3. COMPARISON OF THEORY AND EXPERIMENT

#### 3.1 Comparison of the Flutter Boundaries

Our experimental plate was clamped at the leading edge and partially restrained at the trailing edge. The predicted flutter boundaries for such panels are assumed to be intermediate between the boundaries calculated for simply supported and clamped edge panels and the experimental results are compared against these two limiting cases. This assumption is supported by the results of Reference 21 and by the results of Section 2 of the present paper. The experimentally determined damping coefficient  $g$  for three different test panels was 0.0095, 0.010 and 0.012. The calculations employed in our comparison were therefore taken for  $g = 0.01$ .

The "flat" panel flutter boundary from Figure 12 is replotted in Figure 18 against the theoretical flutter boundaries calculated from two mode analyses of simply supported and clamped edge panels. It is immediately seen that although the experimental and predicted flutter boundaries exhibit the same general trend, namely increased stiffness requirements in the low supersonic region, the magnitude of the respective requirements may differ appreciably. The difference is particularly pronounced at Mach numbers less than about 1.4. The theoretical predictions are seen to be conservative in this region, the maximum predicted thickness requirements being of the order of two to three times the experimental value. Agreement between theory and experiment appears to improve as the Mach number increases. This trend towards better agreement at the higher Mach number is further supported by the results of some preliminary flat panel flutter tests carried out at a Mach number of 2.81 by W. Anderson at Caltech. These experiments are reported in Reference 22. The pertinent data from these experiments revealed that the experimental thickness ratio requirements ( $h/2b$ ) at the two-dimensional flutter boundary are between 3 per cent and 18 per cent above the theoretically predicted values for clamped edge panels.

Can the discrepancy between the theory and experiment at the low supersonic speeds be explained by the neglect of mid-plane stress and plate curvature effects in the analysis? The answer must be in the negative because the flexure at the trailing edge of the panel model limits the development of mid-plane stresses to less than 20 psi, which is less than 4 per cent of the Euler buckling stress of the panel even for the smallest ( $h/2b$ ) ratio. The inclusion of mid-plane stresses of such a magnitude in the flutter analysis would produce very small changes in the theoretical predictions from the zero mid-plane stress results and would not explain the

large differences in question.\* The same conclusion also applies to the structural effect of plate curvature, which is greatly reduced by the flexure support (see Section 2).

### 3.2 Flutter Modes

Although there is considerable disagreement between the theoretical and experimental flutter boundaries at supersonic Mach numbers less than 1.4 it is found that certain other features of the flutter phenomenon are predicted quite closely by the ideal theory even at  $M < 1.4$ . In particular, the predicted frequency ratios ( $\omega/\omega_n$ ) at flutter, obtained from Reference 13 and from our analysis in Section 2, are quite close to the experimental results: the difference between the predicted and experimental values being on the order of 10 - 15 per cent. Furthermore, the agreement between the measured phase shift and the predicted phase shift in the flutter modes appears to be good. Measurements of the phase shift between the plate flutter motion at points located at 0.22 and 0.65 chord lengths aft of the plate leading edge at Mach numbers of 1.18, 1.31 and 1.34 yielded values of  $2.5^\circ$ ,  $1^\circ$ , and  $1^\circ$  respectively. These results compare very closely with values estimated from Reference 6. These findings indicate that the ideal theory can predict the correct flutter mode in the low supersonic region (the non appearance of the critical "second mode" flutter is accounted for by the inclusion of realistic values of structural damping in the analysis) in spite of the disparity in the flutter boundary.

### 3.3 Effect of Panel Deflection upon Flutter

A further source of disagreement between theory and experiment arises when the effect of static deflection of the test panels upon the flutter speed is investigated. It was noticed during the experiments that the flutter speed of a given panel could be altered by causing the test panel to deflect out into the airstream (amplitudes of deflection of the order of 1.5 to 3 plate thicknesses). The changes of the flutter speed that were observed were destabilizing in the sense that the region of instability was enlarged from the "flat" panel region of instability (see Figure 12). It was also found that these effects would be accompanied by an increase in the fundamental plate frequency over the frequency that a "flat" plate would exhibit at the same Mach number, as can be expected from the development of mid-plane tension.

It is most unlikely that the observed changes in the flutter characteristics could arise from potential aerodynamic effects. The non-uniformity of the main flow and the perturbations produced

-----  
\*The order of magnitude of the effect produced by such stresses may be estimated from the results of Reference 13. It is found that the thickness ratio requirements at  $M = 1.3$ , for panels similar to the test panels, are reduced by less than 3 per cent by the introduction of a mid-plane stress of 20 p.s.i.

by the small static deflection are both small and, on the basis of the linear theory, would not affect the unsteady phenomenon. However the flutter analysis of Section 2 indicates that the structural effect of plate curvature and any mid-plane tension introduced by the pressure loading would be stabilizing in this Mach number region and would reduce the region of instability. It is therefore seen that the effect predicted by the ideal theory is directly opposite to the effect observed in the experiments. This is another failure of the ideal theory, at the low supersonic Mach numbers.

#### 3.4 Transonic Panel Flutter

The experimental data indicates that the two-dimensional panel flutter phenomenon is limited to the supersonic flow regime. No subsonic flutter was observed for any of the panels that were tested. These findings support the results of the transonic flutter analysis which indicated, to the degree of approximation employed in the analysis, that panel flutter was not possible at  $M = 1$ . However, the results of the transonic analysis could not be verified directly because of the shock wave interference that arose in the experiments at Mach numbers around unity.

#### 3.5 A Suggestion of the Cause of the Discrepancy

The ideal theory appears to be reasonably accurate for the higher Mach numbers but appears inadequate for supersonic Mach numbers less than 1.4. Why? What are the special features of the flutter phenomenon in the Mach number range  $1.0 \sim 1.4$  that may cause the breakdown of the ideal theory?

The dependence of the agreement between theory and experiment on the Mach number indicates that the trouble arises from the aerodynamic side of the problem. Since the aerodynamic theory employed in the analysis was the complete linearized theory it appears that one or more of the assumptions upon which this theory is based is particularly poor for the accurate description of the flutter phenomenon at the low supersonic Mach numbers.

One might suggest at once that the familiar nonlinear effect of the transonic flow may be the culprit. But one should remember that the disparity in flutter boundary occurs at Mach numbers as high as 1.3, and that the amplitude to chord ratio,  $\bar{\delta}$ , involved in our flutter boundary experiments, was of order 0.005 or smaller, far smaller than in most airfoil experiments.

Although the effect of aerodynamic nonlinearity remains to be investigated, it seems to us that the neglect of the viscosity of the air--the boundary layer effect, is of more immediate concern. There is a plausible reason why the boundary layer should affect the flutter phenomenon in a pronounced way in the lower supersonic Mach number range whilst its effect at higher Mach number is

small. This is suggested by the energy exchange analysis of Section 2 where it is shown that the "non-local" contribution to the aerodynamic pressure plays an important role in flutter at the low supersonic Mach numbers, whereas at the higher Mach numbers the aerodynamic pressures of consequence are of "local" origin. Now, it is conceivable that the boundary layer should influence more readily the "non-local" part of the aerodynamic pressure, since all signals must propagate as waves through the boundary layer. The wave refraction in the non-uniform velocity field of the boundary layer together with the variable convection velocity may cause significant differences in the "non-local" aerodynamic action so that the resulting pressures are different from those that would be obtained in a uniform flow. If the aerodynamic pressures of the "local" origin were only slightly affected by the presence of the boundary layer those changes in the effect of the "non-local" pressures could account for the inadequacy of the ideal theory in the low supersonic range and the apparent success of the theory at the higher supersonic Mach numbers.

The boundary layer effect may also account for the curious changes of flutter speed that were due to static deflection of the test panels (see Figure 12) and which do not appear explainable by the ideal theory. This is because static deflection of the test panels may affect the velocity profile of the boundary layer and may thus alter the effect of the boundary layer upon the flutter phenomenon. To seek evidence to support this suggestion some measurements were made of the velocity profiles of the boundary layer over a surface of constant curvature (the radius of curvature was 9.5"). Figure 2 shows that these profiles are noticeably different from the velocity profiles measured over the flat surface.

The boundary layer effect has been suggested as the cause of the large differences between theory and experiment that were observed in the low supersonic region. To establish the importance of the boundary layer upon the panel flutter phenomenon at these Mach numbers would require the realistic inclusion of the boundary layer effects in the actual prediction of the flutter boundaries. To date the only theoretical analysis of the flutter phenomenon that includes the boundary layer effect has been done by Miles (Ref. 23) for a traveling wave in an infinite elastic plate. No work has yet been done for plates of finite dimensions.

#### 4. CONCLUSIONS

(1) Theory and experiment both indicate that the low supersonic region ( $1 < M < 1.5$ ) is critical for the flutter of two-dimensional flat panels. No subsonic flutter was found for any of the panels that were tested, whereas flutter was found at supersonic Mach numbers. In the transonic region,  $M \approx 1$ , the linearized theory indicated that panel flutter was not possible, but this result could not be verified experimentally because of shockwave



interference in the wind tunnel.

(2) The ideal theory appears to be inadequate for the prediction of flutter boundaries at the lower supersonic Mach numbers. The panel thickness ratio required for the prevention of flutter as predicted by the ideal theory in the low supersonic region is very conservative compared to the experimental data at Mach numbers less than 1.4. The theoretical maximum of the minimum thickness ratio required for the prevention of flutter is of the order of two to three times the experimental value for "flat" panels in the Mach range 1.15 ~ 1.35.

(3) The agreement between the experimental and theoretical flutter boundaries improves with increasing Mach number. This trend is supported by the experimental data presented in Reference 14.

(4) The theory predicts with reasonable accuracy the correct flutter mode at all the supersonic Mach numbers covered by the experiments.

(5) The observed changes of flutter speed that were due to static deflection of the test panels do not appear explainable by the ideal theory.

(6) There is reason to believe that the effect of the viscosity boundary layer is the main cause of the discrepancy between the theoretical and experimental flutter boundaries at Mach numbers below 1.4.

REFERENCES

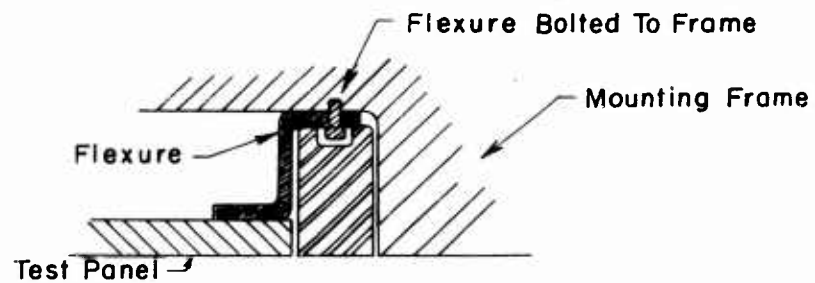
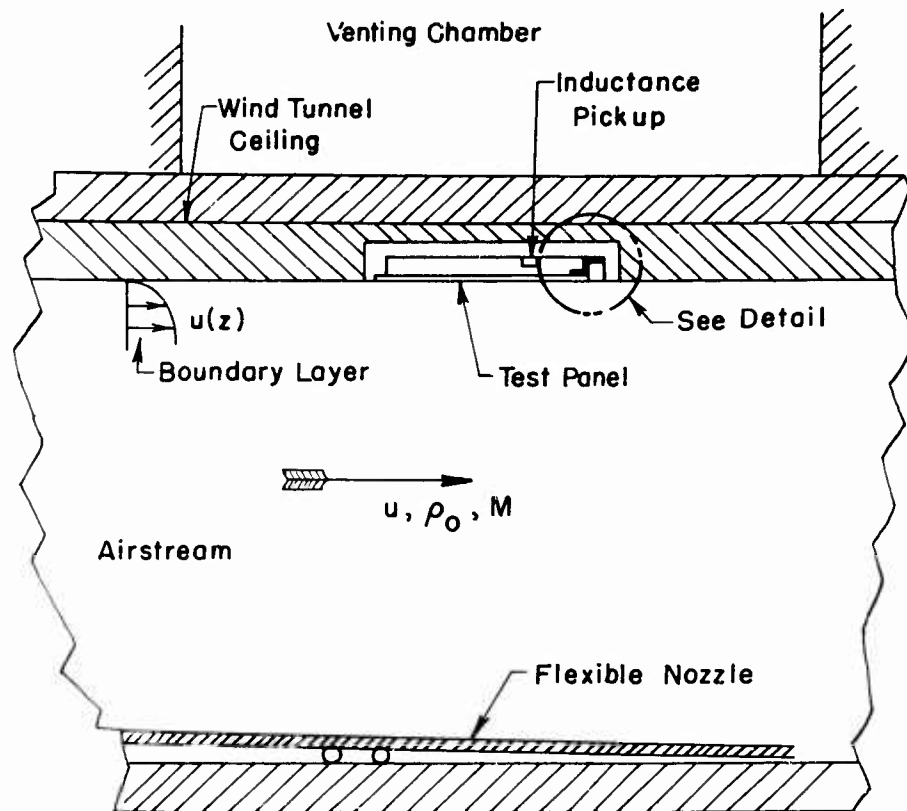
1. Fung, Y. C.: Summary of the Theories and Experiments on Panel Flutter. AFOSR TN 60-224, California Institute of Technology, May 1960. To appear in the AGARD Manual on Aeroelasticity, Pergamon Press.
2. Jordan, P. F.: The Physical Nature of Panel Flutter. Aero. Digest, pp. 34-38, February 1956.
3. Sylvester, M. A., and Baker, J. E.: Some Experimental Studies of Panel Flutter at Mach Number 1.3. NACA TN 3914, 1957.
4. Sylvester, M. A.: Experimental Studies of Flutter of Buckled Rectangular Panels at Mach Numbers from 1.2 to 3.0 Including Effects of Pressure Differential and Panel Width-Length Ratio. NACA RM L55130, 1955.
5. Eisley, J. G.: The Flutter of a Two-Dimensional Buckled Plate with Clamped Edges in a Supersonic Flow. California Institute of Technology, Ph.D. Thesis, July 1956. Published as AFOSR TN 56-296, 1956.
6. Fung, Y. C.: On Two-Dimensional Panel Flutter. Journal of Aeronautical Sciences, 25, 3, pp. 145-160, 1958.
7. Jordan, P., Greenspon, E., and Goldman, R.: Flutter of Thin Panels at Subsonic and Supersonic Speeds. AFOSR TR 57-65, Martin Aircraft, Baltimore, 1957.
8. Stearman, R.: Small Aspect Ratio Membrane Flutter. AFOSR TR 59-45, California Institute of Technology, January 1959. First Award Papers, Institute of Aeronautical Sciences, 1959.
9. Tuovila, W. J., and Hess, R. W.: Experimental Investigation of Flutter of Buckles Curved Panels having Longitudinal Stringers at Transonic and Supersonic Speeds. NASA Memo. 5-18-59L, 1959.
10. Kordes, E. E., Tuovila, W. J., and Guy, L. D.: Flutter Research on Skin Panels. NASA TN D-451, Sept. 1960.
11. Dhawan, S.: The Design and Use of a Flexible Nozzle for the GALCIT Transonic Wind Tunnel. Ae.E. Degree Thesis, Guggenheim Aeronautical Laboratory, California Institute of Technology, 1949.
12. Warburton, G. B.: The Vibration of Rectangular Plates. Proceedings of the Institution of Mechanical Engineers, Vol. 168, pp. 371-384, 1954.

13. Nelson, H. C., and Cunningham, H. J.: Theoretical Investigation of Flutter of Two-Dimensional Flat Panels with One Surface Exposed to Supersonic Potential Flow. NACA Report 1280, 1956. (Supersedes NACA TN 3465).
14. Luke, Y. L., and St. John, A.: Supersonic Panel Flutter. WADC TR 57-252, 1957.
15. Shen, S. F.: Flutter of a Two-Dimensional Simply-Supported Uniform Panel in a Supersonic Stream. Contract No. N5ori-07833, Office of Naval Research, Dept. of Aero. Engineering, Massachusetts Institute of Technology, 1952.
16. Lin, C. C., Reissner, E., and Tsien, H. S.: On Two-Dimensional Nonsteady Motion of a Slender Body in a Compressible Fluid. Jour. of Math. and Physics, Vol. 27, pp. 220-231, 1948.
17. Nelson, H. C., and Berman, J. H.: Calculations on the Forces and Moments for an Oscillating Wing-Aileron Combination in Two-Dimensional Potential Flow at Sonic Speed. NACA Report 1128, 1953 (Supersedes NACA TN 2590).
18. Van Wijngaarden, A., and Scheen, W. L.: Table of Fresnel Integrals. Report R49, Computation Department, Mathematical Centre, Amsterdam, 1949.
19. Yates, J. E., and Zeijdel, E. F.: Flutter of Curved Panels. AFOSR TR 59-163, Midwest Research Institute, 1959.
20. Houbolt, J. C.: A Study of Several Aerothermoelastic Problems of Aircraft Structures. Doctoral Thesis, Eidgenössische Technische Hochschule, Zurich, 1958.
21. Goodman, L. E., and Rattayya, J. V.: Supersonic Speed Flutter Analysis of Circular Panels with Edges Elastically Restrained Against Rotation. WADD TR 60-309, 1960.
22. Anderson, W. J.: Experimental Studies of the Flutter of Flat Panels at Mach Number 2.81. Progress Report No. 9 to the Office of Scientific Research, U. S. Air Force, Contract No. AF 49(638)220, California Institute of Technology, Appendix A, November 1960.
23. Miles, J. W.: On Panel Flutter in the Presence of a Boundary Layer. Journal of the Aero/Space Sciences, Vol. 26, No. 2, pp. 81-93, 1959.
24. Lock, M. H. and Fung, Y. C.: Comparative Experimental and Theoretical Studies of the Flutter of Flat Panels in a Low Supersonic Flow. AF OSR-TN 670. California Institute of Technology, April 1961.

TABLE I  
DETAILS OF THE TEST PANELS

Test Panel No.	Panel Dimensions		Natural Frequencies of Lateral Vibration (cycles/sec)					
	Thickness (inches)	Thickness Ratio ( $\frac{h}{2b}$ )	Experimental			Clamped-Simply Supported		
			Mode 2,0	Mode 3,0	Mode 2,0	Mode 3,0	Mode 2,0	Mode 3,0
3	0.010	0.00297	95	308	91	295	132	364
22	0.0125	0.0033	112	328	90	291	130	360
25	0.0125	0.00353	118	363	103	333	149	412
23	0.0125	0.0037	133	398	114	368	165	455
26	0.0125	0.004	152	471	133	431	193	533
24	0.0155	0.00438	144	440	128	414	185	511
27	0.0155	0.0046	163	505	141	458	205	565

Lock and Fung



Detail Of Flexure Support

Fig. 1 - Schematic Diagram of the test panel installation in the ceiling of the transonic wind tunnel

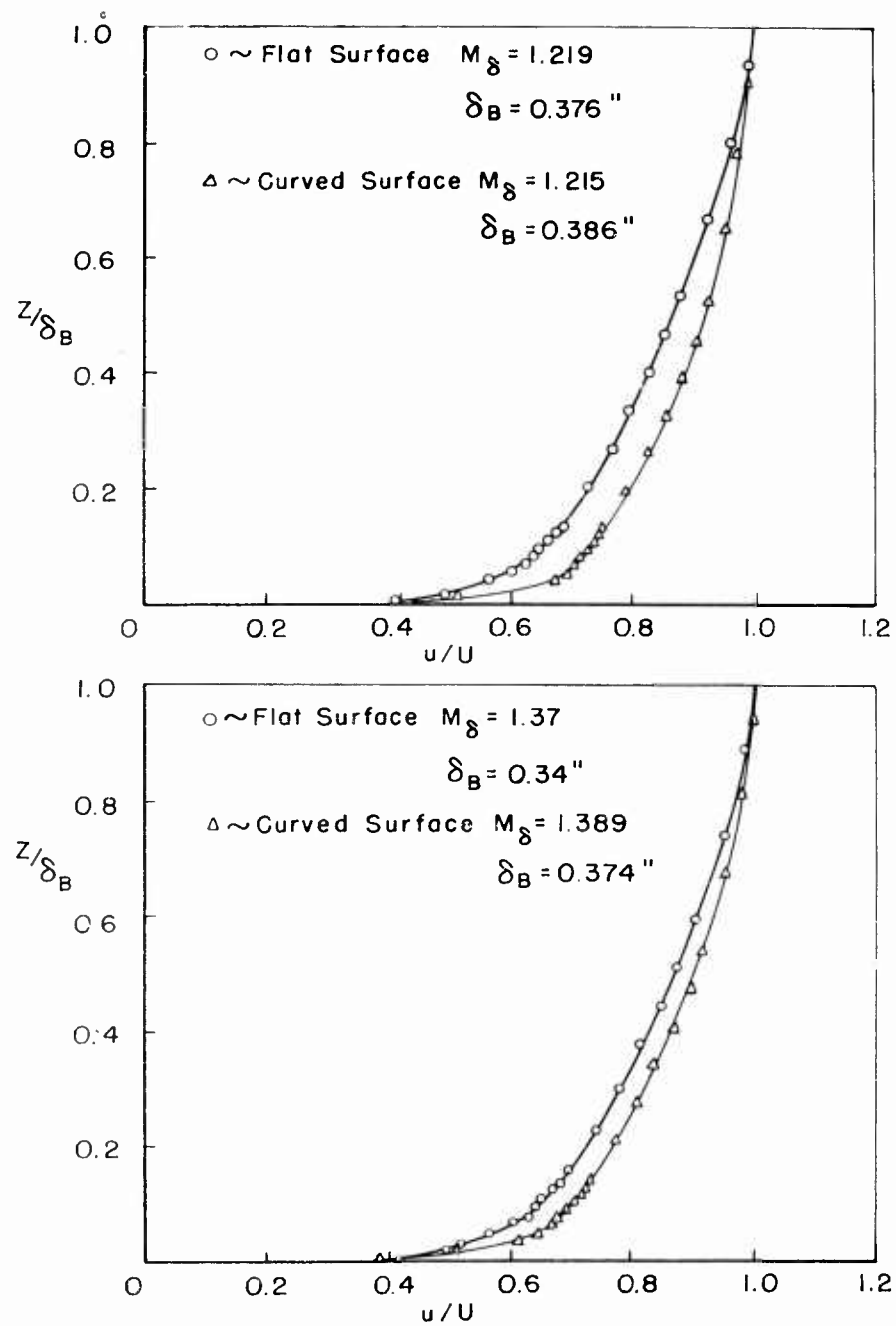


Fig. 2 - Typical velocity profiles of the boundary layer over the test panel installation in the wind tunnel ceiling

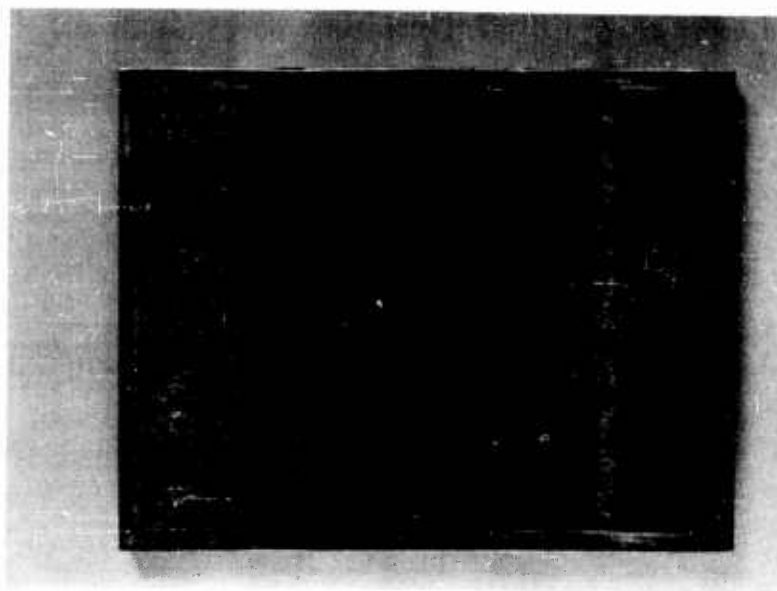


Fig. 3(a) Nodal lines for panel mode (2, 0)

Note: The notation (a, b) denotes the number of nodal lines perpendicular and parallel to the free edges of the plate respectively. The concentrations of salt crystals occur along the nodal lines for the various modes and are clearly visible in the following sequence of pictures.

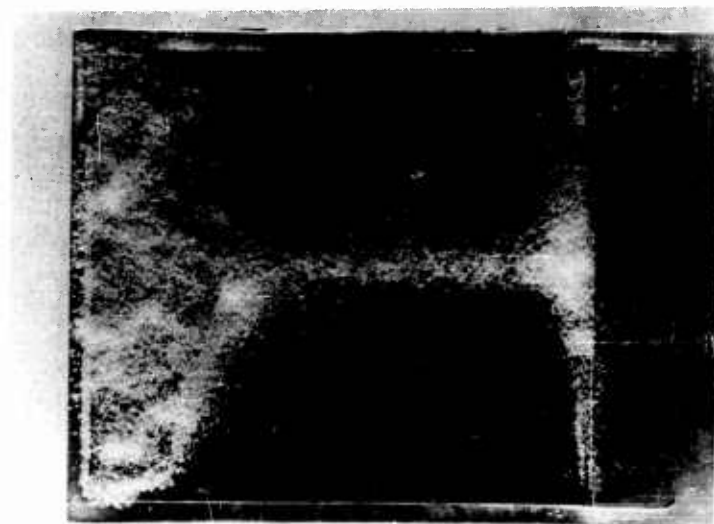


Fig. 3(b) Panel mode (2, 1)

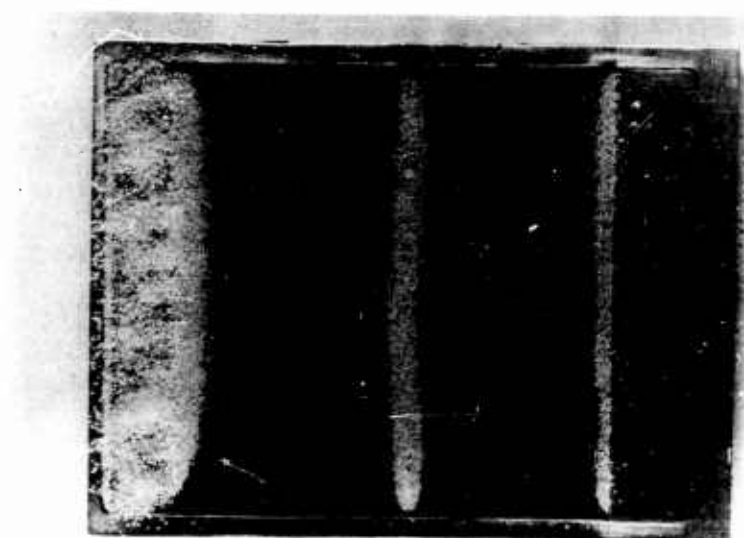


Fig. 3(c) Panel mode (2, 2)



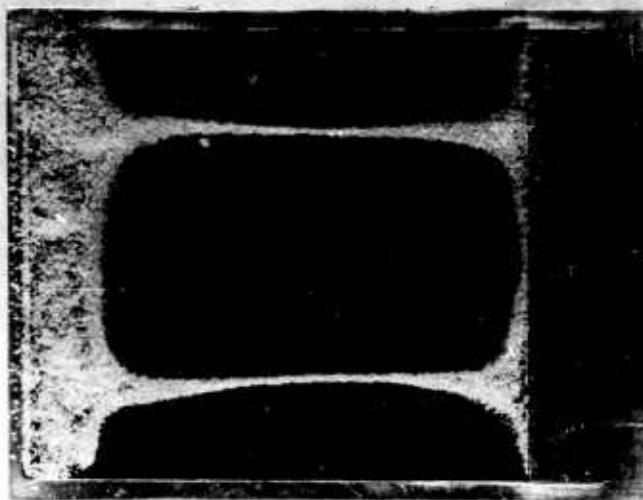


Fig. 3(d) Panel mode (3,0)

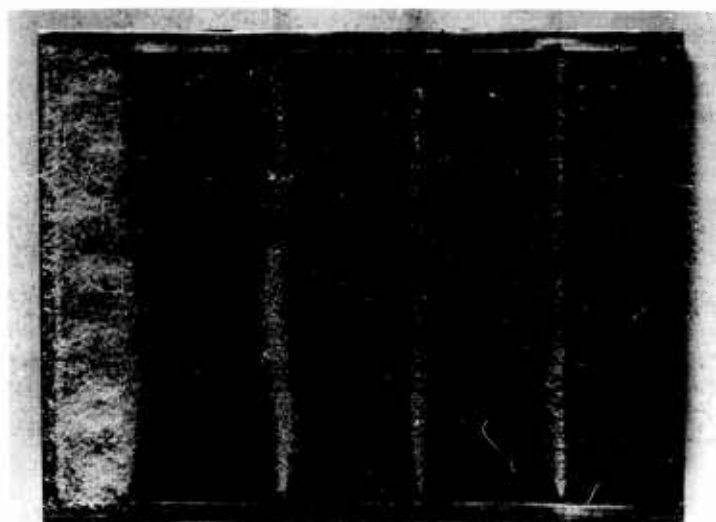


Fig. 3(e) Panel mode (4,0)

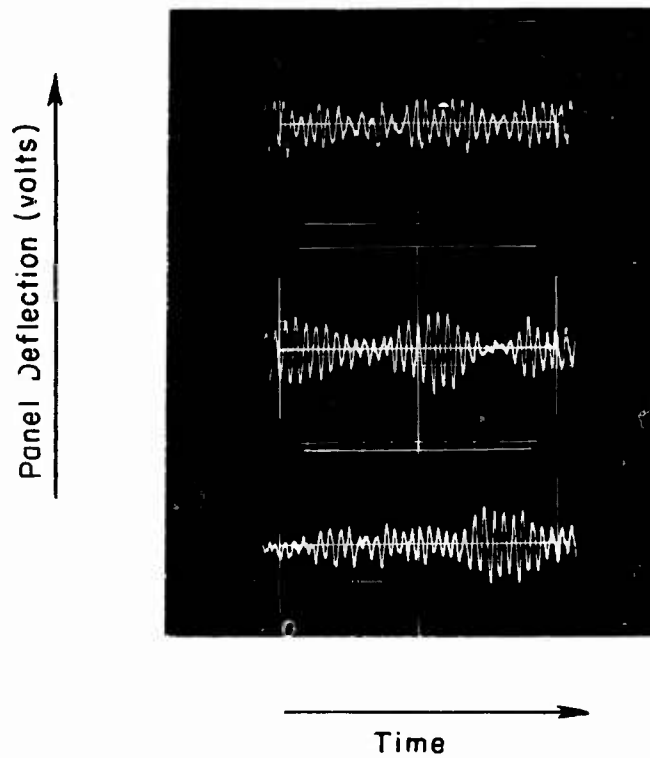


Fig. 4a. Panel response prior to flutter. The oscilloscope trace shows the pre-flutter response of a test panel exposed to a supersonic airstream. The major contribution to the response arises from the frequency band around the fundamental frequency of the panel. Estimated sweep speed was of the order of 0.022 seconds per major division of the scale.

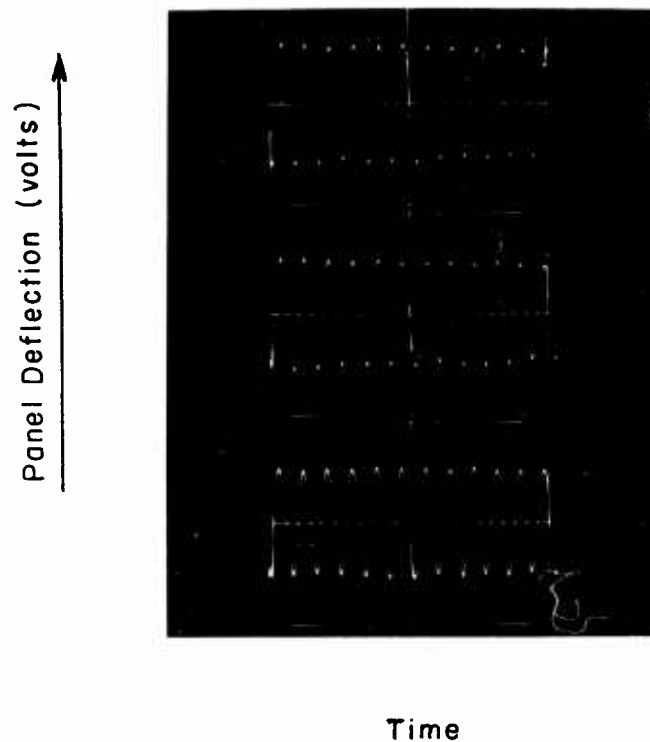


Fig. 4b. Panel response during flutter. The oscilloscope trace shows the response of a test panel at flutter. Estimated sweep speed was 0.0093 seconds per major division of the scale.

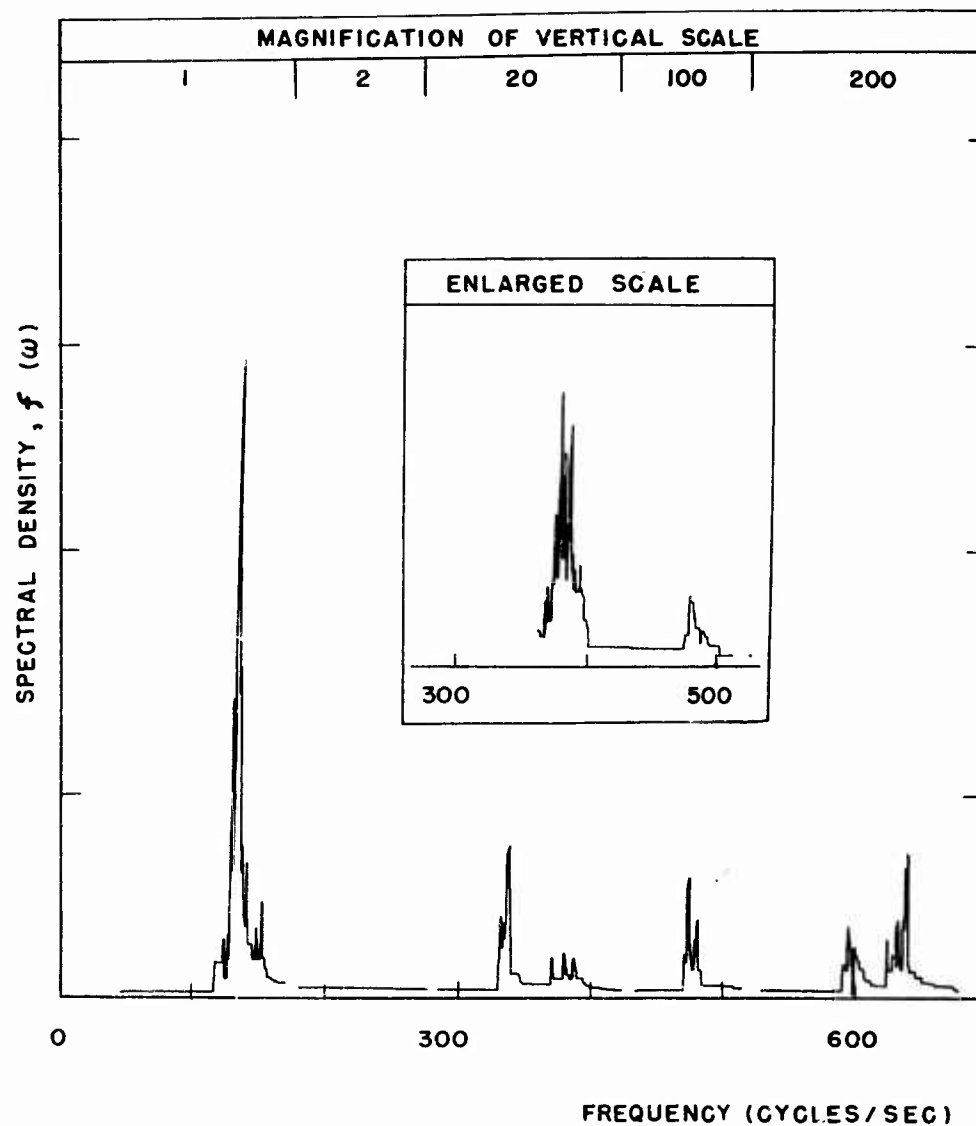


Fig. 5. A typical power spectrum of the test panel response to wind tunnel noise. The spectrum was obtained using a 2 cps bandwidth filter.

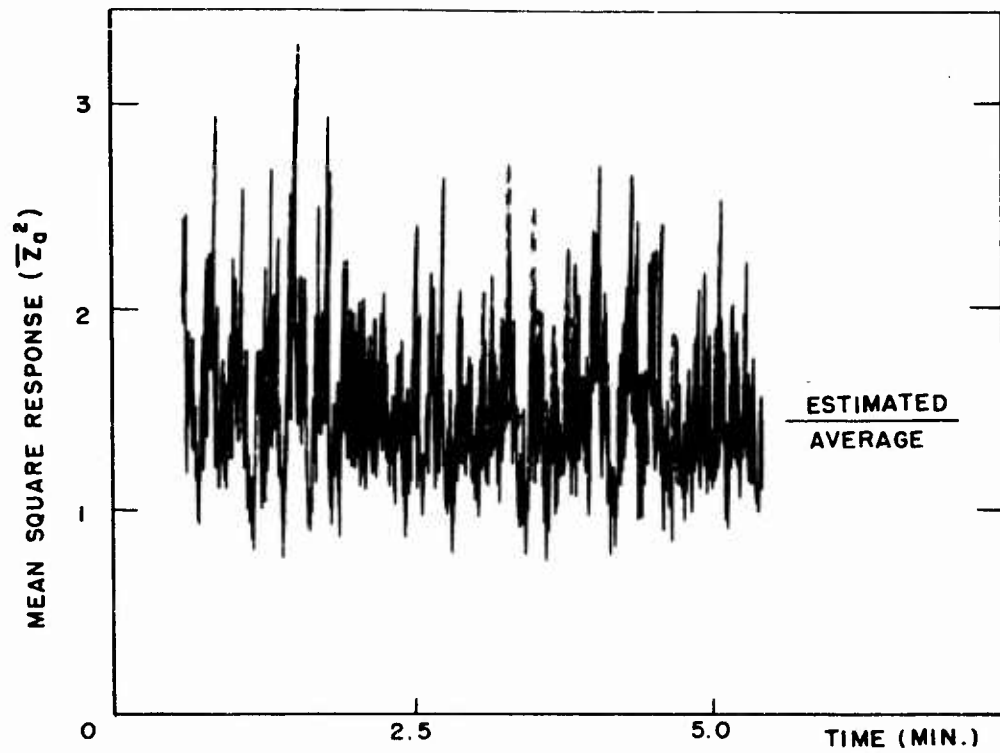


Fig. 6a. Variation of the mean square plate response with time in the non-flutter region.

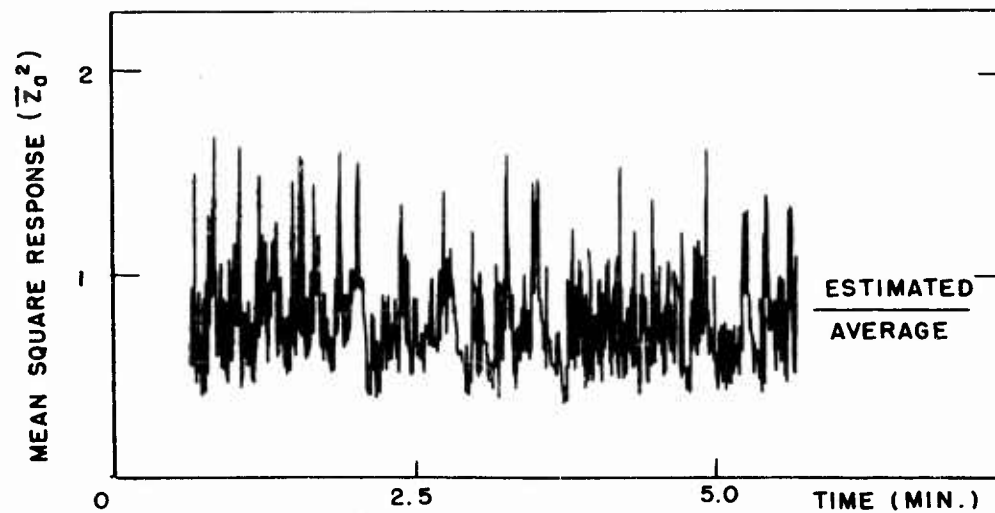


Fig. 6b. Variation of the filtered mean square response with time in the non-flutter region.

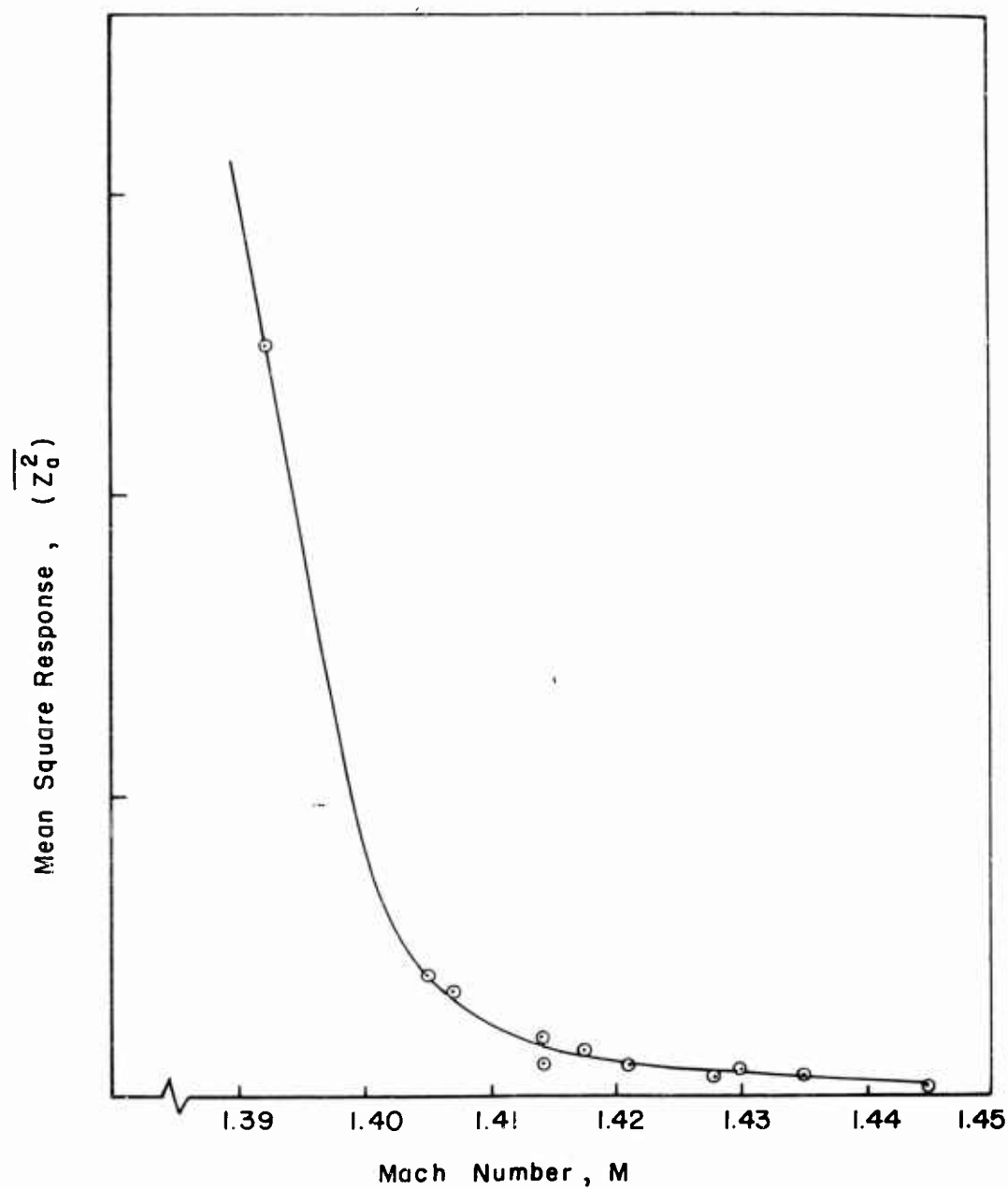


Fig. 7 - Typical variation of the mean square response of a test panel at the flutter boundary

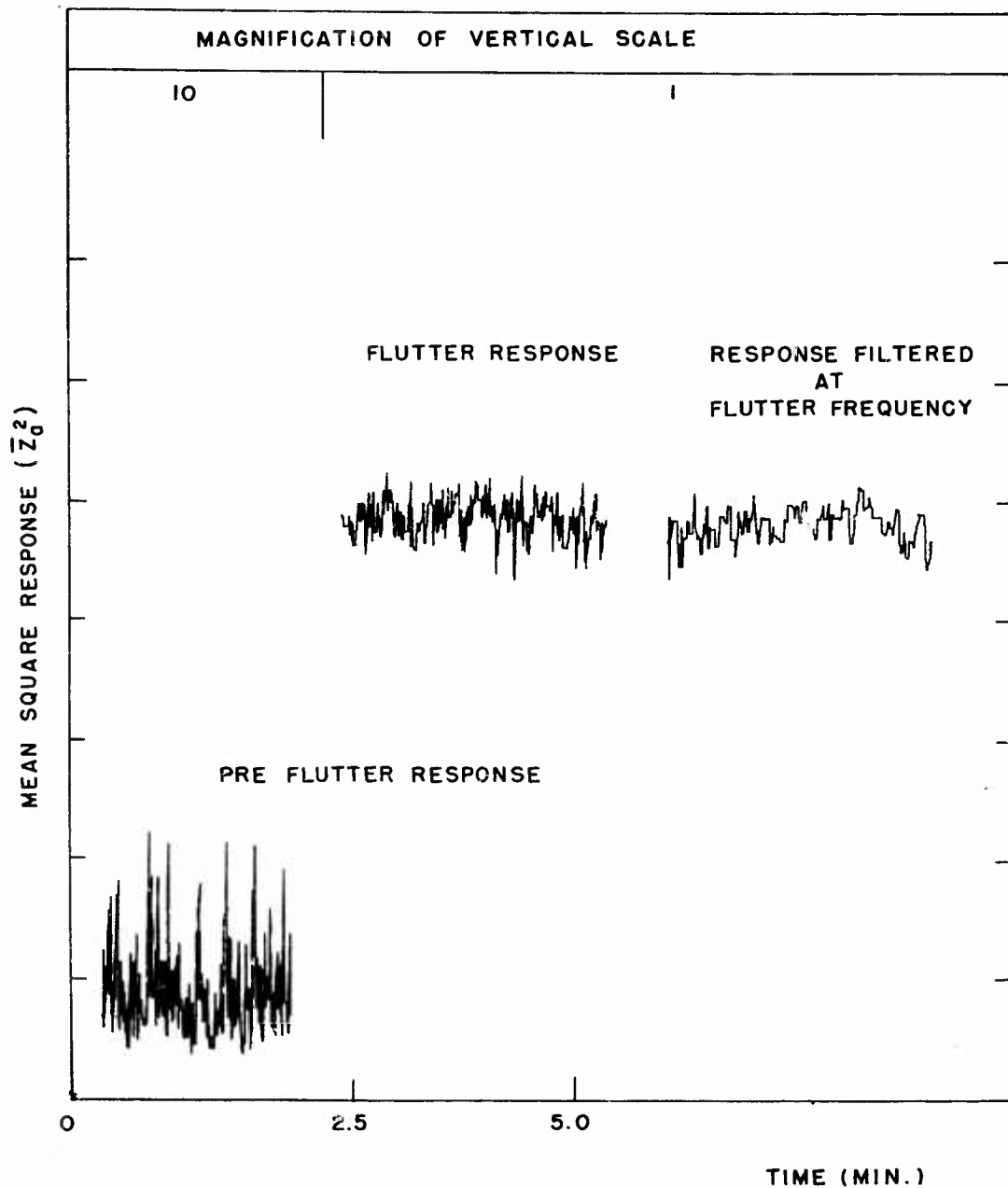


Fig. 8. Comparison of the mean square plate response in the flutter and non-flutter region. The flutter response was filtered at the flutter frequency using a 2 cps bandwidth filter.

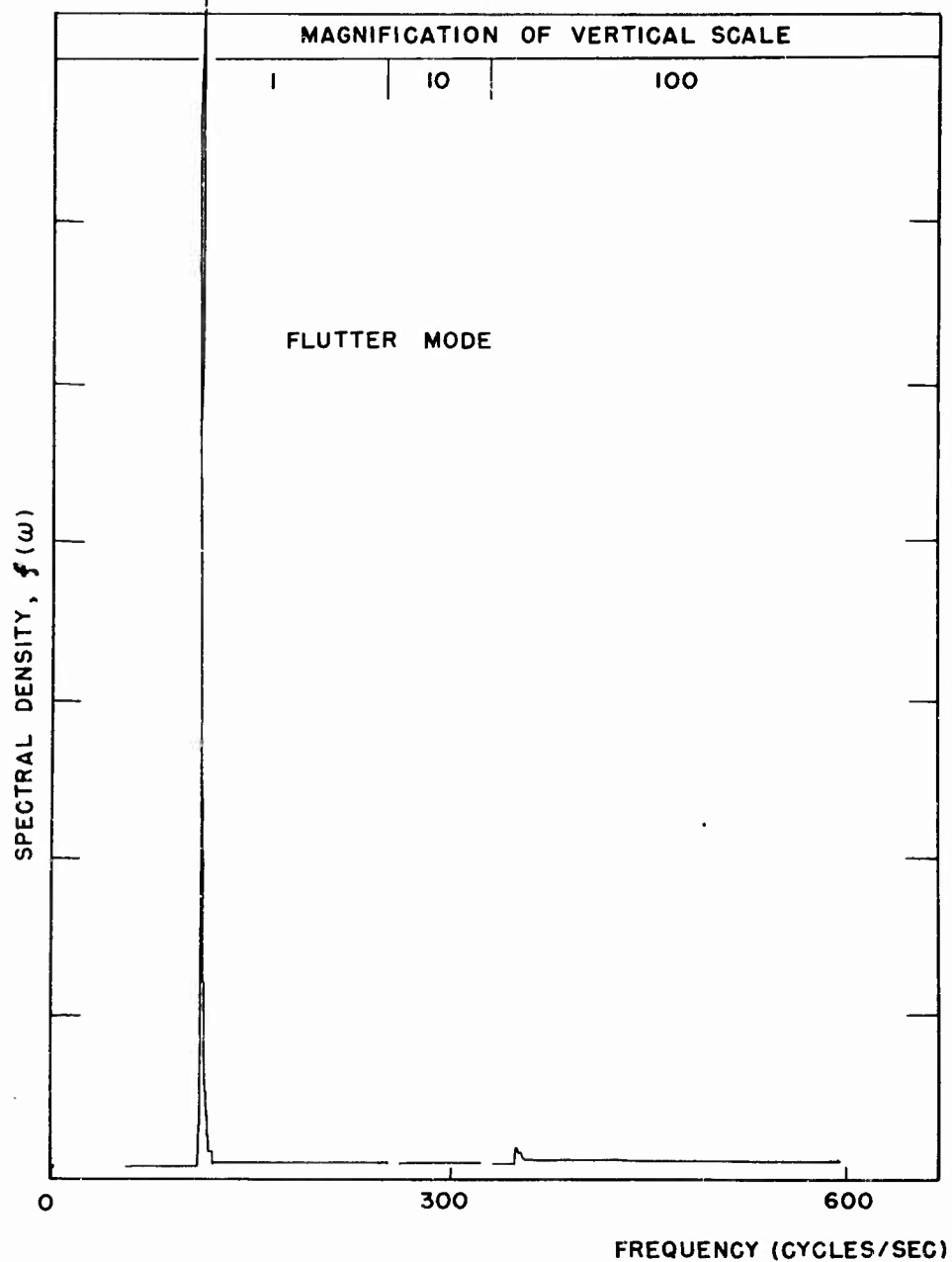


Fig. 9. A typical power spectrum of the test panel at the flutter Mach number. The spectrum was obtained using a 2 cps bandwidth filter.



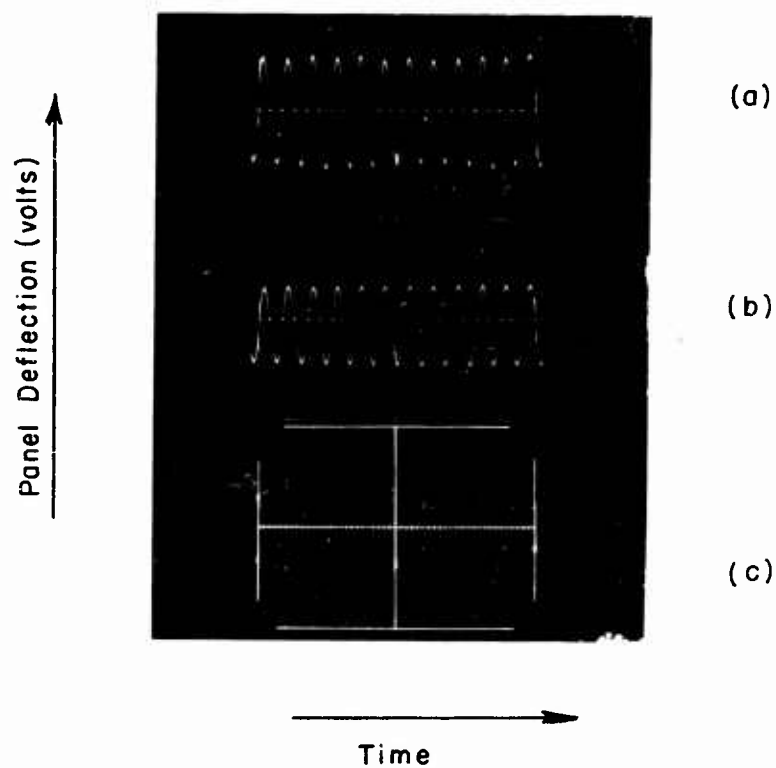


Fig. 10. Panel response during flutter.

- (a) Panel response, total signal
- (b) Panel response filtered at the flutter frequency
- (c) Panel response filtered at the frequency of the second two-dimensional mode

Note: A 2 cycle per sec bandwidth filter was employed to obtain traces (b) and (c). Vertical scales are different for all three traces.

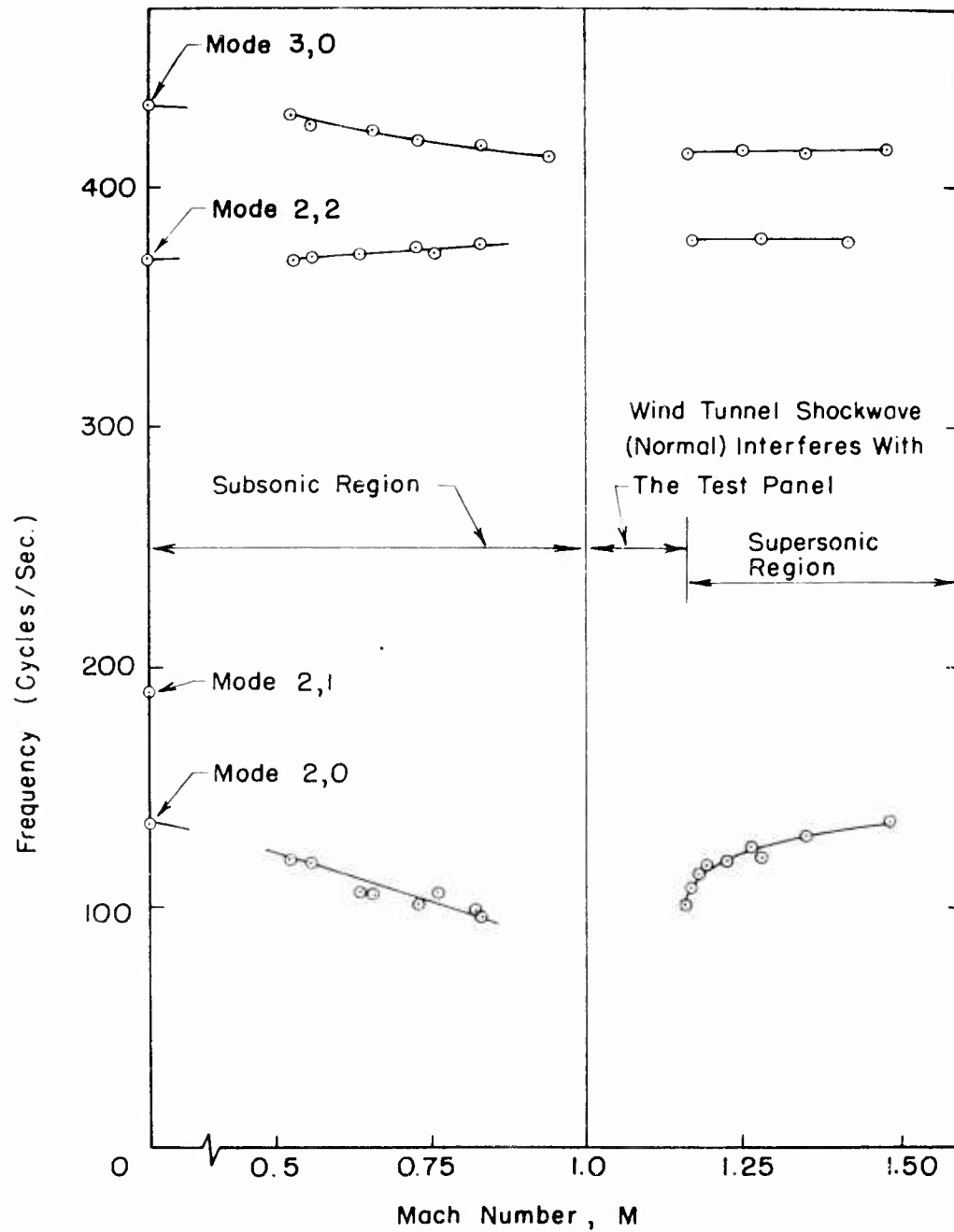


Fig. 11 - The variation with mach number of the frequencies of lateral vibration of a test panel

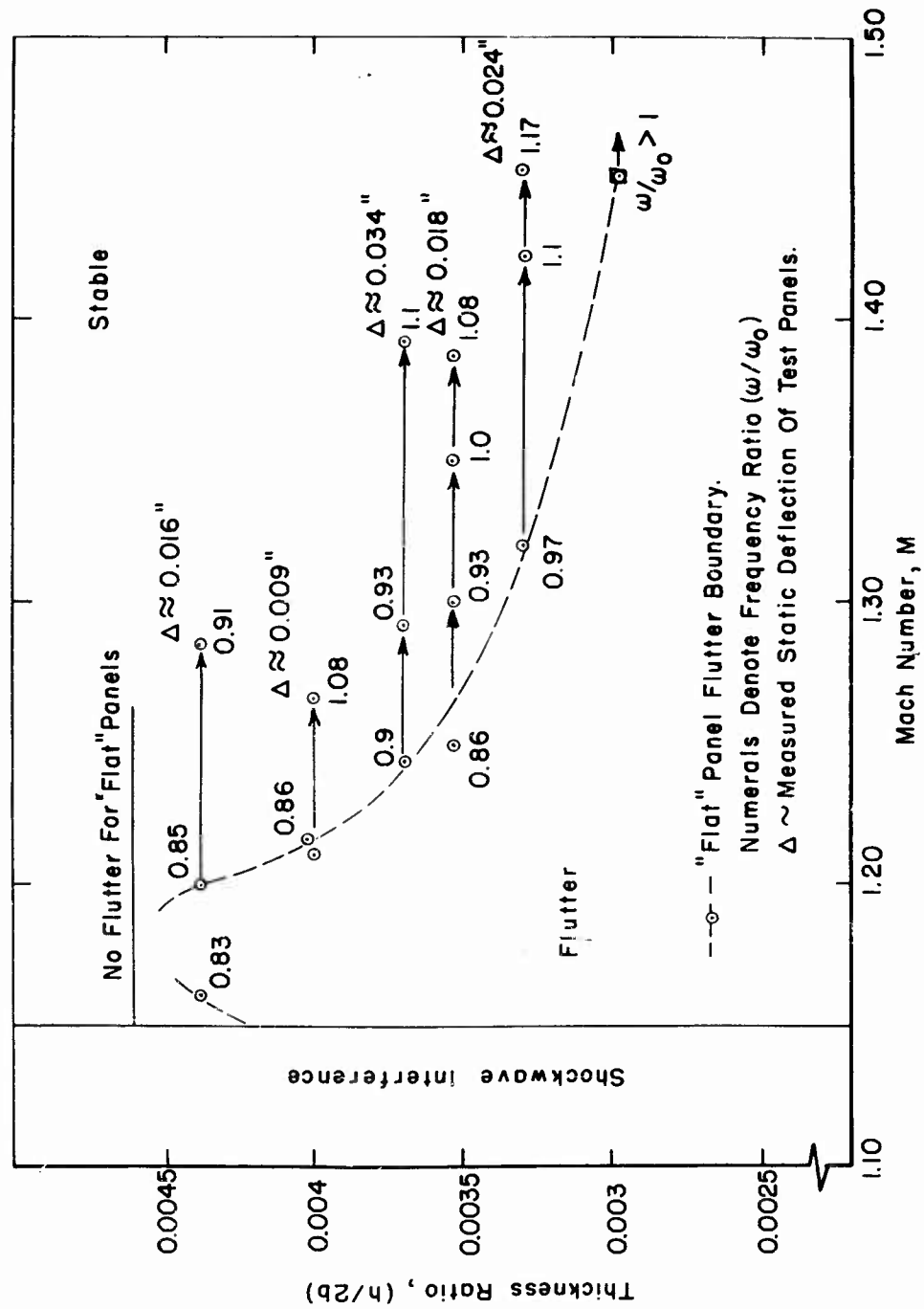


Fig. 12 - Experimental flutter boundaries for brass panels exposed to an airstream with sea level stagnation conditions

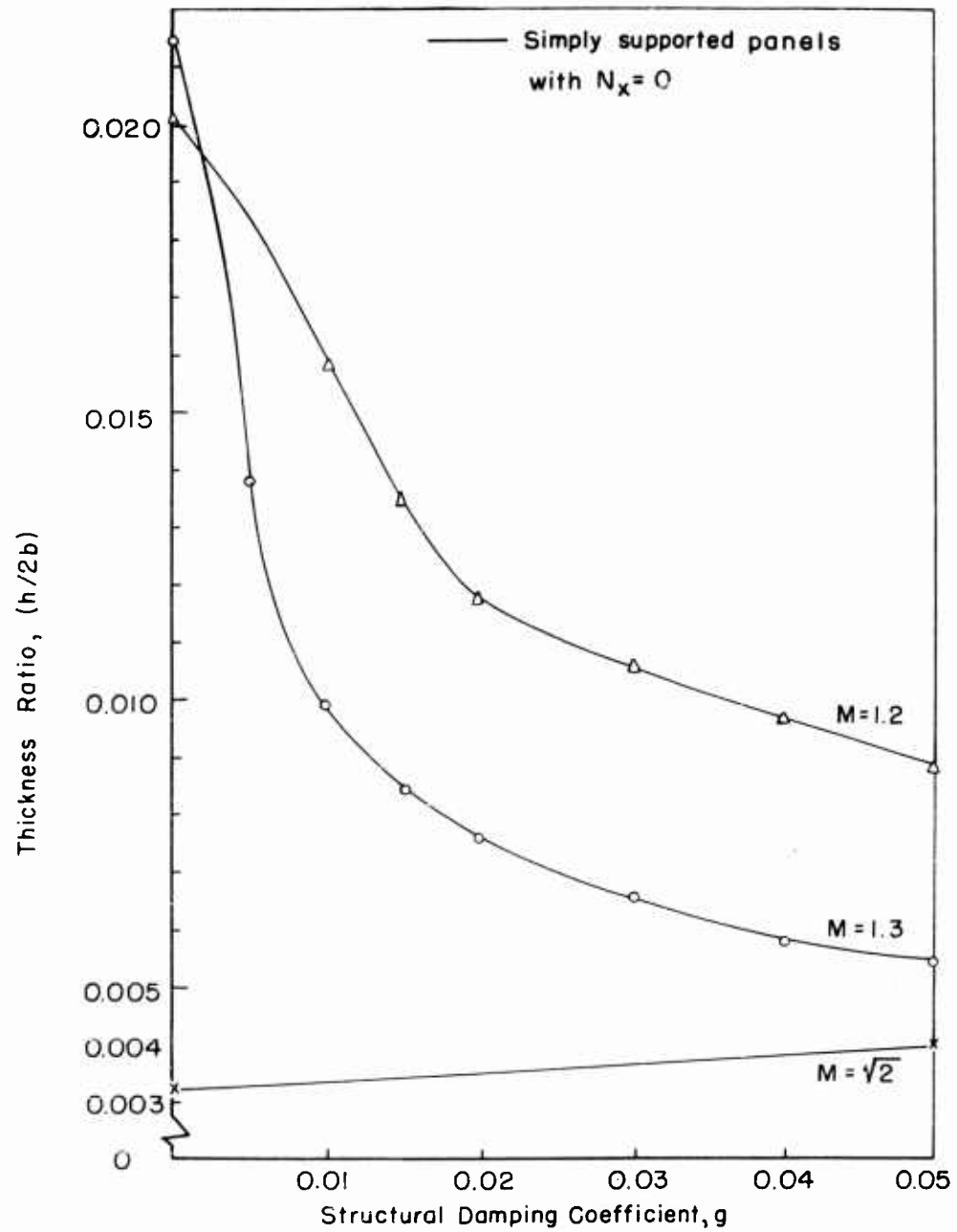


Fig. 13 - Variation of "first mode" thickness requirements with the structural damping coefficient  $g$ . brass panels at constant sea level stagnation conditions

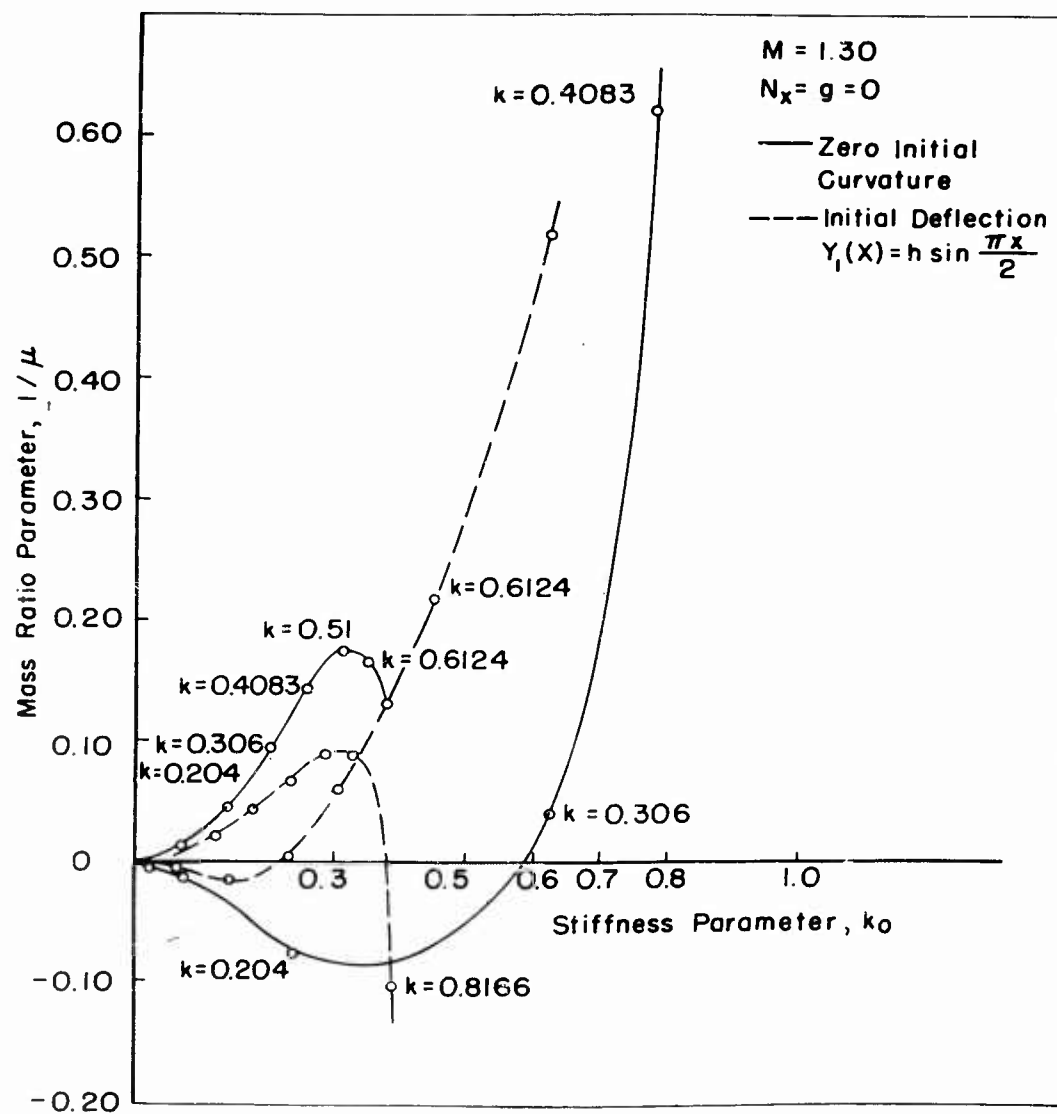


Fig. 14 - Effect of initial curvature upon flutter boundaries of a simply supported panel at  $M=1.3$  according to a two mode analysis

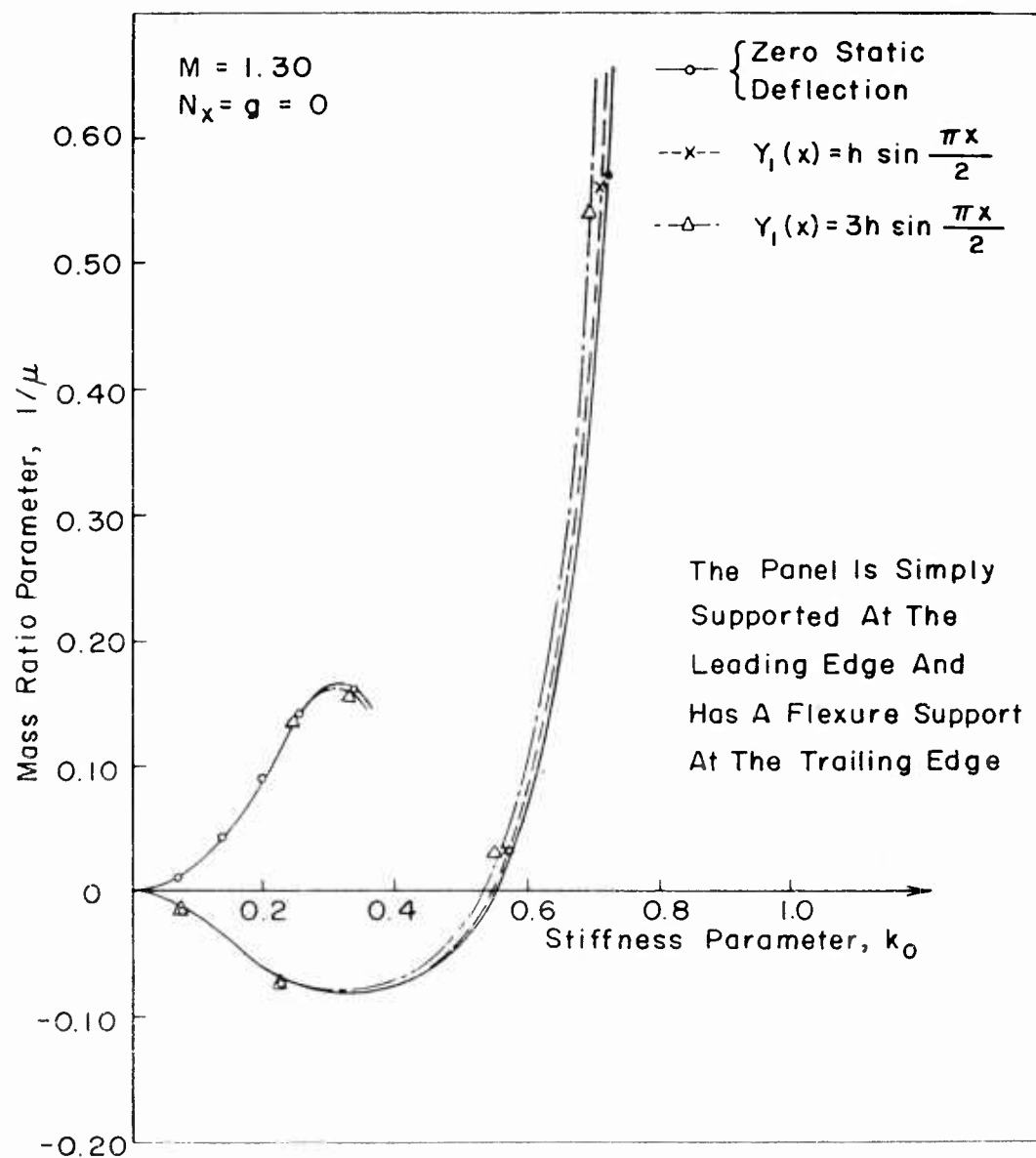


Fig. 15 - The effect of plate curvature upon the flutter boundaries of a panel with a flexure support, according to a two mode analysis

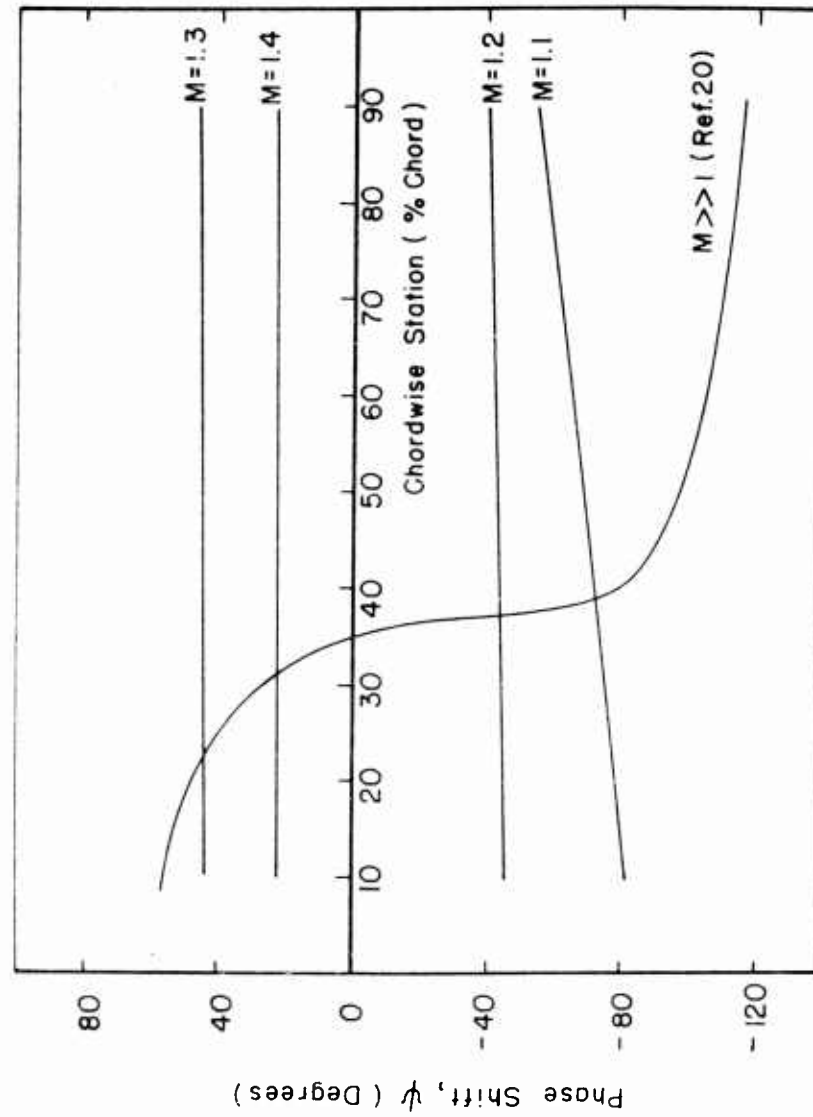


Fig. 16 - Phase shift present in the flutter modes at various mach numbers. The results for mach number 1.1, 1.2, 1.3, 1.4 are estimated from Ref. 6

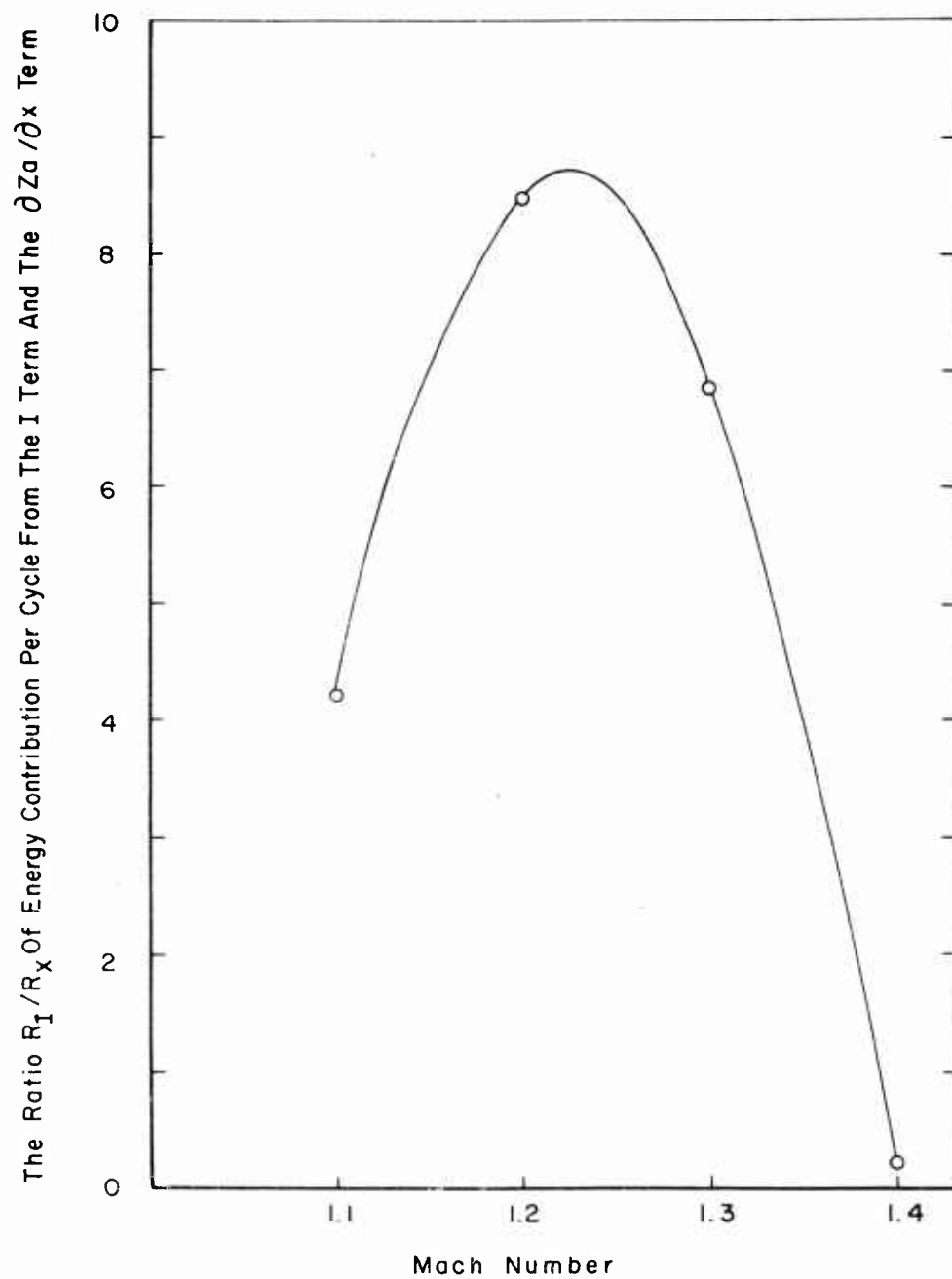


Fig. 17 - Ratio of the energy contribution per cycle at flutter originating from the static aerodynamic term and the integral term in the aerodynamic pressure expression. The results are estimated from the flutter analysis of Ref. 6



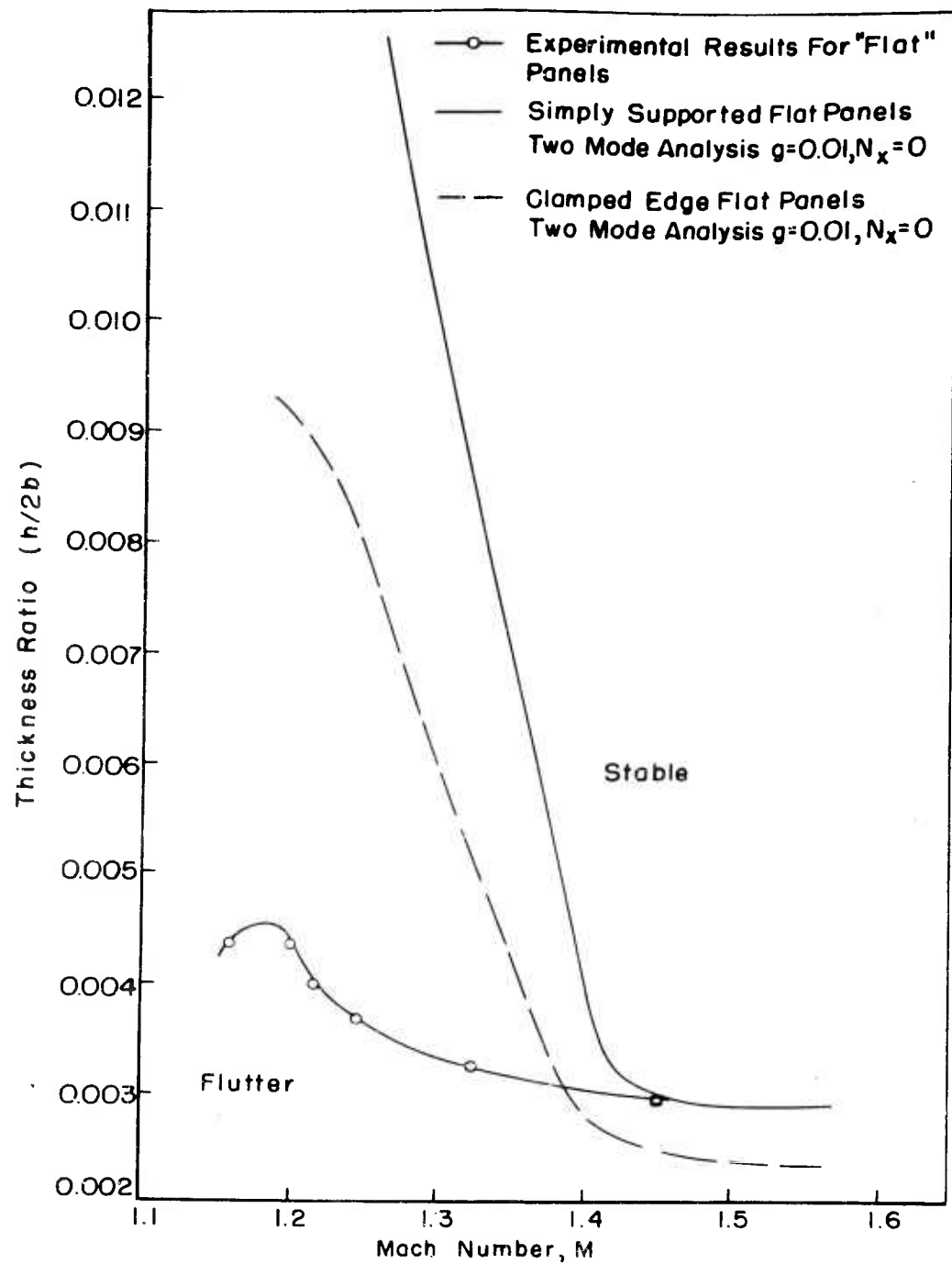


Fig. 18 - Comparison of the theoretical flutter boundaries with the experimental results

## THE EFFECT OF SOME PRACTICAL COMPLICATIONS ON THE FLUTTER OF RECTANGULAR PANELS

H. M. Voss  
Boeing Airplane Company  
Seattle, Washington

### Introduction

Various authors over the past decade have considered the effect of the many and varied influences on panel flutter. Perhaps due to the unusual possibility of "exact" statement of a flutter problem in differential or integral equation form, most authors have chosen this more elegant approach in considering each effect. Thus the literature has developed to include the two-dimensional panel with varying fore-and-aft edge conditions, tension or compression, multiple spans, buckling, and cross stream curvature, for rectangular, circular, and elliptical panels, for circular and conical panels and shells, and for infinite panels. Work on these problems is well summarized by Fung in Ref. 1.

Experimental attempts at verification have largely paralleled the theory in that the attempt was to duplicate an ideal situation while ignoring or minimizing all other effects. Unfortunately, it is very nearly impossible to identically reproduce the theoretical configuration or environment in the wind tunnel. For example, Fig. 1, taken from Ref. 2, presents the results of a number of panel flutter tests with panel aspect ratio as the primary variable. The ordinate is a dynamic pressure-stiffness parameter appropriate to panel flutter. Superimposed is the theoretical boundary for a simply supported plate as determined by Hedgepeth<sup>(3)</sup>. Such results can hardly be said to substantiate or refute the analysis.

Furthermore, the same deviations from ideal occur in all practical applications. It would appear desirable then, both for verification of prediction methods and for consideration of design margins, to evaluate the effect of several possible imperfections and design variations. In the following, then, the panel flutter problem is presented in terms of normalized coordinates, both somewhat more familiar to the aeroelastician and suggestive of a means of assessing the overall influence of extraneous effects. For illustrative

purposes, the simply supported rectangular panel will be used as a base point. Further, the two degree of freedom case will be relied upon, for the most part, for numerical evaluations.

### Formulation

The equations of motion of the dynamic system can be characterized by the set of simultaneous equations,

$$M_{mn}(\omega^2 - \omega_{mn}^2)\omega_{mn} = Q_{mns} \quad m, n = 0, 1, \dots \quad (1)$$

where the normal deflection is given by,

$$w(x, y, t) = \sum_m \sum_n \omega_{mn} f_{mn}(x, y) e^{i\omega t} \quad (2)$$

The remaining definitions are (see Fig. 2),

$$M_{mn} = \int_0^a \int_0^b \rho h f_{mn}^2(x, y) dx dy \quad (3)$$

$$Q_{mr, ns} = \sum_r \sum_s \int_0^a \int_0^b f_{mn}(x, y) \Delta p_{rs}(x, y) \omega_{rs} dx dy \quad (4)$$

with  $\omega_{mn}$  the natural frequencies of the panel,  $\rho$  is the plate density and  $h$  the thickness, and  $\Delta p_{rs}$  the aerodynamic loading. The subscripts  $m$  and  $n$  denote the streamwise and cross-stream mode number, respectively. The functions  $f_{mn}(x, y)$ , are the natural mode shapes which satisfy the appropriate plate equations.

The adequacy of various aerodynamic theories has been considered elsewhere<sup>(3)</sup>; here the static two-dimensional approximation will be used, equivalent to piston theory<sup>(4)</sup> without damping for high Mach numbers

$$\Delta p_{rs} = \frac{-2g}{\sqrt{M^2 - 1}} \frac{\partial f_{rs}}{\partial x} \omega_{rs} \quad (5)$$

$$\begin{aligned}
 Q_{mr,ns} &= \frac{-2q}{\sqrt{M^2-1}} \sum_r \omega_{rn} \int_0^b \int_0^b f_{mn}(x,y) f'_{rn} dx dy \\
 &= \frac{-2q}{\sqrt{M^2-1}} \sum_r A_{mr} \omega_{rn}
 \end{aligned} \tag{6}$$

with  $q$  the dynamic pressure and  $M$  the Mach number. Eq. (1) becomes

$$M_{mn} (\omega^2 - \omega_{mn}^2) \omega_{mn} + \frac{2q}{\sqrt{M^2-1}} \sum_r A_{mr} \omega_{rn} = 0 \tag{7}$$

This is the basic form of the system of equations to be considered. The form of the assumed aerodynamic loading eliminates spanwise coupling. Further, from consideration of Eq. (3) and (6), for the case of separable modes,

$$f_{mn}(x,y) = X(x) Y(y) \tag{8}$$

spanwise effects such as stiffness and boundary conditions will only be apparent in fixing the frequency spectrum. Alternatively, streamwise conditions can affect the generalized mass, the frequency spectrum and the aerodynamic loading. As a further consequence of the separable behavior, for a given streamwise configuration, all cross-stream configurations (finite span, edge support, etc.) can be uniquely related to the two-dimensional or infinite span case. Physically, spanwise conditions contribute to fixing the stiffness level and hence frequency level; the frequency separation is determined solely by streamwise configuration. These ideas will be exploited further in the following sections; although many of the conclusions will be generally applicable, for simplicity attention will be restricted to the panel with simple supports fore and aft.

#### The Fore-and-Aft Simply Supported Panel

For the simply-supported panel, the normal modes are half-sine waves and the generalized mass and force can be evaluated. Eq. (7) then becomes:

$$\frac{\rho h a^4}{D} (\omega_{mn}^2 - \omega^2) \omega_{mn} - \lambda \sum_r D_{mr} \omega_{rn} = 0 \tag{9}$$

where

$$\lambda = \frac{2ga^3}{D(m^2-1)} \quad (10)$$

$$D_{mr} = \begin{cases} 4mr/(r^2-m^2) & r+m \text{ odd} \\ 0 & r+m \text{ even} \end{cases} \quad (11)$$

and  $D$  is the plate stiffness. For discussion purposes it will be useful to consider the form of the two mode solution,

$$\begin{aligned} \lambda &= \frac{\rho ha^4}{D} \frac{(\omega_{rn}^2 - \omega_{mn}^2)}{2D_{mr}} \\ &= \frac{\rho ha^4}{D} \frac{(\omega_{rn} + \omega_{mn})(\omega_{rn} - \omega_{mn})}{2D_{mr}} \end{aligned} \quad (12)$$

Here the combined significance of frequency level (the sum) and frequency separation (the difference) is quite apparent. For the uniform flat panel, the critical modes usually correspond to the first two:  $m=1$ ,  $r=2$ , and the two-mode calculation has been shown to be conservative<sup>(3)</sup>. Eq. (12) will therefore be used to obtain numerical estimates here. However, in the presence of curvature, non-homogeneity or extreme dimensions this need not be true.

Next consider the frequency equation for the flat, uniform panel, simply supported fore and aft:

$$\begin{aligned} \frac{\rho ha^4 \omega_{mn}^2}{D\pi^4} &= m^4 - m^2 \left( \frac{\sigma_{xx} ha^2}{D\pi^2} - 2 \frac{a^2}{\pi^2} \frac{\int_0^L (\gamma')^2 dy}{\int_0^L \gamma^2 dy} \right) \\ &\quad - \frac{\sigma_{yy} ha^4}{D\pi^4} \frac{\int_0^L (\gamma')^2 dy}{\int_0^L \gamma^2 dy} + \frac{a^4}{\pi^4} \frac{\int_0^L (\gamma'')^2 dy}{\int_0^L \gamma^2 dy} \end{aligned} \quad (13)$$

In this  $\sigma_{xx}$  and  $\sigma_{yy}$  are the compressive (uniform) mid-plane stresses. Forming the difference of the squares of the frequency for the first two streamwise modes,

$$(\omega_2^2 - \omega_1^2) \frac{\rho ha^4}{D} = \pi^4 \left[ 15 - 3 \left( \frac{\sigma_{xx} ha^2}{D\pi^2} - 2 \frac{a^2}{\pi^2} \frac{\int_0^L (\gamma')^2 dy}{\int_0^L \gamma^2 dy} \right) \right] \quad (14)$$

For the familiar case of simple support, for  $\sigma_{xx} = 0$ , this becomes,

$$(\omega_z^2 - \omega_1^2) \frac{\rho h a^4}{D} = 3\pi^4 \left(5 + 2 \frac{a^2}{b^2}\right) \quad (15)$$

Since most of the panel flutter effects are interrelated, a base point of evaluation is necessary. For this purpose, the panel simply supported on four edges will be assumed. For specific calculations, a panel aspect ratio  $a/b = 2$ , length  $a = 20$  in., and thickness  $h = 0.10$  in. are considered. For such a panel, the approximate value of the flutter parameter from the two-mode solution is  $\lambda_0 = 732$ . The value from an exact analysis is  $\lambda = 893$ . Since the evaluation of extraneous influences will be based on the two-mode solution, the value of  $\lambda_0$  will be used in percentage evaluations.

Finally, the evaluation considered here is based on the experimental viewpoint, namely the difference in the observed and predicted dynamic pressure at flutter. Except for the case where dimensions are intentionally varied, percentage changes in dynamic pressure correspond directly to the percentage change in the flutter parameter  $\lambda$ . These can be related to changes in required thickness through Eq. (10).

#### Pre-Stress

From Eq. (14), spanwise pre-stress will have no effect on the flutter speed. To give physical meaning to the streamwise pre-stress effect, set

$$\sigma_{xx} \cong -E \frac{\Delta a}{a} \quad (16)$$

This would indicate the effect of a slight misalignment of supports. Therefore, the simply-supported panel

$$\frac{\Delta \lambda}{\lambda_0} \cong \frac{1}{[5 + 2(a/b)^2]} \left(\frac{a}{h}\right)^2 \frac{\Delta a}{a} \quad (17)$$

This deviation is plotted in Fig. 3 for several panel aspect ratios. For the example panel mentioned previously, and a misalignment  $\Delta a = \pm 0.001$ ,  $\Delta \lambda / \lambda_0 \pm 15\%$ .

#### Dimensions

In practical applications, there may be some question as to manufacturing tolerance on dimensions, or effective dimensions due to non-ideal support. For the simply-supported panel,

considering all variations in dimensions,

$$\frac{\Delta \lambda}{\lambda_0} \approx 3 \left( \frac{\Delta h}{h} - \frac{\Delta a}{a} \right) + \frac{4(a/b)^2}{[5 + 2(a/b)^2]} \left( \frac{\Delta a}{a} - \frac{\Delta b}{b} \right) \quad (18)$$

For the example panel listed allowing a deviation of one-tenth inch in planform dimensions and five-thousandths in thickness, the deviation in flutter dynamic pressure,  $\Delta \lambda / \lambda_0 \pm 16\%$ . It should be noted that this effect is primarily due to thickness variation.

#### Boundary Conditions

It has previously been pointed out that all panels with a prescribed fore-and-aft boundary condition, but differing in side edge conditions and aspect ratio, are uniquely related. In practice, ideal edge conditions are seldom attained. Here this effect will be considered by investigating all combinations of the ideal boundary conditions for the side edges. Again the panel, simply supported on all four edges is used as the reference.

This effect may be evaluated from Eq. (12) and (14) as,

$$\frac{\Delta \lambda}{\lambda_0} = \frac{5 - 2(a/b)^2 I}{5 - 2(a/b)^2} - 1 \quad (19)$$

$$I = \frac{b^2}{\pi^2} \frac{\int_0^b (\gamma')^2 dy}{\int_0^b (\gamma)^2 dy} \quad (20)$$

Approximate mode shapes, satisfying the appropriate boundary conditions, were employed to evaluate I, with the following results:

<u>Condition</u>	<u>I</u>
Pin-Pin	1.0
Pin-Free	0.30
Pin-Clamp	1.14
Clamp-Clamp	1.33
Clamp-Free	0.60
Free-Free	0

The results of Eq. (20) are shown in Fig. 4. While a physical case will usually not correspond to any one of these, it is apparent that the effect of side edge conditions is significant.

Furthermore, the present example has considered only pin-edged supports fore and aft. Variation of these edge conditions is even more important, as indicated by the fact that for the semi-infinite clamped plate the flutter parameter is 85% higher than for

the simply-supported case.

### Isotropy

Recently, the corrugation stiffened panel has gained considerable favor as a light-weight structure providing high strength characteristics in one direction. For the corrugation direction aligned with the stream the previous considerations apply, although, in general, spanwise effects would appear to be negligible. When the corrugations are normal to the stream, the situation is quite different. Although the corrugation-stiffened plate does not fully fit the description, the simply-supported, homogeneous, orthotropic plate equations<sup>(5)</sup> will be used to indicate the problem. The principal axes are aligned with the boundaries, and it is assumed that the effective moduli are greatly different,  $E_{xx} \ll E_{yy}$ . Then Eq. (13) is replaced, for no pre-stress, by

$$\frac{\rho h a^4 \omega^2}{D_{yy} \pi^4} = \frac{D_{xx}}{D_{yy}} m^4 + 4 \frac{D_{xy}}{D_{yy}} m^2 n^2 \left(\frac{a}{b}\right)^2 + n^4 \left(\frac{a}{b}\right)^4 \quad (21)$$

where  $D_{xy}$  is the plate shear stiffness. Eq. (15) is replaced, for low  $m$ , by:

$$(\omega_r^2 - \omega_m^2) \frac{\rho h a^4}{D_{yy}} \approx 4 \pi^4 \frac{D_{xy}}{D_{yy}} (r^2 - m^2) \left(\frac{a}{b}\right)^2 \quad (22)$$

Then, combining with Eq. (11) and (12),

$$\lambda \approx \frac{\pi^4}{2} \frac{D_{xy}}{D_{yy}} \frac{(r^2 - m^2)^2}{mr} \left(\frac{a}{b}\right)^2 \quad (23)$$

For the combination of the first two longitudinal modes, by comparison to an isotropic panel of the same stiffness level,

$$\frac{\lambda_{\perp}}{\lambda_0} \approx \frac{4 (D_{xy}/D_{yy}) (a/b)^2}{[5 + 2(a/b)^2]} \quad (24)$$

A final comparison of interest is with the plate with the principal stiffness direction oriented streamwise:

$$\frac{\lambda_{\perp}}{\lambda_{\parallel}} \approx \frac{4 (D_{xy}/D_{yy}) (a/b)^2}{[5 + 4 (D_{xy}/D_{yy}) (a/b)^2]} \quad (25)$$



considering all variations in dimensions,

$$\frac{\Delta \lambda}{\lambda_0} \approx 3 \left( \frac{\Delta h}{h} - \frac{\Delta a}{a} \right) + \frac{4(a/b)^2}{[5 + 2(a/b)^2]} \left( \frac{\Delta a}{a} - \frac{\Delta b}{b} \right) \quad (18)$$

For the example panel listed allowing a deviation of one-tenth inch in planform dimensions and five-thousandths in thickness, the deviation in flutter dynamic pressure,  $\Delta \lambda / \lambda_0 \pm 16\%$ . It should be noted that this effect is primarily due to thickness variation.

#### Boundary Conditions

It has previously been pointed out that all panels with a prescribed fore-and-aft boundary condition, but differing in side edge conditions and aspect ratio, are uniquely related. In practice, ideal edge conditions are seldom attained. Here this effect will be considered by investigating all combinations of the ideal boundary conditions for the side edges. Again the panel, simply supported on all four edges is used as the reference.

This effect may be evaluated from Eq. (12) and (14) as,

$$\frac{\Delta \lambda}{\lambda_0} = \frac{5 - 2(a/b)^2 I}{5 - 2(a/b)^2} - 1 \quad (19)$$

$$I = \frac{b^2}{\pi^2} \frac{\int_0^b (\gamma')^2 d\gamma}{\int_0^b (\gamma)^2 d\gamma} \quad (20)$$

Approximate mode shapes, satisfying the appropriate boundary conditions, were employed to evaluate I, with the following results:

<u>Condition</u>	<u>I</u>
Pin-Pin	1.0
Pin-Free	0.30
Pin-Clamp	1.14
Clamp-Clamp	1.33
Clamp-Free	0.60
Free-Free	0

The results of Eq. (20) are shown in Fig. 4. While a physical case will usually not correspond to any one of these, it is apparent that the effect of side edge conditions is significant.

Furthermore, the present example has considered only pin-edged supports fore and aft. Variation of these edge conditions is even more important, as indicated by the fact that for the semi-infinite clamped plate the flutter parameter is 85% higher than for

the simply-supported case.

### Isotropy

Recently, the corrugation stiffened panel has gained considerable favor as a light-weight structure providing high strength characteristics in one direction. For the corrugation direction aligned with the stream the previous considerations apply, although, in general, spanwise effects would appear to be negligible. When the corrugations are normal to the stream, the situation is quite different. Although the corrugation-stiffened plate does not fully fit the description, the simply-supported, homogeneous, orthotropic plate equations<sup>(5)</sup> will be used to indicate the problem. The principal axes are aligned with the boundaries, and it is assumed that the effective moduli are greatly different,  $E_{xx} \ll E_{yy}$ . Then Eq. (13) is replaced, for no pre-stress, by

$$\frac{\rho h a^4 \omega^2}{D_{yy} \pi^4} = \frac{D_{xx}}{D_{yy}} m^4 + 4 \frac{D_{xy}}{D_{yy}} m^2 n^2 \left(\frac{a}{b}\right)^2 + n^4 \left(\frac{a}{b}\right)^4 \quad (21)$$

where  $D_{xy}$  is the plate shear stiffness. Eq. (15) is replaced, for low  $m$ , by:

$$(\omega_r^2 - \omega_m^2) \frac{\rho h a^4}{D_{yy}} \approx 4 \pi^4 \frac{D_{xy}}{D_{yy}} (r^2 - m^2) \left(\frac{a}{b}\right)^2 \quad (22)$$

Then, combining with Eq. (11) and (12),

$$\lambda \approx \frac{\pi^4}{2} \frac{D_{xy}}{D_{yy}} \frac{(r^2 - m^2)^2}{mr} \left(\frac{a}{b}\right)^2 \quad (23)$$

For the combination of the first two longitudinal modes, by comparison to an isotropic panel of the same stiffness level,

$$\frac{\lambda_{\perp}}{\lambda_0} \approx \frac{4 (D_{xy}/D_{yy}) (a/b)^2}{[5 + 2 (a/b)^2]} \quad (24)$$

A final comparison of interest is with the plate with the principal stiffness direction oriented streamwise:

$$\frac{\lambda_{\perp}}{\lambda_{||}} \approx \frac{4 (D_{xy}/D_{yy}) (a/b)^2}{[5 + 4 (D_{xy}/D_{yy}) (a/b)^2]} \quad (25)$$

These results illustrate several important points with regard to use and testing of orthotropic panels. First of all, no orthotropic panel is as efficient as an isotropic panel of the same stiffness level. For  $a/b = 2$ ,  $D_{xy} \approx 0.1 D_{yy}$ ,  $\lambda_1 \approx 12\% \lambda_0$ , and  $\lambda_n \approx 50\% \lambda_0$ . Further, the value of  $\lambda_1$  will be extremely sensitive to streamwise effects such as aspect ratio and edge conditions. The reason for this is the fact that the difference in the squares of the frequencies varies almost linearly with mode number, rather than as the cube in the case of the isotropic panel. In fact, the two mode result, (Eq. (23)), indicates a very nearly constant value of flutter parameter for each modal pair. In actuality, for higher mode numbers,  $m$ , the streamwise stiffness becomes apparent, and the frequency spectrum tends toward the isotropic behavior. In combination these indicate the need for accurate frequency prediction and a many-mode analysis. Along with the increased sensitivity to other influences, and the unpredictability of panel shear stiffness, the prediction of orthotropic panel flutter is a difficult task, indeed.

#### Slight Curvature

In a practical problem it may be anticipated that there will be some deviations from flatness in any installation, due to initial imperfection, mounting, etc. Here the situation will be accounted for as a plate with double curvature (see Fig. 5). The frequency spectrum for this case may be determined from Reissner shallow shell theory, and the resulting effect on the two-mode solution for the first longitudinal pair of modes may be shown to be:<sup>(6)</sup>

$$\frac{\Delta \lambda}{\lambda_0} \approx C \frac{[(a/b)^2 - 1][13 + 7(a/b)^2]}{[5 + 2(a/b)^2][4 + (a/b)^2][1 + (a/b)^2]} \quad (26)$$

$$C = \frac{12(1-\nu^2)}{\pi^4} \left( \frac{a}{b} \right)^4 \left( \frac{8H}{h} \right)^2 \quad (27)$$

Here  $H$  is the rise height of the shell and the radii of curvature have been taken as fixed by the dimensions such that the mid-point of each edge is co-planar. The results of evaluating  $\Delta \lambda / \lambda_0$  from Eq. (26) and (27) are shown in Fig. 6 for  $H/h = 1.0$ . Using a value of half this amount (the total deviation from flatness is  $2 H/h$ ), leads to a 17% increase in the flutter parameter for the example panel. Also shown are the variations due to a curvature in only one direction. Again, for the case cited, cross-stream curvature of the same magnitude leads to a 61% increase, while streamwise curvature results in a 7% decrease.

Thus, even small amounts of curvature can result in rather

large changes in flutter dynamic pressure. Actually, since the corrections are large and change markedly for the higher streamwise and chordwise mode numbers, a more complete modal analysis is indicated,<sup>(7)</sup> however, the results here are accurate for small curvature.

#### Flow Angle

Numerical investigation of the three-dimensional aerodynamic coupling indicates that the spanwise coupling is quite small, as well as the differences in the two- and three-dimensional chordwise couplings. For example, Ref. 3 indicates a maximum difference of only 6% in  $\lambda$  for aerodynamic aspect ratios,  $\beta b/a = 0 \rightarrow \infty$ .

Here, the coupling effects of a flow yawed to the panel are considered. If the velocity component approach is used, at least for small angles,  $\lambda$  would vary as  $(\cos \Theta)^{-2}$ . However, it is known that for  $\Theta = 90^\circ$ , the flutter speed must be finite. This raises a question as to flutter behavior at intermediate angles. A numerical investigation was therefore undertaken for the example panel, using two-dimensional aerodynamic theory but including both velocity components. Whereas all previous calculations have neglected aerodynamic damping, the sea-level value for an aluminum plate was used here. The results are shown in Fig. 7. An eight-mode analysis was used, selected on the basis of frequency: the first five lengthwise modes for the first crosswise mode and the first three lengthwise modes for the second crosswise mode.

This result appears significant, particularly for design purposes, although lower aerodynamic damping ratio cases and panel aspect ratios should be considered. It would indicate that for a panel which may not be aligned with the flow at all times, the lower of the two cases,  $\Theta = 0, 90^\circ$ , should be used to obtain the critical design condition, since the flutter dynamic pressure is nearly constant at the lower value over most of the yaw-angle range. As concerns testing, for the  $\Theta = 90^\circ$  configuration it would appear that flow alignment could be quite important, but difficult to evaluate.

Finally, although the calculations are incomplete, it would appear that the possibility exists, for low aerodynamic damping (high altitude), that the  $\lambda$  vs.  $\Theta$  plot may be triple valued in  $\lambda$  for a fixed  $\Theta$  at high yaw angles. Such behavior would suggest the existence of an unstable-stable-unstable behavior as dynamic pressure is increased, and could be the basis for explaining the mild flutter - no flutter - violent flutter occurrence noted at times in the experimental literature.

#### Summary

In the above evaluation, a number of effects have been considered. While they are, in fact, not independent, it is

impressive to review the complete situation. To reiterate, the example panel is flat, isentropic, simply-supported on all four edges, with zero pres-stress. The dimensions are (see Fig. 2)  $a = 20$  in.,  $b = 10$  in.,  $h = 0.10$  in. The following results are obtained:

<u>Effect</u>	<u>Variation</u>	<u><math>\Delta\lambda/\lambda</math></u>
Pre-Stress	$\Delta a = \pm 0.001$	$\pm 15\%$
Dimensions	$\Delta h = \pm 0.005$	$\pm 15\%$
Curvature	Cross-Stream	$\pm 61\%$
	Compound $H/h = 1.0$	$\pm 17\%$
	Streamwise	$- 7\%$

While it is highly unlikely that all of these deviations could occur simultaneously and independently, this summary indicates a maximum deviation in dynamic pressure of between  $-37\%$  and  $+90\%$  for a length-to-width ratio of two. These direct additions may appear to be an attempt to overprove a point; however, only the estimable deviations considered above have been included, and the myriad of other possible deviations have not been exhausted. The results obtained here have been translated to thickness required range as a function of length-to-width ratio in Fig. 8. The data from Fig. 1 is shown superimposed, and it would appear that the experimental scatter indicated is, perhaps, not without explanation. It should be emphasized that variations in chordwise boundary conditions have not been considered, a factor of significance in determining both the frequency spectrum and streamwise mode shape and hence the aerodynamic coupling.

Finally, it seems apparent that before satisfactory comparisons can be made, a more adequate evaluation of the test specimen must be made. As indicated in an earlier statement, this should include frequency spectrum, mode shape, and generalized mass, the latter an influence which has not been emphasized here. These same influences suggest that complete correlation should not be expected on the basis of the dynamic pressure-stiffness parameter,  $\lambda$ , alone.

References

1. Fung, Y. C. B.: A Summary of the Theories and Experiments on Panel Flutter. AFOSR TN 60-224, California Institute of Technology, May 1960.
2. Kordes, E. E.; Tuovila, W. J.; Guy, L. D.: Flutter Research on Skin Panels. NACA TN D-451, 1960.
3. Hedgepeth, J. M.: Flutter of Rectangular Simply Supported Panels at High Supersonic Speeds. Journal of Aeronautical Sciences, 24, 8, pp. 563-573, August 1957.
4. Ashley, H.; Zartarian, G.: Piston Theory - A New Tool for the Aeroelastician, Journal of the Aeronautical Sciences, 23, 12, pp. 1109-1118, December 1956.
5. Timoshenko, S.: Theory of Plates and Shells. McGraw Hill Book Co., Inc., 1940.
6. Voss, H. M.: The Effect of Slight Curvature on the Flutter of Rectangular Panels. To be published.
7. Voss, H. M.: The Effect of an External Supersonic Flow on the Vibration Characteristics of Thin Cylindrical Shells. Preprint No. 60-45, Institute of Aeronautical Sciences, Presented at the 28th Annual IAS Meeting, New York, January 27, 1960.

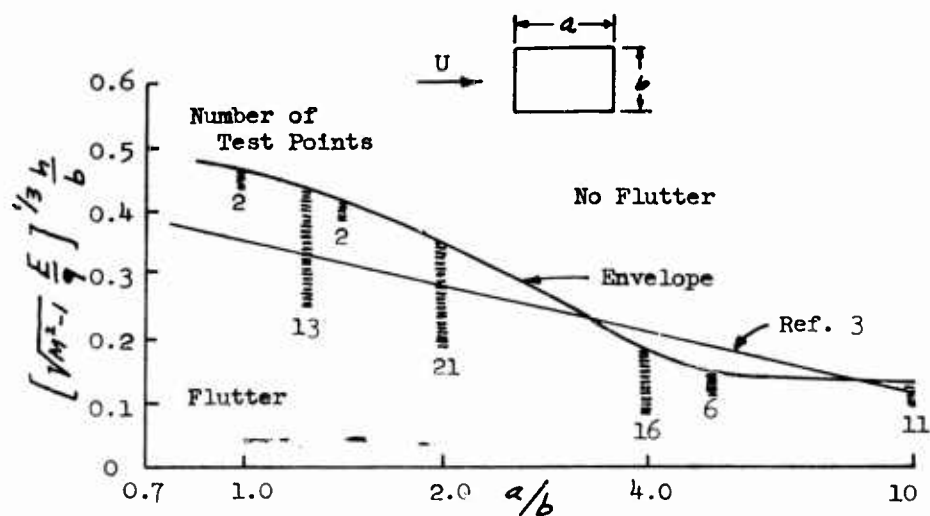


Fig. 1 Flutter of Unstiffened Panels from Ref. 2.

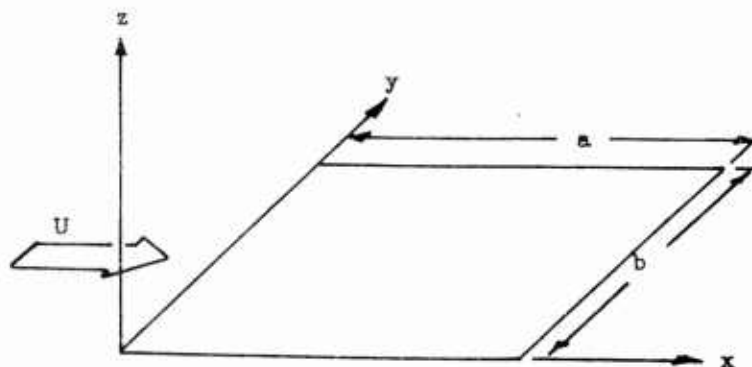


Fig. 2 Rectangular Panel and Coordinate System

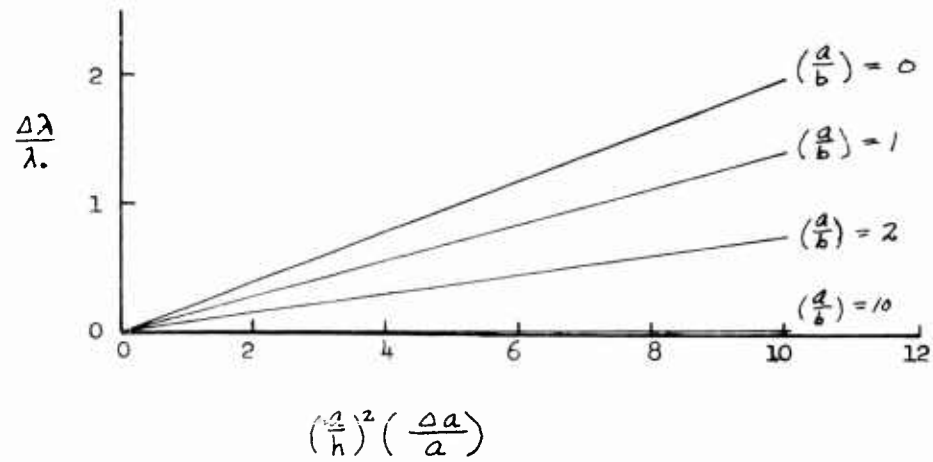


Fig. 3 Effect of Pre-Stress

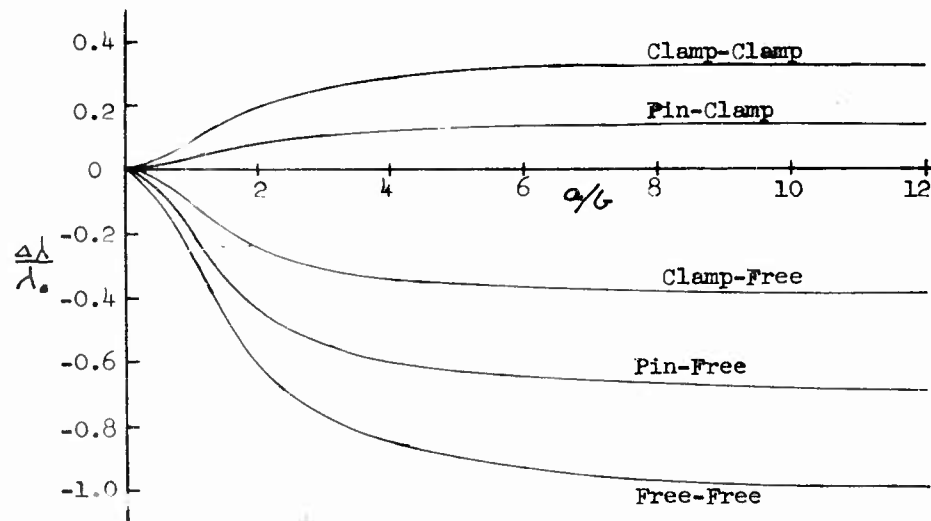


Fig. 4 Effect of Side Edge Conditions



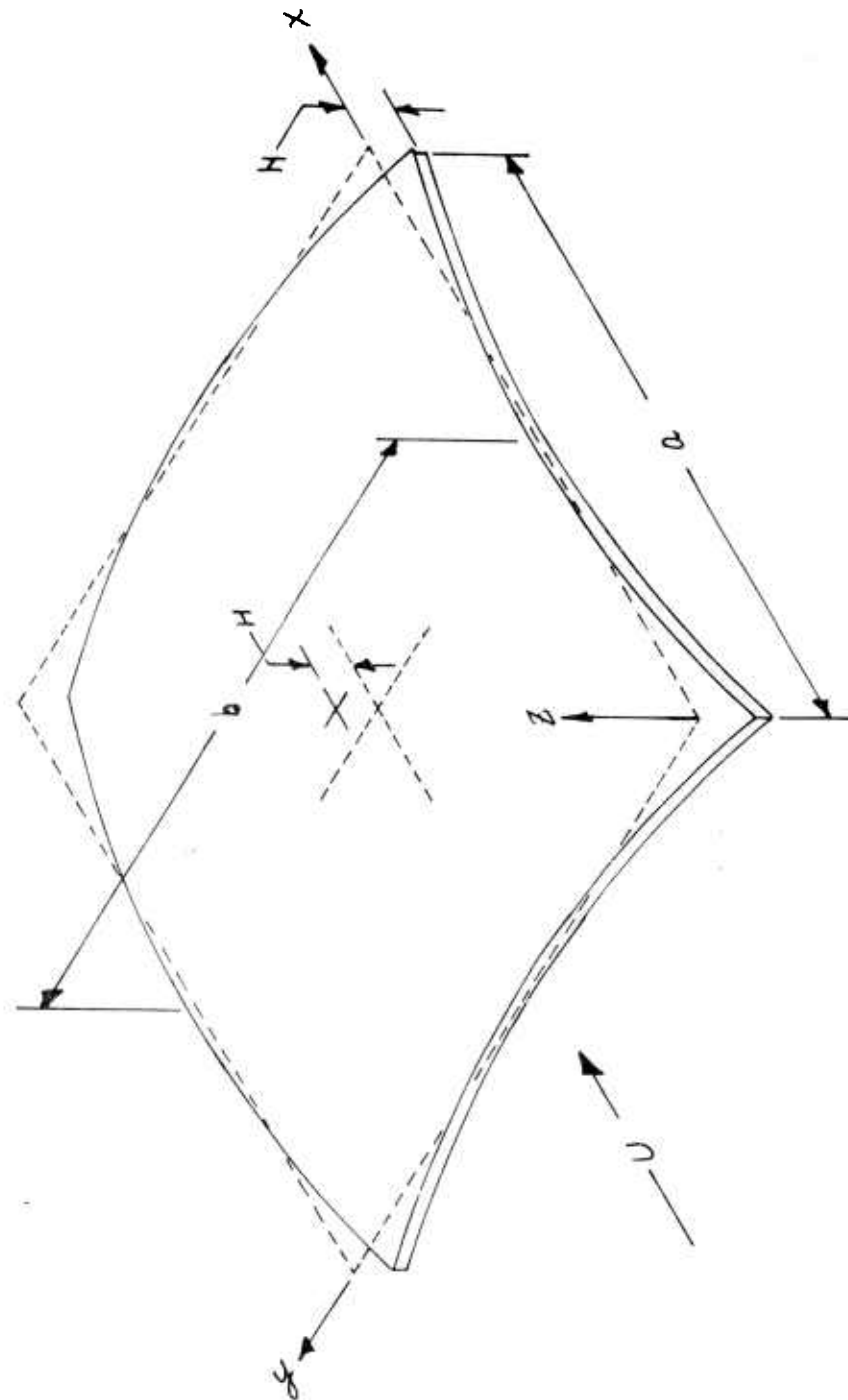


Fig. 5 Plate with Slight Curvature

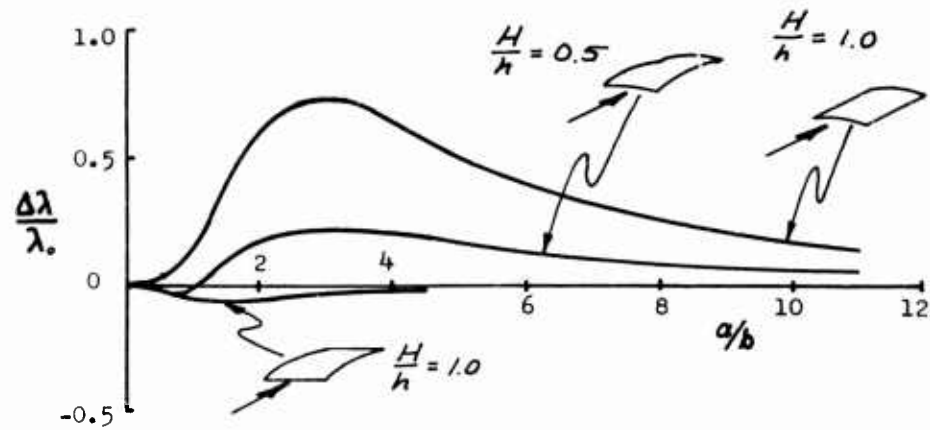


Fig. 6 Effect of Slight Curvature

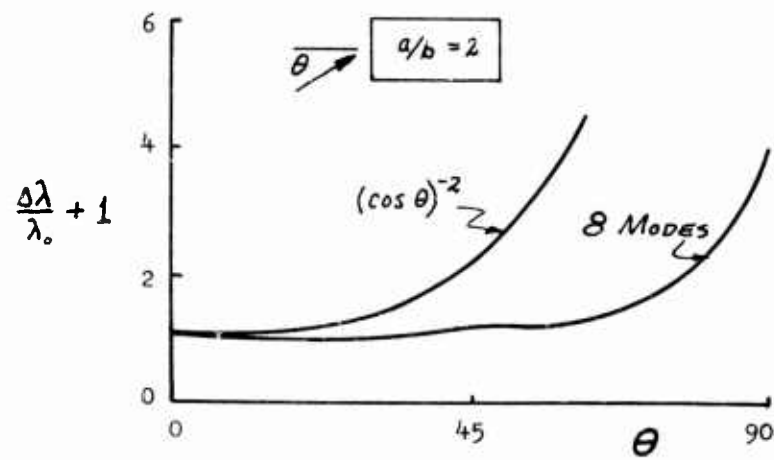


Fig. 7 Effect of Yaw Angle

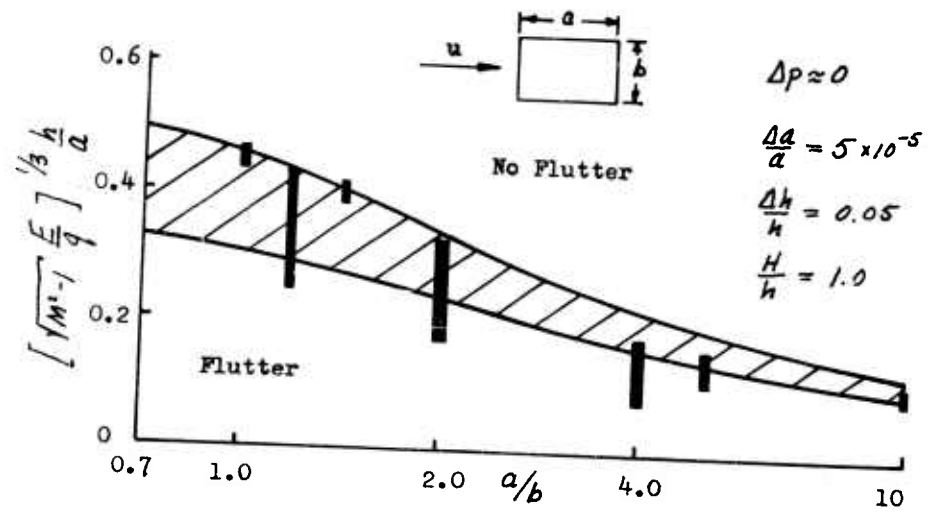


Fig. 8 Predicted Scatter for Example Panel

## SCALE-MODEL FLIGHT DYNAMICS TESTING ON HIGH-SPEED TRACKS

Charles E. Woods  
U. S. Naval Ordnance Test Station  
China Lake, California

The history of high-speed track testing spans little more than 10 years, but in this time its importance in development of ordnance and aircraft components has increased tremendously. Hardly a year has passed in which there have not been several new concepts or capabilities added to the field. Major areas of track testing now include acceleration and environmental testing of guidance systems and associated equipment, aircraft escape system testing and development, simulated flight and acceleration of propulsion systems, and structural dynamics testing of aircraft and missile components. In this latter group fall a variety of tests, including complete aircraft and missile configurations, wings, fins, and radomes.

The Supersonic Naval Ordnance Research Track (SNORT) at the U. S. Naval Ordnance Test Station, China Lake, provides 4.1 miles of precision-aligned rails set at standard railroad gage. Speeds up to Mach 4 have been achieved on this track, and vehicles weighing as much as 40,000 lb have been used. Several test programs have been conducted with scale-model missiles to check flight dynamics during launch and other phases of flight. One of these programs is discussed at length in this paper.

Most scale-model testing is currently conducted in high-speed wind tunnels; however, there are some test objectives that are difficult to achieve in the limited space available, and these can be accomplished more easily in the free flight obtained from a rocket-boosted track vehicle. One of these objectives is thrust termination and separation of the stages or warhead of a missile. Testing of this type can be conducted satisfactorily on a track, and while it is relatively expensive, it may be much less expensive than conducting full-scale flight tests, which are much more difficult to instrument adequately.

In one test program conducted at NOTS a one-third scale-model missile was used to study the dynamics of separation of the missile from its booster motor. It was possible to simulate not only velocity but also the Reynolds number of the full-scale missile at

operational altitude. Since the physical dimensions were scaled by one-third, and full-scale density and velocity modeling were requested, the weight, CG, and moment of inertia were scaled accordingly to give a correctly simulated model. The Appendix gives a complete description of the simulated flight equations for motion and scaling relationships. The complete one-third-scale missile and rocket motor used in the track tests is shown in Fig. 1.

There are basically two types of track vehicles: monorail and dual-rail. Generally, monorail vehicles are less expensive to fabricate and require less propulsive force because of their lighter weight and lower aerodynamic drag. Monorail vehicles are limited, however, in the size and weight of test item which can be safely supported on one rail. This drawback can be overcome, and at the same time significant savings may be realized, by using scale models on monorail vehicles rather than full-scale test items on dual-rail vehicles. The savings become appreciable if a large number of runs with expendable vehicles are required.

Figure 2 shows a complete monorail test vehicle used at NOTS to boost a scale model to a velocity of 3,200 fps. It is a three-stage vehicle, with the first stage consisting of two 11.75-inch Tiny Tim motors and the second and third stages each consisting of three 5.0-inch NOTS Model 124-C motors. The second and third stages, and the missile rocket motor and separation sequence timer, are initiated by ignition-circuit knife blades mounted on the vehicle; the blades cut through electrically-charged screen boxes located along the track rail. There are a number of standard booster-vehicle designs which utilize a variety of readily available rocket motors. Surplus or obsolete motors can often be obtained at no cost to the program.

Supporting the test item on the vehicle so as to allow free flight at the end of the track requires careful design. The designer must see that all support points disengage simultaneously so that motion of the vehicle on the track will not introduce tip-off forces into the missile. In the tests described here, the missile model was supported forward by an auxiliary shoe or skid, shown in Fig. 3. A 'T' lug attached to the missile was fitted into a slot in the skid. The aft end of the missile was supported on the third-stage booster by a ring fitting into a sleeve on the missile motor fairing. Both the aft sleeve and 'T' lug slid free simultaneously as the missile was released. Figure 3 also shows the clamp and explosive bolts that allowed separation of the missile from its booster motor.

In these tests the missile rocket motor was not ignited until after release into free flight, hence the third-stage booster had to be decelerated at the end of the track to allow the missile to slide free. Momentum-exchange water braking was used to accomplish the separation. Approximately 170-g deceleration was applied to the vehicle during the last 40 feet of rail travel; this provided about 6 inches of separation between the booster and the missile at 3,200 fps. The water brake, shown in Fig. 4, consisted of two curved tubes on each side of the rail, which picked up water from sheet metal troughs fastened to the track foundation. The water was turned 90°

CHARLES E. WOODS

to produce a momentum-exchange braking force of approximately 42,000 lb for the last .013 seconds of travel. This method of initiating separation proved to be very satisfactory and was completely reliable throughout the entire program.

In order to eliminate the possibility of the third-stage booster interfering with the missile flight after separation, some means of deflecting the booster away from the flight path at the end of the track had to be found. This was accomplished by virtue of a 100-ft section of rail welded to the end of the track and curving downward to carry the vehicle beneath the missile flight path. The deflector rail is shown in Fig. 5. To avoid the necessity of bending this rail to the proper curvature, the natural curve of the rail, resulting from its own weight was calculated, and the supports built accordingly. When the rail was welded to the existing track it rested on each support and assumed a smooth curve having a total drop of 16 inches in 100 feet. This curve was flat enough that the vertical acceleration of the vehicle did not exceed its 100-g design limit.

Figure 6 shows the missile in free flight at the end of the track, with the third-stage booster below and behind it on the curved rail. The velocity here is about 3,200 fps. Figure 7 covers the entire sequence of separation of the missile from its own booster motor in free flight. The third-stage booster can be seen impacting the ground behind the missile in the lower half of the sequence. Figure 8 shows the shock wave pattern from the missile and booster carriage just prior to water-brake entrance and separation. The reflected shock waves on the track rail make it necessary to actuate the missile functions beyond the influence of the bent rail, hence the usual knife-blade screen-box initiation system could not be utilized.

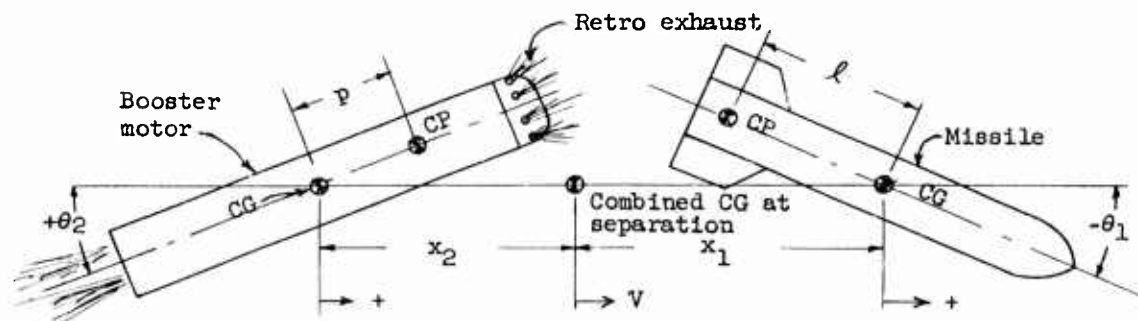
An on-board timer was installed in the missile to fire the booster motor and separation bolts during free flight; the timer circuit is shown in Fig. 9. The timing cycle was initiated at water-brake entrance, and was adjusted for various velocities by changing Resistor R. To insure safe handling during assembly, the capacitors which store the energy for firing the explosive bolts and booster motor were charged remotely five seconds before the run.

Camera coverage of the entire sequence was excellent and of sufficient clarity to permit reasonably accurate measurement of pitch angle vs time.

This program clearly illustrated the feasibility of using high-speed tracks for obtaining dynamic flight information by means of scale models. Although many minor and some major difficulties were encountered during this program, requiring development of some new techniques, usable information was obtained on this particular missile, and much valuable experience in scale-model testing was gained. On the basis of this experience it is felt that much better results could be obtained on similar missile test programs in the future.

## SCALING FACTORS\*

The full scale equations of motion are as follows:



$$m \frac{d^2 x_1}{dt^2} + C_{Dm} A_m \rho \frac{v^2}{2} = F_{jr}(x, \theta) \quad \text{Axial deceleration of the missile}$$

$$M \frac{d^2 x_2}{dt^2} + C_{Db} A_b \rho \frac{v^2}{2} = T_b - T_r \quad \text{Axial deceleration of the booster motor}$$

$$I_m \frac{d^2 \theta_1}{dt^2} + l \theta_1 A_m \left[ \frac{dC_{Lm}}{d\theta_1} \rho \frac{v^2}{2} - k(\theta, x) \frac{dC_{Lm}}{d\theta} \rho_j \frac{v_j^2}{2} \right] = 0 \quad \text{Angular motion of the missile}$$

$$I_b \frac{d^2 \theta_2}{dt^2} - p \frac{dC_{Lb}}{d\theta_2} \theta_2 A_b \rho \frac{v^2}{2} = 0 \quad \text{Angular motion of the booster motor}$$

\* The scale equations of motion and scaling factors were derived by D. P. Ankeney.

Subscript m denotes missile, b denotes booster motor

$m$  = mass of the missile

$M$  = mass of the booster

$x_1$  = Distance of missile C.G. from combined C.G. at release  
Combined C.G. moves at velocity "v" after separation

$x_2$  = Distance of booster motor C.G. from combined C.G.

$C_D$  = Aerodynamic drag coefficient

$A$  = reference area

$\rho$  = mass density of air

$v$  = Release velocity

$T_b$  = Thrust of booster forward

$T_r$  = Effective retro thrust of booster rearward

$F_j(x, \theta)$  = Force of the retro exhaust gases on the missile as a  
function of separation distance and angular motion

$I$  = Moment of inertia about the pitch axis

$\theta_1$  = Angular rotation of missile about C.G.

$\theta_2$  = Angular rotation of booster motor about C.G.

$l$  = Distance from missile C.G. to aerodynamic center of pressure

$p$  = Distance from booster motor C.G. to aerodynamic center of  
pressure

$\frac{dC_{Lm}}{d\theta}$  = Lift coefficient relation

$k(\theta, x)$  = Geometric factor of retro effect on missile as a function  
of angular rotation and separation distances

$\rho_j$  = Mass density of retro exhaust gases

$v_j$  = Velocity of retro exhaust gases

Subscript "s" denotes model dimension and "n" the scale in  
the following discussion

Full scale velocity, "v", and overall model density "σ" are  
requested. Therefore:

$$V_s = V$$

$$\sigma_s = \sigma$$

$$X_s = \frac{X}{n}$$



These relationships imply:

$$\begin{aligned} m_s &= \frac{m}{n^3} \\ A_{ms} &= \frac{A_m}{n^2} \\ F_{jr}(x, \theta)_s &= \frac{F_{jr}(x, \theta)}{n^2} \\ * \theta_s &= \theta \end{aligned}$$

To obtain aerodynamic similarity, it is necessary that the relative angle of attack of the models to the airstream be correctly simulated. The relative angle of attack of the model consists of the vector sum of the free stream velocity "V" and the velocity created by the angular rotation " $\theta$ " of the model.

In order to model this correctly:

$$\begin{aligned} V_s &= V \\ \ell_s \dot{\theta}_s &= \ell \dot{\theta} & \ell = \text{Distance of fin from center of rotation} \\ \text{Now } \ell_s &= \frac{\ell}{n}; \text{ therefore } \dot{\theta}_s = n \dot{\theta} \end{aligned}$$

This  $\dot{\theta}$  scaling can only be accomplished by decreasing the scale time "t" by "n";  $t_s = \frac{t}{n}$ . This means that the events of separation will take place n - times faster than the full scale action. In order to balance the equations of motion involving " $\theta$ " it is necessary to scale the moments of inertia by  $n^5$ . Since " $\theta$ " response is sinusoidal, the scaling of "t" accomplishes the " $\dot{\theta}$ " match as follows:

$$\begin{aligned} \theta &= \theta_{\max} \sin \omega t & \theta_s &= \theta_{\max} \sin \omega \left( \frac{t}{n} \right) \\ \dot{\theta} &= \theta_{\max} \omega \cos \omega t & \dot{\theta}_s &= \theta_{\max} \frac{\omega}{n} \cos \omega \left( \frac{t}{n} \right) \\ & & n \dot{\theta}_s &= \theta_{\max} \omega \cos \omega \left( \frac{t}{n} \right) \end{aligned}$$

\*For further discussion see Sec. 5:17 of Alan Pope, "Wind Tunnel Testing", 2nd edition. New York, John Wiley & Sons, Inc., 1954.

$$\text{so, } \theta = \theta_s$$

$$\dot{\theta} = n \dot{\theta}_s$$

The scale equations of motion are then:

$$\frac{m}{n^3} \frac{d^2 \left( \frac{x_1}{n} \right)}{d \left( \frac{t}{n} \right)^2} + C_{Dm} \frac{A_m}{n^2} \rho \frac{v^2}{2} = \frac{F_{jr}(x, \theta)}{n^2}$$

$$\frac{M}{n^3} \frac{d^2 \left( \frac{x_2}{n} \right)}{d \left( \frac{t}{n} \right)^2} + C_{Db} \frac{A_b}{n^2} \frac{\rho v^2}{2} = \frac{T_b - T_r}{n^2}$$

$$\frac{I_m}{n^5} \frac{d^2 \theta_1}{d \left( \frac{t}{n} \right)^2} + \frac{l}{n} \theta_1 \frac{A_m}{n^2} \left[ \frac{dC_{Lm}}{d\theta} \rho \frac{v^2}{2} - k(\theta, x) \frac{dC_{Lm}}{d\theta} \rho_j \frac{v_j^2}{2} \right] = 0$$

$$\frac{I_b}{n^5} \frac{d^2 \theta_2}{d \left( \frac{t}{n} \right)^2} - \frac{p}{n} \frac{dC_{Lb}}{d\theta} \theta_2 \frac{A_b}{n^2} \frac{\rho v^2}{2} = 0$$

These equations contain the correct scaling factors. The full scale parameters must be divided by the correct power of "n" as listed above to obtain the correct model.

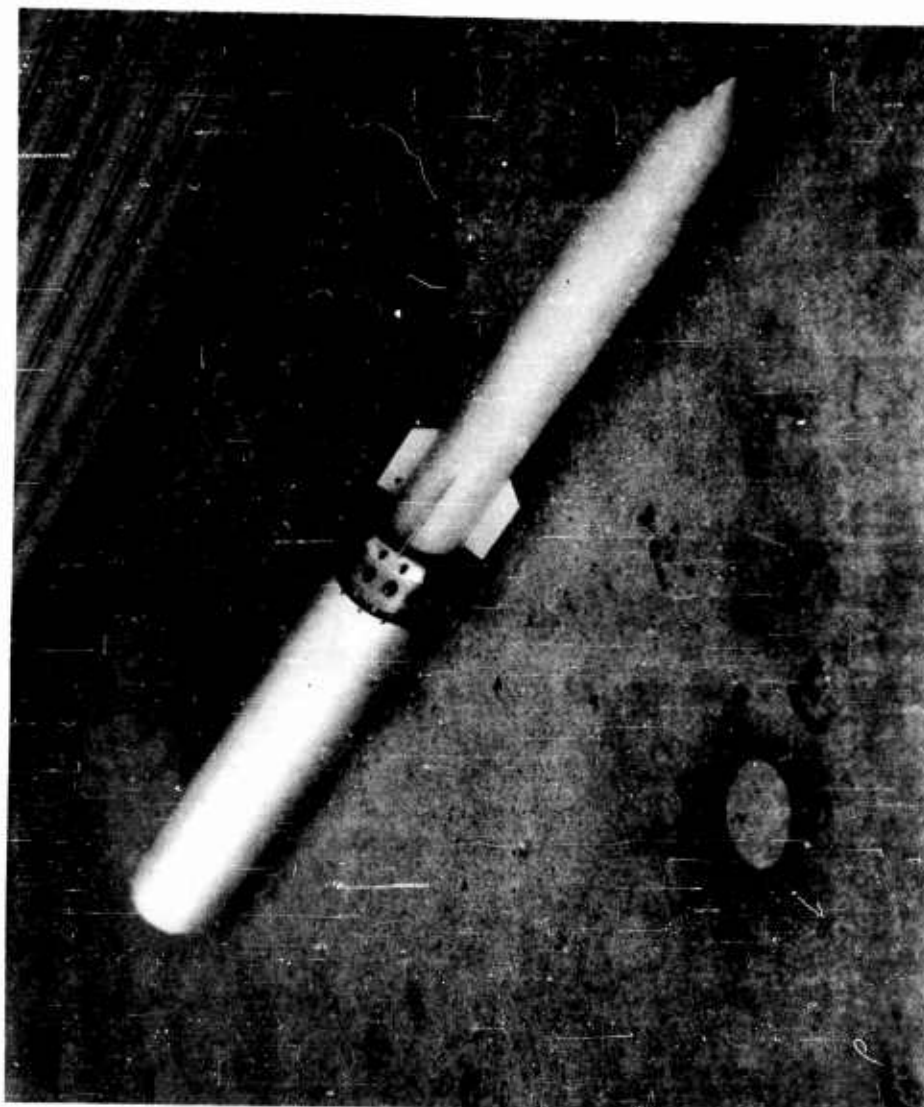


Fig. 1 - One-third scale missile model

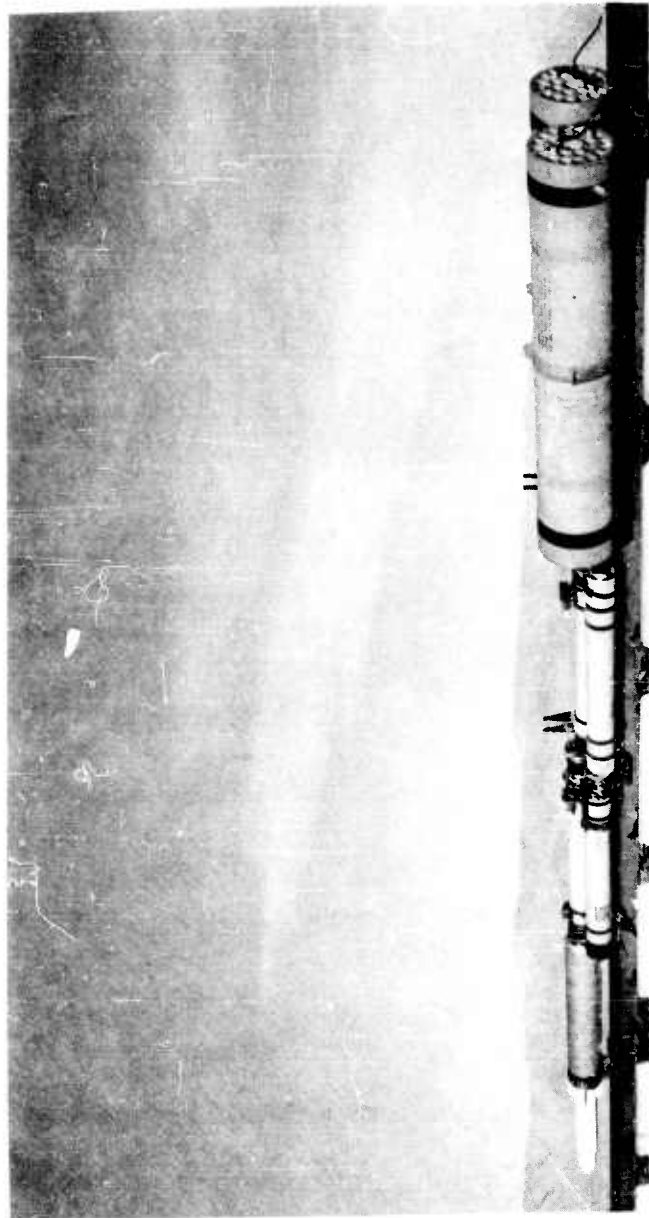


Fig. 2 - 3200 FPS monorail test vehicle



Fig. 3 - Forward auxiliary support slipper

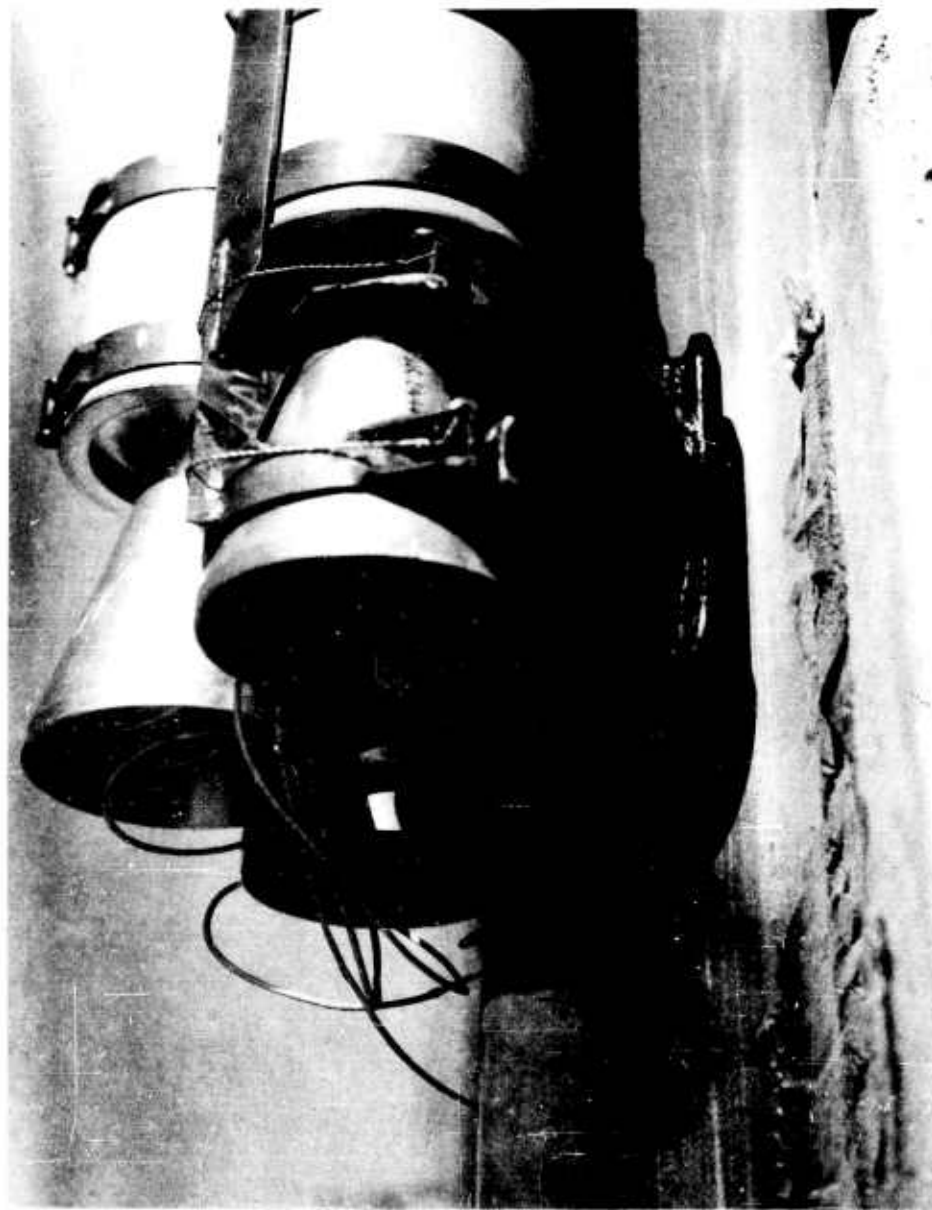


Fig. 4 - Monorail momentum exchange water brake

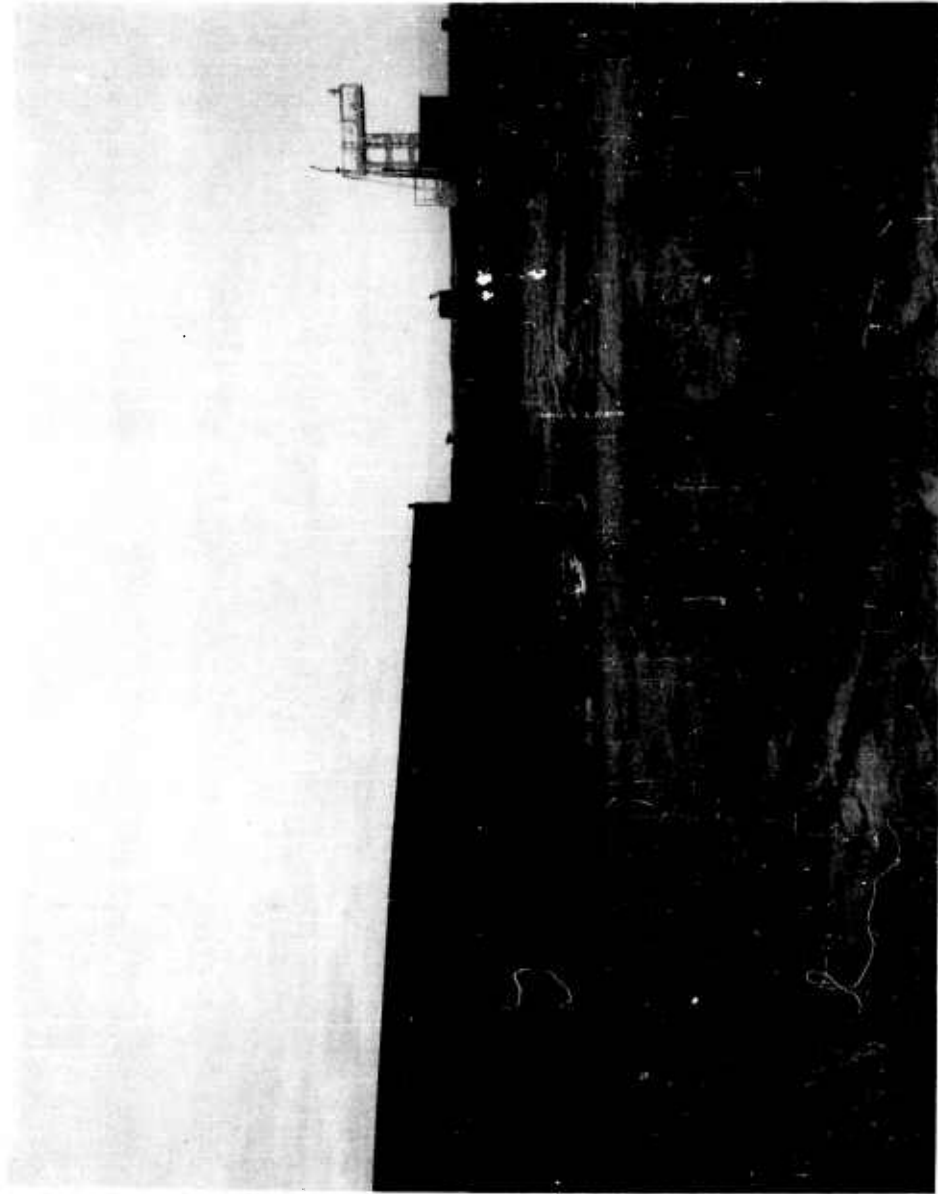


Fig. 5 - Curved rail vehicle deflector

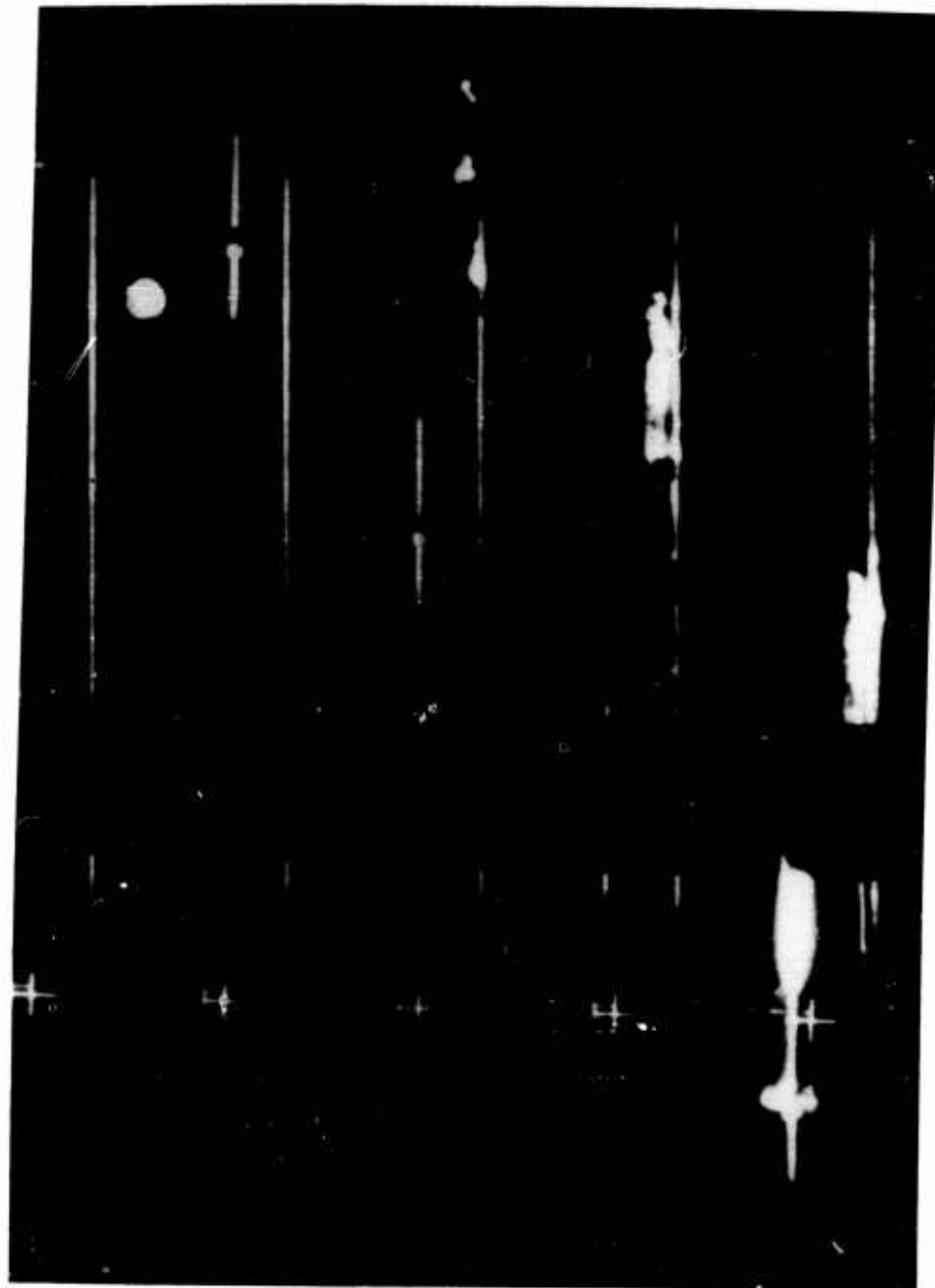


Fig. 6 - Separation sequence



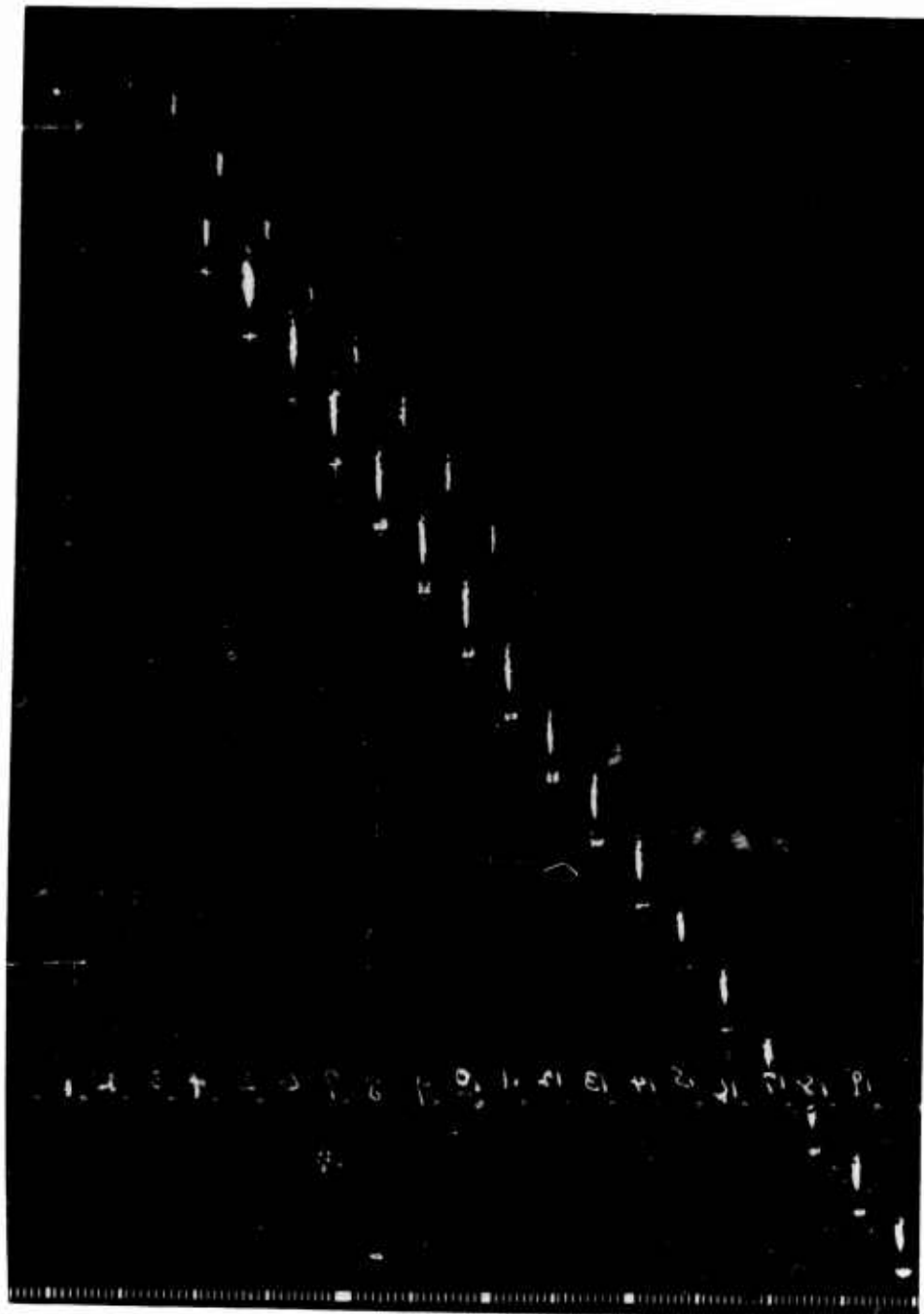


Fig. 7 - Complete separation and actuation sequence

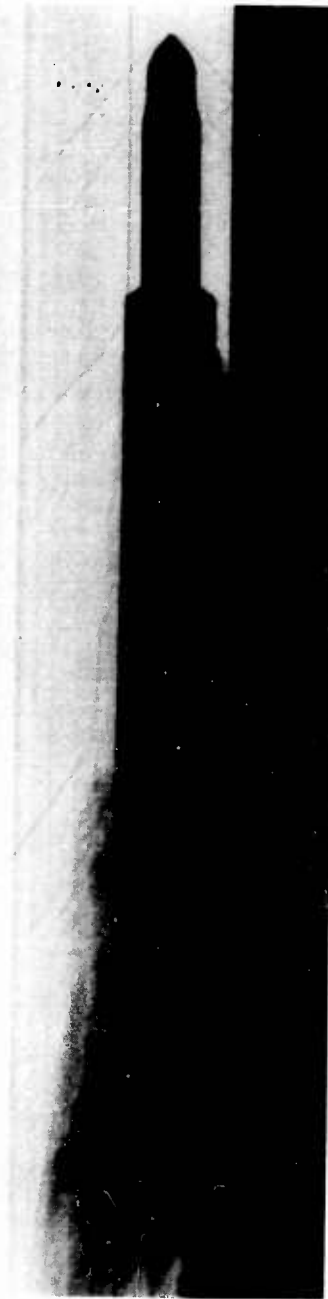


Fig. 8 - Missile shock-wave pattern

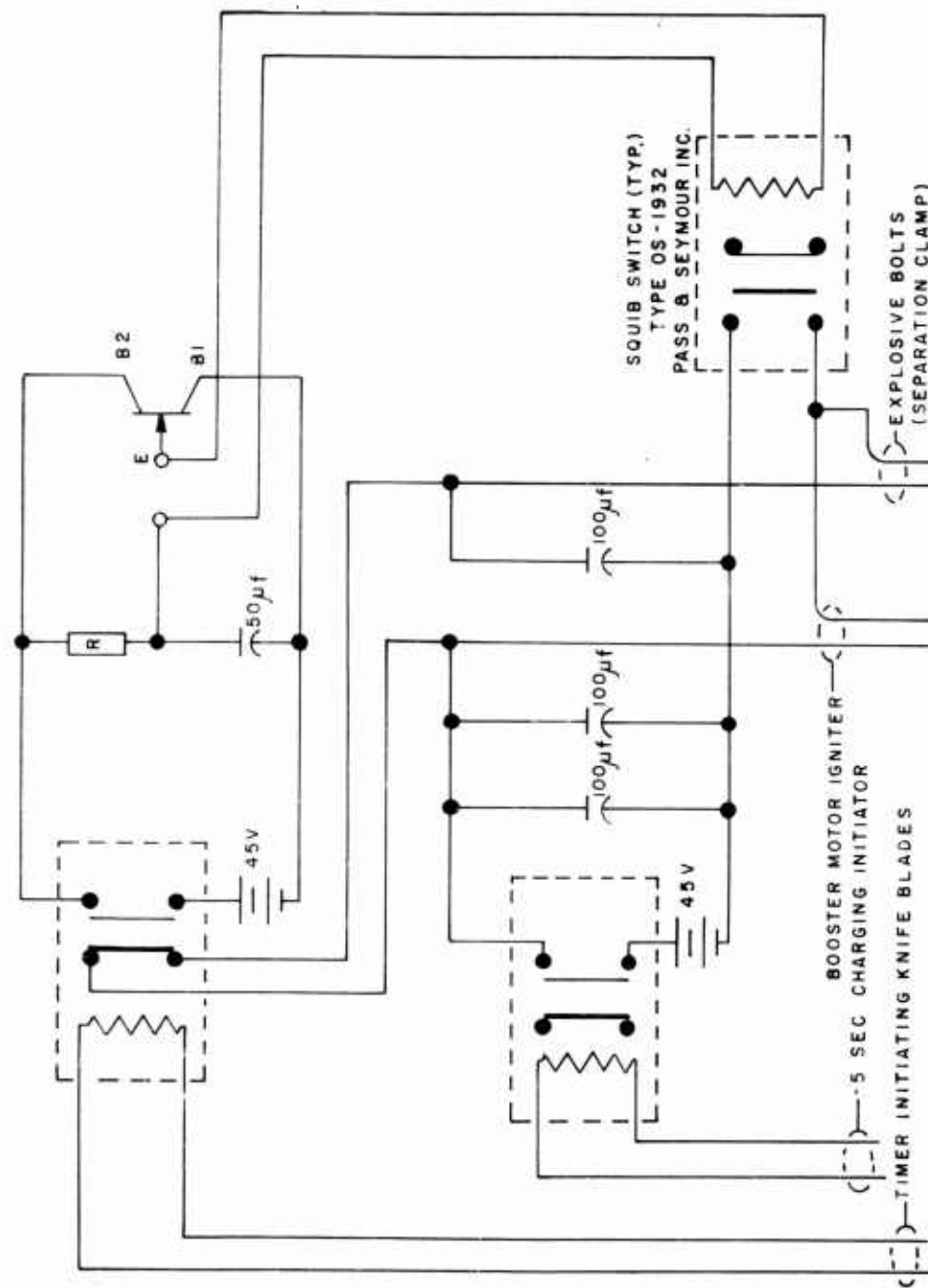


Fig. 9 - Separation sequence timer circuit

**SESSION III | MISSILE SYSTEM DYNAMICS**

Chairman: Dr. Millard V. Barton  
Space Technology Laboratories

## LIQUID DYNAMIC BEHAVIOR IN ROCKET PROPELLANT TANKS

H. Norman Abramson  
Southwest Research Institute  
San Antonio, Texas

### ABSTRACT

Various types of liquid dynamic behavior occurring in rocket propellant tanks are described and discussed. These include normal sloshing, vortexing, liquid impact, bubble and spray formation, and low gravity phenomena. Attention is given to the use of suppression devices and means of evaluating their effectiveness by use of laboratory models, and to the development of equivalent mechanical models for use in analyses of the system dynamics of the vehicle.

### INTRODUCTION

It is well known to everyone that liquids in partially filled containers have a very strong propensity to "slosh" about, under even the slightest of disturbances. Liquid propellants in rocket tanks also possess this same predilection to move about under slight accelerations, thereby leading to highly undesirable consequences with relation to overall performance of the vehicle and even, in extreme cases, to subsequent catastrophic events. The problem is most acute, obviously, when one of the liquid natural frequencies is close to that of one of the lower modes of elastic vibration of the primary structure, say the fundamental body-bending mode, or to one of the principal control system frequencies. In fact, consideration of liquid propellant sloshing effects is now generally accepted as a necessary ingredient of any dynamic stability and control analyses performed in conjunction with rocket design (1).

Unfortunately for the rocket engineer or designer, liquid propellants can exhibit an amazing variety of motions of varying degrees of complexity, none of them really simple and all of them difficult to predict and understand; nevertheless, much new information concerning these various modes of liquid behavior has become available over just the past two or three years and therefore it is perhaps appropriate, by means of this paper, to describe some of the more interesting of these problems of dynamic behavior of liquid propellants and, perhaps even more importantly, to indicate the various theoretical and laboratory techniques employed to study them and the means that are being employed to ameliorate their effects on vehicle performance.

### NORMAL SLOSHING

"Sloshing" is the term usually applied to the most common type of motion of liquid propellants in partially filled rocket tanks. This relatively simple type of back-and-forth motion of the liquid, resulting primarily from translational or pitching motions of the tank, is now fairly well understood in terms of its relation to the general dynamical behavior of the entire rocket system and its interactions with other of the system components(1). The details of the mathematical theory of such "normal sloshing" modes of free surface oscillations of the liquid\* have been quite well-developed so that there is now available a relatively complete body of theoretical knowledge concerning this type of liquid behavior in tanks of various configuration (rectangular, spherical, circular, elliptical, ring, etc.), all of which is well-supported by experimental data(2-5)\*\*.

Figures 1 and 2 show the first and second of such sloshing modes in an upright cylindrical tank and a spherical tank, respectively, produced by horizontal translational excitation of the tanks. One highly interesting and important feature of these sloshing modes is the dependence of natural frequency upon depth, as shown in Figure 3 for the lowest four modes of liquid motion in an upright circular cylindrical tank. The frequency parameter  $\omega_{nd}^2/a$  involves the

---

\* Such analyses are based, of course, on ideal potential flow theory.

\*\* Reference 2 is a review article containing an exhaustive bibliography on normal sloshing; therefore, no attempt at completeness has been made in the list of references for the present paper.

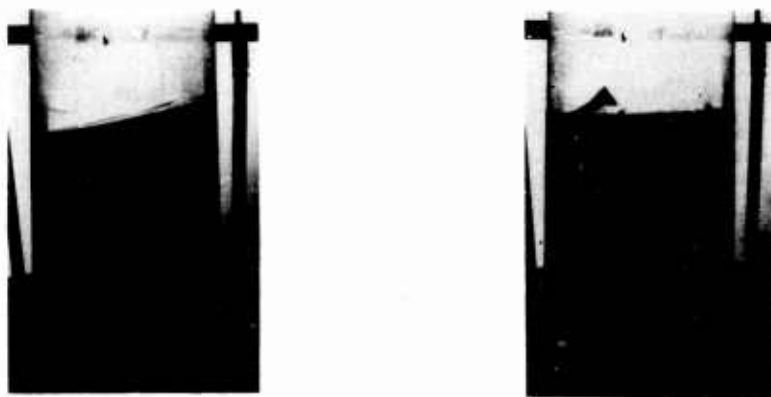


FIGURE 1. FIRST TWO FREE SURFACE MODES OF LIQUID MOTION IN AN UPRIGHT CIRCULAR CYLINDRICAL TANK (PHOTO COURTESY NASA)



FIGURE 2. FIRST TWO FREE SURFACE MODES OF LIQUID  
MOTION IN A SPHERICAL TANK  
(PHOTO COURTESY NASA)



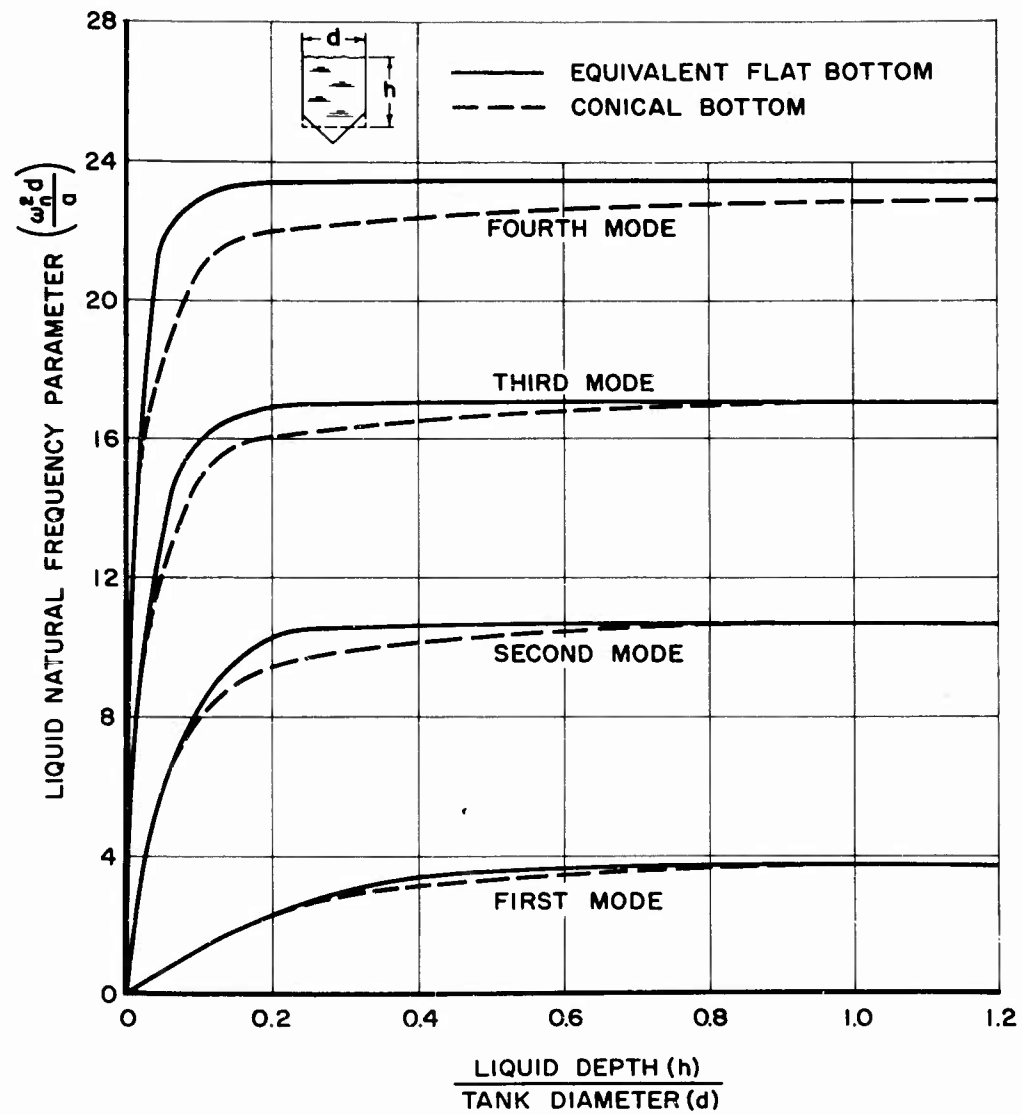


FIGURE 3. CHANGE IN FREQUENCY WITH DEPTH FOR FIRST FOUR NORMAL SLOSHING MODES IN A CIRCULAR CYLINDRICAL TANK WITH BOTH FLAT AND CONICAL BOTTOMS

tank diameter  $d$  and axial acceleration  $a$  in order to make it nondimensional, and is plotted against the liquid depth  $h$ , in terms of tank diameter. For such a circular cylindrical tank with a flat bottom, the frequency relation is given by

$$\omega_n^2 = \frac{2a\xi_n}{d} \tanh\left(2\xi_n \frac{h}{d}\right)$$

where  $\xi_n$  are the zeros of the first derivative of the Bessel function of the first kind. Most of the change in frequency occurs for shallow liquid depths, i. e., less than one tank diameter for the first mode, and even less for higher modes; therefore, it is anticipated that the effect of a conical tank bottom shape, for example, would be most pronounced at the shallow liquid depths(4, 6). Corresponding frequency curves for a circular cylindrical tank with a conical bottom are therefore shown also in Figure 3, with the comparison made on the basis of the two tanks having equal liquid volumes. Similar frequency curves for the first three modes in a spherical tank(5) are shown in Figure 4.

While the mathematical details of the theory governing liquid sloshing modes produced by both translational and pitching excitations, even to consideration of wall pressure distributions(7), have been worked out rather completely, the theory does not yield required information in at least three important instances. One of these involves extremely large amplitude liquid motions ("breaking" waves) which occur near resonance, as shown in Figure 5. Another involves rotational type motions of the liquid about the tank longitudinal axis, but induced by translational excitation and occurring very near to the resonances of the normal sloshing motions, and superimposed on the normal sloshing motion(8, 9)\*. The third such instance of the inapplicability of the mathematical theory arises from the introduction of mechanical suppression devices, or arrangements of baffles of one type or another, that are now almost universally employed in rocket liquid propellant tanks. In all three of these situations, the complexity of the liquid flow behavior, and particularly in combination with mechanical suppression devices, precludes detailed mathematical study and therefore recourse must be made to experimental (laboratory) investigations.

---

\* This problem will be discussed in greater detail later in this paper.

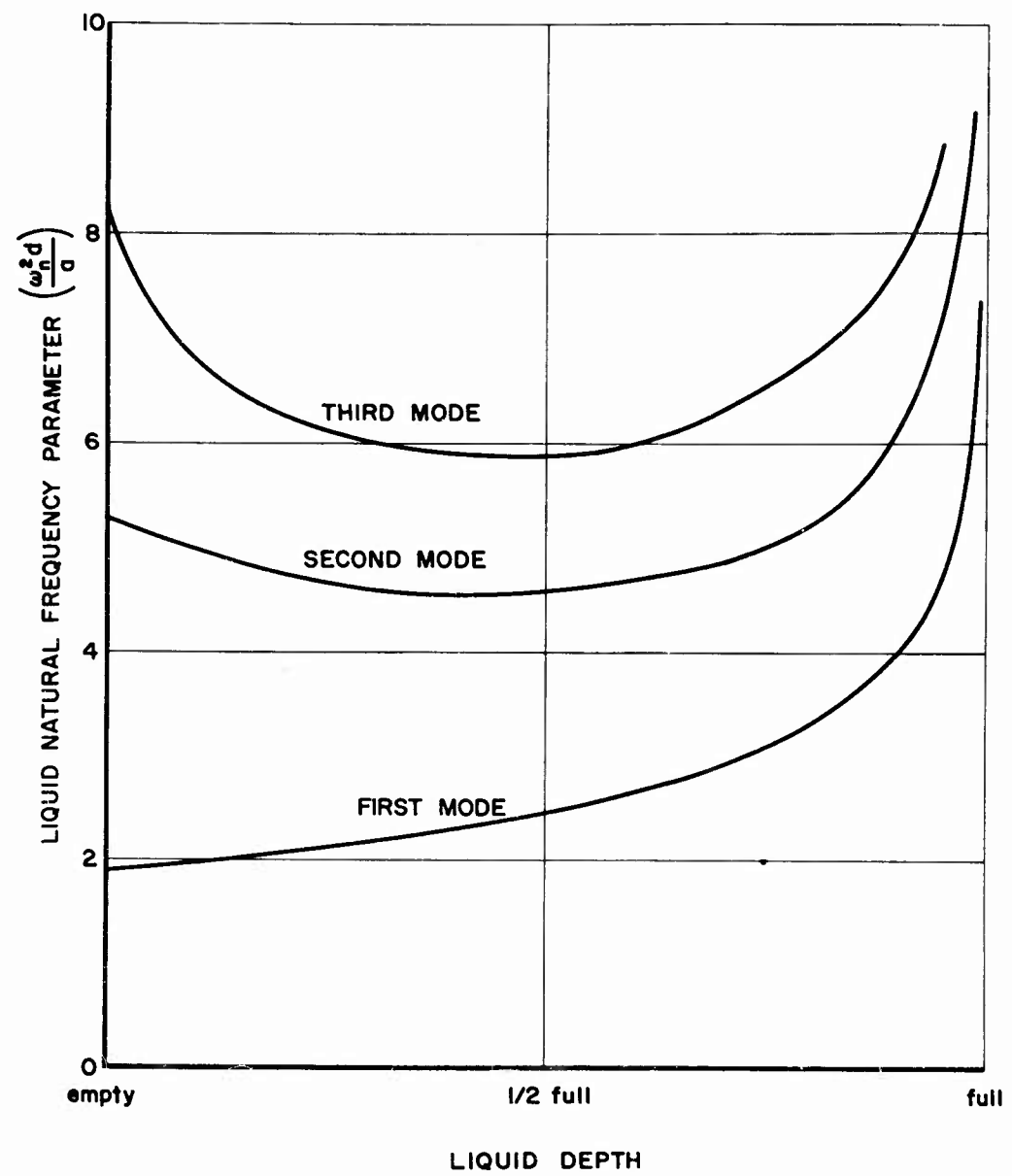


FIGURE 4. CHANGE IN FREQUENCY WITH DEPTH FOR FIRST THREE NORMAL SLOSHING MODES IN A SPHERICAL TANK

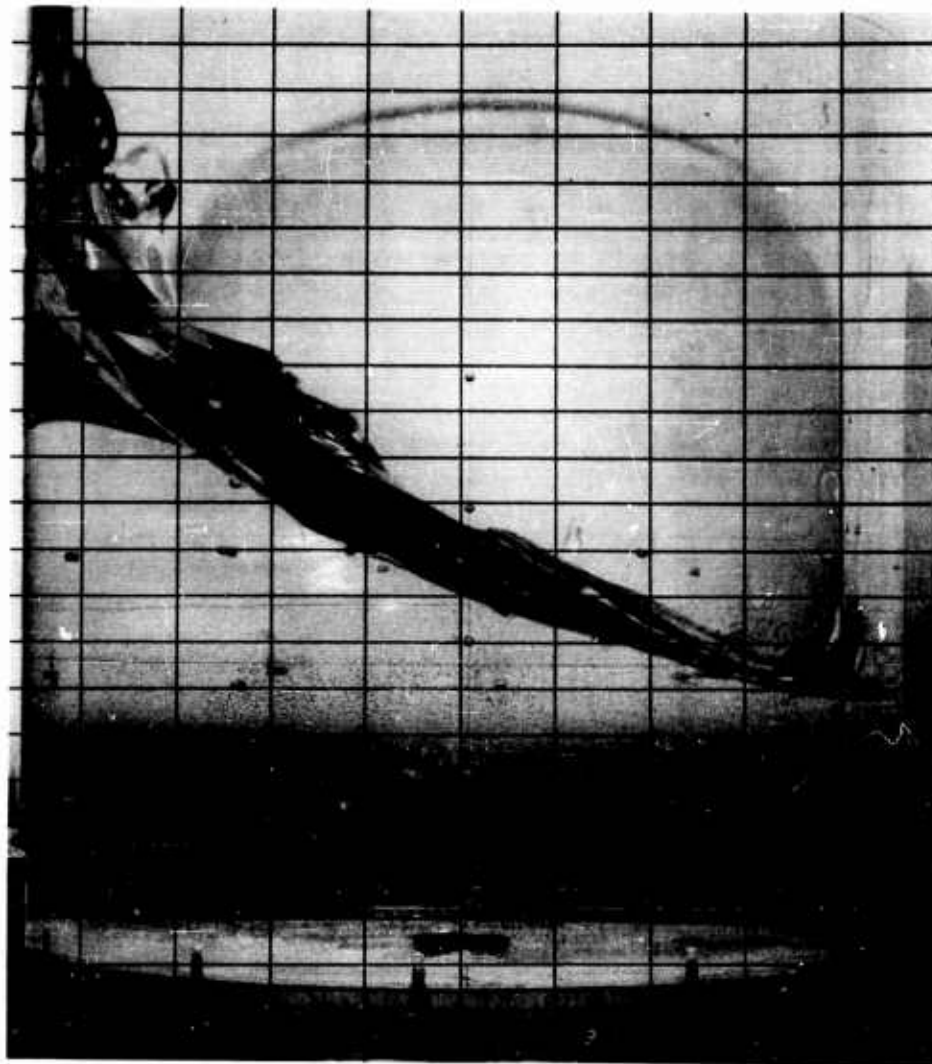


FIGURE 5. LARGE AMPLITUDE LIQUID MOTION ("BREAKING"  
WAVE) OCCURRING DURING TRANSVERSE SLOSHING  
NEAR FIRST MODE RESONANCE

## LABORATORY SIMULATION OF NORMAL SLOSHING

The use of small laboratory models (1/10 to 1/5 scale, say) to simulate liquid sloshing behavior has been found to be particularly valuable in three important respects: (a) to obtain experimental data for quantitative evaluation of a particular theoretical analysis; (b) to explore the fundamental flow mechanisms involved in the occurrence of a little-understood and particular type of liquid motion; and (c) to obtain quantitative data for use in prototype design problems, particularly where no mathematical theory exists, as for example when mechanical suppression devices are involved. Model tests have been found to be particularly successful for the last of these, especially when proper attention is given to the selection of the model liquids to insure dynamic similarity with the liquid propellants employed in the prototype vehicle (10, 11) since the damping provided by baffles and other mechanical devices is usually a function of both the liquid properties and the excitation amplitude and frequency. The modeling relationships derived from a similitude analysis require that (10)

$$d_r = \left( \frac{\mu}{\rho} \right)_r^{2/3} a_r^{1/3}$$

where  $d_r$  is the geometric scale factor ratio of model to prototype,  $a_r$  is the ratio of longitudinal acceleration of model to prototype\*, and  $(\mu/\rho)_r$  is the ratio of kinematic viscosity of model to prototype, which governs the selection of the model fluid. \*\* Surface tension effects have been neglected in comparison with inertial and viscous forces. A series of experiments conducted in accordance with these requirements make it entirely feasible to determine not only the total force and moment exerted on the tank by the sloshing liquid but the effectiveness of various suppression devices in terms of damping factor, as well. An example of such data on damping factor is shown in Figure 6 for conical ring type baffles, as a function of the dimensionless excitation amplitude  $X_0/d$  and at one value of effective Reynolds number (10). The damping provided by these baffles is very nearly the same for both translational and pitching motions of the tank, and tends to decrease with increasing Reynolds number (as provided by different model liquids and tank sizes). Of course, for suppressors

\* The model, of course, is usually tested at 1G.

\*\* For certain cryogenic liquids (e. g., liquid hydrogen), it is virtually impossible to find a model liquid that possesses the required properties.

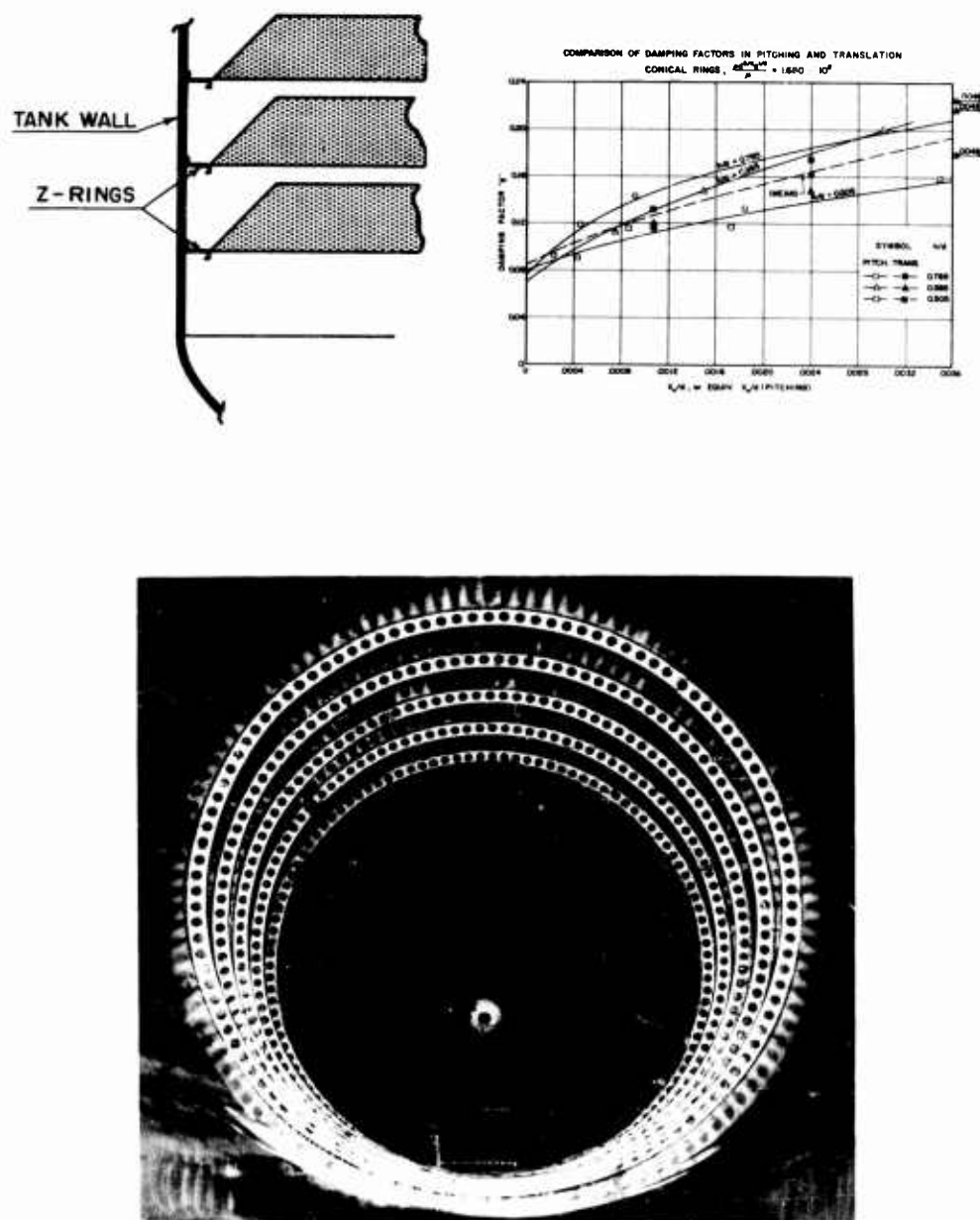


FIGURE 6. CONICAL RING TYPE BAFFLES FOR SUPPRESSION OF NORMAL SLOSHING SHOWING BAFFLES MOUNTED IN MODEL TANK AND DAMPING FACTOR AS A FUNCTION OF EXCITATION AMPLITUDE

such as these conical rings, which are fixed in position in the tank, the amount of damping is also a function of the liquid depth, while for other types of devices (which may float on the liquid surface, for example) the effects of liquid depth are relatively unimportant.

The integration of this knowledge into the problem of analysis of the overall dynamic behavior of the complete vehicle system is, however, still a formidable task.

#### EQUIVALENT MECHANICAL MODEL REPRESENTATION FOR NORMAL SLOSHING

For purposes of vehicle dynamic analyses it is desirable to be able to represent the effects of the sloshing liquid, at least as regards the force and moment that the liquid transmits to the tank, in as simple a manner as possible because of the great complexity of the overall system. One valuable technique for accomplishing this is to represent the dynamic effects of the sloshing liquid by an equivalent mechanical model composed of sets of simple spring-mass-dashpot elements. This (mathematical) model can then be combined with similar representations for other dynamic elements of the vehicle and thus the overall system dynamic behavior can be analyzed by digital or analog techniques.

Several different types of such equivalent mechanical systems have been proposed (2) employing various arrangements of spring-mass or pendulum elements. Figure 7 shows an arrangement involving a single fixed rigid mass and a series of spring-mass-dashpot elements located at varying distances from the liquid center of gravity (12). This system is based on derived equations for small damping with the assumption that the parameters of the equivalent mechanical system are frequency independent and are the same as those for zero damping, which then renders the height of each of the spring-mass-dashpot elements also independent of frequency. This implies that when large damping is present the only substantial change in the characteristics of the system is in the damping coefficient. The height location of each of the spring-mass elements does, however, depend upon the liquid depth being represented. Figure 8 shows the height of the spring-mass elements corresponding to the first two liquid natural resonant modes ( $n = 1, 2$ ) as functions of liquid depth. In order to insure that only one mechanical model is required for both translational and pitching tank motions, it is necessary to establish a basis for determining equivalent excitation amplitudes in translation and pitching at which damping factors may





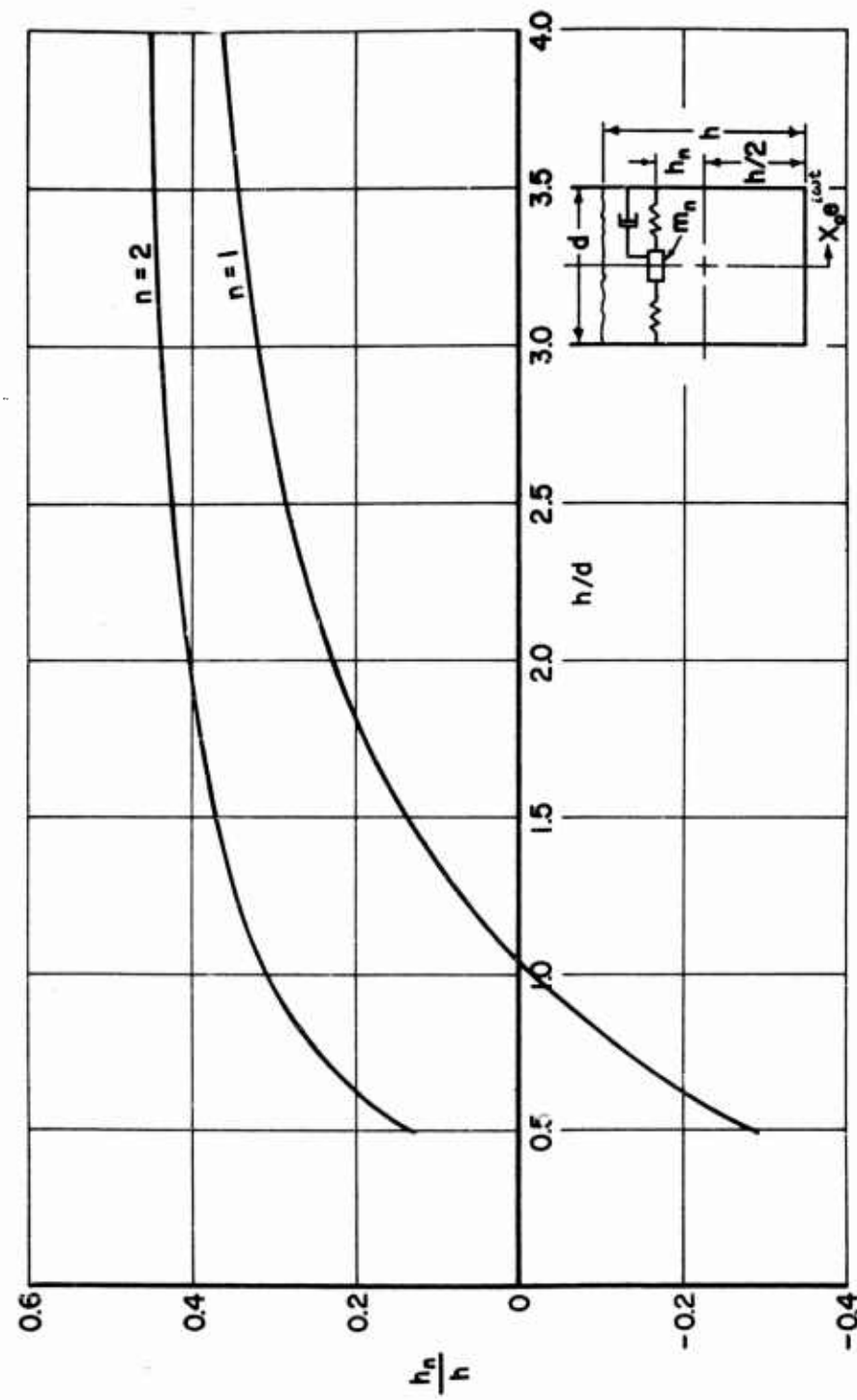


FIGURE 8. LOCATION OF SPRING-MASS-DASHPOT ELEMENTS IN THE EQUIVALENT MECHANICAL SYSTEM

be correlated. Figure 9 shows the variation of the pitching amplitude required to displace the  $n = 1$  mass by an equivalent translational displacement, where  $h_1/h$  is obtained from Figure 8. Experimentally determined damping factor data for both translation and pitching can then be presented as in Figure 6 for use with the equivalent mechanical system. Comparisons of total force response in tanks with conical ring baffles calculated by such a mechanical model and measured directly showed very good agreement in both amplitude and phase (12).

### NORMAL SLOSHING AND VEHICLE DYNAMICS

Generally speaking, it is clear that large rockets must be studied as elastic systems rather than as rigid bodies, primarily because of the stringent requirements for light weight and strength with the consequent sacrifice in stiffness. And, of course, all large rockets also involve another important dynamical element, the control system. Normal sloshing of liquid propellants interacts with both the control system dynamics and the flexible body dynamics, and the latter two elements interact between themselves, thus greatly complicating the problem of evaluation of the overall vehicle dynamics, including stability and control.

The normal sloshing frequencies are often closer to the rigid body control frequencies than to the flexible body frequencies and therefore might ordinarily be expected to be the more important; fortunately adequate damping can be introduced into the liquid system, as discussed earlier, or the tank design can be modified by compartmentation into sectors or concentric rings(3), or clustering, so as to increase the sloshing frequencies. Interaction between the elastic structure and the control system, with the consequent risk of dynamic instability, then becomes of more importance because of the difficulty of providing adequate damping(1).

The question of modifying tank design so as to raise the sloshing frequencies is an interesting one. In the case of compartmented(3) tanks (by sectors or concentric rings, e. g. ), not only are the frequencies increased but phasing of the liquid motions in the different compartments may also result in lower total force and moment responses. Frequencies are also increased in the case of clustered tank configurations (over that for a single tank of the same capacity), but additional complications are introduced in two ways: first, coupling in roll, pitch, and yaw may be produced by the liquid sloshing induced by axial accelerations in the tanks located at some distance from the axial centerline of the vehicle and, second, a new

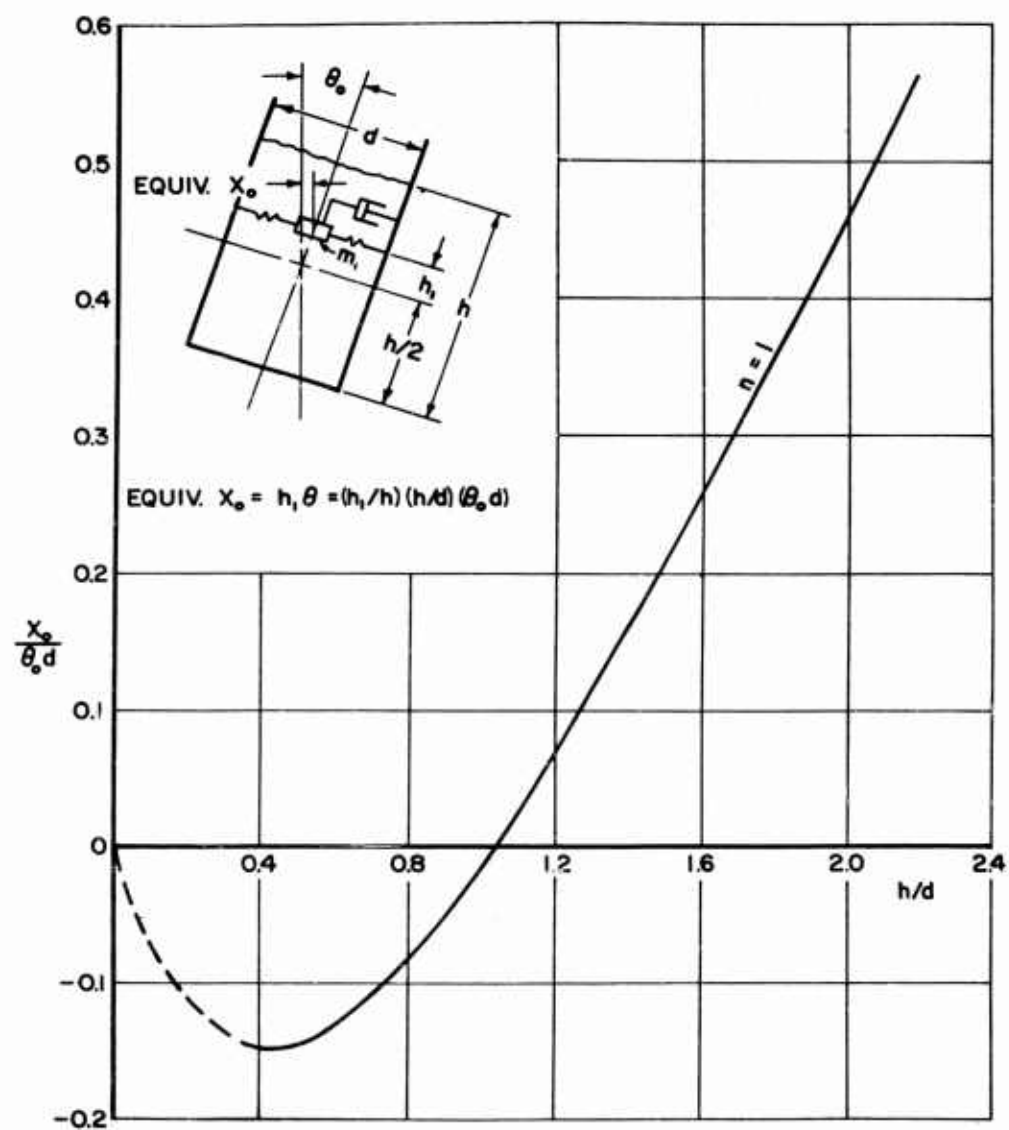


FIGURE 9. EQUIVALENCE OF TRANSLATION AND PITCHING AMPLITUDES IN THE MECHANICAL SYSTEM

low-frequency sloshing mode may be present as a result of the exchange of liquid between the interconnected tanks. \*

The problem of the dynamic interaction between liquid motions and elastic deformations of the walls of the tank or container is of fundamental interest and importance with respect to several different types of questions. For example, there is the problem of bending oscillations in long tubes containing static or flowing liquids as is encountered in many piping systems, the effect of nonrigid walls on the transmission of acoustic or pressure pulses in liquids or gases in long tubes, and also there is the effect of a free surface on the overall response of a liquid-tank system, as will be considered here. The presence of the free surface results in additional liquid sloshing modes that would not be present were the liquid restrained or "capped" (by a movable lid, for example) so as to remain in a plane normal to the tank wall. These additional sloshing modes will affect the total response of the structure, and hence the overall dynamics of the vehicle, so that a determination of the magnitude of these effects becomes important.

Three of the more fundamental and important types of tank vibrations that may occur are torsional, beam bending, and breathing. Unless viscous forces are exceedingly important, because of the particular liquid involved, or unless the tank has a noncircular cross section, the torsional vibration modes will be largely unaffected by the presence of liquid. Bending vibrations of tanks may be excited over a wide range of frequencies and therefore forced bending vibrations at very low frequencies may very well be expected to interact with the normal sloshing modes of the liquid (13, 14). Breathing vibrations are largely influenced by the resistance of the structure to circumferential expansion, both elastically and inertially; internal pressurization is important for the higher modes of breathing vibration (15).

The effect of forced low-frequency bending of the tank wall on the resulting liquid oscillations is similar to that of the translation of a rigid tank, except that the total force and moment produced by the liquid sloshing are generally less for a given maximum bending amplitude than for a translational motion of the same magnitude (13). The maximum dynamic effects are produced when the liquid free surface is coincident with the point of maximum bending

---

\* This sloshing mode may be fairly heavily damped, however, if the interconnecting lines are small.

displacement. At higher bending frequencies, in the neighborhood of the fundamental bending frequency of the liquid filled tank, the effect of the liquid free surface is to increase the resonant bending frequency relative to that which would occur if the free surface were not present, i. e., if the sloshing modes were completely suppressed. The determination of this coupled liquid-tank bending frequency is most significant with respect to dynamic stresses produced in the tank walls. The effect of the free surface has been estimated to increase the coupled bending frequency of a cantilever tank, with a liquid depth equal to one diameter, by 5% while the increase in frequency for a free-free tank of the same liquid depth-diameter ratio is 27%(14). Normal sloshing therefore has a considerable effect on shifting the resonant bending frequency of partially filled tanks and thus has important consequences with regard to any study of vehicle stability and control.

#### LIQUID ROTATION AND VORTEXING

Liquid propellant behavior that involves rotational type motions about the tank longitudinal axis are of special interest because of the torque exerted on the tank, changes in inertial distributions, and reductions in flow rate during tank draining as a result of vortex formation. One interesting motion of this general type can be observed during translational excitation of a partially filled tank at frequencies near resonances of the free surface motions of the liquid (normal sloshing) and can best be described simply as an apparent "rotation" of the liquid about the vertical axis of symmetry of the tank, superimposed on the normal sloshing motion(8, 9). The motion is even more complicated as a type of "beating" also seems to exist: the first mode normal sloshing first begins to transform itself into a rotational motion increasing in angular velocity in (say) the counter-clockwise direction, which reaches a maximum and then decreases essentially to zero and then reverses and increases in angular velocity in the clockwise direction, and so on alternately. The frequency of rotation is less than that of the surface wave motion and therefore the liquid appears to undergo a vertical up and down motion as it rotates about the tank axis; the rotational frequency about this up and down axis is about the same as that of the wave motion. The liquid free surface, at least at relatively low excitation amplitudes, is essentially plane and it is the apparent rotation of this inclined plane about a vertical axis that we are attempting to describe. This phenomenon almost invariably occurs in laboratory tests at frequencies in the immediate neighborhood of one of the resonances of the normal sloshing modes, as mentioned above, and occurs whether the liquid has any initial gross rotation or not; the rotational mode can,

however, be initiated at any excitation frequency by introducing some disturbance which provides a substantial initial rotation to the fluid. The phenomenon is obviously quite complex and certainly involves essential nonlinear effects. Some effort at providing an analytical description of this motion has been made on the basis of the behavior of an equivalent conical pendulum (8). Although the theory is linear and does not consider the apparent reversal of direction of rotation it does demonstrate the general features of the motion in the neighborhood of the normal sloshing resonances.

It may be noted that this type of liquid motion, i. e., rotational motion excited by translational excitation of the tank, is however not of great importance in most practical applications. This is so because of the fact that suppression devices or baffles are almost universally employed in actual liquid propellant tanks to suppress normal sloshing, and these same devices are equally effective in suppressing the liquid rotational motions. In particular, it has been found that the conical ring baffles described earlier (Fig. 6), which are very effective for suppression of normal sloshing, appear to eliminate the rotational motions completely (9). Perforated vertical baffles, mounted normal to the direction of the translational motion, decrease the amplitude of normal sloshing by some 50% - 70% and also completely eliminate rotational motions; when mounted parallel to the direction of translation, such vertical baffles have no effect on normal sloshing but again completely eliminate the rotational motion.

Another interesting and not completely unrelated problem concerns vortex formation as a result of draining of liquid from the tank (Fig. 10). Vortexing is undesirable, of course, because of the consequent reduction in flow rate by reduction of the effective cross-sectional area of the drain outlet and because of deterioration of pumping efficiency as a result of entrained gas and vapor, particularly near burn-out where flow conditions may be quite critical. The formation of a vortex during tank draining is very dependent upon the degree of initial rotation of the liquid and the liquid depth; thus, neglecting other considerations, rotational modes induced by normal sloshing near a resonance, as discussed above, would tend to reinforce and encourage strong vortex formation. Fortunately, a number of factors are present to assist in the prevention of vortex formation: first, sloshing itself tends to break up the vortex as it forms; second, the growth of the rotational motion is largely suppressed by conventional baffling employed for normal sloshing; and third, it is relatively simple to provide small but effective antivortexing baffles at or near the drain outlet which break up the vortex and prevent it from extending into the outlet (9).

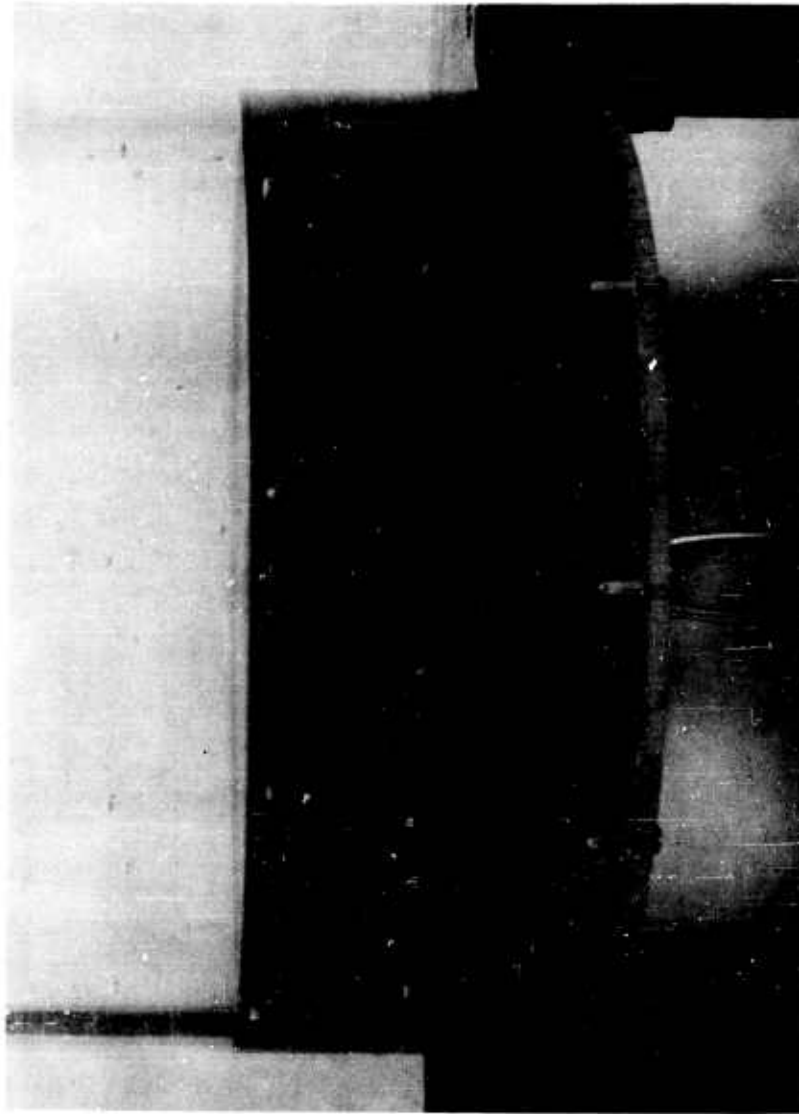


FIGURE 10. VORTEX FORMED DURING STEADY DRAINING FROM A  
CYLINDRICAL TANK

Other interesting rotational type motions of the liquid occur when the tank itself rotates about its longitudinal axis with some prescribed angular velocity (16-18). Free surface oscillations (sloshing) of a liquid in a vertical and rotating circular cylinder have been investigated analytically (16) with the interesting result that new resonant frequencies are found that have no counterpart in the nonrotating tank case, which obviously could have importance with regard to stability characteristics of spin-stabilized vehicles. In fact, it has been noted that instabilities do occur with such spinning vehicles, resonance between the fundamental mode of motion of the liquid and natural nutational frequency of the vehicle apparently being the principal cause of instability (17). Another related aspect of the problem of rotating liquid-tank systems is the role of centripetal acceleration, as compared with the effect of axial acceleration (gravity) for normal sloshing in the nonrotating tank (18).

Some analytical consideration has also been given to the influence of liquid propellants on the behavior of a vehicle undergoing rolling oscillations (19). It appears that the participation of the liquid in the rolling motion is strongly dependent upon the roll frequency; the effective moment of inertia of the liquid decreases with increasing roll frequency while the damping (viscous forces between liquid and tank wall only) increases with increasing roll frequency.

It should be emphasized that these problems involving tank rotation have only been subject to analytical examination and, at best, to only very limited laboratory studies designed to confirm the theoretical results. Thus, there is little or no information available as to the practical consequences of these types of liquid motions or as to the effectiveness of the baffles or other suppression devices.

#### LIQUID BEHAVIOR RESULTING FROM AXIAL EXCITATION

In addition to the liquid dynamic behavior resulting from translational, pitching, and rolling motions of tanks, as discussed so far in this paper, it is of interest also to observe liquid dynamic behavior resulting from tank excitation or vibration in the longitudinal direction (20). At relatively low vibration frequencies (less than 10 cps, say) a large amplitude surface wave can be generated, as shown in the double exposure photograph of Figure 11, with the interesting property that the surface wave frequency is just one-half of the exciting frequency. This type of "sub-harmonic" response is well-known in nonlinear mechanical and electrical systems and therefore this liquid dynamic problem has been studied by analogy with the



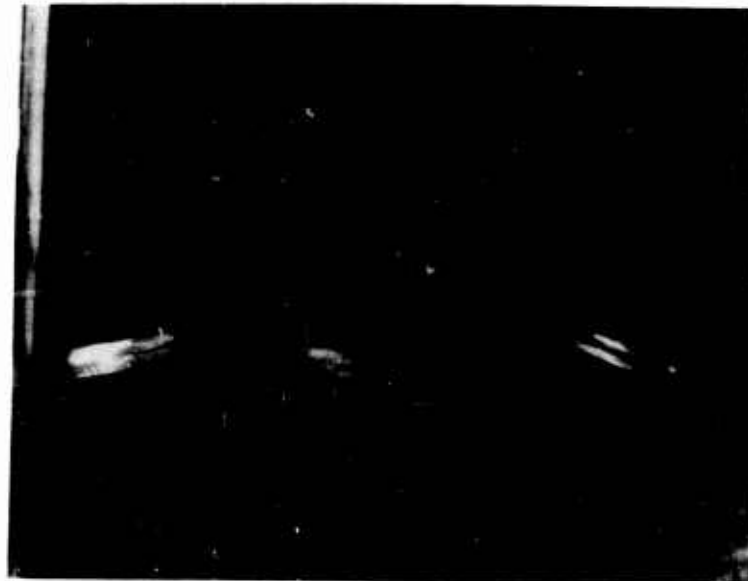


FIGURE 11. FREE SURFACE LARGE AMPLITUDE WAVE  
PRODUCED BY LOW FREQUENCY AXIAL VIBRATION OF  
TANK (PHOTO COURTESY DR. M. I. YARYMOVYCH)

large amplitude oscillations of a simple pendulum with a vertically oscillating support. When the tank is subjected to vertical (axial) vibrations at much higher frequencies, it is found that the surface wave response is still of very low frequency (and thus a very low order sub-harmonic) but of essentially different nature. In this case, the free surface is characterized by the formation of a spray, as shown in Figure 12, which occurs as the result of an instability of very small ripples (capillary waves) that form on the liquid free surface under these conditions.

The axial vibrations of a partially filled tank also raise interesting questions concerning the elastic response of the side walls and the impulsive pressures imposed on the bottom(21). It is found that the elasticity of the bottom is quite important and must be considered in the dynamic response analysis of the upper portion of the tank.

Another interesting phenomenon that occurs during axial vibration of a liquid filled tank involves the motion of small gas bubbles(22). These bubbles are formed in the liquid near the bottom of the tank as a result of the surface disturbances but, contrary to normal expectation, do not rise to the liquid surface but remain at or near the bottom. At certain frequencies of excitation the bubbles tend to cluster together in certain regions.

## LIQUID IMPACT

Certain flight profiles or engine restarts from coasting or orbital flight may result in a reversal in the direction of net acceleration; in such cases the liquid may undergo large displacement motions and, in fact, may move from one end of the tank to the other and thus impact upon the opposing tank bulkhead. Once again, mathematical analysis is virtually impossible because of the complexity of the liquid motions and therefore recourse is made to dynamically similar laboratory experiments(23) in which both the model liquid and the acceleration-time history must be properly scaled. High speed motion picture films (Fig. 13) of such dynamically scaled models show that as the net acceleration reverses the liquid first flows away from the free surface along the side walls (Fig. 13c); this is followed by a breaking up of the free surface into streamers or jets which progress rapidly down the tank (Fig. 13d) and are followed closely by the remaining bulk of the liquid (Fig. 13e); finally, the entire flow becomes very confused as the front running portions and streamers of liquid begin to rebound from the impacted end of the tank (Fig. 13f).

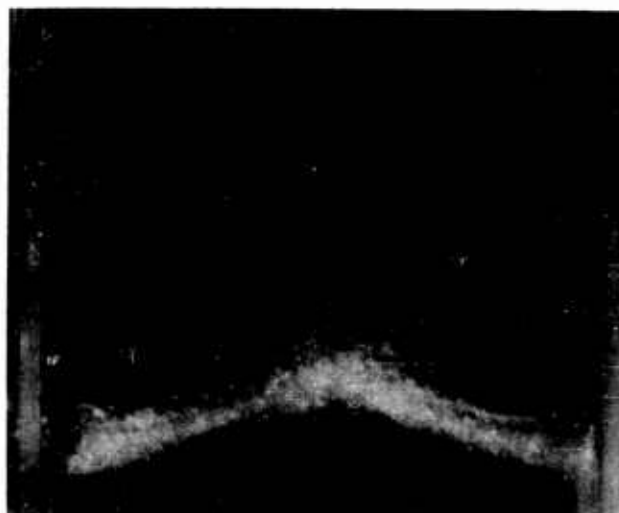
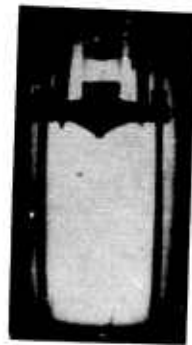


FIGURE 12. FORMATION OF SPRAY FROM THE FREE SURFACE  
PRODUCED BY HIGH FREQUENCY AXIAL VIBRATION OF  
TANK (PHOTO COURTESY DR. M. I. YARYMOVYCH)

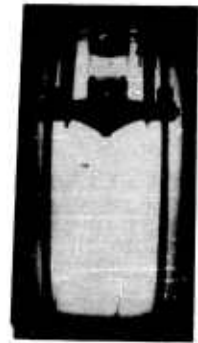
Abramson



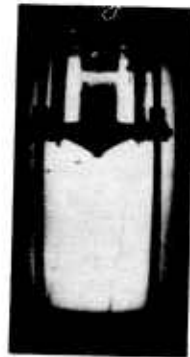
(a)



(b)



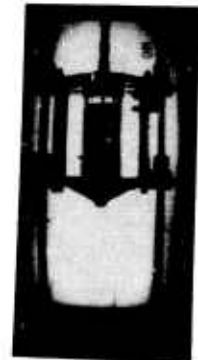
(c)



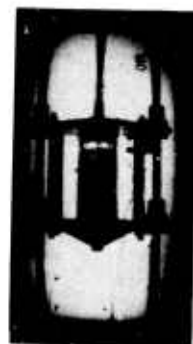
(d)



(e)



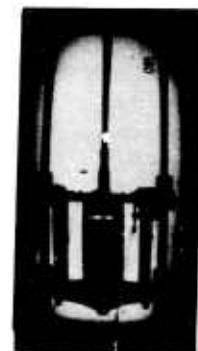
(f)



(g)



(h)



(i)

FIGURE 13. SEQUENCE OF FRAMES FROM HIGH-SPEED MOTION  
PICTURE FILM ON LIQUID IMPACT (LIQUID MOVES  
UPWARD IN THESE PHOTOS)

Measurements of the impact pressures indicate that they are approximately proportional to (net) acceleration but vary considerably according to the shape of the impacted bulkhead. Almost any type of fixed baffling, or even small tank ring stiffeners, are effective in reducing the impact pressures.

In the case of engine restarts from coasting or orbital flight the problem is further complicated by the initial state of the liquid; this is governed by the reduced or zero gravity conditions, as discussed in the following section.

### LIQUID BEHAVIOR AT REDUCED GRAVITY

The behavior of liquids under conditions of reduced or zero gravity offers an entirely new host of phenomena of great interest. Foremost among these is that, during near zero gravity conditions, wetting liquids (conventional fuel, water, etc.) will tend to flow along the tank walls, while nonwetting liquids (such as mercury, e. g.) will tend to globulate and float free (Fig. 14) inside of the tank (24, 25). These two types of stable configuration for liquids in a zero G field have also been predicted theoretically (26). This configurational change forms the basis for almost all other problems engendered by the reduced gravity environment.

A dimensional and order-of-magnitude analysis (27) leads to a number of interesting results. The first of these is that the viscous forces are negligible in comparison with surface tension forces, because of the low velocities of liquid motion involved, so that the governing dimensionless parameter becomes  $\sigma/\rho ad^2$ , where  $\sigma$  is the surface tension. This then indicates that capillary phenomena are governing and (for typical liquids in a small tank) an acceleration of something less than  $10^{-4}G$  is required before essential configurational changes can occur! Second, the time for the configurational change to take place is governed by the relation

$$t \cong \sqrt{\rho d^3/\sigma}$$

which (for typical liquids in a small tank, again) leads to values on the order of twenty seconds! Thus it is seen that any attempt to undertake experimental work must be made with the realization that two rather stringent requirements must be met: a virtually zero G field and a relatively long test time. These considerations now lead directly to the question of experimental techniques and facilities.

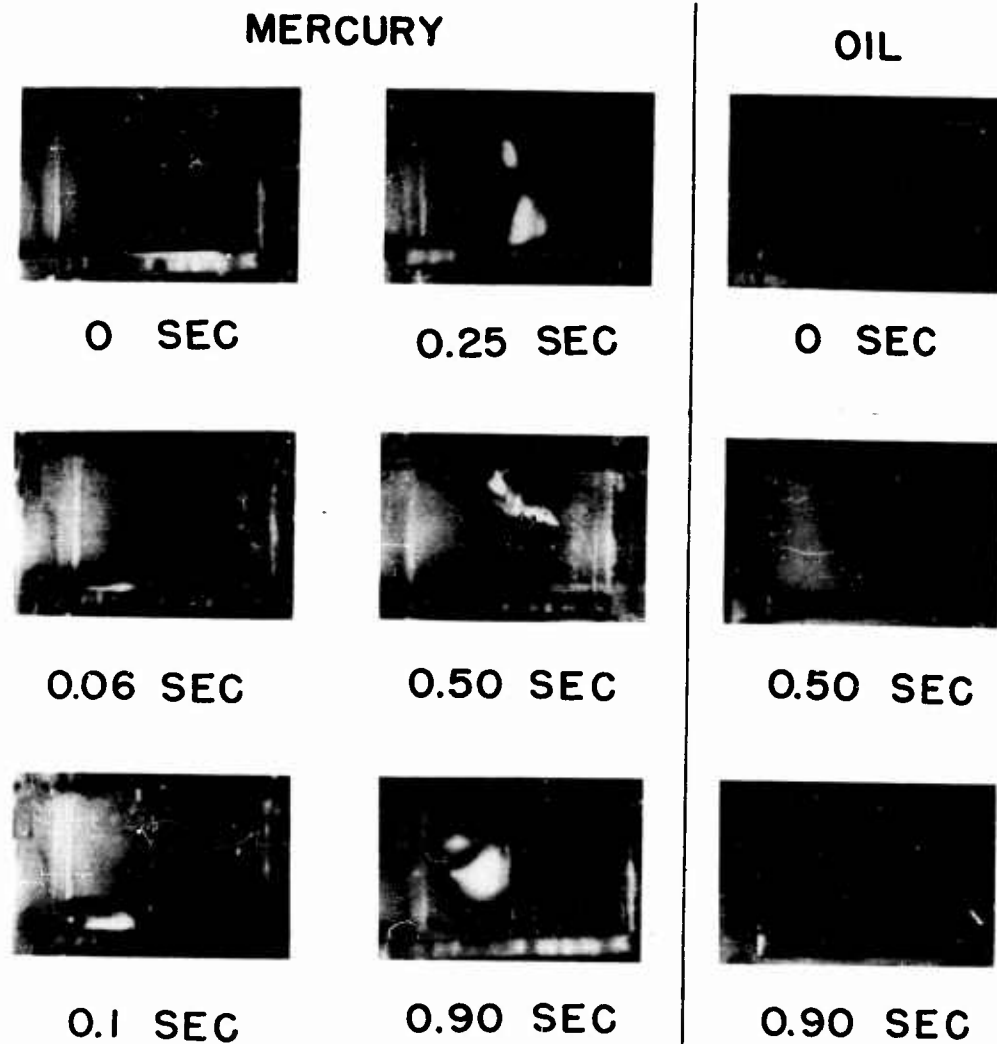


FIGURE 14. LIQUID BEHAVIOR IN FREE FALL (PHOTO COURTESY  
PROF. W. C. REYNOLDS AND THE IAS)

A zero G field can be produced, at present, only by free fall (drop test) or by vehicle flight along a specific trajectory (airplane, missile, or satellite). In order to provide adequate instrumentation and controlled conditions, free fall experiments in a laboratory (24) appear quite attractive, and by careful design of the test capsule it is possible to achieve accelerations at least as low as  $10^{-2}$  or  $10^{-3}G$ . However, it must be noted that the test time is proportional to the square root of the drop height so that it is exceedingly difficult to obtain sufficiently long test durations. Some advantage may be gained by imparting a slight negative acceleration to the test liquid just at the instant of dropping. Aircraft flights have been used relatively successfully as a means of obtaining test periods of the order of 45 seconds (25); however, this is still too brief a time for any degree of sophisticated experimentation and is relatively expensive; missile and satellite flights offer long test times, but only at extreme cost and with attendant difficulties in installation and recovery of appropriate instrumentation.

Consider now some of the problems that may be of concern with relation to liquid behavior in a reduced gravity field, all of which arise from the configurational changes. For example, the problem of restarting an engine from coasting or orbital flight raises the question of how to move the liquid, which may be located arbitrarily within the tank, to the proper location for pumping into the engine. Ways of accomplishing this might involve such techniques as briefly applying low-level thrust by compressed gas or solid propellants, or such devices as expulsion pistons or bladders. The first of these gives rise to the related problem of liquid impact as the tank bulkhead encounters the liquid mass, while the other two give rise to mechanical problems. Expulsion bladders may offer even other problems because many of the liquid propellants of primary concern are cryogenic and thus the bladder materials must retain their flexibility at extremely low temperatures. In fact, fluid transfer in a zero G field, in general, is a potential problem because similar situations exist with respect to all pumps and pressurization devices employed within the vehicle for accomplishing such transfers. Further, cryogenic liquids impose additional problems in that conventional means of venting cannot be employed because an excessive amount of liquid, rather than vapor, may be lost.

The behavior of boiling liquids and problems of heat transfer are also of considerable interest under low gravity conditions. When heat transfer in a liquid is so great that vaporization (boiling) takes place in a system under normal conditions, the vapor will rise to the liquid free surface in the form of bubbles. Under zero G conditions, however, this vapor will not rise but will remain near the

heat transfer surface as a vapor front, because of the absence of natural convection. This vapor front may then serve as an insulation region and thus govern heat dissipation from the heating surface(25). Again, some time is required in these heat transfer problems before equilibrium is attained. For example, Figure 15 shows pool boiling from the bottom of a cylindrical tank during free fall(28). At the beginning of free fall the bubbles continue to move upward through the liquid as in normal boiling, but then remain suspended in the liquid as the free fall continues and increasing quantities of vapor become entrained within the liquid. Clearly, a much more desirable experiment, and one which might reveal more important data on the fundamental heat transfer mechanisms at zero G, would be one in which the heat to the fluid is applied only after zero G conditions have prevailed for some time; unfortunately, sufficiently long test times for such an experiment are not yet available.

#### ACKNOWLEDGEMENTS

The author is grateful for this opportunity to express his indebtedness to his colleagues at SwRI who have contributed so effectively to our research programs on liquid dynamic behavior over the past few years, and to the former Army Ballistic Missile Agency, and now NASA, for continued sponsorship of our work.



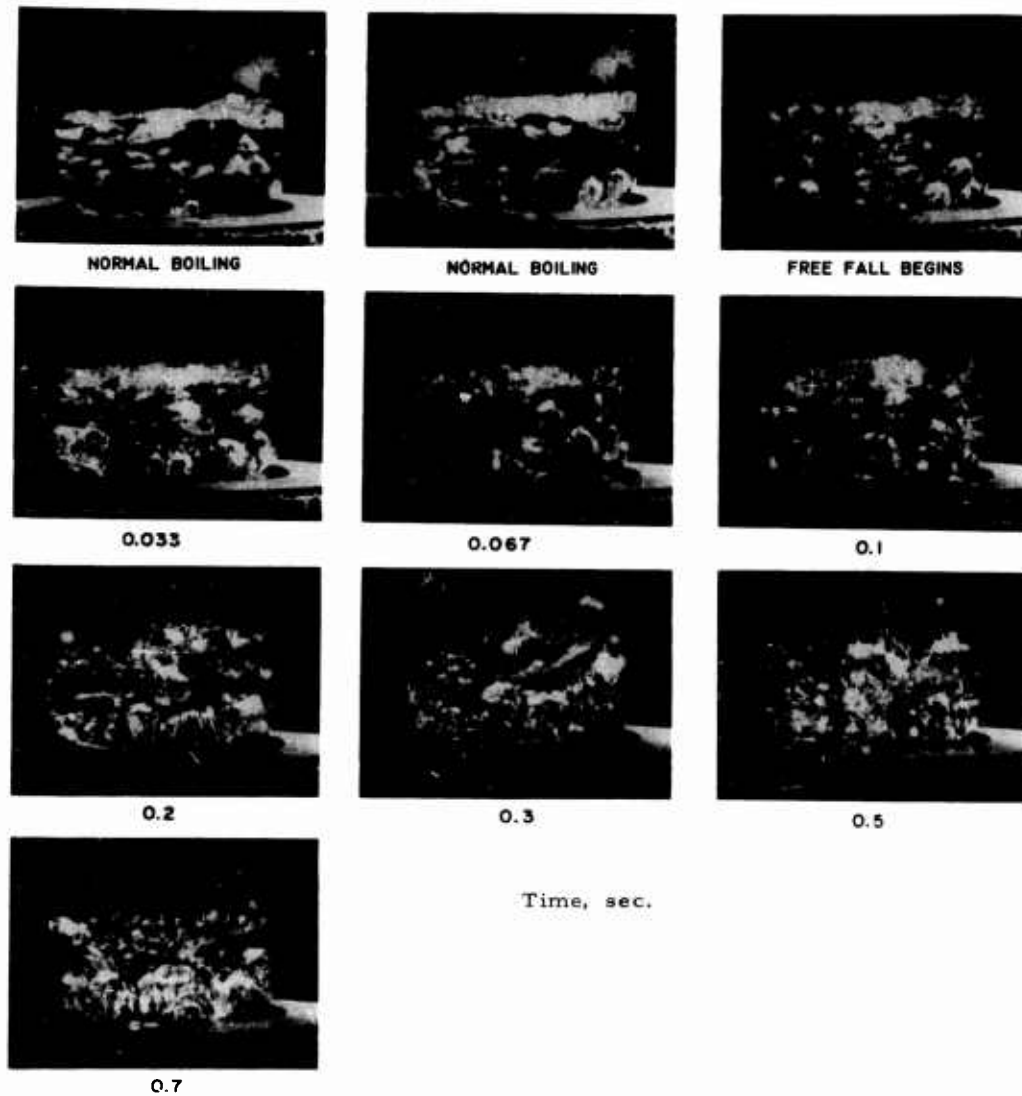


FIGURE 15. POOL BOILING DURING FREE FALL  
(PHOTO COURTESY NASA)

REFERENCES

1. Geissler, E. D., "Problems of Attitude Stabilization of Large Guided Missiles," Aero/Space Engineering, 19, pp 24-29, 68-71, October 1960.
2. Cooper, R. M., "Dynamics of Liquids in Moving Containers," ARS Journal, 30, 8, pp 725-729, August 1960.
3. Bauer, H., "Theory of the Fluid Oscillations in a Circular Cylindrical Ring Tank Partially Filled With Liquid," NASA Tech. Note D-557, December 1960.
4. Lawrence, H. R., Wang, C. J., and Reddy, R. B., "Variational Solutions of Fuel Sloshing Modes," Jet Propulsion, 28, pp 729-736, November 1958.
5. Budiansky, B., "Sloshing of Liquids in Circular Canals and Spherical Tanks," Jour. Aero/Space Sciences, 27, 3, pp 161-173, March 1960.
6. Abramson, H. N. and Ransleben, G. E., Jr., "Some Comparisons of Sloshing Behavior in Cylindrical Tanks with Flat and Conical Bottoms," ARS Journal, to appear April 1961.
7. Abramson, H. N. and Ransleben, G. E., Jr., "A Note on Wall Pressure Distributions During Sloshing in Rigid Tanks," ARS Journal, to appear April 1961.
8. Berlot, R. R., "Production of Rotation in a Confined Liquid Through Translational Motions of the Boundaries," Jour. App. Mechs. (Trans. ASME, Ser. E), 26, 4, pp 513-516, December 1959, (also, discussion by Ransleben and Abramson, same source, p 365, June 1960).
9. Abramson, H. N., Chu, W. H., Garza, L. R., and Ransleben, G. E., Jr., "Some Studies of Liquid Rotation and Vortexing in Rocket Propellant Tanks," Tech. Rept. No. 1, NASA Contract NASw-146, Southwest Research Institute, December 1960.
10. Abramson, H. N. and Ransleben, G. E., Jr., "Simulation of Fuel Sloshing Characteristics in Missile Tanks by Use of Small Models," ARS Journal, 30, 7, pp 603-612, July 1960.

Abramson

11. Sandorff, P. E., "Principles of Design of Dynamically Similar Models for Large Propellant Tanks," NASA Tech. Note D-99, January 1960.
12. Abramson, H. N., Chu, W. H., and Ransleben, G. E., Jr., "Representation of Fuel Sloshing in Cylindrical Tanks by an Equivalent Mechanical Model," Tech. Rept. No. 8, Contract DA-23-072-ORD-1251, Southwest Research Institute, June 1960.
13. Bauer, H., "Fluid Oscillations in a Circular Cylindrical Tank Due to Bending of the Tank Wall," ABMA Tech. Rept. DA-TR-3158, April 1958.
14. Miles, J. W., "On the Sloshing of Liquid in a Flexible Tank," Jour. Appl. Mechs., 25, pp 277-283, June 1958.
15. Reissner, E., "Notes on Forced and Free Vibrations of Pressurized Cylindrical Shells Which Contain a Heavy Liquid with a Free Surface," STL Rept. AM No. 6-15, GM TR 87, November 1956.
16. Miles, J. W., "Free Surface Oscillations in a Rotating Liquid," Jour. of Physics of Fluids, 2, 3, pp 297-305, May-June 1959.
17. Ash, J. E. and Gunderson, R. M., "Investigation in the Exterior Ballistics of Shell with Nonsolid Fillers," U. S. Air Force, APGC-TR-60-23, March 1960.
18. Knopp, M. and Troesch, B., "Centrifugal Sloshing," STL Memo PA-2297-02/1, July 1959.
19. Reismann, H., "Liquid Propellant Inertia and Damping Due to Airframe Roll," Jet Propulsion, 28, 11, pp 746-747, November 1958.
20. Yarymovych, M. I., "Forced Large Amplitude Surface Waves," D.Sc. Thesis, Columbia University, December 1959.
21. Bleich, H. H., "Longitudinal Forced Vibrations of Cylindrical Fuel Tanks," Jet Propulsion, 26, 2, pp 109-111, February 1956.

22. Bleich, H. H., "Effect of Vibrations on the Motion of Small Gas Bubbles in a Liquid," Jet Propulsion, 26, 11, pp 958-978, November 1956.
23. Epperson, T. B., Brown, R. B. and Abramson, H. N., "Dynamic Loads Resulting from Fuel Motion in Missile Tanks," PROCEEDINGS OF THE FOURTH SYMPOSIUM ON BALLISTIC MISSILE AND SPACE TECHNOLOGY, Vol II, Pergamon Press, New York, 1961.
24. Reynolds, W. C., "Behavior of Liquids in Free Fall," Jour. Aero/Space Sci., 26, 12, pp 847-849, December 1959.
25. Neiner, J. J., "The Effect of Zero Gravity on Fluid Behavior and System Design," WADC Tech. Note. 59-149, AD No. 215428, April 1958.
26. Li, T., "Liquid Behavior in a Zero-G Field," IAS paper 61-20, January 1961.
27. Benedikt, E. T., "Scale of Separation Phenomena in Liquids Under Conditions of Nearly Free Fall," ARS Journal, 29, 2, pp 150-151, February 1959.
28. Siegal, R. and Usiskin, C., "A Photographic Study of Boiling in the Absence of Gravity," Jour. Heat Transfer (Trans. ASME, Ser. C), 81, 3, pp 230-236, August 1959.

## DYNAMICS OF LIQUID PROPELLANT VEHICLES

Helmut F. Bauer  
Marshall Space Flight Center  
Huntsville, Alabama

### ABSTRACT

The paper presents the results of theoretical investigations of the response of the liquid in annular cylindrical tanks and circular quarter-tanks. The equivalent mechanical model which leads the way to the introduction of damping into the theoretical nonviscous results and which is used in the stability analysis of the spacecraft will be described.

The basic requirements for the stability with respect to the location of tanks, their configuration, and control sensor characteristics will be presented.

### INTRODUCTION

The danger of instability resulting from propellant sloshing for rigid or elastic spacecrafts is well known. While the exact treatment of these phenomena, especially in the latter case, leads to rather unwieldy equations, very useful general results can be obtained from a simplified stability investigation. The elastic behavior of the structure of the craft influences the stability, especially if its lowest bending frequency is close to the sloshing and control frequency. A parametric study investigates the possibility of eliminating instabilities due to propellant sloshing in the tanks of a space vehicle by proper choice of the tank form, tank location, gain values of the control system, and by proper choice of the vibrational characteristics of additional control sensors (accelerometer). Finally, as a last resort, the amount of damping necessary in the tanks to maintain stability is indicated. The stability boundary was determined in terms of the amount of damping of the propellant in the tank required for various tank locations along the vehicle.

For simplification in the treatment of the equations of motion of space vehicles, an equivalent mechanical model which describes the motion of the propellant in the tanks is derived. This model consists of masses, springs, and dampers, and a massless disc with a moment of inertia and is chosen such that it exerts the same forces and moments and has the same natural frequencies as the propellant in the containers. The motion of this mechanical model, however, must fall into the scope of linearization processes as used in the derivation of the fluid dynamics analysis. The results of the ideal fluid dynamics analysis are only applicable for frequencies which are not too close to one of the natural frequencies of the liquid. Therefore, damping has to be introduced to obtain values at or near resonances. Especially around the lower resonances very high values may occur which can be dangerous to the stability behavior of a vehicle. The introduction of damping is performed in the equivalent mechanical model in form of velocity proportional damping forces. The results of the theoretical fluid dynamics investigations are then transformed into forms as represented in the mechanical model. In the resonance terms an imaginary value is introduced and the damping factor is obtained by experiments.

For pitching oscillation of the tank, the moment of the liquid has an additional damping term besides the resonance terms. This is due to the fact that only part of the liquid is participating in the rotation, as can be seen if the free fluid surface is considered solidified.

# I. FLUID DYNAMICS THEORY AND MECHANICAL MODEL

To determine the response of the liquid with a free surface in a circular cylindrical tank (of circular annular or quarter circular cross section) with a flat bottom due to forced translational and pitching oscillations, the Laplace equation  $\nabla^2 \Phi = 0$  has to be solved with certain time- and space-wise dependent boundary conditions.

The linearized boundary conditions are:

$$\frac{\partial \Phi}{\partial r} = i\omega (x_0 - \theta_0 z) \cos \varphi e^{i\omega t} \quad \text{at the tank walls } r = a, b$$

$$\frac{\partial \Phi}{\partial z} = 0 \quad \text{at the tank bottom}$$

$$\frac{1}{r} \frac{\partial \Phi}{\partial \varphi} = 0 \quad \text{at the radial wall } \varphi = 0$$

$$\frac{1}{r} \frac{\partial \Phi}{\partial \varphi} = i\omega e^{i\omega t} [\theta_0 z - x_0] \quad \text{at the radial wall } \varphi = \frac{\pi}{2}$$

$$\frac{\partial^2 \Phi}{\partial t^2} + g \frac{\partial \Phi}{\partial z} = 0$$

at the free fluid surface

From the velocity potential  $\Phi$ , the wave form of the free fluid surface, the pressure and velocity distribution in the tank, the fluid force on the tank wall, and the moment of the liquid about the center of gravity of the undisturbed fluid can be obtained.

### 1. Cylindrical Tank with Circular Annular Cross Section

The natural frequencies of the liquid are (Ref. 1 and 2)

$$f_n = \frac{1}{2\pi} \sqrt{\frac{g}{a} \xi_n \tanh \left( \xi_n \frac{h}{a} \right)} \quad n = 1, 2, 3 \dots$$

where the  $\xi_n$  (Table 1) are the roots of

$$\Delta_1(\xi) = \begin{vmatrix} J_1'(\xi) & Y_1'(\xi) \\ J_1'(k\xi) & Y_1'(k\xi) \end{vmatrix}$$

$g$  is the longitudinal acceleration,  $h$  the fluid height and  $a$  the outer tank radius.

The diameter ratio of inner to outer tank is  $k = \frac{b}{a}$ .

$$\text{With } C_1(k\xi) = \begin{vmatrix} J_1'(\xi) & Y_1'(\xi) \\ J_1'(k\xi) & Y_1'(k\xi) \end{vmatrix}$$

$$\text{and } A_n = 2 \frac{\left[ \frac{2}{\pi \xi_n} - k C_1(k\xi) \right]}{\frac{4}{\pi^2 \xi_n^2} (\xi_n^2 - 1) + C_1^2(k\xi_n) (1 - k^2 \xi_n^2)}$$

the fluid forces and moments are:

a. For translational oscillations  $x = x_0 e^{i\omega t}$

$$F_x = m\omega^2 x_0 e^{i\omega t} \left\{ 1 + \sum_{n=1}^{\infty} \frac{\bar{A}_n \omega^2 \tanh \left( \xi_n \frac{h}{a} \right) \left[ \frac{2}{\pi \xi_n} - k C_1(k\xi_n) \right]}{\left( \xi_n \frac{h}{a} \right) (\omega_n^2 - \omega^2) (1 - k^2)} \right\}$$

where the first term in the parenthesis is due to the inertial force.

Table 1  
ROOTS OF THE DETERMINANT  
 $\Delta_1(\xi) = 0$

$\frac{n}{k}$	0	.1	.2	.3	.4	.5	.6	.7	.8	.9
1	1.84	1.80	1.71	1.58	1.46	1.35	1.26	1.18	1.11	1.05
2	5.33	5.14	4.96	5.14	5.66	6.56	8.04	10.59	15.78	31.45
3	8.53	8.20	8.43	9.31	10.68	12.71	15.80	21.00	31.45	62.85
4	11.70	11.36	12.17	13.68	15.85	18.94	23.62	31.46	47.15	94.26
5	14.85	14.63	15.99	18.12	21.05	25.20	31.46	41.92	62.85	125.57



$$M_y = m\omega^2 x_0 e^{i\omega t} a \left[ \frac{1+k^2}{4 \frac{h}{a}} + \sum_{n=0}^{\infty} \frac{\bar{A}_n \left[ \frac{2}{\pi \xi_n} - kC_1(k\xi_n) \right] \omega^2}{2\xi_n (1-k^2) (\omega_n^2 - \omega^2)} \right. \\ \left. \cdot \left[ \tanh \left( \xi_n \frac{h}{a} \right) + \frac{2}{\xi_n \frac{h}{a}} \left( \frac{2}{\cosh \left( \xi_n \frac{h}{a} \right)} - 1 \right) \right] \right]$$

The first term is the moment due to the lateral displacement of the center of gravity for a plane free fluid surface of the form  $r \cos \varphi$ .

b. For pitching oscillations  $\theta = \theta_0 e^{i\omega t}$  (about the center of gravity of the undisturbed liquid),

$$F_x = -mg \theta_0 e^{i\omega t} - 2am\omega \theta_0 e^{i\omega t} \sum_{n=0}^{\infty} \frac{\bar{A}_n \left[ \frac{2}{\pi \xi_n} - kC_1(k\xi_n) \right] \omega^2}{(\omega_n^2 - \omega^2) (1-k^2) \xi_n} \\ \cdot \left[ \left( \frac{g}{a\omega^2} + \frac{1}{2} \right) \tanh \left( \xi_n \frac{h}{a} \right) + \frac{2}{\xi_n \frac{h}{a}} \left( \frac{1}{\cosh \xi_n \frac{h}{a}} - 1 \right) \right]$$

The first term is, in tank-fixed coordinates, the component due to gravitation force.

$$M_y = -mg \theta_0 e^{i\omega t} \frac{a(1+k^2)}{4 \frac{h}{a}} - m\omega^2 \theta_0 e^{i\omega t} a^2 \left\{ \frac{1}{12} \left( \frac{h}{a} \right)^2 - \frac{1}{8} (1+k^2) \right. \\ \left. + \sum_{n=0}^{\infty} \frac{\bar{A}_n \omega^2 \left[ \frac{2}{\pi \xi_n} - kC_1(k\xi_n) \right]}{(\omega_n^2 - \omega^2) (1-k^2) \xi_n} \cdot \left[ \left( \frac{1}{4} \frac{h}{a} - \frac{3g}{2a\omega^2} - \frac{4}{\xi_n^2 2 \frac{h}{a}} \right) \tanh \left( \xi_n \frac{h}{a} \right) \right. \right. \\ \left. \left. + \frac{1}{\xi_n \cosh \left( \xi_n \frac{h}{a} \right)} \cdot \left( 2 - \frac{4g}{a\omega^2} \frac{1}{\frac{h}{a}} + \left( \frac{5g}{a\omega^2} \frac{1}{\left( \xi_n \frac{h}{a} \right)} + \frac{1}{2\xi_n} \right) \right) \right] \right\}$$

The first term is the moment due to the lateral displacement of the center of gravity for a plane free fluid surface, which is obtained for very slow oscillations.

For an inner radius  $b = 0$  ( $k = 0$ )

$$\Delta_1(\xi) = 0 \quad \text{has to be substituted by } J_1'(\epsilon_n) = 0$$

and the zeros  $\xi_n \rightarrow \epsilon_n$

$$\epsilon_1 \approx 1.84$$

$$\epsilon_2 \approx 5.33$$

$$\epsilon_3 \approx 8.53$$

The value  $\bar{A}_n \left[ \frac{2}{\pi \xi_n} - kC_1 (k\xi_n) \right]$  will be substituted by  $\frac{2}{(\epsilon_n^2 - 1)}$ .

Thus the forces and moments of the liquid for a circular cylindrical tank with circular cross section can be obtained.

## 2. Cylindrical Quarter Tank (Ref. 3)

The natural frequencies are

$$f_{nm} = \frac{1}{2\pi} \sqrt{\frac{g}{a} \epsilon_{nm} \tanh \left( \epsilon_{nm} \frac{h}{a} \right)}$$

$$n = 1, 2, 3, \dots$$

$$m = 0, 1, 2, \dots$$

where the  $\epsilon_{nm}$  are roots of  $J'_{2m}(\epsilon_{nm}) = 0$

$$\epsilon_{10} \approx 3.83$$

$$\epsilon_{11} \approx 3.05$$

$$\epsilon_{12} \approx 5.32$$

$$\epsilon_{21} \approx 6.71$$

The fluid forces and moments are:

a. For translational oscillations:

$$F_x = m\omega^2 e^{i\omega t} x_0 \left\{ 1 + \frac{64 \omega^2}{\pi^2} \sum_{n=1}^{\infty} \sum_{m=0}^{\infty} A_{nm} \frac{\tanh \left( \epsilon_{nm} \frac{h}{a} \right)}{\left( \epsilon_{nm} \frac{h}{a} \right)} \left[ \frac{J_{2m}(\epsilon_{nm})}{(4m^2 - 1)} + L_0(\epsilon_{nm}) \right] \right\}$$

The first term is due to the inertial force.

$$\begin{aligned}
M_y = m\omega^2 a x_0 e^{i\omega t} & \left\{ \frac{1}{4} \frac{h}{a} + \frac{32 \omega^2}{\pi^2} \sum_{n=1}^{\infty} \sum_{m=0}^{\infty} B_{nm} \left[ \frac{J_{2m}(\epsilon_{nm})}{(4m^2 - 1)} \right. \right. \\
& + L_0(\epsilon_{nm}) \left. \right] \left[ \tanh\left(\epsilon_{nm} \frac{h}{a}\right) + \frac{2}{\epsilon_{nm} \frac{h}{a}} \left( \frac{1}{\cosh\left(\epsilon_{nm} \frac{h}{a}\right)} - 1 \right) \right] \right. \\
& \left. + \frac{2L_2(\epsilon_{nm}) \epsilon_{nm}^2}{(4m^2 - 1) \epsilon_{nm} \frac{h}{a} \cosh\left(\epsilon_{nm} \frac{h}{a}\right)} \right\} + \frac{4}{3} mga.
\end{aligned}$$

where

$$A_{nm} = \frac{\epsilon_{nm}}{(\omega_{nm}^2 - \omega^2)(\epsilon_{nm}^2 - 4m^2) J_{2m}^2(\epsilon_{nm})} \sum_{\mu=1}^{\infty} \frac{J_{2m+2\mu+1}(\epsilon_{nm})}{(2m+2\mu-1)(2m+2\mu+3)};$$

$$B_{nm} = \frac{A_{nm}}{\epsilon_{nm}};$$

$$L_0(\epsilon_{nm}) = \frac{2}{\epsilon_{nm}} \sum_{\mu=0}^{\infty} J_{2m+2\mu+1}(\epsilon_{nm})$$

$$L_2(\epsilon_{nm}) = \frac{2(4m^2 - 1)}{\epsilon_{nm}} \sum_{\mu=0}^{\infty} \frac{J_{2m+2\mu+1}(\epsilon_{nm})}{(2m+2\mu+1)(2m+2\mu+3)}$$

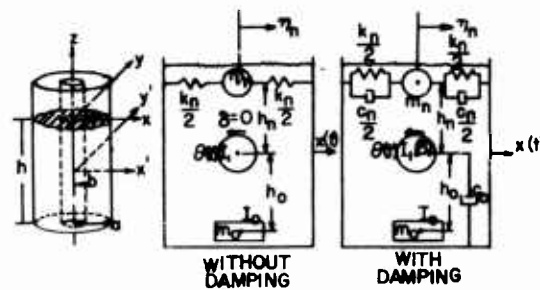
(It may be noted that for  $m = 0$  a factor  $\frac{1}{2}$  has to be included in the A's and B's.)

b. For pitching oscillations similar formulas can be obtained.

## II. THE EQUIVALENT MECHANICAL MODEL

The sloshing mass points  $m_n$  are attached with a spring at a height  $h_n$ , while the fixed mass  $m_0$  has a distance  $h_0$  from the center of gravity of the undisturbed liquid (Fig. 1). The spring constants of the model slosh vibrator are chosen in such a way that the ratio to the sloshing mass represents the square of the natural circular frequency of a liquid mode.

$$\omega_n^2 = \frac{k_n}{m_n} \quad n = 1, 2, 3 \dots \quad (1)$$



COORDINATES AND MODEL

FIG. 1

The mass points have frictionless guidance in the horizontal plane for translational oscillations.

The fluid mass  $m$  is

$$m = m_0 + \sum_{n=1}^{\infty} m_n \quad (2)$$

and since second order terms are neglected, the center of mass law is

$$m_0 h_0 = \sum_{n=1}^{\infty} m_n h_n . \quad (3)$$

Introducing damping forces proportional to velocity in the form of dampers results in

$$c_n = m_n \omega_n \gamma_n \quad (4)$$

where  $\gamma_n$  is a constant damping factor. It is twice the critical damping.

Considering the motion of translation along the  $x$ -axis and rotation about the  $y$ -axis in a space-fixed coordinate system, we obtain the kinetic energy,  $T$ , of the mechanical model:

$$T = \frac{m_0}{2} (\dot{x} + h_0 \dot{\theta})^2 + 1/2 I_0 \dot{\theta}^2 + 1/2 \sum_{n=1}^{\infty} m_n (\dot{x}_n + \dot{x} - h_n \dot{\theta})^2 + 1/2 I_D (\dot{\theta} + \dot{\psi})^2 \quad (5)$$

$\xi_n$  being the coordinate of the mass point  $m_n$  (displacement of  $m_n$  relative to the center line).

The dissipation function  $D$  is

$$D = 1/2 \sum_{n=1}^{\infty} c_n \dot{\xi}_n^2 + 1/2 c_0 \dot{\psi}^2 = 1/2 \sum_{n=1}^{\infty} \omega_n m_n \gamma_n \dot{\xi}_n^2 + 1/2 c_0 \dot{\psi}^2 \quad (5)$$

The potential energy is

$$V = 1/2 g \theta^2 m_0 h_0 - 1/2 g \theta^2 \sum_{n=1}^{\infty} m_n h_n + g \theta \sum_{n=1}^{\infty} m_n \xi_n + 1/2 \sum_{n=1}^{\infty} k_n \xi_n^2 \quad (7)$$

The first term in the kinetic energy is due to the translation and rotation of the fixed mass  $m_0$ ; the second term in the kinetic energy is due to the rotation about the center of gravity of the fixed mass  $m_0$ ; the third term is due to the translation and rotation of the slosh mass points, while the last term is due to the massless disc.

The first term in the potential energy is due to the lifting of the fixed mass  $m_0$  during rotation, the second and third terms represent the same fact for the sloshing mass points, while the last term is the potential energy stored in the springs with stiffness  $k_n$ . In the dissipation function  $D$ , the terms can be identified as the damping of the sloshing masses and the damping of the disc.

The generalized coordinates are here,  $x$ ,  $\theta$ ,  $\psi$ , and  $\xi_n$  and the generalized forces are

$$\begin{aligned} Q_x &= -F_x \\ Q_\theta &= \bar{M}_y \\ Q_{\xi_n} &= 0 \\ Q_\psi &= 0 \end{aligned} \quad (8)$$

With the Lagrange equation

$$\frac{d}{dt} \frac{\partial T}{\partial \dot{q}_i} + \frac{\partial V}{\partial q_i} + \frac{\partial D}{\partial \dot{q}_i} = Q_{q_i} \quad (q_i = x, \theta, \psi, \xi_n) \quad (9)$$

we obtain with Equations 5, 6, and 7

$$m_n (\ddot{x} + \ddot{\xi}_n - h_n \ddot{\theta}) + k_n \xi_n + g \theta m_n + \omega_n m_n \gamma_n \dot{\xi}_n = 0 \quad \text{Slosh Equation} \quad (10)$$

$$m_0 (\ddot{x} - h_0 \ddot{\theta}) + \sum_{n=1}^{\infty} m_n [\ddot{\xi}_n + \ddot{x} - h_n \ddot{\theta}] = -F_x \quad \text{Force Equation} \quad (11)$$

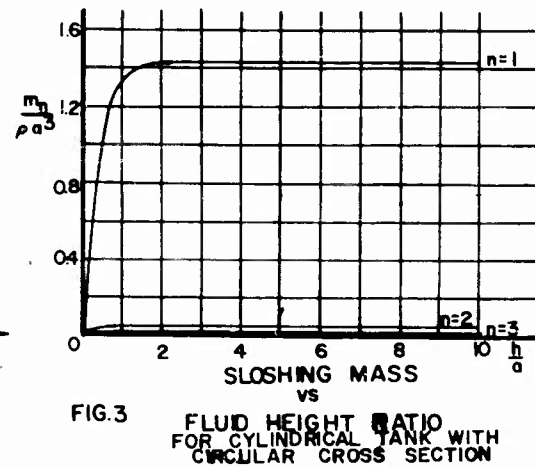
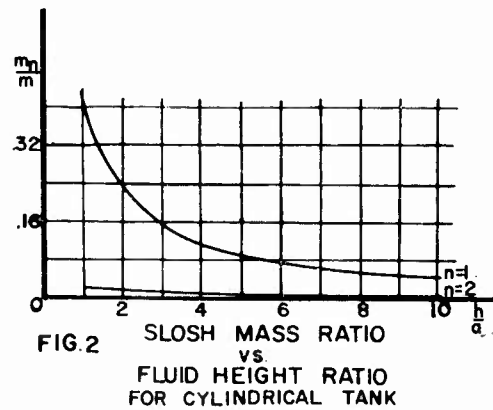
$$I_0 \ddot{\theta} + m_0 h_0 (\ddot{x} + h_0 \ddot{\theta}) + g \sum_{n=1}^{\infty} m_n \xi_n - \sum_{n=1}^{\infty} h_n m_n [\ddot{\xi}_n + \ddot{x} - h_n \ddot{\theta}] + I_D (\ddot{\theta} + \ddot{\psi}) = \ddot{M}_y \quad \text{Moment Equation} \quad (12)$$

$$I_D (\ddot{\theta} + \ddot{\psi}) + c_D \dot{\psi} = 0 \quad \text{Disc Equation} \quad (13)$$

Comparison with the previous fluid dynamics results, which in some cases have to be transformed in a proper form results in the mass ratios and height ratios (Ref. 4).

#### 1. Circular Cylindrical Tank with Circular Cross Section

$$\frac{m_n}{m} = \frac{2 \tanh \left( \epsilon_n \frac{h}{a} \right)}{\epsilon_n \frac{h}{a} (\epsilon_n^2 - 1)} \quad (\text{Fig. 2 and 3}) \quad (14)$$



$$\frac{h_n}{h} = \frac{1}{2} \left[ 1 - \frac{4}{\epsilon_n \frac{h}{a}} \tanh \left( \frac{\epsilon_n}{2} \frac{h}{a} \right) \right] \quad (\text{Fig. 4}) \quad (15)$$

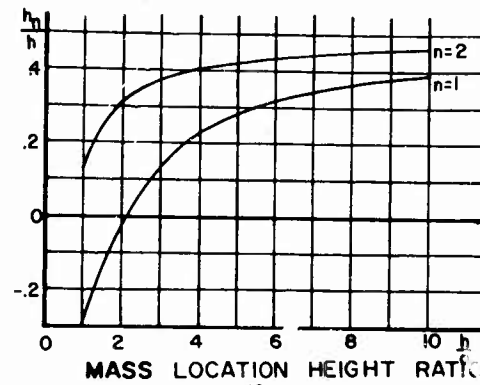


FIG. 4  
FLUID HEIGHT RATIO  
FOR CYLINDRICAL TANK

2. Cylindrical Tank with Annular Cross Section

$$\frac{m_n}{m} = \frac{\bar{A}_n \left[ \frac{2}{\pi \xi_n} - k G_1(k \xi_n) \right] \tanh \left( \xi_n \frac{h}{a} \right)}{(1 - k^2) \left( \xi_n \frac{h}{a} \right)} \quad (\text{Fig. 5 and 6}) \quad (16)$$

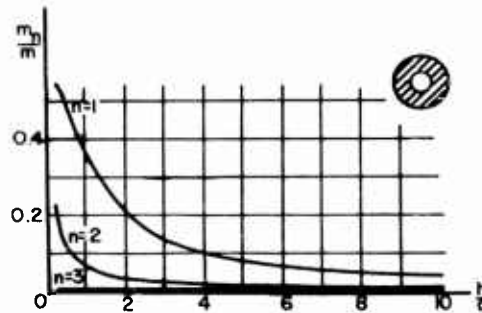


FIG. 5 SLOSH MASS RATIO  
vs.  
FLUID HEIGHT RATIO  
 $K=0.5$

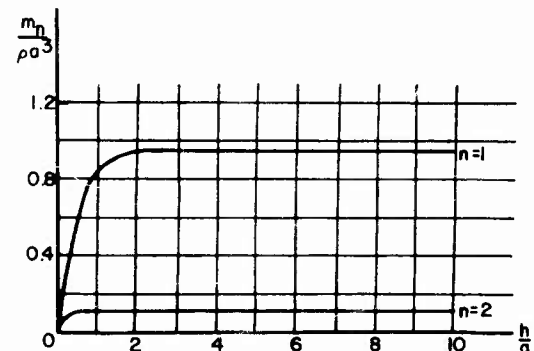


FIG. 6 SLOSHING MASS  
vs.  
FLUID HEIGHT RATIO  
FOR CYLINDRICAL TANK WITH ANNULAR  
CROSS SECTION  
 $K=0.5$

$$\frac{h_n}{h} = \frac{1}{2} \left[ 1 - \frac{4}{\xi_n \frac{h}{a}} \tanh \left( \frac{\xi_n}{2} \frac{h}{a} \right) \right] \quad (\text{Fig. 7}) \quad (17)$$

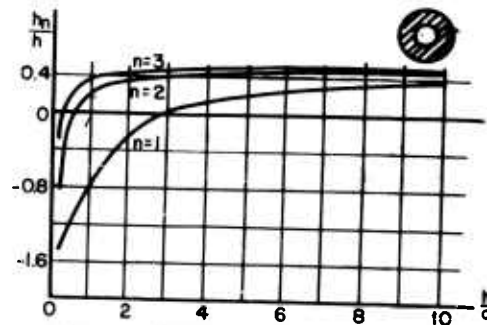


FIG. 7 MASS LOCATION HEIGHT RATIO  
vs.  
FLUID HEIGHT RATIO  
K = 0.5

### 3. Four Quarter Tanks

$$\frac{m_{nm}}{m} = \frac{64 \epsilon_{nm} \tanh \left( \epsilon_{nm} \frac{h}{a} \right)}{\pi^2 (\epsilon_{nm}^2 - 4_m^2) J_{2m}^2 (\epsilon_{nm}) \epsilon_{nm} \frac{h}{a}} \sum_{\mu=0}^{\infty} \frac{J_{2m+2\mu+1} (\epsilon_{nm})}{(2m+2\mu-1)(2m+2\mu+3)}$$

$$\cdot \left\{ \frac{J_{2m} (\epsilon_{nm})}{4_m^2 - 1} + \frac{2}{\epsilon_{nm}} \sum_{\mu=0}^{\infty} J_{2m+2\mu+1} (\epsilon_{nm}) \right\} \quad (\text{Fig. 8 and 9}) \quad (18)$$

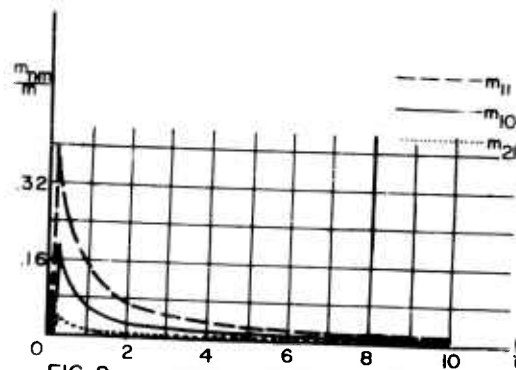


FIG. 8 SLOSH MASS RATIO  
vs.  
FLUID HEIGHT RATIO  
FOR FOUR CYLINDRICAL QUARTER  
TANKS



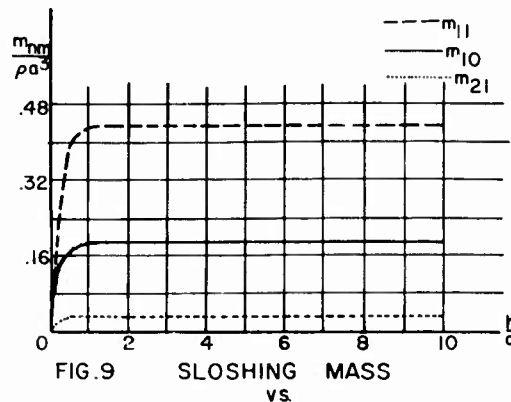


FIG.9 SLOSHING MASS  
vs  
FLUID HEIGHT RATIO  
FOR FOUR CYLINDRICAL QUARTER TANKS

It can be seen that the tank geometry plays an important role in the amount of sloshing mass. For long tanks, i.e., large fineness ratio  $\frac{h}{a}$ , the slosh mass ratio due to the first liquid mode is small while for short tanks a large percentage of the mass is sloshing. This indicates that tanks with small fineness ratios ( $\frac{h}{a} < 3$ ) exhibit considerable liquid motion and, therefore, need to be considered with special care (pressurization). It should be mentioned that the actual sloshing mass has a constant value for decreasing fineness ratio  $\frac{h}{a}$  to about  $h/a \approx 1$ . It furthermore can be concluded that the mass of the second sloshing mode in a circular cylindrical tank is usually smaller than 3% of the sloshing mass of the first mode. The second mode can reach about 8.4% of the first mode only for very low values  $\frac{h}{a} \ll 1$ . In most practical cases, therefore, all higher sloshing modes ( $n > 1$ ) can be neglected. The location of the sloshing mass points is for large fineness ratio close to the free fluid surface and shifts with decreasing fluid height ratio towards the center of gravity of the liquid in the tank. For short tanks ( $\frac{h}{a} \approx 2$ ), the sloshing mass (first mode) is located near the center of gravity of the liquid. For increasing mode number the sloshing mass is approaching the free fluid surface, i.e., the mass points of higher modes are closer to the free liquid surface. With decreasing fineness ratio  $h/a$  the mass points approach the center of gravity of the liquid slowly ( $\frac{h}{a} \approx 1/2$ ). For very small values  $h/a$ , they are located below the center of gravity of the liquid and approach the tank bottom with decreasing fluid height ratio  $h/a$ . The nonsloshing mass can be considered to be located slightly below the center of gravity of the liquid.

The liquid in a circular cylindrical tank with annular cross section exhibits features similar to that in a tank of circular cross

section. The first sloshing mass is decreasing with increasing tank diameter ratio  $k = \frac{b}{a}$  where  $b$  is the inner tank radius and  $a$  the outer tank radius. The sloshing masses of the liquid decrease with increasing mode number, but not as rapidly as in a cylindrical tank with circular cross section. Depending on the tank diameter ratio, values of the second to the first sloshing mass of about 12% can be obtained. With decreasing tank diameter ratio, the location of the first sloshing mass point approaches the free fluid surface. Higher modes show a similar behavior for the location of their slosh masses as in the cylindrical tank with circular cross section. For decreasing fluid height ratio, the first sloshing mass location shifts faster towards the bottom for increasing diameter ratio  $k$ , while the masses of higher slosh modes remain very close to the free liquid surface. The larger the diameter ratio  $k$ , the closer they stay to the free fluid surface. The nonsloshing mass stays very close to the center of gravity of the liquid and exhibits essentially the same behavior as in a tank with circular cross section.

In four quarter tanks the trends are essentially the same except for the fact that the sloshing masses are considerably smaller and that additional modes appear which cannot be neglected any more. The next pronounced sloshing mode is about 43% of the lowest one and has, therefore, to be included in a stability analysis. The total sloshing mass in four quarter tanks, however, is less than half of that of a tank with circular cross section.

## II. STABILITY INVESTIGATIONS

The stability of a liquid propellant spacecraft is affected by the motion of the propellants in the tanks. It is influenced by the tank form, which determines the amount of sloshing propellant and its location in the tank, and by the tank location, i.e., the slosh mass location with respect to the total vehicle. Proper choice of the tank form, thus decreasing the sloshing propellant mass and increasing the natural sloshing frequency will enhance the stability of a vehicle. These, however, are not the only means to suppress the hazard in control due to propellant sloshing. Proper selection of type, location, gain values, and vibrational characteristics of the control sensors can enhance the stability considerably. Since baffles mean additional weight penalty, they shall be employed only as a last resort.

Some simplified stability investigations have been performed which exhibit the influence of the various parameters. The stability boundary was determined in terms of the amount of damping of the propellant in the tank required for various tank locations (slosh mass location). The parameters considered are:

1.  $\mu = \frac{m_s}{m}$  the ratio of the sloshing mass to the total mass of the vehicle
2.  $\omega_c$  the natural circular control frequency
3.  $\zeta_c$  the control damping factor
4.  $\omega_s$  the natural circular sloshing frequency
5.  $a_o$  the gain value of the attitude control system
6.  $\omega_B$  the first natural circular bending frequency
7.  $\omega_a$  the circular accelerometer frequency
8.  $\zeta_a$  the accelerometer damping factor
9.  $x_a$  the accelerometer location
10.  $g_2$  the accelerometer gain value.

For reasons of simplification, only the first bending mode was considered. The propellant sloshing of only one tank was included. All effects due to aerodynamics, inertia and compliance of the swivel engines are neglected. It is furthermore assumed that only half of the thrust is available for control purpose.

The equations of motion are: (Fig. 10)

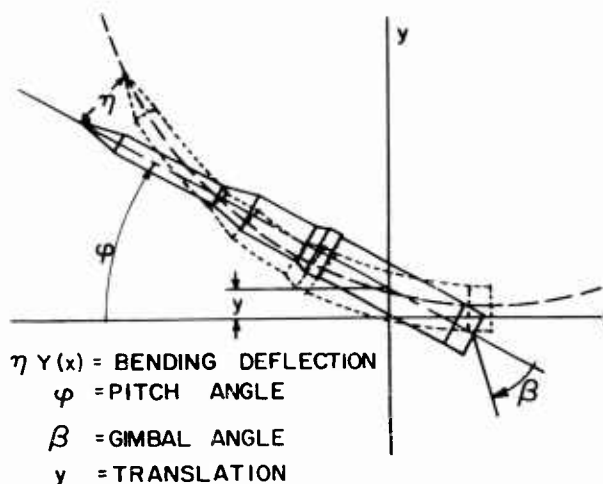


FIG. 10 MISSILE COORDINATE SYSTEM

1. Equation of Lateral Translation

$$m\ddot{y} + m_s \ddot{\xi}_s - F\varphi - \frac{F}{2} \beta + F\eta Y'_E = 0 \quad (19)$$

where  $m$  represents the total mass of the space vehicle,  $m_s$  the sloshing mass of the first propellant mode, and  $F$  the total thrust. The factor  $1/2$  on the right hand side of Equation 19 is due to the availability of only half of the thrust to be gimbaled.  $\xi_s$  is the displacement of the sloshing mass  $m_s$  relative to the center line of the tank.  $\beta$  is the engine deflection. The last term represents the generalized translational force of the thrust due to bending, where  $\eta$  is the generalized bending coordinate and  $Y'_E$  is the bending mode slope at the swivel point of the engine.

2. Equation of Pitching Motion

$$I\ddot{\varphi} - m_s x_s \ddot{\xi}_s - m_s g \xi_s + \frac{F}{2} x_E \beta - F(x_E Y'_E - Y_E) \eta = 0 \quad (20)$$

$I$  represents the effective moment of inertia of the vehicle about its center of gravity. It can be written as

$$I = \int x^2 m'_A dx + \int I'_O dx + m_O x_O^2 + I_O + m_s x_s^2 = m k^2$$

$x_E$  is the distance of the swivel point of the gimbal engine from the origin.  $m'_A$  is the mass per unit length of the air frame,  $I'_O$  its geometric moment of inertia,  $m_O$  the fixed (non-sloshing) mass of the propellant, which is located at the station  $x_O$ ,  $I_O$  is its moment of inertia about its center of gravity and  $x_s$  is the location, at which the sloshing propellant mass point is placed. The symbol  $k$  is the radius of gyration of the vehicle. The last term of Equation 20 represents the generalized rotational force of the thrust due to bending.  $Y_E$  is the lateral displacement of the bending mode at the swivel point of the engines.

3. Equation of Bending Vibration

As already mentioned, only one bending mode is considered for simplification. Because the sloshing and control frequencies are below the lowest bending mode, the first bending mode was chosen in this analysis. It is designated by the letter  $\eta$ . The equation of the bending vibration is then

$$\ddot{\eta} + \omega_B g_B \dot{\eta} + \omega_B^2 \eta + \frac{m_s}{M_B} Y_s \ddot{\xi}_s + \frac{m_s}{M_B} g Y'_s \xi_s - \frac{g}{\left(2 \frac{M_B}{m}\right)} Y_E \beta = 0 \quad (21)$$

where  $\omega_B$  is the circular bending mode frequency (first bending mode) and  $g_B$  is the structural damping. The dissipation of the structural damping, which usually is considered as being proportional to the amplitude (restoring force) of the elastic system and in phase with the velocity of the vibration, is treated here as an equivalent linear viscous damping proportional to the velocity and opposing the oscillation. This was preferred to avoid complex coefficients in the stability polynomial, thus making the treatment less complicated. It is justified as long as the damping forces are small, and it is only of importance in the neighborhood of the bending frequency.

The generalized mass  $M_B$  is

$$M_B = \int m_A' Y^2 dx + \int I_O' Y'^2 dx + m_O Y_O^2 + I_O Y_O'^2 + m_s Y_s^2$$

where  $Y_O, Y_O'$  is the displacement and slope of the bending mode at the non-sloshing mass location,  $Y_s, Y_s'$  is the bending mode displacement and slope at the sloshing mass location. The last term in Equation 21 represents the generalized bending force of the thrust due to bending. The longitudinal acceleration of the spacecraft is represented by

$$g = \frac{F}{m}$$

#### 4. Equation of Propellant Motion

$$m_s \ddot{\xi}_s + \omega_s \gamma_s m_s \dot{\xi}_s + k_s \xi_s - m_s x_s \ddot{\phi} - g m_s \phi + m_s \ddot{\phi} + m_s \ddot{\eta} Y_s' + m_s g \eta Y_s' = 0 \quad (22)$$

$\omega_s$  is the natural circular frequency of the first propellant mode,  $\gamma_s$  is the damping factor of the propellant and  $k_s$  is the spring constant of the equivalent mechanical model describing the fluid motion in the tank.

$$\left( \frac{k_s}{m_s} = \omega_s^2 \right)$$

#### 5. Control Equation

A simplified control equation of the form

$$\beta = a_0 \phi_i + a_1 \dot{\phi}_i + g_2 A_i \quad (23)$$

is used. Derivatives of  $\beta$  which produce increasing phase lags with increasing frequency are neglected. They are not a basic argument in low frequency ranges. The gimbal angle is called  $\beta$  and  $\phi_i$  is the indicated attitude deviation from a space fixed reference (as measured from a position gyro). Gain values of the attitude control system are represented by  $a_0$  and  $a_1$ . The gain value of the accelerometer control

channel is  $g_2$ , and  $A_i$  represents the indicated acceleration. For an elastic spacecraft, the indicated attitude deviation  $\phi_i$  is composed of the attitude deviation  $\phi$  of the rigid vehicle and the bending deviation. It is

$$\phi_i = \phi - \eta Y'_G$$

where  $Y_G$  is the slope of the bending mode at the gyro location.

#### 6. Accelerometer Equation

$$\frac{\ddot{A}_i}{\omega_a^2} + \frac{2\zeta_a}{\omega_a} \dot{A}_i + A_i = \ddot{y} + x_a \ddot{\phi} + g\phi + \ddot{\eta}Y_a + g\eta Y'_a \quad (24)$$

where  $\omega_a$  is the natural circular frequency of the accelerometer,  $\zeta_a$  is the damping of the accelerometer and  $x_a$  is its location. The slope and displacement at the accelerometer location due to bending is represented by  $Y'_a$  and  $Y_a$ . If the accelerometer is considered ideal ( $\omega_a \gg 1$ ) the equation reads

$$A_i = \ddot{y} + x_a \ddot{\phi} + g\phi + \ddot{\eta}Y_a + g\eta Y'_a$$

Four special cases are treated here: (Ref. 5 and 6)

1. Rigid spacecraft with attitude control system (differentiating network)
2. Rigid spacecraft with attitude control system and ideal accelerometer control
3. Rigid spacecraft with attitude control system and "real" accelerometer control
4. Elastic spacecraft with attitude control system.

Assuming solutions of the previous differential equations with the time dependency  $e^{st}$ , where  $s$  is the complex frequency,  $s = \sigma + i\omega$ , the stability polynomial can be obtained. The stability boundaries will be determined in the  $(x_s, \gamma_s)$  plane. The coefficients of the

stability polynomials  $\sum_{\lambda=1}^n A_\lambda s^\lambda = 0$  are real. The boundary of the stability region is

$$A_n = 0 \quad \text{and} \quad H_{n-1} = 0$$

where  $H_{n-1}$  is the Hurwitz determinant.

Stability is achieved for all points  $(x_s, \gamma_s)$  above the boundary curve. The stability boundary breaks off at the left and right due to the results of  $A_n = 0$ . Therefore, stability is only exhibited inside

these boundaries, that is, above the stability curve, left of the right boundary of  $A_n = 0$  and right of its left boundary. Sometimes these latter boundaries are outside the spacecraft and are, therefore, not indicated.

#### A. Rigid Spacecraft with Attitude Control System

It can be seen in Figure 11 that the danger zone where baffling has to be employed for a rigid spacecraft with small values of

$\frac{\omega_c^2}{a_0 \omega_s^2}$  is approximately between the center of gravity and center of

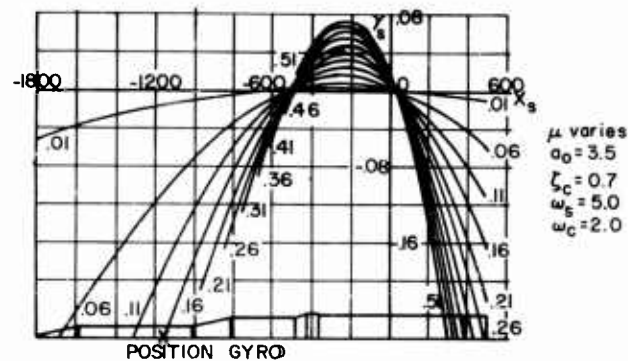


FIG. 11 STABILITY BOUNDARY FOR RIGID SPACECRAFT  
(NO ADDITIONAL CONTROL)

instantaneous rotation. With increasing slosh mass ratio  $\mu$ , the stability is decreasing in this region, that is, more damping has to be employed in a tank in which the slosh mass is located in the danger zone. Considering a damping factor of the magnitude of  $\gamma_s = 0.02$  for an unbaffled tank, the vehicle is always stable for a slosh mass ratio  $\mu < 0.15$ .

In Figure 12 the influence of an increase in the circular control frequency indicates a rather strong increase of the danger zone toward the base of the craft. The sloshing mass ratio was considered to be  $\mu = 0.1$ . The increase in the control frequency also demands more baffling in the danger zone. For a control frequency of approximately double the magnitude of the nominal control frequency of 0.3 cycle/sec, approximately three times as much damping has to be introduced in the tank to obtain stability. The case of  $\omega_c > \omega_s$  is very unfavorable because it demands more baffling and exhibits a larger danger zone. Keeping the control frequency somewhat below the first sloshing mode frequency in the danger zone can, with relatively low baffling, avoid instability and keep the danger zone restricted to the approximate region between the center of gravity and the center of instantaneous rotation. For a sloshing mass ratio  $\mu$  of 10%, the wall friction is

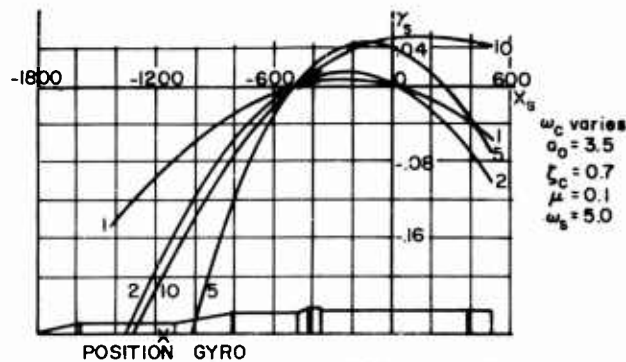


FIG.12 STABILITY BOUNDARY FOR RIGID SPACECRAFT  
(NO ADDITIONAL CONTROL)

sufficient to maintain stability as long as the control frequency is below 0.3 cycle/sec. The change of the control damping  $\zeta_c$  can be seen in Figure 13. It exhibits the following trend: For increasing subcritical control damping ( $\zeta_c < 1$ ), the stability is decreasing in the danger zone; that is, more damping has to be introduced to maintain stability. The danger zone is unchanged by the change of the

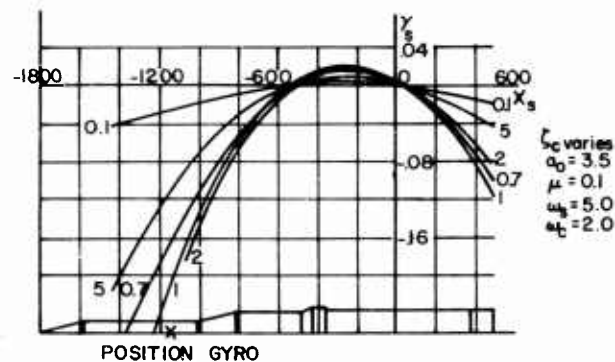


FIG.13 STABILITY BOUNDARY FOR RIGID SPACECRAFT  
(NO ADDITIONAL CONTROL)

control damping. For increasing supercritical control damping ( $\zeta_c > 1$ ) the stability increases; that is, less damping is required in tank locations in the danger zone. No baffling is required for a sloshing mass of  $\mu = 0.1$  in the danger zone if the control damping  $\zeta_c \leq 0.5$  or if  $\zeta_c \geq 2$ . This means that for the parameters considered ( $\omega_s = 5.0$ ,  $\omega_c = 2$ ,  $a_0 = 3.5$ , simple attitude control system with lead network), the wall friction in the tank is sufficient to maintain stability for a rigid space vehicle of the Saturn type.



A further question that always presents itself to the design engineer is the problem of tank design. Tanks with large diameters exhibit low sloshing frequencies which are in many cases too close to the control frequency of the vehicle. Partitions in the tank or clustering the tanks increases not only the sloshing frequency but also reduces the sloshing mass considerably. The effect of the change of the sloshing frequency is shown in Figure 14. The danger zone

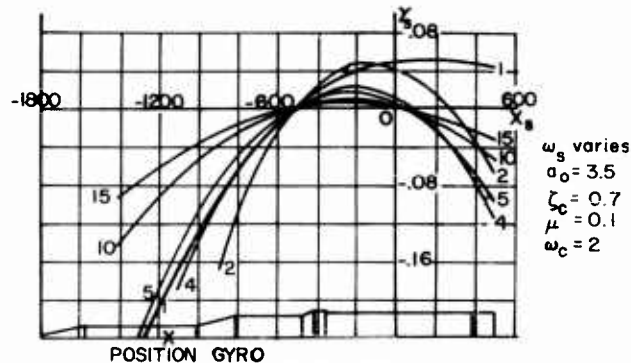


FIG. 14 STABILITY BOUNDARY FOR RIGID SPACECRAFT  
(NO ADDITIONAL CONTROL)

increases toward the aft of the craft with decreasing slosh frequency, and the stability is considerably decreased. An increase of the slosh frequency enhances the stability, that is, decreases the danger zone and reduces the amount of baffling necessary to maintain stability. For the treated case of a rigid spacecraft with a sloshing mass ratio of  $\mu = 0.1$ , the wall friction will be sufficient to maintain stability at any tank location if the natural sloshing frequency is above 3.0 cycle/sec.

The control factor  $a_0$  of the attitude control system exhibits a slight increase of the danger zone toward the base of the craft and a slight decrease in stability for decreasing values (Fig. 15).

#### B. Rigid Spacecraft with Attitude Control System and Ideal Accelerometer Control

The stability boundaries with respect to propellant sloshing are treated for an accelerometer controlled spacecraft employing an ideal accelerometer ( $\omega_a \gg 1$ ) in addition to the control system of the previous Case.

Figure 16 exhibits the influence of increasing slosh mass ratio. The most favorable gain value  $\lambda = 1.0$  ( $\lambda = g_z/g$  where  $g$  is the longitudinal acceleration) for an ideal accelerometer controlled space vehicle was employed. The danger area is considerably decreased to a very short zone below the center of instantaneous rotation where wall friction for the liquid in the tanks already is sufficient

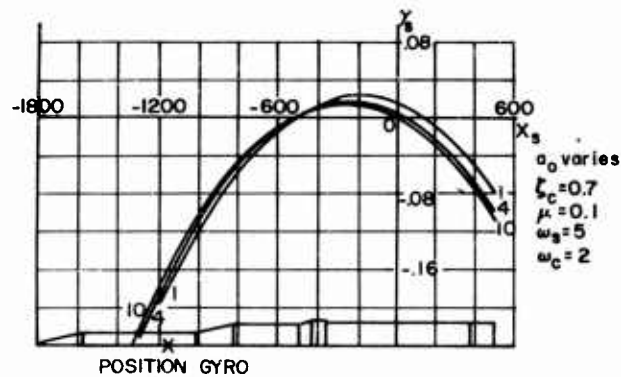


FIG. 15 STABILITY BOUNDARY FOR RIGID SPACECRAFT  
(NO ADDITIONAL CONTROL)

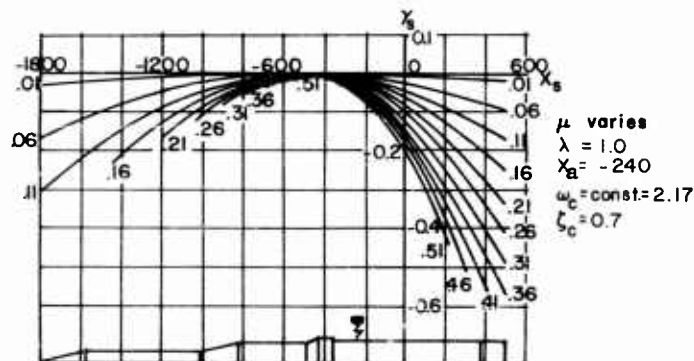


FIG. 16 STABILITY BOUNDARY FOR RIGID SPACECRAFT  
(WITH ACCELEROMETER CONTROL)

to maintain stability. The increase of the control frequency above the slosh frequency results in a decrease in stability and an increase of the danger zone towards the base of the craft. Due to ideal accelerometer control, however, the damping necessary to obtain stability for sloshing mass of 10% of the vehicle mass is very small, even in the case when the control frequency is twice the sloshing frequency. For  $\omega_s = 5.0$  radian/sec and  $\omega_c = 10.0$  radian/sec the necessary damping  $\gamma_s = 0.01$  (Fig. 17). The change of the control damping exhibits the same behavior as in the previous Case. It decreases the stability for increasing subcritical damping and increases the stability for increasing supercritical damping. The effect in the already small danger zone is hardly recognized (Fig. 18). If the slosh frequency is below the control frequency  $\omega_s < \omega_c$ , the danger zone is large and covers nearly the complete region behind the center of instantaneous rotation. Small damping, however, already guarantees stability (Fig. 19). For increasing slosh frequency, a considerable decrease in the danger zone is noticed and an increase in stability is obtained.

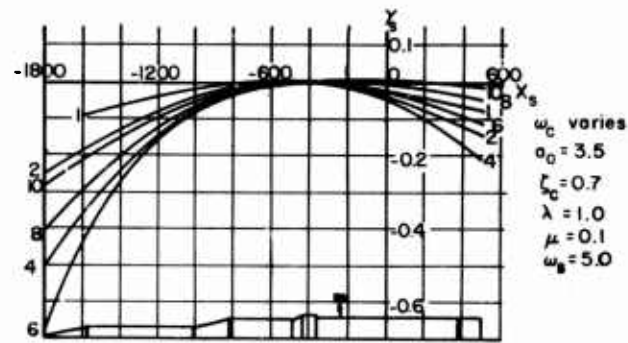


FIG. 17 STABILITY BOUNDARY FOR RIGID SPACECRAFT (WITH ACCELEROMETER CONTROL)

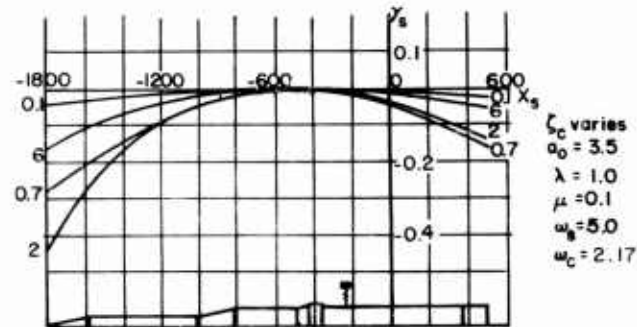


FIG. 18 STABILITY BOUNDARY FOR RIGID SPACECRAFT (WITH ACCELEROMETER CONTROL)

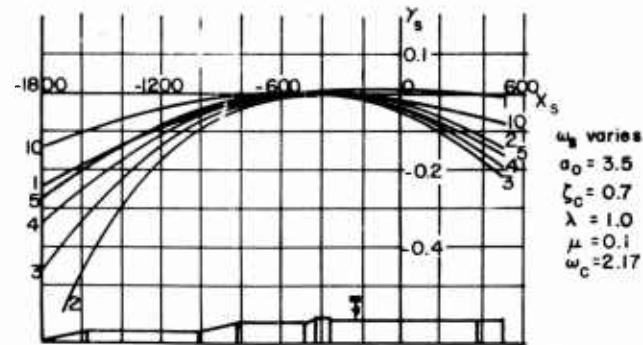


FIG. 19 STABILITY BOUNDARY FOR RIGID SPACECRAFT (WITH ACCELEROMETER CONTROL)

Figure 20 shows that no appreciable stability is encountered by change of the attitude control value  $a_0$ . The accelerometer gain value  $\lambda = 82.8$  has a very pronounced influence on the stability behavior of the vehicle. In Figure 21 it can be seen that, for  $\lambda < 1$  the danger zone

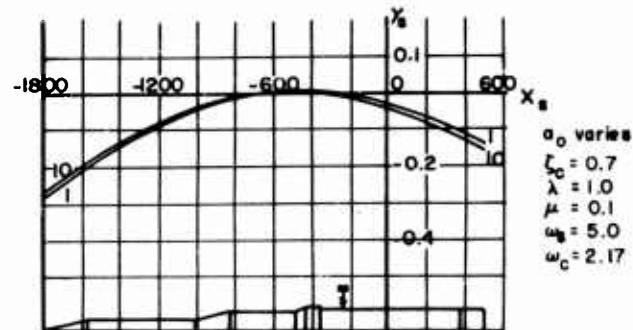


FIG. 20 STABILITY BOUNDARY FOR RIGID SPACECRAFT (WITH ACCELEROMETER CONTROL)

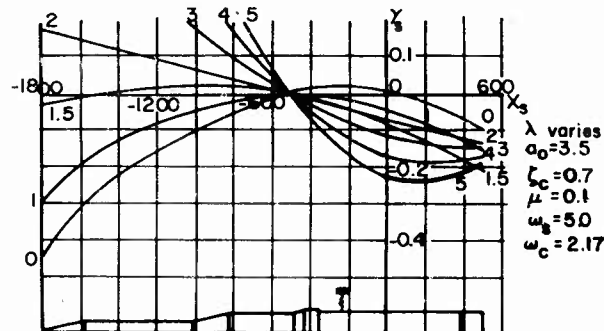


FIG. 21 STABILITY BOUNDARY FOR RIGID SPACECRAFT (WITH ACCELEROMETER CONTROL)

is behind the center of instantaneous rotation and increases towards a value of slightly behind the center of gravity as  $\lambda$  approaches the value zero. A loss in stability takes place in the danger zone while  $\lambda$  is decreasing. For increasing  $\lambda > 1$ , the danger zone shifts forward of the center of instantaneous rotation and increases the magnitude of the zone and the required damping for tanks in this location. From a certain value  $\lambda > 1.5$  on, propellant motion in all tanks in front of the center of instantaneous rotations leads to instabilities while, for tanks behind the center of instantaneous rotation, the motion of the propellant is stable. The value  $\lambda = 1$  is the most favorable gain value for which all other parameter changes were performed. In Figure 22, the influence of the location of the accelerometer upon the stability can be seen. For the most favorable gain value  $\lambda = 1$ , the change of the location of the accelerometer did not lead to instabilities. For other gain values, however, the location of the accelerometer definitely has an influence on the

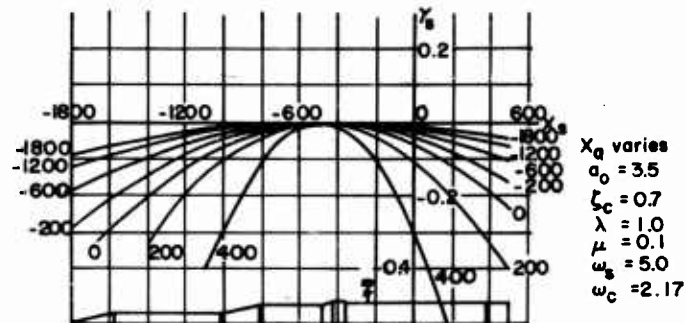


FIG. 22 STABILITY BOUNDARY FOR RIGID SPACECRAFT  
(WITH ACCELEROMETER CONTROL)

stability. For gain values  $\lambda$  larger than 1.5, the fluid motion in all tanks behind the center of instantaneous rotation exhibits strong instabilities for accelerometer locations behind the center of gravity. The propellant motion in tanks in front of the center of instantaneous rotation shows instabilities if the accelerometer is located in front of the center of gravity. For gain values  $\lambda$  smaller than unity, the behavior of the stability boundary is similar to the one without accelerometer control. The previous results are only valid for an ideal accelerometer, which means for an accelerometer frequency of large value ( $\omega_a \gg 1$ ). For an accelerometer with vibrational characteristics  $\omega_a$  and  $\zeta_a$  (noted as a real accelerometer), the stability behavior is quite different from that of an ideal accelerometer depending, of course, mainly on the value of its natural frequency.

C. Rigid Spacecraft with Attitude Control System and Real Accelerometer Control

Two circular frequencies for the accelerometer were treated;  $\omega_a = 12$  and 55 radians/sec. In Figure 23, the influence of increasing slosh mass ratio can be seen for a spacecraft with additional

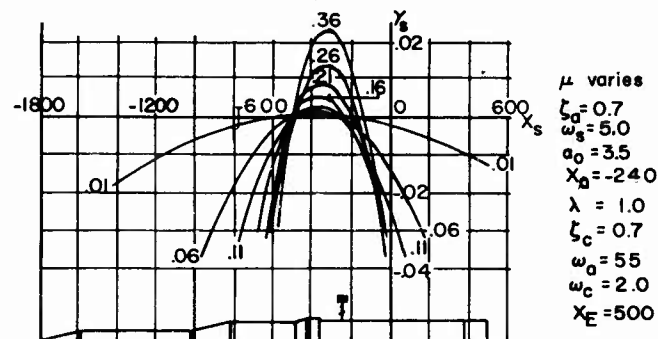


FIG. 23 STABILITY BOUNDARY FOR RIGID SPACECRAFT  
(WITH REAL ACCELEROMETER CONTROL)

accelerometer control, where the accelerometer has a circular natural frequency of  $\omega_a = 55$  radians/sec and a subcritical damping of  $\zeta_a = 0.7$ . With increasing slosh mass ratio, the danger zone increases aft of the center of instantaneous rotation and the stability decreases. That is, in the danger zone more damping is needed to maintain stability. It can be noted, however, that for wall friction only, ( $\gamma_s = 0.02$ ), the vehicle is stable for sloshing mass ratio  $\mu < 0.30$ . Increasing the gain value to  $\lambda = 1.5$  (an optimal value for stability) with an accelerometer of circular natural frequency of  $\omega_a = 55$  radians/sec, no instabilities are obtained for slosh mass ratios of  $\mu < 0.21$  (Fig. 24). For larger slosh mass ratios, the vehicle becomes

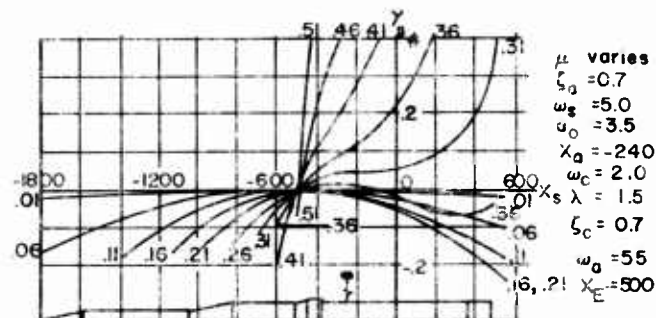


FIG. 24 STABILITY BOUNDARY FOR RIGID SPACECRAFT (WITH REAL ACCELEROMETER CONTROL)

very strongly unstable. It may be noted that the stability curve breaks off at the left at the indicated values, thus pointing out the instability beyond this point. For low accelerometer frequency ( $\omega_a = 12$  radians/sec), the stability situation is becoming very hopeless from the standpoint of sloshing (Fig. 25). Sloshing is

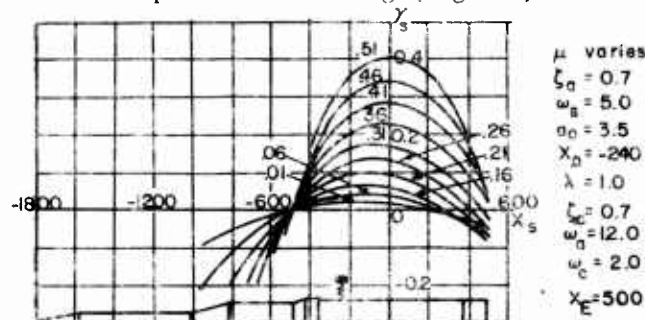


FIG. 25 STABILITY BOUNDARY FOR RIGID SPACECRAFT (WITH REAL ACCELEROMETER CONTROL)

even excited by the accelerometer control and creates a situation which is worse than in a craft with simple attitude control only. The danger zone is increased and increases with increasing slosh mass ratio. Very high baffling would be necessary in order to maintain

stability. The damping required in this case is about three to four times larger than in the case without accelerometer control. From this we can conclude that the accelerometer frequency should be well apart from the slosh and control frequency. With increasing gain value  $\lambda$ , this situation is even becoming more unfavorable, i.e., the danger zone increases over almost the entire vehicle and stability requires tremendous damping values. Figure 26 exhibits the effect of the change of the control frequency for a vehicle with an

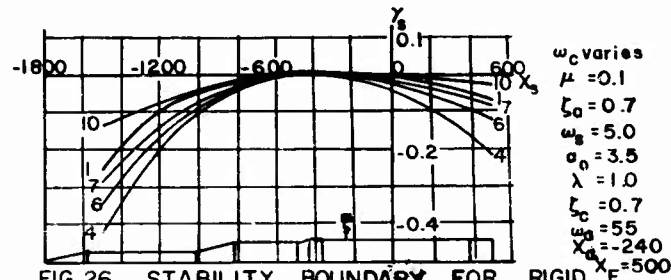


FIG. 26 STABILITY BOUNDARY FOR RIGID SPACECRAFT  
(WITH REAL ACCELEROMETER CONTROL)

accelerometer frequency of  $\omega_a = 55$  radians/sec. An increase of the control frequency below the slosh frequency decreases the danger zone slightly, while an increase of the control frequency above the slosh frequency increases the danger zone towards the aft of the craft. The damping during the increase of the control frequency remains comparatively small ( $\gamma_s = 0.01$  and less). For an accelerometer frequency of  $\omega_a = 12$  radians/sec the stability behavior can be seen in Figure 27. Increase of the control frequency results in a decrease

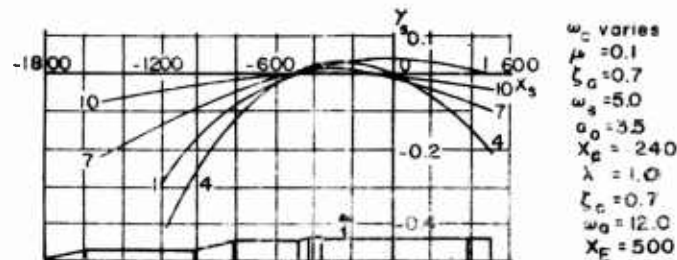


FIG. 27 STABILITY BOUNDARY FOR RIGID SPACECRAFT  
(WITH REAL ACCELEROMETER CONTROL)

of the danger zone and an increased stability. The effect is more pronounced than in the previous case and the vehicle is less stable for equal control frequencies in comparison with the case of  $\omega_a = 55$  radians/sec. Figure 28 exhibits the influence of control damping. Increasing control damping decreases the danger zone, and increases the stability. For the use of the low accelerometer frequency  $\omega_a = 12$  radians/sec, the stability behavior can be seen in Figure 29, which exhibits, for increasing subcritical damping,

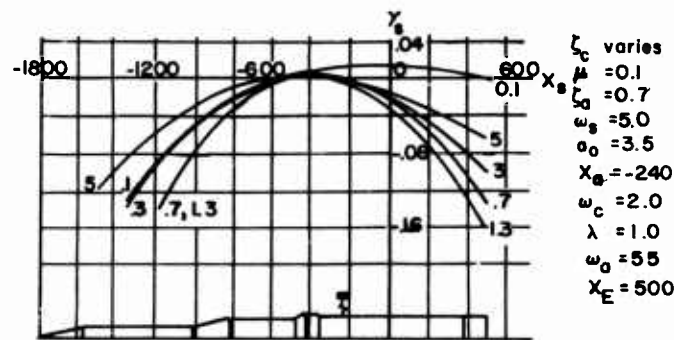


FIG. 28 STABILITY BOUNDARY FOR RIGID SPACECRAFT  
(WITH REAL ACCELEROMETER CONTROL)

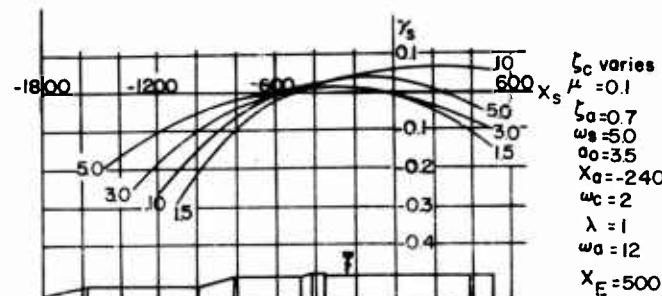


FIG. 29 STABILITY BOUNDARY FOR RIGID SPACECRAFT  
(WITH REAL ACCELEROMETER CONTROL)

decreasing danger zone and increasing stability, while for increasing supercritical damping increase of the danger zone and loss of stability area are encountered. Low subcritical damping, however, seems in both accelerometer frequency cases unfavorable; especially in the low accelerometer frequency case, more baffling has to be applied in order to maintain stability. The effect of changes in the sloshing frequency is shown in Figures 30 and 31. Slosh frequencies below the control frequency exhibit a large danger zone from a value slightly in front of the center of instantaneous rotation almost to the base of the spacecraft. For low accelerometer frequency ( $\omega_a = 12$  radians/sec), this is even more pronounced. Increasing slosh frequency shows a decrease in the danger zone and an increase in stability. Increasing slosh frequency above the control frequency  $\omega_s > \omega_c$  decreases the stability and increases the danger zone towards the base of the craft again. For low accelerometer frequencies, these effects are more magnified. For a slosh frequency in the vicinity of the accelerometer frequency, the stability is decreased and the danger zone is increased. The gain value  $a_0$  of the attitude control system has only very small influence upon the stability boundary for an accelerometer frequency  $\omega_a = 55$  radians/sec, which is large compared to the control frequency



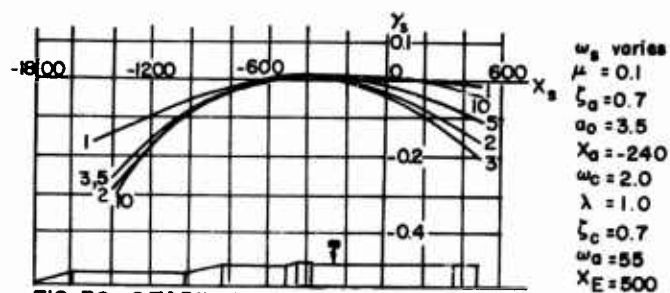


FIG. 30 STABILITY BOUNDARY FOR RIGID SPACECRAFT (WITH REAL ACCELEROMETER CONTROL)

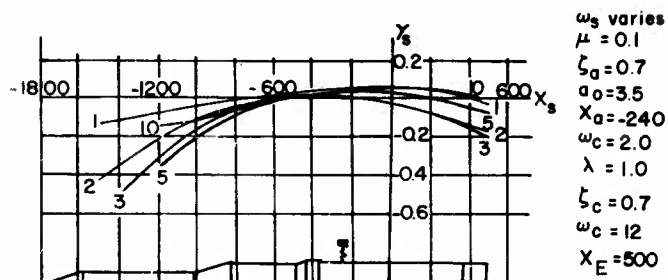


FIG. 31 STABILITY BOUNDARY FOR RIGID SPACECRAFT (WITH REAL ACCELEROMETER CONTROL)

$\omega_c = 2$  radians/sec (Fig. 32). The danger zone is only a short length behind the center of instantaneous rotation. With the wall friction

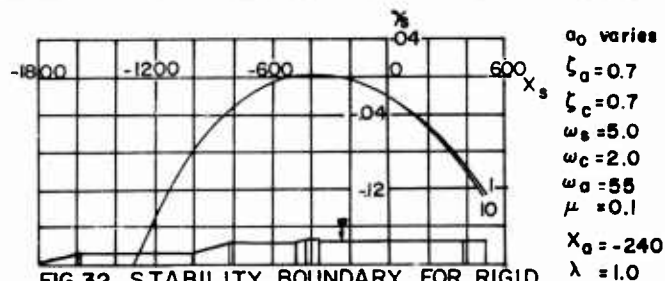
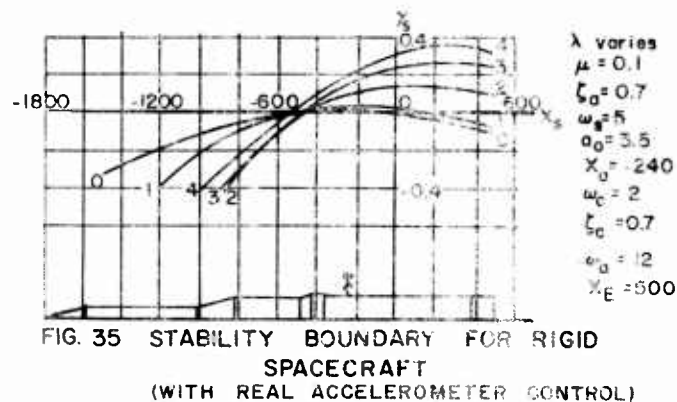
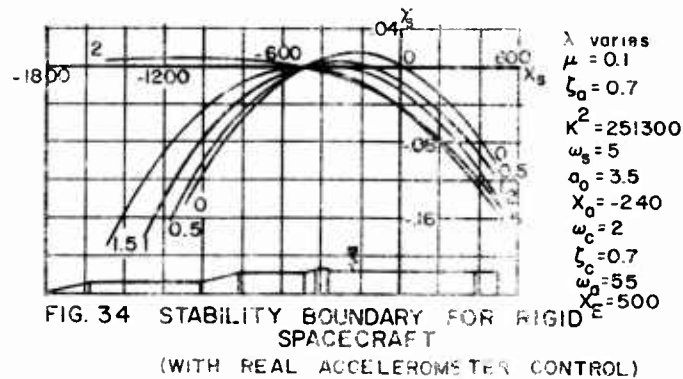
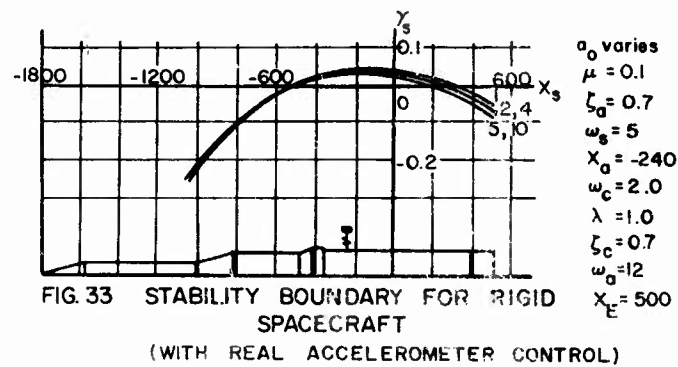


FIG. 32 STABILITY BOUNDARY FOR RIGID SPACECRAFT (WITH ACCELEROMETER CONTROL)

damping value ( $\gamma_s = 0.02$ ), the vehicle is already stable for the given parameters. For small accelerometer frequency ( $\omega_a = 12$  radians/sec), a small effect can be observed. The danger zone and stability region, however, are unfavorable (Fig. 33).

Figures 34 and 35 exhibit the influence of the change of the accelerometer gain value  $\lambda = g_2 g$ . For an accelerometer frequency of  $\omega_a = 55$  radians/sec, an increase of the gain value to about  $\lambda = 1.5$



enhances the stability and decreases the danger zone to a very small region between center of instantaneous rotation and the center of gravity. Further increase of  $\lambda$  extends the danger zone in front of the center of instantaneous rotation. The larger  $\lambda$  becomes the more baffling is required. If the accelerometer frequency is only  $\omega_a = 12$  radians/sec, the situation is quite different. For increasing gain value the danger zone increases from the center of instantaneous rotation to the aft of the craft. Very strong damping is the

tanks has to be introduced in order to maintain stability. Further increases decrease the stability region again, but still require a large zone to be baffled very strongly, while in the case of a large accelerometer, low damping is already sufficient for stability. A damping twenty to thirty times larger is required for the case of low accelerometer frequency. Again we can conclude that large accelerometer frequency eliminates the greatest part of the problem. To obtain the influence of the very important parameter, the natural frequency of the accelerometer, Figure 36 shows that for increasing accelerometer frequency the danger zone enlarges and requires more damping. Above

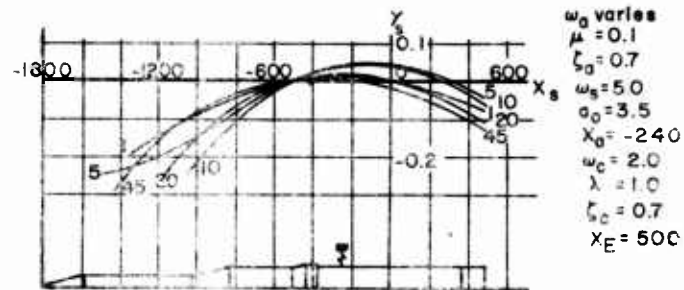


FIG. 36 STABILITY BOUNDARY FOR RIGID SPACECRAFT (WITH REAL ACCELEROMETER CONTROL)

the slosh frequency for  $\frac{\omega_a}{\omega_s} > 2$ , a decrease of the danger zone and an increase in the stability area are noticed. The larger the ratio  $\frac{\omega_a}{\omega_s}$ , the less damping is required in order to obtain stability.

The increase of the damping of the accelerometer exhibits an increase of the danger zone and requires more damping in the tanks. This effect is more magnified for small accelerometer frequencies (Fig. 37 and 38). It can be noticed that for twice the critical

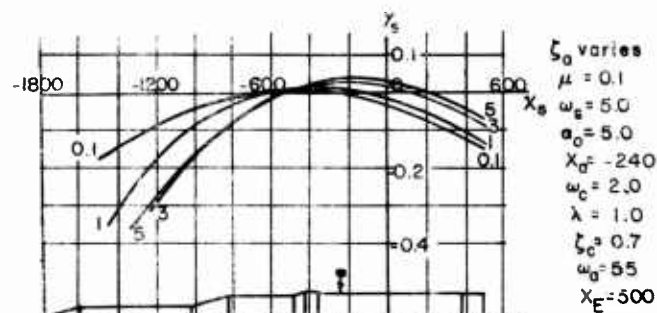


FIG. 37 STABILITY BOUNDARY FOR RIGID SPACECRAFT (WITH REAL ACCELEROMETER CONTROL)

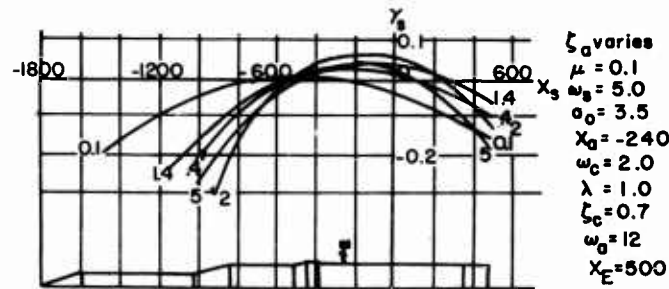


FIG. 38 STABILITY BOUNDARY FOR RIGID SPACECRAFT  
(WITH REAL ACCELEROMETER CONTROL)

damping on, small accelerometer frequency  $\omega_a = 12$  radians/sec, a further increase of the accelerometer damping slightly decreases the danger zone and slightly enhances the stability. A very important parameter in the design of a control system is the location of an accelerometer as indicated in Figures 39 and 40. A location of the

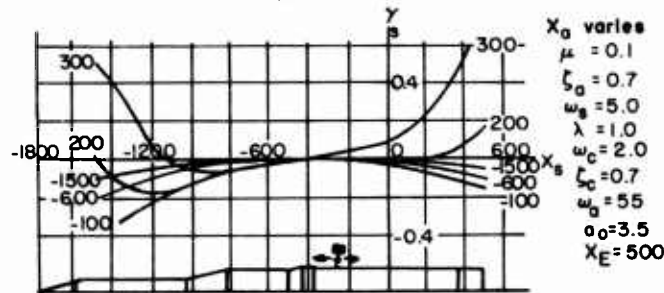


FIG. 39 STABILITY BOUNDARY FOR RIGID SPACECRAFT  
(WITH REAL ACCELEROMETER CONTROL)

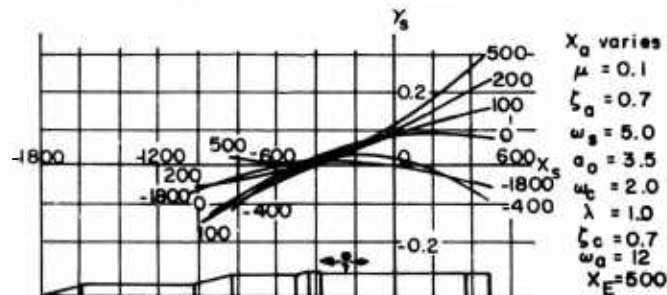


FIG. 40 STABILITY BOUNDARY FOR RIGID SPACECRAFT  
(WITH REAL ACCELEROMETER CONTROL)

accelerometer behind the center of gravity must be avoided. For a natural frequency of  $\omega_a = 55$  radians/sec of the accelerometer any location in front of the center of gravity requires low damping only for stability in a small danger zone. For an accelerometer frequency  $\omega_a = 12$  radians/sec, a location of an accelerometer behind the center

of gravity requires high baffling in the tanks between the base and the center of instantaneous rotation. Further shifting of the accelerometer towards the nose of the vehicle enhances the stability and decreases the danger zone. All these results are valid for a rigid spacecraft. It should, however, be noted that bending in an accelerometer-controlled craft plays an important role. Gain factor  $\lambda$ , location of the accelerometer and the ratio of the bending frequency to the accelerometer frequency as well as to the control frequency are having some definite influence. If the bending and control frequencies are sufficiently apart, only negative bending mode displacements are permissible. This indicates that for the control of the first two bending modes a location in front of the center of gravity, where both bending modes exhibit negative deflection, is favorable. This location also would remedy the sloshing problems with little baffling but must be treated with care with respect to the gain value  $\lambda$  of the accelerometer, since it exhibits limitations in magnitude due to rigid body control.

#### D. Elastic Spacecraft with Attitude Control

All previous statements were only valid for rigid space vehicles or such crafts where the bending frequency is considerably higher than the control and sloshing frequency. (Only the first sloshing frequency need be considered because, for higher sloshing frequencies, the sloshing mass is of insignificant magnitude; thus it is unable to affect the stability.) However, for spacecraft with considerably lower bending frequencies, the influence of the elastic behavior on the stability definitely has a very pronounced effect which needs to be considered. Baffling based on a rigid vehicle would be inadequate and could result in a detrimental situation, such as the saturation of the control system and even destruction of the craft. With increasing size of vehicles, the elastic effect of the structure can no longer be neglected in a sloshing stability analysis.

From Figure 41, it is seen that for an elastic space vehicle the danger zone is enlarged to both sides, especially toward the aft of the craft. Furthermore, about three times as much damping is needed compared with a rigid craft to maintain stability. Considering only the friction of the liquid at the tank wall would guarantee stability as long as  $\mu < 0.05$ . Increasing sloshing mass ratio decreases the stability.

In Figure 42, the influence of an increase in the circular control frequency exhibits a rather strong increase of the danger zone and required damping for stability. A small increase of the control frequency from 0.3 cycle/sec to 0.5 cycle/sec indicates a tremendous baffling requirement of more than three times as much as at 0.3 cycle/sec and for nearly the complete vehicle length. Further increases of the control frequency toward the bending frequency eliminate stability completely and a change in the control system must be performed by attenuation and phase changes. This has not been executed here because, from the view of sloshing stability, it

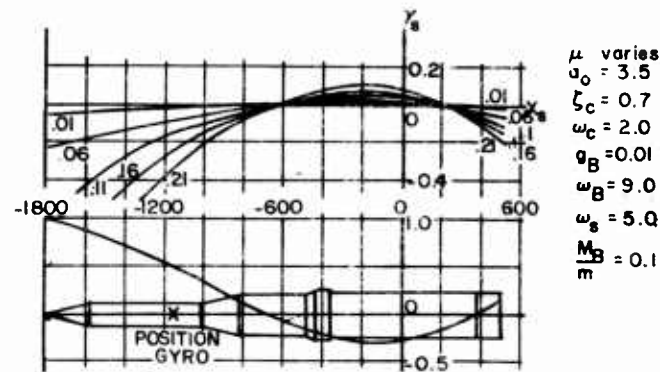


FIG. 41 STABILITY BOUNDARY FOR ELASTIC SPACECRAFT  
(NO ADDITIONAL CONTROL)

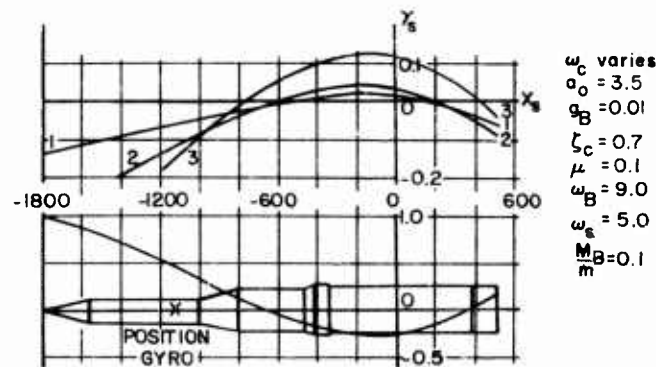


FIG. 42 STABILITY BOUNDARY FOR ELASTIC SPACECRAFT  
(NO ADDITIONAL CONTROL)

is no basic argument. With no baffles in the tanks and a 10% sloshing mass ratio, the vehicle is only stable for a control frequency smaller than 0.15 cycle/sec. The case of  $\omega_c > \omega_s$  is very unfavorable not only from the standpoint of sloshing but also from the bending mode stability standpoint.

The influence of the control damping can be seen in Figure 43. The trend is similar to the rigid space vehicle case: For increasing subcritical control damping ( $\zeta_c < 1$ ), the stability decreases. The danger zone, however, decreases with increasing control damping. For increasing supercritical control damping ( $\zeta_c > 1$ ) the stability increases. This means that less damping in the tanks is required to maintain stability. No baffling would be required for a supercritical control damping of larger than 5.0 if ten percent of the mass of the vehicle is considered to be sloshing ( $\omega_s = 5.0$ ,  $\omega_c = 2.0$ ,  $a_0 = 3.5$ ,  $\omega_B = 9.0$ ). Comparison with the rigid vehicle exhibits again a two to three times larger damping requirement for stability.

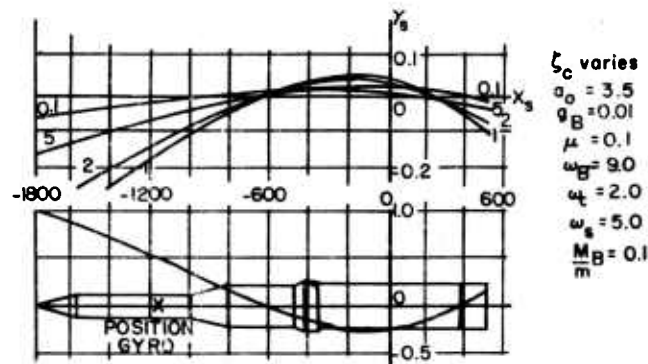


FIG.43 STABILITY BOUNDARY FOR ELASTIC SPACECRAFT  
(NO ADDITIONAL CONTROL)

The effect of the slosh frequency can be seen in Figure 44. An increase in the sloshing frequency increases the stability and

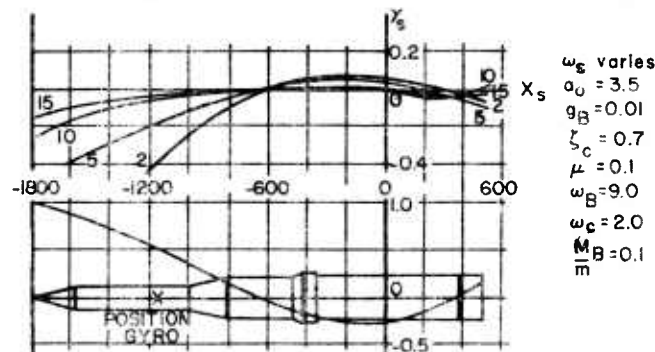


FIG.44 STABILITY BOUNDARY FOR ELASTIC SPACECRAFT  
(NO ADDITIONAL CONTROL)

decreases the danger zone. Especially if the sloshing frequency is above the bending frequency, the danger zone is considerably decreased and the damping necessary to maintain stability is rather small. For a slosh frequency to bending frequency ratio of larger than

$3/2 \left( \frac{\omega_s}{\omega_B} > 1.5 \right)$ , the wall friction in the tank is already sufficient to maintain stability. The damping necessary for an elastic vehicle is about two to three times that necessary for a rigid spacecraft.

The influence of the control factor  $a_0$  of the attitude control system is considerably more pronounced than in the case of a rigid craft. With decreasing gain values, the danger zone increases tremendously over almost the complete vehicle length and demands considerable damping in the tanks to maintain stability (Fig. 45). For low gain values ( $a_0 = 1$ ) a damping factor is needed in an elastic vehicle which is five times larger than that of a rigid spacecraft.

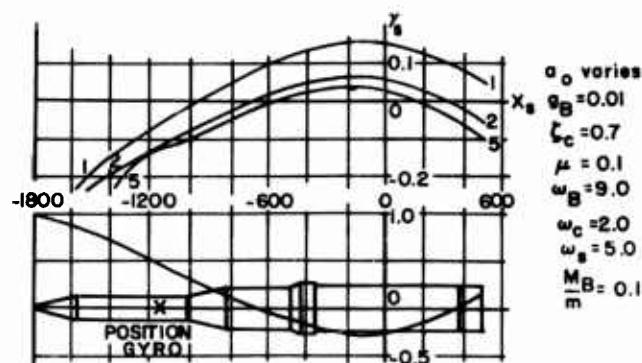


FIG. 45 STABILITY BOUNDARY FOR ELASTIC SPACECRAFT  
(NO ADDITIONAL CONTROL)

One strong effect in the stability of elastic spacecraft is the influence of the bending frequency (Fig. 46). For large bending frequencies, of course, the stability is enhanced and approaches with increasing bending frequency the values of a rigid vehicle. Also the danger zone shrinks to the one of the rigid craft. With decreasing bending frequency the stability decreases and stronger baffling is required.

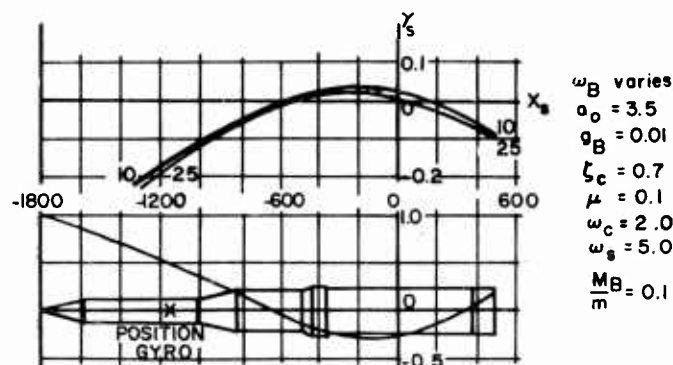


FIG. 46 STABILITY BOUNDARY FOR ELASTIC SPACECRAFT  
(NO ADDITIONAL CONTROL)

### III. CONCLUSION

For spacecraft of increasing size, the influence of propellant sloshing upon the stability becomes more pronounced. Aerodynamically instable spacecraft create loads and require control torques, which can be a potential hazard to the flight performance of the vehicle. Therefore, artificial stabilization such as angle-of-attack meter and/or accelerometer control is employed. This helps alleviate the required control deflections of the gimbal engines, jet vanes or air vanes. For a given configuration the control requirements are



strongly dependent upon the gain settings of the control system (attitude and  $\alpha$ -control). Sloshing propellant requires additional control torques. To minimize this effect proper choice of the control values, tank geometry and tank location and, as a last resort, baffles will enhance the stability situation. The amount of sloshing mass is determined by the tank geometry, the mass density of the propellant and the liquid height. The tank location, i.e., slosh mass location, plays an important role. The conclusions drawn from the results of a rigid space vehicle even with additional ideal accelerometer control lead to optimistic results concerning the baffling of the tanks to maintain stability. An actual accelerometer has its own natural frequency; therefore, the relation of control, sloshing and accelerometer frequency are of utmost importance. Furthermore, low bending frequencies of the vehicle have a very pronounced effect and require much more damping along an enlarged danger zone as anticipated by the results of a rigid spacecraft.

#### REFERENCES

1. Helmut F. Bauer, "Fluid Oscillations in a Circular Cylindrical Tank", ABMA Report DA-TR-1-58.
2. Helmut F. Bauer, "Theory of the Fluid Oscillations in a Circular Cylindrical Ring Tank Partially Filled with Liquid", NASA TN D-557, 1960.
3. Helmut F. Bauer, "Theory of Fluid Oscillations in a Partially Filled Cylindrical Quartertank", (not yet published), (Excerpt from "Fluid Oscillations in Cylindrical Tanks", unpublished).
4. Helmut F. Bauer, "Mechanical Analogy of Fluid Oscillations in Circular Cylindrical Tanks with Circular and Annular Cross Section", MSFC Report MTP-AERO-61-4.
5. Helmut F. Bauer, "Stability Boundaries of a Liquid Propelled Elastic Spacecraft", MSFC Report MTP-AERO-61-7.
6. Helmut F. Bauer, "The Effect of Propellant Sloshing on the Stability of an Accelerometer Controlled Rigid Space Vehicle", MSFC Report MTP-AERO-61-16, 1961.
7. D. R. Fuller, "Stability Criteria for Linear Systems and Realizability Criteria for RC Networks", Proc. of Camb. Phil. Soc., Vol. 53 (1957).

## DISCUSSION OF AN AERO-INERTIAL CONTROL SYSTEM

Robert M. Hunt  
NASA, Marshall Space Flight Center  
Huntsville, Alabama

### SUMMARY

Current production and transportation facilities set a practical limit on the diameter of today's space flight vehicles. Hydrogen fuel and more powerful engines are making these vehicles longer. Long-slender vehicles with conventional engine gimbal control develop large bending moments when traversing their design wind profiles.

Recognizing the fact that serious loads problems are upon the structural engineer, a method is proposed which can reduce and by proper selection of control may eliminate the problem in one specific locality of the vehicle almost entirely or minimize the overall moment distribution.

This method is called an aero-inertial control system. The basic concept is to hinge the nose similarly to current engine gimbal practice. This produces an eccentric mass relative to the thrust vector, and reduces the angle of attack locally at the nose section. The predominant mass of the system experiences lower loads both in terms of lift forces on the nose and control forces on the rear, thus reducing the bending moment.

### INTRODUCTION

A review of the simplified loads produced when placing a rigid body in static equilibrium, using the current practice of engine control is shown in Fig. 1.

The aerodynamic lift for the configuration shown might be distributed as depicted in Fig. 1 (a). Particularly notice that the distributed area is greatest along the forward portion of the vehicle. Fig. 1 (b) shows this integrated lift as vector  $A_z$  at the

center of pressure. Fig. 1 (c) shows the location of the center of gravity and the stabilizing control vector  $F\beta$ . The static equilibrium conditions are completed by addition to Fig. 1 (d) of the inertial vector  $M\ddot{Z}$ .

Now the shear diagram can be drawn in as shown in Fig. 1 (e) and the bending moment diagram as Fig. 1 (f).

There are two significant facts which should be remembered from Fig. 1 and these are: (1) the lift distribution is greatest along the conical nose segment, and (2) the vector  $F\beta$  exists only to place the lift vector in rotational equilibrium.

The lift vector  $A_z$  and the control vector  $F\beta$  are in the same direction and add to produce the large inertial vector  $M\ddot{Z}$ . This inertial vector creates a high bending moment at the vehicle center of gravity.

It can be rationalized that should the lift vector  $A_z$  be nulled the stabilizing control vector would vanish and the ideal case of zero shear and zero bending moment could be realized. A search for this utopian condition for launch vehicle design is the basis of this paper.

#### DISCUSSION

The hypothesis is made that by placing a gimbals on the nose section as indicated in Fig. 2 and by appropriate control of the motion between the two segments a desirable regulation of the aerodynamic forces could be achieved. Fig. 2 (a) shows a cut-away section of a possible scheme for gimbals. The point S represents the swivel point and C the actuator or control mechanism. Figures 2 (b) and (c) show the vehicle in the uncanted and canted position respectively.

The aerodynamists will recognize that this is no panacea since a large lift will now occur aft of the junction of the two bodies, however, the center of pressure has moved rearward. No further discussion of the aerodynamics will be attempted since that subject would be lengthy. However, it will be assumed that the aerodynamic forces on any segmented portion are known linear springs in terms of the attitude of the system they are connected to.

In Fig. 3 (a) it may be seen that the inertial force has an eccentricity to the force vector produced by its cant. This results in a rotational moment on the system in the direction the nose is pointing. It appears that this is advantageous to the attitude control.

It is the aerodynamic force regulation feature and the inertial force eccentricity gained in such a system which leads to the

name "Aero-Inertial Control System".

From Fig. 3 (b) and equation (1) underneath it, a condition may be placed on the cant angle,  $\delta$ , which would result in static rotational equilibrium for the system.

If ideal conditions existed, adequate control could be maintained throughout the powered flight regime for such a vehicle. Thrust vector misalignment and uncertainties which may not be determinable within acceptable limits make it questionable whether this Aero-Inertial Control System should be attempted as a sole means of controlling. Also for multi-engine vehicles, the directional shift of thrust vector as well as the change in magnitude produced by an engine out may make it desirable to maintain the engine-gimbal capability.

#### DESCRIPTION OF MODEL

Consideration of the principles previously mentioned lead to the establishment of the model depicted in Fig. 4 with the symbols as defined within the paper.

It will be seen that this is a three mass system coupled together with pin connections. The three masses, as the subscripts imply, represent the engine, body (or booster), and the nose. The pin connections are designated G for gimbals of the engine and S for swivel of the nose. While the latter is recognized as being misleading nomenclature in that the action of both joints are about parallel axis, perpendicular to plane of the figure, it does allow a separate name for each. There is an aerodynamic-spring-force ( $A_{zi}$ ) attached to each segment at its center of pressure  $P_i$  for that segment plus an assumed steady drag force ( $A_{xi}$ ) at this location acting axial to its segment. In addition there is a thrust vector acting through the engine mass and axial to that segment.

#### DISCUSSION OF DYNAMICS

This will be seen to be a 5-degree-of-freedom system. Namely translation in the x and z direction of some mass, say  $M_N$ , rotation of the same  $M_N$  relative to the fixed references, rotation of  $M_B$  relative to  $M_N$ , and rotation of  $M_E$  relative to  $M_B$ . By neglecting relative motion between the masses in the x direction and by retaining the acceleration in the x direction for inertial effects, the problem is set up as a 4 degree of freedom system.

The equations are as follows:

The force equation is

$$\begin{aligned}
 \sum F_z &= 0 \\
 -F(\phi_N - \delta - \theta) - A'_{ZE}(\phi_N - \delta - \theta) + A_{XE}(\phi_N - \delta - \theta) \\
 &\quad + A'_{ZB}(\phi_N - \delta) + A_{XB}(\phi_N - \delta) \\
 &\quad + A'_{ZN}(\phi_N) + A_{XN}\phi_N = (-A'_{ZE} - A'_{ZB} - A'_{ZN})\alpha_w \\
 + M_E(\ddot{Z}_B - (G_B + G_E)(\ddot{\phi}_N + \ddot{\delta}) - \dot{G}_E \dot{\theta}) \\
 + M_B \ddot{Z}_B \\
 + M_N(\ddot{Z}_B + (S_B + S_N)(\ddot{\phi}_N + \ddot{\delta}) - S_N \ddot{\delta})
 \end{aligned} \tag{2}$$

The moment equation about cg. is

$$\begin{aligned}
 -F \left[ G_{cg} \theta + (Z_B - Z) + (G_{cg} - G_B) \phi_B \right] \\
 + A_{XE} \left[ G_{cg} \theta + (Z_B - Z) + (G_{cg} - G_B) \phi_B \right] \\
 - A'_{ZE} (\alpha_w + \phi_E - \frac{Z_E}{V} - \frac{P_{EF}}{V} \phi_E) (G_{FE} + G_{cg}) \\
 + A_{XB} \left[ (Z_B - Z) + (G_{cg} - G_B) \phi_B \right] \\
 - A'_{ZB} (\alpha_w + \phi_B - \frac{Z_E}{V} - \frac{P_{BB}}{V} \phi_B) (G_{PB} - G_{cg}) \\
 + A_{XN} \left[ S_{cg} \delta + (Z_B - Z) + (G_{cg} - G_B) \phi_B \right] \\
 - A'_{ZN} (\alpha_w + \phi_N - \frac{Z_N}{V} - \frac{P_{NN}}{V} \phi_N) (S_{cg} + S_{PN}) \\
 = I_E \ddot{\theta}_E + M_E \dot{V} (Z - Z_E) - M_E \ddot{Z}_E (G_{cg} + G_E) \\
 + I_B \ddot{\theta}_B + M_B \dot{V} (Z - Z_B) - M_B \ddot{Z}_B (G_{cg} - G_B) \\
 + I_N \ddot{\theta}_N + M_N \dot{V} (Z - Z_N) + M_N \ddot{Z}_N (S_{cg} + S_N)
 \end{aligned} \tag{3}$$

The force equation (2) may be re-written in the following form by assuming steady state conditions (zero translation and zero rotation) and by making some equation substitutions, namely geometric relations. These equations with expressions for the angle coefficients will be found in the appendix of the paper. The steady state condition allows the ejection of all derivatives including the aerodynamic damping terms from this force equation.

Thus:

$$C_F \phi_N + C_F \delta + C_F \beta = C_F \alpha_W \quad (4)$$

By making similar substitutions of geometry and again by neglecting the aerodynamic damping terms (since the immediate goal is to solve for the undamped natural frequency of the system), the moment equation is:

$$C_M \phi_N + C_M \delta + C_M \beta + I_M \ddot{\phi}_N + I_M \ddot{\delta} + I_M \ddot{\beta} = C_M \alpha_W \quad (5)$$

where the equation

$$\alpha_N = \alpha_W - \phi_N \quad (6)$$

is the undamped relation between wind angle  $\alpha_W$ , angle of attack of nose  $\alpha_N$ , and attitude angle of nose  $\phi_N$

$$\alpha_N = \alpha_W - \phi_N - \frac{\dot{z}_N}{V} + P_{NN} \frac{\dot{\phi}_N}{V} \quad (7)$$

would be the expression for including the induced angles of attack.

The force equation (4) is, as previously stated, in the steady state condition. By dropping the derivative terms, equation (5) is set in the steady state; i.e., no rotation (or translation in Z direction). Now adding a control equation which slaves  $\beta$  to  $\delta$ , there are three equations with three unknowns in terms of the wind angle  $\alpha_W$ . Thus:

$$\beta = \delta \quad (8)$$

$\beta$  and  $\delta$  are the engine "gimbal-angle" and nose "swivel-angle" respectively. The gain  $c_o$  is the slaving factor between the systems. This  $c_o$  is an interesting number and more will be said about it later.

Solving these three equations results in the following transfer functions:

$$\left. \frac{\delta}{\alpha_W} \right)_{SS} = \frac{C_F \alpha C_{M\delta} - C_M \alpha C_F \phi}{C_{M\delta}(C_F \delta + C_O C_{F\beta}) - C_F \phi(C_{M\delta} + C_O C_{M\beta})} \quad (9)$$

$$\left. \frac{\phi_N}{\alpha_W} \right)_{SS} = \frac{C_F \alpha (C_F \delta + C_O C_{M\beta}) - C_M \alpha (C_F \delta + C_O C_{F\beta})}{C_F \phi(C_{M\delta} + C_O C_{M\beta}) - C_{M\delta}(C_F \delta + C_O C_{F\beta})} \quad (10)$$

The basic control equation is:

$$\delta = a_0 \phi_N + b_0 \alpha_W + a_1 \dot{\phi}_N \quad (11)$$

Substituting equation (6) into (11) and dropping the  $\phi_N$  term for steady state gives,

$$\delta = a_0 \phi_N + b_0 (\alpha_W - \phi_N) \quad (12)$$

Hunt

Solving equations 9, 10 and 12 results in

$$\begin{aligned}
 & a_0 [(C_{M\delta} C_{F\delta} - C_{F\alpha} C_{M\delta}) + c_0 (C_{M\alpha} C_{F\beta} - C_{F\delta} C_{M\beta})] \\
 & + b_0 [(C_{M\phi} C_{F\delta} + C_{F\alpha} C_{M\delta} - C_{F\phi} C_{M\delta} - C_{M\alpha} + C_{F\delta}) + c_0 (C_{M\phi} C_{F\beta} - C_{F\alpha} C_{M\beta} \\
 & - C_{F\phi} C_{M\beta} - C_{M\alpha} C_{F\beta})] = C_{F\alpha} C_{M\phi} - C_{M\alpha} C_{F\phi}
 \end{aligned}
 \tag{13}$$

Another relationship involving  $a_0$  and  $b_0$  is required to determine these gain constants. This is given in the equation for the undamped natural frequency of the system and is obtained from equations 5, 7, 8 and 12 under the assumption that  $\alpha_w$  vanishes allowing the attitude to be the angle of attack.

Thus,

$$C_{M\phi} \phi_N + C_{M\delta} \delta + C_{M\beta} \beta + I_{M\phi} \ddot{\phi}_N + I_{M\delta} \ddot{\delta} + I_{M\beta} \ddot{\beta} = 0
 \tag{14}$$

and reduces in terms of  $\phi_N$ 's and  $\omega^2$

to,

$$C_{M\phi} + (a_0 - b_0)(C_{M\delta} + c_0 C_{M\beta}) = \omega^2 \{ I_{M\phi} + (a_0 - b_0)(I_{M\delta} + c_0 I_{M\beta}) \}
 \tag{15}$$

which yields,

$$\omega = \sqrt{\frac{C_{M\phi} + (a_0 - b_0)(C_{M\delta} + c_0 C_{M\beta})}{I_{M\phi} + (a_0 - b_0)(I_{M\delta} + c_0 I_{M\beta})}}
 \tag{16}$$



It should be noted that the rotation mode shapes are fixed by the two control conditions and that translation affects only the damping of this frequency.

Equations 13 and 16 establishes the relationship between the two gains  $a_0$  and  $b_0$  in terms of known structural and aerodynamic parameters, the undamped natural frequency in rotation of the system, and the gain  $c_0$ .

Since the rotational natural frequency is a problem common to all flight vehicles and since it is influenced by wind profile criteria, design philosophy, et cetera, it is assumed that this is a known parameter for solving these equations.

#### DISCUSSION OF GAIN $c_0$

The heuristic approach of determining  $c_0$  revealed some very interesting facts.

By making  $c_0$  infinitely large,  $\delta$  would become zero and conventional engine control would exist. Conversely when  $c_0$  is zero,  $\delta$  vanishes and only nose control exists. As might be expected several intermediate, but arbitrary, values were selected.

In order to study variations in the gain  $c_0$ , a configuration was used which had the gimbals at about 7% of the length and the swivel at about 70%. The swiveled nose had a slightly smaller diameter than the booster with the usual nose taper to the base of a winged vehicle.

The aerodynamic forces of the uncanted vehicle were applied according to the angle of attack of the segment it was acting on.

The vehicle was placed in steady state drift minimum equilibrium with  $\alpha_w$  constant. This drift minimum is defined by Dr. Hoelker (Ref. 1) as  $Z = 0$ . Keeping  $\alpha_w$  constant while varying  $c_0$  amounts to shifting the attitude to allow all the external forces to balance out for this condition of wind and velocity.

It is important to keep in mind that this represents a study of the same system varying only  $c_0$ .

Fig. 5 shows the results of the investigation under the stated conditions. The  $c_0 = \infty$  curve shows engine control. The  $c_0 = 0$  curve shows nose control.

The segment from about 80% of the length forward did not change sign in bending moments but even here the minimum value is about 17% of the maximum at that station.

With such a system this  $c_0$  term can be a powerful tool. By proper selection of its value the bending moment (or shear) can be

minimized for any station. Should angle of attack on the payload be a problem, this could also be minimized.

There are numerous "gain" terms in common usage today, such as, attitude gain  $a_0$  and aerodynamic gain  $b_0$  for the control equations. Conceding that what is to be mentioned is abstract from the previous terminology, the structural engineers that generated this paper have dubbed  $c_0$  the "structures gain".

Originally it was intended to discuss strictly Aero-Inertial Control, the case where  $c_0 = 0$ . However, this set of curves show that there would be advantages to a combined control system, therefore, a more general study was made. A more descriptive title would have been "Aero-Inertial-Engine Control" or even  $\alpha - \delta - \theta$  control.

The second from the bottom curve represents what is considered the minimum overall bending moment. After the five previous curves were generated, a scheme was devised to locate this  $c_0$  value. A cross plot of the moment diagram for four key points in bending moment versus  $c_0$  resulted in the curves shown in Fig. 6. The dashed line is the arithmetical mean of the curves and where it crossed the zero moment gave a  $c_0$  value for minimum moments on the system.

#### FUTURE STUDIES

A similar study is underway to investigate the influence of the dynamic response for each of these cases on the bending moment.

The effects of sloshing, bending mode coupling, torsional mode coupling and roll control with a variable roll moment of inertia, all should be given careful consideration. Time permitting these will be investigated.

Before any serious consideration could be given to actual application of such a system, extensive investigation of the aerodynamics would be required.

#### CONCLUSIONS

The purpose of this paper has been to establish a concept of Aero-Inertial Control, to show trends in terms of structural loads which might be expected from such a concept, and to provide an outline of procedure which might be followed in arriving at an end product.

Should bending moments be a problem on a particular vehicle, nose control alone is good, adding engine control to this is better, and proper selection of the ratio between these two controls is best.

Hunt

REFERENCE

1. Hoelker, R. F.: The Principle of Artificial Stabilization of Aerodynamically Unstable Missiles (U), ABMA Report No. DA-TR-64-59, 25 Sept 1959

## DEFINITION OF SYMBOLS

A	aerodynamic force	lb
$a_0$	control gain factor	non-dimensional
$a_1$	damping gain factor	non-dimensional
B	station of booster body center of gravity	inches
$b_0$	control gain factor	non-dimensional
$c_0$	slaving factor	non-dimensional
CG; cg	center of gravity	non-dimensional
$C_F$	force coefficient	lb/deg
$C_M$	pitching moment coefficient	$\frac{\text{in-lb}}{\text{deg}}$
E	station of center of gravity of the engine	inches
e	eccentricity distance of the inertial force vector of the swiveled nose to the thrust vector	inches
F	thrust	lbs
G	station of engine gimbals	non-dimensional
I	moment of inertia	slug ft <sup>2</sup>
i	arbitrary point	non-dimensional
M	mass	slugs
N	station of nose center of gravity	inches
$P_i$	station of the center of pressure of segment i	inches
S	swivel point of the nose	non-dimensional
V	velocity	ft/sec
W	relative wind	non-dimensional
X	distance along the abscissa	inch
Z	distance along the ordinate	inch

## Hunt

$\alpha$	relative wind angle	degree
$\beta$	engine gimbal angle relative to longitudinal axis of engine and body	degree
$\delta$	angle of nose deflection relative to longitudinal axis of nose and body	degree
$\emptyset$	angle of longitudinal axis relative to velocity vector	degree
$\omega$	angular frequency	rad/sec

### Examples of the use of the subscripts

$A_{2N}$	aerodynamic lift force in the Z direction on the nose
$P_{NB}$	distance from the center of pressure on the nose to the cg of the body. This would be a negative distance

APPENDIX

The following are auxiliary equations and coefficient definitions for both the force and moment equations, (4) and (5) respectively.

$$\phi_B = \phi_N - \delta$$

$$\phi_E = \phi_N - \delta - \beta$$

$$Z_N = Z_B - B_N \phi_B - S_N \delta$$

$$Z_t = Z_B - B_E \phi_B - L_G \beta$$

$$\begin{aligned} -F(\phi_N - \delta - \beta) + A'_{ZE}(\alpha_W - \phi_N + \delta + \beta) + A_{XE}(\phi_N - \delta - \beta) \\ + A'_{ZB}(\alpha_W - \phi_N + \delta) + A_{XB}(\phi_N - \delta) \\ + A'_{ZN}(\alpha_W - \phi_N) + A_{XN}\phi_N = 0 \end{aligned}$$

FORCE EQUATION (4)

$$C_{F\phi}\phi_N + C_{F\delta}\delta + C_{F\beta}\beta = C_{Fa}\alpha_N$$

$$C_{F\phi} = \{F + A'_{ZE} + A'_{ZB} + A'_{ZN} - A_{XE} - A_{XB} - A_{XN}\}$$

$$C_{F\delta} = -\{F + A'_{ZE} + A'_{ZB} - A_{XE} - A_{XN}\}$$

$$C_{F\beta} = -\{F + A'_{ZE} - A_{XE}\}$$

$$C_{Fa} = \{A'_{ZE} + A'_{ZB} + A'_{ZN}\}$$

MOMENT EQUATION (5)

$$C_{M\phi}\ddot{\phi}_N + C_{M\delta}\ddot{\delta} + C_{M\beta}\ddot{\beta} + I_{M\phi}\ddot{\phi}_N + I_{M\delta}\ddot{\delta} + I_{M\beta}\ddot{\beta} = C_{M\alpha}\ddot{\alpha}_w$$

$$C_{M\phi} = \{FB_{CG} + A'_{ZE}P_{ECG} - A_{XE}B_{CG} + A'_{ZB}P_{BCG} - A_{XB}B_{CG} \\ + A'_{ZN}P_{NCG} - A_{XN}B_{CG} - M_E\dot{V}E_B + M_N\dot{V}B_N\}$$

$$C_{M\delta} = + \{-FB_{CG} - A'_{ZE}P_{ECG} + A_{XE}B_{CG} - A'_{ZB}P_{BCG} + A_{XB}B_{CG} \\ + A_{XN}B_{CG} - A_{XN}S_{CG} + M_E\dot{V}E_B - M_N\dot{V}B_N\}$$

$$C_{M\beta} = + \{-FG_{CG} - A'_{ZE}P_{ECG} + A_{XE}G_{CG} + M_E\dot{V}E_G\}$$

$$I_{M\phi} = - \{I_E - M_E E_{CG}E_B + I_B + I_N + M_N N_{CG}B_N\}$$

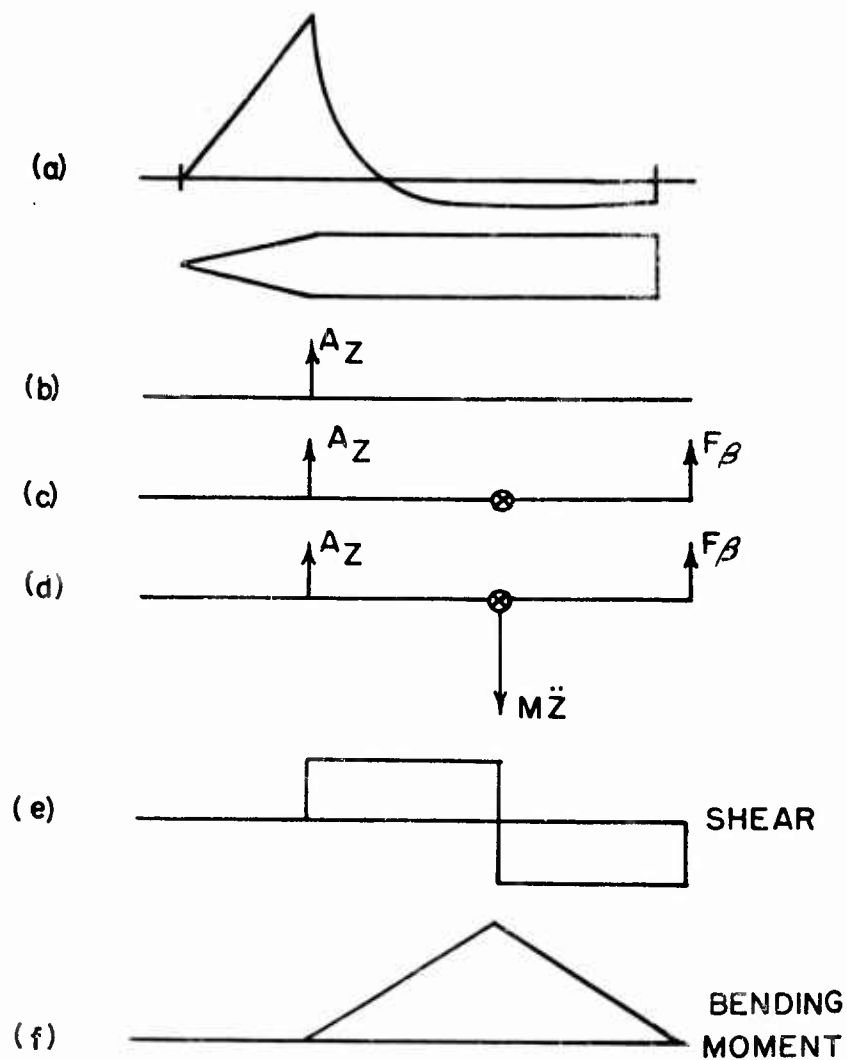
$$I_{M\delta} = - \{-I_E + M_E E_{CG}E_B - I_B - M_N N_{CG}B_N\}$$

$$I_{M\beta} = - \{-I_E + M_E E_{CG}E_G\}$$

$$C_{M\alpha} = \{A'_{ZE}P_{ECG} + A'_{ZB}P_{BCG} + A'_{ZN}P_{NCG}\}$$

$$(Z_B - Z)(-F + A_{XE} + A_{XB} + A_{XN} + M_E\dot{V} + M_B\dot{V} + M_N\dot{V}) = 0$$

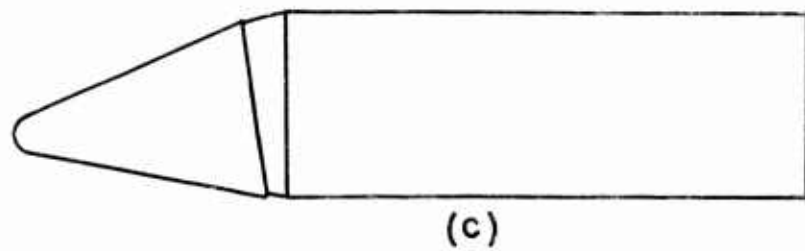
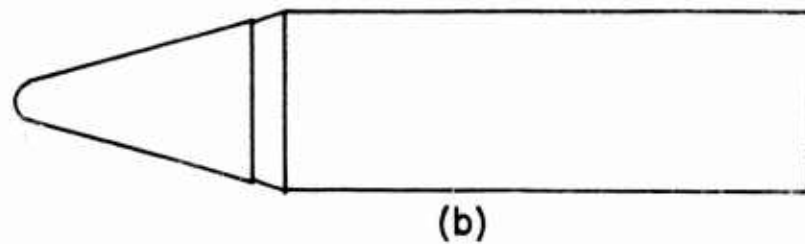
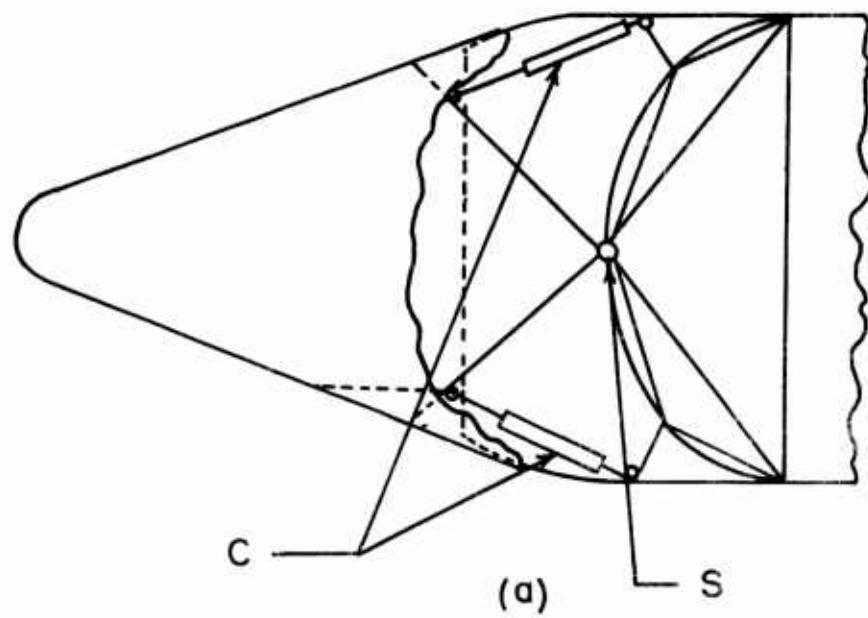
$$\ddot{Z}_B \{-(G_{CG} + G_E)M_E - (G_{CG} - G_B)M_B + M_N(S_N + S_{CG})\} = 0$$



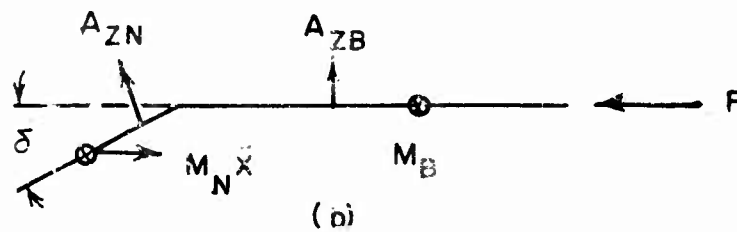
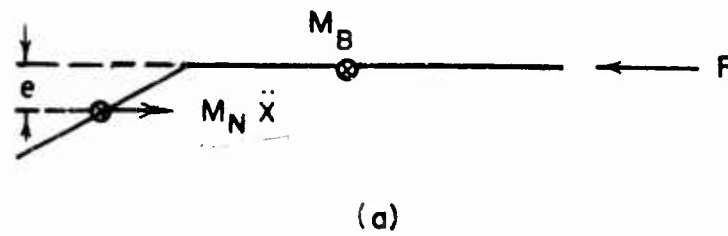
SIMPLIFIED LOADS DIAGRAM

FIG. 1





SKETCH OF POSSIBLE NOSE GIMBAL SCHEME  
FIG. 2

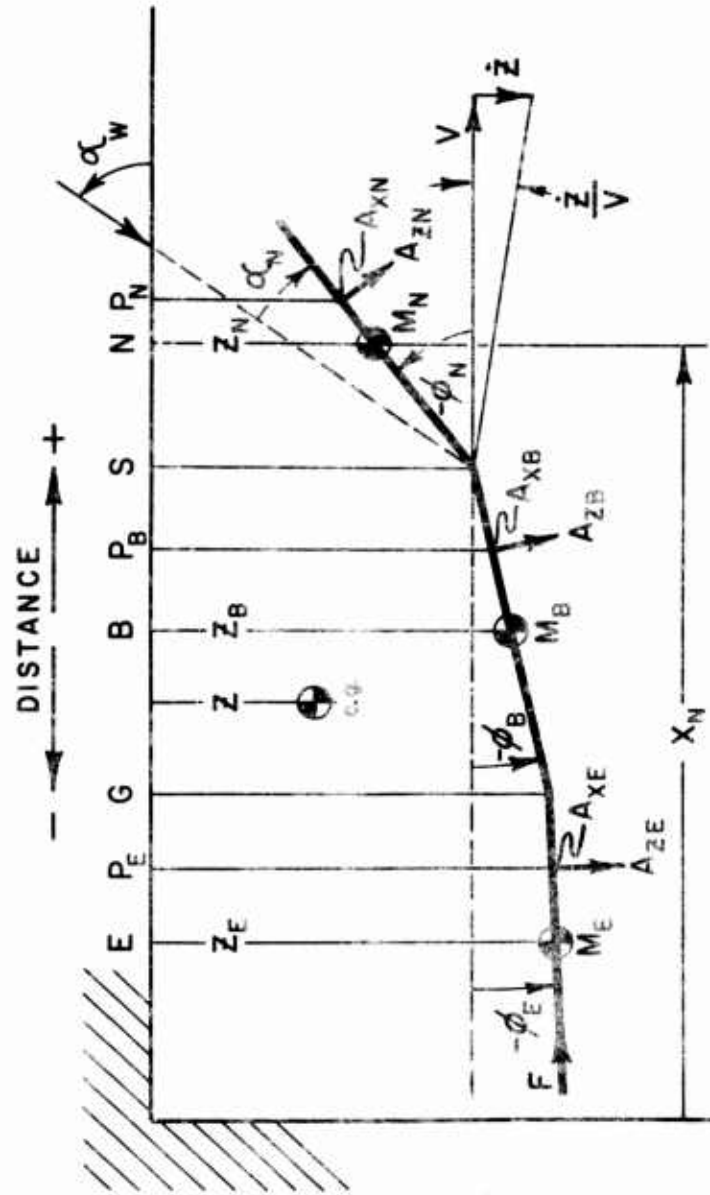


SIMPLE FORCE DIAGRAM FOR AERO INERTIAL  
CONTROL SYSTEM

STATIC EQUILIBRIUM ABOUT  $M_B$

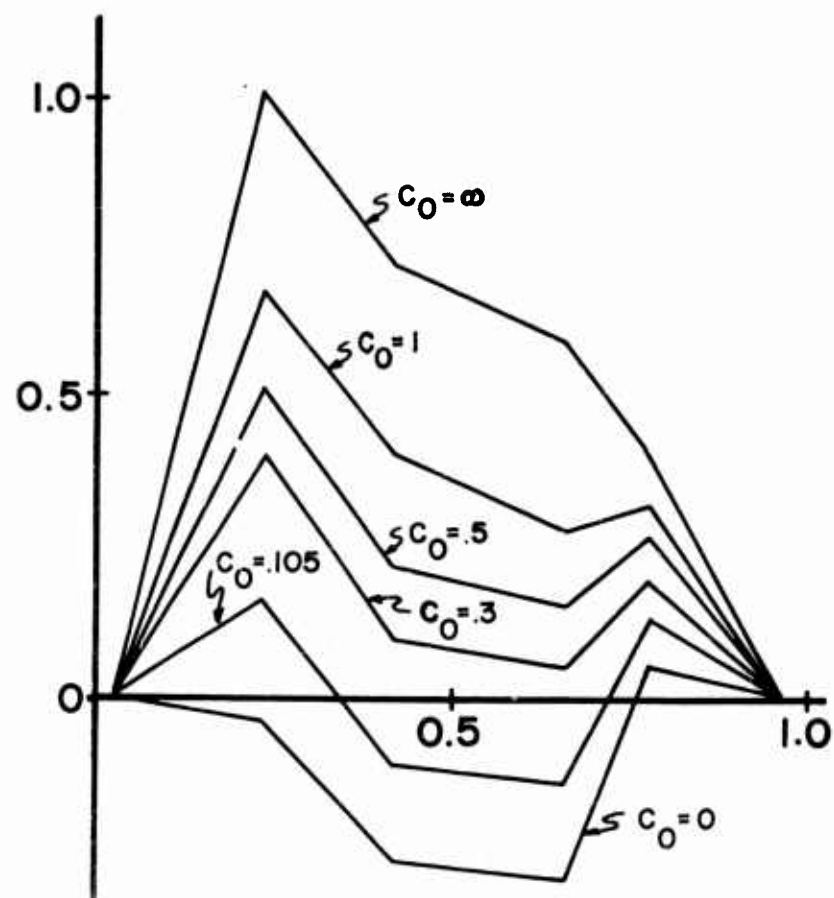
$$A_{ZN} P_{NB} + A_{ZB} P_{BB} = M_N \ddot{X} S_N \delta \quad (1)$$

FIG. 3



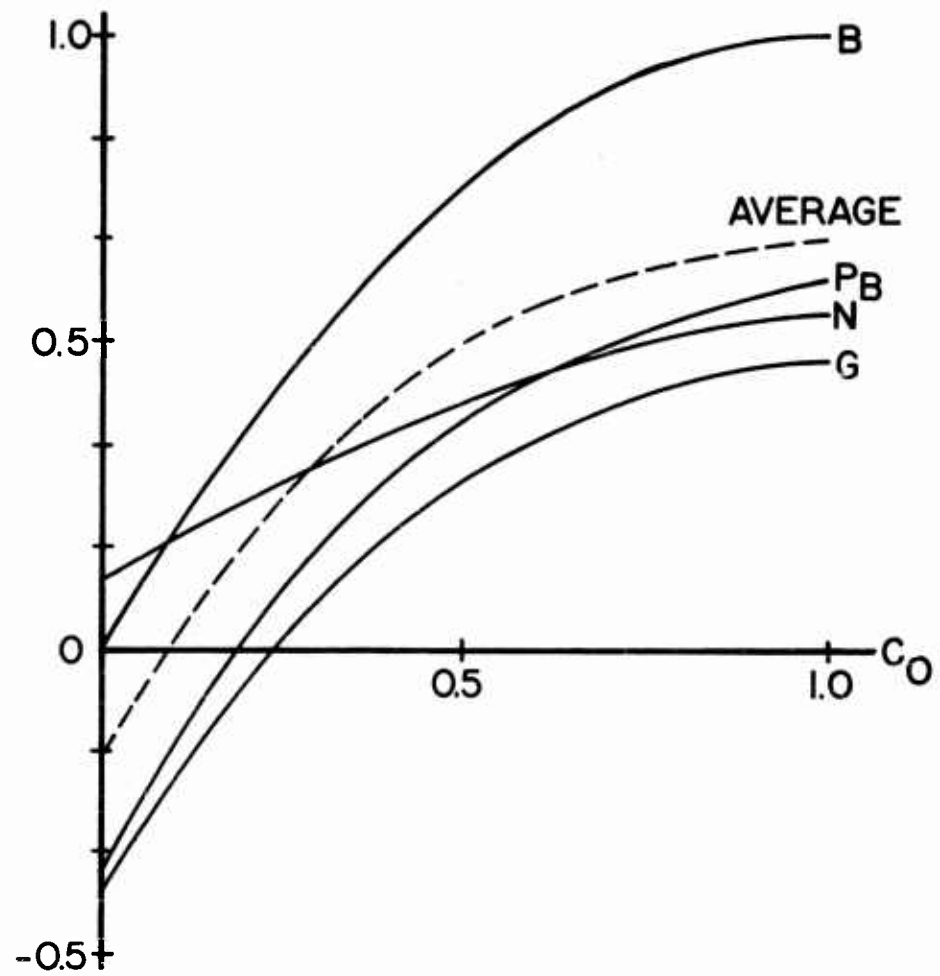
SKETCH OF DYNAMIC MODEL

FIGURE 4



NORMALIZED BENDING MOMENT  
V.S.  
BODY STATION AS FUNCTION OF  
ENGINE ACTUATOR GAIN

FIGURE 5



MINIMIZING BENDING MOMENT BY VARYING  $C_O$

FIGURE 6

A DYNAMIC LOADS COMPARISON FOR A RANGE OF MISSILE  
CONFIGURATIONS UTILIZING TWO CONTROL SYSTEM CONCEPTS

R. T. Wagner  
Boeing Airplane Company  
Aero-Space Division  
Seattle, Washington

SUMMARY

Boost phase dynamic loads due to wind shear are analyzed for a range of vehicle sizes and thrust-to-weight ratios. Bending moment comparisons are shown for each configuration initially using an attitude referencing control system and subsequently utilizing a control system which references angle of attack and attitude.

Configurations consist of winged payloads ranging from 80 to 1666 square feet of lifting area. Thrust-to-weight ratio varies from 1.2 to 2.5. Payload weights range from 1000 pounds to 100,000 pounds. Each vehicle was specifically designed to place its payload in a 200 nautical mile polar orbit. The vehicles are launched from a vertical position and fly a gravity turn trajectory through a single Vandenberg AFB wind sounding estimated at less than 1% probability. The entire group of hypothetical study vehicles was designed to a consistent set of ground rules.

Loads analyses were carried out utilizing two rigid and one flexible degree of freedom. Time varying parameters were used in a digital program which applies a finite difference technique to solve the differential equations.

For the Vandenberg wind sounding, the results of the comparison study show a substantial decrease in bending loads for the attitude plus angle of attack referencing control system.

INTRODUCTION

The preliminary design dynamic loads specialist is

sometimes desirous of quick estimates of loads magnitudes for typical but unanalyzed configurations. Due to the many couplings which exist and the general complexity associated with several time varying parameters, loads generalization from one configuration to another is risky. It was therefore desired that a large range of configurations be selected so that results could be of wide use. While a handbook approach to dynamic loads is impossible for optimum design, a "feel" for loads magnitudes is helpful in preliminary structural design and in assessing results of more detailed loads analyses. The study results permit a look at dynamic loads for a broad range of booster sizes, payload sizes, and thrust-to-weight ratios and a choice of two control systems. The mission, firing site, type of payload, and environment are arbitrary but selected to be of interest.

In addition to covering a wide range of vehicles, it was an objective of this paper to completely redesign each configuration to carry out its orbital mission such that each changing parameter reflects the influence of it upon the other major parameters. As an example, the increase of thrust-to-weight ratio results in a resized booster due to decreased propellant requirement and different engine size. New trajectory, new skin gage sizing, and new mode shapes are utilized. This approach is in contrast to the type of trade study which changes a parameter, and assumes all other parameters stay constant. Each approach has its limitations but both are useful tools in developing design trends. Much of the usefulness of the approach taken here depends upon the soundness of the design ground rules. They must be typical of systems for which they are used. The ground rules selected for this study are considered typical of current systems with some favoritism in the designs towards keeping loads as low as possible.

#### THE STUDY VEHICLES

Nine study vehicles were utilized with two control systems, making a total of eighteen vehicles analyzed. The overall configurations are shown in Figures 1, 2 and 3. Summary weights are given in Table 1. Three payload weights of 1000, 10,000, and 100,000 pounds and three thrust-to-weight ratios of 1.2, 1.85, and 2.5 comprise the matrix of nine vehicles. A relative comparison of vehicle size is shown in Figure 4 for a thrust-to-weight ratio of 1.2.

The ground rules which designed all vehicles were selected to be typical of current systems. Payloads are boosted into a 200 nautical mile circular polar orbit, using liquid rocket boosters. First stages utilize a liquid oxygen and RP-1 propellant combination and all upper stages use liquid oxygen and liquid hydrogen. Engines are "rubberized" to provide the desired thrust-to-weight ratio. A gravity turn, non-

rotating earth trajectory is used with the total required velocity increment equally divided between the number of stages. Velocity losses were assumed to vary from 35% for a thrust-to-weight ratio of 1.2 to 25% for a thrust-to-weight ratio of 2.5.

Delta winged lifting payloads were selected with a 75° sweepback angle. The fuselage consists of a simple right circular cylinder with diameter equal to one fourth of the wing span. Lifting areas were arrived at by the payload weight, geometry, and a constant density of 14 pounds per cubic foot within the fuselage. Structural weight of the payload vehicle is assumed .4 of the total payload weight.

Tandem booster design is used with two stages for the 1000 and 10,000 pound payloads and a three stage booster for the 100,000 pound payload. Stage  $\lambda$  values assumed are shown in Table 2. Tanks are pressurized monocoque construction using 301 stainless steel. Oxidizer tanks are located forward of fuel tanks except for the third stage. Tank heads have a height to diameter ratio of .35. Tank diameters selected are shown in Figures 1, 2, and 3. Interstages are aluminum alloy stringer stiffened construction. The distance between tank heads is equal to engine nozzle length +  $L_f$  + 10 inches where  $L_f = 6.38 \times (T/1000)^{.246}$ . See Reference (1). A 20° semivertex angle is used for the forward interstage. Aft skirt lengths are equal to the aft tank head height +  $L_f$  + .75 (engine nozzle length). All tanks are designed to accommodate 3% excess propellant by weight and allow for ullage space equal to 1% of the useable propellant volume.

Skin gages are designed on the basis of tank pressure necessary to satisfy elastic stability and subsequent stressing for hoop tension. A safety factor of 1.4 is applied to limit combined load. The preliminary loads for sizing structure and determining overall bending stiffness consider ground wind, axial load, and bending moments at maximum dynamic pressure obtained by static pitch trim analysis.

Control systems are assumed perfect with no time lags. Sensors do not sense bending, thus eliminating flexibility from the control laws. Gains are adjusted to provide constant pitch frequencies of .5 cps, .3 cps, and .2 cps for the 1000 pound, 10,000 pound, and 100,000 pound payload vehicles respectively. This is a convenience for obtaining a consistent loads comparison. Ordinarily gains are determined by stability and guidance requirements and the vehicle short period characteristics are a result of these gains.

#### CONTROL SYSTEM CONCEPTS

Two control system concepts were applied to each



missile configuration to illustrate the effect of control system concept on the dynamic loads for a wide range of configurations. Each system depends upon gimbaling of all first stage rocket thrust to provide a control moment. The basic difference is the feed-back input sensed and the resulting response of the vehicle.

The attitude sensing system used has a simple control law as follows:

$$\delta\tau = K_{\theta} \theta_s + K_{\dot{\theta}} \dot{\theta}_s$$

where:  $\delta\tau$  = gimbal angle

$K_{\theta}$  = attitude gain

$K_{\dot{\theta}}$  = rate gain

$\theta_s$  = sensed pitch displacement  
or attitude error ( $\theta_s = \theta$ )

In our simple case the rigid pitch only is sensed when the lift due to the wind induced angle of attack causes the missile to rotate out of the wind flow. The thrust vector required to rotate the missile back to the flight path is in the same direction as the lift force and hence the missile translates freely.

The angle of attack and attitude sensing control system is outlined in (2). The simple control law for this system is as follows:

$$\delta\tau = K_{\theta} \theta_s + K_{\alpha} \alpha_s$$

where:  $K_{\alpha}$  = angle of attack control gain

$\alpha_s$  = sensed angle of attack =  $\theta + \frac{W_s \cdot h}{U}$

$h$  = translational velocity

$W_s$  = wind speed (normal component)

$U$  = flight velocity

$\theta$  = rigid pitch

Here again only rigid responses are sensed with flexibility omitted from the control law. With this control system the angle of attack and attitude gains are programmed in such a fashion as to rotate the perturbed missile back through the flight path and into the wind flow. An equilibrium of lateral forces is achieved through a proper ratio of gain magnitudes such that the drift or lateral translation velocity of the vehicle with respect to the flight path is kept to a minimum. The steps leading to derivation of gain values are given in Reference (2). The rigidly derived expressions used here are as follows:

$$K_0 = \frac{\omega_0^2}{\frac{T l_T}{I_0} \left[ 1 + \frac{(g \sum C_{L\alpha_k} S_k)(1 + l_P/l_T)}{T-D} \right]}$$

$$K_\alpha = \left[ \frac{(g \sum C_{L\alpha_k} S_k)(1 + l_P/l_T)}{T-D} \right] K_0 + \frac{g \sum C_{L\alpha_k} S_k}{T} \left( \frac{l_P}{l_T} \right)$$

In order to keep a constant pitch frequency, both gains must be programmed throughout the trajectory. While zero drift is not attained when inserting the rigidly derived gains in a flexible system, the drift is considerably minimized.

#### METHOD OF ANALYSIS

A lumped mass three degree of freedom representation of the system was utilized with rigid pitch and translation modes and the first bending mode included. Mode shapes were obtained by use of a digital program based upon a Myklestad type of solution. (3)

The trajectories used are characterized by a vertical rise to a velocity of 350 feet per second, an instantaneous tilt, gravity turn through first stage burnout, and upper stage programming to arrive at the desired burnout velocity, altitude and attitude. Since the vehicles were launched into a polar orbit, a non-rotating earth trajectory was used. Trajectories were based on the 1959 ARDC model atmosphere. (4)

Lift curve slopes for the winged payloads are shown in Figure 5. Momentum theory was utilized for the conical inter-stages with the center of pressures moved aft to correspond with a typical distribution obtained by second order shock expansion theory. (5) The resulting modal, aerodynamic, vehicle geometry, and trajectory data were inserted into a digital computer program which calculates the required control gains (6), the equations of motion, and the loads equations. (7). The program calculates these equations at a specified number of time points throughout the flight trajectory, stores the data, and automatically feeds it into the final portion of the program which solves the variable coefficient equations of motion with the desired forcing function and uses the time history of the vehicle responses to solve the loads equations. Since the maximum bending moment occurs prior to first stage burnout the program was terminated at five seconds beyond the peak wind speed.

Six time points were used for the equations of motion and loads coefficients, and 15 time points were used in the forcing function. Linear interpolation was used throughout, and the time varying systems of differential equations were solved at .01 second intervals to form the "continuous" simulation solution. The numerical finite difference solution uses the Adams-Moulton formulas and is based upon a method outlined in Reference (8).

The forcing function is shown in Figure 6. A 17 February 1959 wind sounding for Vandenberg AFB was selected. (9). It is estimated at less than 1% probability and is one of two such profiles recommended for design of vehicles launched from this particular site. It is unique in its lack of a sharp nosed wind shear spike.

## RESULTS

In the interpretation of the results of this study it is important to keep in mind that our variation in range of payloads implies a range of different size boosters each of which is designed according to the study ground rules to specifically put this payload into a 200 nautical mile polar orbit. Hence, the mode shapes, frequencies, flight parameters, vehicle responses, and the wind shear loads reflect the combined effect of all the contributing parameters and we cannot isolate the effect of a single parameter. The sole exception to this is in the comparison of the two control systems. The vehicles undergo no design modification in the interchange of control systems.

### Modal Results

Typical mode shapes are shown in Figure 7 for vehicles with 1,000, 10,000 and 100,000 pound payloads. The vehicles are designed quite stubby, particularly at the extremes of the payload range. This is shown in Figure 8 which plots a fineness parameter. Hence, the vehicles possess good rigidity, with the largest vehicle having a minimum first bending mode frequency of 1.6 cycles per second. The range of first bending mode frequencies is shown in Figure 9. One can refer back to Figure 8 to find the fineness parameter which is associated with these frequencies.

### Trajectory Results

The equations of motion and the loads equations are heavily dependent upon the time histories of dynamic pressure and the dynamic pressure divided by the flight velocity. A feel for the maximum values of these flight parameters as a function of vehicle size and thrust to weight ratio is shown in Figures 10 and 11. They are primarily influenced by thrust-to-weight ratio, but vary somewhat with the size of the missile.

### Vehicle Responses

The variation in vehicle responses as a function of control system concept is illustrated for a 10,000 pound payload vehicle with a thrust-to-weight ratio of 1.85. Figure 12 shows the two pitch responses as the vehicle is flown through the wind sounding. With an aerodynamically unstable vehicle and attitude referencing control the vehicle tends to rotate out of the wind flow. With angle of attack plus attitude feedback and a proper ratio of gains the missile rotates into the wind flow. The gains are ratioed in such a fashion that drift velocity is minimized. The drift velocities for the two control schemes are shown in Figure 13. The drift velocity for the attitude plus angle of attack control reaches a sizeable magnitude since these gains were not optimized. However, there is considerable lag and for a given time in the trajectory the drift velocities are quite different. The effect of thrust-to-weight ratio on the drift velocity responses is shown by comparing Figures 13 and 14. The comparison shows that drift velocities are decreased for a lower thrust-to-weight ratio, and that the greater reduction occurs with the attitude plus angle of attack control system. Typical time histories of the control gains for the two control systems are given in Figure 15. Angle of attack gain must be set zero at launch due to the large angles of attack which are possible immediately following the launch.

### Wind Shear Bending Moments

The loads results are summarized in plots of the peak bending moment obtained versus the size of payload boosted into orbit. Size of payload is plotted in terms of weight in Figures 16 and 17. Figure 16 illustrates the attitude control concept and Figure 17 shows the loads for the attitude plus angle of attack control system. Figures 18 and 19 repeat the loads for each control system with the payload size plotted in terms of lifting area instead of weight.

Figures 20, 21 and 22 illustrate typical bending moment distribution over the entire length of the missile. Control system comparisons are shown in each figure. Figures 20 and 21 are similar in shape since both are two stage vehicles. Figure 22 shows the load distribution for the three stage design with the second stage oxidizer tank located forward of the fuel. The result is a flat peak since the bending moment built up by the glider aerodynamics is leveled off by the inertia force of the heavy second stage oxidizer tank located well forward.

Figure 23 is a plot of peak bending moments versus thrust-to-weight ratio for payload sizes of 1,000, 10,000 and 100,000 pounds. The control system comparison is shown here also.

Figure 24 illustrates a typical time history plot of the maximum bending moment on the vehicle as it flies through the Vandenberg wind sounding. Each control concept is illustrated. For the attitude control the loads peak at the maximum  $q/U$  point of the trajectory. The attitude plus angle of attack control scheme causes the loads to typically peak a few seconds later than the maximum  $q/U$  time point.

It is of interest to note the results of a comparison between the three degree of freedom IBM-704 solution which includes all unsteady responses, and a hand solution which assumes that the unsteady responses in pitch and bending can be neglected (10). Setting these terms equal to zero allows one to reduce the three degree of freedom system to a single differential equation in which translational velocity is the dependent variable. The hand solution employed five time increments in which the forcing function is considered linear and the variable parameters are taken at the midpoint of each increment. The response at the end of each time increment serves as initial conditions for each successive time increment. Results are compared in Table 3 for a single vehicle using both control system concepts. The technique has proven remarkably accurate for vehicles with high rigidity and forcing functions without high frequency disturbances likely to cause large dynamic magnification.

#### CONCLUSIONS

From the loads comparison between the two control system concepts, the major conclusion is that bending moments are substantially reduced by the attitude plus angle of attack control system when the flight environment contains no high frequency disturbances. It is of interest to note here that for gusts and sharp shear reversals previous analyses comparing the attitude control with the attitude plus angle of attack control show that the loads are not changed significantly using a wind profile with a 50 feet per second per 1000 feet shear reversal, and that a (1-cosine) critically phased gust could produce larger loads with this control system. (11).

The results also show that the major loads increase for a given size winged payload occurs in the thrust-to-weight range of 1.2 to 1.85. Increasing the thrust-to-weight ratio from 1.85 to 2.5 produced a substantially smaller increase for the larger size vehicles. For small vehicles the increase in bending moment was nearly linear for the range of thrust-to-weight ratios from 1.2 to 2.5. The increase of translational velocity with thrust-to-weight ratio appears to be an important factor. The effect of increased drift is to alleviate the wind induced angle of attack, and increase the inertia forces which

Wagner

tend to cancel loads built up by the glider aerodynamics. This effect becomes less important as the payload aerodynamics become smaller. Ballistic payloads would probably show a more linear increase in loads with increasing thrust to weight ratio. Another effect of importance is the shorter length of the missile as thrust-to-weight ratio is increased. This is due to lower velocity losses in boost and hence less propellant is required to boost the same weight into the same orbit.

#### ACKNOWLEDGEMENT

The author wishes to express his gratitude to personnel in the Structures Technology Department and the Flight Technology Department for their programming assistance and recommendations in the preparation of the manuscript.

REFERENCES

- (1) Report No. LRP 153, Revision A, Aerojet General Corporation
- (2) Hoelker, R. F., "The Principle of Artificial Stabilization of Aerodynamically Unstable Missiles", Army Ballistic Missile Agency Report No. DA-TR-64-59.
- (3) Holt, J. F., "Lateral Vibrations of Single Beams, Description of Input and Output", Space Technology Laboratories, Inc., October, 1959.
- (4) Minzner, R. A.; Champion, K.S.W.; Pond, H.L.; The ARDC Model Atmosphere, 1959", AFCRC-TR-59-267, August, 1959
- (5) Muth, D. V., "On the Limits of Missile Flexibility Using a Proportional Feedback Autopilot System", Boeing Airplane Company Document D2-6764, July, 1960.
- (6) Clingan, B. E., "Effect of Refinements in Control System Representation and Variation of Control System Parameters on Dynamic Loads Due to Wind Shear", Loads and Acoustics Research Memorandum No. 9, Boeing Airplane Company, March, 1960.
- (7) Belanger, J. R., "An IBM Method for Calculating Coefficients to Equations Describing Missile Motion", Loads and Dynamics Unit Research Memorandum No. 26, Boeing Airplane Company, December, 1960.
- (8) Conte, S. D., "Some Experiments in the Numerical Solution of Differential Equations at the Ramo-Wooldridge Corporation", Proceedings of the Mathematics Committee of the USE Organization, Dayton, Ohio, April 25-26, 1957.
- (9) Saimeia, H. A.; Sissenwine, N., "Additional Note - Strong Vertical Wind Profiles and Upper Level Maximum Wind Speeds over Vandenberg Air Force Base", April, 1960
- (10) Ayvazian, M., "Quasi-Steady Wind Shear" Structures Technology Department Coordination Sheet 5523CS-2-53, Boeing Airplane Company, June, 1960.
- (11) Ayvazian, M.; Holsapple, K., "Saturn C-2 Vehicle Loads Study", Boeing Airplane Company Document D2-10730, March, 1961.

## LIST OF SYMBOLS

$\sum C_{L_k} S_k$	Summation of lifting area increments times their lift curve slopes
D	Total drag
D	First stage diameter
$\dot{h}$	Translation or drift velocity
$I_o$	Pitch inertia about the missile c.g.
$K_\theta$	Attitude control gain
$K_{\dot{\theta}}$	Attitude rate control gain
$K_\alpha$	Angle of attack control gain
L	Total length of the missile
$l_T$	Distance from missile c.g. to the thrust center
$l_P$	Distance from missile c.g. to the aerodynamic center of pressure
$L_F$	Distance from aft end of tank head to throat area of engine
q	Dynamic pressure
S	Lifting area of winged payload
t	Trajectory burn time
T	Sea level thrust
T/W	Sea level thrust-to-weight ratio
U	Flight velocity
W	Gross weight of missile at launch
$W_{PL}$	Payload weight
$W_s$	Normal component of wind speed
$\alpha_s$	Sensed angle of attack
$\chi'$	Propellant weight to stage weight ratio
$\theta_s$	Sensed pitch displacement or attitude error
$\theta$	Rigid pitch displacement
$\omega_1$	First bending mode frequency
$\omega_\theta$	Pitch or short period frequency



Wagner

$W_{PL} = 1,000 \text{ lbs.}$

T/W= 1.2 1.85 2.50

Payload Weight	1,000	1,000	1,000
Second Stage Propellant	3,852	3,465	3,196
Second Stage Inerts	525	473	436
First Stage Propellant	60,508	54,325	47,618
First Stage Inerts	4,554	4,724	4,710

Launch Gross Weight = 70,439 63,987 56,960  
(lbs.)

$W_{PL} = 10,000 \text{ lbs.}$

T/W= 1.2 1.85 2.50

Payload Weight	10,000	10,000	10,000
Second Stage Propellant	38,520	36,300	34,811
Second Stage Inerts	5,253	5,424	5,667
First Stage Propellant	606,333	568,416	521,624
First Stage Inerts	45,638	49,427	51,589

Launch Gross Weight = 705,744 669,567 623,691  
(lbs.)

$W_{PL} = 100,000 \text{ lbs.}$

T/W= 1.2 1.85 2.50

Payload Weight	100,000	100,000	100,000
Third Stage Propellant	180,059	171,229	162,352
Third Stage Inerts	36,880	37,587	38,082
Second Stage Propellant	518,920	481,972	445,718
Second Stage Inerts	77,540	78,461	78,656
First Stage Propellant	3,209,864	2,913,124	2,624,409
First Stage Inerts	279,119	288,111	291,601

Launch Gross Weight = 4,402,382 4,070,484 3,740,818  
(lbs.)

SUMMARY WEIGHT STATEMENTS  
TABLE 1

T/W = 1.2 1.85 2.50 1.2 1.85 2.50 1.2 1.85 2.50

1st Stage	.93	.92	.91	.93	.92	.91	.92	.91	.90
2nd Stage	.88	.88	.88	.88	.87	.86	.87	.86	.85
3rd Stage	-	-	-	-	-	-	.83	.82	.81

$W_{PL} = 1000 \text{ lbs.}$   $W_{PL} = 10,000 \text{ lbs.}$   $W_{PL} = 100,000 \text{ lbs.}$

# PROPELLANT WEIGHT TO STAGE WEIGHT RATIOS

TABLE 2

Inches Bending Moments  $\sim 10^6$  in-lb

Body Station	IBM Solution	Hand Solution	IBM Solution	Hand Solution
0	.00	.00	.00	.00
208	.38	.38	.23	.23
252.5	.62	.64	.37	.37
352	1.26	1.27	.74	.74
477	1.81	1.82	1.07	1.08
547.5	2.15	2.16	1.27	1.30
622.5	1.42	1.43	.84	.85
672	.83	.84	.49	.49
722	.00	.00	.00	.00

Attitude Control Attitude Plus Angle of Attack Control

$W_{PL} = 1000 \text{ lbs.}, T/W = 1.2$

# SOLUTION COMPARISON

TABLE 3

Wagner

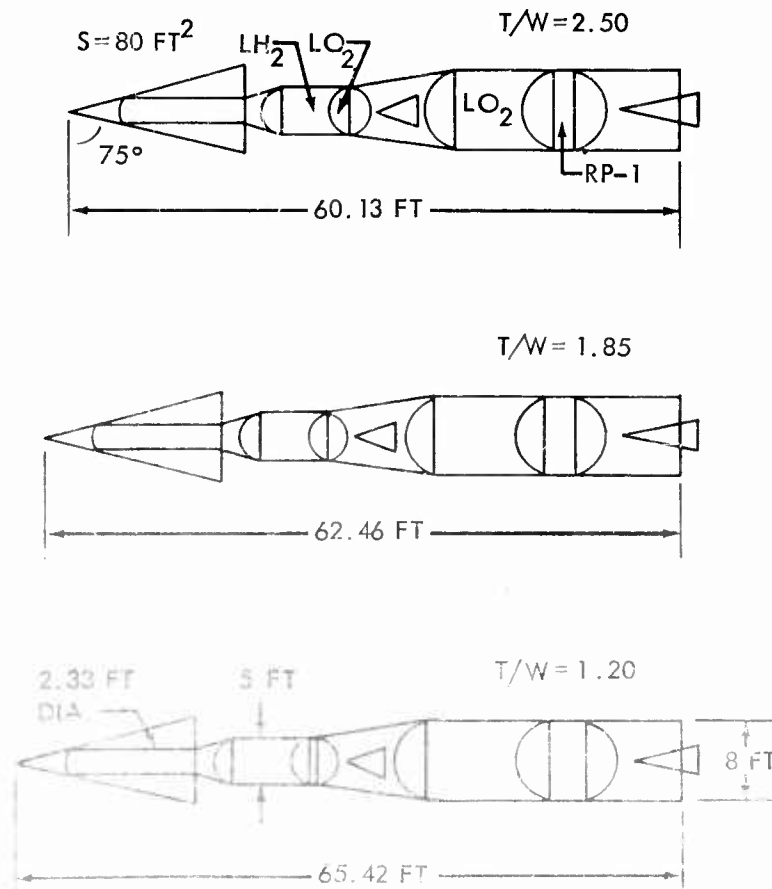


FIGURE 1 - 1000-POUND PAYLOAD VEHICLES

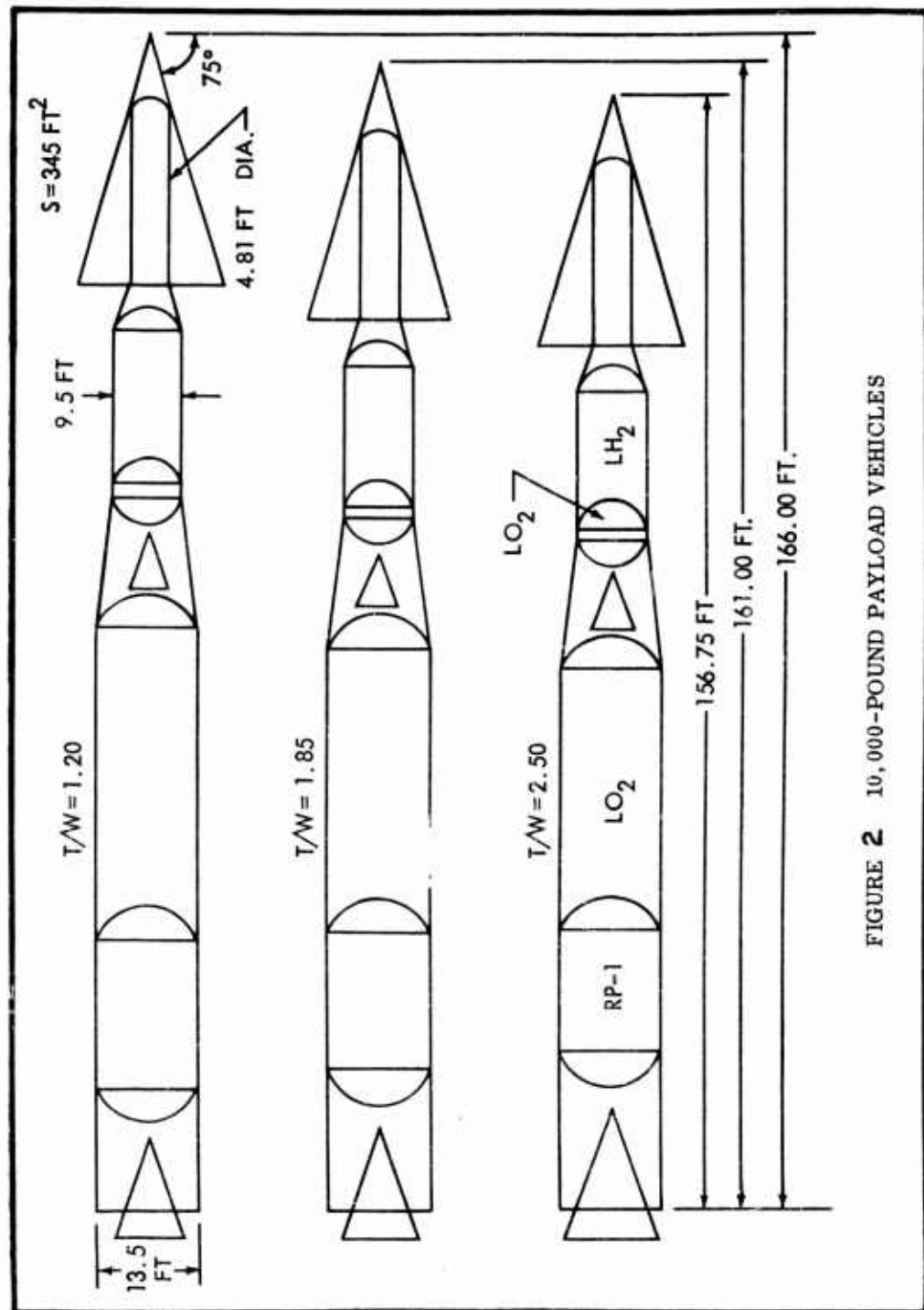


FIGURE 2 10,000-POUND PAYLOAD VEHICLES

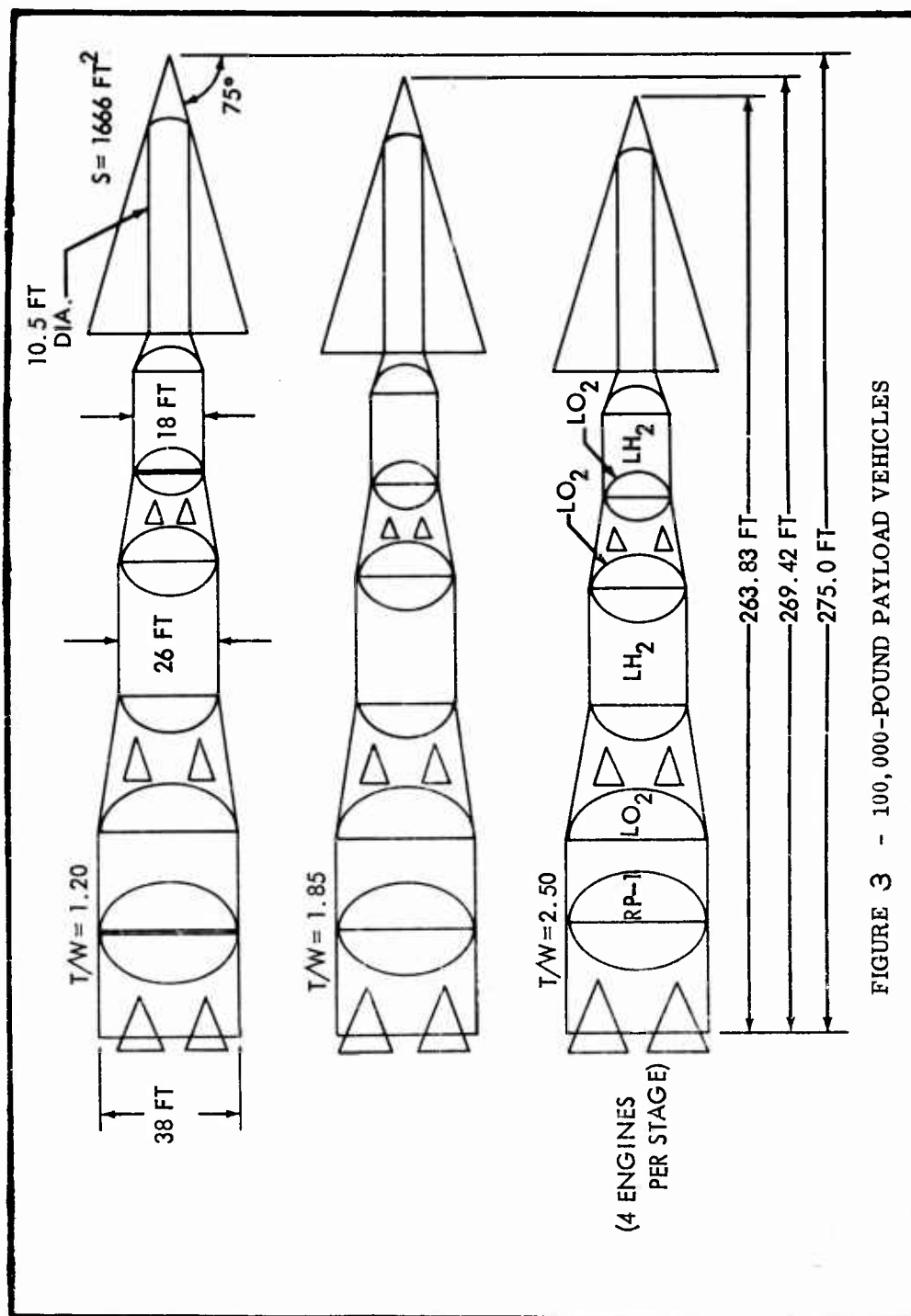


FIGURE 3 - 100,000-POUND PAYLOAD VEHICLES

Wagner

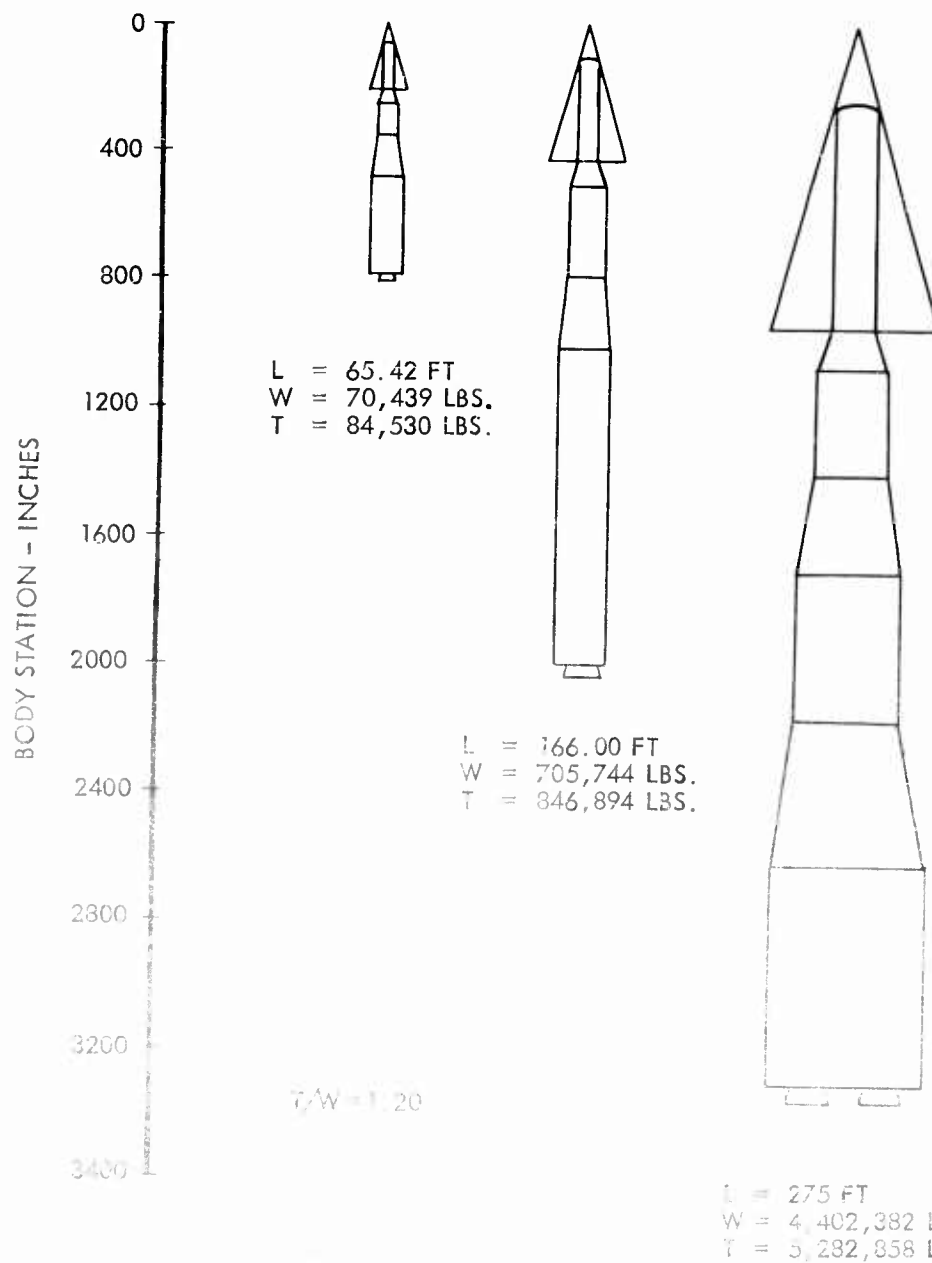


FIGURE 4 - VEHICLE SIZE COMPARISON

Wagner

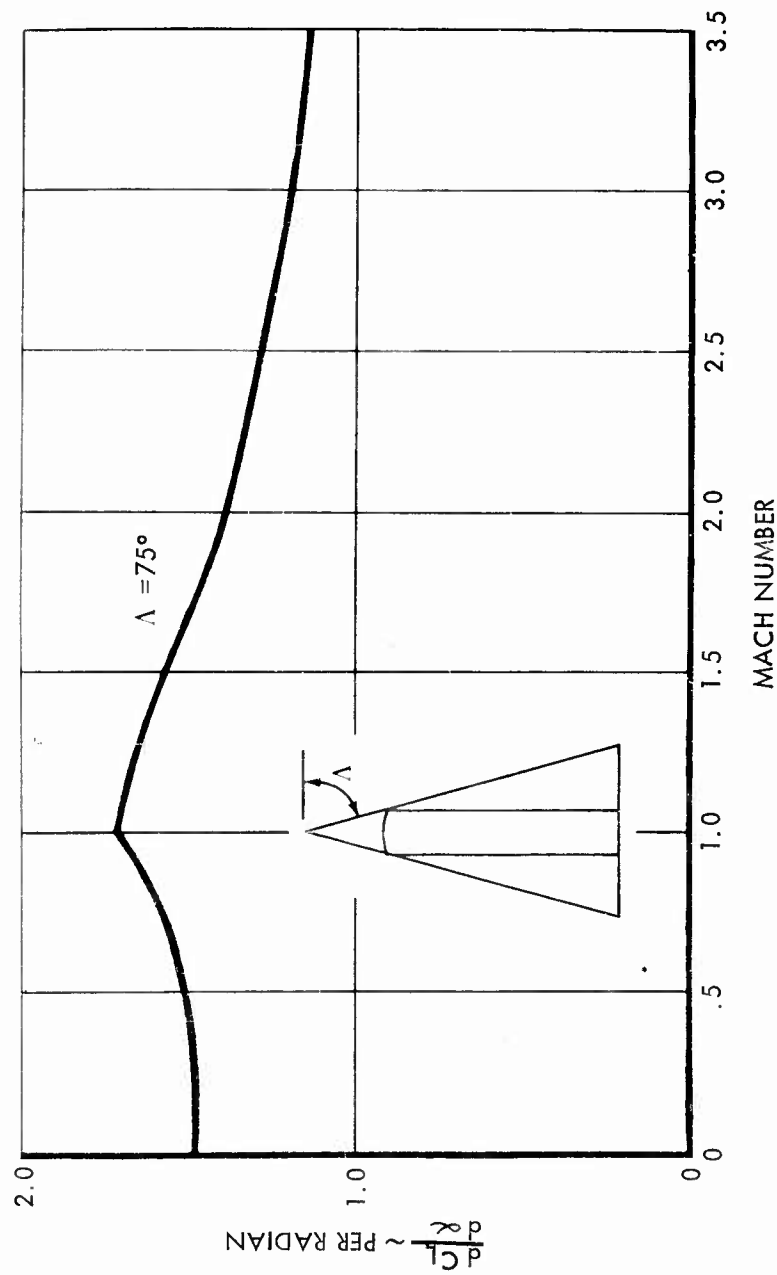


FIGURE 5 - GLIDER AERODYNAMICS

Wagner

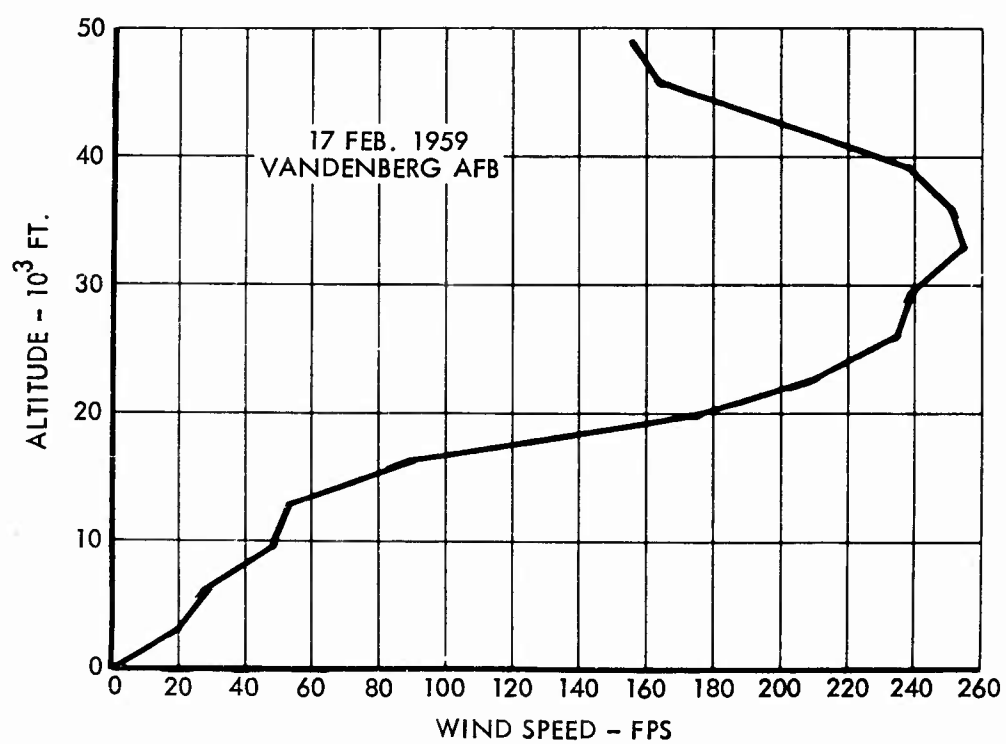


FIGURE 6 - FORCING FUNCTION



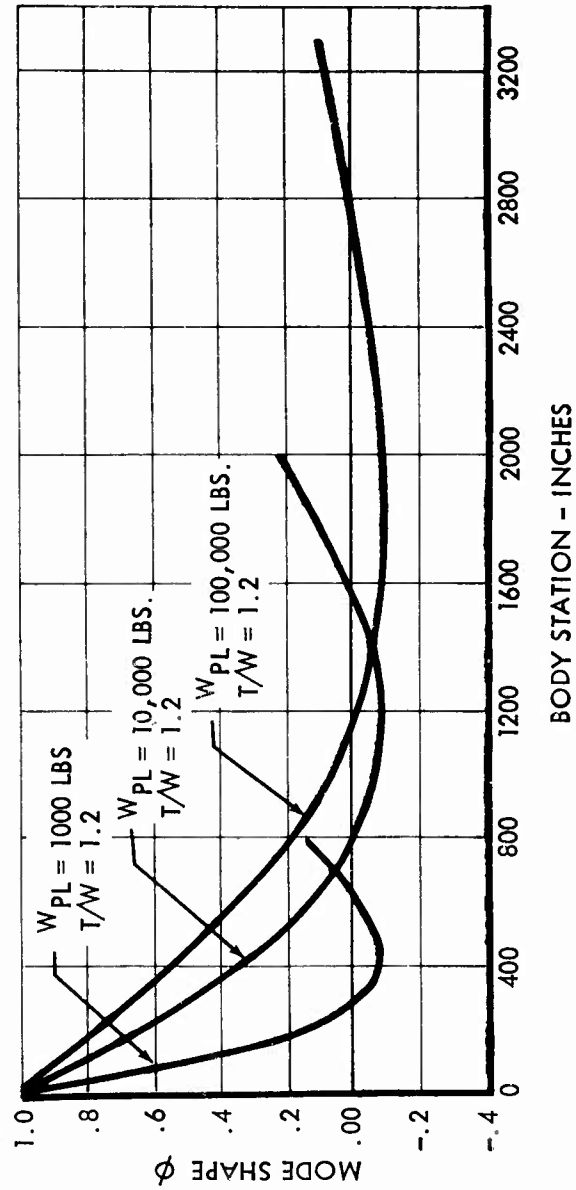


FIGURE 7 - MODE SHAPES

Wagner

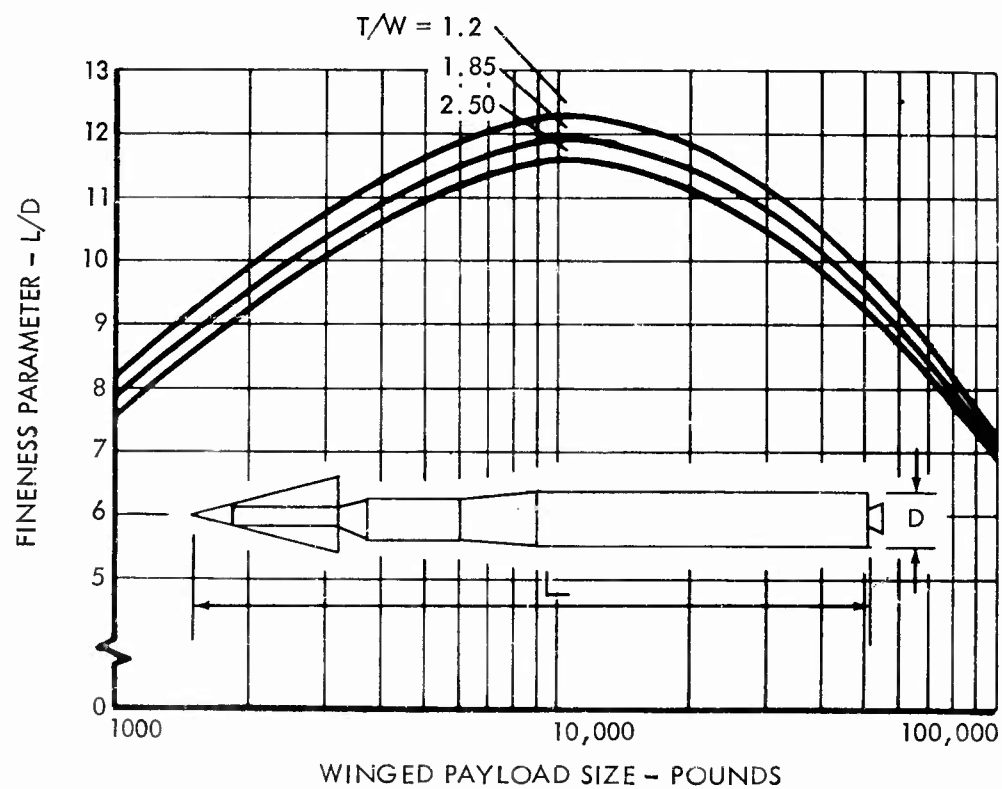


FIGURE 8 - FINENESS PARAMETER

Wagner

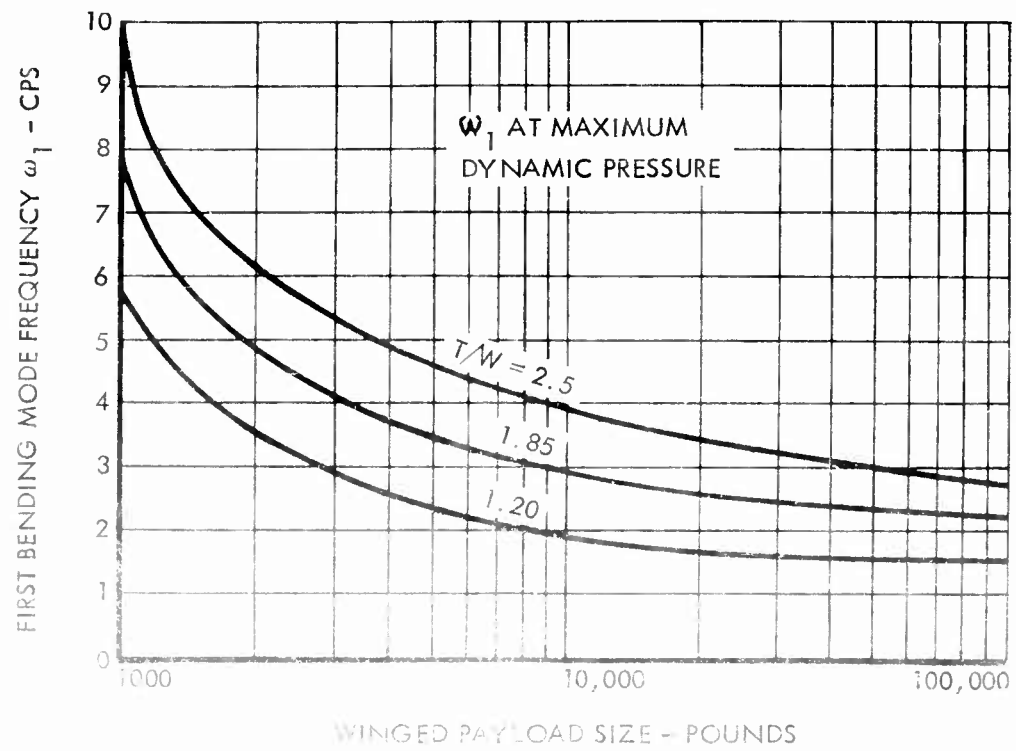


FIGURE 9 - FIRST BENDING MODE FREQUENCIES

Wagner

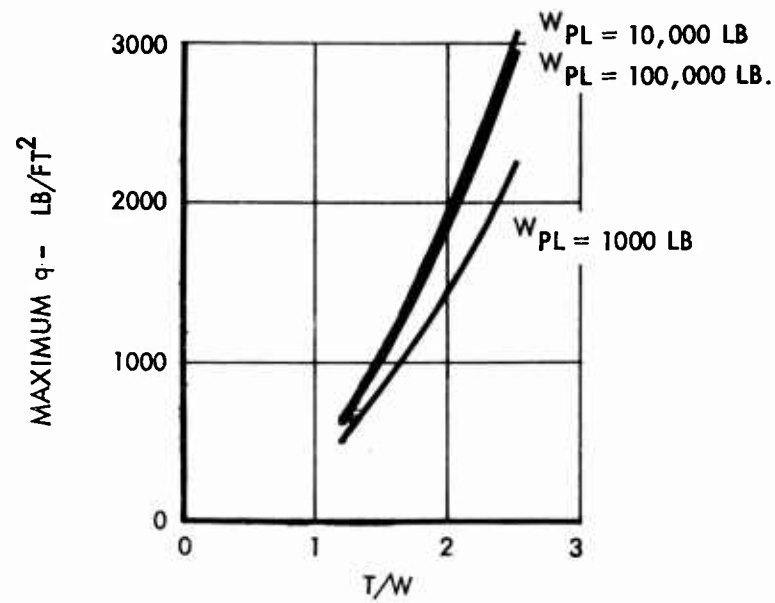


FIGURE 10 - MAX. DYNAMIC PRESSURE

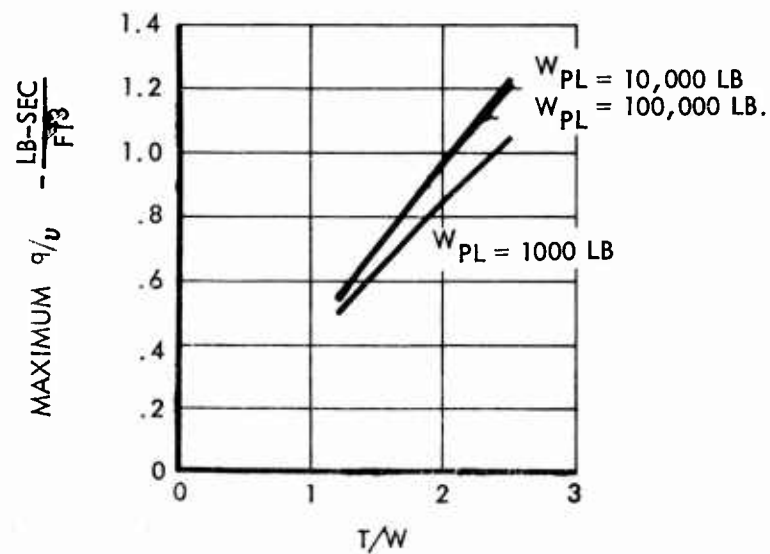


FIGURE 11 - MAXIMUM DYNAMIC PRESSURE/FLIGHT VELOCITY

Wagner

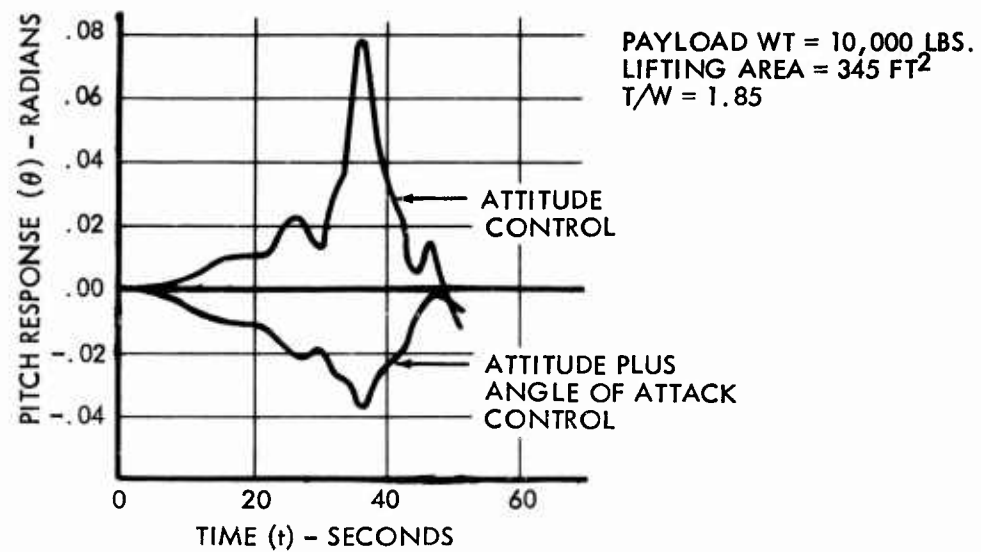


FIGURE 12 - PITCH RESPONSES

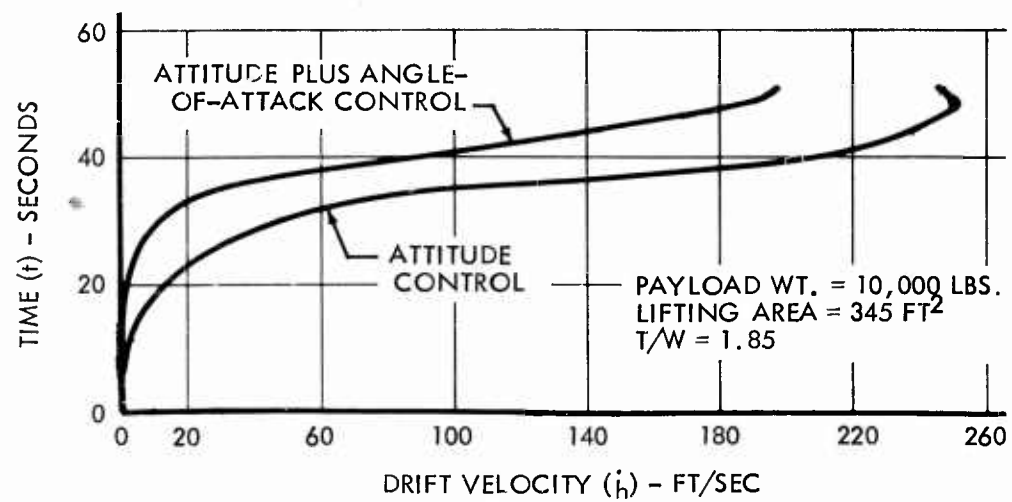


FIGURE 13 - DRIFT VELOCITY

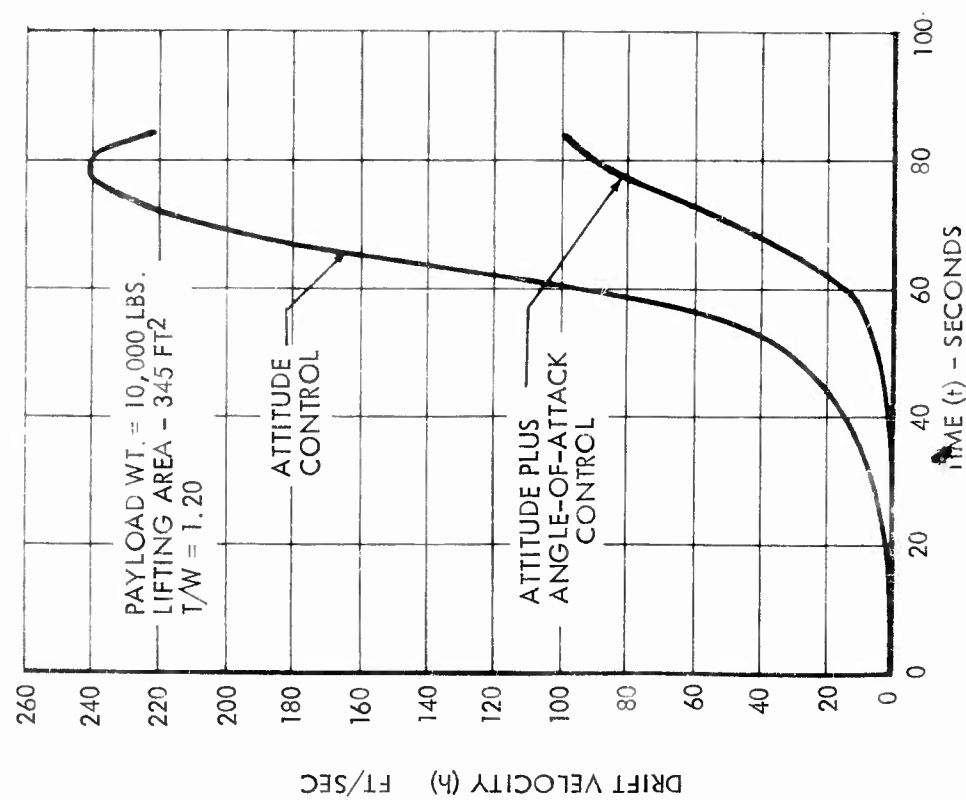


FIGURE 14 - DRIFT VELOCITY

Wagner

$$\delta r = K_{\theta}\dot{\theta}_s + K_{\theta}\ddot{\theta}_s$$

$$\delta r = K_{\theta}\dot{\theta}_s + K_{\alpha}\ddot{\alpha}_s$$

PAYLOAD WT. = 10,000 LBS.  
LIFTING AREA = 345 FT<sup>2</sup>  
T/W = 1.85

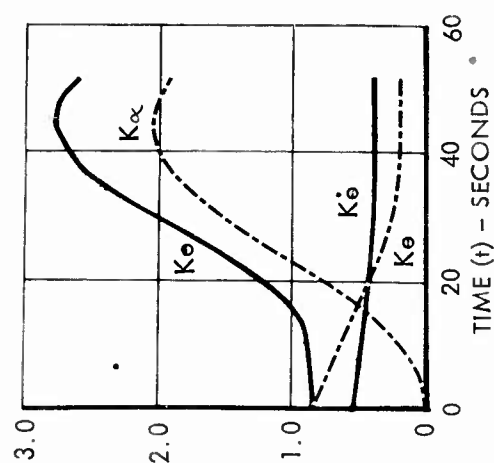


FIGURE 15 - CONTROL GAINS

Wagner

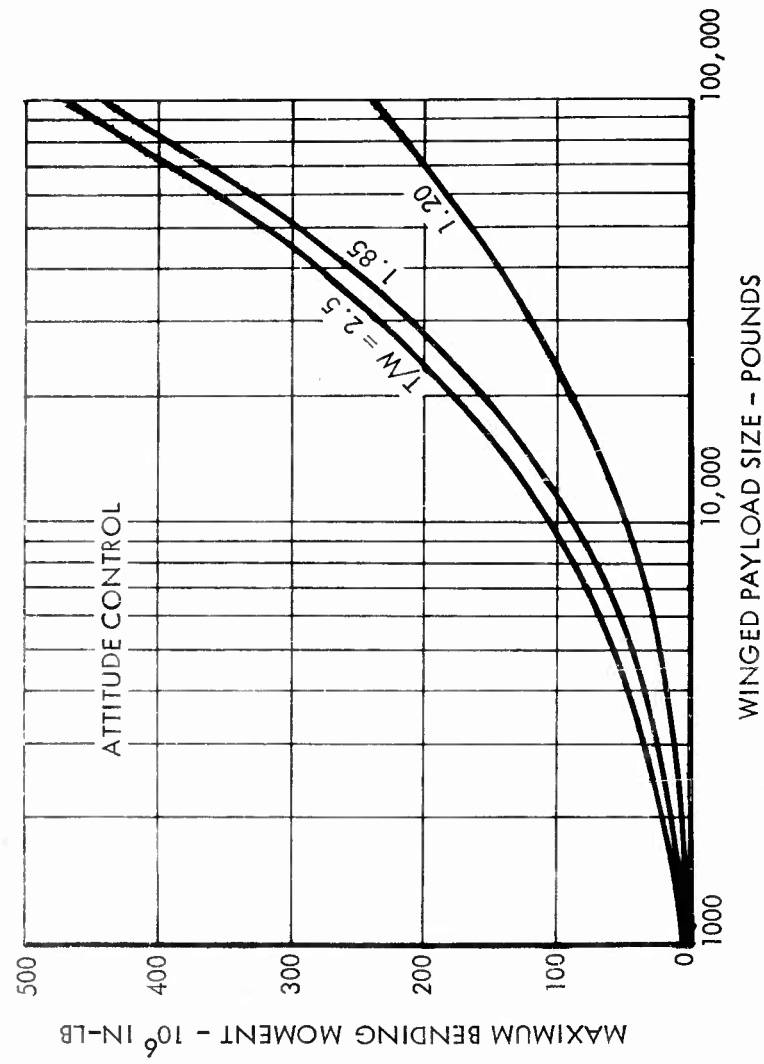


FIGURE 16 - WIND SHEAR BENDING MOMENTS

Wagner

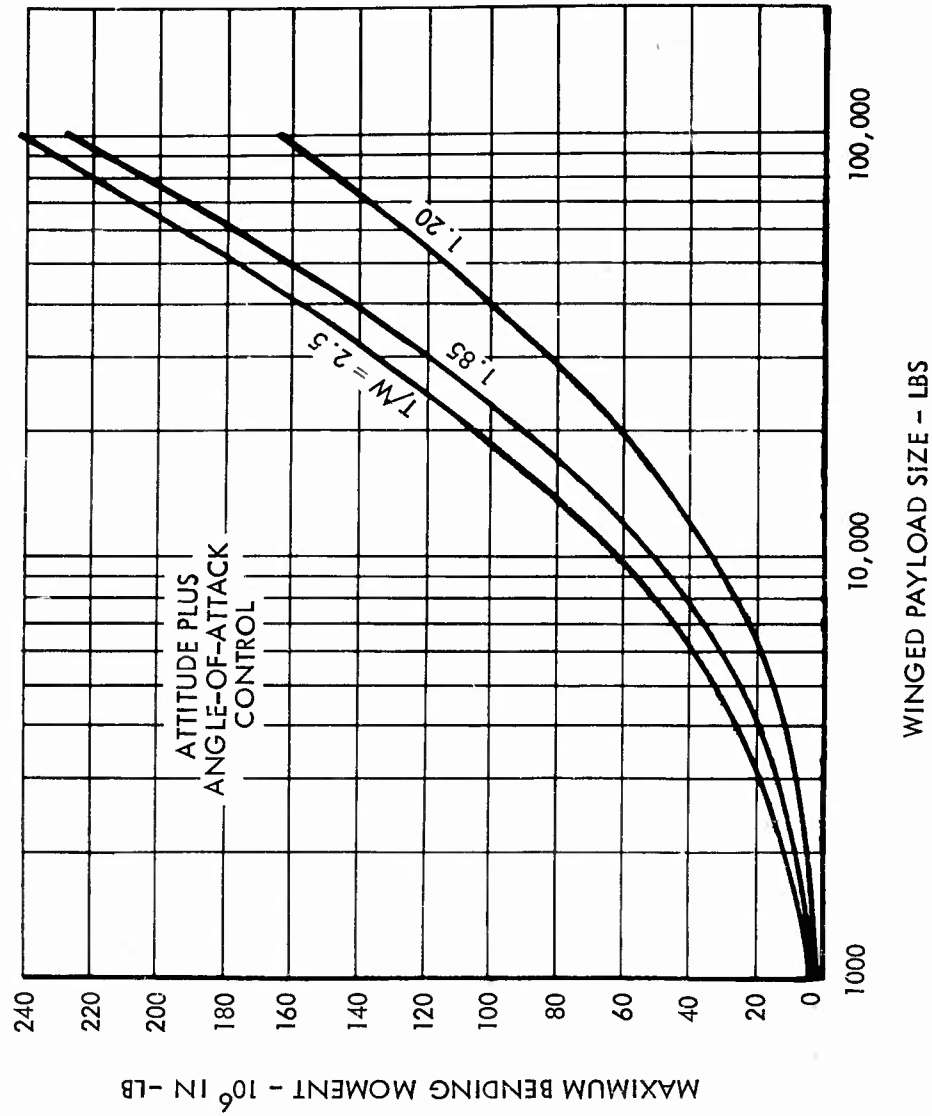


FIGURE 17 - WIND SHEAR BENDING MOMENTS



Wagner

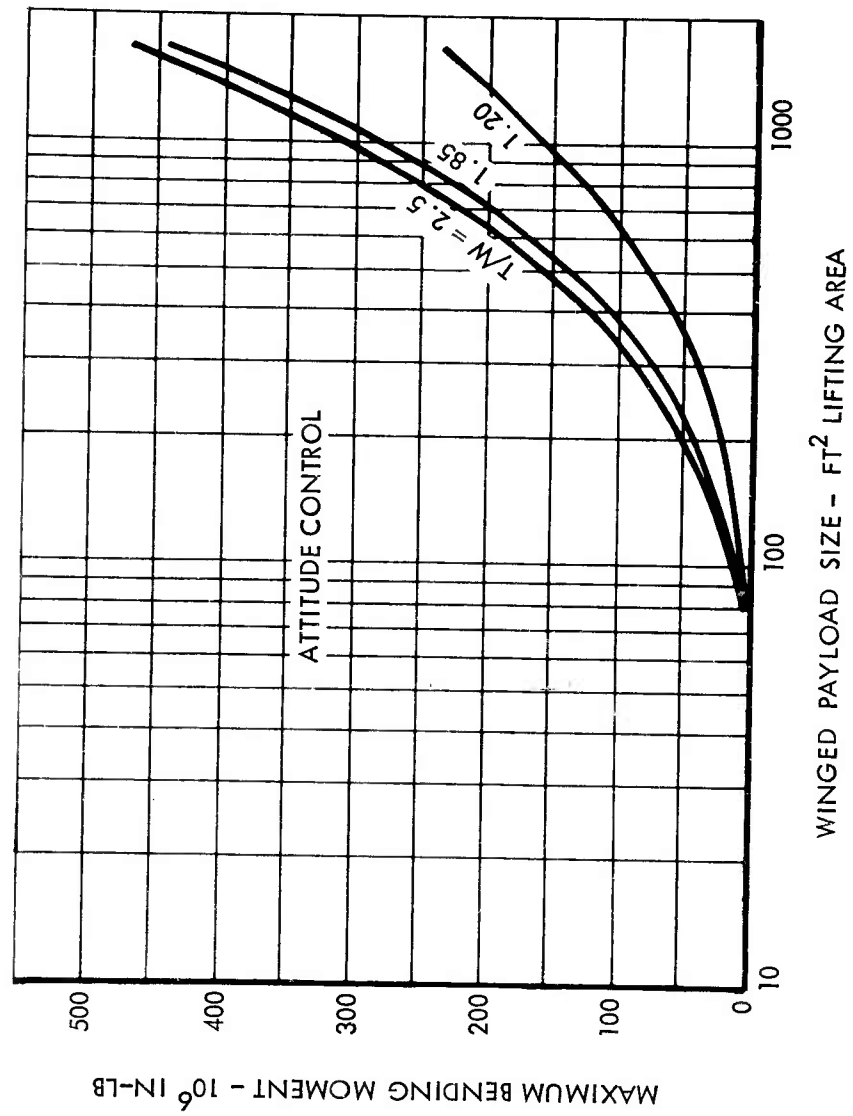


FIGURE 18 - WIND SHEAR BENDING MOMENTS

Wagner

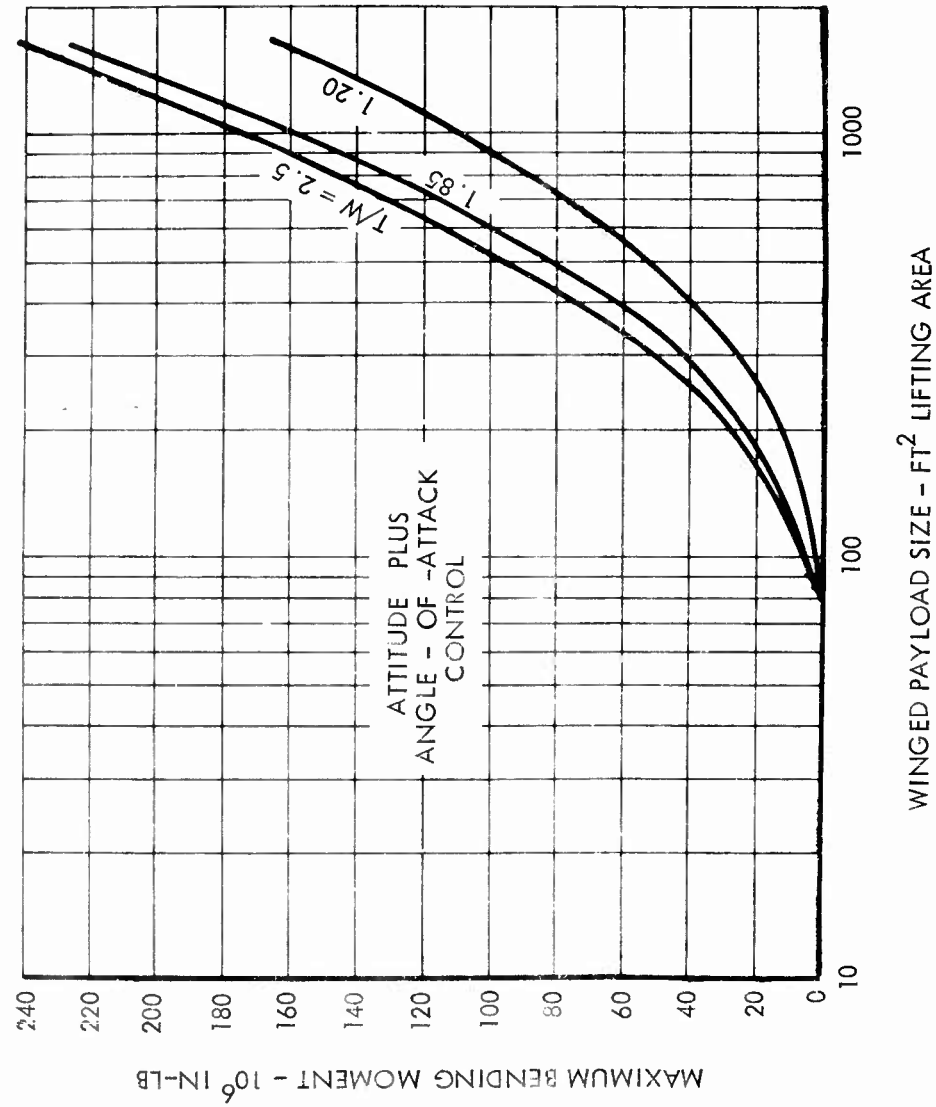


FIGURE 19 - WIND SHEAR BENDING MOMENTS

Wagner

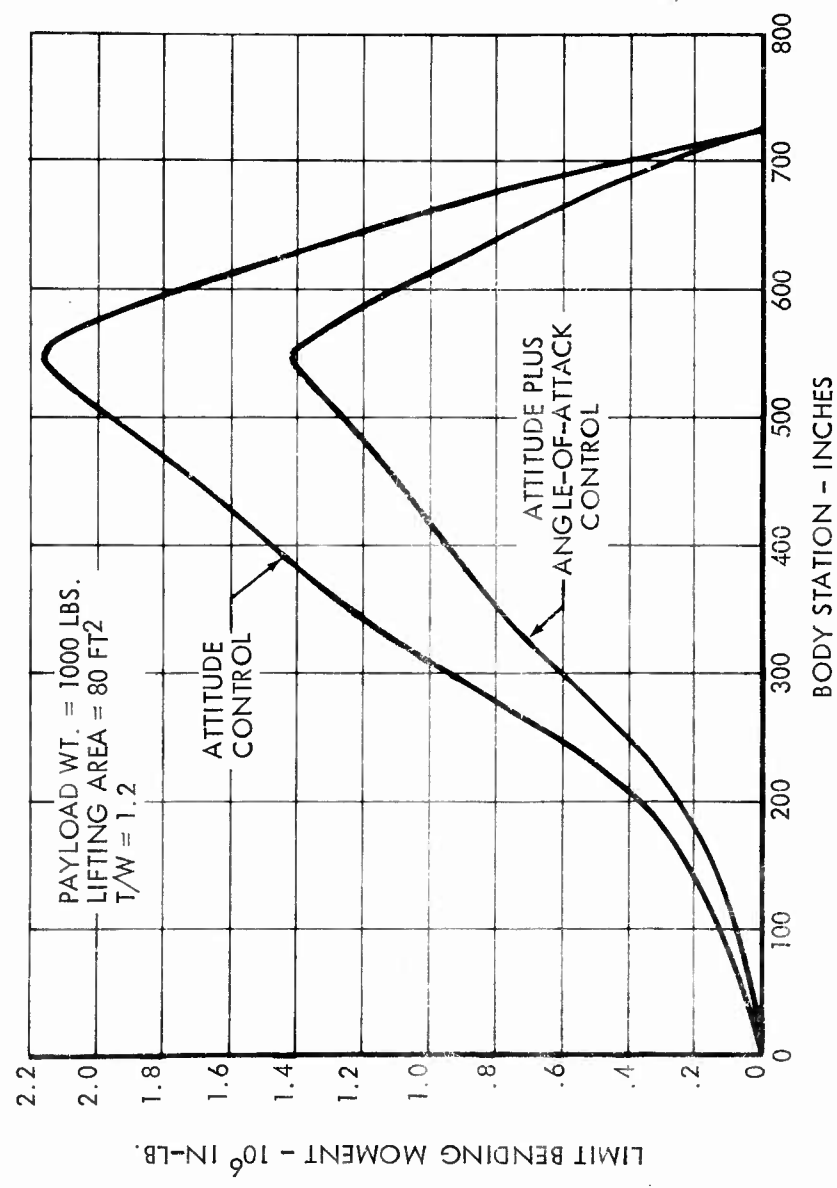


FIGURE 20 - WIND SHEAR BENDING MOMENTS

Wagner

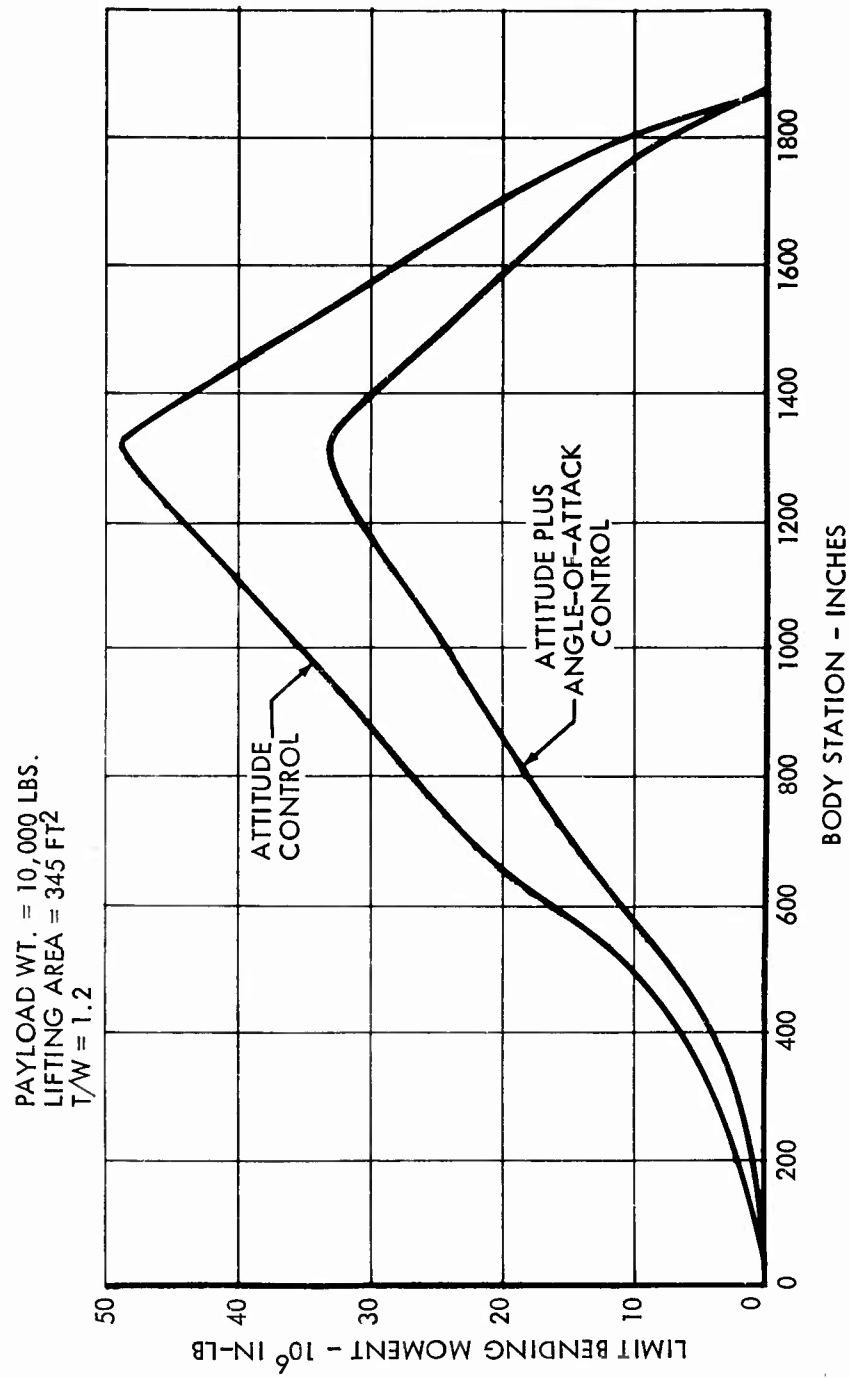


FIGURE 21 - WIND SHEAR BENDING MOMENTS

Wagner

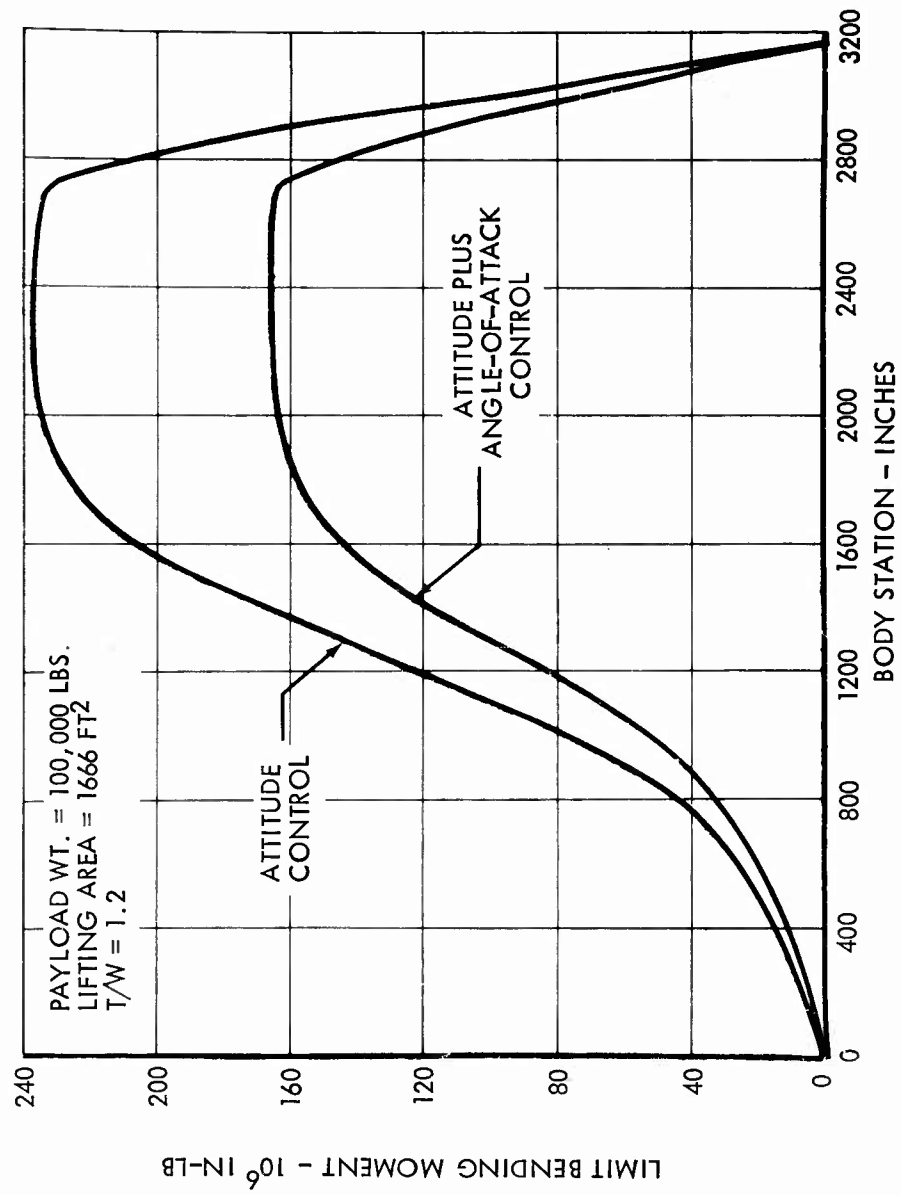


FIGURE 22 - WIND SHEAR BENDING MOMENTS

Wagner

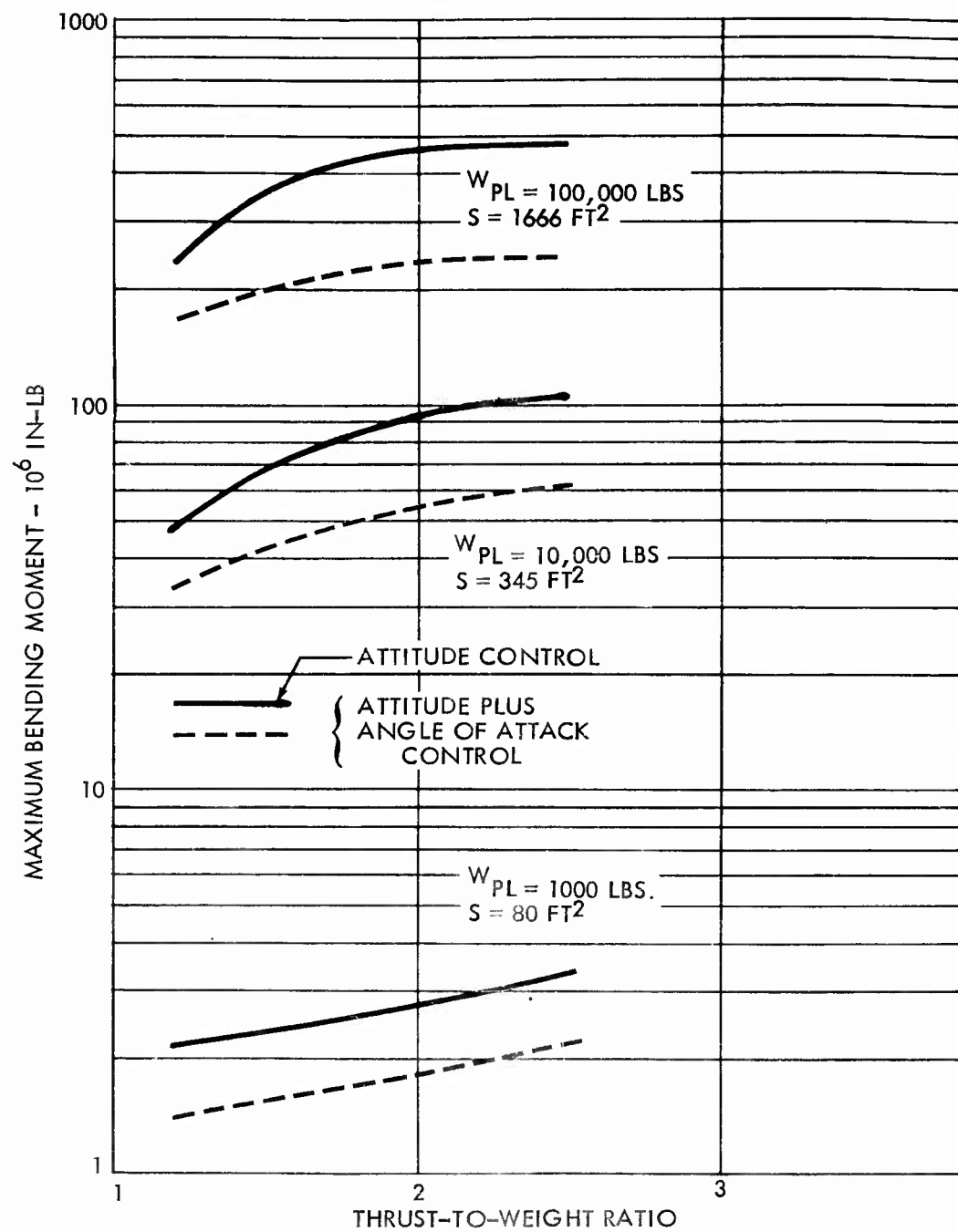


FIGURE 23 - WIND SHEAR LOADS VERSUS T/W RATIO

Wagner

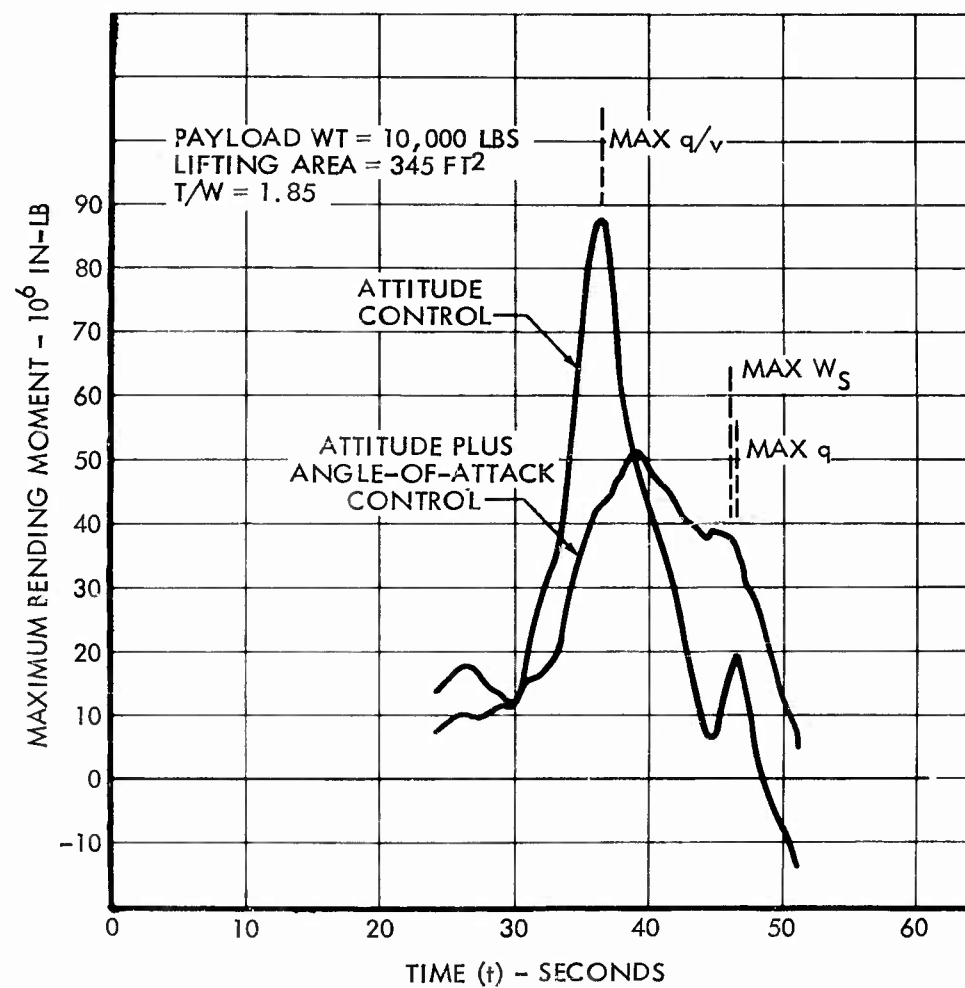


FIGURE 24 - WIND SHEAR LOADS TIME HISTORIES

## SESSION IV | DYNAMIC LOADS

Chairman: Mr. I. Edward Garrick  
NASA, Langley Research Center



WIND LOADS ON A VERTICALLY RISING VEHICLE INCLUDING  
EFFECTS OF TIME-VARYING PARAMETERS\*

Homer G. Morgan and Sheldon Baron  
NASA Langley Research Center  
Langley Field, Virginia

SUMMARY

An analytical investigation of the loads and responses of a simplified elastic rocket vehicle flying a vertical trajectory has been conducted. The external forces assumed acting on the rocket were produced by a series of wind shear reversals and several measured wind profiles. The system was described by three rigid-body modes and three elastic modes, and was stabilized by a simplified control function. The differential equations had time-dependent coefficients and were solved on an analog computer.

Time-dependent coefficients of the differential equations were found to be necessary to predict loads when the wave length of the wind shear reversal became sufficiently long. Errors which would result from using time-fixed coefficients were shown to depend on, among other factors, the ratio of bending frequency to control frequency, the thrust-to-weight ratio, and the control system of the rocket.

Detailed wind profiles measured by a smoke-trail technique were generally found to produce larger loads on the rocket than wind profiles measured by balloon-sounding techniques. These differences were as large as 15 to 20 percent, depending on the parameters of the system. It was noted that the character of the bending-moment response to these profiles, whether primarily inertial or aerodynamic, and the magnitude of bending mode excitation, depended on the type of control system as well as the rocket's thrust-to-weight ratio and bending-mode frequency to control frequency ratio.

---

\*The information presented herein will be offered as a thesis in partial fulfillment of the requirements for the degree of Master of Science, The College of William and Mary, Williamsburg, Va., by Sheldon Baron.

## INTRODUCTION

The critical loads which design the structure of a missile or booster vehicle usually occur along the launch trajectory during ascent through the atmosphere. These loads result from response to guidance and control commands, buffeting, noise, engine transients, atmospheric disturbances, and the response of the vehicle to these loads and disturbances. This paper is concerned with those loads which result from atmospheric disturbances such as wind shears and gusts. Usually the critical loading condition from this source is associated with the "maximum  $q$ " or "maximum  $aq$ " point in the launch trajectory, where the aerodynamic forces are greatest and where loads from the other sources are often critical as well.

An exact analytical description of a rocket in its launch trajectory would necessarily require a set of differential equations having time-dependent coefficients and representing both the rigid and elastic degrees of freedom. A detailed knowledge of the motion of the atmosphere is also required to provide the forcing functions acting on the differential equations in order to predict wind loads. However, simplification of analysis procedures and lack of better atmospheric data have resulted in certain arbitrary criteria to define wind loads being established within the various companies of the aerospace industry. Usually two distinct analytical models have evolved, associated with two available types of atmospheric data. First, wind loads due to the gross motion of the atmosphere, as determined by balloon soundings, are computed using a model consisting of a set of simultaneous differential equations having variable coefficients but neglecting elastic effects. Then the loads resulting from the detailed wind motions, i.e., gusts and turbulence, are found by considering the booster rocket at several discrete points along the trajectory, using constant coefficient differential equations, and including structural elasticity. Total wind loads are then determined by some form of superposition of the loads calculated from the two types of atmospheric disturbances.

The first objective of this paper is to attempt to demonstrate significant effects of time-dependent coefficients of the governing differential equations by using a more fundamental analytical model than those usually used, i.e., one which has time-dependent coefficients and includes structural elasticity. Wind shear reversals, corresponding to the peak of a balloon-measured profile, are used as forcing functions in order to examine the response of the system. Reference 1 is a related study which delineates some effects of time-varying aerodynamic coefficients on an aeroelastic system.

The second purpose of this paper results from improved atmospheric wind data having recently become available. These data, determined by a photographic triangulation technique developed at Langley Research Center and described in reference 2, contain the small horizontal fluctuations of the atmosphere as well as its gross

motion. Loads which result when a rocket flies through this detailed wind profile will be compared with loads which result when the rocket is flown through a wind profile determined by conventional balloon-sounding techniques.

## LIST OF SYMBOLS

$a_i, i = 1, 2, 3$	characteristic values of a uniform beam with free-free boundary conditions
B.M.	bending moment, ft-lb
$C_{ij}$	generalized aerodynamic coefficients appearing in equation (6a)
$D_m, D_{nj}$	constants appearing in equation (14a)
EI	stiffness constant of a uniform beam, lb-ft <sup>2</sup>
$F_{xA}, F_{yA}$	components of aerodynamic force in body axes, lb
$g$	gravitational constant, ft/sec <sup>2</sup>
$h$	altitude, ft
$h_0$	initial altitude, ft
$I_{sp}$	specific impulse of rocket, sec
$K_1, K_2, K_3$	gain constants of the control function, equation (2)
$L$	length of the rocket, ft
$M$	mass of the rocket at any instant, lb-sec <sup>2</sup> /ft
$M_0$	lift-off mass of the rocket, lb-sec <sup>2</sup> /ft
$M_{zA}$	aerodynamic pitching moment, lb-ft
$q_i, i = 1, 2, 3$	generalized coordinate of $i$ th mode, divided by $L$ , nondimensional
$Q_{iA}$	generalized aerodynamic force, lb
$S$	base area of the vehicle, ft <sup>2</sup>
$t$	time, sec

Morgan and Baron

$T$	thrust, lb
$V_m$	velocity of the rocket, ft/sec
$V_{mw}$	velocity of rocket relative to air, ft/sec
$V_w$	horizontal velocity of wind, ft/sec
$W_o$	lift-off weight of rocket, lb
$\dot{x}_o, \dot{y}_o$	center-of-gravity velocity of rocket in body axes, divided by $L$ , per sec
$x$	distance along rocket elastic axis, measured from aft end, divided by $L$ , nondimensional
$x_n$	distance from aft end to nth station, divided by $L$ , nondimensional
$\alpha$	angle of attack, radians
$\alpha_w$	angle of attack due to wind, radians
$\gamma$	angle between vertical reference and inertial velocity vector, radians
$\delta$	angle of deflection of thrust vector from rocket center line, radians
$\theta$	angle between vertical reference and body axis, radians
$\Lambda$	wave length of input wind, ft
$\xi_p$	damping ratio of rigid-body pitch mode, dimensionless
$\rho$	density of atmosphere, lb-sec <sup>2</sup> /ft <sup>4</sup>
$\rho_o$	density of atmosphere at sea level, lb-sec <sup>2</sup> /ft <sup>4</sup>
$\omega_i, i = 1, 2, 3$	natural frequency of ith mode, radians/sec
$\omega_p$	natural frequency of pitch mode, radians/sec

A dot indicates a differentiation with respect to time.

## ANALYSIS

### Physical System

The rocket vehicle is considered to be flying vertically through horizontal winds and gusts. For simplicity, the analytical model will consider angular deviations from the vertical to be small and elasticity will be represented by three uniform beam modes with no structural damping. Aerodynamic coefficients were obtained by slender body or momentum theory and aerodynamic drag was neglected. Gimballed engine dynamics were not included and the control system had perfect notch filters resulting in no structural feedback.

The loads and responses predicted for a real system would certainly be influenced by factors that are neglected. It is recognized that including some of these effects, such as inertia of the gimballed motor and structural damping, would be desirable and may be accomplished in further studies. However, the model retains essential features required to study the particular effects considered. It is believed that the simplifications may actually serve to clarify some aspects of the loads problem.

### Equations of the System

The equations developed for this study are described in the appendix. They are written in terms of nondimensional parameters in the right-handed body axis coordinate system illustrated in figure 1. The system has six degrees of freedom - three rigid-body modes and three elastic modes. The coefficients of these equations all vary with time. They become constant coefficient equations by fixing the mass, altitude, and velocity at some particular point along the trajectory. It should be noted that the fixed coefficient equations actually have only two rigid-body freedoms since longitudinal velocity is constant. The equations were programmed and solved on an analog computer.

Initial conditions were determined at the instant the rocket entered a wind profile by using the equation for an ideal vertically launched rocket to determine time, velocity, and altitude. All other initial displacements and velocities were assumed to be zero.

### Additional Considerations

The change in mass is assumed to occur in a uniform manner over the length of the rocket, similar to the situation to be expected on a solid-propelled single-stage vehicle. Both the rate of change of mass and the specific impulse of the rocket motor are assumed constant over the time interval of the problem. Thus, the motor produces constant thrust according to the relation

$$T = -gI_{sp}\dot{M} \quad (1)$$

where  $T$  is thrust,  $g$  is acceleration due to gravity,  $I_{sp}$  is specific impulse of the rocket, and  $\dot{M}$  is the mass rate of change.

Aerodynamic forces were obtained from momentum theory applied to an unfinned parabolic body of revolution. This results in an aerodynamically unstable configuration which was stabilized by deflecting the thrust vector according to the control function

$$\delta = K_1\theta + K_2\dot{\theta} + K_3(\alpha + \alpha_w) \quad (2)$$

where  $\delta$  is the thrust vector deflection angle;  $\theta$  and  $\dot{\theta}$  are attitude and attitude rate, respectively;  $(\alpha + \alpha_w)$  is the total angle of attack of the vehicle relative to the airstream; and  $K_1$ ,  $K_2$ , and  $K_3$  are gain constants. The gain constants were selected to give a prescribed value of frequency and damping in the rigid-body pitch mode at maximum dynamic pressure as described in reference 3. The values of rigid-body uncoupled pitch mode frequency and damping chosen were  $\omega_p^2 = 10(\text{radians/sec})^2$  and  $\xi_p\omega_p = 2$  per sec.

As a matter of interest, since previous studies have shown significant differences in response when using attitude or angle-of-attack control, parallel studies using both systems were made. This was accomplished by always keeping one of the gains,  $K_1$  or  $K_3$ , zero. When  $K_1$  is zero, the rocket is essentially aerodynamically stable and will be referred to as  $\alpha$ -controlled. When  $K_3$  is zero, the vehicle will be referred to as attitude-controlled. However, since no effort was made to optimize these control systems, comparisons of the relative merits of the two systems on the basis of these parallel studies should not be attempted.

Three uniform beam elastic modes describe the deformation of the rocket. The frequencies of these free-free modes increase as the mass of the system decreases, but their ratios remain fixed. Variation of the ratio of first bending frequency to rigid-body pitch frequency permits variation of the stiffness level of the structure.

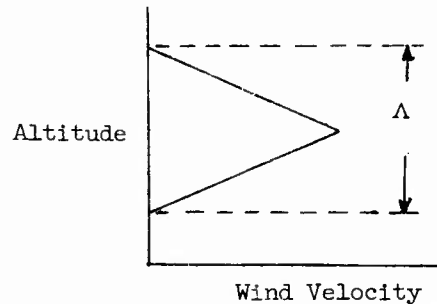
Several parameters appear in the equations of motion for which it was necessary to select values for this study. Values selected were, for the density ratio,  $\frac{\rho_0 SL}{M_0} = 0.0025$ ; for the length,  $\frac{g}{L} = \frac{1}{2}$ , or vehicle length  $\approx 65$  feet; and, for specific impulse,  $I_{sp} = 250$  seconds.

## RESULTS AND DISCUSSION

### Response to Wind Shear Reversals

The first objective to this paper was to attempt to determine significant effects resulting from using variable coefficient differential equations in a wind loads analysis of an elastic rocket. This was done, first, with the variable coefficient equations using a wind input which was a function of altitude, and second, using fixed coefficients with the wind input as a function of time. The input winds, parameter ranges covered, and pertinent results are discussed in the following sections.

Description of wind shear reversals.- The wind shear reversals which produce the loads on the rocket are triangular waves, illustrated by this sketch:



The wave is symmetric, peaking at 35,000 feet altitude near the point of maximum dynamic pressure in each trajectory. The wave length,  $\Lambda$ , is the total vertical distance over which the wind velocity persists. For the variable coefficient cases, the wave is symmetric about 35,000 feet altitude. When constant coefficient cases are examined, the coefficients of the differential equations are fixed at their values at 35,000 feet, while this wind becomes a function of time rather than altitude. The time required to pass through the shear reversal, or the period, is now determined by dividing the wave length by the fixed velocity of the rocket. The maximum wind velocity occurs at one-half the period.

Bending-moment distribution.- A bending-moment distribution along the body of the vehicle is shown in figure 2 for the two basic types of control. The loads in this case resulted from a wind shear reversal of 10,000-foot wave length. In other words, the wind velocity increased linearly from zero at 30,000 feet altitude to 100 ft/sec at 35,000 feet, and then decreased linearly to zero at 40,000 feet. The maximum bending moments were determined for each type of control as the rocket ascended through this wind profile. The  $\alpha$ -control, i.e., the control system which seeks zero angle of attack, is seen to produce larger loadings than the  $\theta$ -control which maintains a constant attitude angle. This loading situation may be contrary to

the usual expectations for such a system. However, the large loads when the vehicle is operated in the  $\alpha$ -control mode result directly from large inertia loads induced by the motor. The system has no lag in the motor equation, permitting the thrust vector to follow the wind inputs, with their discontinuities, exactly as commanded by the control function. This produces large angular accelerations as well as significant excitation of the elastic modes. On the other hand, operation in the  $\theta$ -control mode produces negligible inertia loads, since the thrust is vectored just enough to cancel the destabilizing aerodynamic moment, and does not excite the elastic modes to any great extent. This will be illustrated later in the paper. Also, the momentum theory aerodynamics predict very low normal forces and pitching moments on a body of revolution, such that the bending moments remain low despite the large angles of attack permitted by the  $\theta$ -control system. Therefore, an evaluation of  $\alpha$ -control compared to  $\theta$ -control should not be attempted from the results presented herein, due to the dependence of the loads on the analytical model used in the study.

The maximum bending moments for these cases occur at the 0.3 and 0.5 body stations. For the remainder of the paper, the bending moment at one of these two stations was arbitrarily chosen for examination.

Bending-moment variation with frequency ratio.- Figure 3 illustrates a case where the use of variable coefficients can cause a difference in predicted loads on the rocket. The maximum bending moment at station  $x = 0.5$  is shown as a function of the ratio of first bending frequency to rigid-body pitch frequency. Note that the frequency ratio,  $\omega_1/\omega_p$ , is a measure of the stiffness of the structure since  $\omega_p$ , the rigid-body pitch frequency, has been kept constant throughout the study. The input is a 10,000-foot wave-length shear reversal with a maximum velocity of 80 ft/sec. With  $\theta$ -control, the bending moments calculated using fixed coefficients are about 20 percent higher than those calculated with variable coefficients. Neither shows appreciable variation with frequency ratio, indicating small response in the elastic modes. However, the  $\alpha$ -control behaves quite differently. The elastic modes are now contributing a large percentage of the total bending moment, causing a variation with stiffness. There is also an effect from using the variable coefficients, changing from a reduction in predicted load at low stiffness levels to an increase at higher stiffnesses. Thus, use of fixed coefficients may be either conservative or unconservative in loads prediction. The magnitude of the predicted loads differs by over 30 percent in some ranges.

Consideration of the effects illustrated in this figure will show that they arise from the nature of the input wind. To fix the coefficients of the equations of motion, the wind becomes a function of time rather than altitude, while the rocket flies through this wind at constant velocity. In the variable coefficient case, the rocket is



traveling slower at lower altitudes, and thus takes a longer time to reach the point of maximum wind. So, the transients associated with the reversal of the wind shear will occur with different phasings with respect to the previously induced motions of the vehicle. Then, depending on this phasing, which in turn will depend on the speed with which the rocket is traveling, the wave length of the shear reversal, and the frequencies of the elastic modes, the loads predicted using fixed or variable coefficients can certainly differ.

Bending-moment variation with wave length.- The differences illustrated were those due to frequency changes of the bending modes. It is anticipated that differences would also occur due to changing the wave length of the input. These are illustrated in figure 4, where bending moment is plotted against wave length of the shear reversal for two frequency ratios using angle-of-attack control. The use of fixed coefficients predicted larger loads than obtained using variable coefficients at the longer wave lengths, for the frequency ratios illustrated. However, at wave lengths below about 6,000 feet, again no difference was detectable. This is certainly in agreement with expectations for such a system - at short wave lengths, the maximum responses occur within a very short time span such that changes within the system (variable coefficients) do not have a chance to alter responses. Similar results were obtained with the attitude-control system.

Bending-moment variation with thrust-to-weight ratio.- The differences in predicted bending moments, with and without variable coefficients, which may be anticipated at different thrust-to-weight ratios are illustrated in figure 5. Bending moments at two frequency ratios are shown for the vehicle flying through a shear reversal of 10,000-foot wave length. The deviation in bending moment is largest at low  $T/W_0$ , reaching almost 20 percent, but becomes insignificant at the high values. At the high thrust-to-weight ratios, the rocket passes through the shear reversal too rapidly for the change in system parameters to effect response. The deviation in predicted bending moment appears to be about the same percent of the total for both frequency ratios at thrust-to-weight ratio 1.5. For the frequency ratios shown, the fixed-coefficient analysis predicted conservative, or high, bending moments.

#### Response to Measured Wind Profiles

The second objective of this paper was to demonstrate the response of an elastic rocket to measured atmospheric wind data. All of the wind profile data which have been available to designers until recently were obtained by tracking sounding balloons. Such data are recognized to omit the small-scale fluctuations, i.e., gusts or turbulence, from the picture they present of atmospheric motion. Recently, a technique has been developed at Langley Research Center which permits these small perturbations of the wind to be measured

along with the wind's gross motion. This portion of the paper will present loads for the rocket flying through one of these detailed profiles and compare them with loads produced by flying through profiles measured by conventional techniques.

Measured wind profiles.- The wind profiles are taken from reference 2 and are presented in figure 6. The detailed profile, identified as the rocket smoke trail, was determined at 100-foot altitude increments by photographic triangulation methods utilizing the exhaust trail of the rocket. Two balloon profiles are indicated - number 1 being from a balloon released three hours before the rocket was launched, while number 2 came from a balloon released three-quarters of an hour after rocket launch. The balloon data are seen to define the wind velocity with points about 2,000 feet apart, contrasted to the 100-foot increments in the smoke-trail data. These profiles actually extend from near sea level to over 40,000 feet altitude, but, due to limitations in the computer program, the cases reported herein cover the 20,000- to 40,000-foot altitude range.

All the profiles are random in nature, but the maximum velocities measured for this case are comparatively low, never exceeding 80 ft/sec. Such mild winds would not be suitable for design purposes, but will serve for the comparisons which it is desired to make. However, to make the loads from the balloon data more severe and to make it more representative of design profiles, a third balloon profile, number 3, was artificially created from profile number 2 by extending one point, at 32,500 feet, until the wind velocity matched the maximum wind velocity on the smoke-trail profile. This effectively adds a wind shear reversal, with a wave length of about 4,500 feet and maximum velocity of 40 ft/sec to the existing balloon profile.

Bending-moment time histories with  $\alpha$ - and  $\theta$ -control.- Before comparing the responses due to the various input winds, it is convenient to examine the differences in these responses from the two types of control. Figure 7 illustrates these differences. The input wind is the balloon profile number 3 which was just described. The time history of engine gimbal angle is shown for the  $\alpha$ -control case, along with the bending-moment response at station 0.3. The other response trace illustrated is the bending moment at station 0.3 for  $\theta$ -control. With  $\alpha$ -control, the bending moment follows the engine angle very closely. The predominant characteristics of this load are the large transient peaks, corresponding to peaks in engine angle, which occur in the regions of rapid changes in the wind input. The main component of the load would seem to be inertial, resulting from the angular accelerations of the vehicle as it follows the motor. The loads with  $\theta$ -control do not exhibit this type behavior, but follow the input wind directly. With this type control, rocket attitude is being controlled which prevents large angular accelerations from occurring and large and sudden engine deflections are not required. The angle of attack follows the wind profile so that the bending moment is primarily due to aerodynamic loads. Also, since the  $\alpha$ -control results

in large, rapid engine motions, the elastic modes are responding with greater magnitude than with  $\theta$ -control.

Bending-moment time histories when flying through smoke-trail wind profile.- Examples of bending-moment responses to the smoke-trail wind profile are illustrated in figure 8. In figure 8(a), the bending moment at missile station 0.3 is shown for the two types of control being considered -  $\alpha$ -control and  $\theta$ -control. The rocket parameters are  $\omega_1/\omega_p = 7$  and  $T/W_0 = 5$ . The wind profile, shown at the top as a function of time, begins at 20,000 feet altitude and ends at about 41,000 feet. Maximum dynamic pressure for this trajectory occurs at 35,000 feet, near the peak wind velocity. However, this is not necessarily the point of maximum load, as the responses show. With  $\alpha$ -control, equal loads are produced at about 25,000 feet altitude, corresponding to the first peak on the wind profile. With  $\theta$ -control the maximum bending moment does occur near the maximum wind velocity. Again, notice the difference in the form of the response of the two types of control. The  $\alpha$ -control seeks to reduce angle of attack to zero, and, in following the wind, produces large rigid-body inertia loads as well as considerable excitation of the first and second elastic modes. On the other hand, the  $\theta$ -control maintains constant attitude so that rigid-body inertia loads remain low but aerodynamic loads, due to the angle of attack induced by the wind, now become large. (Dynamic pressure for the case illustrated is approximately 5,000 lb per sq ft, so loads become large despite the small angles involved.) The net result is to produce approximately equal maximum moments at this station for both types of control.

Figure 8(b) shows the bending-moment response to the smoke-trail wind profile for three rockets of different thrust-to-weight ratios. In each case,  $\alpha$ -control was used along with a very low stiffness - a first mode frequency only three times the rigid-body pitch frequency. Changing the thrust-to-weight ratio of the rocket changes the speed with which it traverses the wind profile and alters the dynamic pressure which the vehicle sees. It is notable, then, that the maximum loads are not too different. This comes about because, for the low thrust-to-weight ratio cases, the control system is able to keep the net angle of attack near zero, but induces large elastic responses in the process. For the  $T/W_0 = 5$  case, the control system is not able to reduce the net angle of attack to zero, but the elastic response is much reduced. The elastic response is the most noticeable difference between the various cases. This is to be expected since the effective frequency content of the wind changes, due to different rocket speeds, while the frequency spectrum of the structure has been held constant.

Bending-moment time histories for different wind profiles.- The differences in loads experienced by the rocket with  $\alpha$ -control when flying through different wind profiles are illustrated in figure 9. The bending-moment response of a rocket with thrust-to-weight ratio 3 and frequency ratio 7 is shown at station 0.3 for two winds. The

bending-moment time history at the top of the figure is due to the smoke-trail profile, while the bending moment shown in the bottom portion is due to the balloon profile which has been called number 3. This is the balloon-measured wind which has been adjusted by adding a shear reversal near 35,000 feet to bring the peak velocity up to that measured by the smoke-trail technique. Again, note the differences in the bending-moment response. Response to the smoke-trail profile is characterized by large first-mode contributions, while the response to the balloon profile shows larger inertia loads with greatly reduced elastic response.

It should be pointed out that the other balloon profiles, designated number 1 and number 2, give similar response pictures except for considerable smoothing out in the region of the shear reversal present on number 3. Without the shear reversal, the maximum loads for the balloon-measured profiles sometimes occur during the initial transient period. This transient response results from starting the wind velocity at zero at 20,000 feet for convenience in the computer program. As mentioned previously, the measured data started at lower altitudes and indicated a continuous wind velocity of finite value at 20,000 feet. However, the loads resulting from this transient response, which was artificially induced by the balloon profiles, are still less than the loads produced by the smoke-trail profile in which a large wind shear was actually measured at this altitude.

Maximum bending-moment variation with frequency ratio.- The maximum bending moments resulting from the various wind profiles are shown in figure 10 for the rocket with thrust-to-weight ratio 5. The bending moment at station 0.5 is plotted as a function of frequency ratio for  $\theta$ -control in figure 10(a), and for  $\alpha$ -control in figure 10(b). With attitude control, the loads exhibit little variation with frequency ratio, due to slight excitation of the elastic modes. Slightly larger loads do occur at lower stiffness, as would be expected. The magnitude of the loads from the various profiles seems to correlate with the maximum wind velocities of that profile. For example, balloon profile number 2 has the lowest loads and also had the lowest wind velocities. The largest wind velocities from the balloon-measured winds were on profile number 3, seem to produce the largest loads of the three balloon profiles. However, the smoke-trail produced loads exceed those produced by balloon number 3 by 8 to 12 percent, although their maximum velocities were the same. Flying through the wind from the smoke-trail measurement produces the largest loads due to greater excitation of the elastic modes.

The picture is slightly different with  $\alpha$ -control, figure 10(b). Now, since angle of attack is being controlled, inertia loads predominate. The balloon profile producing the largest loads is number 1, rather than number 3, due to the large transient inertia loads induced by it. In fact, the smoke-trail wind produces larger loads only at very low stiffnesses where large responses of the bending modes occur. In general, for this simple system, it would

seem that bending moments are more sensitive to frequency ratio when  $\alpha$ -control is used.

Maximum bending-moment variation with thrust-to-weight ratio.- The results just examined applied to a rocket with lift-off thrust-to-weight ratio 5.0. The loads are also influenced by this parameter, as shown in figure 11, where the maximum bending moment is plotted against thrust-to-weight ratio for two frequency ratios,  $\omega_1/\omega_p = 3$  and 7, and two inputs - the smoke-trail wind profile and balloon profile number 3. The bending moment at station 0.5, with  $\theta$ -control, is presented in figure 11(a), and with  $\alpha$ -control, in figure 11(b). With attitude control, the loads increase almost linearly with thrust-to-weight ratio for both frequency ratios. Again, this is because the load is almost entirely aerodynamic resulting from the angle of attack built up by the wind. The bending moments due to the smoke-trail wind are greater than those due to flying the balloon-measured profile in every case, ranging up to almost 15 percent at the higher thrust-to-weight ratios. And again, it should be noted that the lower stiffness produced higher loads, for both inputs, over the entire range of thrust weight ratios investigated.

The observations that lower stiffnesses and the smoke-trail input produce higher bending moments carry over to the  $\alpha$ -control case, figure 11(b). But now the trend with thrust-to-weight ratio is reversed. Where, with  $\theta$ -control, loads increased with this ratio, they decrease when using  $\alpha$ -control. This is explained by recalling that, with  $\alpha$ -control, loads are primarily inertial, produced by engine deflections as the rocket tries to keep angle of attack zero. At high thrust-to-weight ratios, rocket velocity is higher so that effective angle of attack due to the wind is reduced. Thus, less control is required to keep the net angle of attack zero and loads go down. Also, with this type control, where bending response produces a larger portion of the load, the differences between the loads produced by the two wind profiles are seen to vary much more with frequency ratio. The low stiffness,  $\omega_1/\omega_p = 3$ , shows a very large increase in load, while the frequency ratio 7 case shows only moderate increases.

In comparing the loads produced by the smoke-trail profile and balloon profile number 3, it should be emphasized that the balloon profile is an artificial one, created by adding a wind shear reversal to the measured balloon profile number 2, such that the maximum wind velocity equaled the maximum velocity measured by the smoke-trail method. Loads produced by flying through the actual number 2 profile, which was taken from a balloon sounding made only three-quarters of an hour after the smoke-trail firing, were in all cases considerably lower than loads from this artificial profile.

The bending moments resulting from flying through smoke-trail measured wind profiles which are presented in figures 10 and 11 are illustrations of the applications of the smoke-trail data which

are being made. However, a number of questions regarding the application of these data to design problems remain to be resolved. For example, is it necessary to superimpose loads induced by gusts or turbulence on loads from the smoke-trail profile as is usually done with loads from balloon-measured profiles? Or, are the loads calculated by superposition of gust loads and balloon-measured wind loads comparable to loads from the smoke-trail wind? Questions such as these remain to be answered by future studies.

#### CONCLUDING REMARKS

Loads for a simplified elastic rocket flying through several wind profiles have been shown. Time-dependent coefficients of the governing differential equations were found to produce significant differences in the bending moment when the wave length of a wind shear reversal was sufficiently long. When the rocket was flown through a group of measured wind profiles, loads were usually largest when the measured profile had been determined by the rocket smoke-trail technique, rather than by the use of balloon soundings made at approximately the time the rocket was launched. The magnitude of the loads was shown to depend on the control system, the stiffness, and the thrust-to-weight ratio of the rocket. The differences in predicted booster loads which result from using the various wind inputs are large enough to warrant further investigations of more realistic systems, including flight tests for correlation with analysis.

## APPENDIX

## Equations of Motion

The equations of motion for the system being studied have been developed using Lagrange's equations in a body axis coordinate system as described in reference 4. Planar motion on a flat earth is considered. The jet forces acting on the body were derived by momentum considerations, described, for example, in reference 5. The vehicle is assumed to be a uniform beam and to lose mass uniformly along its length. The equations are restricted to small deviations of flight path and attitude angles from the vertical.

The rigid-body equations are:

$$\left. \begin{aligned} \ddot{x}_O &= \dot{\theta} \dot{y}_O - \left(\frac{g}{L}\right) - \left(\frac{g}{L}\right) I_{sp} \left(\frac{\dot{M}}{M}\right) + \left(\frac{F_{xA}}{ML}\right) \\ \ddot{y}_O &= -\dot{\theta} \dot{x}_O + \left(\frac{g}{L}\right) \theta - \left(\frac{g}{L}\right) I_{sp} \left(\frac{\dot{M}}{M}\right) (\delta - 4.64726q_1 - 7.85929q_2 - 10.99522q_3) \\ &\quad - \left(\frac{\dot{M}}{M}\right) \left(\frac{1}{2}\dot{\theta} - \dot{q}_1 - \dot{q}_2 - \dot{q}_3\right) + \left(\frac{F_{yA}}{ML}\right) \\ \ddot{\theta} &= 12 \left(\frac{g}{L}\right) I_{sp} \left(\frac{\dot{M}}{M}\right) \left(\frac{1}{2}\delta - 1.32364q_1 - 2.92963q_2 - 4.4976q_3\right) \\ &\quad + \left(\frac{\dot{M}}{M}\right) \left[2\dot{\theta} - 6(\dot{q}_1 + \dot{q}_2 + \dot{q}_3)\right] + 12 \left(\frac{M_{zA}}{ML^2}\right) \end{aligned} \right\} (1a)$$

The equation of motion for the  $i$ th elastic mode ( $i = 1, 2, 3$ ) is given by

$$\begin{aligned} \ddot{q}_1 &= -4 \left(\frac{g}{L}\right) I_{sp} \left(\frac{\dot{M}}{M}\right) (\delta - 4.64726q_1 - 7.85929q_2 - 10.99522q_3) \\ &\quad + 4 \left(\frac{\dot{M}}{M}\right) \left(\dot{y}_O - \frac{1}{2}\dot{\theta} + \dot{q}_1 + \dot{q}_2 + \dot{q}_3\right) + a_1 \left(\frac{EI}{M_0 L^3}\right) \left(\frac{I_{sp}}{\left(\frac{T}{W_0}\right)}\right) \left(\frac{\dot{M}}{M}\right) q_1 \\ &\quad - \left(\frac{\dot{M}}{M}\right) \dot{q}_1 + 4 \left(\frac{Q_{iA}}{ML}\right) \end{aligned} \quad (2a)$$

where the mode shapes have been normalized to unity at the trailing edge.

The total mass of the vehicle was assumed to be a linearly decreasing function of time, given by

$$M = M_0 + \dot{M}t \quad (3a)$$

where  $M$  is the mass at time  $t$ ,  $M_0$  is the initial or lift-off mass, and  $\dot{M}$  is the time rate of change of total vehicle mass. Then the variable mass parameter which appears in equations (1a) and (2a) is given by

$$\left(\frac{\dot{M}}{M}\right) = \left[t - \frac{I_{sp}}{\left(\frac{T}{W_0}\right)}\right]^{-1} \quad (4a)$$

since the thrust is related to the mass rate by the expression

$$T = -gI_{sp}\dot{M} \quad (5a)$$

Aerodynamic drag on the vehicle was neglected. The other aerodynamic forces were derived using momentum theory, as developed in reference 6, and a body shape corresponding to a parabolic body of revolution. Aerodynamic forces due to elastic bending, angular acceleration, and time rate of change of angle of attack due to wind were neglected. The resulting expressions for the aerodynamic terms appearing in equations (1a) and (2a) are

$$\left. \begin{aligned} \left(\frac{F_{xA}}{ML}\right) &= 0 \\ \left(\frac{F_{yA}}{ML}\right) &= -\left(\frac{\rho_0 SL}{M_0}\right) \frac{I_{sp}}{\left(\frac{T}{W_0}\right)} \left(\frac{\dot{M}}{M}\right) \left(\frac{\rho}{\rho_0}\right) \left\{ \left(\frac{V_{mw}}{L}\right)^2 (\alpha + \alpha_w) + \left(\frac{V_{mw}}{L}\right) \left[ \frac{8}{15} \dot{\alpha} + \frac{1}{2} \dot{\theta} \right] \right\} \\ \left(\frac{M_{zA}}{ML^2}\right) &= -\left(\frac{\rho_0 SL}{M_0}\right) \frac{I_{sp}}{\left(\frac{T}{W_0}\right)} \left(\frac{\dot{M}}{M}\right) \left(\frac{\rho}{\rho_0}\right) \left\{ \left(\frac{V_{mw}}{L}\right)^2 \frac{(\alpha + \alpha_w)}{30} - \left(\frac{V_{mw}}{L}\right) \left[ \frac{1}{10} \dot{\alpha} + \frac{3}{20} \dot{\theta} \right] \right\} \\ \left(\frac{Q_i}{ML}\right) &= -\left(\frac{\rho_0 SL}{M_0}\right) \frac{I_{sp}}{\left(\frac{T}{W_0}\right)} \left(\frac{\dot{M}}{M}\right) \left(\frac{\rho}{\rho_0}\right) \left\{ \left(\frac{V_{mw}}{L}\right)^2 C_{i1}(\alpha + \alpha_w) + \left(\frac{V_{mw}}{L}\right) [C_{i2} \dot{\alpha} + C_{i3} \dot{\theta}] \right\} \end{aligned} \right\} \quad (6a)$$

The  $C_{ij}$  terms which appear in the generalized aerodynamic force were evaluated numerically and are listed in table I for the first three elastic modes.



The vehicle is assumed to have an ideal control system with no structural feedback and negligible inertia forces associated with the rotating thrust vector. The control equation is

$$\delta = K_1\theta + K_2\dot{\theta} + K_3(\alpha + \alpha_w) \quad (7a)$$

where  $K_1$ ,  $K_2$ , and  $K_3$  are gain constants.

Several additional equations are required to solve the response problem. They are

angle of attack

$$\alpha = -\frac{\dot{y}_O}{\dot{x}_O} \quad (8a)$$

angle of attack due to wind

$$\alpha_w = \left( \frac{V_w}{V_{mw}} \right) \quad (9a)$$

flight-path angle

$$\gamma = \theta - \alpha \quad (10a)$$

inertial velocity

$$\left( \frac{V_m}{L} \right)^2 = \dot{x}_O^2 + \dot{y}_O^2 \quad (11a)$$

velocity relative to airstream

$$\left( \frac{V_{mw}}{L} \right)^2 = \left( \frac{V_w}{L} \right)^2 + \left( \frac{V_m}{L} \right)^2 - 2 \left( \frac{V_w}{L} \right) \left( \frac{V_m}{L} \right) \gamma \quad (12a)$$

altitude

$$\frac{h}{L} = \frac{h_O}{L} + \int_0^t \left( \frac{V_m}{L} \right) dt \quad (13a)$$

Bending moments at any station  $x_n$  along the center line of the missile are computed by the modal acceleration method considering aerodynamic and inertial loads. They are given by

$$\begin{aligned}
 \left( \frac{B.M.(x_n)}{W_0 L} \right) = & \left( \frac{\rho_0 S L}{M_0} \right) \left( \frac{\rho}{\rho_0} \right) \frac{1}{\left( \frac{g}{L} \right)} \left\{ \left( \frac{V_{mw}}{L} \right)^2 D_1 (\alpha + \alpha_w) + \left( \frac{V_{mw}}{L} \right) \left[ D_2 (\dot{\alpha} + \dot{\alpha}_w) + D_3 \ddot{\theta} \right] \right\} \\
 & - \frac{T/W_0}{I_{sp} \left( \frac{g}{L} \right) \left( \frac{\dot{M}}{M} \right)} \left\{ D_4 \left[ \ddot{y}_0 + \dot{\theta} \dot{x}_0 - \left( \frac{g}{L} \right) \theta \right] + D_5 \ddot{\theta} + \sum_j D_{nj} \ddot{q}_j \right\} \quad (14a)
 \end{aligned}$$

The constants appearing in equation (14a) were evaluated for stations of interest and are listed in table I.

REFERENCES

1. MacNeal, Richard H., Hill, Jack H., and Mazelsky, Bernard: The Effects of Time-Varying Aerodynamic Coefficients on Aeroelastic Response. WADD TR 60-390, April 1960.
2. Henry, Robert M., Brandon, George W., Tolefson, Harold B., and Lanford, Wade E.: A Method for Obtaining Detailed Wind Shear Measurements for Application to Dynamic Response Problems of Missile Systems. Proposed TN.
3. Geissler, Ernst D.: Problems in Attitude Stabilization of Large Guided Missiles. Aerospace Engineering, vol. 19, no. 10, October 1960, pp. 24-29, 68-72.
4. Thomson, William T.: Lagrange's Equations for Moving Coordinates. STL Report No. EM 9-15, July 1959.
5. Hausner, George W., and Hudson, Donald E.: Applied Mechanics Dynamics. Van Nostrand Company, Inc., Princeton, New Jersey, 1950.
6. Miles, J. W., and Young, Dana: Generalized Missile Dynamics Analysis, III - Aerodynamics. STL Report No. EM 8-9, April 1958.

TABLE I.- NUMERICAL DATA

$C_{ij}$			
$i \backslash j$	1	2	3
1	-0.223	-0.0108	-0.0169
2	0	-.0185	-.0739
3	-.0181	.00136	.00983

$x_n$	$D_1$	$D_2$	$D_3$	$D_4$	$D_5$	$D_{n1}$	$D_{n2}$	$D_{n3}$
0	0.533	0.1667	0.100	-0.500	-0.0833	0	0	0
.10	.434	.118	.05528	-.405	-.0810	-.00423	-.00369	-.00326
.20	.339	.0797	.02185	-.320	-.0747	-.0138	-.00979	-.00649
.30	.251	.0503	-.00017	-.245	-.0653	-.0245	-.0122	-.00407
.35	.211	.0388	-.00718	-.211	-.0598	-.0290	-.0111	-.00114
.40	.174	.0292	-.01181	-.180	-.0540	-.0325	-.00844	.00190
.45	.140	.0214	-.01434	-.151	-.0479	-.0348	-.00459	-.00414
.50	.110	.0151	-.01510	-.125	-.0417	-.0355	0	-.00490
.55	.0842	.0103	-.01446	-.101	-.0354	-.0348	.00459	-.00414
.60	.0618	.0066	-.01280	-.080	-.0293	-.0325	.00844	-.00190
.65	.0432	.0040	-.01049	-.061	-.0235	-.0290	.0111	-.00114
.70	.0284	.0022	-.00792	-.045	-.0180	-.0245	.0122	-.00407
.80	.0091	.0005	-.00321	-.020	-.0087	-.0138	.00979	-.00649
.90	.0012	.00007	-.00053	-.005	-.0023	-.00423	.00369	-.00326
1.00	0	0	0	0	0	0	0	0

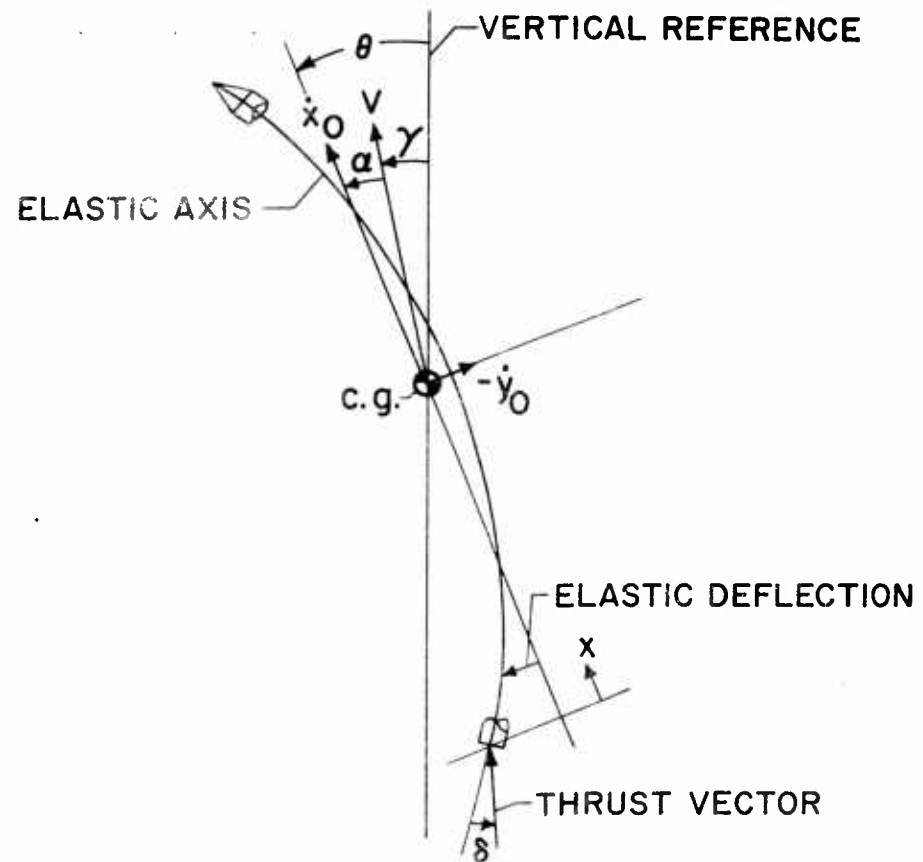


Figure 1.- Coordinate system for ascending rocket.

NASA

NASA

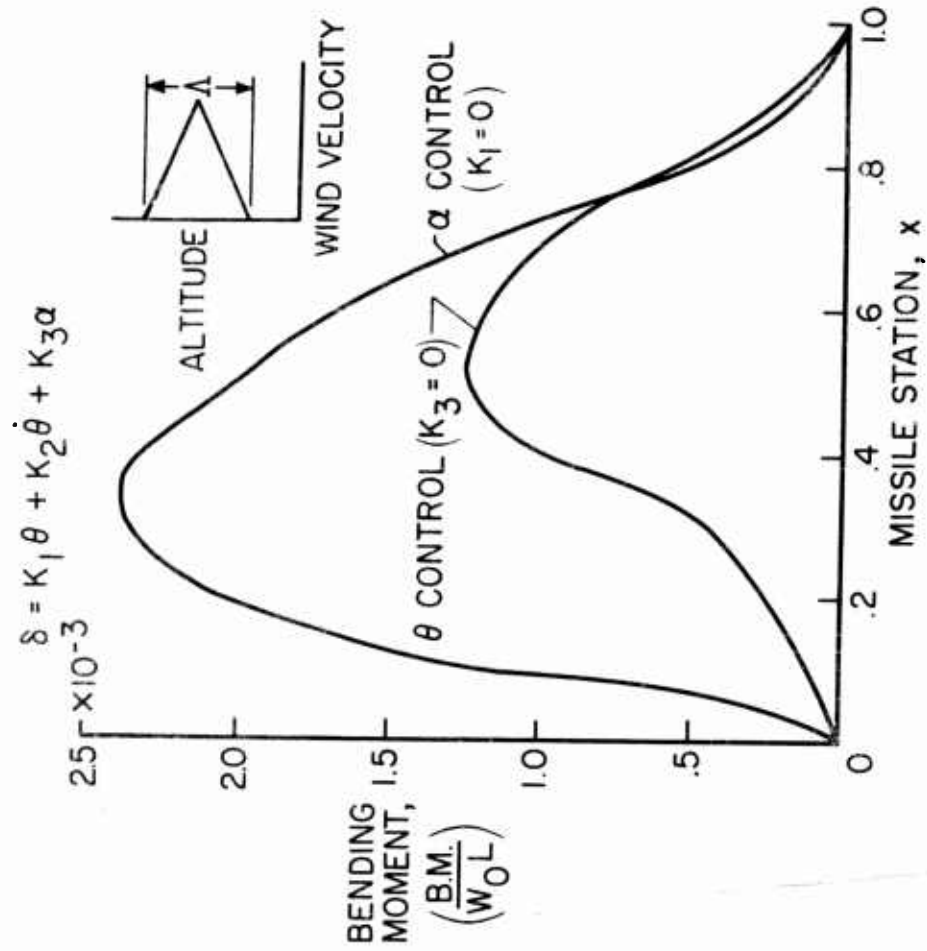


Figure 2.- Bending-moment distribution along missile.  $\Delta = 10,000$  ft,  
 $(V_w)_{\max} = 100$  ft/sec,  $\frac{\omega_1}{\omega_p} = 8.66$ .

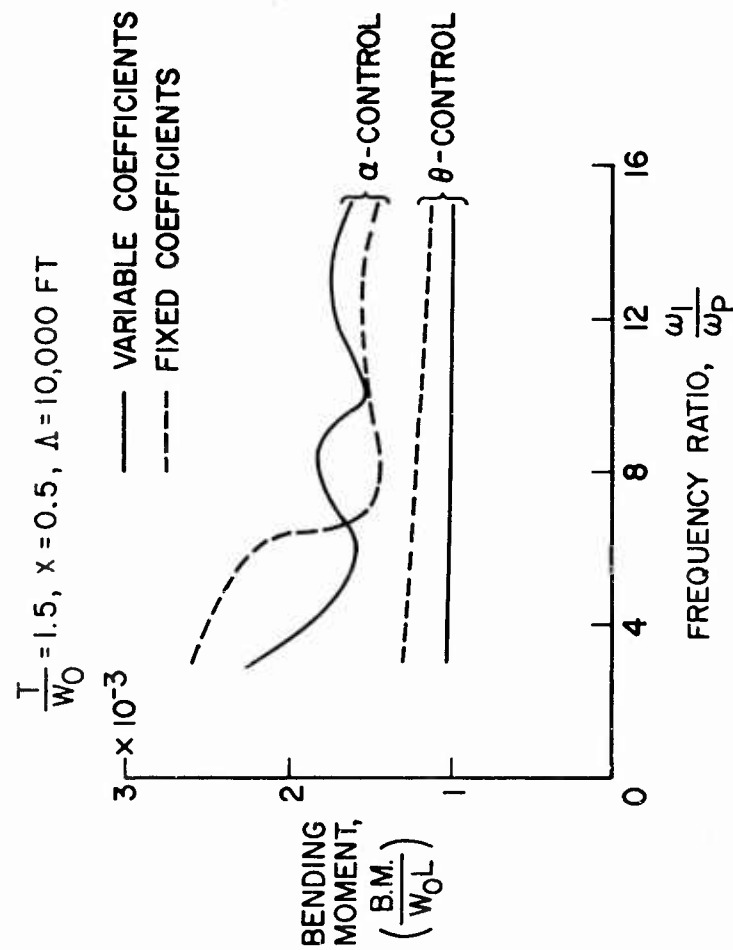


Figure 3.- Maximum bending-moment variation with frequency ratio.  $(V_{\dot{w}})_{\max} = 80 \text{ ft/sec.}$

NASA

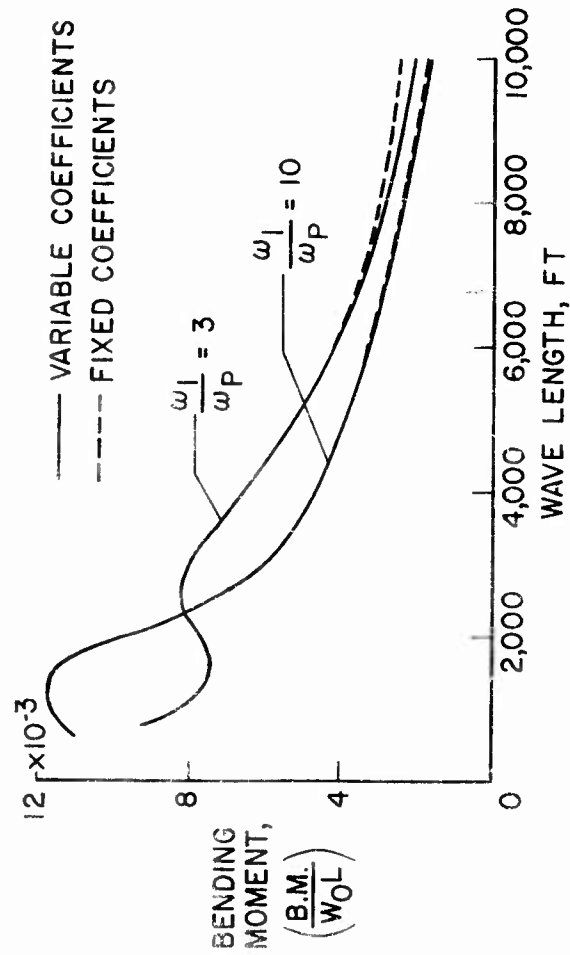
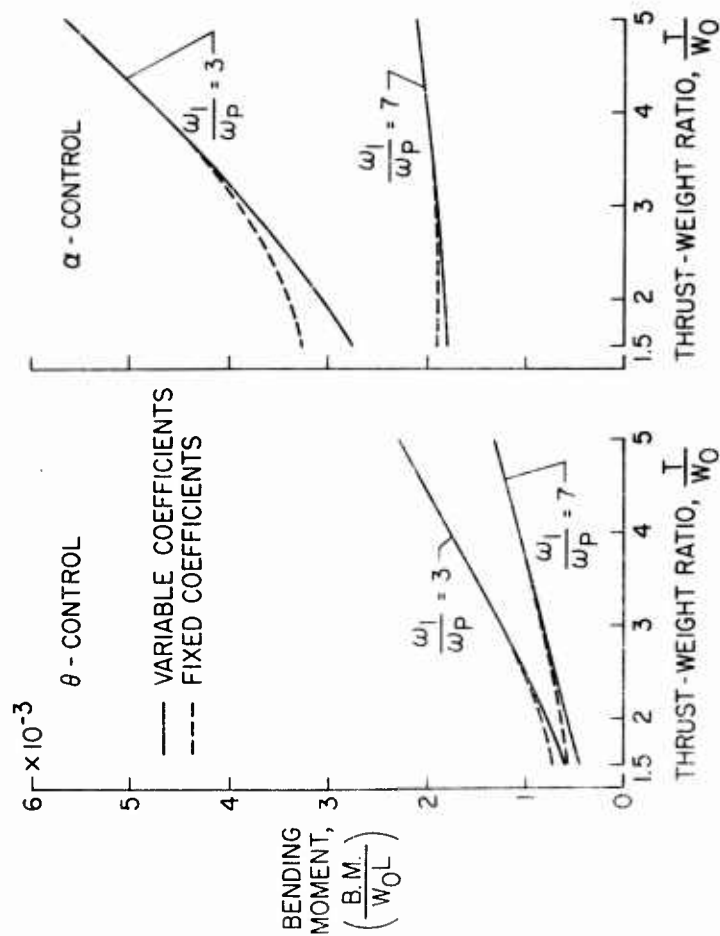


Figure 4.- Maximum bending-moment variation with wave length of shear reversal using  $\alpha$ -control.  
 $\frac{T}{W_0} = 1.5, \quad \alpha = 0.5, \quad (V_w)_{\max} = 100 \text{ ft/sec.}$

NASA





NASA

Figure 5.- Maximum bending-moment variation with thrust-to-weight ratio.  $x = 0.3$ ,  $\Lambda = 10,000$  ft,  $(V_w)_{\max} = 80$  ft/sec.

NASA

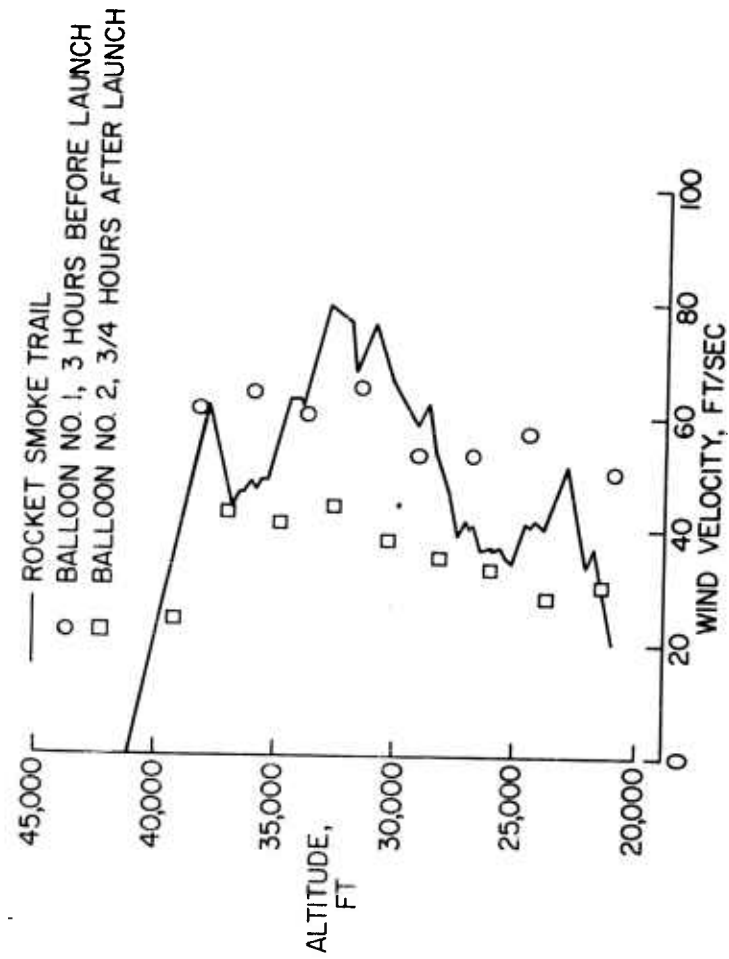
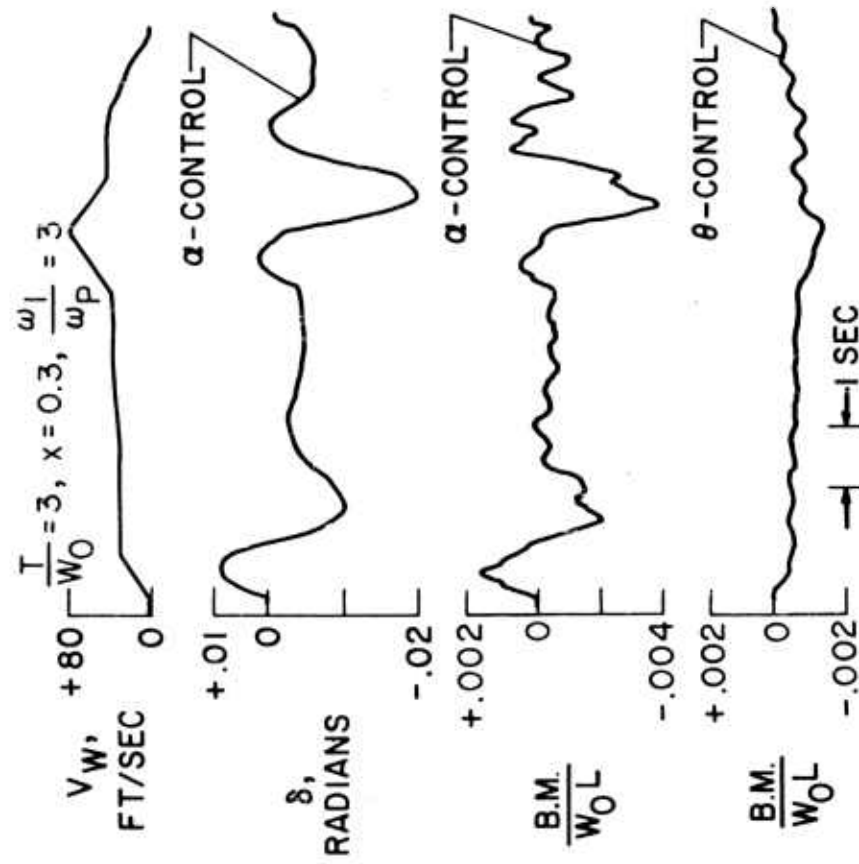
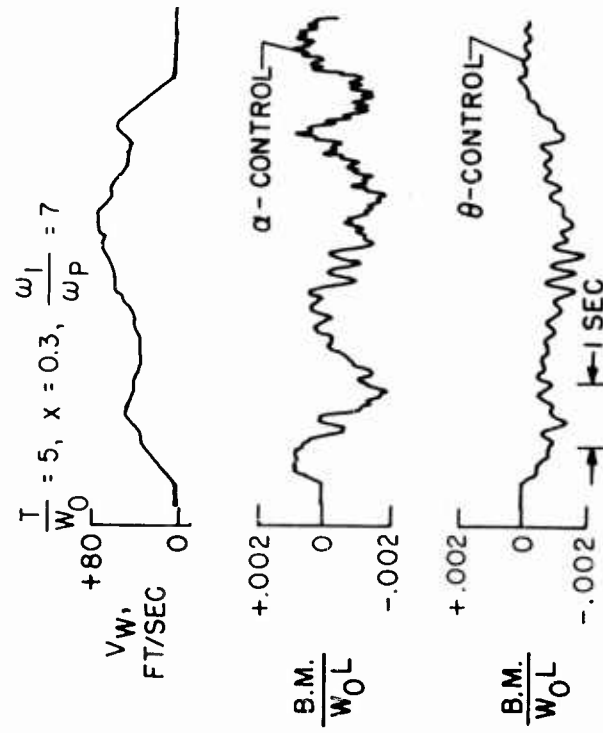


Figure 6.- Measured wind profiles (ref. 2).



NASA

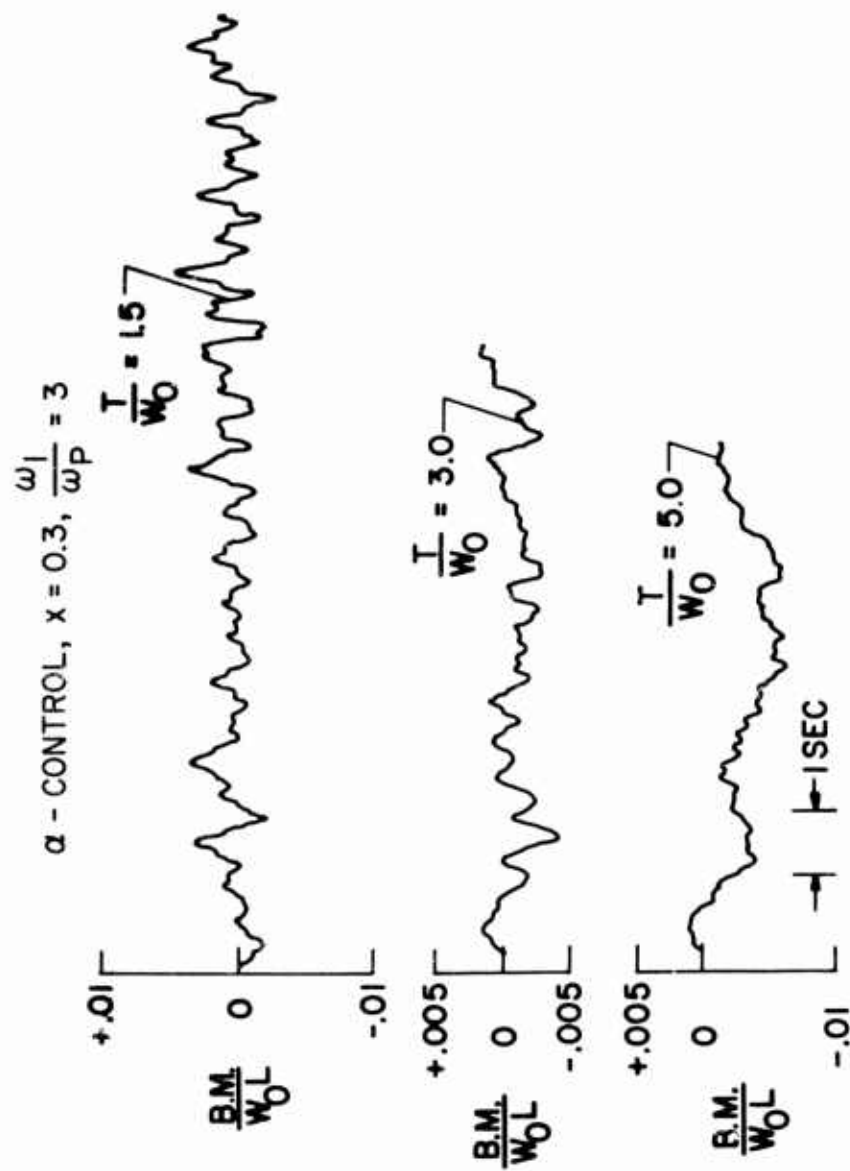
Figure 7.- Response time history due to flying through balloon wind profile no. 3.



(a)  $\alpha$ -control and  $\theta$ -control.

NASA

Figure 8.- Bending-moment time histories due to flying through the smoke-trail wind profile.

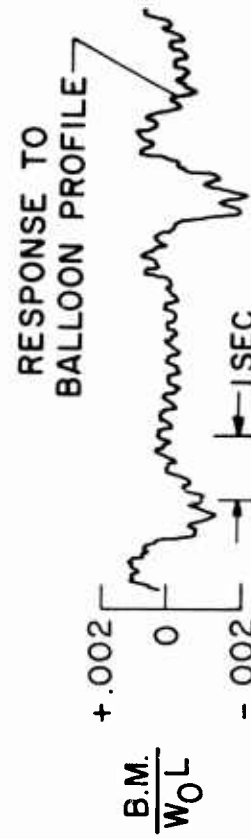


(b) Comparison at three thrust-to-weight ratios.

Figure 8.- Concluded.

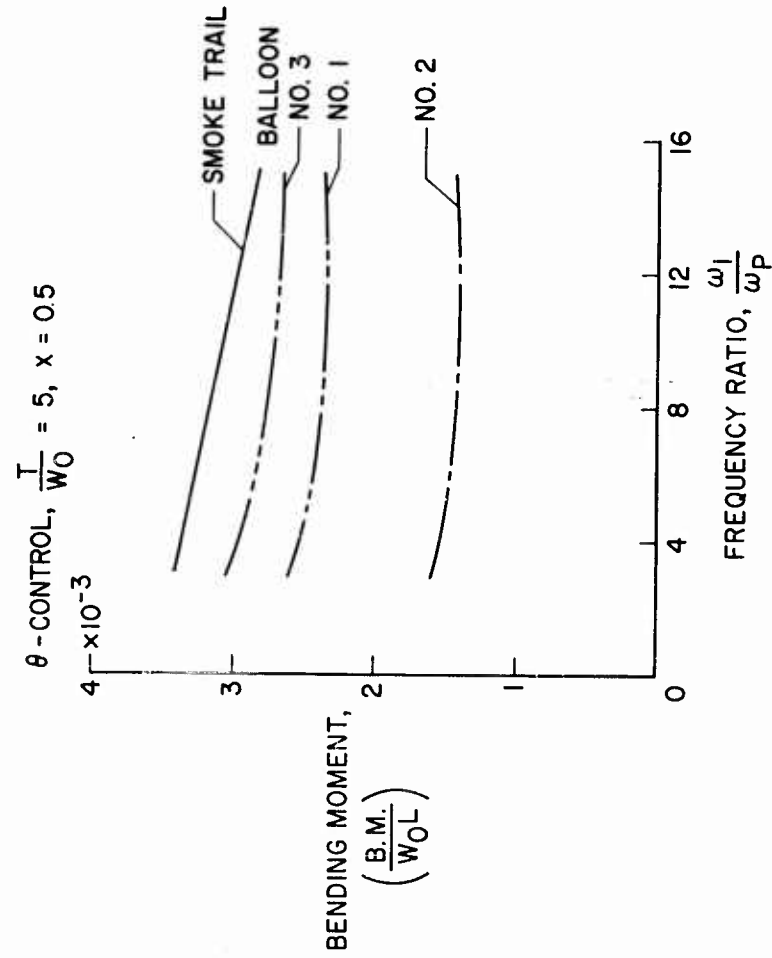
NASA

$\alpha$  - CONTROL,  $\frac{T}{W_0} = 3$ ,  $x = 0.3$ ,  $\frac{\omega_1}{\omega_p} = 7$



NASA

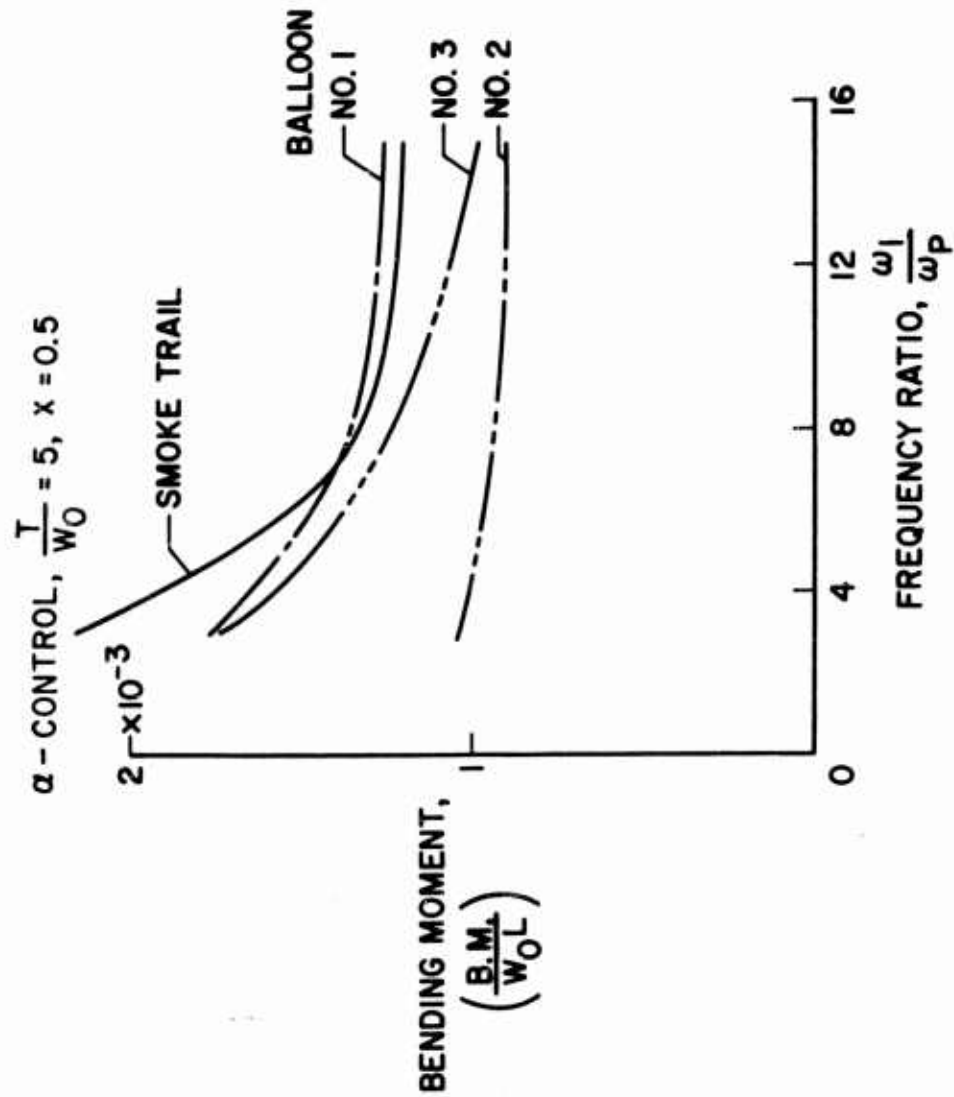
Figure 9.- Bending-moment time histories from flying through two wind profiles with  $\alpha$ -control.



(a)  $\theta$ -control.

NASA

Figure 10.- Maximum bending-moment variation with frequency ratio resulting from smoke-trail and balloon-measured wind profiles.

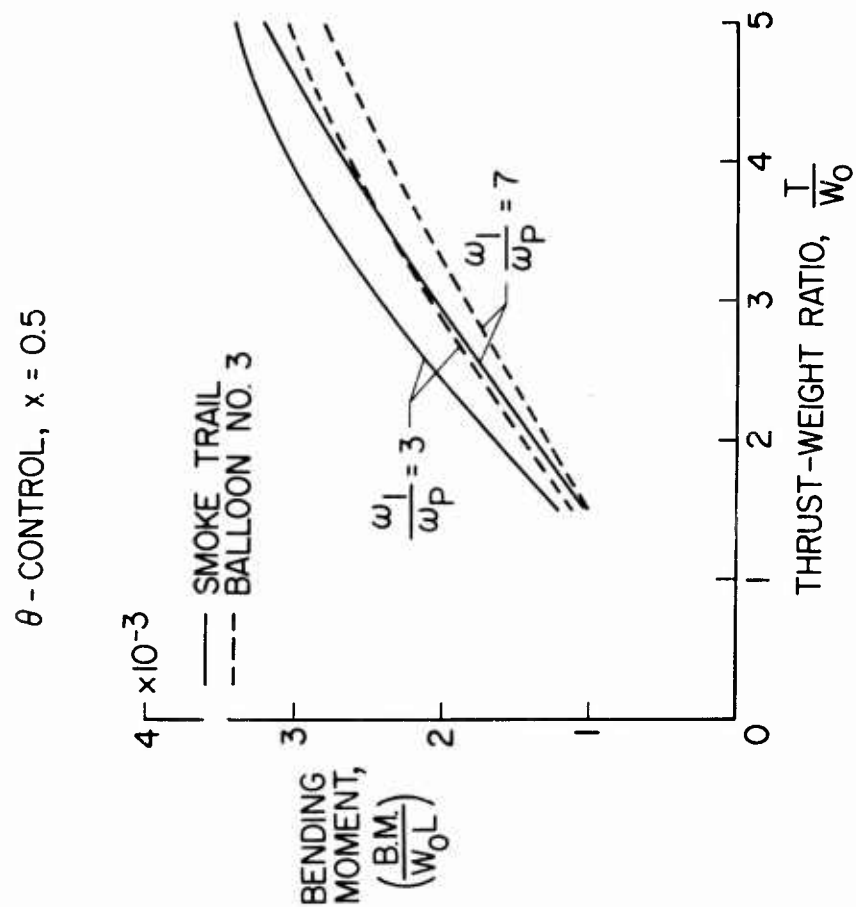


(b) α-control.

Figure 10.- Concluded.

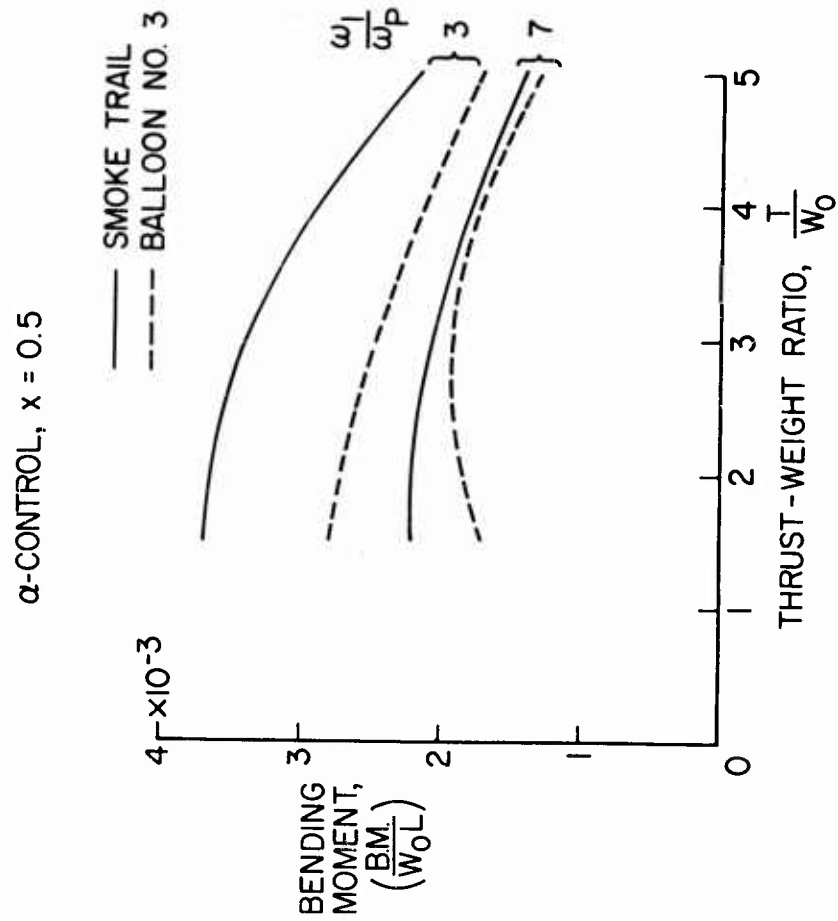
NASA



(a)  $\theta$ -control.

NASA

Figure 11.- Maximum bending-moment variation with thrust-to-weight ratio resulting from smoke-trail and balloon-measured wind profiles.



(b)  $\alpha$ -control.

Figure 11.- Concluded.

NASA

CALCULATION OF RANDOM GUST AND TAXI RESPONSE AND  
DEVELOPMENT OF FATIGUE TEST LOADING FOR DELTA WING  
AIRCRAFT

R. P. Peloubet  
Project Structures Engineer  
Convair, A Division Of General Dynamics Corporation  
Fort Worth, Texas

INTRODUCTION

A B-58 airplane is currently undergoing a cyclic loading test to determine its fatigue life. These tests are being conducted in compliance with the present Air Force policy requiring cyclic fatigue tests of all new aircraft. Loads are being applied to simulate the effect of the ground-air-ground cycle, maneuvers, flight through random turbulence, landing, nose gear touchdown, high speed taxi, braking, turning, ground handling, etc. All loads were determined analytically. This paper discusses those loads which were determined using power spectral density methods, viz. loads produced by flight through random turbulence and high speed taxiing over runways with random roughness. The major portion of the paper is directed toward the problem of obtaining gust loads. The latter portion discusses the differences in the somewhat similar problem of determining taxi loads.

The fatigue life of the B-58 is of special interest because of its low load factor design and because of its capability of high speed performance at low altitude.

The purpose of the cyclic fatigue tests was to generate realistic fatigue damage in the structure. Therefore, the primary effort in the analyses was directed toward determining realistic stress histories. The root mean square (r.m.s.) of the stress response to flight through continuous turbulence was computed for several points in the structure. Next the stress histories in terms of the probable number of stress peaks per unit of time exceeding specified stress levels were computed. Finally, a loading was developed which when cyclically applied to the test airplane produced approximately the computed stress histories at a number of points in the structure simultaneously.

Other possible approaches to the problem were

considered in the beginning of the project. One alternate method would compute the r.m.s. acceleration of the center of gravity and then the c.g. acceleration history. A 1-g load distribution would then be associated with the c.g. acceleration and applied to the test airplane. The amplitude of the cyclic load would be proportional to the magnitude of the acceleration peaks. It would be assumed that the stresses would be related to the c.g. acceleration by a constant factor at least throughout the frequency range of importance. This approach was rejected because of the flexibility of the B-58 in both the spanwise and chordwise directions. In addition, visual inspection of stress traces recorded during flight tests show high response at frequencies near the first symmetric mode as well as the short period mode. Therefore, realistic stress histories were not expected to be produced by cycling a 1-g load distribution in accordance with the c.g. acceleration history.

Another approach would compute the r.m.s. external bending moment of the combined airloads and inertia loads and to apply any load distribution which would produce the required bending moment history. This approach was rejected due to the highly redundant multi-spar construction of the B-58 wing. The spar and bulkhead structure of the B-58 wing is illustrated in figure 1. It is readily apparent that stresses at a specified span station cannot be determined simply from a knowledge of the external bending moment, shear or torque at that station but are dependent upon the spanwise and chordwise load distribution. In general, r.m.s. stresses would not be simply related to r.m.s. bending moments, shears, or torque.

Consequently, emphasis was placed on computing stress histories directly at a number of locations on the airplane. The goal in developing the loading for the test airplane was to duplicate the computed stress histories in the structure. It was speculated that such a loading would also be likely to produce the correct fatigue damage in intermediate regions.

#### SYMBOLS

- $\bar{A}$  Root mean square acceleration per unit root mean square gust velocity.
- $b_1, b_2$  Scale parameters used to define r.m.s. gust velocity probability density function.
- $\bar{C}$  Maximum response to a discrete gust with unit amplitude.

$\hat{f}(\bar{w}_G)$	R.M.S. gust velocity probability density distribution.
$\rho_n$	Structural damping for the $n$ th generalized coordinate.
$G(u_{de})$	Average number of derived gust velocity peaks per mile above the $u_{de}$ level.
$G_0$	Average number of derived gust velocity peaks per mile above the zero level.
$h$	Vertical amplitude.
$j$	$\sqrt{-1}$
$K$	Multiplying factor to be applied to the r.m.s. stresses and the unit equivalent load.
$L$	Atmospheric scale of turbulence.
$M_n$	Generalized Mass associated with the $n$ th generalized coordinate.
$m$	Mass per unit area.
$N(\sigma)$	Average number of crossings per second (with positive slope) of the $\sigma$ level.
$N_0$	Average number of crossings per second (with positive slope) of the zero level.
$\Delta p_s$	Pressure difference between upper and lower surface of the wing due to unit amplitude of the generalized coordinate.
$p_1, p_2$	Fraction of time spent or distance traveled in clear air turbulence and thunderstorm turbulence respectively.
$Q_n$	Generalized aerodynamic force.
$q_n$	Generalized coordinate.
$t$	Time variable.
$T$	Time period.
$\bar{T}, \bar{p}$	Indices used to indicate rigid body translation and pitch respectively.
$w_G$	Gust velocity.

$\bar{w}_G$	R.M.S. gust velocity.
$x, y, z$	Coordinate system with the $x$ -axis in the free stream direction.
$\delta$	Translational or angular deflection.
$\phi_\sigma$	Stress power spectrum.
$\phi_w$	Gust power spectrum.
$\sigma$	Stress.
$\bar{\sigma}$	R.M.S. stress.
$\omega$	Exciting frequency.
$\omega_n$	Natural frequency of the $n^{\text{th}}$ natural mode of vibration.

#### CONFIGURATIONS

Initially, six basic configurations were chosen to be analyzed. A configuration was defined by a Mach number, an altitude, and a gross weight. The number of configurations were extended to ten in the course of the analyses. The configurations were based on past and predicted future usage of the airplane.

#### POWER SPECTRAL DENSITY METHODS

For each configuration r.m.s. stresses were computed using power spectral density methods. This approach is often illustrated by referring to three curves such as are shown in figure 2. The upper curve describes the atmospheric turbulence by means of the gust power spectrum. The area under the curve within any frequency band is the contribution of that frequency band to the total mean square of the gust velocity. The middle curve is the square of the magnitude of the stress transfer function for some particular point in the structure. The stress transfer function is the stress response to an oscillatory gust velocity of unit amplitude. The product of the gust power spectrum and the square of the magnitude of the transfer function yields the stress power spectrum shown as the lower curve. The area under this curve within any frequency band is the contribution of that frequency band to the total mean square stress.

The analytical effort is mainly centered about the computation of the middle curve, the stress transfer function. The following sections describe the steps which were employed in the calculation of the stress transfer function.

# EQUATIONS OF MOTION

Lagrange's equations of motion were employed. The deflection of any point on the aircraft was assumed to be expressible as a superposition of a finite number of pre-assigned deflection shapes. For example, the vertical deflection was expressed as shown in equation 1.

$$h(x, y, z, t) = \sum_{n=1}^n h_n(x, y, z) q_n(t) \quad (1)$$

Where  $h_n(x, y, z)$  is the vertical deflection at point  $x, y, z$  for unit amount of the  $n$ th generalized coordinate,

$q_n$  is the  $n$ th generalized coordinate,

$x, y, z$  is a coordinate system with the  $X$  axis parallel to the free stream direction. The origin is stationary with respect to the airplane in the free stream direction but does not partake of the airplane vertical or lateral motion.

When natural modes of vibration and rigid body modes are used as generalized coordinates, the equations of motion can be reduced to the following matrix equation for harmonic motion.

$$\left[ A_{rs} \right] \left\{ \bar{q}_n \right\} = - \left\{ A_{nG} \right\} \quad (2)$$

Where  $q_n = \bar{q}_n e^{i\omega t}$

$$A_{nn} = \left[ 1 - \left( \frac{\omega_n}{\omega} \right)^2 (1 + jg_n) \right] M_{nn} + Q_{nn}$$

$$A_{ns} = Q_{ns} \quad n \neq s$$

$$Q_{ns} = \frac{1}{\omega^2} \iint_{\text{Surface}} h_n \Delta p_s(\omega) dx dy$$

$$Q_{nG} = \frac{1}{\omega^2} \iint_{\text{Surface}} h_n \Delta p_G(\omega) dx dy$$

- $m_{rr}$  is the generalized mass
- $\omega_r$  is the natural frequency of the  $r^{\text{th}}$  natural mode
- $\omega$  is the frequency of the excitation forces
- $\Delta p_s(\omega)$  is the oscillatory pressure difference between upper and lower wing surfaces due to oscillation of the  $r^{\text{th}}$  generalized coordinate with unit amplitude.
- $\Delta p_g(\omega)$  is the oscillatory pressure difference due to the gust velocity.

#### OSCILLATORY AERODYNAMICS

Because of the low aspect ratio of the wing and because of its flexibility in the chordwise as well as the spanwise direction, it was considered necessary to employ finite span, compressible flow lifting surface methods to predict the oscillatory pressure distribution. In the subsonic range the kernel function method was employed. The method presented in reference 1 was used to solve the integral equation relating pressure, downwash and the kernel function. Twenty-five downwash collocation points on each wing semi-span were employed. In the supersonic range, the oscillatory pressure distribution was computed using the box method as presented in reference 2. Fifty boxes were used to represent the wing area on each side of the fuselage centerline. In both cases it was possible to use IBM 704 programs previously coded for flutter analysis work. Equation 2 reduces to the equations of motion used in the flutter analyses when the right hand side is set equal to zero.

The vertical velocity of the gust was represented as a sine wave with unit amplitude traveling with the free stream.

$$w_g(x, t) = e^{i\omega(t - x/U)} \quad (3)$$

Where  $w_g$  is the vertical gust velocity

$U$  is the free stream velocity.

#### NATURAL MODES OF VIBRATION

A direct analogy electric analog computer was used to determine the natural modes of vibration. The mass and stiffness properties of the entire airplane were simulated. Approximately 60 lumped masses were used to represent the mass distribution over one half the air-



plane. The bending stiffness in both the spanwise and chordwise directions together with the torsional stiffness of the torque boxes were simulated. The underslung engines were elastically attached to the wing with freedom to respond vertically, laterally, fore-and-aft and to pitch, roll, and yaw.

Natural modes of vibration were first obtained for a configuration simulating the airplane on its landing gear. The natural frequencies and mode shapes were compared with those previously obtained during the full scale B-58 ground vibration tests. Small adjustments were made in the mass and stiffness simulation until good correlation was obtained for the first six symmetric natural modes of vibration. The landing gear simulation was then removed to obtain natural frequencies of the airplane freely suspended in space. The natural frequencies and mode shapes for the first four symmetric modes of vibration for a 93,000 lb. gross weight configuration are shown in figure 3.

#### STRESS LOCATION

The location of the wing stress points to be analyzed were chosen on the basis that some of them should be as close to fatigue critical locations as was known at the time and some of them were to be located such that representative stresses could be obtained over all regions of the wing. Ten stress points on the wing were chosen. Their locations are shown in figure 4. Points 2 and 8 were web shear stresses. The remaining stresses were axial skin stresses.

#### STRESS ANALYSES

An IBM 704 program was used to conduct the required stress analyses. The method is described in reference 3. The method involves the concept of computing a stiffness matrix. The structure of the entire airplane was represented as a gridwork of intersecting spars and bulkheads. The bending stiffness of small segments of each beam and bulkhead was represented including spar caps and skin. The torsional stiffness of each torque box was represented. By inverting the stiffness matrix, a flexibility matrix of order 200 was obtained relating deflections and loads as shown in equation 4.

$$\left\{ \delta \right\} = \left[ S \right]^{-1} \left\{ L \right\} \quad (4)$$

$S$

represents the elements of the stiffness matrix,

$L$

represents loads or moments,

$\delta$  represents translational or rotational deflections.

For a specified external loading the resulting deflections were computed. From the known deformation of each structural element of the idealized structure the internal loads and stresses compatible with the deflections were computed. This procedure had previously been shown to predict stresses that were in close agreement with stresses measured from a three eighths scale elastic model of the B-58.

#### STRESS TRANSFER FUNCTIONS

An IBM program was coded to solve equation 2 for the magnitude and phase angle of the generalized coordinates. The generalized mass, generalized aerodynamic forces and frequency data were supplied as input. In order to define the transfer function it is necessary to solve equation 2 for a large number of frequencies. These equations were solved for over 200 values of the exciting frequency, ranging from 0.5 rad/sec to 60 rad/sec. However, the generalized aerodynamic forces were computed for a much smaller number of frequencies. The generalized aerodynamic forces vary with frequency in a very "smooth" manner and can be interpolated very accurately. An interpolation procedure was coded into the IBM program that would permit equation 2 to be solved for many intermediate frequencies. In this manner, the transfer function peaks and valleys could be defined very accurately.

After the magnitude and phase of the generalized coordinate response is computed, there are essentially two approaches to determining the stress response. One method called the mode displacement method computes the stress response by associating a stress distribution with each generalized coordinate. The stress at station  $i$  is computed by summing the products of each generalized coordinate response times the corresponding stress per unit generalized coordinate for  $n$  flexible generalized coordinate.

$$\sigma(x_i, y_i, z_i) = \sum_{n=1}^n \sigma_n(x_i, y_i, z_i) \bar{q}_n \quad (5)$$

Where

$\sigma(x_i, y_i, z_i)$  is the total stress at any point  $i$

$\sigma_n(x_i, y_i, z_i)$  is the stress at point  $i$  due to unit deflection of the  $n$  generalized coordinate.

The stress per unit displacement of the  $r^{\text{th}}$  generalized

coordinate is determined by computing the stress due to the inertia loading associated with  $r$ th natural mode of the airplane freely suspended in a vacuum.

The other approach called the load summation method would compute the total inertia plus aerodynamic load distribution at each excitation frequency for  $n$  flexible generalized coordinates plus rigid body translation and pitch.

$$L(x, y) = \sum_{n=1}^{nTP} \Delta \rho_n \Delta x \Delta y \bar{q}_n + \Delta \rho_G \Delta x \Delta y + \sum_{n=1}^{nTP} \omega^2 \delta_n m(x, y) \Delta x \Delta y \bar{q}_n \quad (6)$$

Where  $L(x, y)$  is the total load on a small area  $\Delta x \Delta y$   
 $m(x, y)$  is the mass per unit area.

Substituting, this combined loading into equation 4 the stress distribution could be computed. For a sufficient number of degrees of freedom the two approaches should yield identical results. It has been demonstrated (4) that in general the second method converges more rapidly than the first. However, when the magnitude of the task of developing a loading from equation 6 for each excitation frequency and then conducting a stress analysis for each loading is realized, the mode displacement method becomes more attractive even at the expense of including more generalized coordinates. Accordingly, it was decided to use the first four natural modes of vibration plus rigid body translation and pitch in the equations of motion and employ the mode displacement method. The stress distributions associated with each of the natural modes used in the analysis of the 93,000 lb. gross weight configuration are shown in table 1. Each natural mode of vibration was normalized to a one foot deflection at the maximum deflection point.

The stress transfer functions for the 93,000 lb. gross weight configuration, were obtained by substituting the data from table 1 into equation 5 together with the generalized coordinate response per unit sinusoidal gust velocity computed from equation 2.

#### ATMOSPHERIC TURBULENCE

Because of the low aspect ratio of the B-58, the assumption of one dimensional atmospheric turbulence was considered to be adequate. The vertical gust velocity was considered to be random in the flight direction but constant in the spanwise direction. The analytic expression for the gust velocity power spectrum recommended in

reference 5, normalized for a one foot per second r.m.s. gust velocity was used.

$$\phi_w(\omega) = \frac{L}{\pi U} \frac{\left[1 + 3 \left(\frac{\omega L}{U}\right)^2\right]}{\left[1 + \left(\frac{\omega L}{U}\right)^2\right]^2} \quad (7)$$

Where  $\phi_w$  is the gust power spectrum  
 $L$  is the scale of turbulence.

#### R.M.S. STRESSES AND CHARACTERISTIC FREQUENCIES

The stress power spectrums were computed by multiplying the square of the absolute value of the stress transfer functions by the gust velocity power spectrum.

$$\phi_\sigma(\omega) = \left| \frac{\sigma}{w_G} \right|^2 \phi_w(\omega) \quad (8)$$

The r.m.s. stress and characteristic frequency were computed in the usual way by the following expressions

$$\sigma = \left[ \int_0^\infty \phi_\sigma(\omega) d\omega \right]^{1/2} \quad (9)$$

$$N_0 = \frac{1}{2\pi} \frac{\left[ \int_0^\infty \omega^2 \phi_\sigma d\omega \right]^{1/2}}{\left[ \int_0^\infty \phi_\sigma d\omega \right]^{1/2}} \quad (10)$$

Equation 9 and 10 were approximated by integrating over the frequency range from 0 to 10 cps.

#### SCALE OF TURBULENCE

The scale of turbulence was assumed to be 500 feet for sea level conditions and 1000 feet for high altitude conditions. The probability density distribution of the r.m.s. gust velocity magnitude as presented in reference 6 was used for conditions in which the scale of turbulence was assumed to be 1000 feet. This data can be used with Rice's equation to compute the expected number of occurrences per second in which a trace of the stress response crosses any specified level with a positive

slope.

$$N(\sigma) = N_0 \left[ p_1 e^{-\sigma/b_1\sigma} + p_2 e^{-\sigma/b_2\sigma} \right] \quad (11)$$

The terms  $p_1$  and  $p_2$  are the fractions of total time spent in clear air turbulence and thunderstorm turbulence respectively. The terms  $b_1$  and  $b_2$  are scale parameters. The products  $b_1\sigma$  and  $b_2\sigma$  determine the slopes of a plot of  $N(\sigma)$  vs.  $\sigma$  for clear air turbulence and thunderstorm turbulence, respectively. The r.m.s. gust velocity probability density function was developed (6) from measured velocity-c.g. acceleration-altitude data. The acceleration peaks above specified levels were counted and converted to derived gust velocity peaks. The average number of derived gust velocity peaks per mile above specified levels, obtained in this manner, were then equated to the integral of the product of the number of gust velocity crossings as predicted by Rice's equation for a constant r.m.s. gust velocity, times the unknown r.m.s. gust velocity probability density function.

$$G(U_{de}) = G_0 \int_0^{\infty} e^{-U_{de}^2 / 2 \left( \frac{\bar{A}}{\bar{C}} \right)^2 \bar{w}_G^2} \hat{f}(\bar{w}_G) d\bar{w}_G \quad (12)$$

Where $G(U_{de})$	is the number of peaks above the $U_{de}$ level.
$G_0$	is the number of peaks above the zero level.
$U_{de}$	is the derived gust velocity.
$\bar{A}$	is the r.m.s. C.G. acceleration response per unit r.m.s. gust velocity.
$\bar{C}$	is the peak C.G. acceleration response per unit discrete gust.
$\bar{w}_G$	is the r.m.s. gust velocity.
$\hat{f}(\bar{w}_G)$	is the r.m.s. gust velocity probability density functions.

The integral equation was then solved to determine the r.m.s. gust velocity probability density function. In

order to carry out the procedure, it was necessary to assume a value of the scale of turbulence so that the term  $\bar{A}$  could be evaluated. In reference 6, the scale of turbulence was assumed to be 1000 feet for all altitudes. It is consistent with the above reasoning to modify the r.m.s. gust velocity probability density function if the scale of turbulence is assumed to be any value other than 1000 feet. This modification is reflected only in the calculation of the scale parameters  $b_1$  and  $b_2$  for clear air and thunderstorm turbulence respectively. The computed values of  $b_1$  and  $b_2$  for sea level conditions using data from reference 6 are shown in table 2 for two additional assumed values of the scale of turbulence.

TABLE 2

Comparison Of Scale Parameters  $b_1$  and  $b_2$  For  
Several Values Of The Scale Of Turbulence (Sea Level)

$L$	$b_1$	$b_2$
1000	4.6	9.4
500	3.57	7.29
300	3.13	6.66

In order to determine the importance of the scale of turbulence in the prediction of the number of stress crossings per unit of time, r.m.s. stresses were computed for sea level conditions first for a scale of turbulence of 500 feet and then 300 feet. A comparison of the r.m.s. stresses and characteristic frequencies computed for the ten points using the two values of the scale of turbulence is shown in table 3. Although the r.m.s. stresses computed using a scale of turbulence of 300 feet are approximately 20 percent higher than those computed for a scale of turbulence of 500 feet, the products  $b_1\sigma$  differ by less than 5 percent and the products  $b_2\sigma$  differ by less than 10 percent. In addition, the change in characteristic frequency due to the change in the scale

of turbulence is small. Hence, the increase in the number of crossings of specified levels, as predicted by equation 11 due to a decrease in the scale of turbulence is not nearly so great as might be expected from the increase in the r.m.s. stress values. A comparison of the number of crossings per hour in clear air turbulence is shown in figure 5 for stress point one.

#### STRESS HISTORY

The predicted stress history for each point was computed using equation 11. The number of crossings of a stress level which is  $k$  times the r.m.s. stress was expressed as

$$TN(K) = TN_0 \left[ p_1 e^{-K/b_1} + p_2 e^{-K/b_2} \right] \quad (13)$$

where  $T$  is the total time (seconds) in which the airplane is expected to operate in a specified Mach-altitude-gross weight configuration during its lifetime. The number of peaks occurring in small incremental  $\Delta K$  bands were computed by taking the difference between the number of positive slope crossings of two levels that are  $\Delta K$  apart.

$$N_p(K) = T \left[ N \left( K - \frac{\Delta K}{2} \right) - N \left( K + \frac{\Delta K}{2} \right) \right] \quad (14)$$

A full stress cycle with amplitude  $K\bar{\sigma}$  was assumed to occur about the 1-g mean stress level for each peak predicted by equation 14 for the purpose of fatigue analyses.

#### EQUIVALENT LOADING

It was desired to obtain a single load distribution which when cyclically applied to the test airplane, would simultaneously produce the correct fatigue damage at each of the ten stress point locations. It was speculated that such a loading would be likely to produce the correct fatigue damage in intermediate regions. The cyclic loads were to be applied to the test airplane suspended in a 1-g level flight attitude and consequently would need to be balanced such that the summation of the loads in all directions would be zero as well as the summation of the moments about all axes. The loads were to be applied with hydraulic rams. To reduce the complexity of the load application it was also specified that the load at each application point should be either in phase ( $0^\circ$ ) or out of phase ( $180^\circ$ ) with the load at every other application point.

As can be seen from equation 14 the number of stress cycles to be applied to each stress point with cyclic amplitude  $K$  times the local r.m.s. would be the same if each of the ten points had the same characteristic frequency. Table 3 shows the characteristic frequency to be different for each of the ten points. So the number-of-cycles condition cannot be satisfied exactly for all points. However, the characteristic frequencies are somewhat similar for the majority of the points, especially those with the high r.m.s. levels. Hence, the number-of-cycles condition is approximated by choosing a value of the characteristic frequency which is in the same neighborhood as the characteristic frequency for the majority of the points (say  $N_0 = 1.95$  cps for  $L = 500$ ).

If a loading could then be developed which would produce a stress that equalled the r.m.s. stress at each point, approximately the correct stress history would be produced at each point. In order to develop such a loading attention was turned to the power spectrums of each of the ten stress points shown in figure 6. It can be seen that the general shape of these spectrums are quite similar except for points 2, 8, and 10. The short period frequency for this configuration is almost 6 rad/sec. and the response peak at this frequency merges into the response peak associated with the first natural frequency of the structure. It is readily apparent that the largest contribution to the r.m.s. stresses occurs in this frequency range for the majority of the ten points. The response of the elastic generalized coordinates at the peak frequency 13.5 rad/sec. due to the unit sinusoidal gust velocity is shown in table 4, column one. Converting the generalized coordinates to polar form and normalizing on the first generalized coordinate shows the phase angles to be close to either 0 or 180 degrees as can be seen in column 2. An approximation of the generalized coordinated,  $\tilde{q}_n$ , is shown in column 3 with magnitude equal to column 2, but with a plus or minus sign attached depending on whether the phase angle in column 2 is closer to 0 or 180 degrees. Therefore, the phase angles of the approximate generalized coordinates are either 0 or 180 degrees exactly. Under column 1 of table 5 are listed the stresses at the ten points if the stresses per generalized coordinate are superimposed in the same ratio as the approximate generalized coordinates.

$$\tilde{\sigma}(x_i, y_i, z_i) = \sum_{n=1}^4 \sigma_n(x_i, y_i, z_i) \tilde{q}_n \quad (15)$$

Column 2 shows the stresses normalized on the highest



r.m.s. stress, that is, stress point one. It can be seen by comparing column 2 to column 3 that there is a certain amount of similarity between the stresses obtained in this manner and the r.m.s. stresses.

The load distribution that produces the stress distribution in column 2 of table 5 can easily be obtained by superimposing the zero airspeed inertia loads associated with each of the flexible generalized coordinates in the same ratio as the approximate generalized coordinates  $\tilde{q}_n$  and normalized to produce the r.m.s. stress at point one. This loading is called an equivalent loading because it produces approximately the same elastic deformation as predicted by the equations of motion at the frequency 13.5 rad/sec. However, it is not the total inertia response load or the total inertia plus airload response at this frequency. The equivalent load is balanced in all directions and about all axes since the same is true of each of the zero airspeed inertia loads associated with each flexible generalized coordinate. The stresses produced by applying unit amount of the equivalent loading differ from the r.m.s. stresses by less than 10 percent with the exception of points 2, 8, and 10. From the stress power spectrums it can be seen that stress points 2, 8, and 10 have large contributions to their total r.m.s. value from higher frequencies. An equivalent loading would need to be developed at a higher frequency to produce a stress distribution that would satisfy these three points. However, the r.m.s. stresses at these three points are lower than the other seven. Therefore, if a single loading has to be chosen it would be better to choose a loading that produces a stress distribution compatible with the points that are expected to experience the highest fatigue damage.

Multiples of the unit equivalent loading were applied to the test airplane such that the stress history predicted by equation 14 is satisfied exactly for point one and the stress history at each of the other points is approximated.

This procedure was repeated for all Mach-altitude-gross weight configurations that were considered.

#### HIGH SPEED TAXI ANALYSES

The stress response to taxi over a runway with random roughness was computed in substantially the same manner as was used in the random gust analyses. The differences will be briefly discussed. The natural modes were computed with the airplane resting on its landing gear. The input force for computing the transfer functions consisted of the mass coupling between the first six natural modes of vibration and the combined rigid body translation and pitching motion produced by the main gear and nose gear motion in following the path of a

sinusoidal runway. It was found that the wing stress transfer functions were almost independent of taxi speed. The primary effect of speed is to vary the ratio of the translation to pitching motion for any particular frequency due to the difference in wave length needed to produce the same frequency at two different taxi speeds. The speed effect was found to be negligible on the wing stress transfer functions.

The runway roughness power spectrum was obtained from 34 power spectrums in reference 7 and 2 power spectrums in reference 8 and 9. These spectrums were averaged by passing a regression line through the combined power spectral data, (10). The following expression was obtained for the average runway power spectrum.

$$\phi_R(\omega) = \frac{.000005777}{u} \left( \frac{\omega}{u} \right)^{-2.576} \quad (16)$$

$$\phi_R(\Omega) = .000005777 \Omega^{-2.576}$$

$$\Omega = \frac{2\pi}{\lambda}$$

The minimum value of  $\Omega$  in the averaged data was .05.

Since the stress transfer function was assumed to be independent of the taxi speed, the ratio of the r.m.s. stress at two taxi speeds using equation 16 reduced to the following.

$$\frac{\bar{\sigma}(u_2)}{\bar{\sigma}(u_1)} = \left( \frac{u_2}{u_1} \right)^{.788} \quad (17)$$

$$\text{Or} \quad \bar{\sigma}(u) = \bar{\sigma}(1) u^{0.788}$$

where  $\bar{\sigma}(1)$  is the r.m.s. stress for a 1 ft/sec. taxi speed. Assuming the runway roughness to be a stationary, Gaussian process, Rice's equation was again used to predict the number of stress crossings of specified levels per second.

$$N(\sigma) = N_0 e^{-\frac{\sigma^2}{2\bar{\sigma}^2}} \quad (18)$$

The majority of the taxi fatigue damage was found to occur during the take-off and landing runs in which the speed was continually varying. In these cases, the take-off or landing velocity was expressed as a function of time.

$$U = U(t) \quad (19)$$

The r.m.s. stress expressed in equation 17 as a function of velocity was then expressed as a function of time

$$\bar{\sigma}(t) = \bar{\sigma}(1) [U(t)]^{0.788} \quad (20)$$

Hence, the number of crossings per second for the fraction of time  $dt/T$  during which the taxi speed was of magnitude  $U$ , was expressed as

$$dN(\sigma) = N_0 e^{-\sigma^2 / 2 \bar{\sigma}^2(t)} dt/T \quad (21)$$

The total number of crossings per second during a take-off or landing was expressed as

$$N(\sigma) = \frac{N_0}{T} \int_0^T e^{-\sigma^2 / 2 \bar{\sigma}^2(t)} dt \quad (22)$$

where  $T$  is the total take-off or landing time.

#### EVALUATION OF CYCLIC FATIGUE TESTS

During the cyclic fatigue test the stress history is being recorded by many strain gages on the airplane. Currently another B-58 airplane is being equipped with a gust boom and is being instrumented with strain gages and accelerometers. Time histories of the gust velocity and the response data will be recorded during flight through turbulence. The data will be reduced to power spectrum and cross spectrum form and combined to obtain experimental transfer functions. These transfer functions will then be used in the same manner as previously described for the theoretical transfer functions to compute stress histories. The stress histories computed with the experimental transfer functions will then be compared to the stress histories recorded during the cyclic fatigue tests to reevaluate the accumulated fatigue in terms of airplane life.

REFERENCES

1. Hsu, P. T., Flutter Of Low Aspect Ratio Wings, Part I. M.I.T. Aeroelastic and Structures Research Laboratory Report 64-1, October 1957.
2. Pines, S., and Dugundji, J., Application Of Aerodynamic Flutter Derivatives To Flexible Wings With Supersonic And Subsonic Edges, Republic Aviation Report E-SAF-2, April 1954.
3. Archer, J. S., A Stiffness Matrix Method Of Natural Mode Analysis. Proceedings Of The IAS National Specialists Meeting, Dynamics and Aeroelasticity, November 6-7, 1958.
4. Bisplinghoff, R. L., Ashley, H., and Halfman, R. L., Aeroelasticity. Addison-Wesley Publishing Company, Inc., 1955.
5. Press, H., Meadows, M. T., and Hadlock, I., A Reevaluation Of Data On Atmospheric Turbulence And Airplane Gust Loads For Application In Spectral Calculations, NACA TR 1272, 1956.
6. Press, H., and Steiner, R., An Approach To The Problem Of Estimating Severe And Repeated Gust Loads For Missile Operations, NACA TN 4332, September 1958.
7. Thompson, W. E., Measurements And Power Spectra Of Runway Roughness At Airports In Countries Of The North Atlantic Treaty Organization, NACA TN 4303.
8. Walls, J. H., Houbolt, J. C., and Press, H., Some Measurements And Power Spectra Of Runway Roughness, NACA TN 3305, November 1954.
9. Data Published in NASA Conference On Some Problems Related To Aircraft Operation, November 5-6, 1958.
10. Murphy, A. C., Power Spectra Of Runway Roughness For Use In B-58 Taxi Analysis, Convair Fort Worth Structures Dynamics Memorandum Report SDGM-94, February 1959.

TABLE 1  
Stress At Station 1 Due To Unit Deflection  
Of The  $r$ th Generalized Coordinate

$i \downarrow r \rightarrow$	1	2	3	4
1	-24261	1989	-12747	10083
2	-507	-1805	1376	-6648
3	-8282	-14540	-1451	4526
4	-29139	-4244	-3805	1849
5	-7920	3520	-10623	13900
6	-18632	3237	-12822	13094
7	-17113	4202	-5468	6743
8	-623	3647	-14513	18016
9	-9580	3750	-14430	17730
10	-7688	-31594	-6363	-2476

TABLE 3  
Comparison Of R.M.S. Stresses, Characteristic  
Frequencies For Two Values Of The Scale Of Turbulence

L	500					300				
	$\bar{\sigma}$	$N_0$	$b_1 \bar{\sigma}$	$b_2 \bar{\sigma}$	$\bar{\sigma}$	$N_0$	$b_1 \bar{\sigma}$	$b_2 \bar{\sigma}$		
1	392.	1.956	1399.	2858.	469.	2.034	1468.	3124.		
2	37.5	3.254	133.9	273.4	46.0	3.384	144.0	306.4		
3	122.	1.953	435.5	889.4	146.	2.048	457.0	972.4		
4	377.	1.903	1346.	2748.	453.	1.969	1418.	3017.		
5	205.	2.212	731.9	1494.	245.	2.322	766.9	1632.		
6	337.	2.012	1203.	2457.	403.	2.108	1261.	2684.		
7	259.	1.963	924.6	1888.	310.	2.038	970.3	2065.		
8	169.	2.675	603.3	1232.	203.	2.813	635.4	1352.		
9	260.	2.223	928.2	1895.	311.	2.334	973.4	2071.		
10	125.	2.347	446.3	911.3	151.	2.454	472.6	1006.		

TABLE 4

Response Of Each Of The Flexible Generalized Coordinates  
To A Unit Sinusoidal Gust At 13.5 Radians Per Second

Col.	1		2		3
r	$\bar{q}_n$		$\bar{q}_n/\bar{q}_1$		$\bar{q}_n$
	Real	Imaginary	Magnitude	Phase Angle	Approximation
1	.0198256	-.03377244	1.000	0°	1.000
2	-.001048743	.00167238	.0504	181.68°	-.0504
3	.01200454	-.00791560	.3672	26.2°	.3672
4	-.007218734	.004627009	.2189	206.95°	-.2189

Peloubet

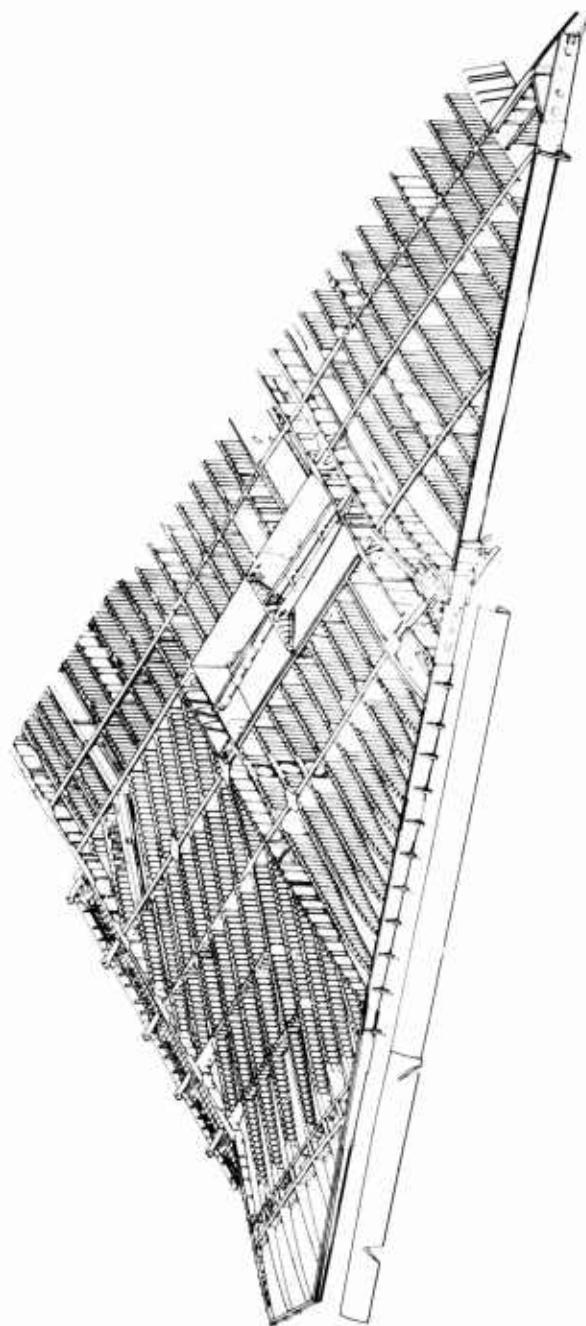
TABLE 5

Comparison Of The Stresses Produced By Unit  
Amount Of The Equivalent Loading With The R.M.S. Stresses

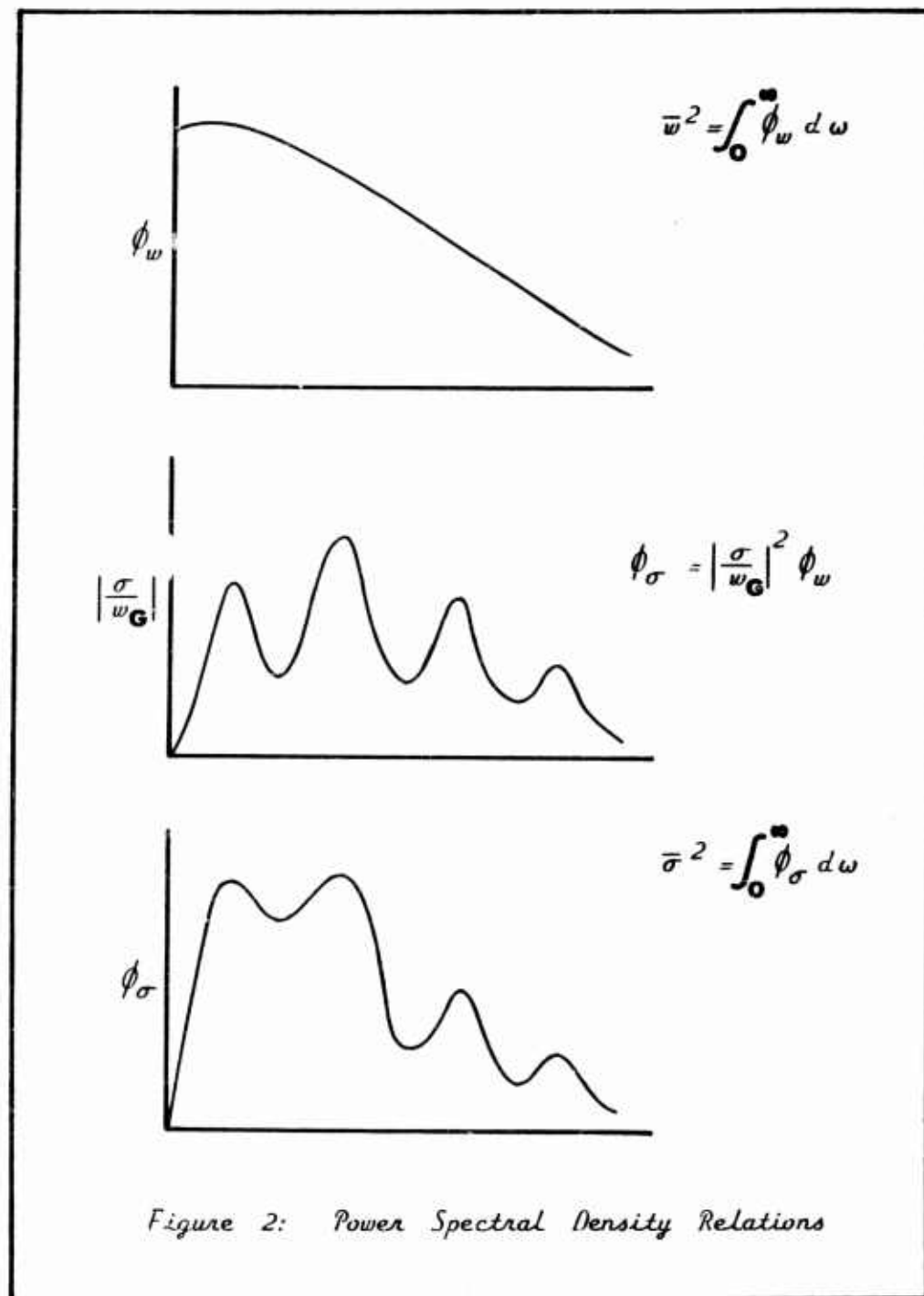
Col.	1	2	3
$i$	$\tilde{\sigma}(x_i, y_i, z_i)$	$ \bar{\sigma} $ Normalized	$\bar{\sigma}$
1	-31249.	392.	392.
2	1544.9	19.4	37.5
3	-9072.7	113.8	122.
4	-30727.	385.4	377.
5	-15041.	188.7	205.
6	-26370.	330.8	337.
7	-20808.	261.0	259.
8	-10079.	126.4	169.
9	-18949.	237.7	260.
10	-7891.3	99.0	125.



Peloubet



**B-58 WING STRUCTURE**



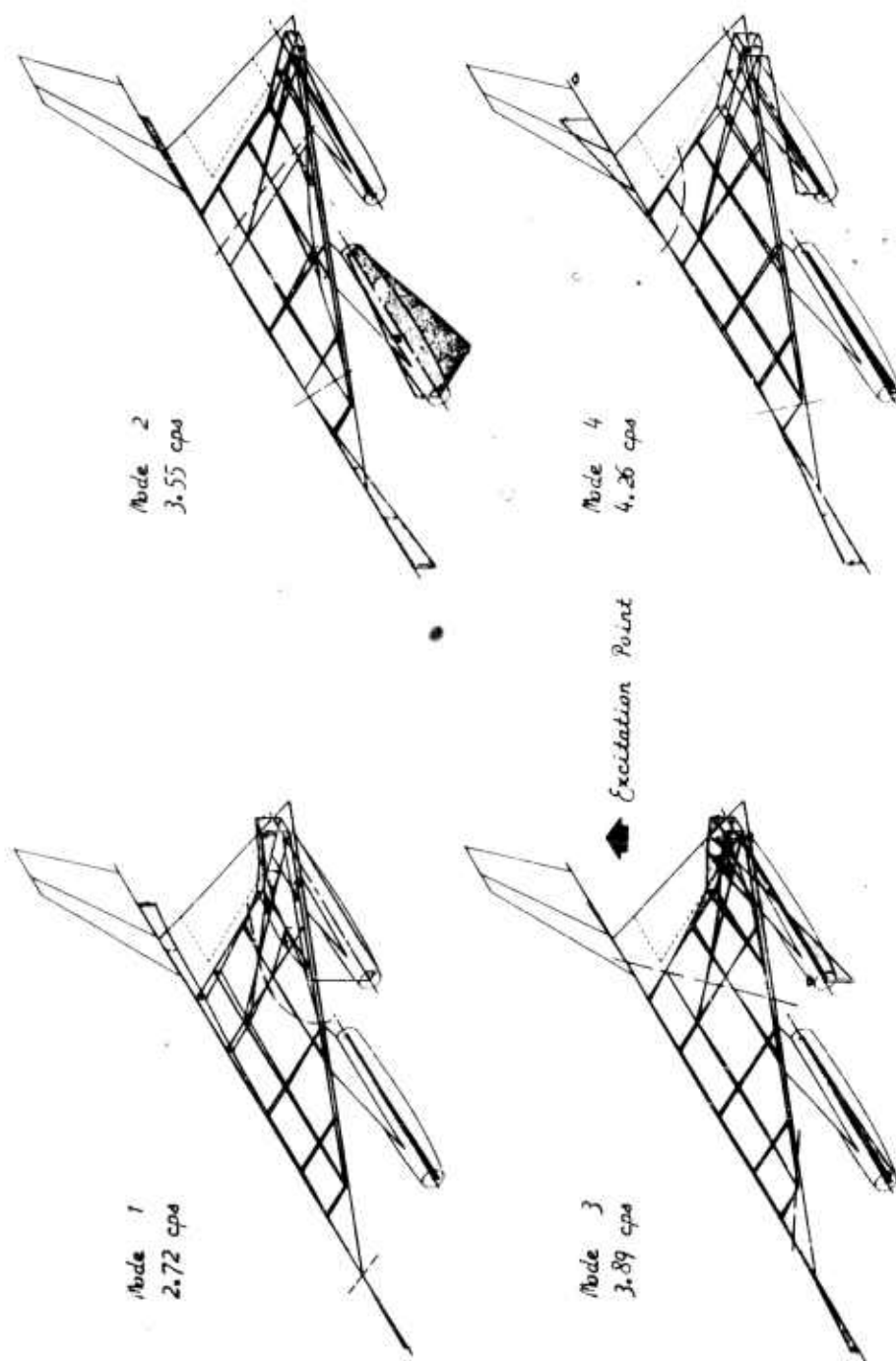


Figure 3: Symmetrical Natural Modes Of Vibration For A 93,022 Lb. G. W. B-58 Airplane

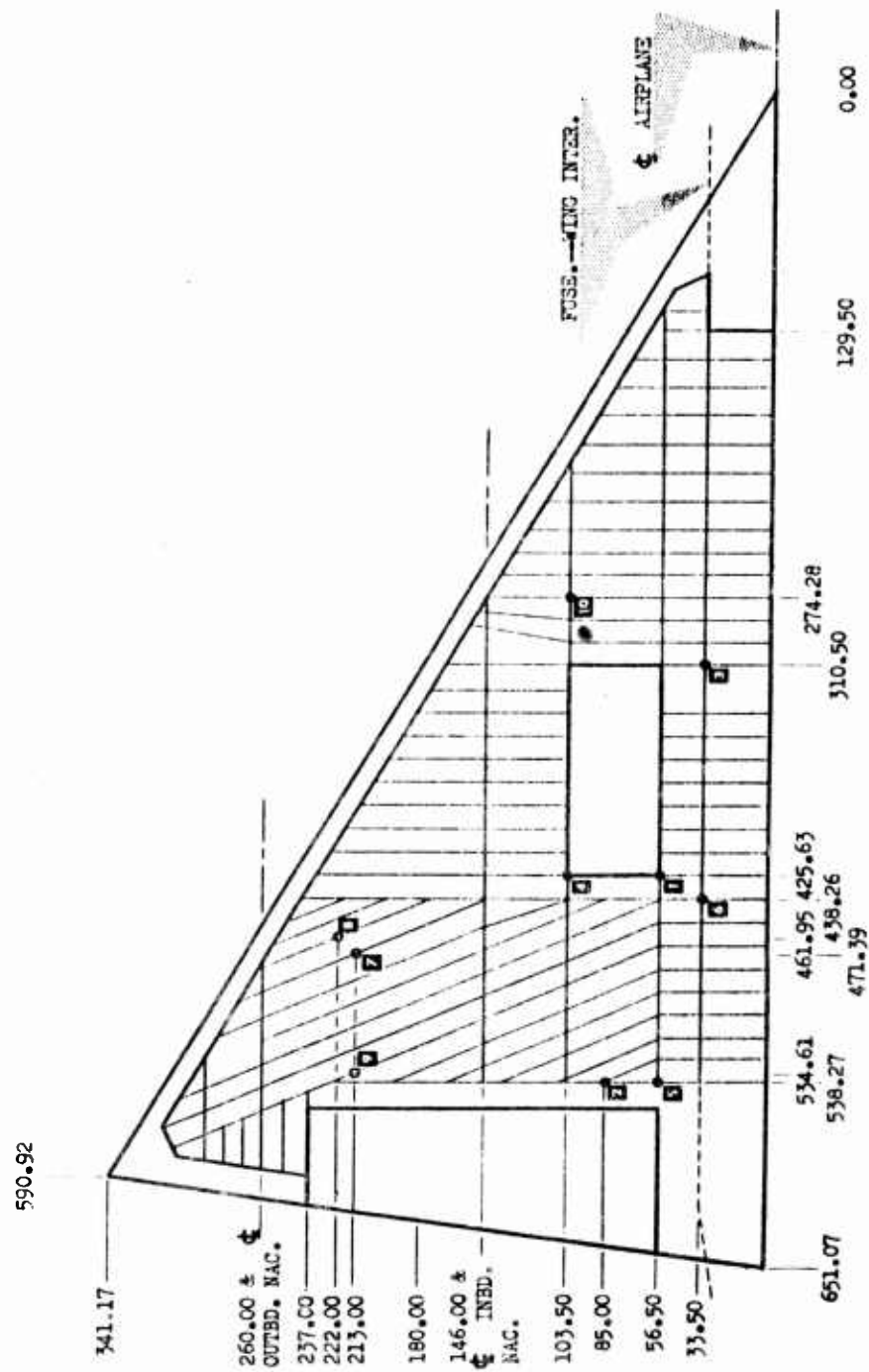
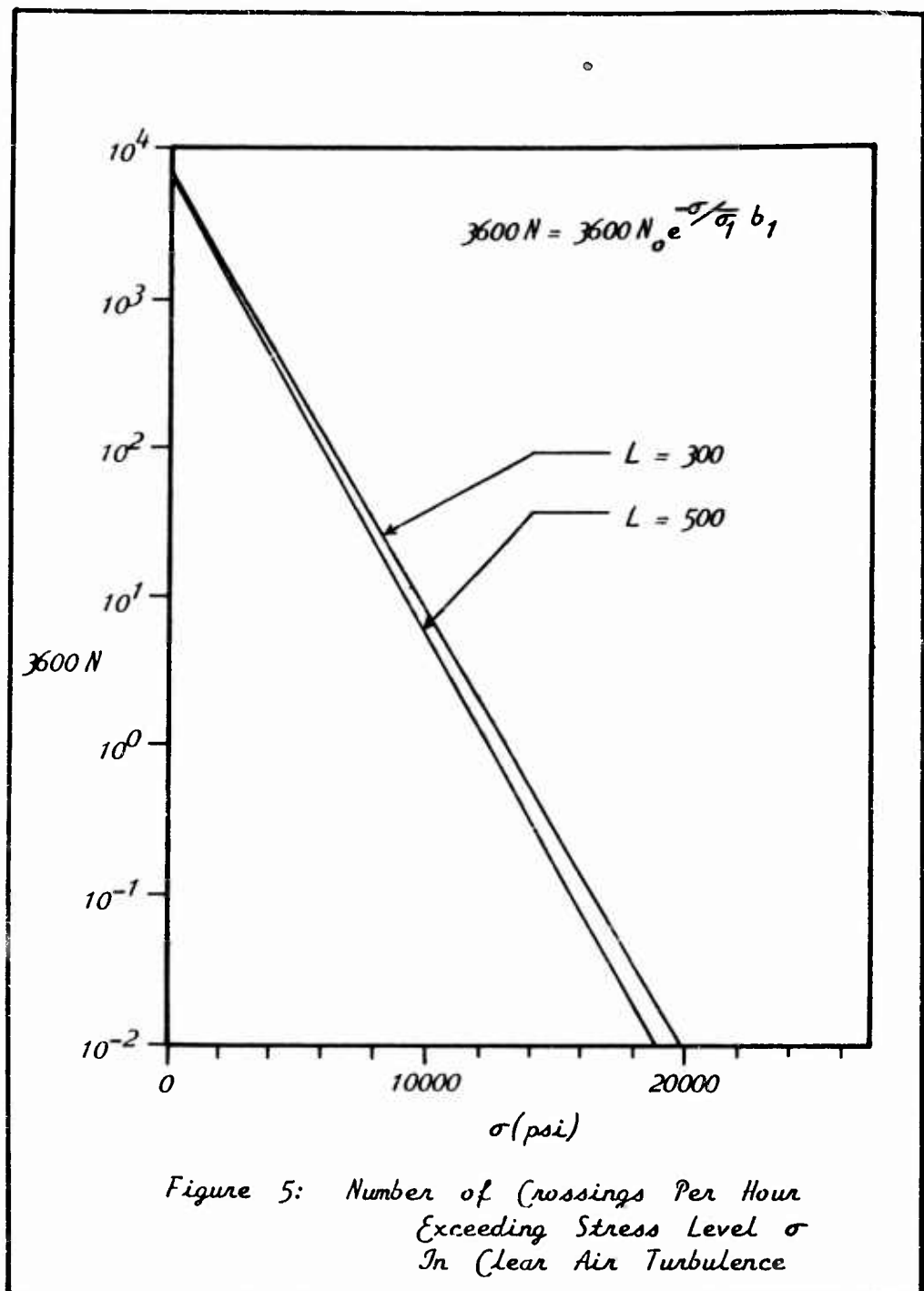


Figure 4: Location Of Wing Stress Points



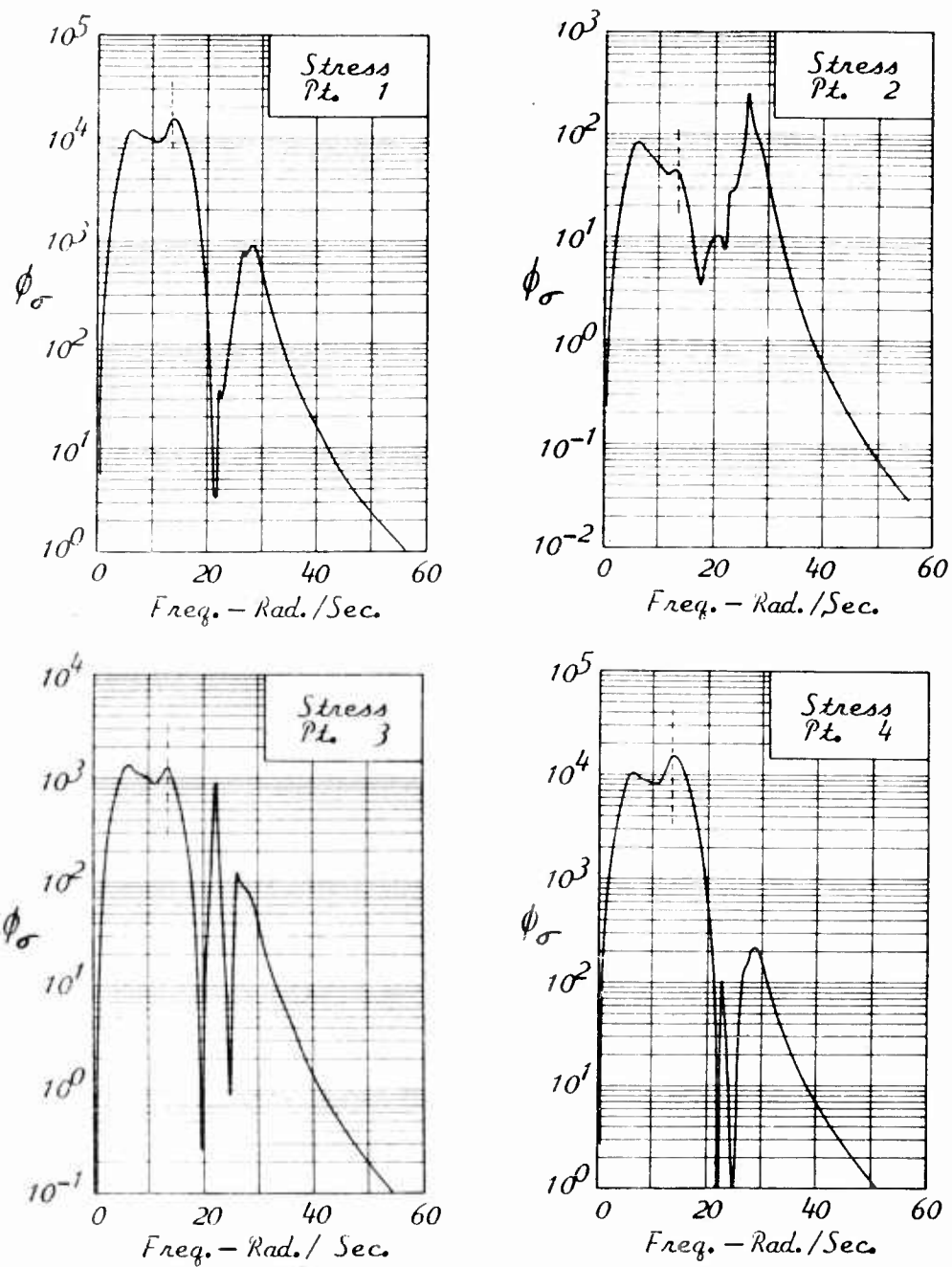


Figure 6: Stress Power Spectrums

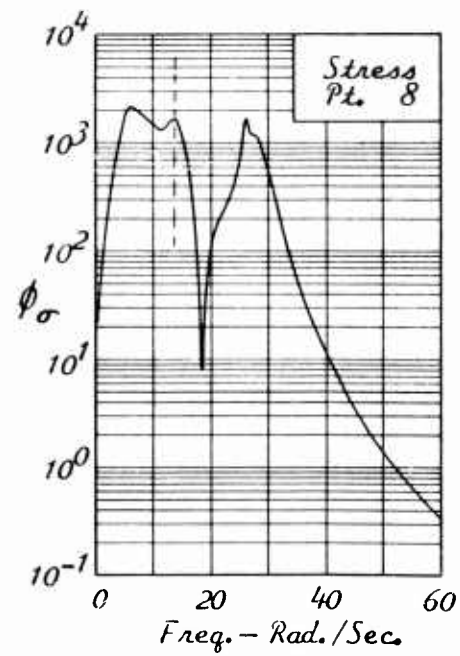
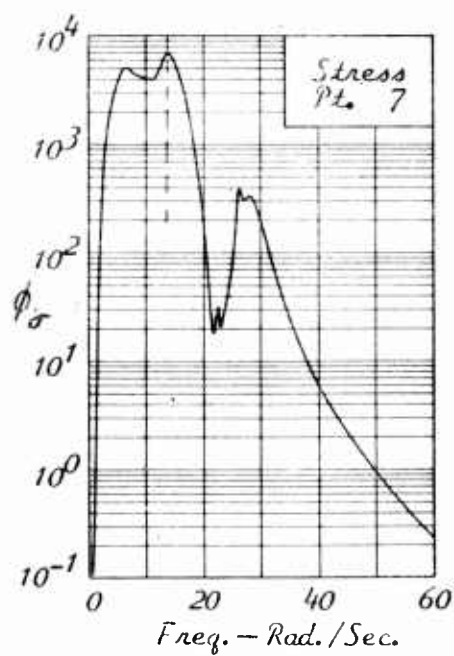
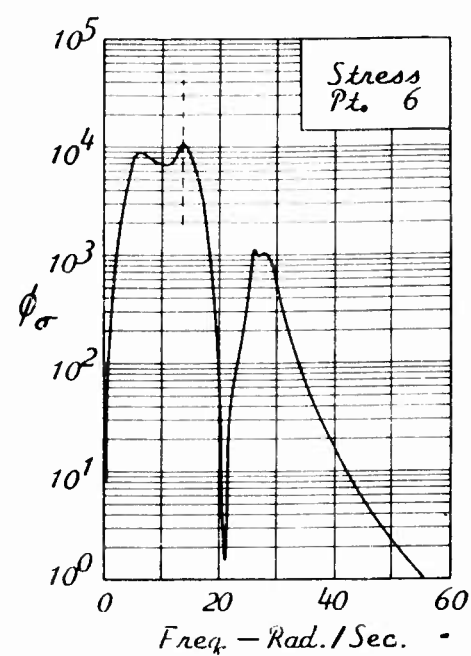
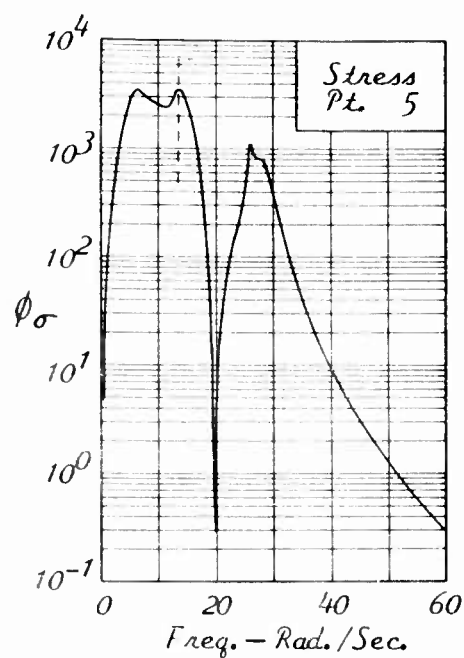


Figure 6: Continued

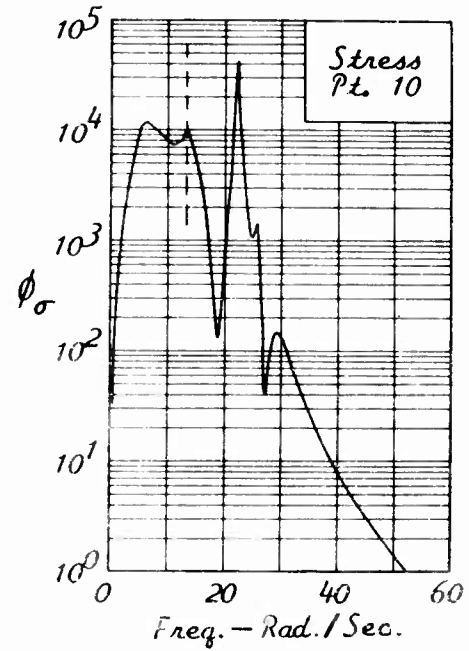
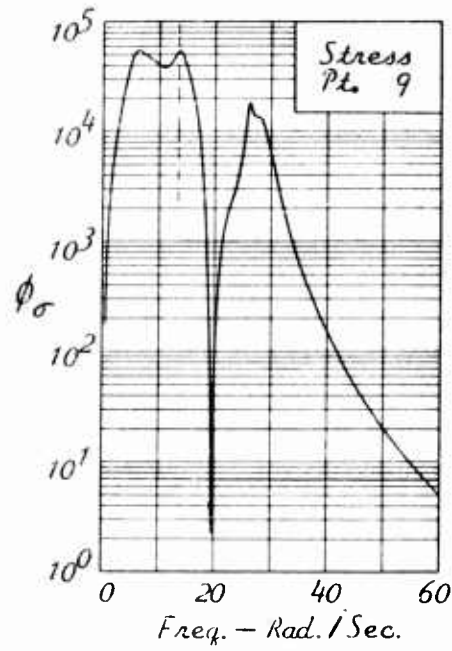


Figure 6: Concluded



## SHOCK-TUBE STUDIES OF BLAST-LOADING ON AIRFOILS

J. R. Ruetenik, W. Herrmann and E. A. Witmer  
Aeroelastic and Structures Research Laboratory  
Massachusetts Institute of Technology  
Cambridge, Massachusetts

### Introduction

The interception of a wing by a strong blast wave, Fig. 1, involves several interesting nonlinear phenomena of aerodynamics. These include the production of large entropy changes due to blast strength, and the shedding of strong vortices from all edges of the wing.

In spite of the nonlinear effects occurring at large angles of attack, the blast loads on wings have frequently been estimated by linearized methods of the gust type. The application of the traveling-gust theory of Miles (1), Hobbs, (2), and Drischler and Diederich (3) to blast airloads on wings was proposed by references 2 and 3. Since the theory is linearized, it is expected to apply only with weak blast waves. However, the full extent of its practical applicability should be determined more explicitly.

A program to measure the simulated strong-blast loads on airfoils and wings has been underway at MIT for several years. In references 4 and 5 the traveling-gust theory has been compared with the loads measured in these experiments, and a considerable area of agreement has been found in both the airloads distribution and the normal force at low and fairly large angles of attack during the period the shock front was being diffracted by the airfoil, provided the method was applied in coordinates fixed in the shock-induced flow. One purpose of this present paper is to extend the comparison of the traveling-gust method to larger blast-induced angles of attack.

-----  
+ This investigation has been sponsored by the Flight Dynamics Laboratory of WADD, ARDC, USAF.

At large blast-induced angles of attack, vortices shed from the leading edge of the airfoil become a prominent feature in the flow. A theoretical description of the flow field is afforded by the lumped-vortex method of Edwards (6), Brown and Michael (7) and Cheng (8), which lumps the shed vorticity into discrete vortices; that approach has been modified in the present work in order to represent the blast-induced flow in the post shock-diffraction period. The second purpose of this paper is to present comparisons of this vortex theory with the experimental airloads, using several boundary conditions.

In the following the blast-simulation experiments are described first. Then the prediction methods and the theoretical-experimental comparisons are made separately for the traveling-gust analysis and for the lumped-vortex analysis.

### Experiments

The MIT-WADD shock tube has a constant 8 x 24 inch section. The airfoil is clamped between the middle of the 24 in. walls, and set at a fixed angle of attack. A shock is fired and measurements are made with either an interferometer, or pressure transducers located in the airfoil. The details of these experiments are described in references 9 and 10.

The airfoils in the tests under present discussion had a 4-in. chord and either an NASA 65-010 profile (9) or 64A010 profile (10). The Mach number of the shock-induced flow,  $M_2$ , during the test program ranged from 0.4 to 1.0. The measurements in reference 9 pertained to fixed angles of attack,  $\alpha$ , ranging up to 30, 5 and 4 degrees at  $M_2 = 0.4$ , 0.8 and 1.0, respectively. The present paper extends the  $\alpha$  range to 60 degrees at both  $M_2 = 0.4$  and 0.8.

### Traveling-Gust Calculations

Essentially the traveling-gust method is an extension of the conventional gust methods, except that the gust front is allowed to move. To represent blast loading the velocity of the gust front is set equal to the velocity of the shock fronting the blast wave. The gust-induced angle of attack is equated to the change in angle of attack experienced by the wing as it penetrates the shock front. The present calculations include compressibility.

In the shock-tube experiments the shock-induced flow has essentially a step profile. To represent blast loading of the airfoil for the shock-tube conditions, the downwash is as sketched in Fig. 2. The procedure involved in these calculations is otherwise straightforward, and the details are given in reference 4.

The interferogram in Fig. 3 was taken while the shock was being diffracted by the NASA 64A010 airfoil; while the shock diffracts about the airfoil is called the "diffraction period". Of note is the bifurcated shock with the Mach stem, slip surfaces, reflected shock, and triple points. In this particular interferogram for which  $M_2 = 0.8$ , there is a local supersonic bubble on the upper surface, but otherwise this interferogram is typical of subsonic Mach numbers. There are several fringes near the airfoil due to the clamping stresses in

the optical flats; corrections were applied to account for these clamping effects in the calculations of pressure distribution about the airfoil.

The pressure difference between the lower and upper surface,  $\Delta p$ , computed by the traveling-gust method, indicated by subscript "tg", for the diffraction period at  $M_2 = 0.4$  and reduced by both the dynamic pressure  $\frac{1}{2} \rho_0 V_0^2$  and the angle of attack  $w_0/V_0$  is given by

$$\Delta c_{p_{tg}} = \frac{(\Delta p)_{tg}}{\frac{1}{2} \rho_0 V_0^2 w_0}$$

where  $\rho_0$ ,  $V_0$ , and  $w_0$  are the density, forward velocity of the airfoil, and the vertical velocity of the gust, respectively, is plotted in Fig. 4. The chordwise distance from the leading edge,  $x$ , has been reduced in Fig. 4 by the speed of sound behind the gust or shock,  $a_2$ , and the time subsequent to initial gust or shock penetration. The function  $\Delta c_{p_{tg}}$  computed here for a flat-plate airfoil has two singularities, the usual one at the leading edge and the other at the gust (shock) front. The airloads measured on the airfoils in the shock tube are compared with the traveling-gust theory by setting

$$\Delta c_p = \frac{\Delta p}{\frac{1}{2} \rho_2 u_2^2}$$

where  $\rho_2$  and  $u_2$  are the air density and the material velocity of the shock-induced flow in laboratory coordinates. The loading data have been reduced by  $\alpha$  to indicate the extent of linearity.

Between the leading edge of the airfoil and the chordwise station adjacent to the shock on the upper surface, the measured airloads are surprisingly independent of  $\alpha$  up to 60 degrees, and well represented by the traveling-gust theory. This is considerably beyond the range where linear theory is ordinarily expected to be valid.

The nonlinear effect of the finite shock strength manifests itself at the shock fronts. Several of these features will be discussed in connection with Fig. 4. The shock loading has two discontinuities, one at the location of the shock on the upper surface and one at the shock on the lower surface. These shocks produce a scalloped step in the differential loading distribution. It is of interest to observe how this step approaches the singularity of the gust front when  $\alpha$  is reduced towards zero.

At large values of  $\alpha$  the departure of the airloads distribution from the traveling-gust theory in the vicinity of the shocks is large. But the data of reference 4 demonstrated that this difference in the distribution did not produce a significant effect on the reduced sectional normal-force coefficient,  $c_n/\alpha$ . This conclusion is supported by the present data which are plotted in Fig. 5 as a function of the reduced time  $u_2 t/c$ . However, for angles of attack above 30 degrees the distribution near the shock does have an effect on  $c_n/\alpha$ .

To indicate the effect of gust speed, the fixed-gust function,  $C_{n_g}$ , and the indicial-sinking function,  $C_{n_k}$ , are also plotted in Fig. 5. The first represents the response to penetration of a fixed gust, and the second the response to penetration of a gust moving at an infinite speed. After several chordlengths of flow, the effect of gust speed is small.

The traveling-gust theory is compared with the measured shock loading during the diffraction period at  $M_2 = 0.8$  in Fig. 6. The general characteristics of  $\Delta C_{n_g}$  are similar to the low Mach number shape, with the exception of the distribution along the upper surface near the leading edge where the loading flattens at large  $\alpha$  due to the supersonic bubble. The difference in the distributions near the shock are similar to the low Mach number case. The reduced normal force coefficient  $C_n/\alpha$  is compared in Fig. 7. There is not as much experimental data available during the diffraction period as at the low Mach number, but the  $C_n/\alpha$  data do support the traveling-gust method below 30 degrees and depart above a 30-degree angle of attack.

It should be recognized that these measurements were made on airfoils that were stationary. So the question to be answered is how applicable these results are to an airfoil that is moving. After a period of time the flow is expected to be independent of the initial flow before shock arrival; that is, except for the diffraction loading period and perhaps the early part of the post-diffraction period, the transient loading is expected to depend upon the angle of attack of the airfoil with respect to the post-shock stream and not be influenced by the flow field existing prior to shock or blast envelopment of the airfoil. The question to be answered is how early the airloading achieves this status. The loading distributions demonstrated that during the diffraction period there is a large region between the leading edge of the airfoil and the shock where the linearized theory for a moving airfoil and the measured data from the stationary airfoil are in agreement at subsonic speeds and  $\alpha$  up to 60 degrees. The differences due to the supersonic bubble at high speed would also occur on a moving airfoil. The region of disagreement is principally in the neighborhood of the shocks. In the shock tube the shock wave is generally much stronger than for a moving airfoil with the same blast-induced angle of attack, because in the former case the shock must be strong enough to establish the whole flow field. This implies that differences from the linearized theory due to finite shock strength will generally be greater in the shock-tube tests than with a moving airfoil subjected to blast.

It is concluded that the traveling-gust theory furnishes a good estimate of the normal force during the diffraction period at subsonic speeds up to blast-induced angles of attack of about 30 degrees. The departure from the traveling-gust theory above 30 degrees is generally expected to be less for a moving airfoil than measured in the shock-tube experiments because of the lesser shock strength involved. The traveling-gust theory is expected to apply in the early post-diffraction period; however, this portion of the loading history was not computed for display here because of the complexity arising from the interaction of the wake upon the flow.

### Lumped-Vortex Calculations

Figure 8 is a typical interferogram of the shed vortices in the post-diffraction period at large angles of attack. The classical starting vortex is evident behind the trailing edge, and the leading-edge vortex is well formed at this angle of attack. Below 15 degrees the leading-edge vortex is smeared over a region along the upper surface rather than appearing as a discrete vortex as seen in Fig. 8.

Interferograms of the flow as well as Fastax high-speed pictures of tufts on the upper surface show that there is a stagnation point on the trailing-edge side of the leading-edge vortex. Beneath the vortex the flow direction is toward the leading edge. Between the vortex and the leading edge, there tends to be another stagnation point. The fluid under the vortex and the fluid negotiating the leading edge separate from the surface in the adverse pressure gradient. This forms a low energy zone of roughly triangular shape. Rott (11) and others have identified secondary vortices near the surface just behind the leading edge in the forward moving flow beneath the vortex which are evident in many of the interferograms in these tests, but not in this particular interferogram, Fig. 8.

At high subsonic Mach numbers compressibility complicates the vortex phenomenon. Therefore, present attention is given to formulating a model for low speeds.

The vortex model of Edwards (6), Brown and Michael (7), and Cheng (8) is sketched in Fig. 9a. All vorticity shed from the body in question is idealized to be concentrated in a vortex located at  $z_1$  and which has a circulation  $\Gamma$ ; however, the vorticity shed at the  $z_0$  position on the body in question actually goes into a vortex sheet-like region. This vortex increases in strength by being fed vorticity along the feeding sheet connecting it with the separation or feeding point located at  $z_0$  at which vorticity is considered to be generated. To account for the equilibrium of the forces in the vortex field, a force on the feeding sheet due to the transport of vorticity and a Joukowski force on the vortex due to the relative velocity between the vortex and the local field are equated. The equation of equilibrium in complex notation is

$$(z_1 - z_0) \frac{\dot{\Gamma}}{\Gamma} = u(z_1) - \dot{z}_1 \quad (1)$$

where  $u(z_1)$  is the local fluid velocity at  $z_1$  and  $\dot{z}_1 \equiv \frac{dz_1}{dt}$ .

Edwards (6) and Brown and Michael (7) applied the model to the cross flow on a slender delta as sketched in Fig. 9b to treat the vortex involved. For a boundary condition on the wing, the Kutta condition was applied at the leading edge. This is a reasonable representation for deltas with very small apex angles. As the apex angle increases, the flow at the leading edge tends no longer to be parallel to the chord plane as in the Kutta condition but is inclined upward with respect to the chord plane. In fact, the measured loadings did depart from the theory as the apex angle increased (7). Apparently the boundary condition at this edge is the key to the problem.

Following the method of references 6 to 8, the flow field around the airfoil is represented by two vortices and the free-stream velocity at infinity, as shown in Fig. 9c. The airfoil is represented by a flat plate. It should be noted that in general the strengths of the two vortices are not equal. Two boundary conditions are needed at the airfoil. The Kutta condition is applied at the trailing edge, and the validity of this has been well supported by interferograms, even at very early times in the diffraction period. The other boundary condition is not as apparent.

In addition to the above described use of the Kutta condition at the leading-edge of a slender delta, Pappas and Kunen (12) employed the Kutta condition at the leading edge of a swept wing with leading-edge vortices. In view of this success of the leading-edge Kutta condition in these two cases, it was used to formulate the first model of the present study for the airfoil. This model is sketched in Fig. 9c. The two feeding points are taken at the leading-edge and the trailing edge.

The vortices are started from the two feeding points with zero strength. The differential equations were then solved by finite difference methods on an IBM 704 high-speed computer. The details of these calculations are described in reference 13. Actually the calculations cannot be started with the vortex at the feeding point, as Bryson (14) pointed out, because the feeding point is a saddle point. However, the initial direction can be found (14), and the vortex can be started with a small displacement. This was the procedure employed.

With the leading-edge Kutta condition invoked, however, difficulty was encountered in obtaining convergence of the finite-difference calculations when the initial displacement was made sufficiently small to obtain accurate starting conditions. Therefore, a calculation was made using experimental values of the vortex positions measured in an interferogram on the NASA 64A010 airfoil at  $\alpha = 30$  degrees,  $u_2 t/c = 0.91$ , as starting points for the vortices; this is now a starting condition in which the vortex is at a relatively large distance from the leading edge. The subsequent normal-force behavior with aerodynamic time over the time range for which the calculation has been carried out thus far is plotted in Fig. 10. It should be noted that the normal force decreases and the leading-edge vortex moves toward the leading edge instead of away, contrary to experiment.

It is also of interest to examine by means of interferograms whether the assumption of the applicability of the Kutta condition at the leading edge is verified by the behavior of the observed flow field. A careful examination of many interferograms taken with these two airfoils over this range of angle of attack and Mach number, e. g. Fig. 8, shows that the fluid remains attached to the surface for a considerable distance around the leading edge. Also, unreported measurements in this laboratory on sharp wedges at  $\alpha = 15, 30$

-----  
<sup>+</sup> Later calculations were performed on an IBM 709 machine.

and 90 degrees showed that the flow at the apex had a component normal to the bisector of the wedge. Therefore, it is concluded that the Kutta condition does not provide a satisfactory description of the flow at the leading edge of the two-dimensional airfoil at a large angle of attack. This conclusion was not unexpected.

It is well known that the shape of the leading edge has a significant effect on the type of separation that occurs at relatively small angles of attack. Measurements in this laboratory on wedges and plates that had a wide range of profiles indicated that the fringe distribution is essentially independent of the shape of the leading edge at  $\alpha = 15, 30$  and 90 degrees provided the vortex is at least 3 leading-edge radii from the leading edge. Therefore, the shape of the leading edge is not believed to be an important parameter at large angles of attack.

Bryson (14) employed the lumped-vortex method to estimate the unsteady drag on a circular cylinder. This is not unlike the situation at the leading edge. For a boundary condition Bryson placed two stationary stagnation points on the back side of the cylinder, simulating the separation points of a turbulent boundary layer.

Therefore, in the second model of the present study, the leading-edge Kutta condition is replaced by a stagnation point on the upper surface, Fig. 9e. The feeding point for the vortex is taken to be at the stagnation point. The computations were performed for several locations of the stagnation point. The trailing-edge vortex again behaved well, but when the stagnation point was near the leading edge, the forward vortex moved upstream. At some location of the stagnation point downstream from the leading edge, the vortex moved downstream and away from the surface. But in this case the velocity was very small compared with the actual velocity of the vortex. For most locations of the stagnation point, the vortex would eventually start moving toward the surface, and then the calculations would diverge.

The initial displacement of the vortices from the two feeding points was arbitrarily taken to be equal for the two vortices, specifically equal to 0.05 radii in the circle plane. To examine the consequences of this selection, vortices were started at points observed in the interferograms, specifically the positions for  $u_2 x/c = 0.47$ ,  $\alpha = 60$  degrees, where both vortices could be seen. Again, the forward vortex moved downstream only if the feeding point were well downstream of the leading edge, and then it moved roughly parallel to the plate. It is concluded that this lumped-vortex model with either of the forward boundary conditions does not provide a satisfactory representation of the forward vortex sheet.

However, the calculations with the stagnation point did provide a fair estimate of the normal force, which was essentially independent of the particular location of the stagnation point, until the calculations diverged. The position of the stagnation point did affect the time at which divergence occurred. The calculations that did not diverge in the time interval of interest are plotted in Fig. 10. Of course, the lumped-vortex theory does not represent the diffraction process, but shortly thereafter the normal force does

follow the trend of the shock-tube data.

It is concluded that the normal force is insensitive to the forward vortex during this time in the angle of attack range of 30 to 60 degrees. However, the forward vortex does have a large effect on subsequent developments. This is discussed with reference to Fig. 5. At  $ut/c \approx 3$ , depending upon  $\alpha$ , the  $c_n/\alpha$  data drop severely. It is observed that this drop coincides with the arrival at the trailing edge of the rearward upper-surface stagnation point produced by the leading-edge vortex, and the formation of the second trailing-edge vortex. This stage of the development is shown in the interferogram in Fig. 11. It appears that this second trailing-edge vortex causes the drop in the normal force. In order to predict the growth and motion of this second trailing-edge vortex and the subsequent effect on the normal force, it appears necessary to predict the growth and motion of the first leading-edge vortex.

It appears that an improvement in the estimate of the transient loading at large angles of attack requires a better representation of the flow near the leading-edge. The lumped-vortex method is based upon the so-called perfect-fluid equations. Whether it is necessary to go to a formulation of the equations of motion which incorporates viscosity explicitly is not yet clear.

#### References

1. Miles, J. W., The Aerodynamic Force on an Airfoil in a Moving Gust — A Generalization of the Two-Dimensional Gust Problem, Douglas Aircraft Co., Rep. SM-18598, Oct. 1954 (Also, Jour. Aero. Sci., v. 23, n. 11, pp. 1044-50, Nov. 1956).
2. Hobbs, H. P., Indicial Downwash and Its Structural Effect on the Horizontal Tail, MIT, WADC TR 56-164, AD 97325, Aug. 1956. (Also, Jour. Aero. Sci., v. 24, n. 10, pp. 731-40, Oct. 1957).
3. Drischler, J. A. and Diederich, F. W., Lift and Moment Responses to Penetration of Sharp-Edged Traveling Gusts, With Application to Penetration of Weak Blast Waves, NACA TN 3956, May 1957.
4. Ruetenik, J. R., Evaluation of Traveling-Gust Method for Airfoils in Strong Blast Waves by Shock-Tube Tests, MIT, WADD TR 60-279, May 1960.
5. Ruetenik, J. R., Traveling-Gust Method for Airfoils in Strong Blast Waves, Jour. Aero/Space Sci., v. 27, n. 10, pp. 795-6, Oct. 1960.



6. Edwards, R. H., Leading-Edge Separation from Delta Wings, Jour. Aero. Sci., v. 21, n. 2, pp. 134-5, Feb. 1954.
7. Brown, C. E. and Michael, W. H., Jr., Effect of Leading-Edge Separation on the Lift of a Delta Wing, Jour. Aero. Sci., v. 21, n. 10, pp. 690-94, Oct. 1954.
8. Cheng, H. K., Aerodynamics of a Rectangular Plate with Vortex Separation in Supersonic Flow, Jour. Aero. Sci., v. 22, n. 4, pp. 217-226, Apr. 1955.
9. Transient Aerodynamics of Two-Dimensional Airfoils, MIT, WADC TR 54-368,  
Part 1 — Ruetenik, J. R. and Witmer, E. A., AD 97322, Aug. 1956;  
Part 2 — Ruetenik, J. R. and Witmer, E. A., AD 151018, Mar. 1958;  
Part 3 — Andrews, P. T. and Ruetenik, J. R., AD 209497, Jan. 1959.
10. Ruetenik, J. R. and Herrmann, W., Shock-Tube Measurements of Step-Blast Loads on an NASA 64A010 Airfoil, WADD report in preparation.
11. Rott, N., Diffraction of a Weak Shock with Vortex Generation, Jour. of Fluid Mech., v. 1, p. 111-128, 1956.
12. Pappas, C. E. and Kunen, A. E., An Investigation of the Aerodynamics of Sharp Leading-Edge Swept Wings at Low Speeds, Jour. Aero. Sci., v. 21, n. 10, pp. 649-58, Oct. 1954.
13. Ruetenik, J. R., Lumped-Vortex Calculation of Vortex Separation on an Airfoil, WADD report in preparation.
14. Bryson, A. E., Jr., Symmetric Vortex Separation on Circular Cylinders and Cones, Jour. App. Mech., pp. 643-48, Dec. 1959.

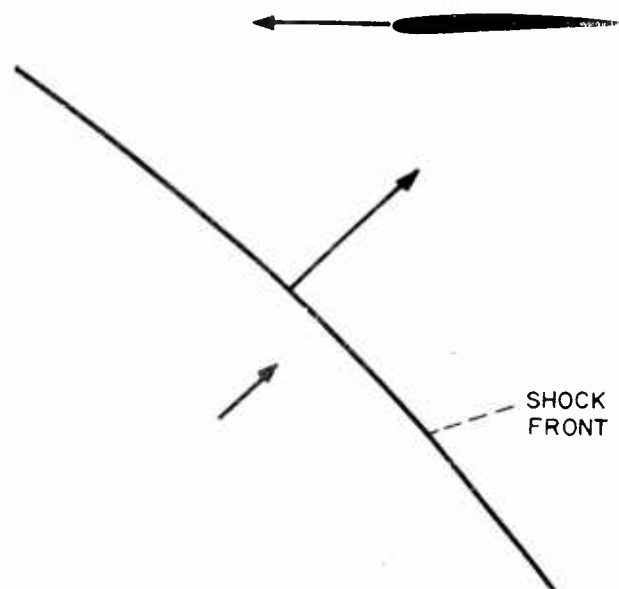


Fig. 1 Sketch of Blast Wave-Airfoil Interception

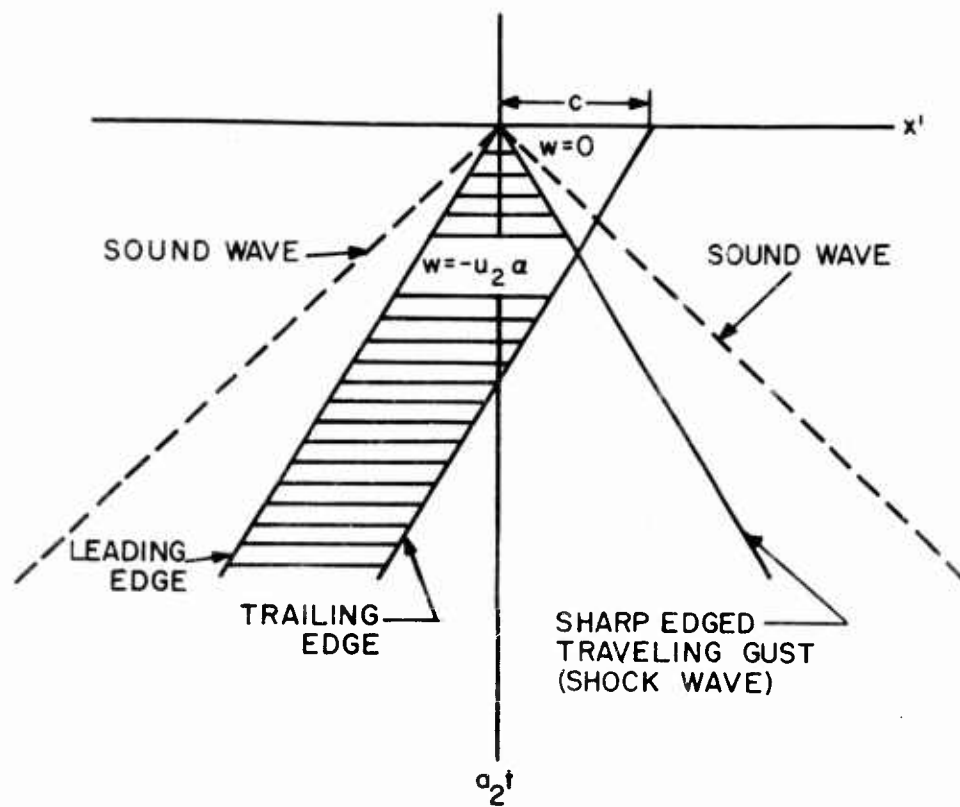


Fig. 2 Two-Dimensional Wing Penetrating a Traveling-Gust

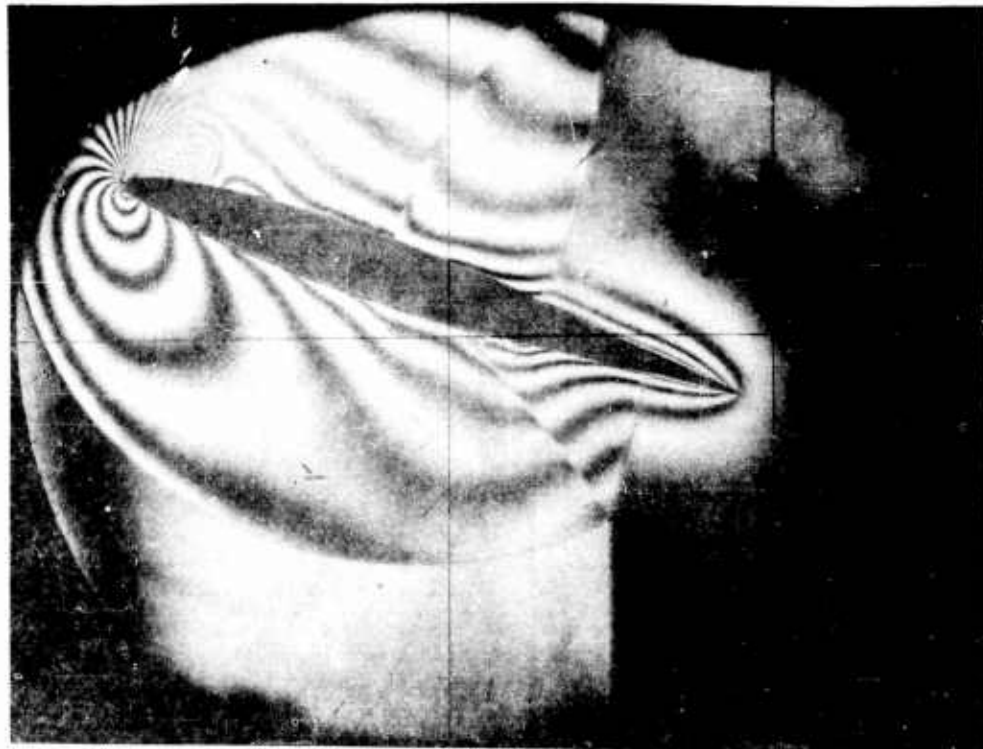


Fig. 3 Single-Fringe Interferogram in Diffraction Period,  
NASA 64A010 Profile,  $\alpha = 20$  degrees,  $M_2 = .80$ ,  $\frac{M_1^*}{\lambda} = .42$ .

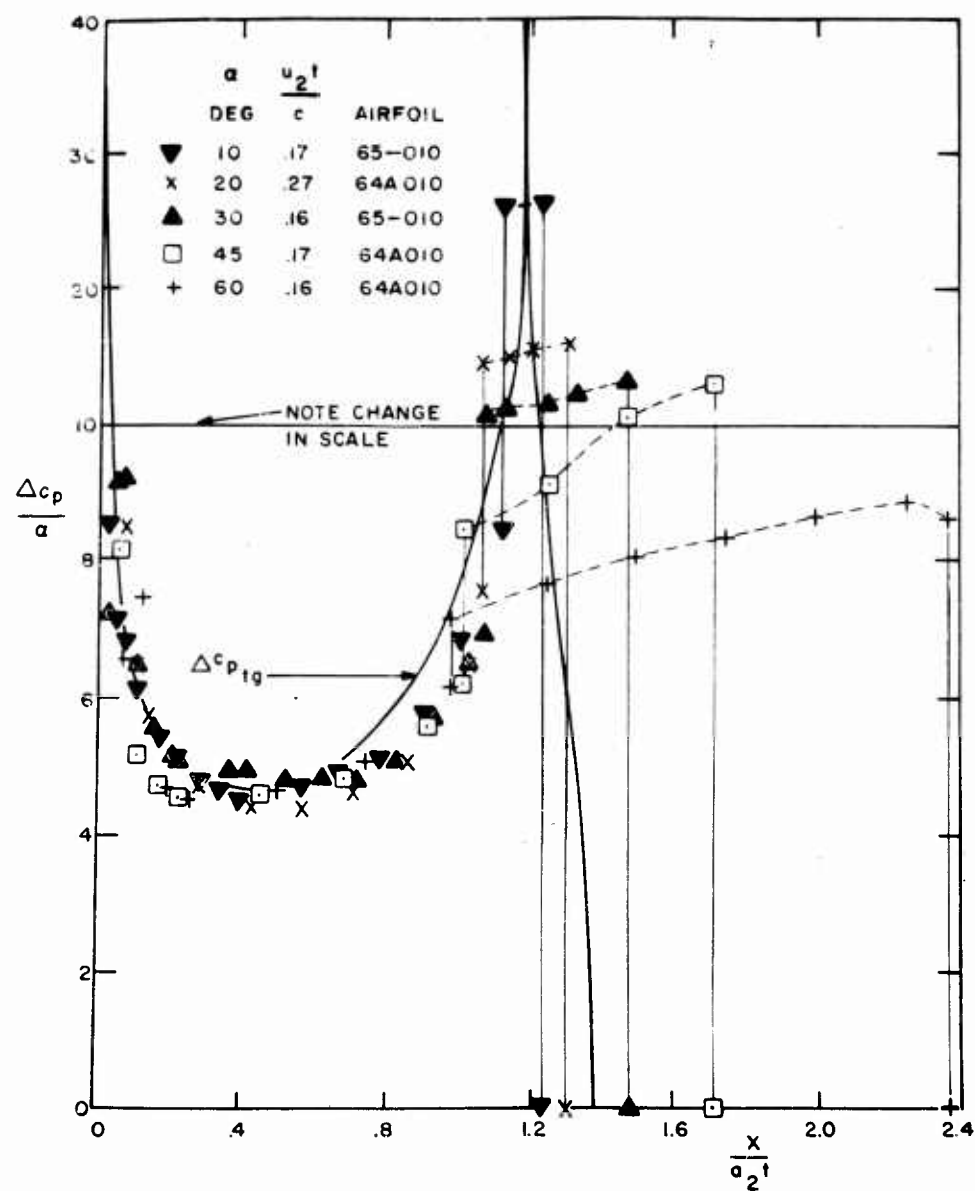


Fig. 4 Pressure Difference Across Airfoil During Diffraction Period,  $M_2 = 0.4$ .

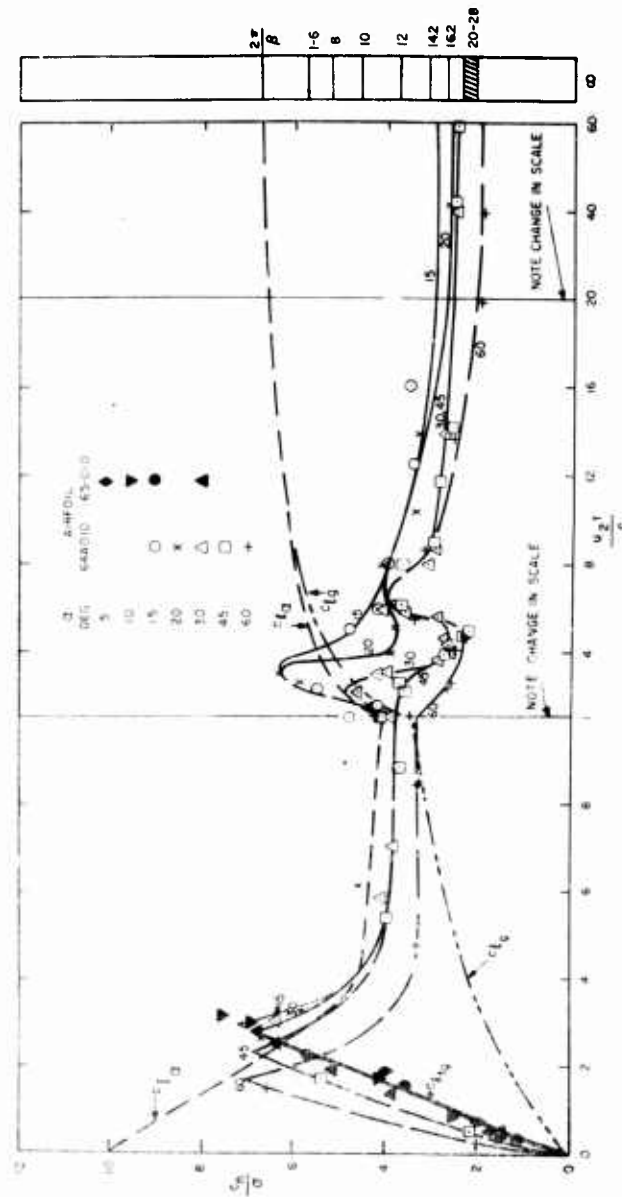


Fig. 5 Reduced Normal-Force Coefficient,  $M_2 = 0.4$ . Wind-Tunnel Data From NACA TN 3162 for a 64A010 Airfoil Are Plotted at Infinite Delay Time.

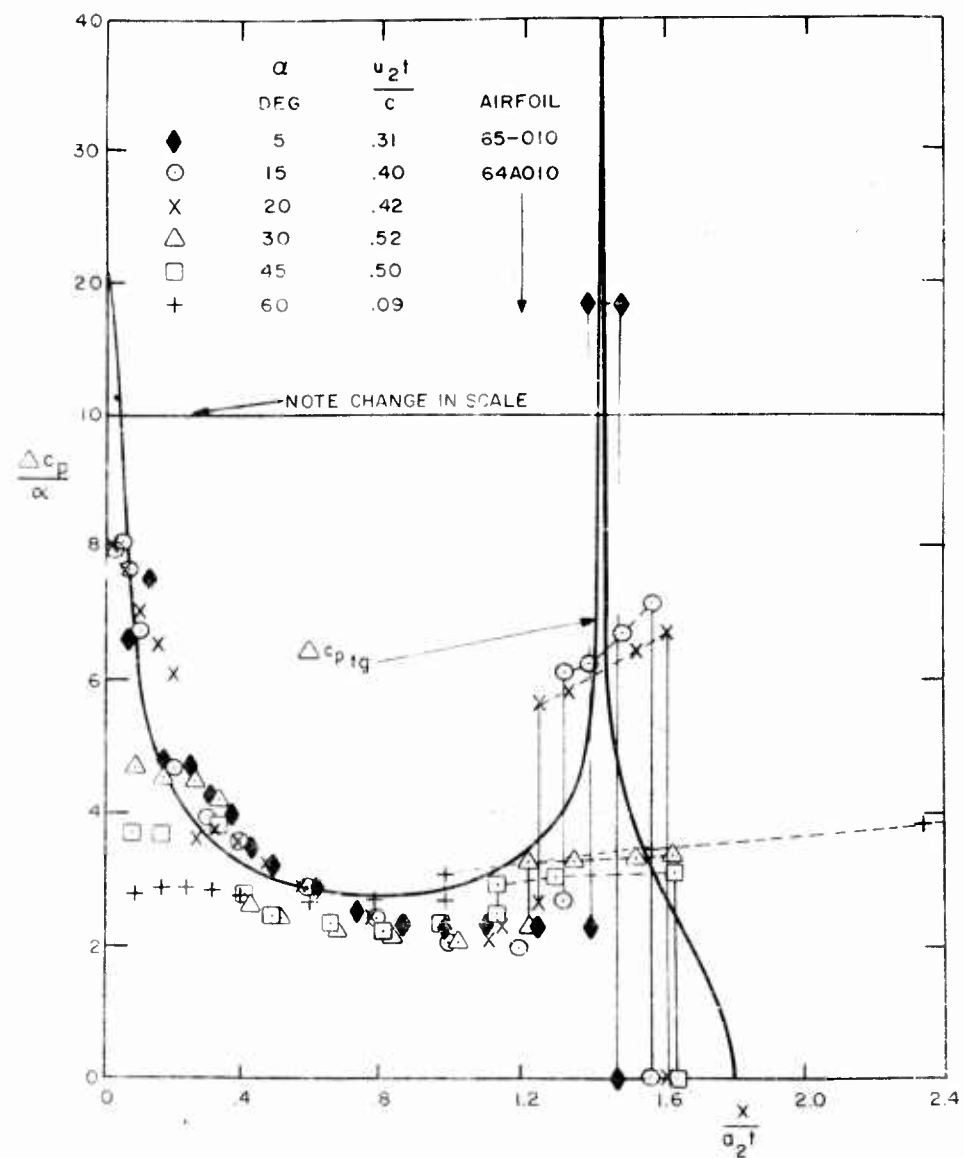


Fig. 6 Pressure Difference Across Airfoil During Diffraction Period,  $M_2 = 0.8$ .

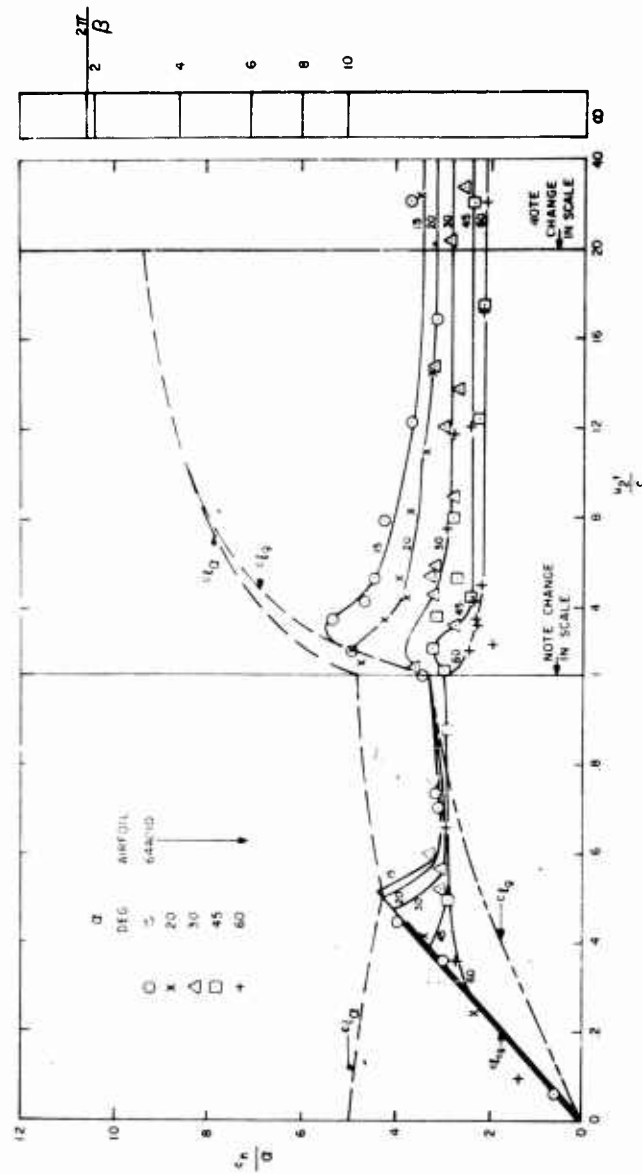
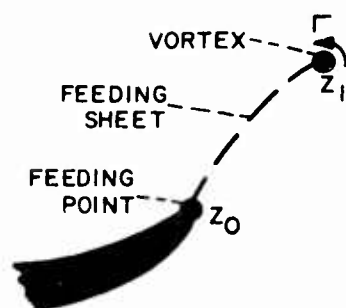


Fig. 7 Reduced Normal-Force Coefficient,  $M_2 = 0.8$ . Wind-Tunnel Data From NACA TN 3162 for a 64A010 Airfoil Are Plotted at Infinite Delay Time.

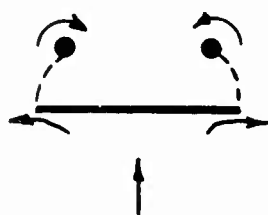




Fig. 8 Single-Fringe Interferogram in Early Post-Diffraction Period,  
NASA 64A010 Profile,  $\alpha = 30$  deg.,  $M_2 = 0.4$ ,  $\frac{u_1 x}{c} = .71$ .



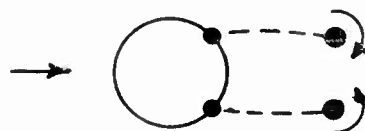
a. Lumped vortex



b. Edwards and Brown-and-Michael model for cross-flow plane of a slender delta wing



c. Airfoil with leading-edge Kutta condition



d. Bryson model for indicial motion of a circular cylinder



e. Airfoil with stagnation point on upper surface

Fig. 9 Sketches of Lumped-Vortex Models

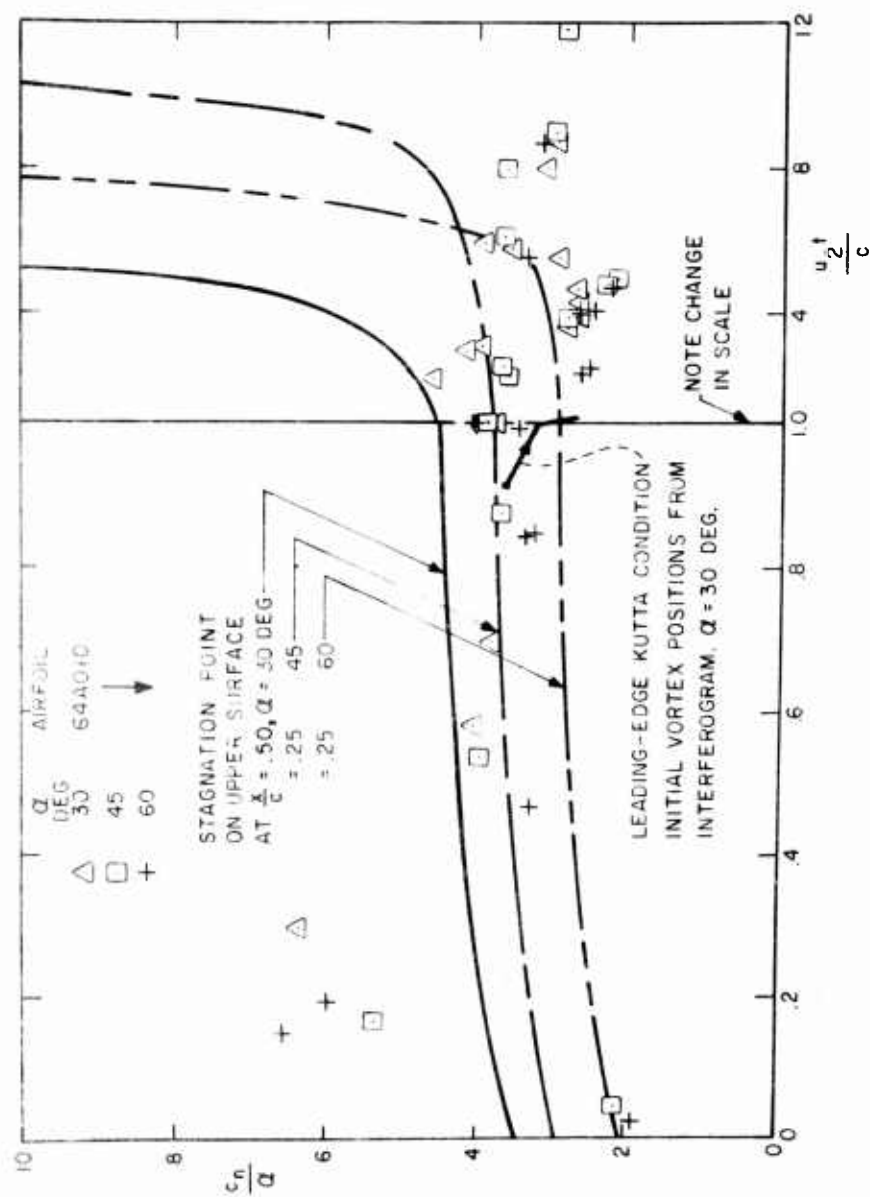


Fig. 10 Comparison of Reduced-Normal-Force History by Lumped-Vortex Calculations with Shock-Tube Data at  $M_2 = 0.4$



Fig. 11 Single-Fringe Interferogram of Formation of Second Trailing-Edge Vortex, NASA 64A010 Profile,  $\alpha = 30$  deg.,  $M_2 = 0.4$ ,  $\frac{x}{c} = 3.08$ .

## AIRPLANE RESPONSE TO STALL BUFFETING LOADS

J.R. Post  
North American Aviation, Inc.  
Columbus, Ohio

### Summary

Aircraft design criteria for horizontal tails due to stall buffeting have long been specified empirically. It is the purpose of this paper to present a first step toward the formulation of more rational buffet design criteria.

Analytical and experimental techniques for evaluating the dynamic response of a tail plane to the forced excitation of the stalled-wing wake are given. The design and instrumentation of an aeroelastic wind-tunnel model and the experimental program conducted to measure horizontal tail response to buffeting are discussed. A scheme for using a hot-wire anemometer system to determine the perturbation velocities in the stalled-wing wake is presented.

An analytical procedure is described to calculate a two-dimensional transfer function for the horizontal stabilizer. A method is given, using this transfer function, for relating the horizontal tail response to the turbulent-wake input through a power and cross-power spectral technique.

The results of this type of analysis are discussed with respect to the determination of probabilities of exceeding various load levels, for use as input to fatigue analyses.

This research was conducted under Bureau of Naval Weapons Contract NOa(s) 59-6172-c.

List of Symbols

The definitions of symbols used other than those defined in the text are given as follows:

$[a]$	A square (no. of modes x no. of modes) matrix giving the generalized force on the surface.
$[AIC]$	A rectangular matrix of aerodynamic influence coefficients relating concentrated forces at structural control points to angles of attack at Kernel Function control points.
$b_o$	reference length, L
$\{b^j\}$	A (number of pressure mode terms x 1) matrix of pressure mode weighting factors.
$c_o$	reference flexibility, $WL^{-1}$
$[C_{nm}]$	A (KFCP x number of pressure mode terms) square matrix of coefficients relating downwash at KFCP to pressure mode factors.
EI	structural bending stiffness, $WL^{-2}$
$\{F\}$	Column matrix (SCP x 1) of concentrated forces at structural control points.
GJ	structural torsional stiffness, $WL^{-2}$
H	transfer function
I	imaginary part of
$k_o$	$\frac{b_o}{U}$
$[\chi]$	$[\omega_n^e] [m_s]$
L, T, W,	scaling factors; length, time, and weight respectively
M	Mach number

# Post

$m$	mass per unit length, $WT^2 L^{-2}$
$[m]$	Diagonal generalized mass matrix, the members of which are the generalized masses for each lifting surface orthogonal mode considered.
$[P]$	A rectangular matrix (SCP x pressure mode terms), each row of which contains the pressure at each SCP x the associated area for each of the assumed pressure mode shapes
$q$	dynamic pressure, $WL^{-2}$
$R$	real part of
$\frac{l}{U}$	angle of attack due to a downwash of 1 ft./sec/ at a forward speed of U ft./sec.
$V$	true airspeed, $LT^{-1}$
$w$	downwash velocity
$\left\{ \frac{\bar{w}}{U} \right\}$	A (KFCP x 1) matrix of downwash at the KFCP's. The members of this matrix are complex if the flow is unsteady.
$\left[ \left( \frac{\bar{w}}{U} \right)_\phi \right]$	A (KFCP x number of surface normal modes) rectangular matrix of complex downwash due to the motion of the surface.
$x$	streamwise coordinate
$y$	spanwise coordinate
$\alpha$	angle of attack
$\xi$	damping ratio
$\frac{\rho_s}{\rho}$	ratio of structural density to air density
$\xi$ KFCP	non-dimensional distance measured stream-wise and perpendicular to a line perpendicular to the centerline of the airplane at the half-rootchord point of the lifting surface.
$\rho$	air density

# Post

$\phi$	power spectral density
$\varphi$	mode shape deflection
$[\varphi]^T$	A (number of surface normal modes x SCP) rectangular matrix, composed of rows which are the deflections at each structural control point for each normal mode shape.
$\omega_o$	reference frequency, $T^{-1}$
$\omega$	forcing downwash frequency
$[\omega_n^2]$	Diagonal matrix of natural frequencies



## Introduction

The problem of aircraft design for buffet loads has been a serious one for quite some time. There have been a number of instances of horizontal tail structural failure which occurred at high normal load factor and relatively low speed such that the angle of attack was close to or beyond stall. Accumulated evidence indicates that the failures were brought on by a superposition of loads due to buffeting upon the already near limit loads associated with the aircraft maneuver condition. Buffet problems have also been experienced by the majority of aircraft designed to operate in or traverse the transonic speed range. This situation is cause for concern because of the detrimental effects on pilot comfort and performance, weapon platform stability, and on the resultant loads which the aircraft structure must sustain.

In the past, the problem has not been amenable to rational prediction and analysis. The only means available for alleviation have been empirical fixes such as surface intersection contouring and filleting, and fences on the lifting surfaces. These fixes have been evaluated either during flight-test programs or with wind-tunnel tests on standard aerodynamic force models. These procedures have quite often involved significant delays in the development of the aircraft. The criteria for design of tail surfaces for loads due to buffeting are quite empirical. Often, weight penalties are paid to make a surface adequate to meet these design criteria, when in reality the buffet loads encountered in flight are considerably lower. On the other hand, there have been several in-flight failures due to buffet loads on surfaces designed to these same criteria. It therefore is appropriate to consider the development and application of rational, straightforward procedures which would be applicable to the analysis and prediction of buffet loads on aircraft structures.

Relatively recently, agencies such as the NASA and various airframe manufacturers have undertaken systematic investigations in this area. Liepmann (Reference 1 ) was among the first to suggest the application of the procedures of generalized harmonic analysis, as developed by Wiener, to the buffet problem. Wind tunnel studies conducted at NASA-Ames (Reference 2 ) based on measurements of the output pressures and strains on airfoil surfaces, indicate strongly that the pertinent statistical characteristics of these quantities are invariant with time, and thus buffeting can be considered as a stationary random process. Also, the output characteristics tend to have Gaussian probability distributions. On this basis, the power spectral density techniques of generalized harmonic analysis become natural tools with which to describe and manipulate the system input-output relations.

Research conducted by NASA-Langley, has resulted in suggestions for extrapolating wind-tunnel wing buffet data to flight-test con-

ditions. The procedure is based on wind-tunnel and flight-test data which indicate that the output spectra of wing buffet loads are for the most part dominated by the wing first-bending mode. Relatively little has been determined concerning the buffet-load spectra for tail surfaces. Available NASA data indicate that horizontal-tail bending, aft-fuselage torsion, and vertical-fin bending appear prominently.

The primary purpose of this research program is to develop an analytical method for the determination of the response of a lifting surface to a vehicle-generated turbulent flow field. The analytical method includes the derivation of power-spectral-density techniques in a usable form for the relation of turbulent input to surface response through a two-dimensional transfer function. To support the analytical development, a wind-tunnel program, utilizing an aeroelastic model, was conducted to obtain a better understanding of the basic mechanism of tail buffeting and to provide measured data to correlate with theory.

#### Experimental Study

The purpose of the experimental study is to provide a better understanding of the phenomenon of aircraft buffet. There are two major sources of buffet loads on an airplane. The first is associated with the transonic region and is caused by the attachment and re-attachment of shock waves to the fuselage and lifting surfaces. The second, which is the type under investigation here, is caused by the turbulent wake of the wing as an airplane approaches stall. This turbulent wake is caused by the separation of the flow over the upper surface of the wing.

Of particular interest are the loads caused by the wing wake on a horizontal tail surface which is located aft of the wing. When an airplane approaches stall at high normal load factor, the load on the horizontal tail nears a maximum. The additional loads resulting from perturbations in the horizontal tail angle of attack caused by random downwash velocities contained in the wing wake, are sometimes sufficient to cause failure. An important factor in the magnitude of these additional loads is the proximity of the horizontal tail to the wing wake.

To ascertain the location and turbulence level of the wing wake, a hot-wire anemometer system is employed. The operational details and the manner in which this device is used are subjects of a subsequent section. Limitations of the type of hot-wire probe that is used prevent a rigorous, quantitative description of the wing wake. However, the data obtained from this model to indicate that the depth of the turbulence behind the wing is contained in a very narrow band, that wing natural frequencies do not appear in

a power spectral density of the turbulence measured in the neighborhood of the horizontal tail and that the level of the turbulence varies along the span.

There are three primary boundary conditions imposed on the design of the aeroelastic model. First, the model must be aerodynamically and dynamically similar to a full-scale airplane. Second, the scaling factors must be adjusted so that the capabilities of the wind tunnel employed will allow the simulation of realistic flight conditions so that it may be possible to make comparisons with flight-test data. Third, the model must be strong enough to withstand the high continuous loads associated with testing at angles of attack approaching stall.

For correct dynamic similarity between model and full-scale data, the following nondimensional parameters must be maintained:

$$M_m = M_{fs} \quad (1)$$

$$\alpha_m = \alpha_{fs} \quad (2)$$

$$\left( \frac{V}{b_o \omega_o} \right)_m = \left( \frac{V}{b_o \omega_o} \right)_{fs} \quad (3)$$

$$(c_o q b_o)_m = (c_o q b_o)_{fs} \quad (4)$$

It can easily be shown that if equations (3) and (4) are satisfied,

$$\mu_m = \mu_{fs} \quad (5)$$

It is interesting to note that equations (3) and (4) are the conditions for the design of a flutter model. It is therefore true that a buffet model could be used for a flutter model and vice versa. The essential difference between the two is that the full-scale Mach number is usually not maintained in the design of subsonic, complete-air-vehicle flutter models as it must be for buffet models, and, instead the frequency ratio, model to full scale, is usually held one to one. Care must be exercised in choosing the scaling factors for a buffet model so that the lifting surfaces will be strong enough to withstand the high-angle-of-attack wind-tunnel conditions necessary for buffet studies.

With the scaling laws determined, the model is designed so that its mass and stiffness properties simulate those of a full-scale airplane as close as possible. The model is constructed around a rigid center-fuselage section fixed to a sting mount which contains the balance mechanism. The forebody is also rigid and accommodates an angle-of-attack indicator. The aft-fuselage bending and torsional stiffness is simulated by a flexible tube cantilevered at the aft end of the center section, but with clearance between it and the sting to allow the aft fuselage plus empennage to vibrate freely as a cantilevered member. The vertical tail is attached at zero incidence angle; however, the horizontal tails are capable of being preset to any desired incidence angle from zero to eighteen degrees in two-degree increments. The wings are mounted to the center section with attachments similar to those used in the full-scale airplane.

The lifting surfaces are constructed of a styrofoam core stiffened by a spanwise aluminum spar and covered with a chem-milled, tapered aluminum skin. All surfaces are closed out with an aluminum root rib. Accelerometers for measuring surface response are set into the styrofoam core during construction and are thus built into the surface. The instrumentation for the model includes seven accelerometers and seven strain gages.

#### Wing-Wake Turbulence Measurements Using a Hot-Wire Anemometer

The calibration and theory of operation of the hot-wire anemometer are discussed in References 3 through 5. The basic principle involved is that a wire's resistance to an electric current is changed as it is heated or cooled. During operation of this device, a small (.04" long x .0005" dia.) cylindrical wire is heated by an electric current and placed in an airstream at a point where turbulence is to be measured. As long as the flow past the wire is of constant velocity, and pressure, the voltage drop across the wire will remain unchanged. However, if a perturbation in either pressure or velocity occurs at the wire, it will be heated or cooled, thus changing its resistance and the voltage drop across it.

There are two basic methods of hot-wire flow measurement. The first, termed the constant-current method, maintains the current constant through the wire and the voltage change across the ends is recorded. The second, termed the constant-temperature method, maintains the temperature and voltage drop constant and records the current fluctuations. The frequency responses of commercially available hot-wire systems are claimed to be flat to 100,000 cps for a constant-current device and to 1000 cps for a constant-temperature device. There are advantages and disadvantages to each system which are discussed at length in the literature.

The hot-wire anemometer used for this study applies the constant-temperature method. This system was chosen because of its comparatively low cost and its adequate frequency response.

Two probes are installed on the model to measure the wing-wake in the neighborhood of the horizontal tail with the horizontal tail removed. This configuration is shown in Figure 1.

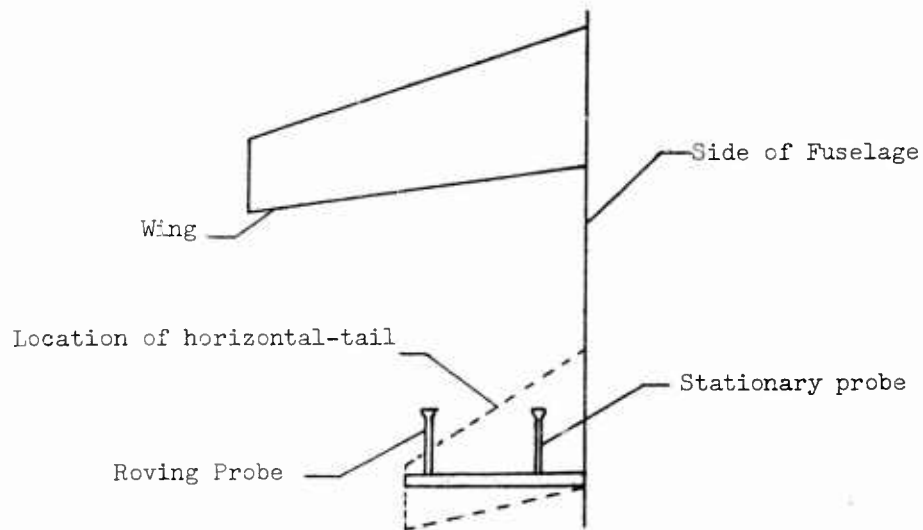
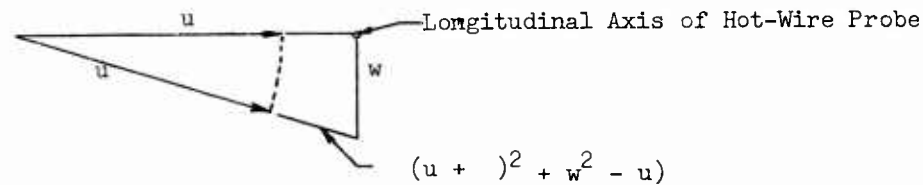


Figure 1

The inboard probe remains stationary as a reference, while the outboard probe is capable of being moved to various spanwise positions as a test is in progress. Each probe contains a single wire, whose longitudinal axis is horizontal and perpendicular to the airstream.

A single-wire probe is sensitive to velocity perturbations only in a plane normal to the longitudinal axis of the wire. For the wire orientation described above, any perturbation from the free-stream velocity vector in the streamwise-vertical plane would be sensed. Letting  $U$  represent the free-stream velocity vector and  $u$  and  $w$  be perturbation velocities in the streamwise and downwash directions respectively, the wire would measure  $u$  and  $w$  through the following relationship:



It is seen from the diagram that the perturbation in  $U$  is

$\left[ \sqrt{(U + u)^2 + w^2} - U \right]$ . Thus, this is the quantity which was measured by the hot-wire probes during the wind-tunnel program. Letting this quantity be denoted by  $p$ , it is seen that

$$p = \frac{2 U u + u^2 + w^2}{2 U + p}$$

If the assumptions are made that  $2U \approx 2U + p$

and that  $u^2$  and  $w^2$  are small with respect to  $2 U u$ , then  $p \approx u$ . Thus, the single-wire probe is predominantly sensitive to the streamwise perturbation,  $u$ , in the free-stream velocity. However, the  $w$  perturbations cause the buffeting loads and it was assumed that the turbulent field would be approximately isotropic, such that  $u$  and  $w$  would have the same statistical properties at a point in the field.

The goals, then, of the hot-wire study, using the two single-wire probes, are to ascertain the location of the wing wake relative to the horizontal tail, to find the depth of the turbulence from the wing at the horizontal tail, to determine whether there is any spanwise variation of the turbulence level and to find whether wing natural frequencies appear in the power spectral density of the measured hot-wire signals.

The hot-wire apparatus is installed at the wind tunnel on the left side of the model only. The current fluctuations are fed through a load resistor and the resulting voltage signal is recorded on magnetic tape. For a given wind-tunnel condition, a 45-second record is taken. The section of tape containing this example is then cut and spliced into a loop for determination of the power spectral density of the signal.

Three Mach numbers ( $M$ ) and pressure conditions were tested corresponding to  $M = .33$  at 20,000',  $M = .56$  at 25,000' and  $M = .74$  at 30,000'. The goals of the program were achieved and answers to the questions posed for the conditions given are as follows.

1. With the horizontal tail removed, turbulence from the wing was found only when the probes were directly behind the wing. For the model used, only at approximately -8.8 degrees of model angle

of attack was any signal received from the probes whatsoever. This results from the horizontal tail being at a water plane station below the wing. From zero to stall at positive angle of attack, there was no response from the hot-wire.

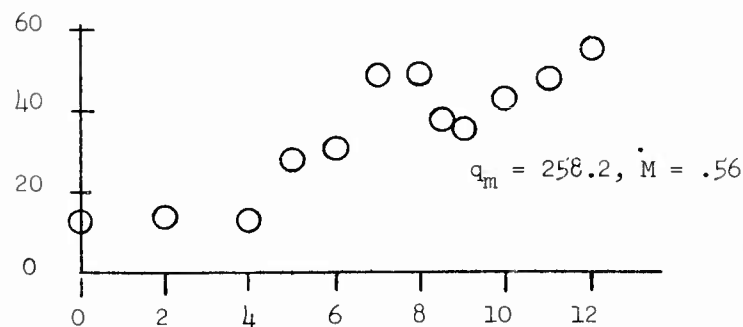
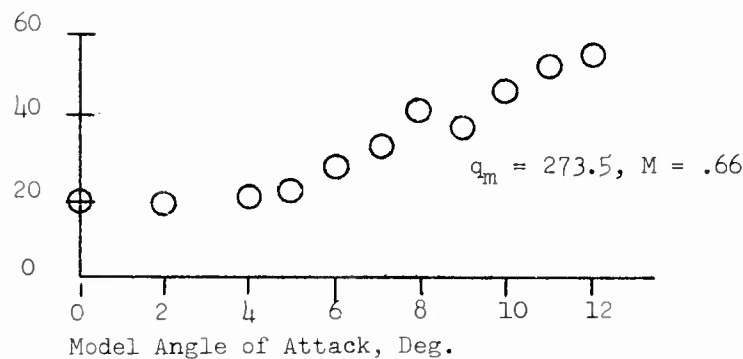
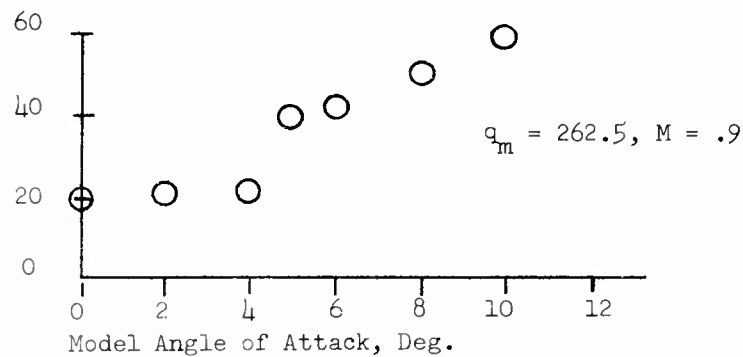
2. The depth of the turbulence from the wing at the horizontal tail location is quite narrow. A variation of  $\pm .1^\circ$  angle of attack is enough to take the probe out of the turbulence.
3. There is a difference in the root-mean-square level of the turbulence as the probe travels from a point corresponding to 25% horizontal tail span to 100% span. For the  $M = .56$  condition, the rms level is approximately 3 times as great at the outboard station as at the inboard station.
4. Power spectral densities taken at all conditions show a smooth decay of power level from zero to higher frequencies with no peaks at any of the wing natural frequencies. This result is surprising since the wing is generating the turbulence and in turn being excited by it. It is therefore hypothesized that sufficient mixing of the flow takes place from the wing trailing edge to the horizontal tail, such that wing frequencies are no longer dominant.

Supporting the hot-wire findings are Figures 3 and 5, which show relatively no change in horizontal tail response over the entire angle-of-attack range. The only time this is not true is when the horizontal tail is placed at a zero incidence angle. In this case, the rms levels look much the same as those for the wing, thus indicating that the horizontal tail itself is stalling.

Figures 2 through 5 show data from the two strain gages monitored during wind-tunnel testing. The horizontal tail is at an incidence angle with the fuselage of 6 degrees leading-edge-down as shown in Figure 6. This is a realistic angle as derived from full-scale airplane flight data. It is seen that the root-mean-square (rms) level of the signal from the wing-root-bending gage begins to increase after approximately  $+4$  degrees angle of attack in all cases, thus indicating the start of flow separation over the upper surface of the wing. The numerical value of the rms level seems to be independent of Mach number and dynamic pressure.

Post

Root-Mean-Square Bending Moment, in.lbs.

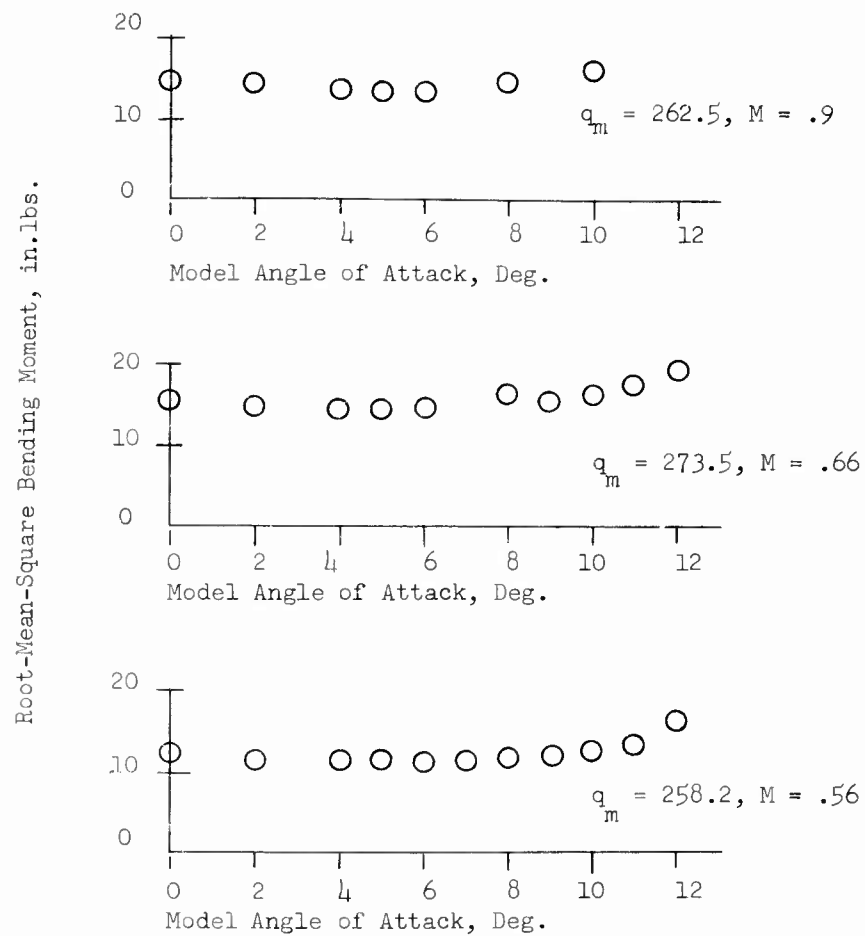


Model Angle of Attack, Deg.  
Root-Mean-Square of Model Left-Wing-Root-Bending  
Gage Due to Buffet ( $q$  - constant, varying  $M$ )

FIGURE 2



Post



Root-Mean-Square of Model Left-Horizontal-Tail-Root-Bending Gage ( $q$  - constant, varying  $M$ )

Figure 3

Post

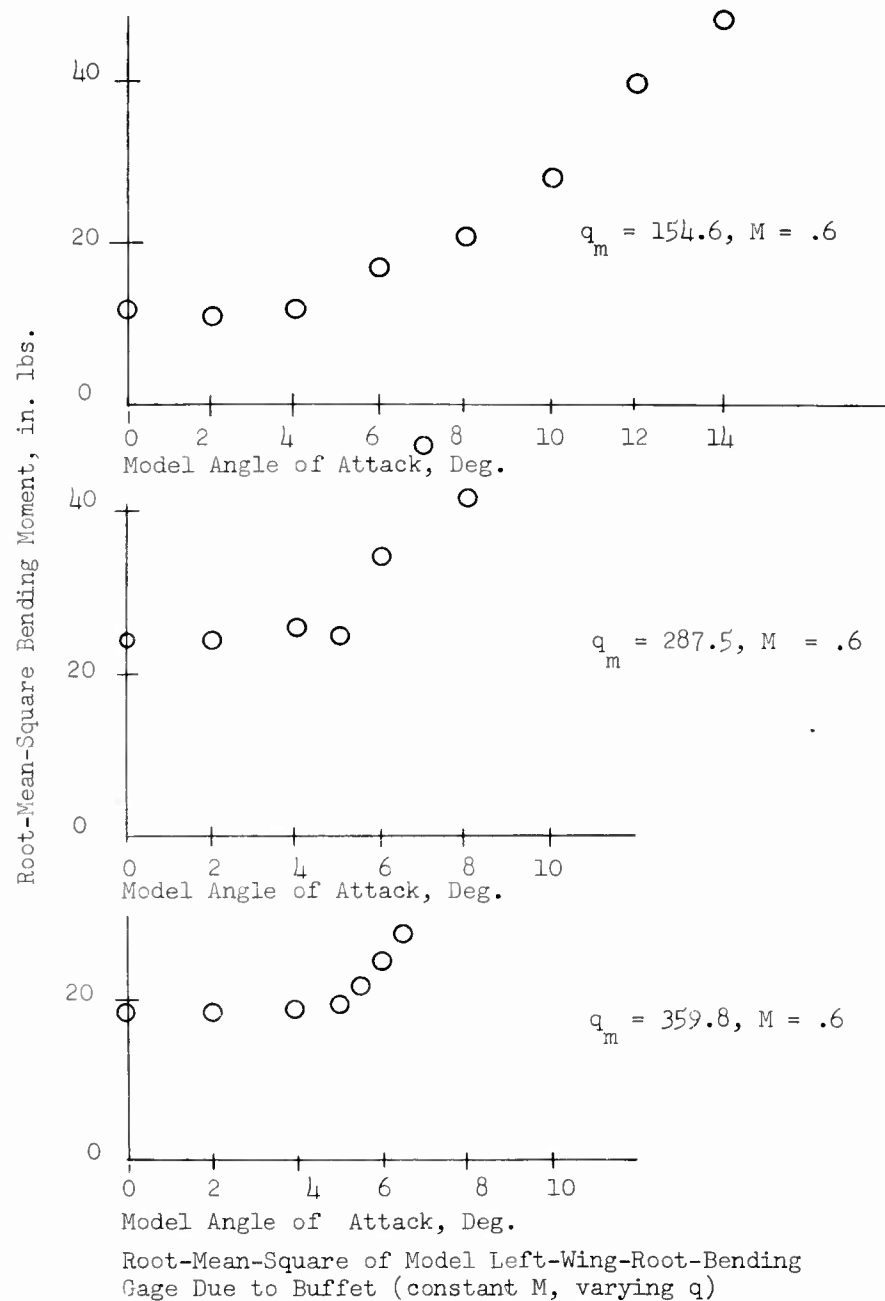
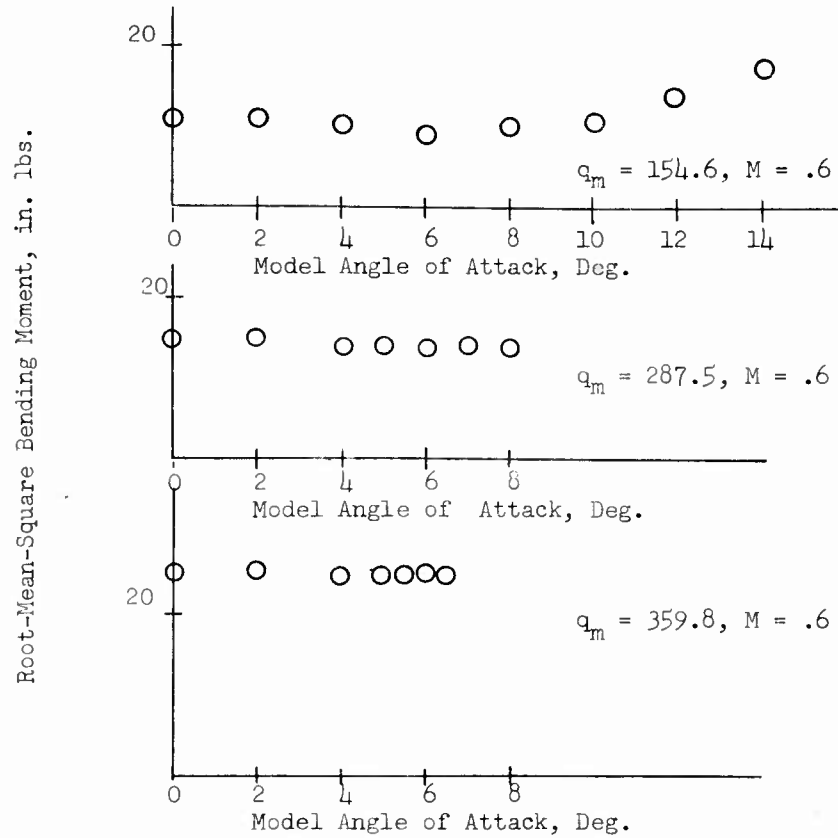


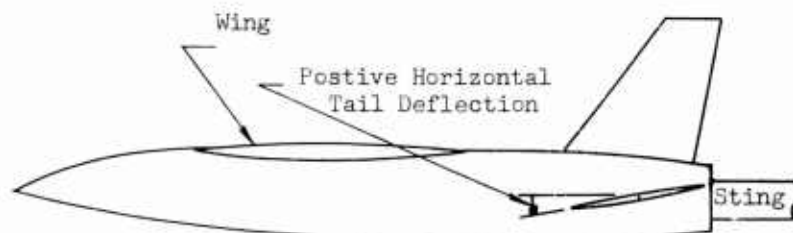
Figure 4

Post



Root-Mean-Square of Model Left-Horizontal-Tail-Root-Bending Gage (constant M, varying q)

Figure 5



Model General Arrangement  
Figure 6

A limited amount of the experimental data has been compared with flight-test results, showing qualitative agreement.

#### Analytical Study

The response of a lifting surface, in this case the horizontal tail, may be related to a random, aerodynamic input through the general relation: (output) = (transfer function) x (input). The method for calculating a horizontal-tail transfer function is the core of this analytical study.

#### The Interpretation of Buffet-Turbulence Measurements

The buffet-turbulence field extends in three dimensions behind and near the wing. In each point in this field the local velocity of the air varies in magnitude and direction in a random fashion. In the following, only excitation of the horizontal stabilizer will be considered. Therefore, the turbulence in the region of interest is supposed to consist of random vertical velocities in a two-dimensional field. The random vertical velocity is statistically different in different points in a chordwise section of the stabilizer. It is assumed that a point exists in each section where the measured power spectrum is statistically representative for the whole section. Statistical variation in the chordwise direction is thus neglected. For a given airplane condition, the random vertical velocity in this point is assumed to be a stationary random process with a Gaussian probability distribution.

Furthermore, it is assumed that the hypothesis of Taylor is valid so that time averages of the turbulence in a point are equivalent to space averages in forward direction from that point. The points on all cross-sections form a straight line which may have a certain sweep-back angle. In general, the statistical properties of the random vertical velocity will change along this line, i.e., the field is inhomogeneous in the spanwise direction.

The response item of interest can be determined by using the frequency-response function  $H(\omega, y)$ , also often called the transfer function, which represents the response to a sinusoidal excitation with frequency  $\omega$  over a strip with unit width at spanwise station  $y$  on the line defined in the preceding paragraph. It can be shown (Reference 6) that the power spectrum of the response is given by

$$\phi_z(\omega) = \iint_{span} H^*(\omega, y_1) H(\omega, y_2) \phi(\omega, y_2 - y_1) dy_1 dy_2 \quad (6)$$

in which  $\phi(\omega, y_2 - y_1)$  represent the cross-power spectrum of the inputs at station  $y_1$  and  $y_2$  along the span, and the star indicates that the complex conjugate is to be taken. The cross-spectrum is defined as the Fourier transform (apart from the constant  $\pi$ ) of the cross-correlation function

$$\phi(\omega, y_2 - y_1) = \frac{1}{\pi} \int_{-\infty}^{+\infty} \psi(\tau, y_2 - y_1) e^{-i\omega\tau} d\tau, \quad (7)$$

and the cross-correlation function is defined as

$$\psi(\tau, y_2 - y_1) = \overline{w(t, y_1) \cdot w(t + \tau, y_2)} \quad (8)$$

with the bar denoting a time average, and  $w$  representing the random downwash velocity.

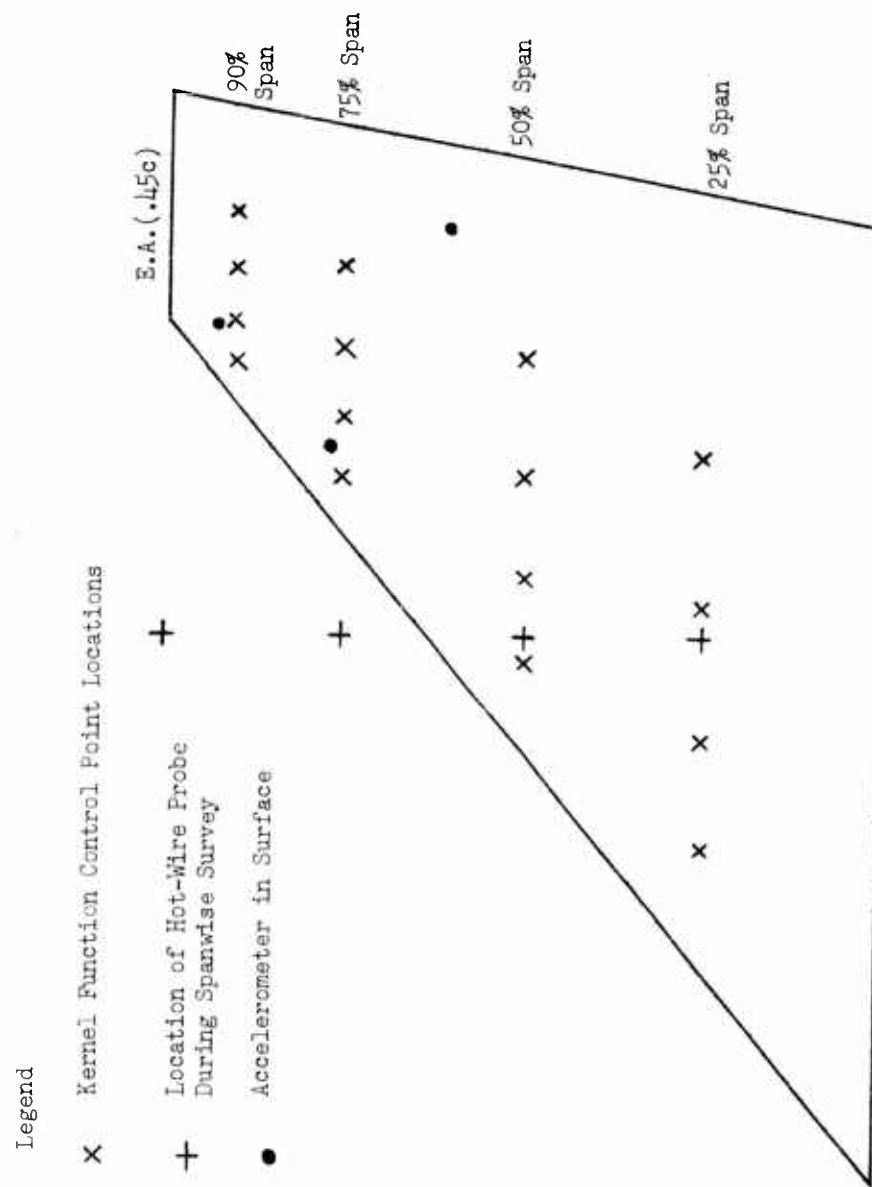
In this program, measurements of the input power-spectra using hot-wire probes were taken in only four spanwise locations, as shown in Figure 7. Hence, not enough information is available to carry out the integrations rigorously. However, an approximate solution can be obtained if it is assumed that the random excitation is constant over finite intervals. Over these intervals the power spectra are constant and can be taken outside the integrals. Introducing the frequency-response function for a finite spanwise interval  $\Delta y$ :

$$H(\omega, \Delta y_i) = \int_{\Delta y_i} H(\omega, y) dy \quad (9)$$

the response equation, can be written in matrix form (see Reference 7).

$$\phi_r(\omega) = [H^*(\omega, \Delta y_i)] [\phi(\omega, y_j - y_i)] \{H(\omega, \Delta y_j)\}. \quad (10)$$

The response equation in matrix form is known mathematically as a Hermitian form, which is always real. Only the matrix of power spectra requires further attention. It is a Hermitian matrix with the property that its real part is symmetric and its imaginary-part skew-symmetric. Simplifying the notation for the power spectra by writing



Model Horizontal-Tail

Figure 7

$$\phi_{ji} = \phi(\omega, y_j - y_i) \quad (11)$$

the matrix of the power spectra simply becomes

$$[\phi_{ij}]$$

and the elements have in general the properties that

$$\phi_{ii} = \text{real}$$

$$\phi_{ij} = \phi_{ji}^*$$

The members of the main diagonal of  $[\phi_{ij}]$  are the power spectra of the downwash-velocity for each spanwise location of a hot-wire probe. The off-diagonal members are cross-power spectra between each spanwise probe location.

In order to generate cross-power spectra between a number of spanwise sensors, all signals along the span must be measured simultaneously. Ideally then, it is desirable to have a number of probes along the span, each measuring only the random downwash velocity.

If a system exists which will yield a time varying signals that can be calibrated to only the downwash velocity, it may not be practical to have more than one or two probes along the span. Another practical difficulty is the measurement of cross-spectra. Not many such machines are in existence. A method for making estimates of the cross power-spectra is given in Reference 7 .

In Equation (6) the power spectrum of a random response  $r(t)$  is expressed as a double integral containing the cross-power spectra of the random inputs at various stations. A more general expression relates the cross-power spectrum of two random responses  $r(t)$  and  $s(t)$  to the cross-power spectra of the inputs at various stations:

$$\phi_{rs}(\omega) = \iint_{\text{span}} H_r^*(\omega, y_1) H_s(\omega, y_2) \phi_{\text{turb}}(\omega, y_2 - y_1) dy_1 dy_2 \quad (12)$$

Any two responses can be considered here. The appropriate

frequency response functions must be used as indicated by the subscripts r and s. In the special case where r is equal to s, Equation (6) is obtained.

The double-integral equation can again be written in matrix form by making the same assumptions used for Equations (9), (10). The result is in general

$$\left[ \phi_{rs} \right]_{m \times m} = \left[ H_{ri}^{*T} \right]_{m \times n} \left[ \phi_{turb}(y_j - y_i) \right]_{n \times n} \left[ H_{sj} \right]_{n \times m} \quad (13)$$

The matrix  $\phi_{turb}$  containing in general the cross-power spectra of the random vertical velocity at the stations  $y_i$  and  $y_j$  has the order  $(n \times n)$  if a total of  $n$  stations are considered. The matrix  $\phi_{rs}$  containing the cross-power spectra of the random responses has the order  $(m \times m)$  if a total of  $m$  responses are considered. The two matrices  $H$  of order  $(m \times n)$  and  $(n \times m)$  contain the frequency-response functions of the appropriate response to the unit sinusoidal excitation at a specific station, and they are mutually complex conjugate and transposed.

It appears to be possible to determine the input power spectra from the response power spectra by inversion of Equation (13). This gives

$$\left[ \phi_{turb} \right]_{n \times n} = \left[ H^{-1*T} \right]_{n \times m} \left[ \phi_{rs} \right]_{m \times m} \left[ H^{-1} \right]_{m \times n} \quad (14)$$

The equation is obtained by post-multiplying  $\phi_{turb}$  by  $H^{-1}$  and pre-multiplying by  $(H^{*T})^{-1}$ . It can be shown that the latter is equivalent to  $(H^{-1})^{*T}$ . Of course  $H^{-1}$  is only well defined if  $H$  is a square, non-singular matrix. From Reference 8, the impression is gained that  $H^{-1}$  can always be defined when  $H$  is rectangular of order  $(n \times m)$  with  $m \geq n$ . This would mean that the inverse equation exists if the number of responses is larger than or at least equal to the number of stations where the input vertical velocity is measured. The definition of the inverse of  $H$  is then:

$$H^{-1} = H^T [H \cdot H^T]^{-1} \quad (\text{See Reference 7}).$$



So far the response equations are valid for any response as long as it has a frequency-response function describing it in terms of the input at the various stations. It is possible to express the response of generalized coordinates in a similar way, the generalized coordinates representing the amount of each normal mode present in the response. These generalized response power-spectra can be obtained as follows; see Reference 7. Let the cross-correlation function of two deflections  $d$  be given by

$$\psi_{ij}^d = \overline{d_i(t) \cdot d_j(t + \tau)}. \quad (15)$$

Express the deflections in the generalized coordinates by means of the modal deflections  $\varphi$ :

$$d_i = L \varphi_{in} \downarrow \left\{ \xi_n \right\}, \quad (16)$$

in which  $\xi_n$  is the  $n$ th generalized coordinate. It is understood that the deflection is completely described by this expression only if all vibration modes in the frequency range of interest are taken into account. Now introducing the cross-correlation function of the generalized coordinates

$$\psi_{mn}^{\xi}(\tau) = \overline{\xi_m(t) \cdot \xi_n(t + \tau)}, \quad (17)$$

and after substitution of the expression for  $d$  in  $\psi_{ij}^d$ , and recognizing that the time-averaging process affects  $\xi$  only, the following expression is obtained,

$$\psi_{ij}^d = L \varphi_{im} \downarrow \left[ \psi_{mn}^{\xi} \right] \left\{ \varphi_{nj} \right\}, \quad (18)$$

or in general for all cross-correlation functions  $\psi^d$ :

$$\left[ \psi^d \right]_{a \times a} = \left[ \varphi \right]_{a \times b} \left[ \psi^{\xi} \right]_{b \times b} \left[ \varphi^T \right]_{b \times a}. \quad (19)$$

Each column of  $\varphi$  represents one of (b) mode shapes, defined in (a) points. Taking Fourier transforms on both sides produces an equivalent expression in power-spectra:

$$[\phi^d]_{a \times a} = [\varphi]_{a \times b} [\phi^f]_{b \times b} [\varphi^T]_{b \times a} \quad (20)$$

Inversion of this equation to give an expression for  $\phi^f$  in terms of  $\phi^d$ , appears to be possible under the same conditions as given for Equation (14), from  $\phi^{-1} = [\phi^T \cdot \phi]^{-1} \phi_T$  for  $a > b$ . The expression becomes:

$$[\phi^f]_{b \times b} = [\varphi^{-1}]_{b \times a} [\phi^d]_{a \times a} [\varphi^{-1}]_{a \times b}^T, \text{ for } a > b. \quad (21)$$

The justification of this limitation on the order of  $\varphi$  is that the number of points (a) in which the mode shapes are known must be equal to or larger than the number of modes (b), in order to well define the (b) modes from measurements in the (a) points.

The power-spectra of the generalized coordinates can now be expressed in terms of the input power-spectra:

$$[\phi^f] = [\varphi^{-1}] [H_d^{*T}] [\phi_{turb}] [H_d] [\varphi^{-1}]^T \quad (22)$$

or

$$[\phi^f] = [H_f^{*T}] [\phi_{turb}] [H_f], \quad (23)$$

in which the generalized frequency-response functions follow from

$$[H_f] = [H_d] [\varphi^{-1}]^T \text{ or } [H_d] = [H_f] [\varphi^T]. \quad (24)$$

The question arises whether it is more useful to determine the power spectra of the generalized coordinates than those of specific responses. It is expected that graphs showing the power spectra of the generalized coordinates will be very helpful in interpreting the behavior of the structure, more so than graphs showing the power spectra of specific responses. Furthermore, any response can be conveniently determined from the responses in the generalized coordinates. In general the relation exists:

$$\{R\} = [A_r] \{f\}. \quad (25)$$

The matrix  $A_r$  consists of rows associated with a specific response and columns associated with the various modes. The power spectra of these responses can be expressed in the power spectra of the generalized coordinates by

$$[\phi^R] = [A_r] [\phi^f] [A_r]^T. \quad (26)$$

If the response is simply the deflection in various points,

$$[A_r] = [\varphi].$$

If the response consists of accelerations in various points,

$$[A_r] = -\omega^2 [\varphi],$$

and the power-spectral relation becomes

$$[\phi^a] = \omega^4 [\varphi] [\phi^f] [\varphi^T]. \quad (27)$$

If the response is a stress, strain, force or moment, the amount of this quantity in each mode must be determined to obtain the matrix  $A_r$ . The coefficients of  $A_r$  represent a response per unit generalized coordinate and are sometimes given as  $\left(\frac{\sigma}{f}\right)$ .

Using the generalized frequency-response function defined in Equation (23) the input-output relations can be written:

$$[\phi_r^f] = [H_f^{*T}][\phi_{turb}][H_f] , \quad (28)$$

and the inverse,

$$[\phi_{turb}] = [H_f^{-1*T}][\phi_r^f][H_f^{-1}] . \quad (29)$$

The similarity of both equations suggests that neither one of the random processes, the turbulence or the response, is to be regarded as an actual input in the mathematical model and the other as an output. They are rather to be considered as interdependent random processes connected by the frequency-response functions. For any given set of frequency-response functions one random process is completely defined by the other.

For a complete description of a partitioned-matrix method for the estimation of all unknown power or cross-power spectra, see Reference 7.

The main limitation in the analysis is probably that the power spectrum of the input turbulence is assumed to be constant in the chordwise direction. If future hot-wire measurements of the random downwash velocity show that the power spectrum of the turbulence varies appreciably in forward direction, it will be necessary to choose a representative power spectrum for each chordwise strip. This may be difficult and it can be the source of differences between measured and calculated responses. It is, therefore, considered to be a major improvement if the variation in chordwise direction can be taken into account. This appears to be possible in a simple way provided the frequency-response functions are available in a somewhat different form.

It can be shown that in the case of variation of the turbulence spectra in the chordwise direction, the power spectrum of the response is given (similar to Equation (6) by)

$$\phi_r(\omega) = \iint_{\text{span}} \iint_{\text{chord}} H^*(\omega, x_1, y_1) H(\omega, x_2, y_2) \phi_{turb}(\omega, x_2 - x_1, y_2 - y_1) dx_2 dy_2 . \quad (30)$$

The integrations can again be approximated to summations over finite intervals  $\Delta x$  and  $\Delta y$  by introducing:

$$H(\omega, \Delta x_i, \Delta y_i) = \int_{\Delta x_i} \int_{\Delta y_i} H(\omega, x, y) dx dy. \quad (31)$$

Then the response equation can be written in the same matrix form as in Equation (10):

$$\phi_r(\omega) = [H^*(\omega, \Delta x_i, \Delta y_j)] \left[ \phi_{turb}(\omega, x_k - x_i, y_l - y_j) \right] \{H(\omega, \Delta x_k, \Delta y_l)\}. \quad (32)$$

The cross-power spectrum of the turbulence relates the random input at station  $(x_i, y_j)$  to that at  $(x_k, y_l)$ . The frequency-response functions must be defined at these stations for finite areas  $(\Delta x_i, \Delta y_j)$  and  $(\Delta x_k, \Delta y_l)$ . The matrix equation can, of course, be generalized as before to give cross-power spectra between various responses.

#### Method for Calculation of Horizontal Tail Transfer Function

The transfer function for a lifting surface is defined as the response of the surface due to a unit sinusoidal downwash input.

The members of the column matrix  $\{H(\omega, y_j)\}$ , defined by Equation (10) are the responses at a point on the horizontal tail due to excitations by unit sinusoidal downwash velocities, each of frequency  $\omega$ , impressed one at a time, on each chordwise strip of width  $y$ , where  $y$  is the spanwise coordinate measured perpendicular to the centerline of the airplane. Thus,  $\{H(\omega, \Delta y)\}$  may be termed a two-dimensional transfer function. The number of chordwise strips to be chosen is equal to the number of points at which the turbulent input to the horizontal tail is measured. The width of each chordwise strip is the area of influence assumed applicable to each spanwise measurement of the turbulent input.

An assumption implicit in the choosing of the chordwise strips is that the power level of the turbulent input remains constant across the chord of the horizontal tail.

The only aerodynamic theory known to be available at the present which is capable of being used to calculate such a transfer function, is known as the Kernel Function method. Until recently, there have been no satisfactory aerodynamic methods of analysis

which rationally account for all the effects of finite-span geometry, compressibility, and lifting-surface oscillation in subsonic flow. However, C. Watkins and his associates at NASA-Langley, have developed and made available, an IBM-704 digital computer program of a Kernel Function method which enables prediction of the pressure distribution under such conditions.

The Kernel Function method may be briefly stated as follows: given the integral equation relating pressure and downwash, and assuming that the pressure is representable as a weighted superposition of basic pressure mode shapes, a numerical solution to the integral equation is obtained in the form of numerical values of the pressure mode shape weighting factors. The theory and digital program are the subjects of References 9, 10, and 11.

To use the Kernel Function program in obtaining the surface transfer function, the following data must be available.

A. Surface Geometry

1. exposed semispan,  $\ell$
2. length of half the root chord,  $b$
3. sweep-back angle of the quarterchord line,  $\Lambda$  c/4
4. taper ratio,  $\lambda$
5. aspect ratio,  $R$

B. Surface Vibration Characteristics

1. For each surface mode of vibration to be used, the following must be determined either by calculated or experimental means:
  - a. surface deflection mode shape,  $\phi$
  - b. natural frequency,  $\omega_n$
  - c. generalized mass,  $M$

A step-by-step procedure for the calculation of the transfer function, is given below.

Step 1

A Kernel Function control point configuration is established as a grid or fixed points on the surface at which the input unit sinusoidal downwash will eventually be applied.

The placing of these points must be carefully done so that the distance between any two adjacent ones spanwise, is not less than approximately 10% of the exposed span. These points should also be no closer than 10% span to either tip or root, and no closer to the leading

and trailing edges than 12% of local chord. The reason for these restrictions is the shapes of the assumed set of basic spanwise and chordwise pressure distributions.

A total of 16 Kernel Function control points are provided for in the current program. For reasons unknown at the present, the best configuration for these control points is a 4 by 4 grid such as the one shown in Figure 7.

## Step 2

A system of equations to solve for the pressure mode weighting factors, given the downwash at the Kernel Function control points (KFCP) is

$$\frac{\bar{w}^j}{U} = [c_{nm}] \{b_j\} \quad (33)$$

The elements of the coefficient matrix  $[c_{nm}]$  are integrals over the lifting surface. The unwieldiness and singular nature of these integrals thwarted early attempts to use this method. However, through the use of modern, high-speed, computing machinery and a high precision numerical integration technique called Gaussian quadrature, the matrix can be evaluated and inverted to yield the pressure mode shape weighting factors in terms of downwash as

$$\{b_j\} = [c_{nm}^{-1}] \left\{ \frac{\bar{w}^j}{U} \right\} \quad (34)$$

The left-hand side of this equation was the output of the NASA program received at NAA-Columbus. However, in light of extensions proposed and developed here, the downwash-independent quantity,  $[c_{nm}^{-1}]$  is a more basic one. Therefore, subsequent minor modifications resulted in Part One of the NASA-NAA-Columbus Subsonic Kernel Function program whose output is  $[c_{nm}^{-1}]$ . This matrix is dependent upon Mach number ( $0 \leq M < 1$ ), reduced frequency, non-dimensional planform geometry of arbitrary (excluding 0 and  $\infty$ ) aspect ratio, downwash symmetry, number and locations of the KFCP, and is complex if unsteady conditions exist. Computing time to obtain  $[c_{nm}^{-1}]$  is approximately 10 seconds and 35 seconds per Kernel Function control point for steady and unsteady conditions, respectively.

## Step 3

A matrix of aerodynamic influence coefficients must be computed which relates the input downwash to forces acting on the lifting surface.

Given a pressure distribution upon a lifting surface, composed of a linear superposition of basic pressure mode shapes, the objective is to predict resultant concentrated forces transmitted through the structure to a set of arbitrarily located structural control points (SCP). The surface is then divided into small areas, one associated with each structural control point. The program calculates the pressure acting on each area, then a force which is considered to act at the structural control point is obtained by pressure  $\times$  area. A maximum of 100 structural control points is provided for in the program.

The governing equation is

$$\{F\} = [P] \{b\} \quad (35)$$

However,

$$\{b\} = [C_{NM}^{-1}] \left\{ \frac{\bar{w}}{U} \right\} \quad (36)$$

therefore,

$$\{F\} = [P] [C_{NM}^{-1}] \left\{ \frac{\bar{w}}{U} \right\} \quad (37)$$

The matrix product,  $[P][C_{NM}^{-1}]$  thus relates the downwash to the forces on the lifting surface, which is the definition of an aerodynamic influence coefficient matrix:

$$[AIC] = [P] [C_{NM}^{-1}] \quad (38)$$



## Step 4

Calculate the generalized aerodynamic force-due-to-surface-motion matrix:

$$[a] = [\varphi^T] \frac{4\pi \rho^2 b_o^2}{k^2} [AIC] \left[ \left( \frac{\bar{w}}{U} \right)_\varphi \right] \quad (39)$$

A very important feature of the matrix  $[\varphi^T]$  is that it allows for chordwise bending of streamwise strips. This is especially important when considering a delta planform or when including higher modes for a conventional swept surface.

The matrix  $\left[ \left( \frac{\bar{w}}{U} \right)_\varphi \right]$  is the downwash input to the surface due to the modal deflections of the surface. The mode displacement and slope are loaded in at each Kernel Function control point in the form  $\frac{\partial \varphi}{\partial x} + i \frac{k}{k_o} \varphi$ .  $\varphi$  is the modal deflection and  $\frac{\partial \varphi}{\partial x}$  is the streamwise slope of the mode shape evaluated for each mode at each KFCP.

The matrix  $[a]$  is then the generalized force on the lifting surface due only to the motion of the surface. This matrix is square of order (no. of modes x no. of modes) and is, in general, complex. The  $ij^{\text{th}}$  member of this matrix is the generalized force in mode  $i$  due to a deflection of mode  $j$ .

## Step 5

Calculate the generalized aerodynamic force-due-to-input-downwash matrix;

$$[\tilde{z}] = [\varphi^T] \frac{4\pi \rho^2 b_o^2}{k_o^2} [AIC] \left[ \left( \frac{\bar{w}}{U} \right)_r \right] \quad (40)$$

Each column of the matrix  $\left[ \left( \frac{\bar{w}}{U} \right)_r \right]$  specifies a unit downwash along one chordwise array of Kernel Function control points. A limitation to the calculation of a two-dimensional transfer function exists here. As explained previously, there are only four chordwise arrays of KFCP's, each containing four KFCP's. This means that under the present program it is possible to divide the lifting surface into only

four chordwise strips.

The procedure for obtaining the first column of  $[\Xi]$  is to excite the lifting surface by impressing a unit sinusoidal downwash on only the first (most inboard) four chordwise KFCP's. This is done by loading into the program:

$$\left(\frac{\bar{w}}{U}\right)_i = \frac{1}{U} \left( \cos k_i F_{KFCP_i} + i \sin k_i F_{KFCP_i} \right), \quad (41)$$

where  $i = 1, 2, 3$  and  $4$ .

The slope and deflection at the other twelve Kernel Function control points are loaded in as zero.

To obtain the second, third and fourth columns of  $[\Xi]$ , excite the second, third and fourth chordwise arrays of KFCP, respectively, while, in each case, zero downwash is loaded in at all other KFCP's.

#### Step 6

Calculate the two-dimensional transfer function  $[H_f]$  as defined by Equation (24).

The governing equation is the well-known second-order-system response equation:

$$[H_f^T] = \left\{ [\chi] - \omega^2 \{ [m] + \rho [a] \} \right\}^{-1} \rho \omega^2 [\Xi], \quad (42)$$

where each column of  $[H_f^T]$  are the modal responses to each corresponding column of  $[\Xi]$ .

#### Step 7

All of the steps thus far have been to obtain the response matrix  $[H_f]$  for one value of the forcing frequency  $\omega$ , at one density  $\rho$ , at one airspeed  $U$ . Theoretically, a transfer function is defined as the matrix  $[H_f]$  evaluated for all forcing frequencies from zero to infinity at each altitude and airspeed.

The transfer function must, of course, be calculated for each Mach number and altitude at which a flight condition is to be investigated.

A sample calculation was made using the above procedure. A one-dimensional transfer function was obtained, due to the fact that it was not possible to get cross-power spectra. Taking an average power spectrum value of the hot-wire input signal across the span of the horizontal tail and the power spectra of accelerometers placed in the horizontal tail, the value of the transfer function obtained by dividing the output by the input was compared with the calculated transfer function. The modulus squared of the experimental transfer function was, on the average, eighty times larger than the modulus squared of the calculated transfer function.

A possible explanation of this discrepancy was shown to be in the hot-wire signal. As outlined previously, the hot wire is sensitive to velocity perturbations in a plane perpendicular to the axis of the wire. It has been shown that if the downwash velocity,  $w$ , is an order of magnitude larger than the perturbation in the forward speed,  $u$ , the experimental and calculated transfer functions would be in agreement. However, this contradicts the assumption made earlier that  $u$  is statistically the same as  $w$ . This assumption was based on a turbulent field being composed of circular eddies; therefore, in order to continue the investigation,  $u$  and  $w$  must be determined separately and cross-power spectra must be obtained.

#### Data Reduction for Use In Fatigue Analyses

There are three pertinent quantities used in fatigue analyses, which can be derived from the power spectrum of a stationary, Gaussian random signal. These are: (1) the number of zero crossings with positive slope per unit time, (2) the number of peaks above a given level per unit time and (3) the total number of all maxima per unit time. Relationships for obtaining these quantities can be found in Reference 12.

It has been found feasible to code a digital computer which will calculate the above data.

Thus, a simple procedure has been developed, whereby inputs to a fatigue analysis may be obtained, given the power spectral density of the output of a critically located accelerometer or strain gage.

# Conclusions and Recommendations

Analytical procedures have been developed for the determination of the response of a lifting surface to a two-dimensional random downwash excitation. An advanced aerodynamic method (Kernel Function) for calculating airload distributions has been applied for establishing the two dimensional transfer function for the lifting surface. Power spectral analysis methods have been developed in matrix form for computing input-output relationships for linear systems excited by two-dimensional random inputs.

A hot-wire anemometer system was successfully applied for the first time for making measurements of turbulence fields generated by a wind-tunnel model in stalled conditions. The turbulence field was found to be of very narrow depth in the region of the tail and above the plane of the wing of the model tested in positive stalled attitudes. No wing frequencies were found present in the measured power spectra of the wing wake and the rms level of turbulence was found to increase by a factor of three from the 25% to 100% spanwise tail station.

Measurements taken by the hot-wire probe that were used are more sensitive to perturbations in the streamwise direction than in the vertical direction. However, it was hypothesized that these perturbations would be of approximately the same magnitude, and, therefore, that these measurements could be directly interpreted as downwash. Comparison of calculated and experimental results show that this hypothesis was not confirmed since, assuming that the horizontal tail transfer function and the measured output are correct, calculations indicate that the downwash velocities must be larger than the streamwise perturbations. It is therefore absolutely necessary, before any significant additional work in this field may be done, to develop a system to record the time histories of the forward-speed perturbations and the downwash separately. This is planned to be undertaken in subsequent work.

A significant step has been taken in this program to develop techniques for the design of aeroelastic buffet models that can simulate both airplane dynamic characteristics and full-scale flight conditions. Although specific comparison with flight test data have not yet been made, the buffet model shows promise for revealing the buffet behavior of the full-scale airplane.

A logical extension of this work is the investigation of horizontal-tail response in abrupt stalls. It is under this condition that most buffeting-type failures occur. It is believed that a peculiar condition exists here, that of a large starting vortex associated with a sudden stall. This may be of greater depth than a continuous turbulence field and affect horizontal tails in a greater range of vertical position.

References

1. Liepman, H. W., "On the Application of Statistical Concepts to the Buffeting Problem", Journal of the Aeronautical Sciences, December 1952
2. Polentz, P. O., Page, W. A., & Levy, L. L., "The Unsteady Normal Force Characteristics of Selected NACA Profiles at High Subsonic Mach Numbers", NACA RM A55C02, May 1955
3. Hinze, J. O., "Turbulence", McGraw-Hill Co., Inc., 1959
4. Efowes Williams, J. E., "Measuring Turbulence with a View to Estimating the Noise Field", A. R. C. 20,381, 1958
5. Kovasznay, L. S. G., "Development of Turbulence Measuring Equipment: NACA-TR 1209, 1954
6. Coleman, T. L., Press, H., Shufflebarger, C. C., "Effects of Airplane Flexibility on Wing Bending Strains in Rough Air:", NACA TN-4055, 1957
7. Botman, M., "The Response of Linear Systems to Inhomogeneous Random Excitation", IAS Paper No. 61-32, Presented at the IAS 29th Annual Meeting, New York, January 1961
8. Gravitz, S. I., "An Analytical Procedure for Orthogonalization of Experimentally Measured Modes", Journal of the Aeronautical Sciences, November 1958
9. Watkins, Runyan, and Woolston, "On the Kernel Function of the Integral Equation Relating Lift and Downwash Distributions of Oscillating Finite Wings in Subsonic Flow", NACA Report 1234, 1955
10. Watkins, Woolston, and Cunningham, "A Systematic Procedure for Determining Aerodynamic Forces on Oscillating or Steady Finite Wings at Subsonic Speeds", NASA TR R-48, 1959
11. Watkins, Woolston, and Cunningham, "An IBM 704 Program of a Kernel Function Procedure for Obtaining Aerodynamic Forces on Finite Wings in Subsonic Flow. Analytical Background and Description of Coding", NASA Internal Memorandum for Files, April, 1959.
12. Bendat, J. S., "Principles and Applications of Random Noise Theory", John Wiley and Sons, Inc., New York, 1958

**SESSION V | HIGH TEMPERATURE EFFECTS**

Chairman: Dr. Harold Liebowitz  
Office of Naval Research

A MATRIX FORCE METHOD FOR ANALYZING  
HEATED WINGS, INCLUDING LARGE DEFLECTIONS

W. Lansing,\* I. W. Jones,\*\* P. Ratner\*\*  
Grumman Aircraft Engineering Corporation  
Bethpage, New York

I SUMMARY

The matrix force method of redundant structure analysis has been shown in previous papers to be well suited for calculating stresses and deflections resulting from non-uniform thermal strain. (ref. 1, 2) However, these papers have dealt only with structures whose responses to external loads are essentially unaltered by the presence of the induced thermal stresses.

The present effort extends the matrix force method as applied to thin wings to include the influence of in-plane thermal stresses upon the resistance of the structures to lateral loads. The limiting case of increased flexibility due to in-plane stresses, specifically the condition critical for buckling, is also solved. Further, a procedure is indicated for handling large deflections and the calculation of the in-plane stresses that result.

For completeness, the lumped stringer and shear panel idealization is reviewed briefly, together with techniques for taking into account the practically important effects of Poisson's ratio coupling and coupling due to sweep.

To illustrate, a built-up structure is analyzed. It is a low aspect ratio model wing with sweep, for which non-uniform temperature test results have previously been published. (ref. 3) The analytical results are shown to compare reasonably well with those of the tests.

\* Structural Methods Group Leader

\*\* Structural Methods Engineer



The same lumped stringer and shear panel idealization also gives rather good agreement with theoretical solutions for simply supported flat plates. Some of these are included as well; one of them serves to illustrate the technique for handling large deflections.

## II INTRODUCTION

The primary problem considered in this paper is already well known. Briefly restated it is this: a thin built-up wing or control surface is subjected to uneven aerodynamic heating, and as a result thermal stresses are induced. These stresses alter the static response of the structure to lateral applied loads, their effect being analogous to that of axial stress on the lateral deflection of a beam column. The problem is to determine the stress distribution in the structure and its flexibility influence coefficients, taking this effect into account.

There are a number of excellent references available which propose systematic calculation procedures for handling this problem. One which is especially good, by Basin, MacNeal and Shields (ref. 4), is a direct analog method which is applicable in the small deflection range. Because of the nature of the direct analog computer, these authors employ an iterative type of solution. Several other references are reviewed in 1960 AGARD meeting papers by Gallagher and Rattinger (ref. 5), and by Huston (ref. 6). With the exception of the previously mentioned direct analog method, all methods known to be available are apparently based either upon an idealized plate or a finite element displacement method approach. Outstanding among the latter is a sequence of papers by Turner and his co-workers at Boeing (ref. 7 - 9). They have been one of the pioneering groups in developing the matrix displacement method, and one cannot help but be greatly impressed by their accomplishments.

At the same time, it is felt that there are good reasons why the matrix force method will continue to find acceptance by a portion of the aerospace industry. Therefore, it is the intent of the present work to provide an extension to the matrix force method to account for the thermal stress effect on flexibility and to include provisions for solving the possibly accompanying problems of thermal buckling or large deflections, should either be of interest.

The plan of the paper is as follows. First, a very brief outline of the matrix force method as it has previously been reported in the literature is presented. Two examples are given: one, the laterally loaded, simply supported square plate, for which a theoretical solution is available (ref. 10); the other, a built-up test wing (ref. 3).

Next, the interaction problem in the small deflection range is discussed. The necessary matrix formulation is presented, and the influence of the interaction is illustrated by different loadings

applied to the structures already examined.

Finally, expressions are developed for the interaction problem in the large deflection range. In this case the square plate only is given as an example; the numerical solution is again compared with a theoretical solution (ref. 11).

### III REVIEW OF THE MATRIX FORCE METHOD

#### A. Formulation

The review given here of the basic formulation of the matrix force method will of necessity be very brief. It is suggested that the publications cited throughout be referred to by readers who are not already familiar with the basic theory.

There are three fundamental matrices required as input data in the matrix force method. In the notation used at Grumman (ref. 12), they are:

1.  $[\mathcal{V}_{im}]$ , the member loads in the statically determinate structure due to unit values of the applied loads.
2.  $[\mathcal{V}_{ir}]$ , the member loads in the statically determinate structure due to unit values of the redundants.
3.  $[\alpha_{ij}]$ , the flexibilities of the individual members making up the structure.

These matrices may be assembled by hand, or they may be obtained from computer sub-routines. More will be said about them later; for the present it is sufficient to point out that the entire remaining sequence of calculations leading to the stress distributions and flexibility influence coefficients for the redundant structure can be performed by the computer in a continuous series of operations. It might also be noted that the program is completely general with regard to the types of structures that can be handled, as long as they are linear.

When thermal strains are to be included, it is necessary to calculate a matrix of strain values in the statically determinate, stress-free structure corresponding to the member loads. With these and another matrix of quantities based upon the geometry of the members, the thermal stress analysis can be formulated in any one of several different ways (See, for example, ref. 1, 2). An approach requiring no additional programming has been developed as an extension to the formulas of ref. 12, and is as follows. A unit diagonal matrix with as many elements as there are member loads is adjoined to the  $\mathcal{V}_{im}$  matrix. The matrix of geometry dependent quantities is adjoined to the  $\alpha_{ij}$  matrix. This is designated  $[L_{ij}]$ ; considering the case of a bar with linearly varying load and strain, for example,

the  $L_{ij}$ 's would be  $l/3$  and  $l/6$ , where  $l$  is the bar length (ref. 2). The expanded matrices now become:

$$1a. \begin{bmatrix} \gamma_{im} & 0 \\ 0 & I \end{bmatrix}$$

$$2a. \begin{bmatrix} \gamma_{ir} \\ 0 \end{bmatrix}$$

$$3a. \begin{bmatrix} \alpha_{ij} & L_{ij} \\ L_{ij} & 0 \end{bmatrix}$$

With the input data arranged in this form, the same computer program that was previously developed for the analysis of "cold" structures can be used without change. The output will now consist of: 1. the same stress distributions for the redundant structure as before, but with an additional square matrix  $[\Gamma_{ij}]$  giving the thermal stress distributions for unit strains; (a typical term would be the  $i^{\text{th}}$  member load due to a unit strain at the  $j^{\text{th}}$  member load) and 2. the same flexibility influence coefficients for the redundant structure as before, but with an additional matrix  $[A_{mj}]$  giving the displacements at the applied loads due to the unit strains.

Solutions for various thermal conditions can be then obtained by a subsequent multiplication of the unit strain results by the matrix of thermal strains referred to previously. For a typical thermal condition, identified by subscript  $\theta$ , these are designated  $\epsilon_{j\theta}$  in the Grumman notation. In the case of the bar with linearly varying load and strain, for example, the  $\epsilon_{j\theta}$ 's would be the  $\alpha \Delta T$  values at the two ends of the bar, where  $\alpha$  is the coefficient of thermal expansion and  $\Delta T$  is the change in temperature. Thus, the column of member loads for the condition  $\theta$  may be designated as

$$\{q_{i\theta}\} = [\Gamma_{ij}] \{\epsilon_{j\theta}\},$$

and the deflections for the same condition will be

$$\{\delta_{m\theta}\} = [A_{mj}] \{\epsilon_{j\theta}\}.$$

Of course, if only one thermal condition is of interest,  $\{\epsilon_{j\theta}\}$  may be submitted initially in place of the unit diagonal

matrix  $[I]$ . In this event the unit solution step is eliminated, and  $\{q_{io}\}$  and  $\{\delta_{mo}\}$  result directly.

#### B. Lumped Stringer and Shear Panel Idealization

One of the standard methods for conducting redundant structure analyses of multi-spar, multi-rib wings is based upon an idealized structure consisting of capstrips carrying axial load only, interconnected by shear panels which can carry tangential edge loads only. Using this approach, one lumps the covers into equivalent capstrips over the spars and ribs; the contributions of the spars and ribs themselves are calculated in the usual way and added in. If appropriate, intermediate shear lag members are introduced as well. Because of the shear panel assumption, the axial loads in the capstrips vary linearly from one panel point to the next.

Based upon this idealization, the member loads in the statically determinate structure may be obtained in any convenient way. The method suggested by Argyris and Kelsey (ref. 2), and by Grzedzielski (ref. 13) is especially recommended; it has worked out very well in a number of applications at Grumman.

The member flexibilities for a swept wing with parallel spars and parallel ribs can be readily obtained from ref. 13. Refer to Fig. 1, which shows a single shear panel, together with two of its adjacent lumped stringers. For the case of uniform cross sectional areas, the necessary expressions are as follows:

$$\alpha_{11} = 2 \alpha_{12} = \alpha_{22} = b / (3 a_r E)$$

$$\alpha_{33} = 2 \alpha_{34} = \alpha_{44} = l / (3 a_s E)$$

$$\alpha_{55} = (1/Et) b l \cos \lambda (2 + 2\nu + 4 \tan^2 \lambda)$$

$$\alpha_{23} = -(1/Et) R_s R_r (\nu - \tan^2 \lambda) \cos \lambda$$

$$\alpha_{25} = (1/Et) R_r b \tan \lambda$$

$$\alpha_{35} = (1/Et) R_s l \tan \lambda$$

In these formulas  $A_s$  is the total lumped spar area in a section normal to the spar, while  $R_s = (\frac{1}{2}bt \cos \lambda) / A_s$ .  $A_r$  and  $R_r$  are similarly defined. The member flexibility  $\alpha_{23}$  introduces Poisson's ratio coupling in the cover material, while  $\alpha_{25}$  and  $\alpha_{35}$  allow for coupling due to sweep.

The preceding are the expressions which were used in the analysis of the swept wing to be given later. They do not include an allowance for the fact that in a stiffened plate, the spar caps and rib caps are working at different stresses than the plate in the corresponding directions. (This is, of course, because there is a Poisson's ratio effect in the plate but not in the caps.) An allowance can be made for this effect, but it is not considered to be sufficiently significant to warrant the necessary discussion at this time.

Referring again to Fig. 1, the geometrical quantities required in the thermal stress analysis are as follows:

$$L_{11} = 2L_{12} = L_{22} = b/3$$

$$L_{33} = 2L_{34} = L_{44} = l/3$$

$$L_{55} = 2b l \sin \lambda$$

The thermal strains  $\epsilon_{T0}$  are the  $\alpha \Delta T$  values associated with the corresponding member loads; in the case of the parallelogram shear panel the average of the four corner values is used.

Techniques can also be developed for taking into account tapering section properties and irregular orientation of internal structure, i.e., quadrilateral shear panels. Space does not permit a discussion of this.

#### C. Square Plate Example

The lumped stringer and shear panel idealization works reasonably well even in the rather extreme case of a solid plate. To illustrate this, a square, simply supported plate with side  $a$  and depth  $h$ , subjected to uniform lateral load, is analyzed. It is simulated by a 2 x 2 grid, shown schematically in Fig. 2, and also by a 4 x 4 and a 6 x 6 grid.

In determining the equivalent capstrip areas, the familiar technique of maintaining identical bending flexibility is observed. The cover shear panels are determined in a similar manner; thus the equivalent thickness is taken as  $h/6$ . The vertical shear webs are assumed to be infinitely stiff; this is in agreement with plate theory assumptions.

The applied loads used to simulate the uniformly distributed loading are concentrated forces acting at the interior grid points. In order to hold down the complexity of the calculations, only unit loads exhibiting double symmetry are considered. Thus it becomes necessary to analyze only one eighth of the plate, giving it of course the proper boundary conditions. The numbering system for designating the applied loads is given in Fig. 3.

Bending moment and deflection distributions along the symmetry axes are presented for the uniform load exact solution (ref. 10) in Fig. 3, together with the semi-monocoque solution results. As can be seen, the central deflection shows a rather extreme variation, the difference ranging from 40% for the 2 x 2 to 4% for the 6 x 6. The 40% value is primarily the result of the excessively crude representation of the distributed load by a single central force. On the other hand, the central bending moment for the 2 x 2 is artificially close to the exact value. As the number of grid points increases, the representation of the distributed load by concentrated loads should improve, and both central deflection and central moment agreement reflect this.

The central deflection due to a unit central load agrees somewhat better with the exact result, as shown by the following table:

	2 x 2	4 x 4	6 x 6	Exact Sol'n Ref. 10
$\frac{W_{max} E h^3}{P a^2}$	.1073	.1221	.1246	.1265

#### D. Test Wing Example - Uniform Temperature Test

A built-up, low aspect ratio wing with sweep has been tested by the Bell Aerosystems Company (ref. 3). Fabricated of A286 stainless steel sheet, its details are summarized in Fig. 4.

For analysis purposes, the wing has been idealized by lumping the cover material into equivalent stringers over the spars and ribs; to these are added the contributions of the spars and ribs themselves. The spar and rib webs are idealized as flexible shear panels of the gauges shown, and extending from the midplane of the upper to the lower cover; no allowance has been made for fastener flexibility. Young's modulus is taken as  $29.9 \times 10^6$  psi. Represented in this way, the structure is redundant 28 times for symmetrical loads. A total of 25 applied loads is considered, one at every intersection point of spar and rib. Only the outboard 15 are numbered in Fig. 4, however.

Fig. 5 shows the analysis prediction for the normal stress in the covers due to a 1000 lb. load at the rear beam tip. All

stresses shown are in the direction normal to the airplane  $\zeta$ , with the exception of the front and rear spar stresses, which are in the spanwise direction. The model demonstrates the characteristic peaking of stress expected at the reentrant corner; see for example, ref. 14. The reversal of sign in the front beam region at the  $\zeta$  is a consequence of the three point tie down system. No test stresses are reported in ref. 3.

Fig. 6 shows a comparison of measured and calculated lateral displacements of the wing for the same applied load. As can be seen, the agreement is reasonably good, with the analysis values on the average about 6.7% less than test at the tip rib.

It is believed that the degree of simplification in the idealized structure as just described might well be adequate in the early design stages of some structures. Later on, as the design becomes firmer, such refinements as additional shear lag members, especially in the root region, would undoubtedly be added.

#### E. Test Wing Example - Temperature Gradient Test

A steady state temperature gradient was induced in the test wing by means of external heating lamps, in combination with cooling tubes running through each of the three interior spar webs. The temperature distribution is symmetrical about the mean chord plane, and peaks sharply at the leading edge; this is shown in Fig. 7. This distribution does not vary by much in the spanwise direction, and is assumed to be uniform.

The temperature level assumed for each of the lumped spars is shown by the stepped curve of Fig. 7. In the case of the interior spars, allowance is made for the depressed temperature of the spar webs. Rib cap temperatures are assumed to vary linearly from one spar value to the next, while each shear panel value is taken as the average of the two adjacent spars.

Based upon the data of ref. 3, the modulus of elasticity for the model during the gradient test varies from  $25.1 \times 10^6$  psi at the leading edge to  $28.1 \times 10^6$  psi at the trailing edge. At the same time, the coefficient of expansion varies correspondingly from  $9.43 \times 10^{-6}$  to  $8.67 \times 10^{-6}$  in./in./°F. For the present purposes it is considered sufficiently accurate to choose constant values for these two material properties; accordingly,  $27.9 \times 10^6$  and  $8.73 \times 10^{-6}$  were used.

The resulting thermal stresses are shown in Fig. 8. As in the case of Fig. 5, stresses in the covers are all normal to the airplane  $\zeta$ , while the rear spar stresses are shown for the spanwise direction. Test values at a few points are listed in ref. 3. They are shown for comparison, and appear to indicate the same trends as the analysis. There is a rather wide difference at the reentrant

corner, however, for which no explanation is readily apparent.

#### IV INTERACTION PROBLEM - SMALL DEFLECTIONS

##### A. Theory

The problem of analyzing a wing under an arbitrary temperature distribution, neglecting the interaction effect, can be handled by considering the wing to be subjected to two component temperature distributions, symmetrical and anti-symmetrical about the mean chord plane respectively, which when superposed, add up to the given distribution. The wing is analyzed under each separately and then the resulting stresses are added algebraically. The two required analyses can be performed by procedures already discussed in Section III. The temperature distribution symmetrical about the mean plane will give rise to stresses symmetrical about the mean plane and displacements in the plane, while the anti-symmetrical temperature distribution will produce anti-symmetrical stresses and displacements normal to the plane. The latter add directly to the stresses and deflections caused by lateral applied loads.

An obvious assumption in the foregoing procedure, and a valid one in many cases, is that the two analyses can be treated independently. However, if the in-plane stresses are large enough, there can be noticeable interaction between the two thermal stress distributions themselves and between the in-plane stresses and the lateral displacements due to applied loads. In this case the flexibility influence coefficient matrix for the structure may be appreciably altered.

In the development of the method for accounting for this effect it is assumed that the deflections are small in the sense that no additional membrane type stresses are developed due to deflections, that the structure is symmetrical about a mean chord plane, and that it has been idealized as a bar-shear panel system. The two idealized structures used in the symmetrical and anti-symmetrical analyses for a given case will be geometrically identical. Element flexibilities however may be different, inasmuch as the stresses in one case depend upon the bending and torsional flexibility and in the other upon the in-plane flexibility. With the "cold" structure flexibility influence coefficient matrix and the symmetrical and anti-symmetrical thermal stress distributions already calculated by the methods reviewed in section III, the two analyses can be coupled by the procedure to follow.

In the development of the coupling formulas it is convenient to consider first the symmetrical thermal stress distribution; in this case the loads in pairs of upper and lower capstrips and shear panels are identical. This load distribution is self equilibrating only as long as the structure remains undeflected laterally. When the spars and ribs bend and the shear panels become warped,



resultant forces normal to the plane are induced. To illustrate, consider the segment of spar or rib shown schematically in Fig. 9. As shown, the average slope between panel points is taken as the element slope. To calculate the magnitude of the lateral force, which will be called a kick load and denoted by  $Z$ , consider vertical components of forces at the panel point. Summation of these forces gives

$$Z = 2q_1 \left[ \frac{(\delta_0 - \delta_1)}{l_1} - \frac{(\delta_1 - \delta_2)}{l_2} \right] , \quad (1)$$

where  $2q_1$  is the total load in the upper and lower capstrips;  $\delta_0$ ,  $\delta_1$ , and  $\delta_2$  are the deflections at three consecutive panel points, and  $l_1$  and  $l_2$  are the distances between them.

Fig. 10 shows a pair of deflected quadrilateral shear panels, together with their projection on the undeflected mean chord plane. The mean positions of the four corners are identified by the four panel point deflections  $\delta_A$ ,  $\delta_B$ ,  $\delta_C$ , and  $\delta_D$ . The in-plane shear flows  $k_{AB}q_1$ , etc. have a lateral resultant which is called  $Z'$  and can be calculated by again summing forces vertically. Thus,

$$Z' = 2q_1 \left[ (k_{AB} + k_{AD})\delta_A - (k_{AB} + k_{BC})\delta_B + (k_{BC} + k_{CD})\delta_C - (k_{AD} + k_{CD})\delta_D \right] . \quad (2)$$

In the case of the shear panels, the force in eqn. (2), which is assumed to act at the intersection of the diagonals, is replaced by a statically equivalent set of forces at the four corners of the panel.

In the formulas to follow, the matrix notation of ref. 12, which is reviewed in part in section III, will be extended and used. The kick loads will be written in column matrix arrangement and designated  $\{P'_m\}$ . They are dependent upon the deflections, which in column order are called  $\{\delta_n\}$ , and the in-plane member loads which, for convenience, are written in diagonal matrix form. The latter are designated  $[q_{10}]$ . The formula from which the kick loads are obtained is then

$$\{P'_m\} = [F_{mn}] \{\delta_n\} , \quad (3)$$

where

$$[F_{mn}] = [B_{mi}] [q_{io}] [C_{in}] \quad (4)$$

The  $[B_{mi}]$  and  $[C_{in}]$  matrices are made up of geometry dependent constants derived from eqns. (1) and (2). They can be obtained in a systematic, routine way; space limitations do not permit a detailed discussion.

Recalling that the deflections due to lateral loads and anti-symmetrical thermal strains are

$$[A_{mn}] \{P_n\} + \{\delta_{no}\} ,$$

the total deflections may be written

$$\{\delta_n\} = [A_{mn}] \{P_n\} + \{\delta_{no}\} + [A_{mn}] [F_{mn}] \{\delta_n\} \quad (5)$$

Solving for  $\{\delta_n\}$  ,

$$\{\delta_n\} = [D_{mn}]^{-1} [A_{mn}] \{P_n\} + [D_{mn}]^{-1} \{\delta_{no}\} \quad (6)$$

where

$$[D_{mn}] = [I] - [A_{mn}] [F_{mn}] .$$

It is seen that  $[D_{mn}]^{-1} [A_{mn}]$  is the required matrix of flexibility influence coefficients. Multiplication of  $[A_{mn}]$  by  $[D_{mn}]^{-1}$  introduces the change in flexibility due to in-plane thermal stresses, while multiplication of  $\{\delta_{no}\}$  by  $[D_{mn}]^{-1}$  takes care of the interaction between the symmetrical thermal stresses and the thermal displacements discussed previously.

With the  $\{\delta_n\}$  known, it is now possible to substitute in

eqn. (3) to determine the kick loads  $\{P'_m\}$ . With these known, the complete stress distribution in the structure can be obtained in a straight forward manner.

### B. Thermal Buckling

It is well known that the increased flexibility of structures for lateral load is related to the proximity of the in-plane load to buckling. The same matrices used to calculate the heated structure flexibilities can be used to determine the factor by which a given in-plane loading distribution must be increased to cause buckling.

If the structure is subjected to in-plane loads only, then according to eqn. (5),

$$\{\delta_n\} = [A_{nn}] [F_{nn}] \{\delta_n\} \quad (7)$$

Examination of eqn. (7) indicates that equilibrium configurations other than the undeflected case may be possible. If they are, then the deflections  $\delta_n$  and the loads  $q_{io}$  entering  $[F_{nn}]$  must satisfy eqn. (7) and can be determined from it. Assuming that the in-plane loads increase proportionally, then a given load distribution becomes at buckling  $\bar{q} [q_{io}]$ .  $\bar{q}$  is the factor which, when multiplied by each of the in-plane loads gives the load distribution causing buckling. Eqn. (7) can now be written as

$$\frac{1}{\bar{q}} \{\delta_n\} = [A_{nn}] [F_{nn}] \{\delta_n\} \quad (8)$$

which is recognized as an eigenvalue equation. The lowest value  $\bar{q}$  satisfying this equation defines the in-plane loading condition for buckling. The corresponding eigenvector  $\{\delta_n\}$  gives the buckled shape.

### C. Square Plate Example - Increased Flexibility and Buckling

The case of increased flexibility of a simply supported square plate under combined lateral and edge loads is easily solved using the theory just given. If it is assumed that the edge loading is uniform in the two directions, the in-plane stress distribution is of course known. It is then a simple matter to combine it with the results already obtained for a laterally loaded square plate by means of eqn. (6).

The results of the calculation are plotted in Fig. 11 for several values of the edge load, using the 2 x 2, the 4 x 4 and the

6 x 6 grid idealization. A theoretical plot from ref. 10, page 390, is shown for comparison; the curve was evaluated letting  $m, n = 1, 3, 5$ . As can be seen, predictions for all three grid idealizations tend to deteriorate somewhat with increasing edge load, although the 6 x 6 is still reasonably good up to 75% of the critical edge load.

The buckling loads for the three idealizations were also obtained by use of eqn. (8). They are listed in the following table, together with the theoretical value.

	2 x 2	4 x 4	6 x 6	Exact Sol'n Ref. 10
$\frac{\sigma_{cr} a^2}{E h^3}$	2.330	1.898	1.846	1.808

#### D. Heated Test Wing Example - Increased Flexibility and Buckling

It will be recalled that the two test wing analyses of section III are uncoupled. In the first, the model was assumed to be at room temperature, and lateral loads only were applied. The analysis yielded stress distributions and flexibility influence coefficients for this condition. In the other, the wing was assumed to be subjected to a fairly severe temperature variation in the chordwise direction, which was symmetrical about the mean chord plane. The analysis in this case gave the corresponding thermal stresses.

The results of coupling the two analyses to account for the thermal stress effect on flexibility are shown in Table I. Three sets of numbers are given. First, the value determined from test as reported in ref. 3 is shown; below this is the calculated value determined from a coupling analysis carried out as outlined in this section. Finally the fractional change in the flexibility influence coefficient caused by the in-plane thermal stress effect is given. This value was determined by dividing the coupled analysis result by the room temperature analysis result altered to account for material property deterioration only.

Ref. 3 introduces the concept of a "deflection parameter" for evaluating the influence of various elevated temperature effects. In the case of the swept wing model, these authors apply 100 lb. loads at panel points 1 through 10, and calculate the deflections at all 25 points. (Deflections at the two support points are zero.) The sum of the 25 deflections is the deflection parameter. A comparison of the present analysis with the test on this basis is given in the following table:

	Deflection Parameter at Room Temperature	Temperature Gradient Condition - % Increase of Parameter over Room Temperature Value	Increase of Parameter due to Reduced $E_{av}$ , %	Increase of Parameter due to Thermal Stress, %
Test	2.111	15.58	7.36	8.22
Analysis	2.044	11.18	6.68*	4.50

\* Different from 7.36 only because in the present report, the average value for  $E$  was assumed to be  $27.9 \times 10^6$  rather than  $27.7 \times 10^6$ .

The thermal buckling case has also been investigated, and the calculated buckled shape for the test wing is plotted in Fig. 12. Eqn. (8) gives 11.81 for the buckling parameter  $\bar{q}$ .

As a point of interest, the latter can be used to obtain an order of magnitude estimate for the maximum increase in lateral displacements to be expected due to the thermal stresses of Fig. 8. The theory of structures indicates that when the loading on a structure consists of components tending to cause instability, as well as the type producing linear displacements only, the resultant displacement of any point can still be represented by a superposition of suitably selected component displacements. However, each component must now be multiplied by a factor of the type  $1/(1 - \alpha_n)$ , where  $\alpha_n$  is the ratio of the actual destabilizing loading to the buckling value in the  $n^{\text{th}}$  mode. (The analysis leading to the curve of Fig. 11 is an example of this.)

In many cases, only the factor for the lowest buckling load is significantly different from unity. When this is the case, this factor should provide an order of magnitude estimate for the maximum magnification of deflections to be expected. (See ref. 15, 16)

In the present instance, the factor for the lowest mode is  $1/[1 - (11.81)^{-2}] = 1.092$ . Inspection of Table 1 indicates that all magnifications are actually less than 1.092, with a few values in the vicinity of load  $P_{11}$  approaching it.

#### V INTERACTION PROBLEM - LARGE DEFLECTIONS

##### A. Introduction

An implied assumption in linear wing analysis methods is

that the lateral deflections are small enough so that the attendant straining of the middle plane is negligible. It is quite possible that this assumption may not be valid for the case of a thin, low aspect ratio wing. On the contrary, as a consequence of large deflections, there may be a stiffening of the wing due to the development of in-plane membrane type stresses which help carry the load.

In this section a method is developed for including this effect. It permits the determination of the deflected shape for a given set of applied loads, together with the attendant stress distribution, and the flexibility of the structure for small displacements about the deflected shape. The latter is stated by means of a tangent flexibility matrix which, of course, is dependent upon the particular loading condition.

The procedure can be broadly divided into three steps which are repeated cyclically until a sufficiently accurate solution is obtained. The steps, each of which is discussed later in detail, are:

1. The calculation of the stress distribution in the middle plane consistent with an assumed or calculated approximate set of deflections
2. The calculation of the lateral loads sustained by the structure in this deflected configuration, and
3. The calculation of the tangent flexibility matrix and its use to obtain a better set of approximate deflections.

#### B. Membrane Stresses - Step 1

The membrane stresses for a given distribution of thermal strains and for a given lateral displacement configuration can be easily calculated using the basic matrix force method reviewed in section III. The procedure is to simply evaluate the in-plane strains due to large deflections, and to add these values to the in-plane thermal strains of the type discussed previously. The combined values are identified hereafter as  $\epsilon_{j0}$  and become the input data for the present problem. The output, namely the in-plane redundant load distribution, is correspondingly identified hereafter as  $q_{i0}$ .

As for the calculation of the large deflection strains, when the panels are rectangular, the usual finite difference plate approximation can be used without change. Referring to Fig. 9, the strain in the segment of stringer shown on the right is thus

$$-\frac{1}{2} \left( \frac{\delta_2 - \delta_1}{l_2} \right)^2$$

Referring to Figure 10, the shear strain in the panel shown (assuming

that it is rectangular) is

$$-\frac{(\delta_o - \delta_B)^2 - (\delta_c - \delta_A)^2}{4 l_{AB} l_{BC}}.$$

In the case of parallelogram shear panels, and the more general quadrilateral shapes, other analogous expressions of comparable accuracy can be formulated.

Later on, for the calculation of the tangent flexibility matrix (step 3) it will be required to know the increments in the in-plane loads  $q_{io}$  corresponding to increments in the various lateral deflections. It is convenient to calculate the associated rates here in step 1. Designating these quantities in matrix form as  $[\partial q_{io} / \partial \delta_n]$ , and recalling from section III that the unit strain analysis yields the matrix  $[\Gamma_{ij}]$ , the formula for step 1 can be written

$$\left[ q_{io} \middle| \frac{\partial q_{io}}{\partial \delta_n} \right] = \left[ \Gamma_{ij} \right] \left[ \epsilon_{jo} \middle| \frac{\partial \epsilon_{jo}}{\partial \delta_n} \right].$$

Since the  $\epsilon_{jo}$ 's are simple quadratic functions in the deflections, calculation of their derivatives with respect to the deflections is straight forward.

#### C. Lateral Loads - Step 2

It will be recalled that eqn (5), which gives a relationship between lateral deflections and lateral loads, was derived to include the effect of in-plane stresses. The same equation clearly applies in the present situation without change. Solving it for the applied loads,

$$\{P_m\} = [K_{mn}^o] \{\delta_n\} - [K_{mn}^o] \{\delta_o\} - [F_{mn}] \{\delta_n\} \quad (9)$$

The superscript  $o$  is henceforth appended to  $[A_{mn}]$  to indicate that it has been calculated based upon the assumption of small deflections; then  $[K_{mn}^o]$  is obtained simply from

$$[K_{mn}^o] = [A_{mn}^o]^{-1}$$

## D. Tangent Flexibility Matrix - Step 3

It is convenient to calculate the tangent flexibility matrix corresponding to a given set of deflections by first calculating its inverse, the tangent stiffness matrix. Differentiation of eqn. (9) with respect to a particular deflection, say  $\delta_t$ , and bearing in mind that  $[F_{mn}]$  is now dependent upon all of the deflections  $\delta_n$ , gives the  $t^{\text{th}}$  column of the required matrix; thus

$$\left\{ \frac{\partial P_m}{\partial \delta_t} \right\} = \left\{ K_{mt}^0 \right\} - \left\{ F_{mt} \right\} - \left[ \frac{\partial F_{mn}}{\partial \delta_t} \right] \left\{ \delta_n \right\} \quad (10)$$

With  $[K_{mn}^0]$ ,  $[F_{mn}]$  and  $\{\delta_n\}$  already determined, there remains only the job of calculating  $[\partial F_{mn}/\partial \delta_t]$ . This is obtained from eqn. (4); thus

$$\left[ \frac{\partial F_{mn}}{\partial \delta_t} \right] = [B_{mi}] \left[ \frac{\partial q_{io}}{\partial \delta_t} \right] [C_{in}]$$

The  $[\partial q_{io}/\partial \delta_t]$  have already been calculated in step 1. Substituting these values, and letting

$$\left[ \frac{\partial F_{mn}}{\partial \delta_t} \right] \left\{ \delta_n \right\} = \left\{ \Delta F_{mt} \right\},$$

the resulting tangent stiffness matrix may be written

$$\left[ \frac{\partial P_m}{\partial \delta_n} \right] = [K_{mn}] = [K_{mn}^0] - [F_{mn}] - [\Delta F_{mn}] \quad (11)$$

The tangent flexibility matrix  $[A_{mn}]$  is simply  $[K_{mn}]^{-1}$ .

## E. Iteration Procedure

The deflections assumed in step 1 and used throughout the cycle are the correct ones for the loads calculated in step 2, and the tangent flexibility matrix also corresponds to these loads. The problem however is usually to calculate these quantities for a given set of loads, so that a set of deflections must first be assumed and



those corresponding to the given loads obtained by successive iterations. To obtain an improved set of deflections, assume that with the structure in the deflected position for which everything is known, the loads are adjusted to the values for which the solution is sought, and that the structure deflects linearly from the known position under the correcting loads. Using the tangent flexibility matrix to describe the linear deflection from the known position, the equation for the improved deflections is

$$\{\delta_n^{(2)}\} = \{\delta_n^{(1)}\} + [A_{nn}^{(1)}] \left( \{P_n\} - \{P_n^{(1)}\} \right). \quad (12)$$

In eqn. (12) the superscript (2) refers to "improved," and (1) refers to the current equilibrium position. The applied loads for which a solution is sought are written without any superscript.

In a given problem, for the initial set of deflections one might well use the values given by the small deflection theory, eqn. (6).

#### F. Example - Square Plate

The method just described was applied to the structure discussed earlier, a simply supported square plate. It was assumed that there exists no resultant loading on the edges but that the latter are constrained to remain straight, making the problem identical to one for which a large deflection plate theory solution is given by S. Levy in ref. 11. The lateral loading (in non-dimensional form,  $qa^4/Eh^4$ ) was chosen as 75, large enough to produce an appreciable large deflection effect. The 4 x 4 grid representation of section III was used, along with some data from the small deflection analysis of section IV. Among these were the deflections, which were used as a first approximation. In Fig. 13 an attempt is made to present a summary of the analysis. The analysis results have been superimposed on a load-deflection graph from ref. 11. The arrows indicate the direction in which the calculation progressed. The numbered points represent calculated large deflection equilibrium positions. Their corresponding loading and deflection parameters are given in the table below, together with the ratios of the loads and deflections at the three grid points, which are given as fractions of  $P_1$  and  $w_1$  respectively. The theoretical results were obtained from a curve in ref. 11.

Equilibrium Configuration No.	$\frac{w_{\text{cr}}}{h}$ ( $w_1 : w_2 : w_3$ )	$\frac{q a^4}{E h^4}$ ( $P_1 : P_2 : P_3$ )
1	3.031 (1 : .717 : .514)	243 (1 : .431 : .101)
2	2.114 (1 : .723 : .529)	115 (1 : .481 : .303)
3	1.857 (1 : .729 : .536)	92.1 (1 : .587 : .485)
4	1.633 (1 : .739 : .548)	76.4 (1 : .862 : .878)
5	1.607 (1 : .741 : .551)	75.0 (1 : 1 : 1)
Exact Sol'n Ref. 11	1.63 ( ... )	75.0 (1 : 1 : 1)

As can be seen, good agreement with the Levy solution was obtained in the fifth iteration. The final rate of growth of the central deflection with loading parameter is of course given by the tangent flexibility matrix for equilibrium configuration 5. If it were plotted on Fig. 13, it would show as a straight line through point 5, and to the eye at least, parallel to the tangent to the curve at  $q a^4 / E h^4 = 75$ .

The corresponding calculated membrane stresses across the mid-section, again compared with the Levy solution, are shown in Fig. 14. For the maximum stress, which occurs at the edge, the calculated value was approximately 6.5% higher than the theoretical.

VI REFERENCES

1. Denke, P.H., "A Matrix Method of Structural Analysis," Proceedings of the Second U.S. National Congress of Applied Mechanics, June 1954.
2. Argyris, J.H., Kelsey, S., "The Matrix Force Method of Structural Analysis and Some New Applications," British A.R.C. Technical Report R & M No. 3034, 1957.
3. Gallagher, R.H., Quinn, J.F., Turrentine, D., "Thermal Effects on Static Aeroelastic Stability and Control, Part III - Experimental and Analytical Methods for the Determination of Thermally - Affected Wing Deflectional Behavior," WADC TR 58-378, December, 1959.
4. Basin, M.A., MacNeal R.H., Shields, J.H., "Direct Analog Method of Analysis of the Influence of Aerodynamic Heating on the Static Characteristics of Thin Wings," Journal of the Aero/Space Sciences, March, 1959.
5. Gallagher, R.H., Rattinger, I., "The Experimental and Theoretical Determination of The Elastic Characteristics of Modern Airframes," AGARD, NATO, September, 1960.
6. Huston, W.B., "Surface Warp and Aerodynamic Heating," AGARD, NATO, September, 1960.
7. Turner, M.J., Clough, R.J., Martin, H.C., Topp, L.J., "Stiffness and Deflection Analysis of Complex Structures," Journal of the Aeronautical Sciences, September, 1956.
8. Turner, J.M., Dill, E.M., Martin, H.C., Melosh, R.J., "Large Deflections of Structures Subjected to Heating and External Loads," Journal of the Aero/Space Sciences, February, 1960.
9. Melosh, R. and Merritt, R., "Prediction of Flexibility and Natural Modes of Low Aspect Ratio Wings Using Stiffness Matrices," Aero/Space Engineering, July, 1960.
10. Timoshenko, S.P., Woinowsky-Krieger, S., "Theory of Plates and Shells," Second Edition, McGraw Hill.
11. Levy, S., "Bending of Rectangular Plates with Large Deflections," NACA Report No. 737, 1942.
12. Wehle, L.B. Jr., Lansing, W., "A Method for Reducing the Analysis of Complex Redundant Structures to a Routine Procedure," Journal of the Aeronautical Sciences, October, 1952.

13. Grzedzielski, A.L.M., "Organization of a Large Computation in Aircraft Stress Analysis," National Research Council of Canada - Aeronautical Report - LR-257, July, 1959.
14. Zender, G.W., "Comparison of Theoretical Stresses and Deflections of Multicell Wings with Experimental Results Obtained from Plastic Models," NACA TN 3813, November, 1956.
15. Vosteen, L.F., Fuller, K.E., "Behavior of a Cantilever Plate Under Rapid - Heating Conditions," NACA RM L55E20c, July, 1955.
16. Heldenfels, R.R., Vosteen, L.F., "Approximate Analysis of Effects of Large Deflections and Initial Twist on Torsional Stiffness of a Cantilever Plate Subjected to Thermal Stresses," NACA TN 4067, August, 1957.

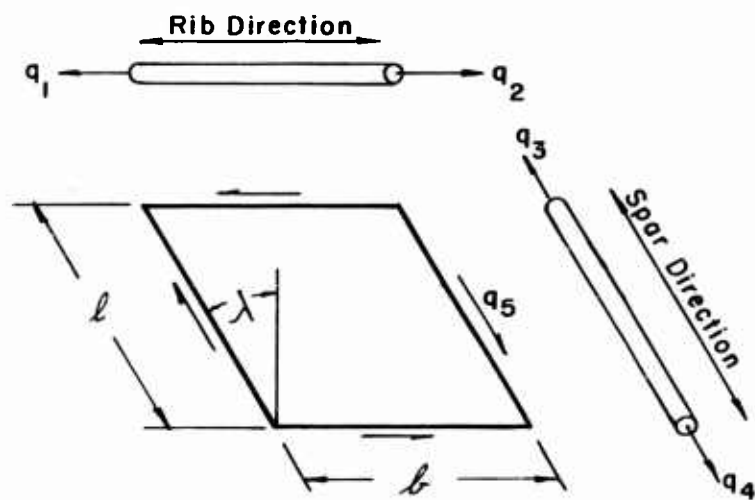


FIGURE 1.

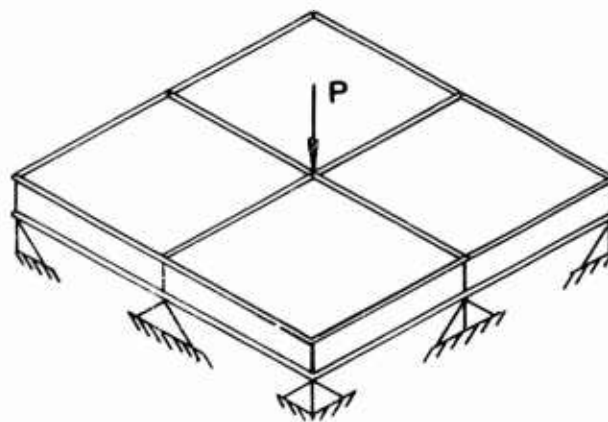


FIGURE 2.

# BENDING MOMENT AND DEFLECTION AT MIDSECTION OF PLATE UNDER UNIFORM LOADING.

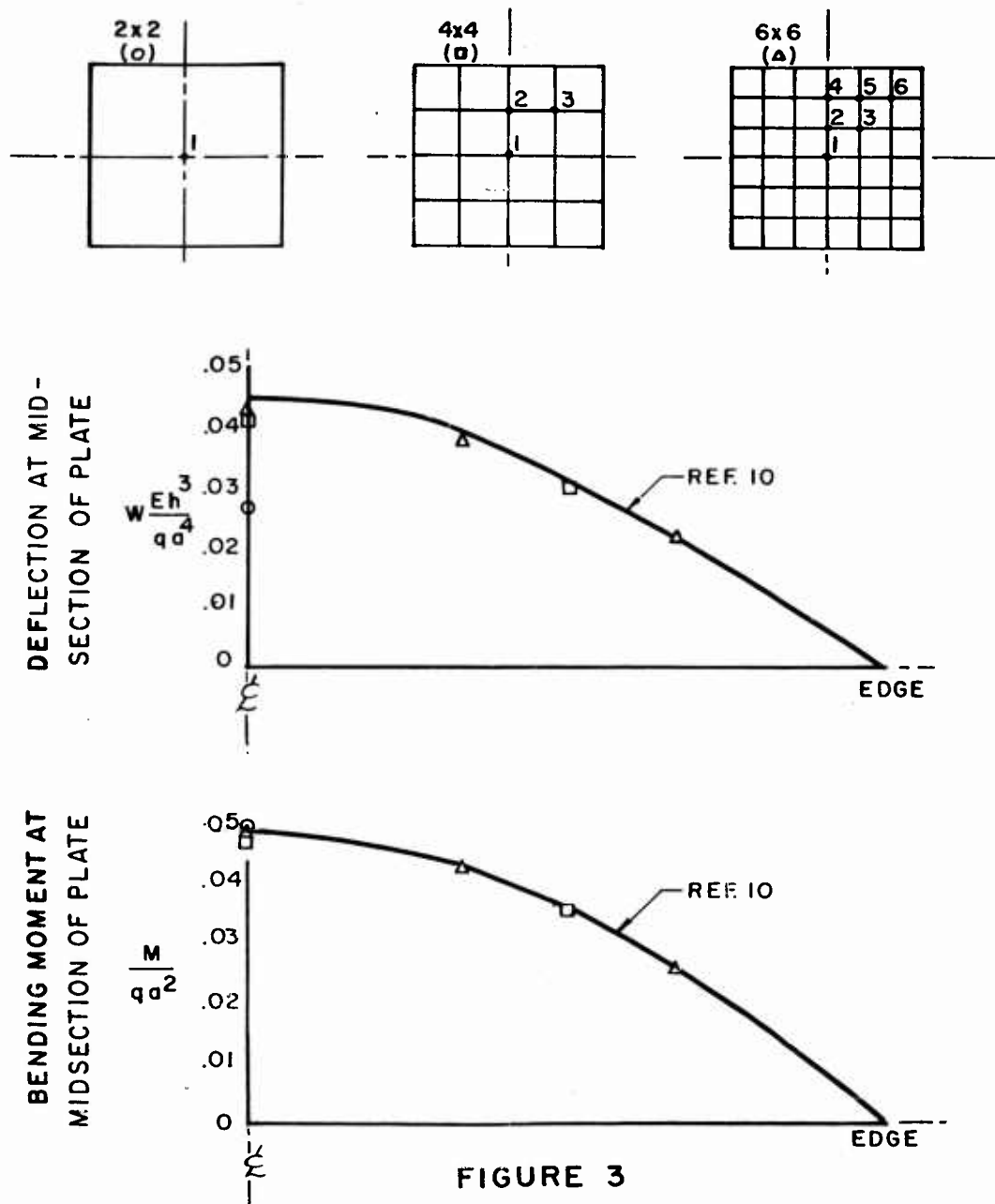
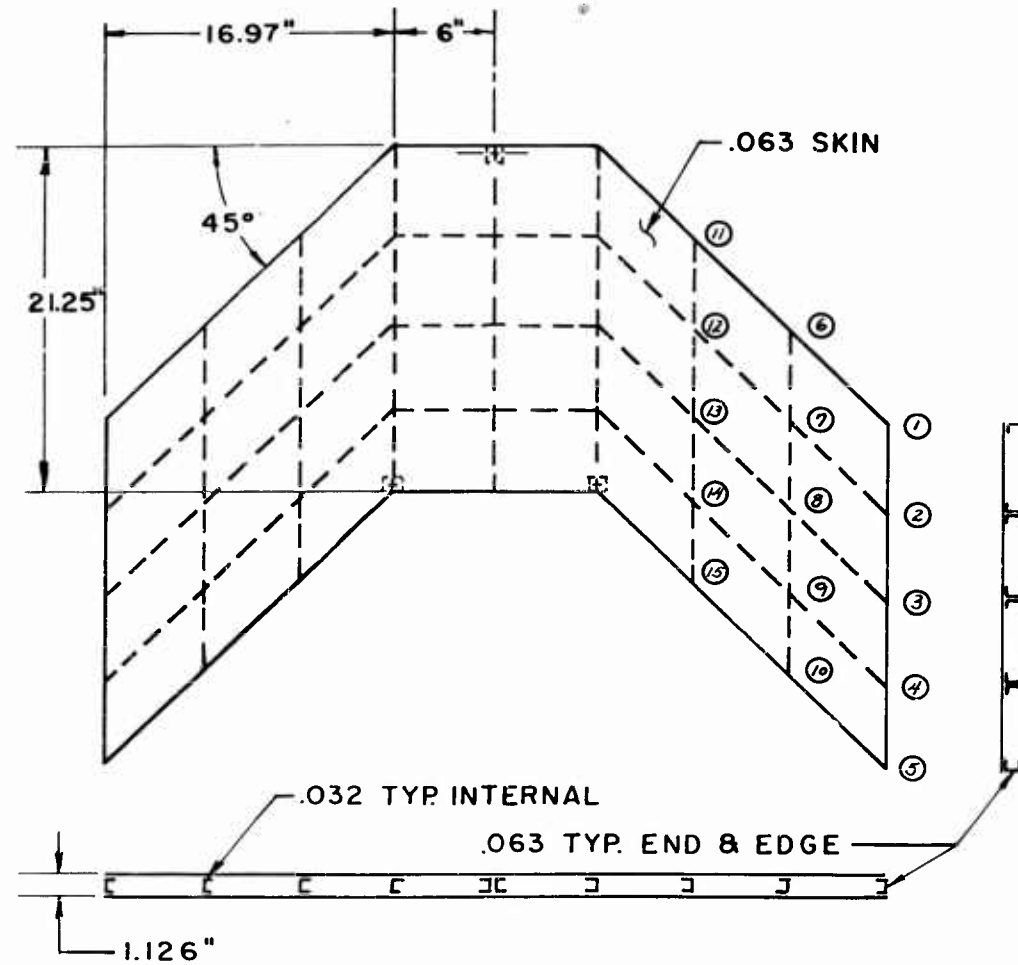


FIGURE 3



TEST WING

FIGURE 4

NORMAL STRESS DISTRIBUTION, TEST WING  
LATERAL LOAD  $P_5 = 1000^\#$

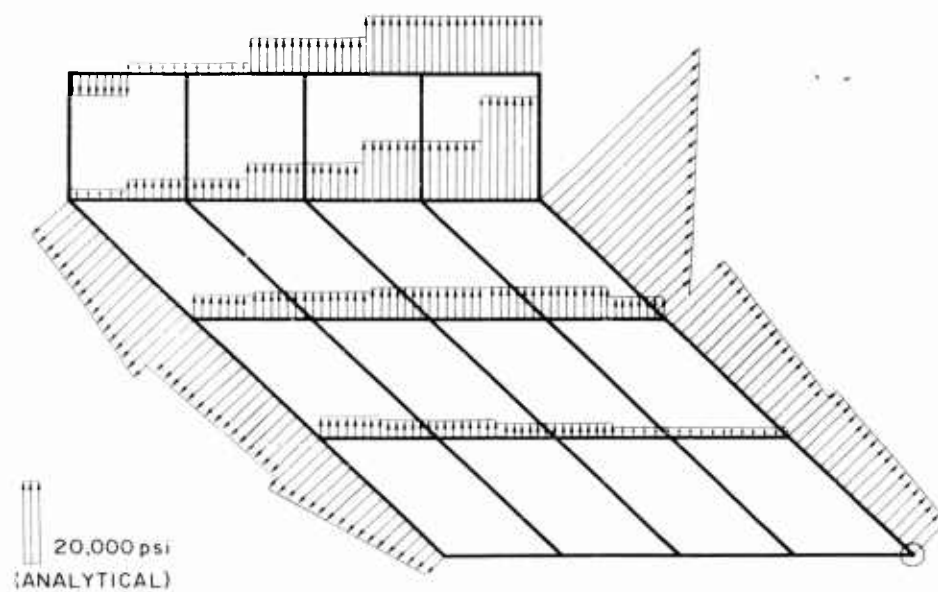


FIGURE 5



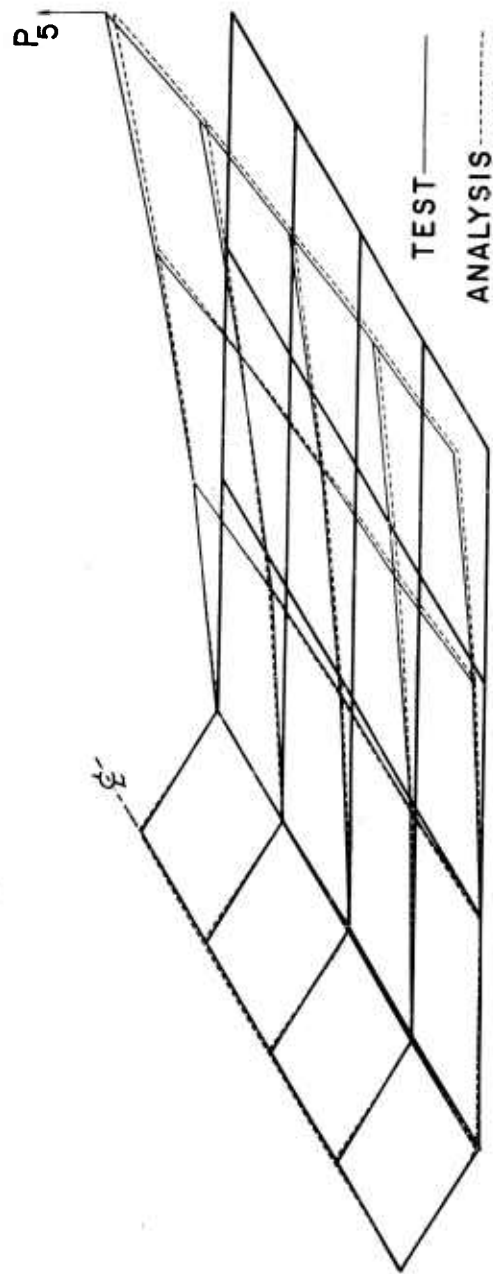


FIGURE 6. DEFLECTED SHAPE - UNHEATED TEST WING

CHORDWISE TEMPERATURE PROFILE-TEST WING

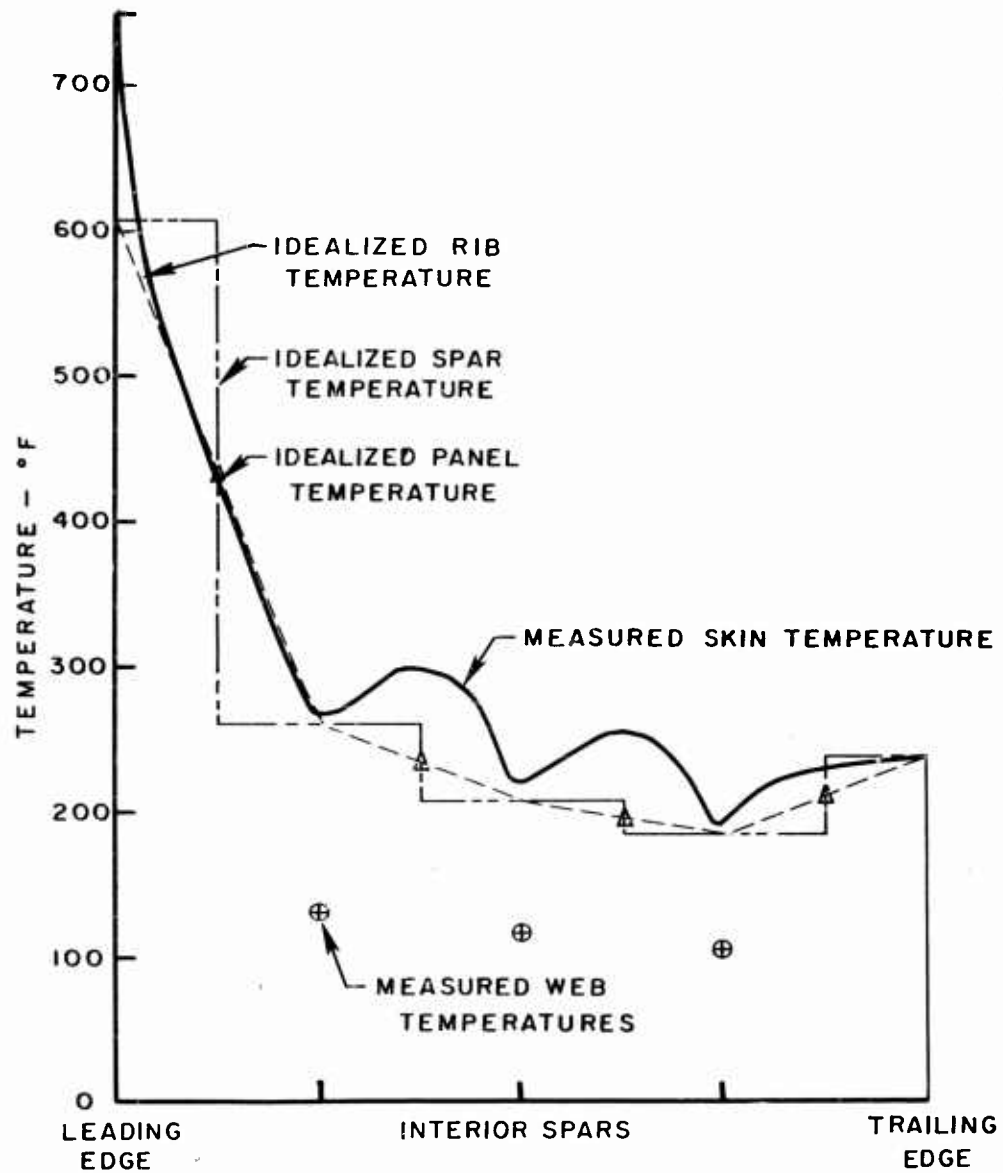


FIGURE 7.

NORMAL STRESS DISTRIBUTION  
TEST WING THERMAL LOADING

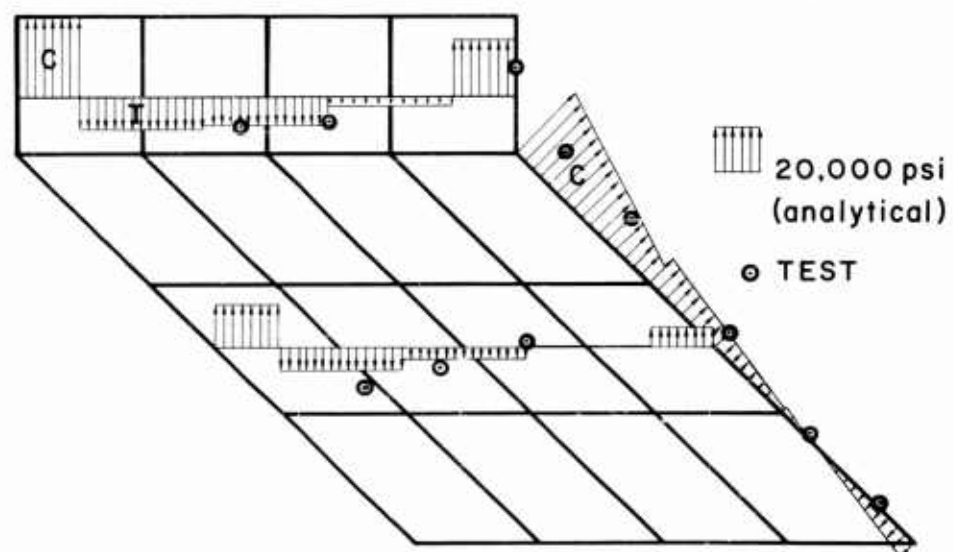


FIGURE 8

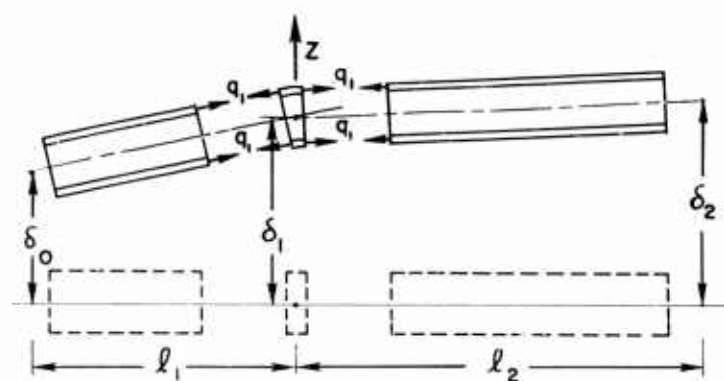


FIGURE 9

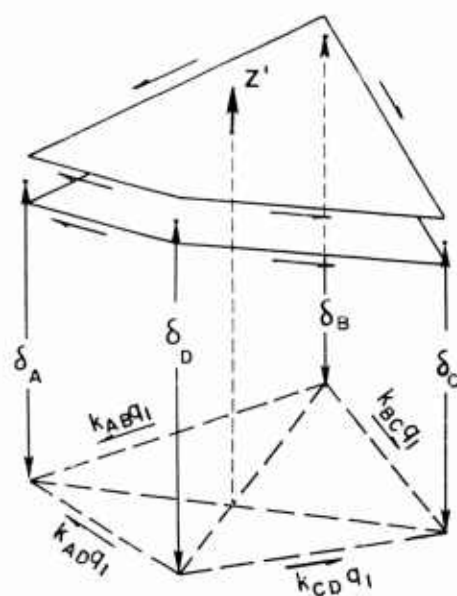


FIGURE 10

# CENTRAL DEFLECTION OF SQUARE PLATE UNDER COMBINED LATERAL & EDGE LOADS (SMALL DEFLECTIONS)

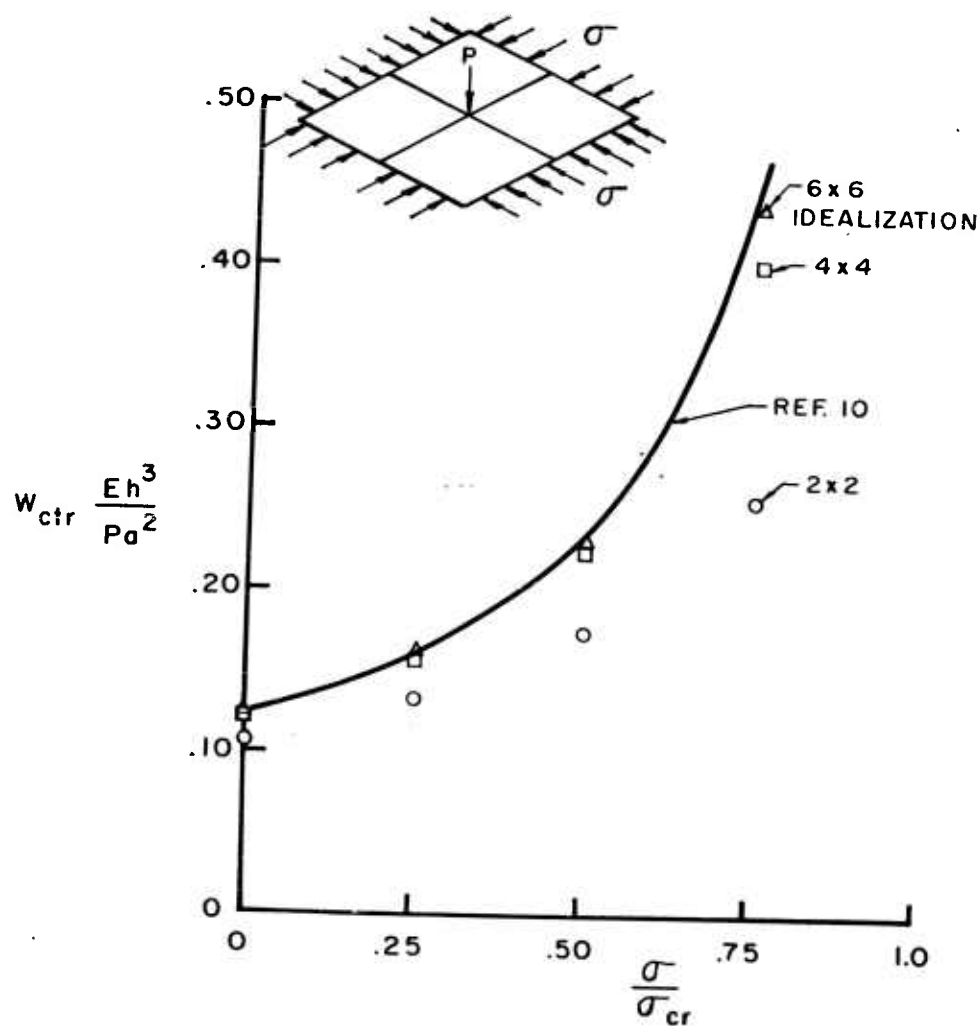


FIGURE II

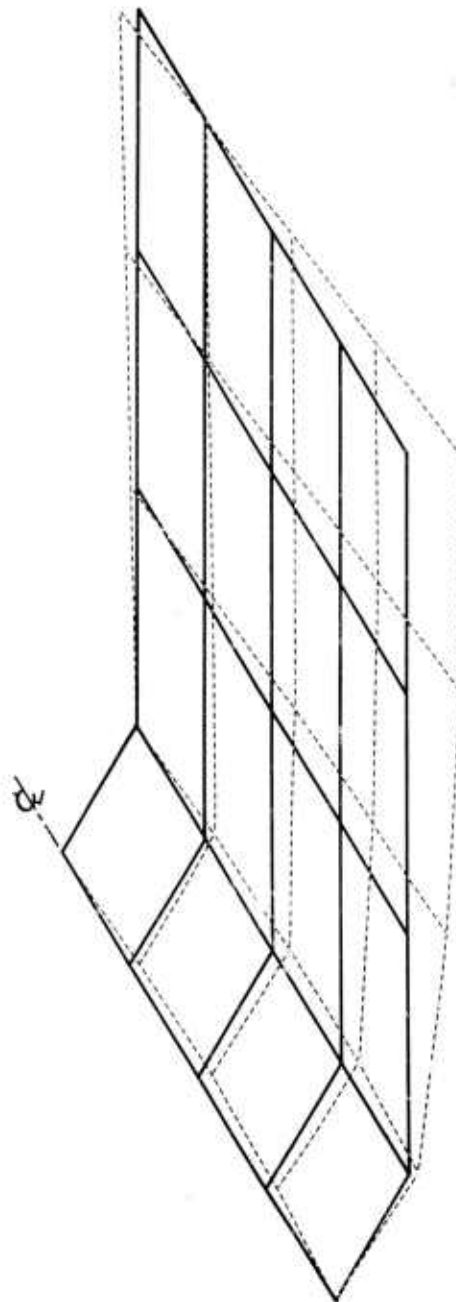


FIGURE 12 DEFLECTED SHAPE THERMALLY BUCKLED  
TEST WING

CENTRAL DEFLECTION OF SQUARE PLATE  
(LARGE DEFLECTIONS)

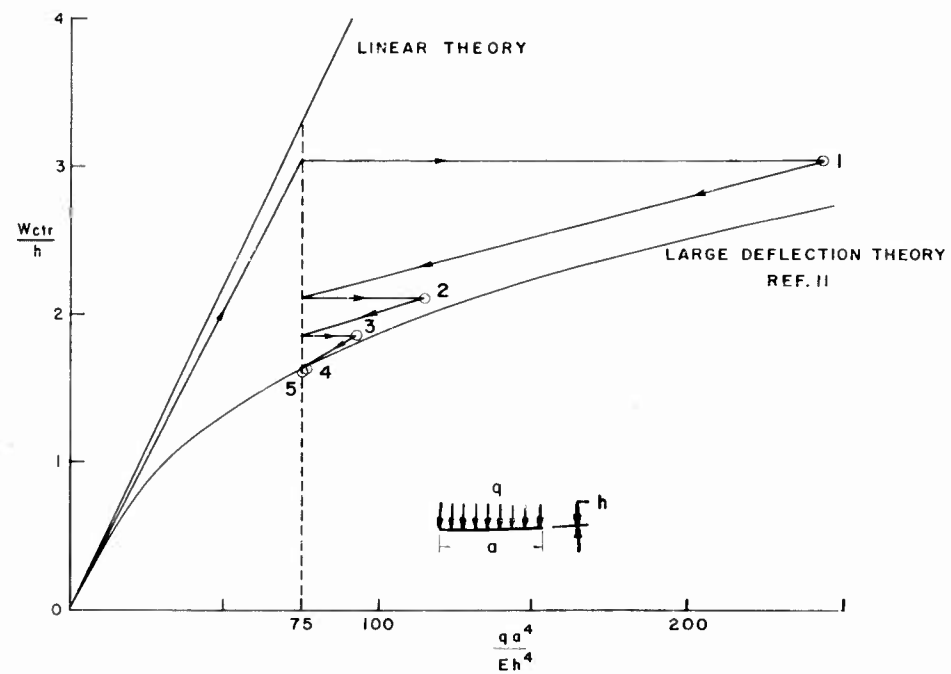


FIGURE 13

# MEMBRANE STRESS AT MIDSECTION OF PLATE

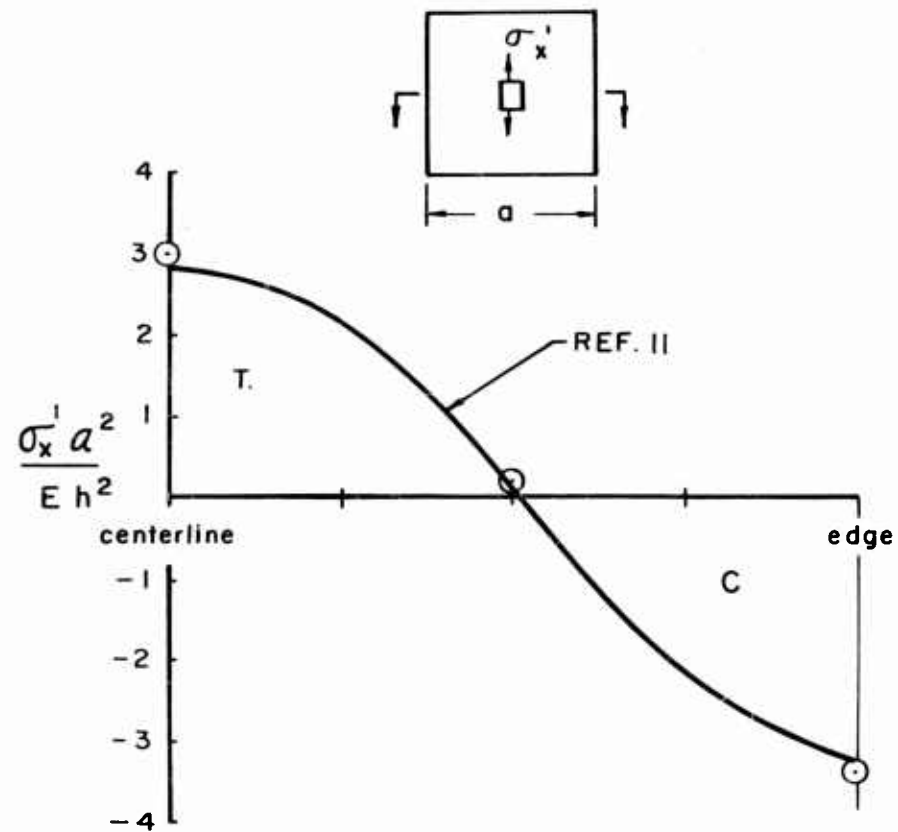


FIGURE 14



## LOAD APPLICATION POINTS

	1	2	3	4	5	6	7	8	9	10	11	12	13	14	15
DEFLECTION LOCATION POINTS	1	.2659 .2658 1.049	TEST ANALYSIS *												
	2	.2408 .2468 1.044	.2850 .2670 1.039												
	3	.2260 .2249 1.035	.2863 .2719 1.034	.3546 .3206 1.032											
	4	.2179 .2032 1.024	.2895 .2742 1.028	.3947 .3576 1.030	.5096 .4505 1.030										
	5	.2127 .1809 1.010	.3096 .2764 1.023	.4290 .3939 1.028	.5811 .5377 1.030	.7583 .7068 1.031									
	6	.1605 .1632 1.062	.1367 .1379 1.053	.1146 .1124 1.039	.0985 .0870 1.016	.0840 .0613 0.979	.1584 .1334 1.070								
	7	.1656 .1616 1.057	.1681 .1554 1.051	.1601 .1448 1.045	.1569 .1334 1.037	.1554 .1221 1.030	.1166 .1098 1.064	.1386 .1135 1.056							
	8	.1455 .1495 1.046	.1696 .1651 1.044	.1914 .1776 1.041	.2026 .1867 1.039	.2170 .1960 1.037	.0835 .0859 1.053	.1082 .1015 1.051	.1383 .1171 1.044						
	9	.1322 .1320 1.030	.1751 .1693 1.033	.2201 .2096 1.034	.2639 .2502 1.035	.3011 .2900 1.036	.0637 .0616 1.027	.0968 .0890 1.041	.1262 .1204 1.040	.1751 .1585 1.037					
	10	.1318 .1126 1.009	.1937 .1728 1.023	.2677 .2435 1.030	.3552 .3236 1.033	.4430 .4089 1.034	.0509 .0370 0.971	.0961 .0774 1.027	.1383 .1269 1.036	.2040 .1907 1.036	.3213 .2723 1.036				
	11	.0695 .0745 1.073	.0494 .0559 1.061	.0313 .0373 1.039	.0193 .0187 0.979	— -.0001 —	.0811 .0722 1.081	.0554 .0537 1.074	.0307 .0351 1.057	.0147 .0167 1.012	— -.0018 —	.0866 .0619 1.080			
	12	.0829 .0824 1.089	.0711 .0690 1.083	.0573 .0546 1.088	.0463 .0399 1.087	.0350 .0253 1.086	.0773 .0697 1.086	.0706 .0603 1.083	.0470 .0458 1.080	.0322 .0305 1.082	.0216 .0156 1.076	.0561 .0465 1.081	.0704 .0498 1.069		
	13	.0713 .0783 1.080	.0725 .0750 1.081	.0704 .0698 1.082	.0671 .0639 1.083	.0619 .0581 1.086	.0526 .0565 1.080	.0585 .0567 1.076	.0587 .0532 1.073	.0457 .0457 1.075	.0395 .0388 1.081	.0290 .0309 1.080	.0373 .0365 1.074	.0533 .0398 1.061	
	14	.0565 .0645 1.052	.0676 .0745 1.052	.0780 .0841 1.053	.0888 .0931 1.053	.0968 .1024 1.056	.0310 .0366 1.052	.0421 .0459 1.058	.0521 .0551 1.054	.0634 .0638 1.053	.0735 .0712 1.053	.0109 .0144 1.059	.0181 .0212 1.076	.0263 .0282 1.068	.0642 .0372 1.051
	15	.0478 .0461 1.002	.0726 .0727 1.021	.1010 .1024 1.029	.1345 .1341 1.034	.1711 .1663 1.037	.0164 .0138 0.939	.0354 .0333 1.018	.0545 .0572 1.034	.0861 .0864 1.037	.1301 .1190 1.039	— -.0031 1.476	.0059 .0057 1.056	.0155 .0181 1.065	.0338 .0375 1.050
FLEXIBILITY INFLUENCE COEFFICIENTS TEST WING — THERMAL GRADIENT CONDITION (DEFLECTIONS — INCHES PER 1000#)															

FLEXIBILITY INFLUENCE COEFFICIENTS  
TEST WING — THERMAL GRADIENT CONDITION  
(DEFLECTIONS — INCHES PER 1000#)

\* FRACTIONAL CHANGE IN FLEXIBILITY DUE TO INTERACTION

TABLE I

Deformational Response Determinations For  
Practical Heated Wing Structures

By

Richard H. Gallagher\*, James F. Quinn\*\*, and Joseph Padlog\*\*  
Bell Aerosystems Company  
Buffalo 5, New York

ABSTRACT

Methods for determining the deformational characteristics of heated lifting surfaces are described. With regard to analysis, the extension of displacement approaches to low aspect ratio wing analysis to account for the effects of aerodynamic heating on stiffness and the shape of the lifting surface are outlined. Compatible testing techniques are also described. Analyses of two types of structures, a plate and a multiweb wing, are performed for static load conditions and the results compared with test data.

ACKNOWLEDGEMENTS

Work described in this paper was performed in connection with Air Force contracts AF33(616)-5014 and -6653, under sponsorship of the Aerospace Mechanics Branch, Flight Control Laboratory, Wright Air Development Division.

- \* Chief, Advanced Airframe Analysis, Bell Aerosystems Company
- \*\* Structures Research Engineer, Bell Aerosystems Company

## I. INTRODUCTION

Methods for analyzing the dynamic behavior of complex low aspect ratio wing structures have reached a stage in their development where the significant effects of shear lag, sweep, cutouts, and two-dimensional stress fields can be taken into account with accuracy. These effects on the structural response input to the dynamic equations are dealt with by means of procedures wherein the structure is represented by an assemblage of discrete elements, each of which is assumed to behave in a simplified manner. The two most widely used approaches to the solution of such systems are the "force" and "displacement" techniques. In the former, a solution is first achieved for the internal forces in the system, i.e., the forces acting upon the discrete elements, and subsequent evaluations are made of the displacements at the element juncture points. Conversely, in the displacement approach, the element juncture point displacements are initially determined, followed by the evaluation of the internal force system.

As a consequence of the operational environment and configuration specified for proposed hypersonic vehicles, there is a need to extend both the force and displacement approaches to account for elevated temperature effects. Severe heating rates will be experienced, resulting in a structural temperature rise that is non-uniformly distributed. The elevated temperatures and the associated thermal stress systems cause stiffness reductions which influence the dynamic response to the extent that the deformational characteristics affect the total dynamic solution.

The primary purpose of this paper is to outline the extension of the displacement approach to account for the more significant of these effects; force methods are dealt with by other authors at this conference. With either approach it is possible to employ various structural idealizations. The complete catalog of associated displacement formulations for these many idealizations would consist of an extremely large number of equations, and it would be beyond the scope of the paper to detail the extension of each. What has been done is to discuss the individual phenomena resulting from heating in terms of physical behavior, their relationship to the various idealizations in common use, their influence on the total formulation of the problem as a set of matrix equations, and their influence on solution procedures. A detailed development of basic relationships is given for one idealization, the equivalent plate representation, and this embodies concepts directly applicable to the other representations treated. While this paper restricts its attention to the inclusion of additional phenomena and their effect on the solution of the final equations, it should be noted that the success of this general approach to analysis is dependent on a high degree of automation in the computer programs to be employed. The latter questions are discussed in References 1 and 2, among others.

For purposes of clarification it is useful to define, briefly, the consequences of elevated temperatures on deformational response before discussing the phenomena of interest individually. The principal effects of aerodynamic heating occur as the result of (a) influences on the material properties, and (b) nonlinear temperature distributions. With regard to material properties, elevated temperatures not only reduce stiffness by elastic modulus deterioration, but also intensify the likelihood of inelastic deformations being experienced. When the wing is inelastically deformed it will have a new shape in the unloaded state.

The most important effects of nonuniform temperature distributions are the change in shape of the lifting surface and the reduction in stiffness with respect to displacements normal to the surface, by what is effectively a compressed-plate action. In past investigations, based on elementary theory, the latter effect has appeared as a reduction in torsional stiffness. This phenomena must be accounted for in a realistic approach to deformational analysis.

The net effect of the above-cited stiffness reductions can be deflections in the presence of loads, and/or dynamic behavior that are many times greater than the thickness of the wing. This will result in the development of a "large deflection" stress system in the midplane of the wing, having the same type of effect on deflectional stiffness as a midplane stress system. The large deflection stress system is nonlinearly related to the deflections, however, and the entire problem becomes nonlinear. Under such conditions initial deformations have a bearing on stiffness. Subsequent paragraphs discuss these and the other phenomena cited above at greater length.

## II. ANALYSIS

### a. Review of the Displacement Approach

Historically speaking, displacement approaches to complex structure analysis did not progress from any particular development that received widespread acceptance as a common basis for practical applications. Dating from 1953, many approaches were presented in the literature, varying in both the procedures to be followed in forming the equations to be solved and in the representation of the structure. Advances in computing machines used to form and solve the governing equations have led to the general acceptance of specific procedures for these purposes, but a diversity in possible structural representations remains. The following representations are most common:

- 1.) The Equivalent Plate. Here, the internal members may be transformed into an equivalent skin thickness and the entire

wing treated as a thin plate in flexure. It is also possible to deal with the internal members as discrete elements (See References 3 and 4).

- 2.) An assemblage of beam segments (flexural elements) and torsion cells. (References 5 and 6).
- 3.) An assemblage of skin panels in a two-dimensional state of stress, and flexural elements representing the internal members. (References 1 and 2).
- 4.) An assemblage of axial force members and shear panels. (Reference 2). For clarity, web shear panels are not shown.

The last representation is most often employed with the "force" approach. Examples of all but the first of the above idealizations are illustrated in Figure 1. The coordinate systems used in succeeding paragraphs are also shown.

In each of the above representations the discrete elements are joined at specified points, and every such element is displaced in an idealized manner under the application of loads to these attachment points. For every type of discrete element, it is necessary to establish general relationships between loads applied to the points and the displacements of the points. Although actual flight conditions result in distributed loads being applied to the lifting surface, only concentrated applied loads at the element juncture points are considered here. This is consistent with the geometric representation. For dynamic analyses it will be necessary to "lump" the distributed masses at the juncture points.

The coordinates used to define the load-displacement properties of a lifting surface will vary, dependent, among other factors, upon whether or not the shear displacements are directly accounted for. If, for example, the wing is to be analyzed as a plate in flexure, then it is possible to deal only with displacements normal to the plane. Generally, however, the representations in use deal with a minimum of three displacement components. When the wing is represented as an assemblage of flexural elements and torsion boxes, the unknowns will be the displacements normal to the plane of the lifting surface and the angular rotations of normals to this surface in each of the two inplane directions. For other representations, the latter two are replaced by the inplane displacement components of points on either the upper or lower surface of the wing.

As complex structure analysis procedures advance to dealing with nonuniform temperature effects, the displacement unknowns will, in effect, increase by two. These are midplane, inplane displacements not bound by the type of conditions which relate the inplane displacements of upper and lower surface points to each other.

For simplicity, subsequent paragraphs will deal primarily with the relationships between the loads and displacements in the Z-direction (See Figure 1), i.e., in the direction normal to the middle surface of a planar wing. It is possible to "reduce" a formulation in three coordinates to a single coordinate as follows: when a flexural element-torsion box idealization is applied in a wing analysis, the resulting governing equations have the form

$$\begin{Bmatrix} P_z \\ M_x \\ M_y \end{Bmatrix} = \begin{bmatrix} K_{zz} & K_{zx} & K_{zy} \\ K_{xz} & K_{xx} & K_{xy} \\ K_{yz} & K_{yx} & K_{yy} \end{bmatrix} \begin{Bmatrix} w \\ \phi_x \\ \phi_y \end{Bmatrix} \quad (1)$$

$P_z$  represents the reference point loads normal to the plane,  $M_x$  and  $M_y$  are applied moments in the  $x$  and  $y$  directions, and  $w$ ,  $\phi_x$  and  $\phi_y$  are corresponding displacement coordinates. The terms  $K_{zz}$ ,  $K_{zx}$ , etc., are the stiffness coefficients for the complete structure. Solving the moment equations (those below the dotted partitioning line) for the displacements  $\phi_x$  and  $\phi_y$ , and substituting the result into the equation for  $P_z$  yields:

$$\begin{aligned} \{P_z\} &= [K_{zz}]\{w\} - [K_{zx} \ K_{zy}] \begin{bmatrix} K_{xx} & K_{xy} \\ K_{yx} & K_{yy} \end{bmatrix}^{-1} \begin{bmatrix} K_{xz} \\ K_{yz} \end{bmatrix} \{w\} \\ &\quad + [K_{zx} \ K_{zy}] \begin{bmatrix} K_{xx} & K_{xy} \\ K_{yx} & K_{yy} \end{bmatrix} \begin{Bmatrix} M_x \\ M_y \end{Bmatrix} \end{aligned} \quad (2)$$

which can be concisely expressed as

$$\{P_z\} = [K_z] \{w\} + \{\lambda\} \quad (3)$$

The definitions of  $[K_z]$  and  $\{\lambda\}$  follow from a comparison of (2) and (3).

The above reduction process demonstrates the transformation of moment loadings into Z-displacements. Also, it is clear from (2) that any addition to the out-of-plane stiffness ( $[K_{zz}]$ ) is not affected by the reduction. For example, if it is found, subsequent to the formation of (3), that the original relationship between  $P_z$  and  $w$  is  $[K_{zz}] + [N]$ , rather than  $[K_{zz}]$  alone, then it is only necessary to add  $[N]$  to (3) thusly.

$$\{P_z\} = ([K_z] + [N]) \{w\} + \{\lambda\} \quad (4)$$

These factors are noted because phenomena described in subsequent paragraphs will be shown to be analytically equivalent to either additional loadings or additional deflectional stiffnesses. The above comments, although based on angle change coordinates ( $\phi_x \neq \phi_y$ ) apply equally well for  $u$  and  $v$  coordinates in either the upper or lower skin surfaces.

#### b. Thermal Stress Effects

Thermal stresses result from the equilibration of thermal strains in a nonuniformly heated structure. Since this paper is concerned with effects on stiffness, details of thermal stress analysis techniques will be avoided to the extent possible. To be consistent with the deformational response determinations, the thermal stress analysis model should correspond to the one used in evaluating displacements due to applied loadings. Also, since the thermal stress evaluation is, in itself, a deformational analysis, the resulting displacements may be so large as to be of concern.

Three types of thermally-induced displacements would appear possible, based on the displacement coordinate choices discussed previously. The first, displacements in the Z-direction, represent the expansions of the wing thickness and will therefore be insignificant. The other two types of displacements are net displacements of the middle surface and equal and opposite displacements of corresponding upper and lower surface points. (These two types may represent a distinction that is made after a solution is affected for all thermal displacements).

For net displacements of the middle surface, the associated thermal stress system is important due to its effect on stiffness, as will be discussed below. The displacements, being entirely in the plane of the wing, will not be of concern in the present context, however. The other type of inplane displacement system involves a curvature of the midplane, occasioning deflections normal to the plane. Reference 8 has shown that the terms required for the evaluation of these deflections, for a flexural element-torsion box idealization, are in the form of applied moments. Hence, from the reduction process described previously, the net effect is to yield equivalent lateral loadings  $[\lambda_m]$ . Specific details for the plate representation are given in the Appendix. The application to the other representations of interest follow directly from the concepts given above and in the Appendix.

In turning to questions of thermally-induced stiffness loss, the physical behavior of concern is most simply illustrated by the action of an axial force member (Figure 2). Consider end point 2. There, in the displaced state, the end force  $F_2$  (evaluated independently in a thermal stress analysis) will have a component in the Z-direction equal to  $F_2 (w_2 - w_1)$ . The other axial force members meeting at point 2 will each have end forces with a Z-

component that is also a linear function of Z-displacements. In an unheated wing, the net effect of these Z-direction components at a planform reference point will be zero; the basic Z-direction equilibrium equation is entirely derivable from the internal vertical shears. With a thermal stress system the net midplane force might not be zero, and such a system contributes to the equilibration of the applied load.

For a system of equations that have been completely reduced to relationships between loads and displacements in the Z-direction, the formulation to account for effects due directly to thermal strains and stresses becomes:

$$\{P_z\} = [K_z] \{w\} + [N_T] \{w\} + \{\lambda_m\} \quad (5)$$

The equivalent loadings,  $\{\lambda_m\}$ , have already been described above.  $[N_T]$  is the matrix of the multipliers of the displacements in the terms representing contributions of the midplane forces to vertical equilibrium.

The example cited above need only be implemented by counter-part relationships for the vertical components of shear panel forces to complete the inclusion of thermal stress effects in an axial force member-shear panel idealization. The necessary details are indicated by the formulations of the Appendix. Also, it is not necessary to extend the above concepts further for the plate segment skin-internal element representation, since it is again a matter of forming the terms of the  $[N_T]$  matrix consistent with the element corner forces at each point. Corner force-displacement equations for the individual elements can be obtained from Reference 7.

The flexural element-torsion cell representation provides a choice in the formulation of the problem. On one hand, as shown in Reference 8, it is possible to derive flexural element force-displacement equations that directly account for the presence of the axial force. This corresponds to a direct formation of the total stiffness matrix  $[K_z] + [N_T]$ , but has an important practical shortcoming in that the element stiffness coefficients involve complicated trigonometric functions. As an alternative, it would appear sufficiently accurate to assume linear displacements when evaluating the out-of-plane components of the midplane. The procedure then corresponds to those discussed above and simplifies the inclusion of the shear panel components.



## c. Large Deflections

With or without the stiffness reducing effects of aerodynamic heating it is possible for a wing to experience large deflections under load. If the wing is sufficiently flexible these deflections will take place elastically. The specific large deflectional phenomena towards which attention has been drawn are the midplane stress systems produced in consequence of the wing assuming a displacement state that is not a developable surface. The simplest example of this effect is a flexural element hinged at either end to fixed walls (Figure 3). The length of the neutral line under transverse load is greater than in the unloaded state, requiring the existence of an axial load whose magnitude is a function of the deflection.

Clearly, in the beam theory representation of a wing as a cantilever, there can be no effects of this type. It follows that the onset of significant large deflection midplane stress systems in low aspect ratio wings, will occur for deflections much greater than the thickness of the wing. The latter value is often used to establish the significance of large deflection effects for beams and plates supported at all boundaries. Nevertheless, the effect may prove of importance for highly solid heated wings where deflections as much as 10, or even more, times the wing thickness have been recorded (Reference 9).

In terms of the effects on deflectional behavior, the midplane stress systems due to large deflections influence stiffness in the same manner as do the midplane stress systems due to temperature. The result, however, will generally be to increase stiffness. Although a fixed midplane thermal stress system will be entirely associated with linear behavior, the large deflection stresses are nonlinear functions of the displacements, which are in turn a function of the large deflection stresses. Of importance to the dynamic analyst under such conditions is the nonlinear relationship between load and displacement with the result that displacement characteristics about an equilibrium state are dependent on the values of the particular equilibrium state.

Since the large deflection effects are in the nature of midplane stress effects it is not necessary to consider the modification to the out-of-plane equations. The terms to be introduced enter into the midplane analysis. Consider again the bar shown in Figure 2. Due to deflection, a differential length  $dx$  along the member axis is deformed to a length  $dL$ . By geometry, the difference ( $d\Delta u$ ) in these lengths can be expressed as

$$d\Delta u = dx \left( 1 - \sqrt{1 + \left( \frac{dw}{dx} \right)^2} \right) \quad (6)$$

and, by expanding the square root by the binomial theorem and discarding higher order terms

$$\delta \Delta u = -\frac{1}{2} \left( \frac{dw}{dx} \right)^2 \quad (7)$$

it follows that the change in length ( $\Delta u$ ) of the ends of the member is given by

$$\Delta u = -\frac{L}{2} \left( \frac{dw}{dx} \right)^2 \quad (8)$$

and the force ( $F_{\Delta w}$ ) required for this displacement is

$$F_{\Delta w} = \frac{AE}{2} \left( \frac{dw}{dx} \right)^2 \quad (9)$$

With regard to phenomena considered thus far, the stiffness of an element can be viewed as the sum of internal forces due to relative displacement, the restraint of thermal expansion, and the above mentioned large deflection force. A summation of the same form will be retained when the stiffness matrix for the complete structure is assembled. The first type of internal force is the inplane stiffness matrix  $[K_{xy}]$  multiplied by the inplane displacements. The second can be simply designated as  $\{T_x, T_y\}$ , and the third as  $\{P_{\Delta w_x}, P_{\Delta w_y}, P_{\Delta w_{xy}}\}$ . The three terms in the "large deflection" loading column does not imply a partitioning of these terms. Such terms will be combined in the matrix assembly operations to yield a number of runs conformable with the number in  $\{T_x, T_y\}$ .

With these definitions, the inplane force-displacement equations can be written as:

$$\{P_x, P_y\} = [K_{xy}]\{u, v\} + \{T_x, T_y\} + \{P_{\Delta w_x}, P_{\Delta w_y}, P_{\Delta w_{xy}}\} \quad (10)$$

The temperature term is retained only for consistency. As mentioned in the previous section, the analysis for thermal displacements can be carried out without distinctions between inplane and out-of-plane behavior. An independent thermal displacement analysis is in fact desirable since it is entirely linear. Also, it is unlikely that loads will be applied in the plane of the wing;  $\{P_x, P_y\}$  is therefore usually zero. These and other factors associated with solutions to Equation (10) are discussed in Paragraph f.

Equation (9) suffices to define the large deflection terms in axial force member relationships. Orientation in the X or Y directions is accounted for by proper coordinate transformations. Analogous terms, based on plate twist, need be evaluated for the shear panels. It is noteworthy that an axial force member-shear panel representation is the midplane analysis counterpart of the flexural element-torsion box representation. Large deflection formulations for the equivalent plate and the skin plate element idealizations are given in the Appendix and Reference 7, respectively.

#### d. Initial Displacements

Under linear conditions the initial displacements of the wing middle surface from a planar form will not influence deformational characteristics. They will effect these characteristics in the presence of nonlinear behavior since the absolute magnitude of a displaced state governs the relationship between applied loads and displacements about this state. For this reason, initial displacements were taken into account in Reference 10 in the analysis of a heated plate. Agreement with test data was achieved. Reference 10 also presented a parametric study of the influence of various pertinent factors, including initial displacements, on the stiffness of a simple heated plate. The results demonstrated that an initial twist did have beneficial effects on stiffness.

Initial displacements can be included in a discrete element analysis by a reformulation of the basic relationships. Their inclusion can be achieved more expeditiously, however, on the basis of direct reasoning. Consider first out-of-plane behavior (Equation 4). Since the basic stiffness  $[K_z]$  represents a change in curvature from the unloaded state, the multiplying column of displacements must be replaced by  $\{w - w'\}$ , where the  $w'$  values are the initial displacements of the reference points. The multiplier of the matrix  $[N]$  is not affected, since these terms represent the upward components of inplane forces and as such depend on absolute displacements, nor is the column of thermal displacements,  $\{\lambda\}$  affected, hence, Equation 4 becomes

$$\{P_z\} = \left[ [K_z] + [N] \right] \{w\} - [K_z] \{w'\} + \{\lambda_M\} \quad (4a)$$

The midplane Equations (Equation 10) are similarly modified. They involve Z-displacements only in the large deflection terms,  $\{P_{\Delta w_x}, P_{\Delta w_y}, P_{\Delta w_{xy}}\}$  which represent slopes. Hence, these slopes are replaced with changes in slope. Designating the latter as  $\{P'_{\Delta w_x}, P'_{\Delta w_y}, P'_{\Delta w_{xy}}\}$ , Equation (10) becomes:

$$\{P_x, P_y\} = [K_{xy}] \{u, v\} + \{T_x, T_y\} + \{P_{\Delta w_x}, P_{\Delta w_y}, P_{\Delta w_{xy}}\} \\ - \{P'_{\Delta w_x}, P'_{\Delta w_y}, P'_{\Delta w_{xy}}\} \quad (10a)$$

### e. Inelasticity

For the convenience of engineering analysis inelastic behavior is assumed to arise from two sources: time independent plastic flow, and creep. The former behavior results from stress levels in excess of the elastic limit, while the latter may occur at any stress level, as a function of time. Elevated temperatures can severely reduce the elastic limit and greatly increase the rate of creep deformation. Thus, either or both forms of inelastic behavior become important to the extent that they cause stress redistributions, residual stresses, and permanent deformation of the lifting surface. As a consequence, the inelastic deformations will have an indirect, but possibly significant, effect on stiffness. These effects can be beneficial, since the stiffness-reducing midplane thermal stress systems will themselves be reduced in magnitude and, as already noted, certain forms of permanent displacements will reduce the displacements due to load in the nonlinear range.

The application of discrete element approaches to the solution of creep and time-independent plastic flow problems is in its beginning stages, and, as far as is known, there has been no such analysis of a practical wing structure performed. In Reference 11, however, a discrete element approach was applied to the inelastic analysis of a plate with a centrally located hole subjected to the cyclic application of loads and temperatures. Rules for the prediction of inelastic strains, the matrix formulation of the problem and procedural details were described at length in the same reference. A necessarily brief outline of the basic concepts is given in the following paragraphs.

To extend element force-displacement relationships to include inelastic behavior the total direct and shear strains at any instant are defined as

$$\epsilon_x = \epsilon_{x_e} + \epsilon_{x_{pc}} + \alpha T \quad (11)$$

$$\tau_{xy} = \gamma_{xy_e} + \gamma_{xy_{pc}}$$

where the subscripts  $e$  and  $pc$  indicate the elastic and plastic strain components of the total strain, respectively. The plastic strain component is the sum of both the time-independent plastic and creep strains. The  $X$  and  $Y$  coordinates are employed for convenience; similar expressions can be written with reference to all three coordinates.

The inelastic strain components will be a nonlinear function of stress and temperature and their histories and it is not possible to effect a closed-form solution for deformational response. An approximate solution can be achieved, however, by assuming the accumulated inelastic strains to be constant at the beginning of a finite time interval. An analysis for stress and displacement for the beginning of the interval can then be achieved. By using the so-determined stresses to evaluate the inelastic strains accumulated during this interval, stresses and displacements at the end of the time interval can be determined. Many such determinations will be required to accurately analyze a given flight plan.

Consider as an illustration of the required stiffness matrix formulation an axial force member of the type shown in Figure 2. In the presence of inelastic strain, the following relationships can be written:

$$\text{Strain-Displacement:} \quad \epsilon = (u_2 - u_1) / L \quad (12)$$

$$\text{Applied Load-Stress:} \quad F_{x_2} = \sigma A \quad (13)$$

$$\text{Modified Hooke's Law:} \quad \sigma = E (\epsilon - \alpha T - \epsilon_{pc}) \quad (14)$$

Combining Equations (12) to (14) yields:

$$F_{x_2} = \frac{EA}{L} (u_2 - u_1) - EA\alpha T - EA\epsilon_{pc} \quad (15)$$

In a determination of displacements at a given time,  $\alpha T$  and  $\epsilon_{pc}$  will be known quantities. The last two terms in (15) therefore contribute to the formation of equivalent loadings, thermal and plastic, in the assembly of the stiffness matrices for the complete structure. The nature of thermal loadings has already been discussed, and on this basis, the formulation of the governing equations to include accumulated inelastic strain is seen to be:

For out-of-plane behavior

$$\begin{aligned} \{P_z\} = & \left[ [K_z] + [N] \right] \{w\} - [K_z] \{w'\} + \{\lambda_m\} \\ & + \{\lambda_{pc}\} \end{aligned} \quad (4b)$$

For in-plane behavior

$$\begin{aligned} \{P_x, P_y\} = [K_{xy}] \{u, v\} + \{T_x, T_y\} + \{P_{x_{PC}}, P_{y_{PC}}, P_{xy_{PC}}\} \\ + \{P_{\Delta w_x}, P_{\Delta w_y}, P_{\Delta w_{xy}}\} \end{aligned} \quad (10b)$$

where  $\{\lambda_{PC}\}$ ,  $\{P_{x_{PC}}, P_{y_{PC}}, P_{xy_{PC}}\}$  represents the equivalent loadings due to accumulated inelastic strains.

#### f. Solution Procedures

A solution for the deformational behavior of a heated lifting surface on the basis of the approach described above presents no inherent difficulty, apart from the size of the system under analysis, if the problem is linear. When large deflections or inelasticity are dealt with, the factors involved will not only amplify the complexity of the problem, but may also preclude the possibility of obtaining a convergent solution by means of seemingly useful techniques.

To simplify the discussion of the solution process for a large deflection elastic problem, it can be assumed that initial displacement terms are zero and that the complete deflectional analysis formulation has been reduced to relationships between the Z-displacements and applied loads. This does not restrict the generality of the discussion since the former can be transformed into equivalent loads. The latter operations are performed in Equations (2) and (3) above. The reduced load-deflection relationships can be written as:

$$\{P_z\} = \left[ [K_z] + [N_T] + [N_{\Delta w}] \right] \{w\} \quad (4c)$$

Probably the most straightforward approach to the solution is the following iterative technique. The midplane displacement and force equations are first linearized by neglect of all large deflection terms. Midplane forces evaluated in this manner are the thermal forces. Since these provide for the complete evaluation of  $[N_T]$ , it is convenient to replace  $[K_z]$  +  $[N_T]$  by a single matrix,  $[K_{zT}]$ .  $[N_{\Delta w}]$  is zero and a first-pass solution to (4c) can be effected thusly

$$\{w_1\} = [K_{zT}]^{-1} \{P_z\} \quad (4d)$$

Graphically, (see Figure 4), Equation 4d represents the intersection of a line tangent to the exact solution curve at the origin with a characteristic load  $\{P_{zi}\}$  to yield the corresponding deflection  $w_a$ . The slope of this line is consistent with the stiffness  $[K_{zt}]$ .

The so-determined  $\{w_i\}$  values permit an analysis for the midplane forces due solely to large deflections, leading to a first estimate for  $[N_{\Delta w}]$ . With a revised total stiffness,  $[K_{zt}] + [N_{\Delta w}]$ , a second, improved solution for the displacements can now be obtained as  $w_c$ . Diagrammatically (Figure 4), the point b is established on the true solution curve consistent with the displacement  $w_a$ . At point b, the slope to the origin is the revised total stiffness,  $[K_{zt}] + [N_{\Delta w}]$ . This stiffness establishes the improved deflectional solution  $w_c$  at point c, which in turn defines a more accurate large deflection midplane force system and then still better deflectional stiffnesses. The process would have to continue to convergence.

At convergence (point e), the coefficient in the total stiffness matrix,  $[K_z] = [K_{zt}] + [N_{\Delta w}]$ , relating  $P_{zi}$  to the corresponding  $w_i$ , is the slope of the line from the origin to the point on the true solution curve. This is the case for all terms in  $[K_z]$ . Hence,  $[K_z]$  is a "secant" stiffness, representative of an equilibrium solution. Aeroelastic analyses may require the "tangent" stiffness,  $[K_z]$  - the stiffness for incremental displacements about the equilibrium state. Reference 7 developed expressions for the direct determination of tangential stiffness for axial force and triangular plate elements. The resulting equations prove to be of a relatively complicated form. An attempt can be made to derive an approximate tangential stiffness by effecting secant solutions somewhat above and below the load levels of interest and then evaluating the intermediate slope. The most serious defect in this approach would appear to arise from round-off error.

In applying the iterative technique described above to the solution of actual problems, the authors have encountered a difficulty which often precluded true convergence. This difficulty can be characterized as "oscillatory convergence", (see Figure 5). Assume the iterations on Equation 4c have proceeded to the definition of a set of displacements characterized by  $w_a$  for the loading  $P_i$ . Then, a revised stiffness can be determined at point "b" and used to determine the corresponding flexibility (line 0-b), followed by the evaluation of  $w_c$  and the flexibility 0-d. This returns the process to point "a" and the displacement  $w_a$ . Subsequent iterations will therefore continuously follow the path a-b-c-d without convergence. From a physical behavior standpoint, the midplane force components for  $w_a$  are so large that the stiffness is overestimated. This leads to smaller displacements and an underestimation of the stiffness.

Alternate iterative solution approaches include the following. First, Equation 4c can be rearranged to read

$$[K_{zT}]\{W\} = \{P_z\} - [N_{\Delta W}]\{W\} \quad (4e)$$

then, by inversion of the linear stiffness matrix,  $[K_{zT}]$

$$\{W\} = [K_{zT}]^{-1} \{ \{P_z\} - [N_{\Delta W}]\{W\} \} \quad (4f)$$

To effect a solution,  $\{W\}$  is initially assumed zero on the right-hand side. The first approximation to  $\{W\}$  is therefore  $[K_{zT}]^{-1} \{P_z\}$ . This  $\{W\}$  then is used in an evaluation of  $[N_{\Delta W}]$ , and, together with  $[N_{\Delta W}]$ , is employed on the right-hand side to obtain an improved  $\{W\}$  on the left-hand side, and so forth until convergence.

This technique can be improved upon to yield more rapid convergence. For simplicity, let  $[K_{zT}]^{-1}[N_{\Delta W}]$  be designated as  $[\Delta]$ . Also, let  $\{W_0\} = [K_{zT}]^{-1} \{P_z\}$ . Then, Equation 4f becomes:

$$\{W\} = \{W_0\} - [\Delta]\{W\} \quad (4g)$$

Further, let the left-hand side value of  $\{W\}$  determined in a "first pass" be designated as  $\{W\}^{(1)}$ . Thus

$$\{W\}^{(1)} = \{W_0\} - [\Delta]\{W\} \quad (4h)$$

The "second pass" can then be written as:

$$\{W\}^{(2)} = \{W_0\} - [\Delta]\{W\}^{(1)} \quad (4i)$$

Substitution of 4h into 4i yields:

$$\{W\}^{(2)} = [I - [\Delta]]\{W_0\} + [\Delta]^2\{W\} \quad (4j)$$

Equation 4j is a formula that can now be applied in the same manner as Equation 4f. It is clear that any number of additional formulas, involving higher powers of  $[\Delta]$ , could be derived by continued application of the above technique.

### III. EXPERIMENTAL DETERMINATIONS

To assure the integrity of a heated structure design against dynamic failure it would be necessary to perform a wind tunnel test, subjecting the design to a close approximation of the anticipated history of applied loadings and temperatures. This



necessity arises in consequence of the complexity of the phenomena occurring as a result of the elevated temperature conditions. By the same token it is extremely difficult, if not impossible, to obtain from such tests information that would lead to a clarification of the fundamental mechanisms affecting deformational response. The latter objective can be achieved through tests for deflection influence coefficients, which provide a direct experimental comparison with the output of the type of analyses described in previous paragraphs.

The technology of deflection influence coefficient testing is not well documented, due, possibly, to the fact that the need to define the deformational characteristics of a wing in this form has existed only since the advent of the low aspect ratio wing. Many difficulties enter into the problem when elevated temperature conditions are imposed. It proves difficult to simulate the true support conditions realistically. Temperatures and displacements must be simultaneously measured at each point while both the loads and temperatures are applied, and the instrumentation must be protected from the effects of the latter.

A scheme to surmount these difficulties was developed three years ago at Bell Aerosystems Company. Detailed descriptions of the associated apparatus and techniques have been published elsewhere (8) (12), and for this reason only a brief review of the work is given here.

The basic concept is to simply support the model to be tested in a fixture, and surround it with the proper heating apparatus. By orientation of the heating devices and control of their input it is possible to impose and maintain temperature profiles that approximate conditions at a particular time in a flight plan. Temperature differences between internal members and the skins can be simulated by coolant passages incorporated in the internal members.

To apply load, cables are attached to the reference points on the underside of the wing, and to measure deflections variable permeance extensometers can be employed, if they are remote from the heated area and otherwise protected from the temperature effects. The displacement travel is transmitted from the heated area by joining the reference points to the extensometers, with long, small diameter quartz rods when the extensometers are placed above the model.

The use of a simple-support system, in the form of three "point" supports satisfies two objectives. First, a properly designed point support will eliminate constraints that would lead to localized, severe thermal stresses, and will circumvent large heat sinks at the support. Secondly, deflection influence coefficients obtained from a model supported in this fashion can be adapted to other types of support conditions. The necessary analytical procedures are given in Reference 13.

This test scheme was first used in the experimental determination of deflection influence coefficients for two stainless steel multiweb wings. The models possessed a number of geometric similarities, the differences being primarily confined to the planforms. One model was of rectangular planform (Figure 6). The other model was swept  $45^\circ$  (Figure 7). Due to the condition of a three-point support, each wing had a carry-through segment 12" long. Tests were performed at room temperature, at uniform elevated temperatures, and in the presence of a number of nonuniform temperature distributions. Figure 8 illustrates the nonuniform temperature distributions on a typical chordwise cross-section of the rectangular planform wing (temperatures were constant in the spanwise direction). Similar temperature profiles were imposed on the swept wing.

Recently, a fuselage model, fabricated of stainless steel, was subjected to a similar series of tests. The model is illustrated in Figure 9. It is shown attached to the rectangular planform wing described above, since combined wing-fuselage tests were performed. The fuselage was supported at its four corner points and loaded symmetrically about the longitudinal axis at the indicated points. All loads were applied normal to the surface of the structure.

Tests were scheduled for temperature profiles consistent with both the heat transfer characteristics of the fuselage structure and the severity of the conditions imposed on the counterpart wing structures. Gradients along the longitudinal axis, at an average temperature of  $500^\circ\text{F}$ . were maintained by the orientation and voltage regulation of radiant heat lamps. Radial temperature gradients, represented by the differences between the ring and adjacent skin temperatures, were established using coolant tubes attached to the ring surfaces.

In the sequence of planned tests, influence coefficients for the fuselage alone were determined for unheated, uniform elevated temperature, and nonuniform elevated temperature conditions. Then, corresponding tests were performed for the combined wing-fuselage arrangement. Temperature profiles for the wing were in conformity with those imposed on the wing alone in previous tests.

#### IV. TEST-THEORY COMPARISONS

##### a. Cantilevered Plate

The assessment of procedures for predicting elevated temperature effects on wing deformational behavior is at present severely limited by a lack of test data useful for comparison purposes. One set of available data is that given in Reference 9 for a cantilevered plate. Other test information was recorded for the two multiweb wings discussed in the preceding section. Both series of

tests excluded curvature-producing depthwise temperature gradients and none of the structures are believed to have experienced significant inelastic effects during testing.

The cantilevered plate, composed of aluminum alloy, is illustrated in Figure 10. Also shown is the network of points employed in analyses based on the approach shown in the Appendix. The initial displacements of the plate and the measured chordwise temperature profiles for three times in the heating cycle, as reported in References 9 and 10, are given in Figures 11 and 12. Temperatures were constant in the spanwise direction. Figures 11 and 12 also show the analytical idealizations of the initial displacements and the temperature distributions.

In the tests of interest to the present paper, concentrated loads of 20 lb. each were applied to the tip corner points to form twisting action. All conditions-geometric, temperature, and load-were therefore either symmetric or antisymmetric about the 50% chord line, making possible an analysis of half the plate. The gridwork of points employed in the analyses to be discussed is shown in Figure 10.

Since only the measured tip twist angles were reported, the analytical results, which are obtained in terms of the displacements of the reference points, have been transformed into tip chord twist angles by dividing the corner point displacement by the half-chord length. The analytical and test results, in the form of the tip chord twist angle versus elapsed time of the heating sequence, is shown in Figure 13. The representation is based entirely on results for the unheated condition (time zero) and the three times in the heating cycle indicated on Figure 12.

Two approaches to solution had to be attempted before the results were obtained. The first, the conventional iteration technique, encountered numerous difficulties. For one, it was not possible to advance the analysis for the 16.5 seconds case beyond the first iterative cycle due to the fact that the linear portion of the out-of-plane stiffness matrix,  $[K_z + N_T]$ , represented a buckling condition. In addition, both other heated conditions (10 and 30.5 seconds) experienced oscillatory convergence characteristics. The solution technique represented by Equation 4j was therefore resorted to. This proved successful for each condition, requiring less than 10 iterative cycles for convergence to the values plotted in Figure 13.

The test and theoretical results are in reasonable agreement, considering the crudity of the representation. A variational solution, employing a functional representation of all varying quantities, was presented in Reference 10. The results were in closer agreement with test than those given here. This is to be expected in view of the simplicity of actual conditions, each of which could be closely

approximated by a continuous function. It is to be noted, however, that the major advantages of the present approach lie in the ability to deal with built-up wings of irregular planform and thickness taper.

b. Multiweb Wings

Extensive results were obtained from the elevated temperature deflection influence coefficient tests of the multiweb wings shown in Figures 6 and 7. The results were reported in Reference 8, where assessments of the significance of thermal effects on the basis of comparisons of the elevated temperature results with the room temperature tests were effected. Recently, analyses were performed using the flexural element-torsion box representation and are to be published in the near future (Reference 14). The following paragraphs summarize results obtained for the rectangular planform wing. Results obtained for the swept wing lead to conclusions similar to those given below.

The comparison of influence coefficients on a number to number basis often proves unsatisfactory, due to localized phenomena which will have an uncertain effect on the overall behavior under distributed load or in the presence of dynamic response. This problem was heightened in the subject series of tests by difficulties in testing in an elevated temperature environment and by the small differences in stiffness between the various test sets of influence coefficients. These differences were often on the order of a reasonable experimental error. For these reasons, "flexibility" parameters which incorporate all significant values in each test, have been resorted to. It is on the basis of these parameters that the following comparisons are effected.

A comparison of test results for the rectangular planform wing model will provide a fuller explanation of the "flexibility" parameter chosen and its application. As shown in Figure 8, the two most severe temperature conditions imposed on this model occurred during tests IVa and Va. In Case Va, a 300°F. chordwise gradient and a 550°F. average temperature condition prevailed. The recorded influence coefficients exceeded those measured during a room temperature test by about 10%. Material property evaluations of the model material, indicated that the reduction in elastic modulus value between room temperature and 550°F. would be 9%. The other 1% could not clearly be defined at each point in the presence of a reasonable experimental error. This is made more evident when a comparison is made between material property data determinations and deflection measurements for the model in a uniformly heated condition. Results presented in Reference 8 show that this difference may be as much as 2% for a 550°F. uniform temperature condition.

In Case IVa, a similar chordwise gradient (300°F. from leading to trailing edge) and a lower average temperature (310°F.) were imposed on the model. The measured influence coefficients exceeded

those measured at room temperature by about 9% as compared with an elastic modulus reduction for this average temperature condition of 4 $\frac{1}{2}$ %. This was the largest difference between the apparent elastic modulus effect and the total measured change in a thermal environment, for tests performed on this model.

To average out the experimental error and to compress the available data for comparison purposes, all influence coefficients for points 1 through 10 were added together to yield a "flexibility" parameter. This group of points 1 through 10, were the outboard points on the wing, and thus were the points for which deflection measurements were of significant magnitude.

The test and theory "flexibility" parameters are listed in Table I. A comparison between these values is given in Table II, where there is shown the percentage change in these parameters from the corresponding room temperature parameter. Each temperature condition is represented by parameter changes due to both the thermal stress and elastic modulus effects ("total change"), the modulus effect alone, and the thermal stress effects alone ("other effects"). The latter value was obtained as the difference between the first two values.

Comparing the analytical and test changes, it is apparent that although there is a good correlation with regard to the effect of modulus change, the correlation is poor for thermal effects. In each case, small or negligible thermal stress effects are predicted by the analytical method.

To further emphasize these comparisons, Table III has been constructed. This table presents the ratios between the analytical and test changes. For modulus effects it is seen that the analytical predictions were in the range of 89 to 116% of changes indicated by material property tests. In only one case (Case Ia) is the analytical prediction of thermal stress effects in excess of 21% of the value indicated by test data.

The existence of experimental errors would be a possible cause for these discrepancies. It is unlikely that this factor is significant in the present case, due to the extensive averaging of recorded data entering into the test flexibility parameter. It is reasonable to question if the results truly represent the theory upon which they are based. Evidence that they do is given by similar analyses performed elsewhere and reported in Reference 15.

One deformational behavior mechanism not represented by the basic theory employed is the local instability effect on the skin panels. These panels may "bow out" and bend under direct loads, resulting in reduced stiffness. The correlation of surface strain gage measurements with a beam theory thermal stress solution (Reference 8) demonstrated that this mechanism was insignificant in

the presence of thermal stresses alone. It is possible that the addition of applied loading did introduce such effects to a modest extent, and this may account for a portion of the test-theory discrepancy.

In summary of the above results and comparisons, it has been found that small changes in general flexibility were experienced by the actual wing model in consequence of temperature effects other than elastic modulus deterioration. Discrepancies between the stiffness changes predicted by theory and measured during tests are likely due to the following sources of error:

- (a) Experimental error
- (b) Numerical errors in the analyses (round-off errors)
- (c) Phenomena not accounted for by the theory  
(e.g., the bowing out of skin panels)

#### V. SUMMARY

The present paper has discussed how the newer approaches to the deformational response analysis of built-up low aspect ratio lifting surfaces can be extended to account for the effects of aerodynamic heating. Each phenomena introduced by, or intensified by, heating conditions can be incorporated in the basic formulation of these approaches as either loadings or additional stiffnesses. Such concepts provide a physical insight into these effects and should assist in forming an estimate of their importance prior to undertaking the massive sequence of operations required in an application to a practical structure. It has also been indicated that many unique difficulties are to be expected when attempting to effect a solution to a nonlinear formulation of the problem. Negligible experience has been thus far recorded in the analysis of discrete element systems for nonlinear behavior. Although the original studies of heating effects on stiffness could be severe enough to warrant the inclusion of nonlinear midplane stress system effects, the structures involved were simplified and relatively solid. Practical structures that have recently been designed, which required the application of complex structure analysis techniques, have been built-up and have therefore not sustained significant stiffness losses due to heating. The design of vehicles for higher performance continues, however, and it is to be expected that the problem will have to be dealt with in future practical analyses.

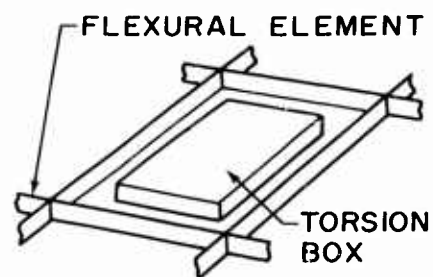
REFERENCES

1. TURNER, M. J., CLOUGH, R. J., MARTIN, H. C., and TOPP, L. J. "Stiffness and Deflection Analysis of Complex Structures" Journal of the Aeronautical Sciences, Sept., 1956.
2. ARGYRIS, J. H., and KELSEY, S. "Energy Theorems and Structural Analysis" Butterworths Scientific Publications, London, England, 1960.
3. WILLIAMS, D. "A General Method (Depending on the Aid of a Digital Computer) for Deriving the Structural Influence Coefficients of Airplane Wings" Parts I and II, A.R.C. R.&M. No. 3048, May, 1956.
4. BENSCOTER, S., and MAC NEAL, R. H. "Equivalent Plate Theory for a Straight Multicell Wing" NACA TN 2786, Sept., 1952.
5. LEVY, S. "Structural Analysis and Influence Coefficients for Delta Wings" Journal of the Aeronautical Sciences, July, 1953.
6. THOMANN, G. E. A. "Aeroelastic Problems of Low Aspect Ratio Wings, Part I - Structural Analysis" Aircraft Engineering, Jan., 1956.
7. TURNER, M. J. DILL, E., MARTIN, H. C., and MELOSH, R. J. "Large Deflections of Structures Subjected to Heating and External Loads" Journal of the Aero/Space Sciences, Feb., 1960.
8. GALLAGHER, R. H., QUINN, J. F., and TURRENTINE, D. "Thermal Effects on Aeroelastic Stability and Control, Part III" WADC TR58-378, Dec., 1959.
9. VOSTEEN, L., and FULLER, K. "Behavior of a Cantilever Plate Under Rapid Heating Conditions" NACA RM L55E20c, 1955.
10. HELDENFELS, R. R., and VOSTEEN, L. F. "Approximate Analysis of Effects of Large Deflections and Initial Twist on Torsional Stiffness of a Cantilever Plate Subjected to Thermal Stresses" NACA TN 4067, Aug., 1957.
11. PADLOG, J., HUFF, R., and HOLLOWAY, G. "Inelastic Behavior of Structures Subjected to Cyclic Thermal and Mechanical Stressing Conditions" WADD TR 60-271, April, 1960.

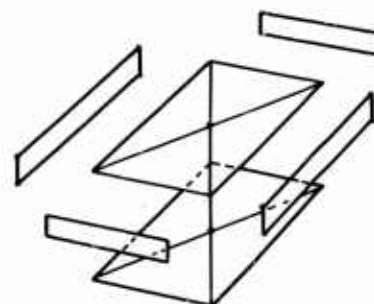
REFERENCES (Continued)

12. GALLAGHER, R. H., QUINN, J. F., and TURRENTINE, D.  
"Techniques for Testing Thermally-Affected Complex Structures"  
Society for Experimental Stress Analysis, May, 1959.
13. STEIN, M. and SANDERS, J. L. "A Method for the Deflection  
Analysis of Thin Low-Aspect Ratio Wings" NACA TN 3640,  
June, 1956.
14. GALLAGHER, R. H., and HUFF, R. "Elastic Response Determinations  
for Severely Heated Wings" WADD TR, in preparation.
15. BASIN, M. A., MAC NEAL, R. H., and SHIELDS, J. H.  
"Direct-Analog Method of Analysis of the Influence of Aero-  
Dynamic Heating on the Static Characteristics of Thin Wings"  
Journal of the Aeronautical Sciences, Dec., 1956.

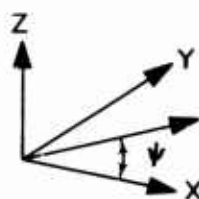




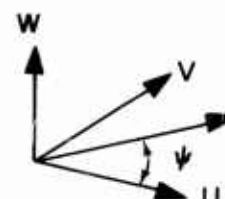
A. FLEXURAL ELEMENT-TORSION BOX IDEALIZATION



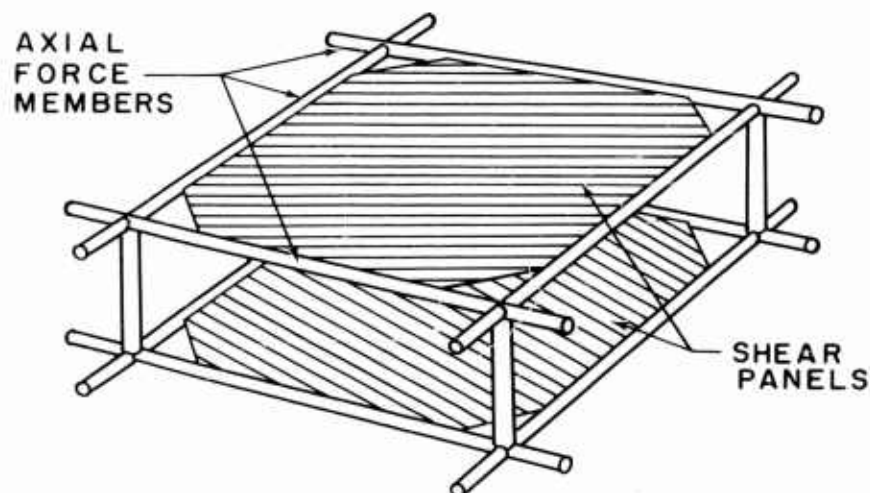
B. SKIN PANEL INTERNAL ELEMENT



WING SURFACE COORDINATES



DISPLACEMENT COORDINATES



C. AXIAL FORCE MEMBER - SHEAR PANEL

FIGURE 1 TYPICAL IDEALIZATIONS AND COORDINATE SYSTEMS

DEFLECTED STATE (FOR PURPOSES OF  
PARA IIc DISCUSSIONS ONLY)

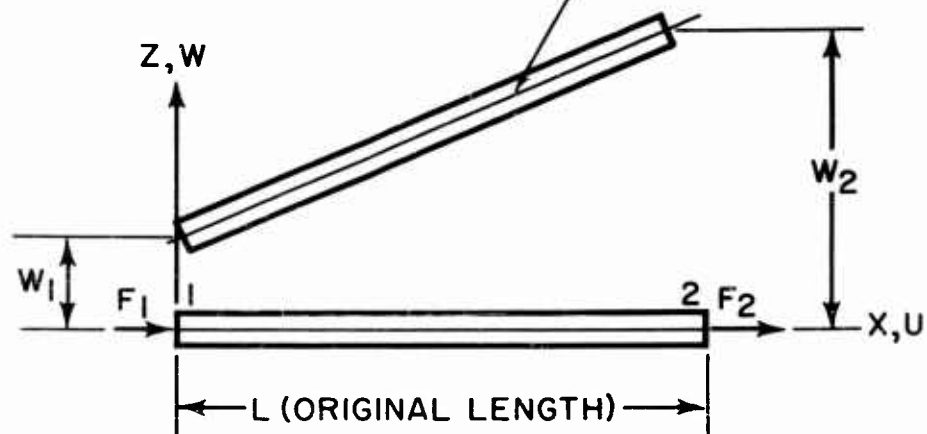


FIGURE 2. AXIAL FORCE MEMBER

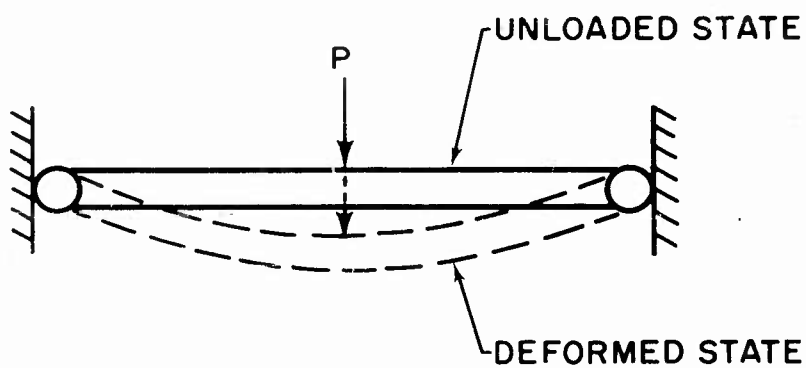


FIGURE 3. BEAM BETWEEN WALLS

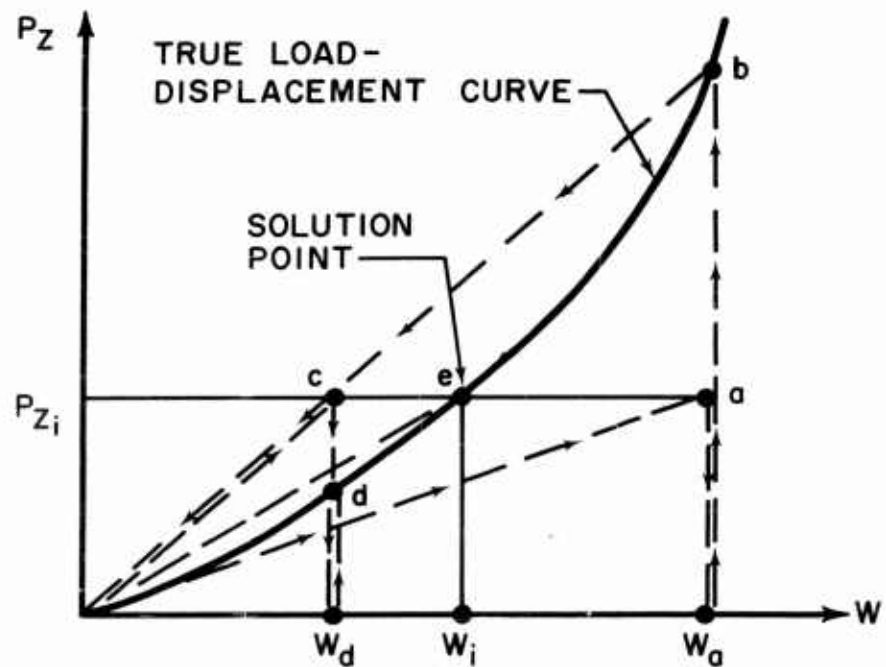


FIGURE 4. ITERATIVE SOLUTION PROCESS

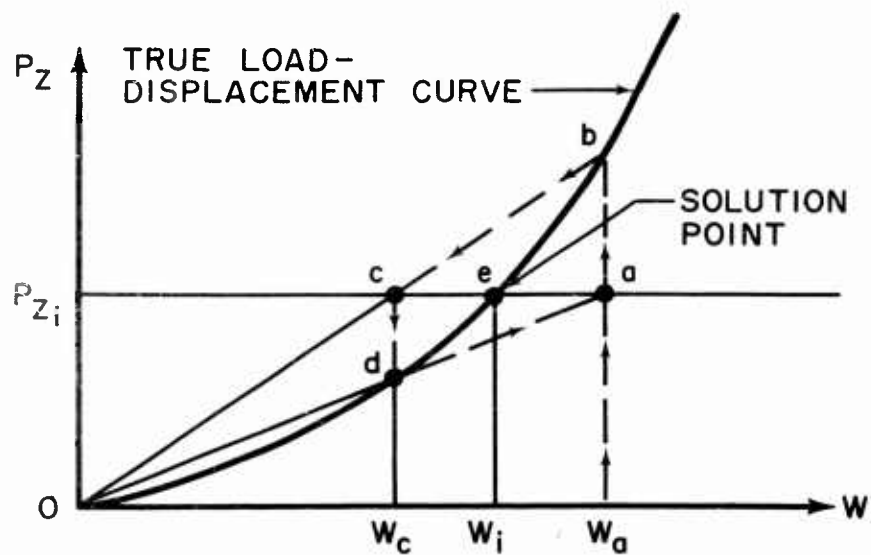


FIGURE 5. OSCILLATORY CONVERGENCE BEHAVIOR

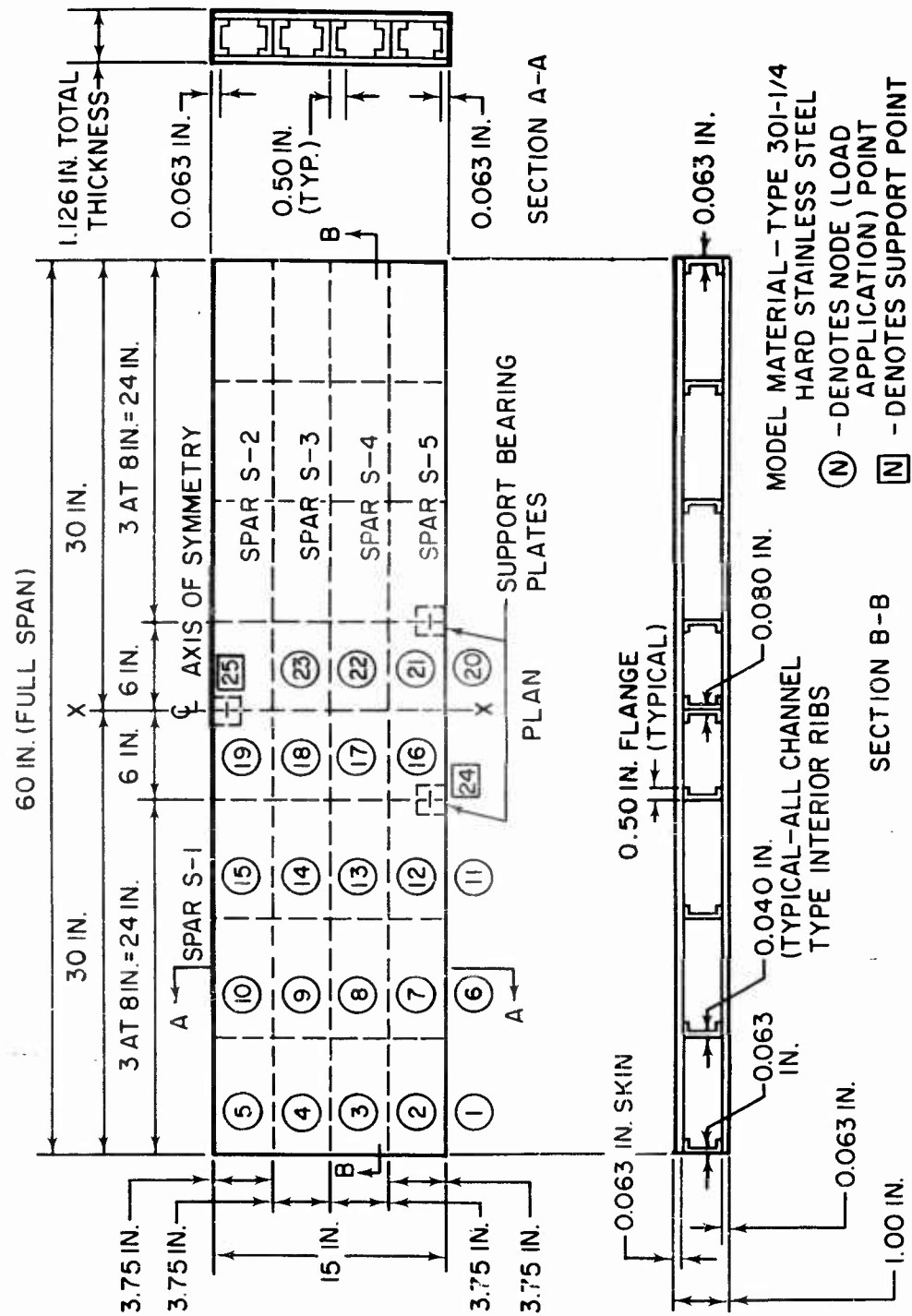


FIGURE 6. FIRST HEATED WING MODEL - GEOMETRY, DIMENSIONS, AND NODE POINTS

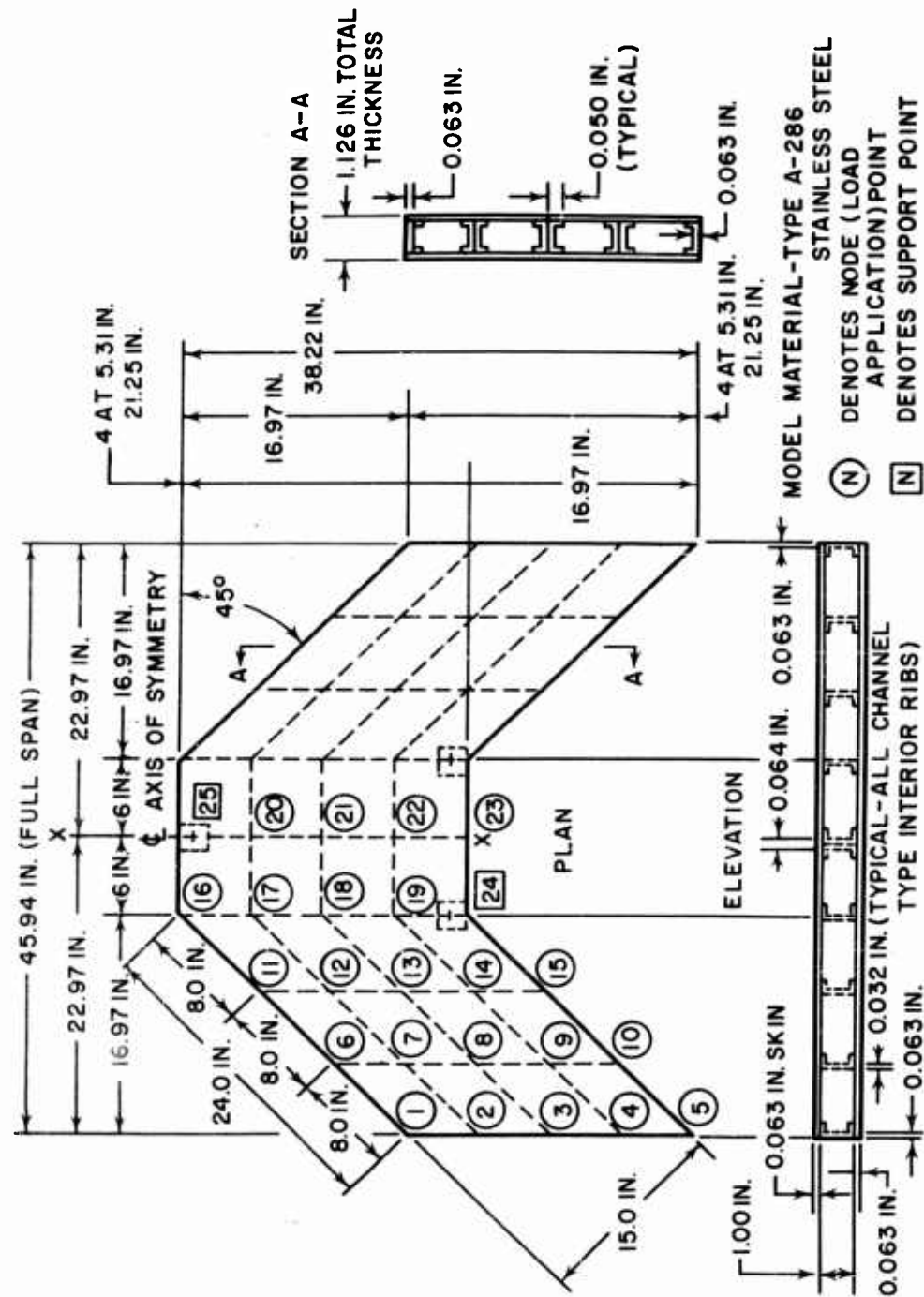


FIGURE 7 SECOND HEATED WING MODEL - GEOMETRY, DIMENSIONS, AND NODE POINTS

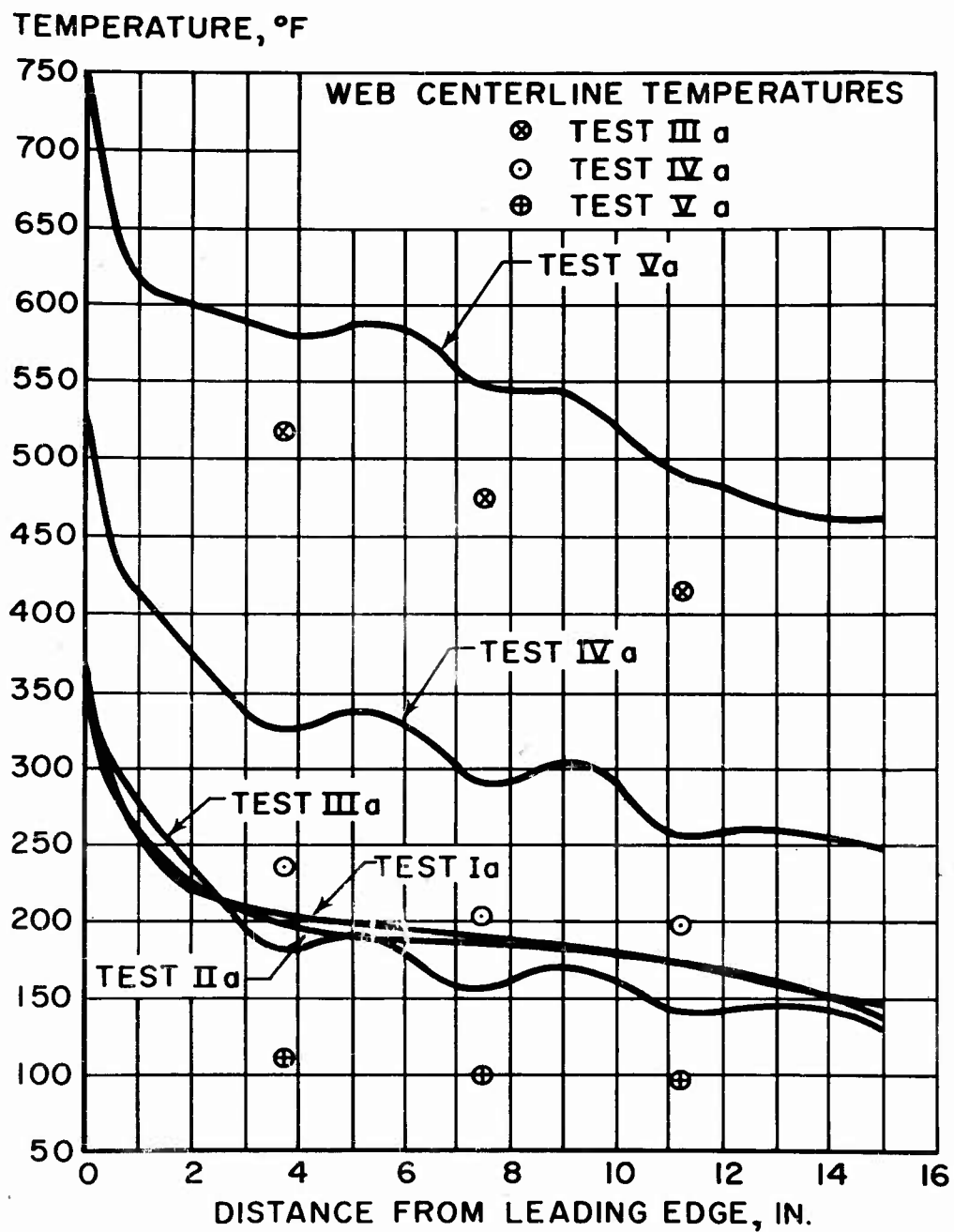
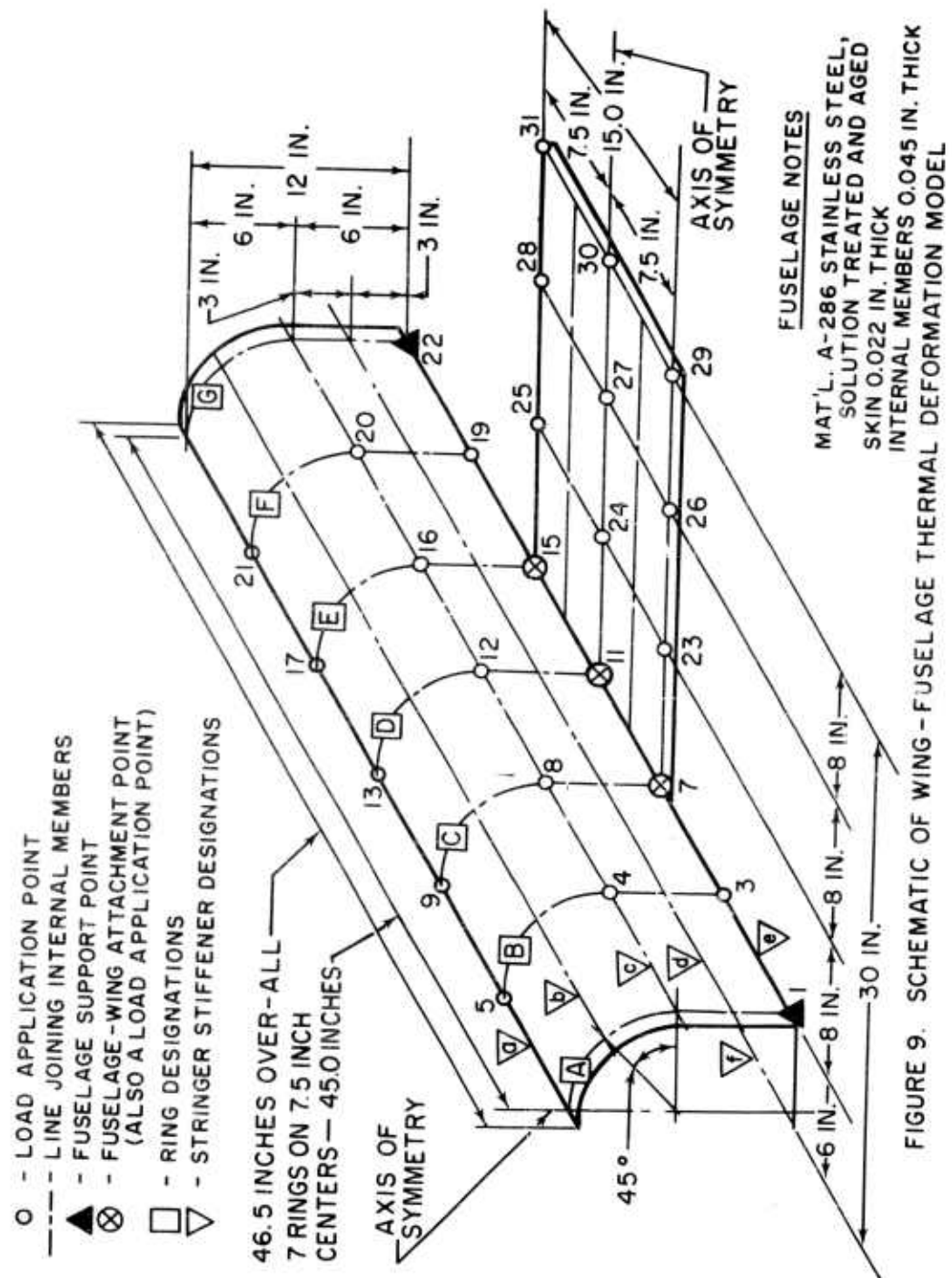


FIGURE 8. SKIN CHORDWISE TEMPERATURE PROFILES - FIRST HEATED WING MODEL



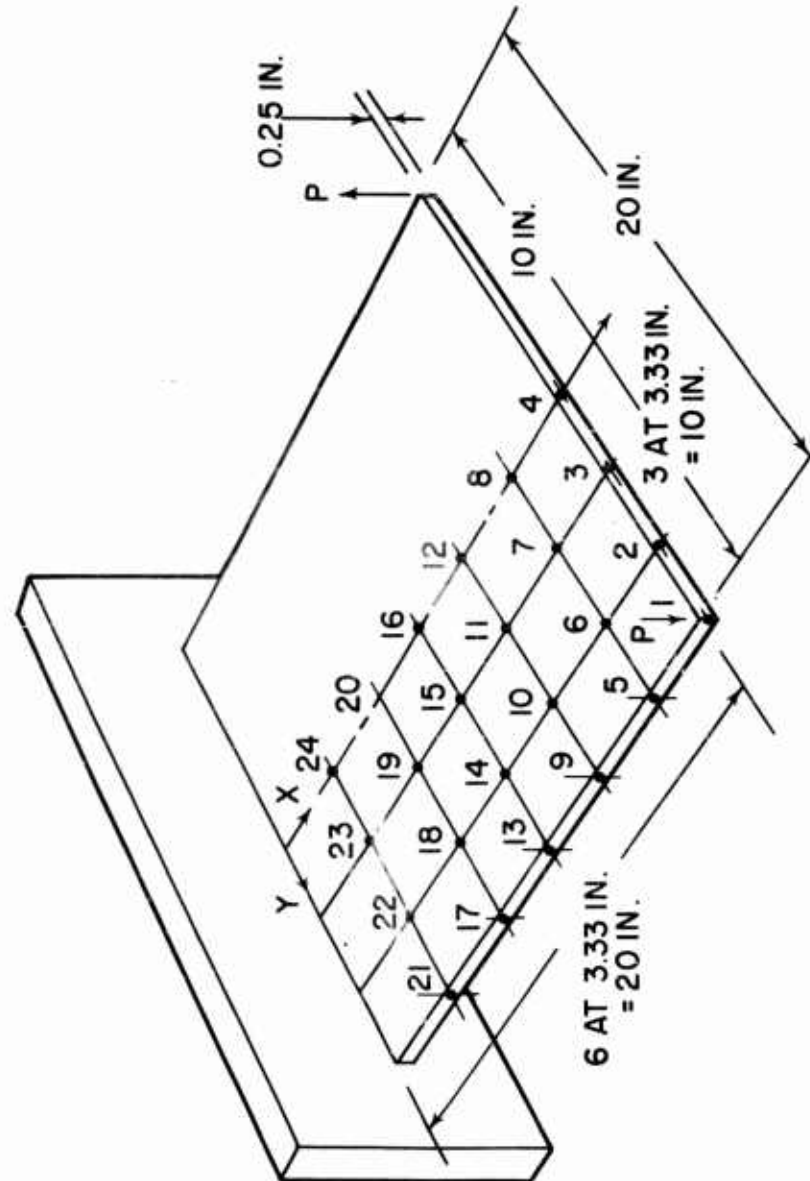


FIGURE 10. CANTILEVER PLATE



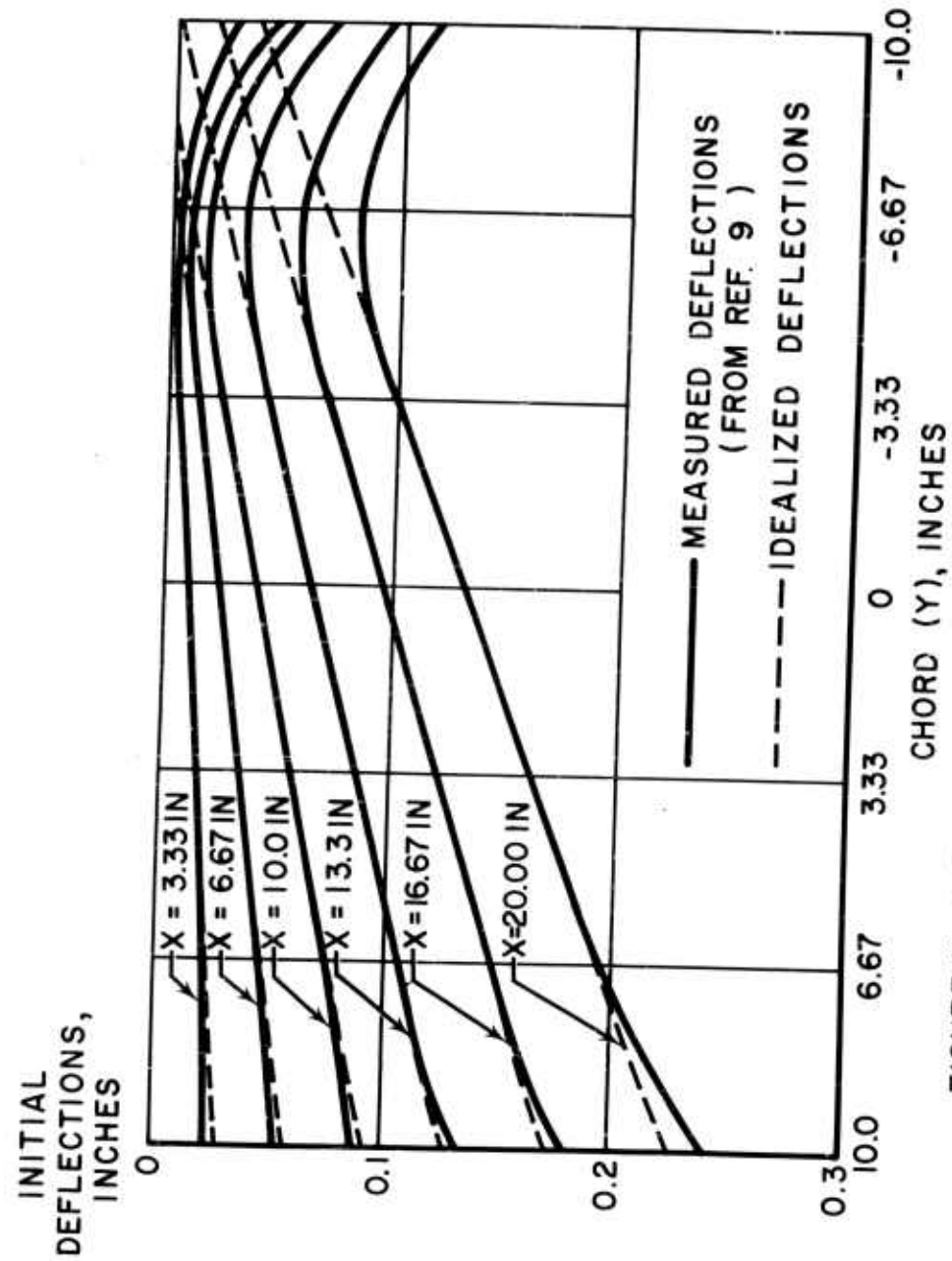


FIGURE 11. INITIAL DISPLACEMENTS-CANTILEVER PLATE

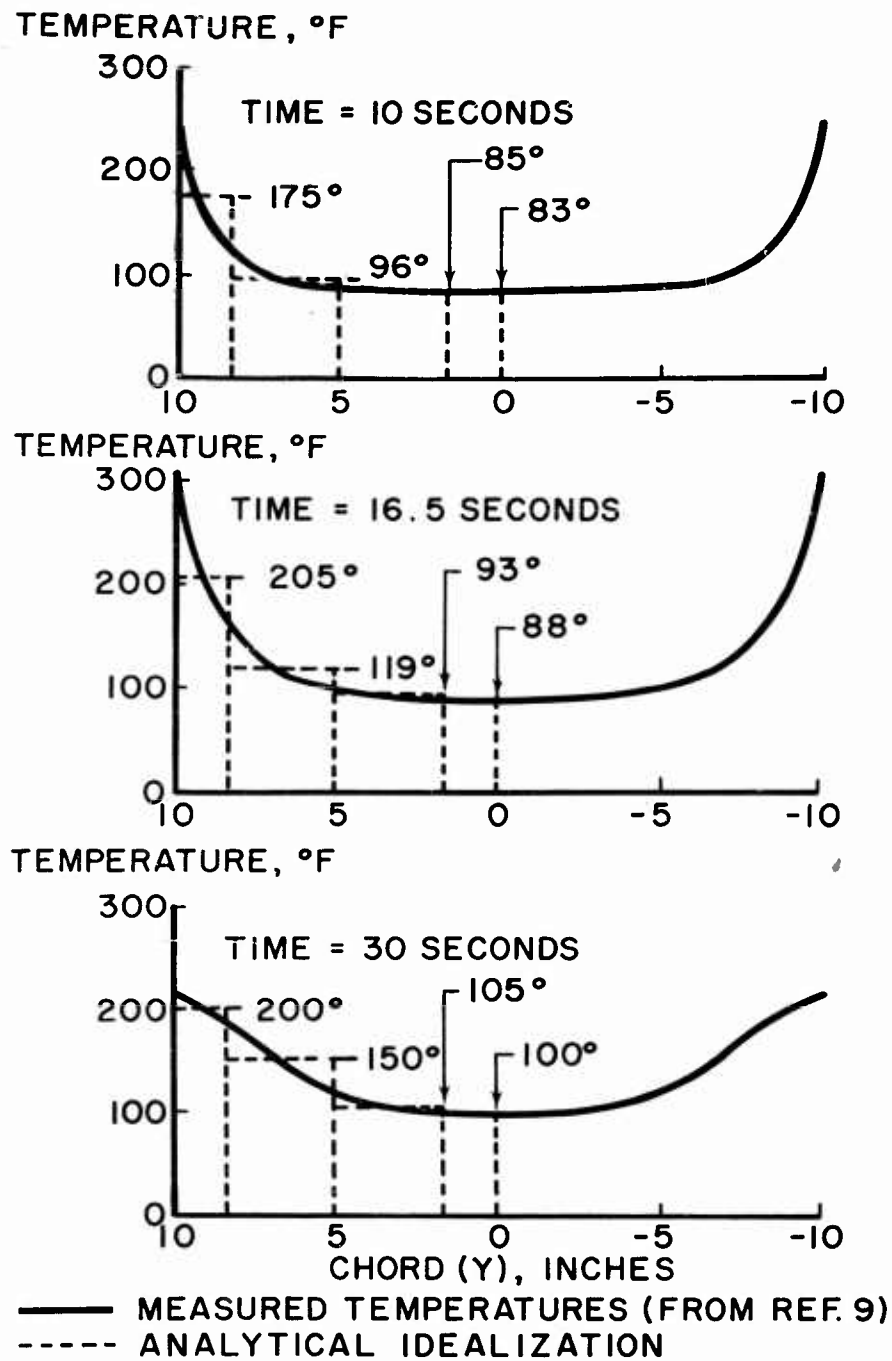


FIGURE 12. TEMPERATURE IDEALIZATIONS—  
CANTILEVER PLATE

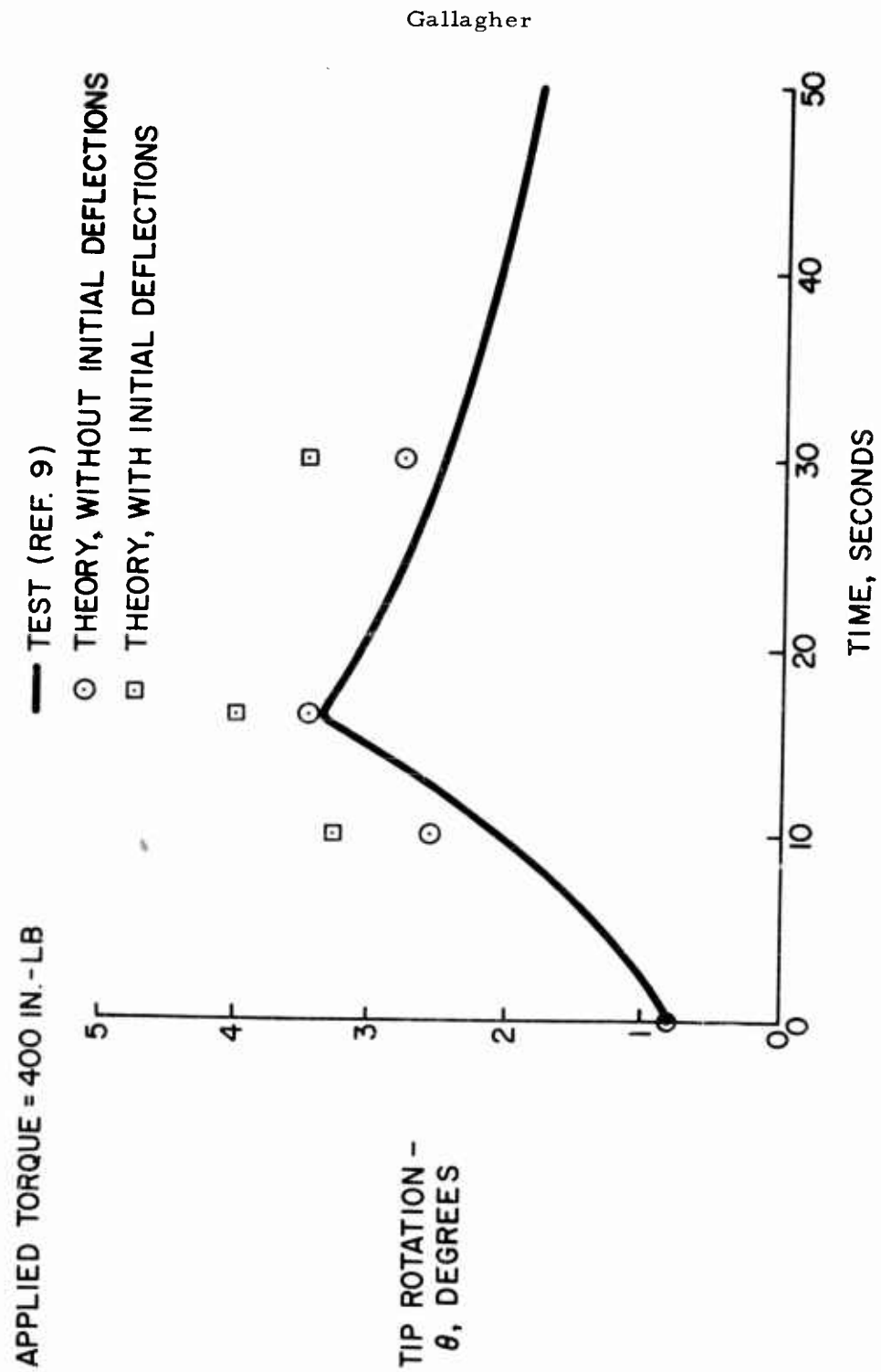


FIGURE 13. RESULTS-HEATED CANTILEVER PLATE

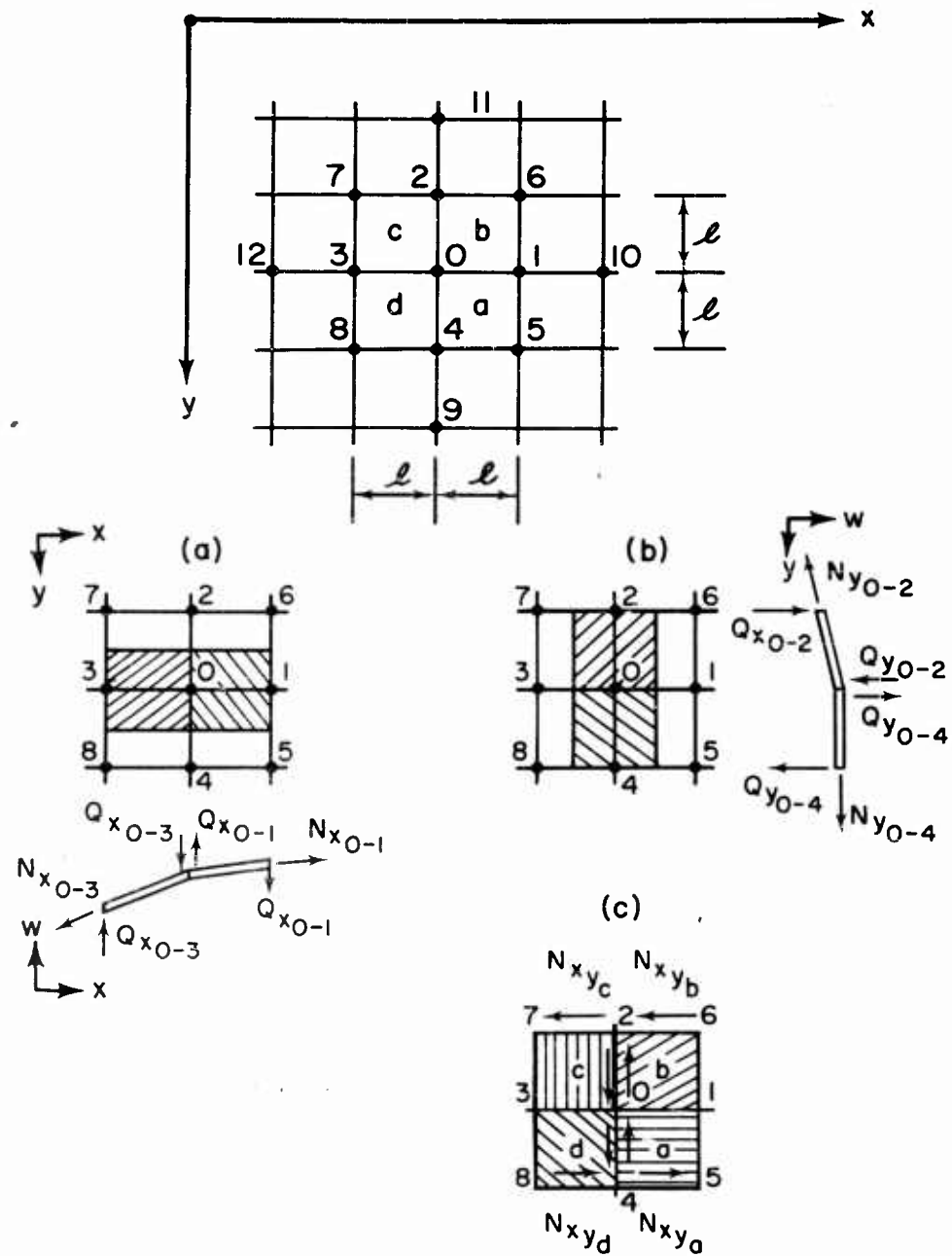


FIGURE 14. TYPICAL REFERENCE POINT ARRAY AND STRUCTURAL IDEALIZATION

Gallagher

TABLE I  
FLEXIBILITY PARAMETERS  
(Values Tabulated Below are in Inches)

Model I	Room Temp.	Case Ia	Case IIa	Case IVa	Case Va
Test	3.668	3.810	3.869	4.006	4.063
Analysis - Mod. Effects Only	3.676	3.779	3.743	3.850	4.036
Analysis Total Effects	3.676	3.784	3.769	3.849	4.022

TABLE II  
PERCENTAGE CHANGES IN FLEXIBILITY PARAMETERS  
DUE TO TEMPERATURE CONDITIONS

	Percentage Changes From Room Temperature Parameter					
	Test			Theory		
	Total Change	Mod. Effects	Other Eff.	Total Change	Mod. Effects	Other Eff.
Case I	3.88	2.41	0.47	2.94	2.79	.15
Case IIa	5.47	2.06	3.41	2.53	1.83	.70
Case IVa	9.23	4.47	4.76	4.71	4.73	-.02
Case Va	10.78	8.59	2.19	9.42	9.88	-.46

TABLE III  
COMPARISON OF TEST AND THEORY FLEXIBILITY  
PARAMETER CHANGES DUE TO TEMPERATURE  
RATIO OF ANALYTICAL AND TEST PARAMETER CHANGES

	Total Change Ratio	Ratio of Change Due to Other Eff.	Ratio of Change Due to Mod. Eff.
Case Ia	.76	.32	1.16
Case IIa	.46	.21	0.89
Case IVa	.51	.00	1.06
Case Va	.87	-.21	1.15

APPENDIX

Let it be assumed for the conditions discussed that the wing is planar, loaded normal to the plane, and experiences a temperature variation chordwise, spanwise, and throughout the depth. Restricting the analysis to the pair of skins or to an equivalent plate that accounts for the stiffness of internal members, the approach considers the structure to be representable by axial stress carrying and shear carrying segments. Direct stress carrying segments exist in both the x and y directions (see Figure 14), lying between successive reference points. The geometric and material properties are assumed constant within each element.

Based on the actual temperature distribution, certain equivalent temperature characteristics must be defined. For the intervals, the average temperatures ( $T_x$  and  $T_y$ ) must be evaluated. Other equivalent temperature characteristics, the thermal curvatures ( $\lambda_x$  and  $\lambda_y$ ), are defined at the reference points. A thermal curvature is that due to a depthwise temperature gradient alone, and is calculated as follows

$$\lambda = \frac{12\alpha}{t^3} \int_{-\frac{t}{2}}^{\frac{t}{2}} T \tau d\tau \quad (A-1)$$

The coordinate  $\tau$  is measured normal to the wing midplane and  $t$  is the thickness of an equivalent solid plate.

Because it is characteristic of plate analysis to consider distinct in-plane and out-of-plane behaviors, it is possible to formulate one group of relationships between midplane forces and displacements, and another group between the loads and displacements normal to the plane. Consider first, the behavior normal to the plane. The vertical shears,  $Q_x$  and  $Q_y$ , are taken as constant in each axial stress element. The axial element forces,  $N_x$  and  $N_y$ , and shear element forces,  $N_{xy}$ , are each constant within the respective elements. The net upward value of the shears at point O, expressed in terms of reference point deflections, forms a contribution to the equilibrium of the applied load  $P_{z0}$ . (Under distributed load conditions,  $P_{z0} = q_0 l^2$ , where  $q_0$  is the average intensity of distributed load on the area subtended by point O).

The net upward force is

$$\ell(Q_{x_{0-1}} - Q_{x_{0-3}}) - \ell(Q_{y_{0-4}} - Q_{y_{0-2}})$$

where, for example

$$Q_{x_{0-1}} = D \frac{\partial}{\partial x} \left( \frac{\partial^2 W}{\partial x^2} + \frac{\partial^2 W}{\partial y^2} + \lambda_x + \nu \lambda_y \right) \quad (A-2)$$

and, in terms of finite difference approximations to the differentials

$$Q_{x_{0-1}} = \frac{D}{\ell^3} \left\{ 5W_0 - 5W_1 - W_2 - W_3 - W_4 + W_5 \right. \\ \left. + W_6 + W_{10} \right\} + \ell^2 \left\{ \lambda_{x_1} - \lambda_{x_0} + \nu \lambda_{y_1} - \nu \lambda_{y_0} \right\} \quad (A-3)$$

The plate flexural rigidity ( $D = Et^3/12(1-\nu^2)$ ) can be taken as the value at point 0, or consistent with the wing average temperature. This parameter actually varies from point to point and inclusion in this form would appear in a more exact development. Its effects should be insignificant, however.

The midplane forces also contribute to the equilibration of  $P_{z_0}$ . As indicated by Figure 14b, the differences in value and inclination between  $N_{y_{0-2}}$  and  $N_{y_{0-4}}$  result in a net upward component

$$N_{y_{0-2}}(W_0 - W_2) - N_{y_{0-4}}(W_4 - W_0)$$

Similarly (Figure 14a), the  $N_x$  forces contribute a net upward force of

$$N_{x_{0-3}}(W_0 - W_3) - N_{x_{0-1}}(W_1 - W_0)$$

and the shear forces have an upward component

$$0.5 \left[ (N_{xy_a} + N_{xy_c} - N_{xy_b} - N_{xy_d}) W_0 - N_{xy_a} W_5 \right. \\ \left. + N_{xy_b} W_6 - N_{xy_c} W_7 + N_{xy_d} W_8 \right]$$

Thus, the complete expression for  $P_{z_0}$  is

$$P_{z_0} = \left( \frac{20D}{\ell^2} + N_{x_{0-1}} + N_{y_{0-2}} + N_{x_{0-3}} + N_{y_{0-4}} \right. \\ \left. + \frac{N_{xy_a}}{2} + \frac{N_{xy_c}}{2} - \frac{N_{xy_b}}{2} - \frac{N_{xy_d}}{2} \right) W_0 - \left( \frac{8D}{\ell^2} + N_{x_{0-1}} \right) W_1 \\ - \left( \frac{8D}{\ell^2} + N_{y_{0-2}} \right) W_2 - \left( \frac{8D}{\ell^2} + N_{x_{0-3}} \right) W_3 - \left( \frac{8D}{\ell^2} + N_{y_{0-4}} \right) W_4 \\ + \left( \frac{2D}{\ell^2} - \frac{N_{xy_a}}{2} \right) W_5 + \left( \frac{2D}{\ell^2} + N_{xy_b} \right) W_6 + \left( \frac{2D}{\ell^2} - N_{xy_c} \right) W_7 \\ + \left( \frac{2D}{\ell^2} + N_{xy_d} \right) W_8 + \frac{D}{\ell^2} (W_9 + W_{10} + W_{11} + W_{12}) \\ + D \left\{ (\lambda_{x_1} + \lambda_{y_2} + \lambda_{x_3} + \lambda_{y_4}) - 2(1+\nu)(\lambda_{x_0} + \lambda_{y_0}) \right. \\ \left. + \nu(\lambda_{y_1} + \lambda_{x_2} + \lambda_{y_3} + \lambda_{x_4}) \right\} \quad (A-4)$$



A similar equation can be written for each loaded point. A full set of equations for the complete structure is, in matrix form,

$$\{P_z\} = \left[ [K_z] + [N] \right] \{w\} + \{\lambda\} \quad (A-5)$$

Here,  $[K_z]$  is the familiar plate flexure stiffness matrix,  $[N]$  represents terms dependent on  $N_x$ ,  $N_y$ , and  $N_{xy}$ , and  $\{\lambda\}$  is the column of values due to the thermal curvatures. Equation A-5 is identical to Equation (4) of the text.

Three mechanisms can contribute to the development of midplane stresses: (1) Externally applied midplane forces, (2) nonlinear chordwise and spanwise temperature gradients, and (3) the midplane strains arising in consequence of the deflections of such a nondevelopable surface. As discussed in Paragraph 2c, if this last effect is significant enough to merit attention, the problem is nonlinear.

The disregard of explicit compatibility conditions for regions between reference points and their satisfaction at the reference characterizes the approach to the solution for midplane behavior. For an arbitrary plate element, the usual stress-strain, strain-displacement, and equilibrium relationships yield

$$N_x = \frac{Et}{(1-\nu^2)} \left[ \frac{\partial u}{\partial x} + \nu \frac{\partial v}{\partial y} \right] - \frac{Et\alpha T}{(1-\nu)} \quad (A-6)$$

$$+ \frac{Et}{2(1-\nu^2)} \left[ \left( \frac{\partial w}{\partial x} \right)^2 + \nu \left( \frac{\partial w}{\partial y} \right)^2 \right]$$

$$N_y = \frac{Et}{(1-\nu^2)} \left[ \frac{\partial v}{\partial y} + \nu \frac{\partial u}{\partial x} \right] - \frac{Et\alpha T}{(1-\nu)} \quad (A-7)$$

$$+ \frac{Et}{2(1-\nu^2)} \left[ \left( \frac{\partial w}{\partial y} \right)^2 + \nu \left( \frac{\partial w}{\partial x} \right)^2 \right]$$

$$N_{xy} = \frac{Et}{2(1+\nu)} \left[ \frac{\partial u}{\partial y} + \frac{\partial v}{\partial x} + \frac{\partial w}{\partial x} \frac{\partial w}{\partial y} \right] \quad (A-8)$$

where the first derivatives in  $w$  represent the effects of large deflections on the stretching of the middle surface of the wing. Next, consider equilibrium at point 0 with respect to an applied load.

. In equation form, one can write (see Figure 14).

$$\begin{aligned} P_{x0} &= \ell (N_{x_{net}} - N_{xy_{net}})_0 \\ &= \ell (N_{x_{0-3}} - N_{x_{0-1}}) + \frac{\ell}{2} (N_{xy_b} + N_{xy_c} - N_{xy_d} - N_{xy_a}) \quad (A-9) \end{aligned}$$

Equations (A-6) and (A-8) are then substituted in Equation (A-9) and, after applying finite difference approximations, the result is

$$\begin{aligned} P_{x0} &= \frac{Et}{(1-\nu^2)} \left\{ \left[ 2 + \frac{(1-\nu)}{2} \right] u_0 - \left[ 1 - \frac{(1-\nu)}{4} \right] u_1 - \frac{(1-\nu)}{4} u_2 - \left[ 1 - \frac{(1-\nu)}{4} \right] u_3 \right. \\ &\quad \left. - \frac{(1-\nu)}{4} u_4 - \frac{(1-\nu)}{8} (u_5 + u_6 + u_7 + u_8) - \left[ \frac{\nu}{4} + \frac{(1-\nu)}{8} \right] (v_5 - v_6 + v_7 - v_8) \right. \\ &\quad \left. + (1+\nu) \alpha \ell (T_{x_{0-1}} - T_{x_{0-3}}) - \frac{1}{2\ell} \left[ (w_1 - w_0)^2 - (w_0 - w_3)^2 \right] \right. \\ &\quad \left. + \frac{(1-\nu)}{16\ell} \left[ (w_1 + w_6 - w_2 - w_0)(w_1 + w_0 - w_2 - w_6) \right. \right. \\ &\quad \left. \left. + (w_0 + w_2 - w_7 - w_3)(w_0 + w_3 - w_2 - w_1) - (w_1 + w_5 - w_0 - w_4) \right] \right\} \quad (A-10) \end{aligned}$$

$$(W_4 + W_5 - W_0 - W_1) - (W_0 + W_4 - W_3 - W_8)(W_8 + W_4 - W_0 - W_3) \\ - \frac{2l}{32l} \left[ (W_4 + W_5 - W_2 - W_6)^2 - (W_4 + W_8 - W_2 - W_7)^2 \right]$$

A similar equation can be written for equilibrium with respect to applied loads  $P_y$  and for all points in the x and y directions. The complete set of equations, when assembled, will be of the form

$$\{P_x, P_y\} = [K_{xy}] \{u, v\} + \{T_x, T_y\} \\ + \{P_{\Delta W_x}, P_{\Delta W_y}, P_{\Delta W_{xy}}\} \quad (A-11)$$

The thermal and large deflection "loadings",  $\{T_x, T_y\}$  and  $\{P_{\Delta W_x}, P_{\Delta W_y}, P_{\Delta W_{xy}}\}$ , result from corresponding terms in Equations (A-6) through (A-8). Solving Equation (A-11) yields

$$\{u, v\} = [K_{xy}]^{-1} \left[ \{F_x, F_y\} - \{T_x, T_y\} \right. \\ \left. - \{P_{\Delta W_x}, P_{\Delta W_y}, P_{\Delta W_{xy}}\} \right] \quad (A-12)$$

The  $\{u, v\}$  displacements can then be used in Equations (A-6) through (A-8) to effect solutions for  $N_x, N_y, \& N_{xy}$ .

Techniques for solving the entire problem (i.e., both Equations (A-5) and (A-11), in combination), are discussed in Paragraph II.f of this paper.

## AN APPROACH TO THE THERMAL STIFFNESS PROBLEM

L. J. Topp, D. L. Grande, R. R. June, and C. D. Newsom  
Boeing Airplane Company  
Wichita, Kansas

A method is developed for calculating stiffness influence coefficients of plate and stringer type structures with arbitrary boundary conditions, loads, and steady-state temperature distributions. Plate-type elements are approximated by a lattice network of axially loaded members. Increasing the fineness of the lattice network improves the accuracy of results. The method is well suited for use with automatic digital computing equipment.

The method is illustrated by application to a simple truss and a rectangular flat plate.

### SYMBOLS

$A$  = cross-sectional area, in.<sup>2</sup>  
 $c$  = specific heat capacity, in.-lb/in.<sup>3</sup>-deg F  
 $c_L$  = specific heat capacity at constant length, in.-lb/in.<sup>3</sup>-deg F  
 $c_p$  = specific heat capacity at constant pressure, in.-lb/in.<sup>3</sup>-deg F  
 $E$  = modulus of elasticity, lb/in.<sup>2</sup>  
 $E_s$  = isentropic modulus of elasticity, lb/in.<sup>2</sup>  
 $E_T$  = isothermal modulus of elasticity, lb/in.<sup>2</sup>  
 $F$  = force, lb  
 $[K]$  = matrix of thermomechanical stiffness influence coefficients  
 $[K_0]$  = matrix of isothermal stiffness influence coefficients  
 $Q$  = heat flow, in.-lb  
 $S$  = entropy, in.-lb/deg F  
 $T$  = absolute temperature, deg R  
 $T_r$  = reference temperature, deg R  
 $t$  = plate thickness, in.  
 $u, v$  = displacement in x and y directions, respectively  
 $V$  = volume, in.<sup>3</sup>  
 $\alpha$  = linear coefficient of thermal expansion, in./in.-deg F

$\delta$  = displacement, in.  
 $\Theta$  = temperature increment above a reference temperature, deg F  
 $\lambda, \mu$  = direction cosines  
 $\nu$  = Poisson's ratio

## (1) INTRODUCTION

High-speed flight presents to the structural dynamicist many real and practical problems that were only of academic interest a few years ago. Among these is the problem of determining the effects of elevated temperature on the elastic behavior of aircraft structures. Such knowledge is necessary for vibration and flutter analyses, static and dynamic load calculations, and analyses of stability and control.

This paper presents a method for determining the stiffness of complex structures subjected to elevated temperatures as well as conventional loads. The method utilizes simple input data to develop simultaneous equations in matrix form that are easily solved with automatic digital computing equipment.

The method of direct stiffness calculation as presented by Turner, et al. [1] has proved very useful in isothermal analysis of complex elastic structures. The direct stiffness method satisfies the basic conditions of continuity and equilibrium at selected node points on the structure. This type of analysis neglects the small reciprocal coupling between temperature and deformation. Classical thermodynamics, however, shows that under certain conditions a change of temperature produces a deformation and, in turn, a deformation produces a change in temperature.

A more rigorous formulation of the direct stiffness relations would include the reciprocal coupling of deformations and temperatures. This coupling, which is usually quite small for structural applications, becomes a valuable tool for use in the analysis of thermally affected structures. Consideration of this coupling in the analysis of temperature induced stresses has been presented by Biot [2].

The thermomechanical stiffness relation for a heated elastic system is obtained by introducing the concept of entropy "displacement". The entropy displacement is defined such that the temperature at a point in the system may be considered the conjugate "force", i.e. the scalar product of entropy displacement and temperature force represents energy the same way that the scalar product of displacement and force represents energy. Because of the reciprocal coupling relations, a temperature applied at some point on the elastic system produces a mechanical displacement at some other point on the system. For this case temperature is analogous to force and the mechanical displacement is its conjugate. An entropy displacement can also occur

if a mechanical force is applied such that the deformation is isothermal. In this case the entropy is the displacement while the force is its conjugate.

The thermomechanical stiffness matrix is defined in the same way as the isothermal stiffness matrix. That is, the force coefficients for all points are determined by imposing a unit displacement at a particular point while requiring zero displacements at all other points. Therefore, the thermomechanical stiffness matrix has the form

$$\begin{bmatrix} F \\ \Theta \end{bmatrix} = \begin{bmatrix} K_{11} & K_{12} \\ K_{21} & K_{22} \end{bmatrix} \begin{bmatrix} \delta \\ S \end{bmatrix} \quad (1)$$

where

$F$  is the column matrix of mechanical forces;

$\Theta$  is the temperature column matrix;

$\delta$  is the mechanical displacement column matrix;

$S$  is the entropy displacement column matrix.

It is apparent from the form of the thermomechanical stiffness matrix that the  $K_{11}$  and  $K_{21}$  submatrices must be determined for the isentropic case. The elements of  $K_{12}$  and  $K_{22}$  must be determined for the case where all mechanical displacements are equal to zero. A necessary condition for the conservation of energy is that the matrix be symmetrical. In obtaining these relations reference will be made to the work of Parkes [3], particularly in connection with the uniaxial stress system.

It has been common practice to use truss-type structures to evaluate new methods since trusses lend themselves to simple and quick solutions. It is possible to use trusses to approximate plate elements through the use of the lattice analogy. This paper combines the truss analogy and the thermomechanical relations for the analysis of heated, built up structures. The thermomechanical stiffness relations for uniaxial members are developed in the following section. Sections (3) and (4) show the application of this method to a simple truss and a heated plate.

(2) DEVELOPMENT OF THE THERMOMECHANICAL STIFFNESS MATRIX

The direct stiffness method, as given by Turner [1], has force deflection relations of the form

$$\{F\} = [K_0] \{\delta\}$$

where

$\{F\}$  is a column matrix of external forces;  
 $[K_0]$  is the matrix of stiffness influence coefficients;  
 $\{\delta\}$  is a column matrix of displacements.

The following discussion expands this method to include the effects of structural heating. Material properties are assumed to be independent of temperature; the method is, however, readily adaptable to the case of temperature dependent properties.

The submatrices  $K_{11}$ ,  $K_{12}$ ,  $K_{21}$ , and  $K_{22}$  in Eq. (1) are defined as follows:

$K_{11}$  is the coupling between force and displacement at constant entropy;

$K_{12}$  is the coupling between force and entropy at constant length;

$K_{21}$  is the coupling between temperature and displacement at constant entropy;

$K_{22}$  is the coupling between temperature and entropy at constant length.

The coupling between force and displacement at constant entropy is given by

$$K_{11} = f \left( \frac{AE_s}{L} \right) \quad (2)$$

Parkes [3] has derived an expression for the isentropic modulus of

elasticity in terms of the isothermal modulus. The relation is

$$\frac{E_T}{E_S} = 1 - \frac{E_T \alpha^2 T}{c_p} \quad (3)$$

Submatrix  $K_{12}$ , the coupling between force and entropy at constant length, is derived as follows. If a temperature increment  $\Theta$  above a reference temperature  $T_r$  is applied uniformly and slowly to an incremental volume  $A dx$ , the second law of thermodynamics can be written as

$$dS = \frac{dQ}{T_r} = \frac{Ac \Theta dx}{T_r}$$

Integrating the above expression over the length yields

$$\Delta S = \int_0^L \frac{Ac \Theta}{T_r} dx = \frac{AcL \Theta}{T_r}$$

If the entropy is taken as zero at the reference temperature, then

$$S = \frac{AcL \Theta}{T_r} \quad (4)$$

From the definitions of  $\alpha$  and  $E_T$ ,

$$\delta = \alpha L \Theta = \frac{FL}{AE_T}$$

and

$$\Theta = \frac{F}{AE_T \alpha} \quad (5)$$

Substituting the value of  $\Theta$  from Eq. (5) in Eq. (4) and solving for  $F$  yields

$$F = \frac{E_T \alpha T_r}{L c} S \quad (6)$$

The elastic modulus in Eq. (6) must be  $E_T$  since a change in entropy is specified. The process occurs at constant length and requires use of a specific heat capacity defined for this process. Parkes [3]



derives such a specific heat capacity, in terms of the constant pressure heat capacity, for a uniaxial stress system. The relation between  $c_L$  and  $c_p$  is the same as between  $E_T$  and  $E_S$ , or

$$\frac{c_L}{c_p} = 1 - \frac{E_T \alpha^2 T}{c_p}$$

Eq. (6) is thus

$$F = \frac{E_T \alpha T_r}{L c_L} S$$

and

$$K_{12} = F \left( \frac{E_T \alpha T_r}{L c_L} \right) \quad (7)$$

The submatrix  $K_{21}$  represents the temperature change due to isentropic deformation. This relation is obtained by using the Maxwell relation

$$\left( \frac{\partial T}{\partial p} \right)_S = \left( \frac{\partial V}{\partial S} \right)_p \quad (8)$$

Eq. (8) is obtained from the definition of enthalpy and the theorem of the exact differential. For the stringer, deformation at constant pressure is assumed to occur along the longitudinal axis of the stringer with the cross-sectional area remaining constant. This assumption is the same as that made in obtaining the force-deformation relation and hence the force-entropy relation. With this assumption the volume at constant pressure is

$$V_p = AL [1 + \alpha \theta]$$

The relation between entropy and temperature, Eq. (4), is used to express the volume at constant pressure in terms of the entropy, or

$$V_p = AL \left[ 1 + \frac{\alpha T_r}{AL c_p} S \right]$$

Performing the operation indicated on the right hand side of Eq. (8) gives

$$\left(\frac{\partial V}{\partial S}\right)_P = \frac{\alpha T_r}{c_p} \quad (9)$$

By specifying an isentropic process and by making use of Eq. (9), Eq. (8) may be rearranged and put in integral form to give

$$\int_{T_r}^T dT = \int_0^P \frac{\alpha T_r}{c_p} dP \quad (10)$$

Treating  $\alpha$  and  $c_p$  as being independent of the pressure (stress) and by using the relation for uniaxial stress,  $P = F/A$ , Eq. (10) yields

$$T - T_r = \theta = \frac{\alpha T_r F}{c_p A} \quad (11)$$

For an isentropic deformation the force-deformation relation is given by

$$F = \frac{AE_s}{L} \delta$$

Using this relation for  $F$  in Eq. (11) gives the desired expression for temperature due to isentropic deformation

$$\theta = \frac{E_s \alpha T_r}{L c_p} \delta \quad (12)$$

Therefore

$$K_{21} = f \left( \frac{E_s \alpha T_r}{L c_p} \right) \quad (13)$$

Since

$$\frac{E_T}{E_s} = \frac{c_L}{c_p} = 1 - \frac{E_T \alpha^2 T}{c_p}$$

then

$$\frac{E_T}{c_L} = \frac{E_S}{c_P} \quad (14)$$

and from Eqs. (7), (13), and (14) it is obvious that the thermo-mechanical matrix in Eq. (1) is symmetrical. This is a necessary condition for energy to be conserved during any loading and unloading sequence.

The submatrices  $K_{11}$ ,  $K_{12}$ , and  $K_{21}$  are determined from Eqs. (2), (7), and (13). Submatrix  $K_{22}$  may be determined from Eq. (4) by specifying a zero deformation process (constant length). Eq. (1) then has the form

$$\begin{Bmatrix} F \\ \Theta \end{Bmatrix} = \begin{bmatrix} f \left( \frac{A E_S}{L} \right) & f \left( \frac{E_T \alpha T_r}{L c_L} \right) \\ f \left( \frac{E_S \alpha T_r}{L c_P} \right) & f \left( \frac{T_r}{A L c_L} \right) \end{bmatrix} \begin{Bmatrix} \delta \\ S \end{Bmatrix} \quad (15)$$

The individual elements of the submatrices in Eq. (15) are determined by the geometry and boundary conditions of the system. A simple example is presented to illustrate the method.

Consider the stringer of length  $L$  and cross-sectional area  $A$  shown in Fig. 1.

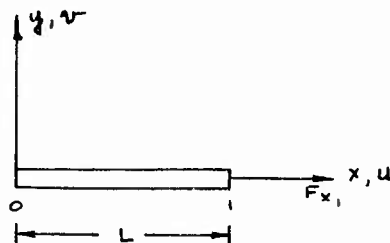


Fig. 1. Stringer.

Assume that the stringer is fixed at the origin and is axially loaded in the  $x$ -direction. The sign conventions used are:

1. A positive force is one that causes a positive displacement in the coordinate system shown.

- 2.. A positive temperature difference, i.e. an applied temperature that is above a reference temperature, causes a positive entropy displacement. It should be noted that the applied temperature and the associated entropy displacement are scalars.

The thermomechanical stiffness relation for the system of Fig. 1 is

$$\begin{Bmatrix} F_{x_0} \\ F_{y_0} \\ F_{x_1} \\ F_{y_1} \\ \hline \theta_{o_1} \end{Bmatrix} = \begin{bmatrix} \frac{AE_s}{L} & 0 & -\frac{AE_s}{L} & 0 & \frac{E_T \alpha T_r}{L c_L} \\ 0 & 0 & 0 & 0 & 0 \\ -\frac{AE_s}{L} & 0 & \frac{AE_s}{L} & 0 & -\frac{E_T \alpha T_r}{L c_L} \\ 0 & 0 & 0 & 0 & 0 \\ \hline \frac{E_s \alpha T_r}{L c_p} & 0 & -\frac{E_s \alpha T_r}{L c_p} & 0 & \frac{T_r}{A L c_L} \end{bmatrix} \begin{Bmatrix} u_0 \\ v_0 \\ u_1 \\ v_1 \\ \hline s_{o_1} \end{Bmatrix} \quad (16)$$

Boundary conditions are imposed by striking out rows and columns corresponding to zero displacements. Thus,

$$\begin{Bmatrix} F_{x_1} \\ \theta_{o_1} \end{Bmatrix} = \begin{bmatrix} \frac{AE_s}{L} & -\frac{E_T \alpha T_r}{L c_L} \\ -\frac{E_s \alpha T_r}{L c_p} & \frac{T_r}{A L c_L} \end{bmatrix} \begin{Bmatrix} u_1 \\ s_{o_1} \end{Bmatrix} \quad (17)$$

Solving Eq. (17) for displacements gives

$$u_1 = \left[ \frac{AE_s}{L} \left( 1 - \frac{E_T \alpha^2 T_r}{c_p} \right) \right]^{-1} \left[ F_{x_1} + E_T \alpha A \theta_{o_1} \right] \quad (18)$$

The substitution of Eq. (3) in Eq. (18) gives

$$u_1 = \frac{L}{AE_T} \left( F_{x_1} + E_T \alpha A \theta_{o_1} \right) \quad (19)$$

For the isothermal case with an applied load, Eq. (19) yields

$$u_1 = \frac{L}{AE_T} F_{x_1}$$

which is in agreement with simple theory. For the case of an applied temperature and no external load, Eq. (19) yields

$$u_1 = \alpha L \theta$$

which is also in agreement with simple theory.

The ratios  $E_T/E_s$  and  $c_I/c_p$  for a typical aluminum alloy at room temperature are about 0.996. While the difference from unity is negligible for most computational purposes, and indeed, available material property values may not be of this accuracy, the concept of the thermomechanical stiffness relation requires cognizance of the distinction. The ratios decrease with increasing temperature, however, and may be significantly less than unity at elevated temperatures.

### (3) APPLICATION OF THE THERMOMECHANICAL STIFFNESS MATRIX TO A SIMPLE TRUSS

The truss shown in Fig. 2 is analyzed to illustrate the method of treatment of structures of more than one member. The method used in forming the matrix of stiffness influence coefficients is similar to that described in Reference [1].

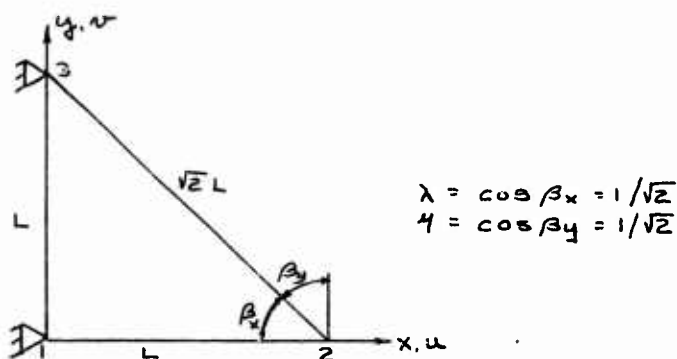


Fig. 2. Simple Truss.

The stiffness relations for members 1-2 and 1-3 of Fig. 2 are found in a manner similar to that used to obtain Eq. (16). The relation for the diagonal member 2-3 is obtained from

$$\begin{Bmatrix} F \\ \Theta \end{Bmatrix} = [\phi]^T [K] [\phi] \begin{Bmatrix} \delta \\ S \end{Bmatrix}$$

where  $[K]$  is of the form of Eq. (16) and

$$[\phi] = \begin{bmatrix} \lambda & -4 & 0 & 0 & 0 \\ 4 & \lambda & 0 & 0 & 0 \\ 0 & 0 & \lambda & -4 & 0 \\ 0 & 0 & 4 & \lambda & 0 \\ 0 & 0 & 0 & 0 & 1 \end{bmatrix}$$

The result for the diagonal member is

$$\begin{Bmatrix} F_{x2} \\ F_{y2} \\ F_{x3} \\ F_{y3} \\ \Theta_{23} \end{Bmatrix} = \frac{1}{2\sqrt{2}} \begin{bmatrix} \frac{AE_s}{L} & -\frac{AE_s}{L} & -\frac{AE_s}{L} & \frac{AE_s}{L} & -\frac{\sqrt{2}E\alpha T_r}{Lc_L} \\ -\frac{AE_s}{L} & \frac{AE_s}{L} & \frac{AE_s}{L} & -\frac{AE_s}{L} & \frac{\sqrt{2}E\alpha T_r}{Lc_L} \\ -\frac{AE_s}{L} & \frac{AE_s}{L} & \frac{AE_s}{L} & -\frac{AE_s}{L} & \frac{\sqrt{2}E\alpha T_r}{Lc_L} \\ \frac{AE_s}{L} & -\frac{AE_s}{L} & -\frac{AE_s}{L} & \frac{AE_s}{L} & -\frac{\sqrt{2}E\alpha T_r}{Lc_L} \\ -\frac{\sqrt{2}E\alpha T_r}{Lc_p} & \frac{\sqrt{2}E\alpha T_r}{Lc_p} & \frac{\sqrt{2}E\alpha T_r}{Lc_p} & -\frac{\sqrt{2}E\alpha T_r}{Lc_p} & \frac{2T_r}{ALc_L} \end{bmatrix} \begin{Bmatrix} u_2 \\ v_2 \\ u_3 \\ v_3 \\ S_{23} \end{Bmatrix}$$

The thermomechanical stiffness relation for the truss is obtained by adding corresponding elements of individual members. The resulting 9 x 9 matrix is the complete thermomechanical stiffness matrix and it is necessary to apply the appropriate boundary conditions to this matrix for static equilibrium. This is accomplished by eliminating the rows and columns corresponding to the truss support of

$$u_1 = v_1 = u_3 = v_3 = 0$$

With these boundary conditions imposed, the resulting matrix is

$$\begin{Bmatrix} F_{x_2} \\ F_{y_2} \\ \theta_{12} \\ \theta_{23} \end{Bmatrix} = \begin{bmatrix} \frac{AE_s}{L} \left(1 + \frac{1}{2\sqrt{2}}\right) & -\frac{AE_s}{L} \frac{1}{2\sqrt{2}} & -\frac{E\alpha Tr}{Lc_L} & -\frac{E\alpha Tr}{Lc_L} \frac{1}{2} \\ -\frac{AE_s}{L} \frac{1}{2\sqrt{2}} & \frac{AE_s}{L} \frac{1}{2\sqrt{2}} & 0 & \frac{E\alpha Tr}{Lc_L} \frac{1}{2} \\ -\frac{E\alpha Tr}{Lc_p} & 0 & \frac{Tr}{ALc_L} & 0 \\ -\frac{E\alpha Tr}{Lc_p} \frac{1}{2} & \frac{E\alpha Tr}{Lc_p} \frac{1}{2} & 0 & \frac{Tr}{ALc_L} \frac{1}{\sqrt{2}} \end{bmatrix} \begin{Bmatrix} u_2 \\ v_2 \\ s_{12} \\ s_{23} \end{Bmatrix} \quad (21)$$

For a uniform increment of temperature

$$\theta_{12} = \theta_{23} = \theta$$

and

$$F_{x_2} = F_{y_2} = 0$$

Eq. (21) gives

$$u_2 = \alpha L \theta$$

and

$$v_2 = -\alpha L \theta$$

which are in agreement with simple theory. If an external force but no temperature increment is applied to the truss, then

$$u_2 = \frac{L}{AE_T} (F_{x_2} + F_{y_2})$$

and

$$v_2 = \frac{L}{AE_T} \left[ F_{x_2} + F_{y_2} (1 + 2\sqrt{2}) \right]$$

which are also in agreement with simple theory.

## (4) STIFFNESS ANALYSIS OF A FLAT PLATE

The analyses in the previous sections were concerned with uniaxial stress systems in that structural members were assumed to carry loads and deform only along their longitudinal axes. A similar concept was employed in the lattice approximation of a plate developed by Topp [4]. The lattice approximation is applied to the stiffness analysis of a plate with mechanical loading, a plate with temperature gradient, and a plate with temperature gradient and mechanical loading.

A flat plate in plane stress is replaced by the pin jointed lattice shown in Fig. 3. The areas of the rods are determined such that the basic equations of elasticity are satisfied by the lattice approximation to give the same deflections at the corners.

The required areas of these rods are developed in Reference [4] and are

$$A_1 = \frac{t(b^2 - a^2\nu)}{2b(1 - \nu^2)} \quad (22a)$$

$$A_2 = \frac{t(a^2 - b^2\nu)}{2a(1 - \nu^2)} \quad (22b)$$

$$A_3 = \frac{\nu d^3 t}{2ab(1 - \nu^2)} \quad (22c)$$

where  $b > a$

Poisson's ratio is restricted to  $1/3$  in Eqs. (22).

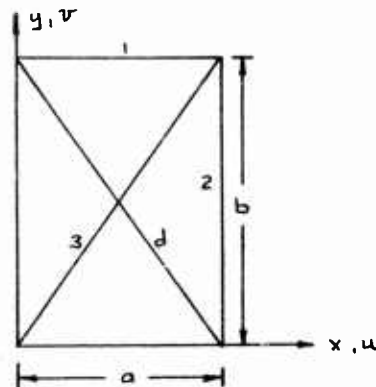


Fig. 3. Lattice Approximation to a Rectangular Plate.



## (a) Stiffness Analysis of a Plate with Mechanical Loading

The plate shown in Fig. 4 was replaced by the lattice network shown in Fig. 5.<sup>1</sup> Only node points 1, 3, 7, and 9 in Fig. 5 were considered in the 4-node method. The deflections due to uniform loading along one edge are tabulated in Table 1.

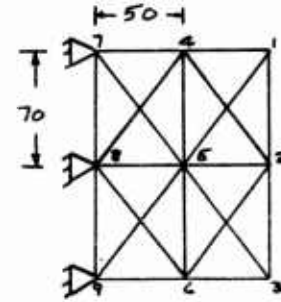
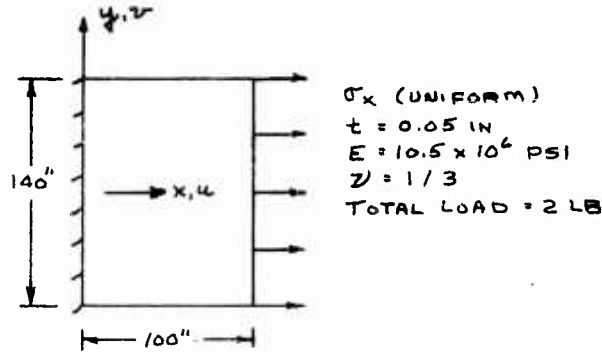


Fig. 4. Clamped Rectangular Plate Subjected to Uniform Tensile Loading.

Fig. 5. Nodes and Supports for Clamped Rectangular Plate.

TABLE 1

Method	Displacements $\times 10^6$ (in.)					
	$u_1$	$u_2$	$u_4$	$u_5$	$v_1$	$v_4$
Relaxation	2.70	2.61	1.39	1.25	-0.686	-0.562
Simple Theory	2.72	2.72	1.36	1.36	-0.635	
Ref. 1 - 4 Node	2.60				-0.740	
Ref. 1 - 9 Node	2.69	2.58	1.36	1.20	-0.680	-0.568
Lattice- 4 Node	2.64				-0.913	
Lattice- 9 Node	2.69	2.60	1.34	1.23	-0.684	-0.606

1. Figs. 4 and 5 and Methods 1 through 4 in Table 1 were taken from Reference [1]. Methods 5 and 6 were taken from Reference [4].

(b) Stiffness Analysis of a Plate with Temperature Gradients

The in-plane displacements of the plate shown in Fig. 6 having the steady state temperature distribution of Fig. 7 were determined.

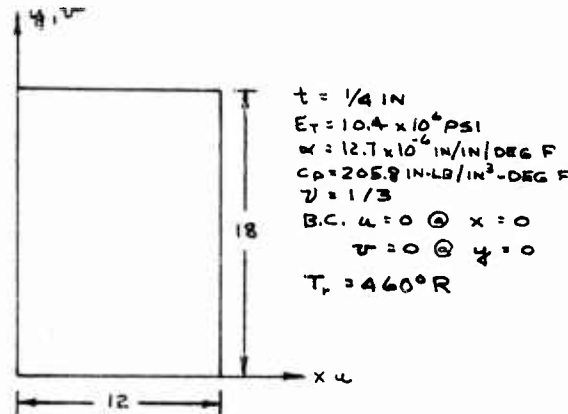


Fig. 6. Rectangular Plate.

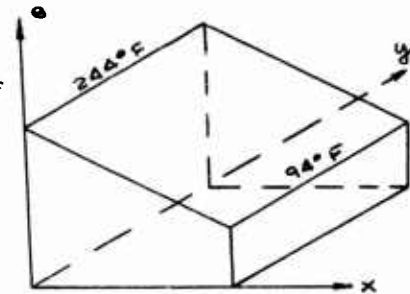


Fig. 7. Temperature Distribution in Rectangular Plate.

As a first approximation, the plate was replaced by the network shown in Fig. 8.

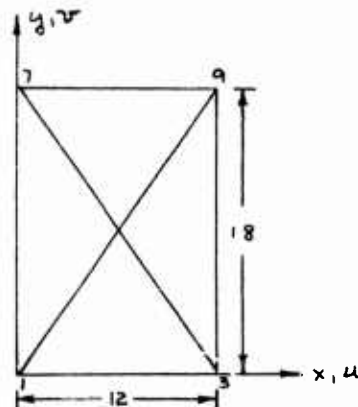


Fig. 8. Four Node Approximation to a Rectangular Plate.

Eq. (15) can be written, for the lattice of Fig. 8, as

$$\begin{Bmatrix} u_3 \\ v_7 \\ u_9 \\ v_9 \\ s_{13} \\ s_{79} \\ s_{17} \\ s_{39} \\ s_{19} \\ s_{37} \end{Bmatrix} = \begin{bmatrix} K_{11} \left( \frac{AE_s}{L} \right) & K_{12} \left( \frac{E_T \alpha T_r}{L c_L} \right) \\ K_{21} \left( \frac{E_s \alpha T_r}{L c_p} \right) & K_{22} \left( \frac{T_r}{A L c_L} \right) \end{bmatrix}^{-1} \begin{Bmatrix} F_{x3} \\ F_{y7} \\ F_{x9} \\ F_{y9} \\ \theta_{13} \\ \theta_{79} \\ \theta_{17} \\ \theta_{39} \\ \theta_{19} \\ \theta_{37} \end{Bmatrix} \quad (23)$$

where  $\theta_{ij}$  is the average temperature difference between member (ij) and the reference temperature.

The inversion of the large matrix of Eq. (23) can be avoided, however, if only mechanical displacements are of interest. Eliminating the entropy from Eq. (15) and solving for displacements gives

$$\begin{Bmatrix} u_3 \\ v_7 \\ u_9 \\ v_9 \end{Bmatrix} = \begin{bmatrix} K_{11} & K_{12} \\ K_{21} & K_{22} \end{bmatrix}^{-1} \begin{Bmatrix} F_{x3} \\ F_{y7} \\ F_{x9} \\ F_{y9} \end{Bmatrix} - \begin{bmatrix} K_{12} \\ K_{22} \end{bmatrix}^{-1} \begin{Bmatrix} \theta_{13} \\ \theta_{79} \\ \theta_{17} \\ \theta_{39} \\ \theta_{19} \\ \theta_{37} \end{Bmatrix} \quad (24)$$

The elements of the submatrices  $K_{11}$ ,  $K_{12}$ ,  $K_{21}$ ,  $K_{22}$  in Eq. (24) require use of the parameters indicated in Eq. (15). A considerable saving of computation time can be realized by the following.

$$\text{Let } \overline{K_{11}} = \overline{K_{11}} - \overline{K_{12}} \overline{K_{22}}^{-1} \overline{K_{21}}$$

By matrix manipulation and the use of Eq. (3), it can be shown that

$$\overline{K_{11}} = \frac{E_T}{E_s} \overline{K_{11}} = f \left( \frac{AE_T}{L} \right)$$

Then Eq. (24) becomes

$$\begin{Bmatrix} u_3 \\ v_7 \\ u_9 \\ v_9 \end{Bmatrix} = [K_{11}]^{-1} \begin{Bmatrix} F_{x3} \\ F_{y7} \\ F_{x9} \\ F_{y9} \end{Bmatrix} - [K_{12}] [K_{22}]^{-1} \begin{Bmatrix} \theta_{13} \\ \theta_{19} \\ \theta_{17} \\ \theta_{39} \\ \theta_{19} \\ \theta_{27} \end{Bmatrix} \quad (25)$$

The cross-sectional areas of the individual members were calculated by use of Eqs. (22). An apparent specific heat capacity was determined for each of the three types of members such that the product of volume and specific heat capacity was the same for all members. The lattice was then made "thermally equivalent" to the plate. This was accomplished by equating the total heat content of the lattice to that of the plate. Submatrix  $[K_{22}]$  is thus reduced to a scalar multiplied by a unit matrix. The submatrices for the conditions shown in Figs. 6, 7, and 8 are

$$[K_{11}] = 10^6 \times \begin{bmatrix} 2.19375 & 0.48750 & 0 & 0 \\ 0.48750 & 0.97500 & 0 & 0 \\ 0 & 0 & 2.19375 & 0.48750 \\ 0 & 0 & 0.48750 & 0.97500 \end{bmatrix} \quad (26)$$

$$K_{21} = K'_{12} = \begin{bmatrix} -70.7304 & 0 & 0 & 0 \\ 0 & 0 & -70.7304 & 0 \\ 0 & -13.8386 & 0 & 0 \\ 0 & 0 & 0 & -13.8386 \\ 0 & 0 & -39.9780 & -59.9670 \\ -39.9780 & -59.9670 & 0 & 0 \end{bmatrix} \quad (27)$$

$$[K_{22}] = 0.24835 \begin{bmatrix} 1 & 0 & 0 & 0 & 0 & 0 \\ 0 & 1 & 0 & 0 & 0 & 0 \\ 0 & 0 & 1 & 0 & 0 & 0 \\ 0 & 0 & 0 & 1 & 0 & 0 \\ 0 & 0 & 0 & 0 & 1 & 0 \\ 0 & 0 & 0 & 0 & 0 & 1 \end{bmatrix} \quad (28)$$

$$\begin{Bmatrix} F_{x3} \\ F_{y7} \\ F_{x9} \\ F_{y9} \end{Bmatrix} = 0 \quad (29)$$

$$\begin{Bmatrix} \theta_{12} \\ \theta_{79} \\ \theta_{17} \\ \theta_{39} \\ \theta_{19} \\ \theta_{27} \end{Bmatrix} = \begin{Bmatrix} 169 \\ 169 \\ 244 \\ 94 \\ 169 \\ 169 \end{Bmatrix} \quad (30)$$

The submatrices of Eqs. (26) through (30) were substituted in Eq. (25) and the indicated operations performed. The results are tabulated in Table 2.

The plate was then replaced by a 9-node and a 25-node lattice.

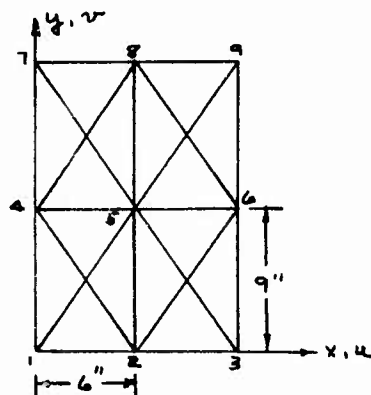


Fig. 9. Node Numbering for Lattice Approximation.

The results of a relaxation solution and 4, 9, and 25-node lattice approximations are tabulated in Table 2. The nodes are numbered as shown in Fig. 9.

TABLE 2				
Displacements $\times 10^2$ (in.)				
	Relaxation	4-Node	9-Node	25-Node
u <sub>2</sub>	1.59		1.60	1.59
u <sub>3</sub>	2.48	2.47	2.49	2.49
v <sub>4</sub>	2.12		2.07	2.12
u <sub>5</sub>	1.58		1.57	1.56
v <sub>5</sub>	1.94		1.96	1.97
u <sub>6</sub>	2.54		2.49	2.49
v <sub>6</sub>	1.68		1.81	1.76
v <sub>7</sub>	4.47	4.35	4.46	4.50
u <sub>8</sub>	2.11		1.80	1.92
v <sub>8</sub>	3.83		3.90	3.90
u <sub>9</sub>	3.23	2.68	2.83	3.00
v <sub>9</sub>	2.94	3.38	3.19	3.07

(c) Stiffness Analysis of a Heated Plate with Mechanical Loading

A uniform stress,  $\sigma_x$ , of 5000 psi was assumed at the right-hand edge of the plate shown in Fig. 6. The temperature distribution was that shown in Fig. 7. Results were obtained from relaxation and lattice approximations of 4, 9, and 25 nodes. The results are tabulated in Table 3, where the nodes are numbered as shown in Fig. 9.

TABLE 3				
Displacements $\times 10^2$ (in.)				
	Relaxation	4-Node	9-Node	25-Node
u <sub>2</sub>	1.85		1.89	1.88
u <sub>3</sub>	3.06	3.05	3.07	3.07
v <sub>4</sub>	1.98		1.93	1.97
u <sub>5</sub>	1.87		1.86	1.85
v <sub>5</sub>	1.80		1.82	1.82
u <sub>6</sub>	3.12		3.07	3.07
v <sub>6</sub>	1.54		1.67	1.62
v <sub>7</sub>	4.18	4.06	4.17	4.22
u <sub>8</sub>	2.40		2.09	2.20
v <sub>8</sub>	3.54		3.61	3.61
u <sub>9</sub>	3.81	3.26	3.40	3.55
v <sub>9</sub>	2.64	3.09	2.91	2.78

(5) CONCLUDING REMARKS

The proposed thermomechanical stiffness matrix extends the direct stiffness method of Turner to cover the case of heated structural elements. This extension is accomplished with a modest increase in complexity. The method can handle complex structure with steady state temperature distributions while retaining the inherent simplicity of the direct stiffness method and its ease of applying boundary conditions.

Examination of Tables 1 through 3 shows that the displacements calculated with the proposed method converge satisfactorily as the lattice network becomes finer. A relaxation solution is given for comparison. Although the relaxation solution solves the exact equations of the plate, it too is an approximation since the equations are satisfied only at pre-selected points. The comparison of the 25-node lattice with the relaxation solution is in all cases good.

The proposed method can be easily extended to the analysis of complex built up structure using the basic structural elements presented herein. The built up structure is replaced by an elastically and thermally equivalent structure made up of uniaxial members pin-jointed at the nodes. Thus a three dimensional thermomechanical stiffness relation can be obtained for the entire structure and displacements determined as shown in the previous sections.

(6) REFERENCES

1. Turner, M. J., Clough, R. W., Martin, H. C., and Topp, L. J., "Stiffness and Deflection Analysis of Complex Structures", Journal of the Aeronautical Sciences, Volume 23, No. 9, pp. 805 - 823, September 1956.
2. Biot, M. A., "New Thermomechanical Reciprocity Relations with Applications to Thermal Stress Analysis", Journal of the Aerospace Sciences, Volume 26, No. 7, pp. 401 - 408, July 1959
3. Parkes, E. W., "Thermoelasticity", AFPSR-TN-60-380, ASTIA Doc. No. AD 238412, February 1960
4. Topp, L. J., "Calculation of Deflection Influence Coefficients of a Complex Structure from Stiffness Considerations", MS thesis, University of Wichita, Wichita, Kansas, 1957

ACOUSTIC FATIGUE TESTS RELATING TO THE DESIGN OF  
STRUCTURES FOR ELEVATED TEMPERATURES

Philip M. Edge, Jr.  
Langley Research Center  
Langley Field, Va.

INTRODUCTION

The supersonic transport and some types of reentry vehicles will have acoustic fatigue problems for which combined acoustic, airflow, and elevated temperature environments may be significant. On the one hand, the supersonic transport will be required to operate for long periods of time at elevated temperature and relatively high dynamic pressures. The reentry vehicle, on the other hand, must withstand the combined acoustic, airflow, and elevated temperature environments during exit flight without failure in order to be able to subsequently perform its reentry mission. At the Langley Research Center, several acoustic fatigue studies relating to such high-speed vehicles have recently been made. These studies have included some effects of intense noise on structures under conditions of elevated temperature and have involved some unique applications of existing research facilities. The purpose of this paper is to describe some of these studies along with the testing techniques employed and to summarize some of the results obtained.

NATURE OF THE ACOUSTIC FATIGUE PROBLEM FOR HIGH-SPEED FLIGHT

The nature of the acoustic fatigue problem is illustrated schematically in figure 1. The response of the structure is noted to be a function of the acoustic, temperature, and airflow environments and the type of structure.

Much of the experience and know-how for minimizing noise-induced structural fatigue has been accumulated to date from jet aircraft operations (refs. 1 and 2). This experience relates largely to the engine noise which is random in nature and is most intense for short periods of high-power operation, such as during ground testing



and take-offs. There is thus a question about the application of the present experience to conditions where elevated temperature is believed to be significant and where airflow and the use of new materials and fabrication methods may be complicating factors.

For conventional aircraft the airflow environment is the primary factor in determining the overall aircraft configuration and the design of its structure. For certain critical regions, however, the acoustic environment may be the dominant factor in determining the detail structural design. For vehicles where elevated temperature is an important design consideration, new materials, configurations, and fabrication methods are required. Structures designed primarily to withstand the high-temperature environment, however, may not be adequate to withstand the airflow and acoustic environments. Thus, for vehicles operating at elevated temperature, all of the factors of figure 1 are believed to be significant and are noted to be inter-related. Of particular significance is the fact that all environments of figure 1 may simultaneously influence the response of the structure.

In the past for acoustic fatigue studies, it has been sufficient to simulate only the acoustic input. It follows that for some future designs, the simulation of combined environments may be a requirement. To date, only limited experience is available in combined environmental testing of this type. The remainder of this paper will deal with acoustic fatigue studies of structures designed for elevated temperature conditions, and of particular interest are some preliminary studies in combined environments.

#### THE SCOPE OF THE PRESENT STUDIES

The scope of the studies and the order in which each will be discussed are indicated in figure 2. Illustrated schematically in the left column are the configurations and at the right are the conditions indicated by means of check marks under which each was investigated. A Project Mercury capsule, complete with escape tower, was tested in an intense noise environment only. There were two rather unusual aspects of this study. A unique application was made of the noise field of a large wind tunnel to accomplish this full-scale test, and the main onboard systems were operational to the extent that an astronaut was on board and participated. Project Mercury full-scale heat shield shingles were investigated in intense noise only, in combined noise and elevated temperature environments, and in combined noise and airflow environments. Corrugation stiffened panels of the type illustrated and which are of interest for application to boost-glide vehicles were investigated in noise only and a combined noise and elevated temperature environment. Of particular interest is a light gage truss-core sandwich panel which was investigated over a range of combined noise and elevated temperature environments. Studies of the first three configurations shown in figure 2 were exploratory in nature and were related to hardware development. In

## Edge

the study of the truss-core sandwich, effort was directed toward a systematic study of the effects of combined elevated temperature and noise environments.

### EXPLORATORY ACOUSTIC TESTS OF STRUCTURES FOR ELEVATED TEMPERATURE APPLICATION

#### Full-Scale Project Mercury Capsule

Environmental studies of the structure and the onboard systems were made for a full-scale Project Mercury capsule in intense noise only. These studies made unique application of the noise field of the Langley 9- by 6-Foot Thermal Structures Blowdown Wind Tunnel (refs. 3 and 4). Illustrated schematically in figure 3 is a plan view of the area near the diffuser exit and the contour lines of overall noise level. Although testing is limited to runs of approximately 30 seconds duration and to ambient temperatures, there is the capability for testing large specimens. As a matter of information, the spectra were noted to vary markedly at various locations along any given contour line. The two test locations indicated in figure 3 were chosen to simulate (1) the Atlas rocket booster engine spectrum, and (2) the aerodynamic boundary-layer noise spectrum, respectively.

Tests were made with the capsule in both manned and unmanned conditions, and the noise measured during the run was found to be closely representative of that predicted for Project Mercury flight conditions (ref. 5). Structural behavior, the operation of onboard systems, and voice communications between the astronaut and the ground station were monitored throughout the tests. Monitoring during the tests and subsequent inspections of the equipment indicated no adverse effects. From a structural standpoint, the heat shield shingles of the capsule were among the primary items of concern in this test. The ability of the shingles to successfully withstand this noise exposure is in general agreement with the results of more extensive random noise tests of the individual shingle components.

#### Project Mercury Capsule Type Heat Shield

From the standpoint of acoustic fatigue, more testing experience has been obtained on Mercury capsule type heat shields in component testing rather than in complete capsule testing. For this type of study and other intense noise tests of structures up to several square feet in size, the noise environment around the exhaust of a 12-inch-diameter air jet is used at the Langley Research Center (ref. 6).

## Edge

Some of the noise spectra obtainable are presented in figure 4 along with schematic illustrations of two model test arrangements for elevated temperature studies. Overall noise levels of above 160 db are obtainable at the model for the arrangement shown in the upper right-hand sketch. It is noted that quartz tube heat lamps are located below the model in such a manner that the model receives the heat from below. Where it is desirable to simulate the condition wherein the heat and the noise are received from the same direction, the test arrangement shown in the lower sketch has been used. Since for this arrangement the model is farther from the noise source, noise levels obtainable at the model are limited to about 155 db.

The noise levels and frequency spectra can be varied somewhat by varying jet exit velocity or by shifting position of the model relative to the exhaust jet. By moving the model into the exhaust stream, effects of partial or total aerodynamic flow attachment can be combined with intense noise. An air jet facility now under construction will have the capability for combined random noise and heated airflow testing at temperatures up to 3,000° F.

By the use of the 12-inch-diameter air jet facility, heat shield shingles of a type designed for the conical portion of the Mercury capsule were tested. Tests were made using fixtures of the same wall construction as the capsule itself and in conditions of intense noise only, of combined intense noise and elevated temperatures up to 1,700° F, and of combined intense noise and airflow.

Illustrations of the types of failure that occurred on a shingle during combined noise and airflow tests are shown in the photograph of figure 5. Shown is an example of an early design of the skin surface heat shield shingle of 0.010 gage stainless-steel construction. Two of the main features to note are the stamped-in beads running perpendicular to the direction of airflow and the oversized holes which allow for expansion due to heat. Also shown in the photograph are examples of three types of failure encountered. The most obvious is the long fatigue crack at the right-hand edge in the area of the termination of the beads. Cracks were noted to originate in or near the radius of the bead, due probably to a stress concentration, and then to link up in the manner shown. Small fatigue cracks were also noted to emanate from the oversized bolt holes as indicated in the top center of the figure. Another significant result is the elongation of the bolt holes such as is indicated in the bottom of the figure. These failures were obtained in the combined intense noise and airflow test which was judged to be more severe than the simpler acoustic tests.

It should be pointed out that the production capsule incorporates shingles having thicker skin gage, longer beads, and somewhat different materials. Acoustic fatigue is not believed to be of serious concern for the present design.

## Corrugation Stiffened Structure

Acoustic fatigue studies have been made of a hot structure designed for lifting reentry vehicles (ref. 7). The skin structure tested consisted of a sandwich of 0.010 gage Inconel X with the construction details illustrated in figure 6. The outer surface is a beaded skin to which is welded an inner surface of corrugated design. Terminating the inner surface is a Z stiffener which is seam welded to the outer skin and spot welded at two points on each corrugation.

Acoustic fatigue tests were conducted at high noise levels for the purpose of determining the weak points in the above structural design. It was determined that initial failure occurred in the spot welds attaching the inner skin to the Z stiffener. Skin cracks were also observed near the termination of the panels in the vicinity of the seam welds attaching the outer skin to the Z stiffener. A panel configuration incorporating rivets instead of spot welds had a time to failure approximately twice as long as that of the spot-welded panel. In this latter test the rivets did not fail and the fatigue cracks in the outer skin again occurred in the region of the seam weld as indicated in figure 6. There is thus a suggestion that a local weakening of the material occurs in the region of the welds for the type and gage material used (0.010-inch-thick Inconel X).

A brief intense noise test has been made of an open-faced sandwich panel of the type shown in figure 7 (back side view) and which is used as a fairing panel on the X-15 airplane. The material of this structure was Inconel X; the outer skin being of 0.020 gage and seam welded to the inner beaded skin of 0.012 gage. A 0.016 gage hat section stiffener was installed down the center of the back side as indicated in the sketch of the figure to prevent the growth of inner skin cracks which were initiated during flutter tests. The purpose of the noise tests was to determine if further crack growth or other damage would result from exposure of the outer surface to high noise levels. The only damage resulting from these tests was failure of the rivets attaching the hat section stiffener to the inner beaded skin. As a matter of interest, some typical rivet failures are illustrated by the photograph in the lower part of figure 7. This photograph is a closeup of a section near the center of the stiffener and shows rivets in various stages of failure. First, the periphery of the rivet head is deformed (see, for example, the rivet in lower right-hand part of photograph). This peripheral deformation progresses inward toward the center of the rivet head until complete failure occurs. The photograph shows an example of progressive fatigue failures of rivets due to acoustic excitation.

EFFECTS OF ELEVATED TEMPERATURE ON ACOUSTIC FATIGUE LIFE  
OF A TRUSS-CORE-TYPE SANDWICH PANEL

A systematic series of acoustic fatigue tests was run on panels constructed from a commercially available lightweight truss-core-type sandwich material. The panels were of welded construction of the type illustrated in figure 8, and were fabricated from type 301 steel. The overall thickness is about 5/32 inches; the skin surfaces being of 0.006 gage and the core of 0.002 gage. One of the main features of this type of construction is the use of rows of tiny spot welds to attach the core to the facing sheets.

Also illustrated schematically in figure 8 are the types of failure observed during these acoustic fatigue tests. It is a general result of these tests that the facing sheet becomes separated from the core due to failure of the welds. This results in a region of localized weakness which grows in extent as more weld failure occurs. As these failures progress and affect larger areas of the panel, looseness of the facing sheets may be detected. Eventually skin surface cracks, as illustrated in figure 8, will occur, usually along the weld lines and will be followed by core deterioration. Core cracks progress along the weld lines also as indicated in figure 8, and in the extreme case small segments of the core become detached. In most cases the first failures were detected at the weld line associated with the overlap joint of the core.

Panels having overall dimensions 15 inches by 15 inches were tested in combined elevated-temperature—intense-noise environments over a temperature range up to 750° F and a noise level range from 151 db to 162 db. The specimens were supported on all four sides with a resulting free panel size of 12 inches by 12 inches. The panels were restrained by clamping frames in such a manner that thermal expansion could be accommodated without panel deformation. As a matter of interest, the noise and heat were applied as indicated in the upper sketch of figure 4.

The results obtained for the panels of figure 8 at a noise level of 162 db and for a range of temperature from about 70° to 575° are shown in the bar graph of figure 9. The length of each bar indicates the total time of the test at each temperature. The test in each case was terminated at the time of the first perceptible skin surface crack. The intermediate times at which inspections were made are indicated by vertical lines within each bar. The shading at the end of the bar indicates the time interval of each test for which local weaknesses were known to exist (thus indicating internal failures).

It can be seen from the data of the figure that for this random noise environment of 162 db the panel fatigue life varied from approximately 3 hours at 70° F to only a few minutes at 575° F. It

## Edge

has been reported in reference 8 that the static shear strength of this type of panel is reduced only about 15 percent due to this order of temperature increase. Thus there is a suggestion that the decrease in fatigue life shown in figure 9 may be due to increased local stress rather than changes in material properties due to increased temperature.

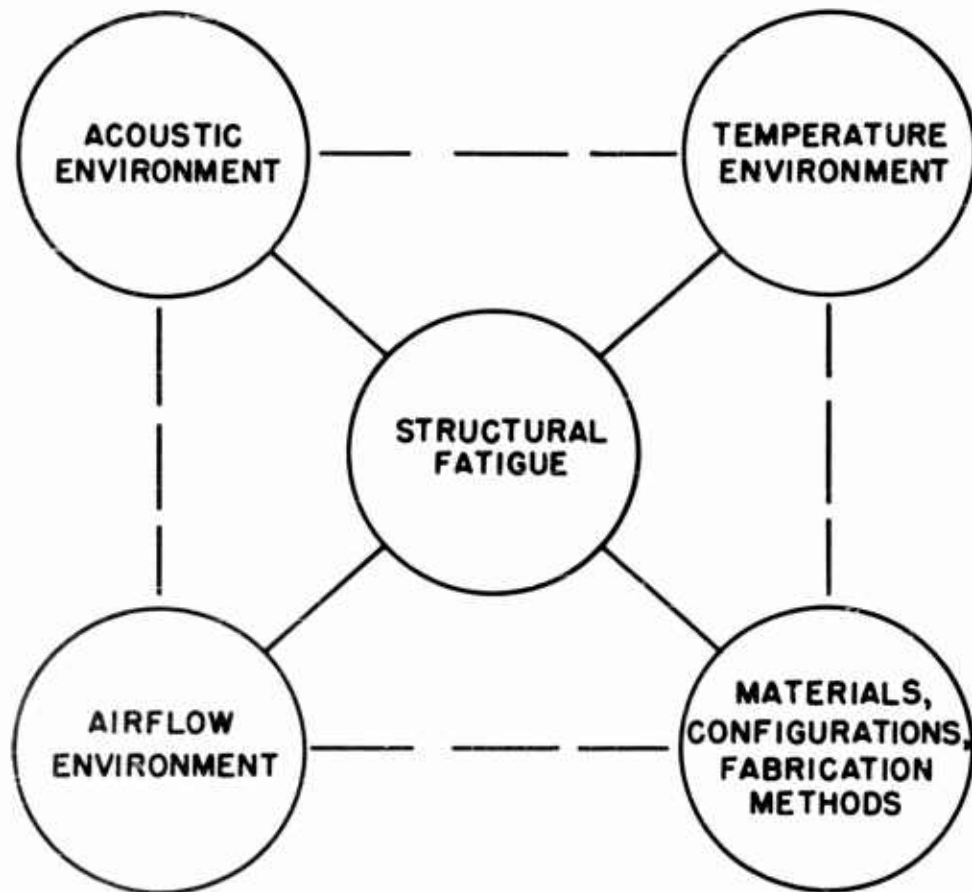
The results of combined elevated temperature and noise environment tests for the above panels are presented for a range of noise levels in figure 10. The data of figure 9 are included and constitute the highest points (162 db). Although not enough data were obtained to properly define the curves, the dashed lines have been drawn in to indicate possible trends in the data. Short segments of bar graph are used to indicate the approximate times at which skin surface failures were observed. The open symbol at 151 db is meant to indicate that no failures occurred for the duration of that test at 750° F. It can be seen that, at a given temperature, the time to failure is decreased markedly by an increase in the noise level. It is concluded that, for a test of combined elevated temperature and noise environments in the range covered by the above tests, both the noise level and the temperature have significant effects.

## CONCLUDING REMARKS

In conclusion, a description has been given of some exploratory experimental studies dealing with acoustic fatigue of some types of skin surface construction proposed for elevated temperature application. Results of these studies indicate that elevated temperature or airflow environments combined with intense noise environments can accelerate acoustic fatigue damage. It is thus concluded that for some future vehicles it is desirable to simulate combined environments for structural testing.

REFERENCES

1. Hubbard, Harvey H., and Houbolt, John C.: Vibrations Induced by Acoustic Waves. Chapter 48, Handbook of Shock and Vibration Control, edit. by C. M. Harris and C. E. Crede. McGraw-Hill Book Co., N. Y., 1961.
2. Richards, E. J.: Introduction to Acoustic Fatigue. WADC TR 59-676, 1959.
3. Mayes, William H., Edge, Philip M., Jr., and O'Brien, James S., Jr.: Near-Field and Far-Field Noise Measurements for a Blowdown-Wind-Tunnel Supersonic Exhaust Jet Having About 475,000 Pounds of Thrust. NASA TN D-517, 1961.
4. Clevenston, Sherman A., Hilton, David A., and Lauten, William T., Jr.: Vibration and Noise Environmental Studies for Project Mercury. Presented at Annual Meeting of the Institute of Environmental Sciences, Washington, D.C., April 5-7, 1961.
5. Hilton, David A., Mayes, William H., and Hubbard, Harvey H.: Noise Considerations for Manned Reentry Vehicles. NASA TN D-450, 1960.
6. Edge, Philip M., Jr.: Random Noise Testing of Aircraft and Missile Components With the Aid of a Laboratory Air Jet. Presented at 27th Shock and Vibration Symposium, Fort Bliss, El Paso, Texas, Feb. 26-27, 1959.
7. Pride, Richard A., Helms, Bobbie F., and Royster, Dick M.: Design and Testing of Hot Structures for Lifting Reentry Vehicles. Presented at Lifting Reentry Vehicles Meeting: Materials and Design, Meeting of American Rocket Society, Palm Springs, Calif., April 4-6, 1961.
8. Anon: Spacemetal Sandwich Engineering Handbook. Prepared by Special Products Engineering Department, North American Aviation, Inc. Report MD 59-108.



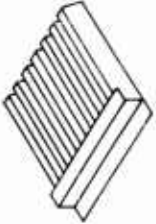



NASA

Figure 1.- Nature of the acoustic fatigue problem.



Edge

CONFIGURATION	ENVIRONMENT		
	ACOUSTIC	ACOUSTIC + TEMPERATURE	ACOUSTIC + AIR FLOW
	✓		
	✓	✓	✓
	✓	✓	
	✓	✓	

NASA

Figure 2.- Scope of recent acoustic fatigue studies.

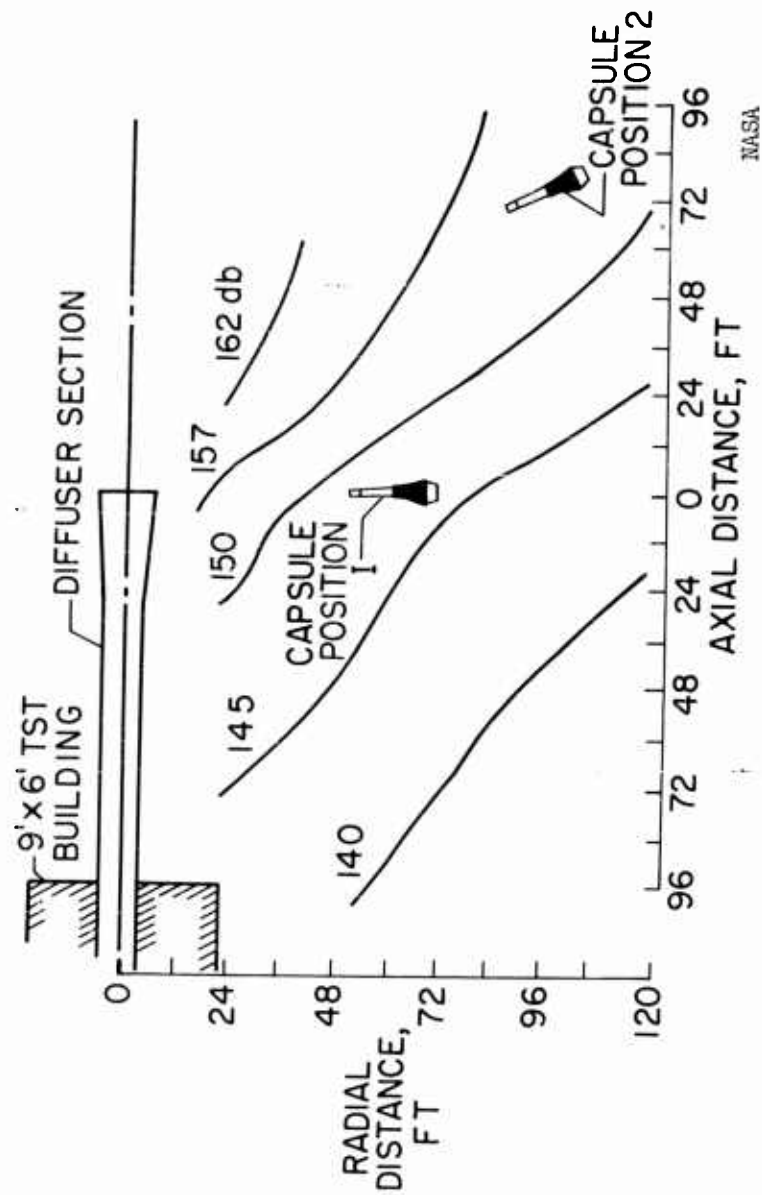


Figure 3.- Near-field overall sound-pressure-level contours for exhaust jet of the Langley 9- by 6-Foot Thermal Structures Tunnel showing two locations for environmental tests of a Project Mercury capsule.

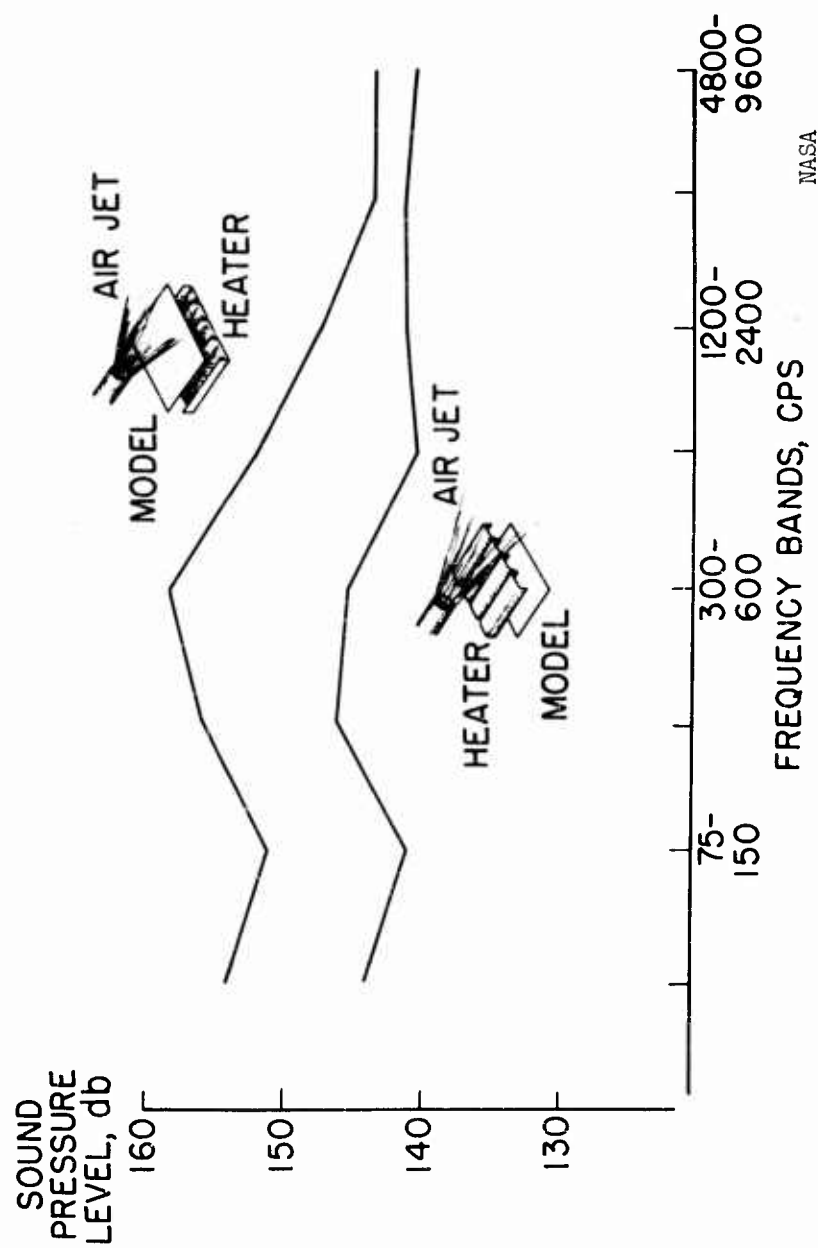


Figure 4.- Random noise spectra obtainable during elevated temperature - acoustic fatigue tests with the Langley air jet facility.

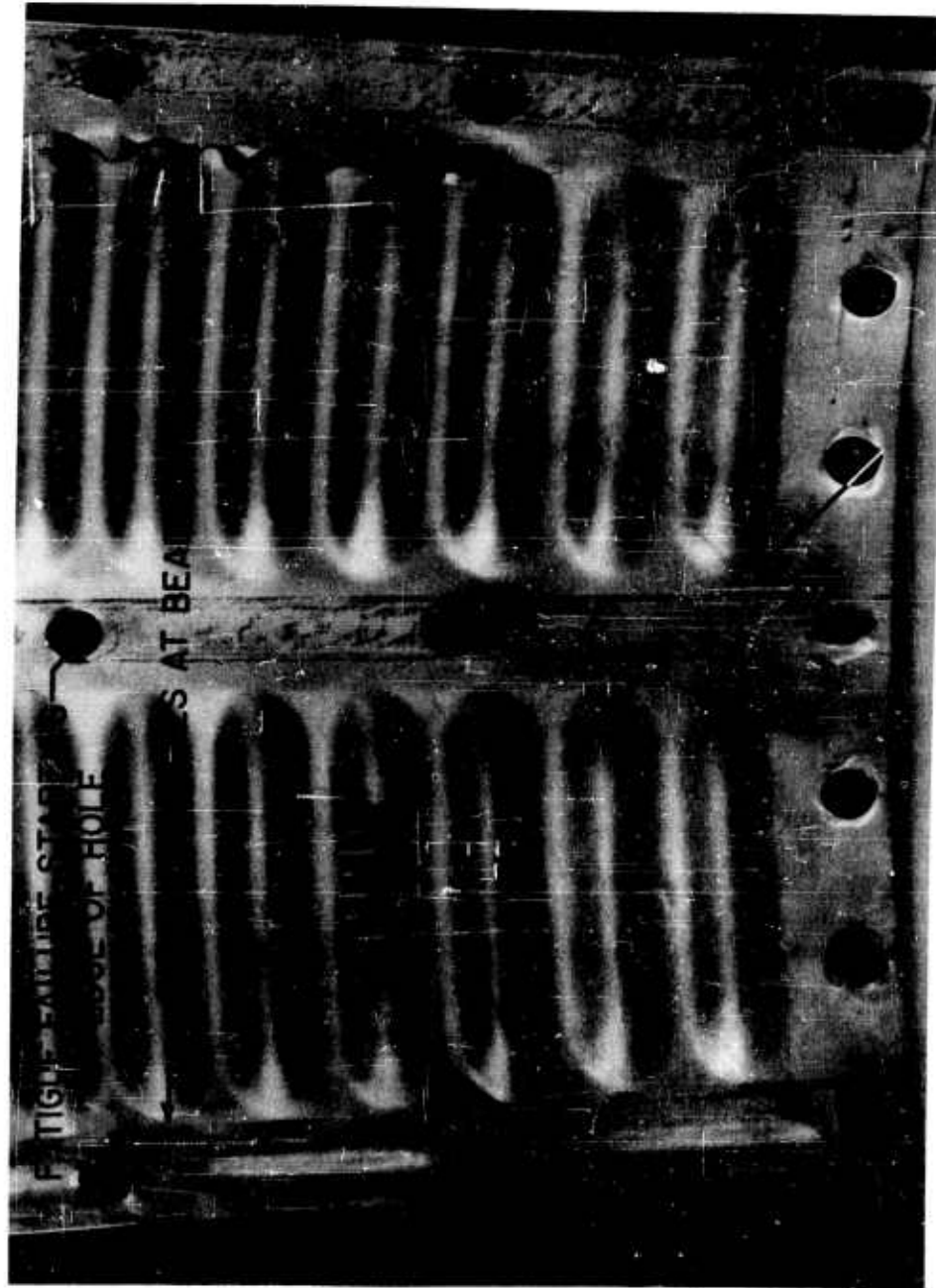
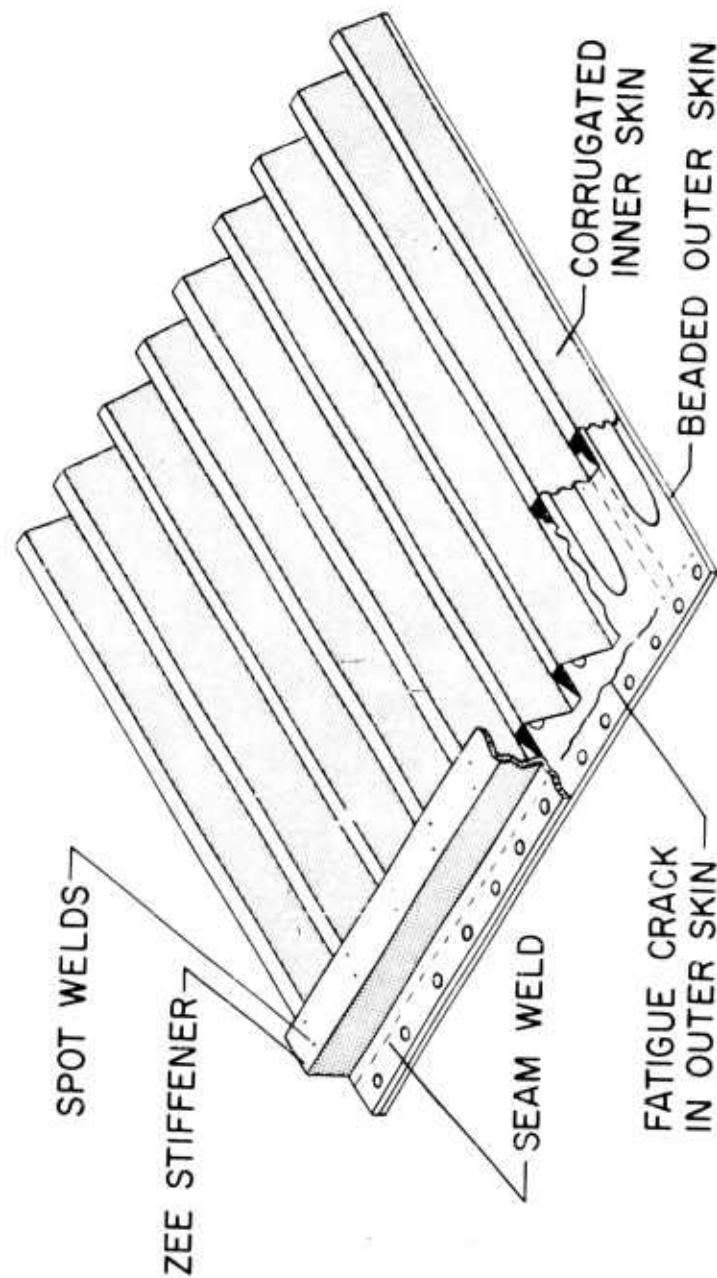


Figure 5.- Photograph of 0.010-inch gage Project Mercury heat shield shingle acoustic fatigue specimen showing three types of failures.

NASA

Edge



NASA

Figure 6.- Acoustic fatigue failure of corrugation-stiffened panel.

Edge

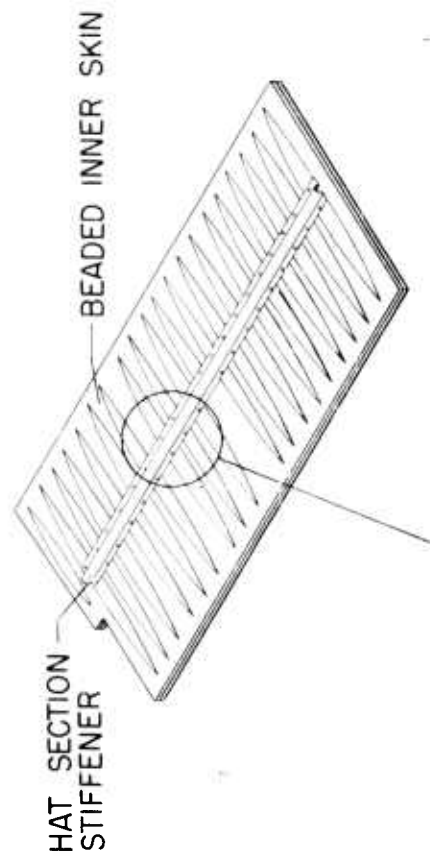
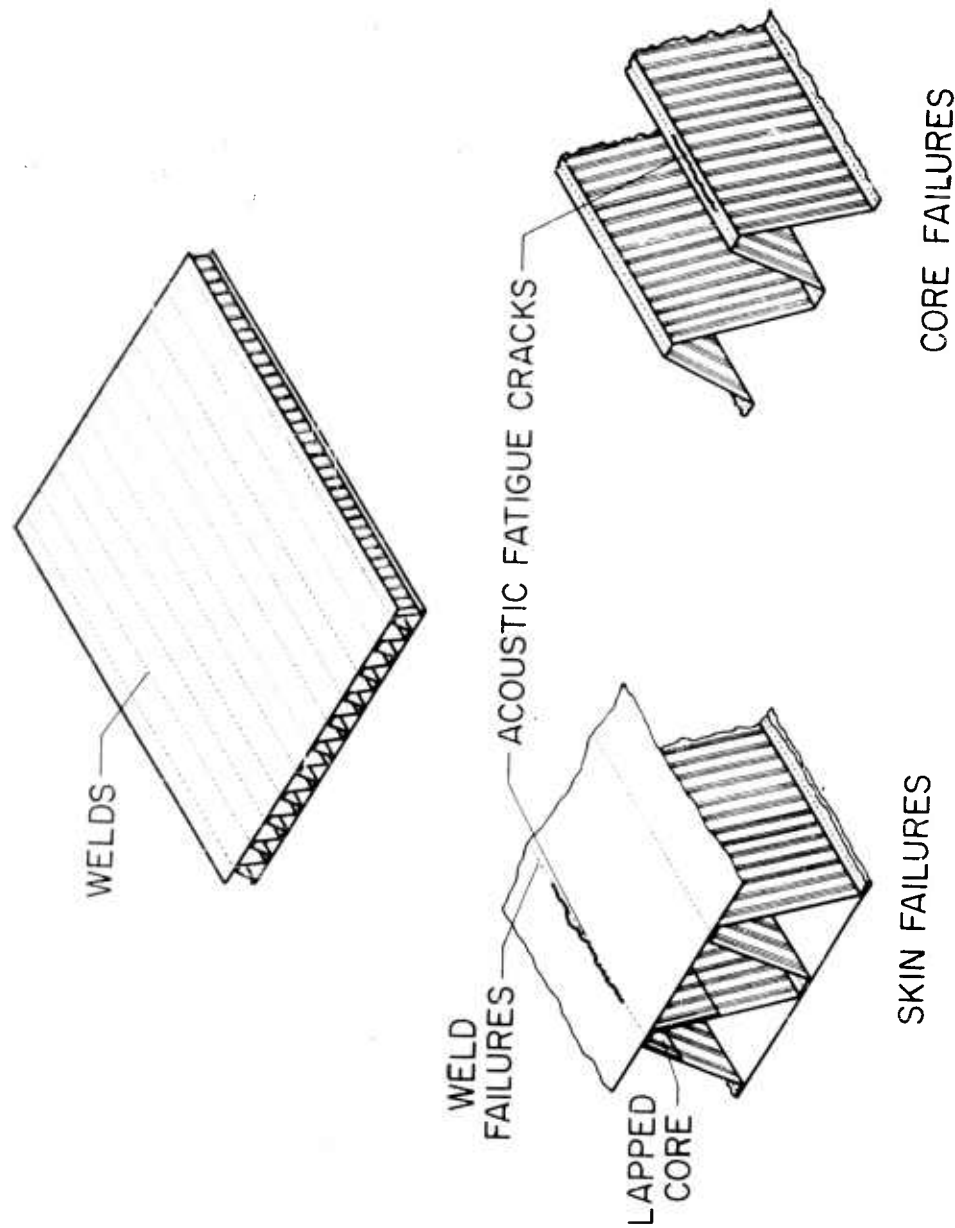


PHOTO OF  
RIVET FAILURES



NASA

Figure 7.- Acoustic fatigue rivet failure.



NASA

Figure 8.- Acoustic fatigue failures of truss-core sandwich panel.

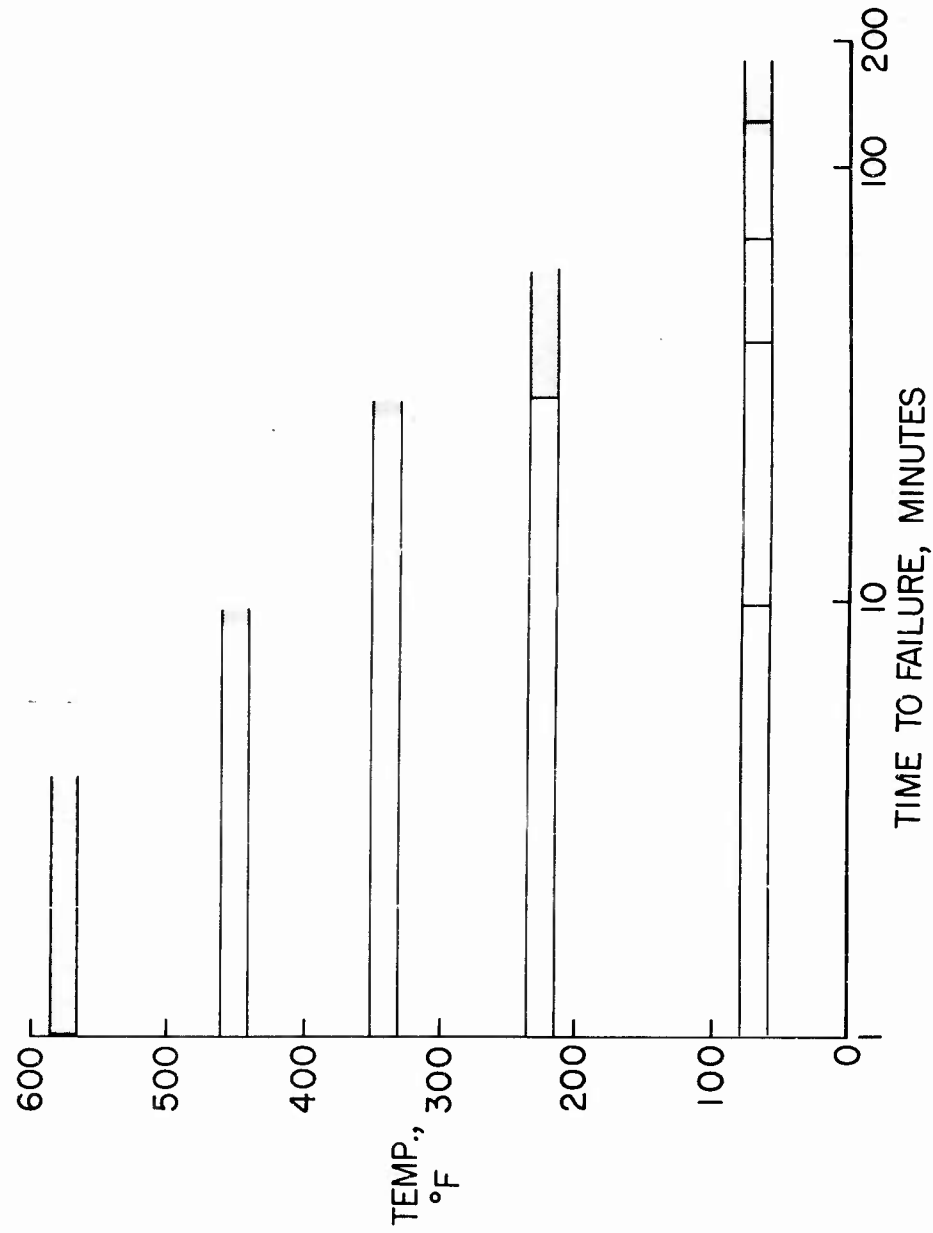


Figure 9.- Effect of temperature on time to failure of truss-core sandwich panels under random noise excitation at an overall noise level of 162 db.

NASA



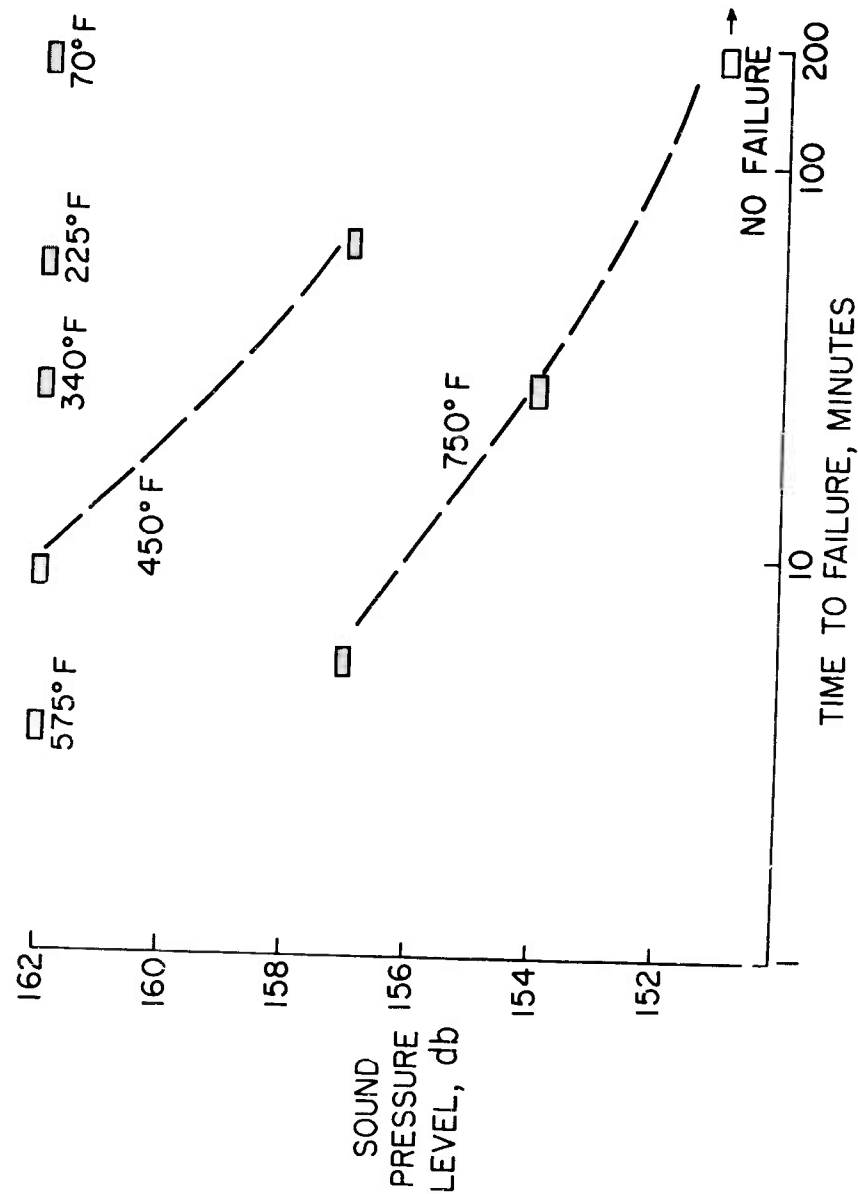


Figure 10.- Effects of noise level and temperature on time to failure of truss-core sandwich panel under random noise excitation.

NASA

**SESSION VI | ENVIRONMENTAL VIBRATION**

Chairman: Dr. Charles T. Morrow  
Aerospace Corporation

## STRUCTURAL VIBRATION IN SPACE VEHICLES\*

Kenneth McK. Eldred  
Western Electro-Acoustic Laboratory, Inc.  
Los Angeles, California

William Roberts  
Robert W. White  
Northrop Corporation, Norair Division  
Hawthorne, California

### I. INTRODUCTION

Throughout the past decade, attention has been increasingly focused on the vibration of flight vehicles. This increased attention, of both industry and government, has been forced by an increasing number of vehicle failures and malfunctions. There is strong reason to suspect that excessive vibration may have contributed to the malfunction of critical components.

These failures and malfunctions have resulted in costly, continuous maintenance programs and occasionally in catastrophic accidents. Further, they have required extensive vibration test programs, with resulting retro-fits to restore the mission capability of existing military flight vehicles. In addition, during the period of test and retro-fit, the mission capability of the class of vehicles is often severely restricted, reducing their effectiveness as military weapons.

Significant advances have been made in the analysis and control of vibration. However, as recent history amply demonstrates, these advances have lagged behind the creation of new problems, each problem seemingly more formidable than the one previously solved.

---

\*The material described in this paper is drawn from a much larger study of Structural Vibrations in Space Vehicles (ref. 1) which has been conducted by the Norair Division of Northrop Corp. and the Western Electro-Acoustic Laboratory, Inc., as co-contractors. The basic study was sponsored by the United States Air Force, Vibration and Acoustical Section, Dynamics Branch, Structures Laboratory, Wright Air Development Division, under Contract AF33(616)-6486.

It is reasonable to ask why this lag has developed; and further, does the recent history portend a similar trend for the future? The answer to the "why" of the present dilemma can be found in three basic factors of our current technological explosion.

First, the rate of advance in the design and concept of flight and space vehicles is increasing at a rapid pace. In former years, new aircraft designs evolved from immediate predecessors, as witness the Douglas series of DC commercial aircraft. Although catastrophic failures often accompanied the introduction of a new aircraft with a few "radical" design features, these problems were usually found during preliminary testing and either corrected or the "radical" approach was discarded. Today, a new design often represents a significant advance in the "state of the art" over a broad front. Consequently, few designs evolve from their predecessors, and the majority represent new design solutions to new problems. Each of these novel designs engenders many potential vibration problems, which must be discovered during the design process or during lengthy vibration tests, if they are not to be discovered later during the vehicle's operational lifetime.

Second, each new design represents a maximum effort to minimize weight and maximize performance. The effort to maximize performance leads to increased propulsion with a concomitant increase in vibratory forcing functions of all types. The effort to minimize weight requires elimination of all unjustifiable safety factors. Thus, the necessity to maximize the thrust/weight ratio makes mandatory the careful design of each part.

The third, and most important factor for space vehicles, is the fantastic increase in the reliability requirement which accompanies the development of the missile, both as a weapon and as a launching vehicle for space exploration. For example, Figure 1 shows that to obtain 10-to-1 odds for survival of the complex electronics in a space vehicle attempting a two-year mission into space, the mean time to failure for the total vehicle system must be 20 years! Similarly, to obtain 10-to-1 odds against occurrence of structural failure during a launch into space requires the mean time to failure for structure exposed to the launch environment to be approximately 22 times the duration of the launch phase.

Regarding future trends, it is clear that the magnitudes of the forcing functions, which historically have kept pace with propulsive power, will increase in the next decade, particularly when one considers the atomic hydrogen rocket and hypersonic flight. Also, the design projects presently under way call for significant new advances in many areas of vehicle design. Thus, the course of future vibration problems depends upon the hindsight and foresight of both industry and government, upon the success of vibration research, and upon the skill utilized in applying the tools of

vibration engineering to the design, construction and test of flight vehicles.

In order to assist in reversing the unfavorable historical trend, it is desirable to assess the probable operational vibration environment of a vehicle during the design stage. Correct evaluation of the probable environment at this early date is required to guide both system and mission concepts toward increased reliability at minimum penalty<sup>(2)</sup>.

The major excitation for vibration in space vehicles and high performance aircraft generally results from jet or rocket noise, power plant vibrations, boundary layer and other aerodynamic pressure fluctuations, which are primarily characterized by continuous frequency spectra and random amplitudes. Hence, the task of predicting vibratory responses and stresses for these vehicles is more formidable than formerly when the exciting forces were primarily sinusoidal in nature. Furthermore, although structural fatigue usually results from excitation at frequencies below 500 cps, the problem of equipment malfunction and electronic component fatigue extends the frequency range of concern to at least 10,000 cps. Therefore, the prediction of vibration response for advanced aircraft and space vehicles must include concern for all frequencies below 10,000 cps.

The vibration of any portion of the vehicle depends upon the characteristics of the source, the path between the source and the receiver, and the characteristics of the receiver itself, as illustrated in Figure 2. At low frequencies, the response of the entire vehicle to external sources is maximum at the basic body modes, and the magnitude of the response depends primarily upon the location relative to the body mode shape, the magnification factor for the mode, and the magnitude of the forcing function over the entire vehicle. At higher frequencies the maximum responses occur at the resonances of the various panels and the magnitude of the response depends on the characteristics of the source, the panel, the transmission path between panel and receiver, and the receiver. At frequencies above the panel fundamental resonances, the factors influencing response become very complex and the possibility of resonances along the path becomes sufficiently high as to suggest that the path be treated with transmission line parameters which, in addition to source and receiver characteristics, determine the vibration response.

From this brief discussion, it is clear that a detailed step-wise approach to the prediction of vibration for any general case would be exceedingly complex and cumbersome. Further, it is clear that a practical analytical solution of the vibration characteristics of a mechanical system must lie in judicious simplification

of the system to a series of sub-systems whose solutions are known. It is also clear that an analytical approach is not feasible for detailed prediction at the early design stages where the structure is not reasonably fixed in concept. However, many preliminary decisions regarding equipment location, isolation and specification, and the definition of potential structural fatigue problem areas must be resolved in the early design stage.

In order to attain the overall vehicle design reliability target, detailed vibration analysis, together with component and sub-assembly testing, must proceed throughout the entire design stage. When completed vehicles are available, they must be tested in their entirety to determine their capability of withstanding their expected environments. However, it must be noted, as seen in Figure 2, that vibration in a vehicle is subject to a complex interaction of many factors. Further, structural or electronic fatigue failures usually begin with the one component in a structural series of components which has the lowest ratio of fatigue strength to vibration stress. Consequently, each component part of the vehicle may be a potential source of vibration failure.

In order to eliminate or minimize potential future vibration problems, it is clear that the vibration specialist must be able to predict the characteristics of each vibration source, the acceptance of vibratory energy by the structure and the responses and stresses at various points in the structure. Further, he must be able to relate the predicted responses to damage - either fatigue failure or malfunction. Then he must be able to design and evaluate tests which demonstrate that the final article has the target probability for reliability for its design mission. These factors will be briefly reviewed in the succeeding sections.

## II. SOURCES OF VIBRATION

In order to obtain a qualitative orientation for some of the major forcing functions, it is helpful to consider an analysis that was recently made of the noise telemetered from a microphone located in a missile nose cone and recorded during flight.

Figure 3,(3), illustrates the several phases of noise or vibration environment which are usually found in missile flight data. The rocket noise at launch provides a high level of vehicle response, which decreases rapidly as the vehicle leaves the pad and accelerates. However, as vehicle velocity increases, the pressure fluctuations in the turbulent boundary layer increase in magnitude and the vehicle response begins to increase. The transients shown on the graphic level recording represent a shock as the vehicle passed through the transonic region, and a second shock when the sustainer engine was ignited. As can be seen, the response continued to increase until the maximum dynamic pressure ( $q$ ) was

reached, at which time in the flight profile the boundary layer pressure fluctuations are maximum. As the vehicle continued to accelerate into less dense atmosphere, the  $q$  decreased, as did the response. However, when the vehicle descended into more dense atmosphere in the terminal portion of the flight, the vehicle  $q$  and response both increased.

It is evident from Figure 3 that the two most severe vibration environments are a result of rocket noise at launch, and aerodynamic phenomena at maximum  $q$ . The relative severity of these two forcing functions and their responses in a specific vehicle depends on many factors, including the flight profile and the launch configurations.

It may be fairly stated at the outset that many of these sources are only now being quantitized with the degree of precision often desired by an engineer. This results both from the complex nature of some of the sources and the short historical transition which is occurring from subsonic-manned aircraft to supersonic and hypersonic missiles and space vehicles. Fortunately, the relative importance of these sources can be readily determined and their parameters can be roughly estimated. Further, and perhaps more important, the fundamentals of the major sources are becoming better understood.

#### Rocket Noise and Vibration

The noise from the rocket engine is generated primarily in the subsonic portion of the rocket's turbulent exhaust gas stream. This noise is characterized by a very broad frequency spectrum of random amplitude extending throughout the audible frequency range. Therefore, because acoustic energy is available in all frequency regions, resonant responses can be excited over the entire skin of the vehicle, transferring acoustic energy into vibratory energy which is transmitted throughout the vehicle.

Fortunately, little of the available acoustic energy in the rocket noise excites the vehicle's low frequency fundamental resonances because the wavelengths of this low frequency noise are generally much larger than the diameter of the vehicle. However, at higher frequencies above approximately 100 cps, where the wavelength of the sound becomes comparable and less than minimum vehicle dimensions, the available external acoustic energy is more readily accepted by the vehicle, exciting resonances in external panels and substructure and higher frequency resonant responses in electronic equipment and other components.

The total acoustic power of free jets and rockets has been found<sup>(1)</sup> to correlate with a modified Lighthill parameter<sup>(4,5)</sup> as shown in Figure 4. The departure of the data from the mean line at the higher values of the Lighthill parameter can be viewed as a

function of temperature as illustrated in Figure 5. Since, for the jet flows which have been studied, both the density ( $\rho$ ) and the speed of sound in the flow ( $a^*$ ) are functions of temperature, Figure 4 gives the net result of both variables. Thus, it may be expected that the first approximation to the deviation of total acoustic power from the Lighthill parameter for a jet whose density at ambient temperature is much lighter than air, may be evaluated from Figure 5 by determining an equivalent temperature of air which is required to give the proper jet density.

The concept of total acoustic power is useful in examining the influence of various rocket parameters. However, it is the sound pressures and their spacial correlations over the vehicle surface which are of importance as vibration sources. These sound pressures are a function of both the total power and its distribution in space. In fact, although interaction of the jet with a surface usually decreases the total acoustic power, the noise environment of the vehicle increases. This paradox results from changes in the distance between the vehicle and noise-producing portion of the flow, and changes in the directional characteristics of the new flow geometry. A hypothetical example of the launch noise exposure for two points on a typical medium sized vehicle is given in Figure 6. Note the large increase in noise exposure between the free jet at  $T = 2$  seconds and the jet impinging on the ground, and the even larger increase found when the missile was launched from a silo which had no acoustical treatment. These increases are particularly evident at the forward vehicle positions where sensitive equipment is often located.

This figure stresses the opportunity to reduce launch noise by the design of the launch configuration. Fortunately, the design configuration can be experimentally investigated by duplicating all flow parameters on a small scale. Here, then is a major vibration source which can be partially controlled by design.

Direct excitation by the rocket engine itself is also a major source of vibration, particularly in structure near the engine mounts. Total RMS accelerations on liquid rocket engines, including all frequencies below 12,000 cps, are generally of the order of 4 to 10 g with peak amplitude during firing as much as 10 times the RMS values. However, in some cases total RMS accelerations of the order of 50 to 500 g have been reported. Further, it appears that random frequency thrust variations from rough burning may be expected to be less than 5% of the engine thrust. However, the screaming resulting from resonant burning in the longitudinal mode of the chamber may result in RMS forces which are as much as 25% of engine thrust. Other combustion instabilities which are capable of producing significantly higher dynamic forces are generally eliminated during engine design, in order to prevent engine failure.



Unfortunately, the majority of available data cannot be generalized in a form useful to the designer because the mechanical impedances of the test stand mounts are unknowns which obviously differ from those of any practical vehicle. One possible experimental solution to this dilemma is the simulation of sufficient vehicle structure in the test stand rig so that the mount impedance would approximate that of the actual vehicle, or at least enable reasonable calculation of impedances and proper interpretation of the resulting data. However, regardless of these technical problems in evaluating existing data, rocket engine vibration environment is very severe, and any engine control equipment mounted on the engine, or its immediate structure, must be very rugged to achieve reliability. Similarly, great care must be exercised throughout the engine area to avoid fatigue failures.

#### Noise From Aerodynamic Phenomena

There are many potential vibration sources which can result from the flow of air over the vehicle. Fortunately, the majority of these aerodynamic sources can be eliminated or minimized by the designer. However, the recurrence of certain of these problems on the prototype vehicles indicates the need for effective cognizance during the design process.

The most familiar and basic aerodynamic source of vibration is the fluctuating pressure on the skin from the turbulent boundary layer. These pressure fluctuations result directly from the turbulent eddies in the boundary layer and are often referred to as pseudo-sound. The level of the RMS fluctuating pressures  $\langle \bar{p}^2 \rangle^{1/2}$

resulting from the normal turbulent boundary layer over a flat surface, are of the order of .005 times the free stream dynamic pressure ( $q$ ) at low Mach numbers. However, recent experimental

data (6) indicates that this ratio of  $\langle \bar{p}^2 \rangle^{1/2} / q$  decreases with increasing Mach number. Figure 7 summarizes these relationships and indicates a prediction of the variation of the ratio with Mach number, based on the variation in density resulting from increased temperature near the skin.

More data are required, particularly at supersonic Mach numbers, if engineering predictions of the vibration response to boundary layer pressure fluctuations are to be refined to an acceptable level. Furthermore, future measurements should not be limited to single microphones but must include several adjacent microphones to enable definition of the area over which a single pressure fluctuation is correlated. Without this latter information, analytical prediction involves severe approximations.

The value of  $\langle \bar{p}^2 \rangle^{1/2} / q = .005$ , which was found for the

normal turbulent boundary layer, can be increased to the order of .1 when flow separation occurs around abrupt geometrical changes behind a normal shock, or during buffet. This higher value of .1 can impose severe dynamic structural loads which have been responsible for failures in many cases, including some of the duct inlet problems. Hence, separated flow phenomena should be eliminated wherever possible by careful aerodynamic design. However, when such phenomena are unavoidable, the structure must be upgraded for the expected high loads and adequate test programs must be initiated if serious failures are to be avoided.

Closely related to some of the separated flow phenomena are the occurrence of oscillating shocks. The forces involved with shock oscillation approximate the pressures across the normal shock at low supersonic Mach numbers, but decrease considerably above Mach 2-3. Oscillating shocks may be anticipated as a general problem for reentry bodies whose high drag design shape often encourages shock oscillation. Recent NASA wind tunnel tests of a Mercury capsule demonstrate the effectiveness of model testing to determine probable occurrence of these oscillations and the effect design modifications which minimize these occurrences. Transient aerodynamic shocks occurring in the transonic speed range must also be considered in addition to mechanical shocks which occur at launch and stage separation.

Many severe vibration problems have resulted in aircraft when bomb bay and other similar compartments have been opened during flight. The investigators of cavity resonance phenomena (7),(8),(9) have all suggested that the resonance results from interaction between an acoustic wave and the boundary layer - vortex flow, where an acoustic wave propagated from the aft bottom corner of the cavity affects the boundary layer flow over the cavity. This interaction with the boundary layer results in a modulation of the momentum transferred from the boundary layer to the vortex and, hence, a modulation of the vortex circulation velocity and the resultant stagnation pressures in corners of the cavity. Although the exact form of this interaction is unknown, experimental evidence suggests that the length of the cavity is on the order of one wavelength at the dominant resonant frequency. Figure 8 gives the cavity Strouhal number associated with the dominant resonant frequency as a function of freestream Mach number for the data of (8) and (9). As can be seen, the fundamental cavity resonant frequency is inversely proportional to its length and directly proportional to approximately the two-thirds power of the freestream velocity. Examination of the full scale data from (7) indicates an additional small altitude effect on the frequency.

Other cavity resonance frequencies, including one-half,

one and one-half, and two times the dominant frequency, have been found together with the dominant frequency. The occurrence of these other frequencies in both the experiments (8) and (9) was dependent upon either boundary layer turbulence or the dimensions of the cavity.

The maximum RMS amplitude of the pressure fluctuation appears to be on the order of .03 to .06 of the freestream dynamic pressure ( $q$ ), (7) and (9). Note that these overall amplitudes represent energy concentrated at the fundamental frequency and its harmonics. Hence, coincidence of cavity resonance frequency with the resonant frequency of the structure enclosing the cavity leads to the imposition of unusually high vibration amplitudes and stresses.

Base pressure fluctuations on dive brakes and blunt based space vehicles represent another class of potential vibration sources. Figure 9 summarizes the frequency spectra obtained in a recent wind tunnel experiment (10) which determined the pressure fluctuations at two positions on the base of a small body of revolution. Values of the overall  $\langle \overline{p^2} \rangle^{1/2} / q$  ranged from .007

in the center of the base to .015 at the 65% radius position. More data, particularly in the supersonic flight region, are required to supplement these low-speed tests if prediction for a full scale vehicle is to be made with confidence.

#### Advanced Propulsion Systems for Space

There are many devices which have been conceived for eventual use in space propulsion and/or providing auxiliary power for space vehicles. Many of these are classified as "exotic" systems and only a few are past the conceptual stage and transferred to the experimental research phase. However, it is possible to evaluate the potential utility of the majority of these conceptual devices for space flight and, in a limited way, to assess their potential as vibration sources.

Figure 10 gives an overall view of the various types of propulsion units which may become practical, together with their thrust weight ratios, specific impulses, advantages, disadvantages and possible applications. This material has been taken from (12). In addition, the table gives the authors' assessment of the categories of vibration sources which will accompany each type of propulsion engine, together with an estimate of present knowledge of these problems.

It is clear from Figure 10 that the major sources of vibratory energy from these propulsion engines will be from auxiliaries. Thus, for the majority of the proposed systems, vibratory problems will be of the conventional types associated with rotating machinery. However, for many of the electrical engines

(Ion and Plasma Drives) the thrust will be either pulsed or follow a full wave rectified alternating current signal. The frequencies which will be encountered range from a few pulses per day to the order of 10,000 per second. The electric engines will be utilized (if they become practical in the distant future) primarily for very low thrust inter-space acceleration. Hence, their vibratory forces involved are expected to be small. It is expected that the thermal engine will be the mainstay of space research for the next decade at least, with a transition occurring from primary reliance on chemical fuels to reliance on nuclear fuels.

It should be noted that the thermal engines will all produce jet noise which will be important during the boost phase at vehicle velocities below Mach 1. Although the magnitude of this noise can be evaluated crudely by existing methods, the velocities expected for nuclear rockets utilizing hydrogen as a propellant are of the order of 20,000 feet per second. This is approximately three times exit velocities for conventional chemical rockets and, hence, prediction of noise should be supplemented by measurement at the earliest practicable date.

#### Summary of Sources

Figure 11 gives a tabular summary of the major sources, including those previously discussed, together with an estimate of the probable relative severity of each source. As can be seen, the sheer number of important potential vibration sources which can be minimized by proper analysis, test and design emphasizes the requirement for thorough evaluation of all potential sources during the design stage. Without such thorough evaluation, vibration sources which could have been controlled in design may be discovered during flight tests and require structural fixes which penalize vehicle capability.

### III. RESPONSE OF STRUCTURE

The prediction of vibration response throughout a vehicle is much more difficult than the prediction of the external forcing function. Although there has been considerable research effort to develop analytical approaches, the application of these approaches is at present confined to simplified analytical models of the vehicle or its sub-structure. Therefore, fundamental and higher modes of the entire vehicle, skin panels, bulkheads, equipment mounting sub-structure, etc., can be defined analytically in useful form. However, the complex transmission pattern throughout the vehicle, or vibratory energy which results from the interaction of a large number of component complex impedances, does not lend itself to analytical solution. Considerable more research is required to define the physical constants required for analysis, and to validate the interpretation of new theoretical parameters.

The prediction of vibration environment for a new vehicle design is required in the earliest design stages, long before the design is sufficiently advanced to be considered analytically. This early estimate of vibration environment enables consideration of vibration in the arrangement of equipment, determination of preliminary vibration specifications for equipment, and evaluation of the probable size and design of the vibration analysis, control, and test program for the new vehicle.

These early estimates of vibration are based, of necessity, upon empirical data from past experience. For this purpose it is desirable to be able to modify earlier data to reflect any differences in source and vehicle parameters between the past and future vehicle. A considerable effort was made in (11) to correlate vibration data from aircraft, and in (1) to correlate vibration data for various classes of missiles. The median curves from these two analyses of data are summarized in Figure 12. It should be realized that these median curves are useful only as trend indicators, since there is a very considerable scatter in the data with a standard deviation, generally on the order of a factor of 2 times the median. Furthermore, the vibration frequency spectrum at any one location in response to the various random forcing functions, is characterized by a series of maxima resulting from local resonances and amplifications in the path between the source and receiver. Thus, the RMS data which are considered in Figures 12 and 14 represent the RMS amplitudes at frequencies when the amplitudes are maximum.

The data for both the aircraft and missiles in Figure 12 were obtained primarily from high power or high dynamic pressure flight regimes. It can be seen in Figure 12 that the median of the data for the B52 exceeds that for the B47, whereas the median for the jet fighter vibration data lies between the medians of these two bombers. The medians for light missile launch and maximum q flight are generally higher than those for the aircraft. However, the medians of the data for the heavy missiles at structural locations forward of the engine compartment have a significantly lower magnitude, and are of the same order as the jet fighter and B47 vibration. Note that the vibration on missile structure located near the rocket engine is considerably higher than any of the other data. This figure clearly demonstrates that the severe portions of the vibration environment in the light missiles generally exceeds those experienced in high performance jet aircraft. However, the vibrations in the heavy missiles of the IRBM and ICBM category have been generally of the same order as those of the aircraft.

It should be emphasized again that Figure 12 only shows trends, since a very large scatter around the median exists for all

the data. Further, it should be noted again that the relative severity of launch and maximum q flight phase vibration depends upon both the flight profile and the launch configuration. For example, all of launch data result from surface launches, rather than silo launches. A comparison of the surface launch noise environment with the silo launch environment, based on the information of (1), indicates that the magnitude of vibration might be on the order of 3 to 10 times greater in a silo than on the surface, depending upon silo design and frequency. Thus, the silo launch vibration equipment for heavy missiles would be expected to exceed the surface launch vibration environment in the light missiles.

It is interesting to note that the slopes of all the trend curves are positive and that the data generally lie between curves of constant velocity and constant acceleration. Therefore, the overall values of acceleration are primarily influenced by the highest frequencies measured. Consequently, comparison of the overall acceleration levels of various data is not useful unless the data have similar spectra and were obtained over identical frequency ranges.

Two attempts have been made recently to obtain a useful correlation between the external noise and internal vibration. Convair (13), (14), (15) suggested a correlation for aircraft structure from the results of their extensive measurements and analysis of B58 data. In this correlation, internal vibrations were compared to adjacent external sound pressures. Thus, vibration measurements in the nose of the aircraft were compared directly to sound pressure levels measured on the external skin of the nose section, and vibration measurements in the aft end of the aircraft were compared to sound pressure levels measured on the external skin of the aft section, etc. Since the external noise environment on the B58, and other types of jet aircraft, varies considerably from the relatively low noise levels forward to the very high levels toward the aft end, a comparison of this type includes a range of external noise levels of the order of approximately 30 db.

A similar comparison of external noise and internal vibration from Snark data (1) is given in the upper portion of Figure 13. The higher sound pressure levels and their associated vibration data are obtained at after-fuselage stations adjacent to the rocket booster exhaust. It should be noted that the small variations in sound pressure level at one microphone position result from data of repeated firings and that the acceleration data include transducers attached to different points of structure and oriented in various directions.

As might be expected, the data exhibit considerable scatter, so that it is possible only to estimate a trend line through the points. However, more significant than the scatter is the slope of the trend line. Note that if the acceleration amplitude increases by a factor of 10 for an increase of 20 db spl, a

direct linear relationship exists between the internal structural vibration amplitude and the adjacent external sound pressure amplitude. In this event, the trend line through the data gives the constant of proportionality between external sound and internal vibration. The slopes of the trend lines for several aircraft are summarized in the lower half of Figure 13. It is clear from the figure that better correlation between adjacent external noise exists above 150 cps for the Snark and at the higher frequencies for the other aircraft where the slopes of the trend curves approach unity.

If the trend line has a slope of less than unity, as is the case for most of the low frequency data, a direct linear relationship between internal vibration and adjacent external sound pressure cannot be proved by the correlation. Several factors might, individually or collectively, be responsible for slopes less than unity. These factors include:

- (a) Structure-borne transmission of vibration from high external noise level areas to those of lower external noise level;
- (b) Non-uniform structure throughout the fuselage (which undoubtedly contributes to scatter);
- (c) Non-linear response of the structure;
- (d) Unfortunate selection of transducer location with respect to modal response.

Since a large number of randomly selected transducer locations are included in the various surveys, it is doubtful that the accidental location of transducers with respect to the various vibration modes accounts for the lower slopes at the lower frequencies. Similarly, since several experiments give the same general conclusion with regard to the trend curves, it is not felt that structural non-uniformity is a particular factor in the determination of the slope of the trend curve, although it undoubtedly is a most significant factor in the scatter of the individual data.

The role of nonlinear behavior in the structure cannot be evaluated with respect to the trend curves from the available data. However, it is considered to be less important than the fact that the response at any general position in the structure is given by the sum of the noise energy transmitted directly to adjacent structure, plus the noise energy received at more remote locations and transmitted as vibratory energy through the structure to the position. Thus, at higher frequencies better correlation would be expected between adjacent acoustical excitation and response because the vibrational energy transmitted through the structure from remote locations has been attenuated and makes only a minor

contribution. Conversely, at low frequencies the vibrational energy transmitted from the areas which have the highest external noise levels to those with lower external noise levels would be expected to exceed the local excitation. This general result might be anticipated since the attenuation of vibratory energy transmitted by bending waves along the fuselage is essentially constant per wavelength. Thus, the high frequency energy suffers considerably more attenuation than does low frequency energy when both are transmitted for the same distance through the fuselage.

An empirical correlation for missile launch data was developed in (1), based on the premise that the natural vibration characteristics of many complex structures can be approximated by individual consideration of each resonance or mode of vibration, assuming it to be essentially unaffected by, or decoupled from, any other mode. The response of the vehicle in any one of these modes can be obtained from expressions similar to those developed for the single degree of freedom system if an appropriate definition can be obtained for the amount of the total mass which is involved in actual vibratory motion, and for the effective or "generalized force" on the vehicle. Viewed in this perspective, the total response of the vehicle at any location is simply the sum of the contributions from all of the vehicle's vibratory modes.

In (1) it was shown that a correlation of this type might be expected at constant  $k r$ , where  $k$  is the wave number and  $r$  is the radius of the vehicle. Utilizing the normal single degree of freedom equation with a factor  $\beta^2$  as the constant of proportionality, then:

$$\left(\frac{a}{g}\right)^2 = \frac{\beta^2 \omega_n Q \overline{F(f)^2}}{4 W^2}$$

at constant  $k r$

where

- $\beta^2$  represents the constant of proportionality
- $\left(\frac{a}{g}\right)^2$  mean square acceleration ratio
- $\omega_n$  resonant frequency in radian/second
- $\overline{F(f)^2}$  mean square forcing function
- $W$  weight
- $Q$  dynamic magnification factor.



It is clear that both the damping in the structure and the type of structure will affect any correlation of response with forcing function, as both additional damping or additional stiffness in a specific vehicle will reduce the response for a given forcing function. Therefore, in absence of sufficient data describing these two factors, a constant  $Q$  of 15 was assumed for all missiles and all natural frequencies. The missile weight ( $W$ ) was taken as the gross launch weight, while the stiffness variable remains in the correlation as an additional unknown. The estimated value of mean square force per cps was obtained by integrating the predicted mean square pressure per cps on the vehicle and multiplying this result by the square of the vehicle's surface area. It is obvious that this quantity cannot represent the true generalized force on the vehicle, but it should be proportional to the generalized force for constant values of  $k_r$ .

The results for eight missiles are given as a function of  $k_r$  in figure 14.  $\beta$  appears to be almost constant, slowly decreasing with increasing wave number. The standard deviation of 20 log is approximately 6 db, indicating that 68% of the values of  $\beta$  are between .5 and 2.0. This is approximately equal to the scatter of the data in any general location on an individual vehicle. Perhaps the most startling result is the fact that the mean value of  $\beta$  is approximately one, as in the single degree of freedom case. This indicates that the ratio of generalized force to generalized mass remains constant with wave number and that the method of obtaining the forcing function used for the correlation fortuitously gives the ratio exactly equivalent to the single degree of freedom case.

Both of these empirical correlation methods are obviously limited by the variation of the vibration data themselves which vary from test to test and vary between transducers which are located in the same region but at different points and types of structure. However, the first method appears useful at high frequencies and the second method appears useful for missiles. It would be expected that their judicious combination, subject to all of the limitations and comments in the previous references, would provide useful preliminary predictions. It would also be desirable to analyze future data in accordance with these two methods to determine the validity of each method and better define its statistical accuracy.

#### IV. VIBRATION FATIGUE, MALFUNCTION AND TESTING

The topics of vibration fatigue and malfunction are closely related to the conception of suitable vibration tests, for the major objective of the test is to insure reliable performance in the anticipated environment throughout the design lifetime of the vehicle.

Metal fatigue from excessive vibration has been known for

a long time in reciprocating machinery, propellers, ships and aircraft. However, until it was necessary to optimize the strength-weight ratio of flight vehicle structure, and to subject this structure to severe external random loads (pressure fluctuations and gusts), the problems were readily solved. The solutions usually resulted in applying sufficient reinforcing to the local areas which experienced the maximum stress reversals to obtain a good safety factor. When the forcing functions were primarily sinusoidal the number of critically stressed structural parts depended on the modal response for the worst resonant frequency. Generally, the number of these critical parts was small and the total weight penalty imposed by simple "fixes" was low.

The problem of "fixing" structure and panels exposed to random frequency external pressures is an order of magnitude more complicated and can involve serious weight penalties. It is no longer possible to stiffen the structure to move its natural frequency above the major forcing frequency, because the random forcing function contains energy at all frequencies. Furthermore, the external pressure fluctuations act over large areas of external skin and its substructure, so that the number of "fixes" must be very large.

Therefore, it is mandatory to design the structure and skin to withstand these external pressure fluctuation, optimizing its fatigue strength - weight ratio. Secondly, it is necessary to prove and optimize these structures by testing them in simulated predicted environments prior to finalizing the vehicle. The appropriateness of the test design depends upon the validity with which it simulates the essential factors of the true environment. Herein lies one of the major dilemmas facing the vibration specialist and management; for the assessment of the degree of simulation required, time of testing, and the number of specimens required for statistical significance involves important economic and schedule considerations.

The difficulty of these assessment is clear upon examination of typical fatigue data. Figure 15 from Ref. 14 shows that the number of cycles to failure for strains above the endurance limit is proportional to the square of the RMS strain ( $\Delta \epsilon$ ) for a variety of materials. This correlation vs strain was proposed by (14) as a much more general correlation than the conventional S-N diagram because a wide variety of materials appear to behave similarly for equal  $\Delta \epsilon$ . Note that the spread of the data is typically of the order of a factor of ten in life and a factor of three in strain. This large scatter requires tests of several structural specimens if any real confidence is to be obtained.

Secondly, utilization of data of the form of Fig. 15 to predict life or to accelerate tests involves serious unknowns. It has been shown by many authors, including Ref. 15, that the Minor's

fraction can be utilized with reasonable accuracy to obtain expected fatigue life for sinusoidal vibration at various amplitudes when the test durations at each constant amplitude are a significant number of cycles. However, when true random forcing functions are imposed on the part, its response at its natural frequency varies in amplitude from cycle to cycle in a random fashion. Hence, successive strains contain all combinations of high and low amplitudes and varying magnitudes of strain reversals. This intermixing of strain amplitudes lowers the cycle life of the part to as little as one-fourth of that predicted by a cumulative damage rule. Although considerable research effort is progressing currently in this problem area, it is presently hazardous to predict fatigue life for a part subjected to a complex random load environment from conventional sinusoidal test data.

It is also difficult to ascertain the degree to which a test can be accelerated without invalidating the results. Since a reduction of test time by a factor of ten can be achieved by increasing the forcing function by a factor of approximately three, it is most tempting to reduce test costs by accelerated testing. Furthermore, when the design life in the maximum environment is to be in the order of days or weeks, it becomes impractical to test without acceleration. Serious hazards impede this approach, primarily because of panel nonlinearities, including appearance of additional damping at higher strain levels, and increased stiffness due to membrane stresses. Consequently, it is necessary to control the increase of test amplitudes by direct measurement of the fluctuating strains, rather than measurement of the forcing function.

#### Equipment Malfunction and Damage

Space vehicle equipment packages range from relatively heavy and rugged components, such as turbopumps, plumbing valves, motors, generators and transformers, to very small and fragile items, such as electron tubes, relays, optical systems, magnetic pickups, etc. The latter are generally sensitive items, having fine tolerances and requiring fine adjustments which must not be excessively disturbed. The probability of malfunction and damage to equipment is high; first, because of the high levels of transmitted shock and vibration through the vehicle structure and base mounts, and, secondly, because of the very large number of equipment items required for instrumentation, data recording, guidance, etc.

Equipment failures are broadly divided into two classes: temporary and permanent failures. Temporary failures, often called malfunctions, are characterized by out-of-tolerance performance of the equipment when the shock and vibration environments are applied and by normal performance when the environments are removed. Permanent failures are characterized by breakage resulting from high amplitude overstressing associated with shocks and cumulative damage leading to fatigue-type failures associated with the cyclical

stressing of vibration over a large number of cycles. These two classes are not necessarily distinct, since temporary failures accompanied by wear and gradual deterioration may promote permanent failures under continued action of the environment.

The internal structures of equipment components are generally quite complex, as are the vibration response modes, the modes of failure, and the environmental excitations which lead to these failures, so that accurate analysis and prediction of equipment failures is difficult. However, since the overall reliability of the vehicle is dependent upon the reliability of the individual equipment components, an assessment of the damage potential of each equipment component must be made. Conceptually, this can be accomplished with a knowledge of the in-service environment and the fragility of the equipment to this environment in terms of time duration, frequency and amplitude of the applied excitation. Because of the statistical nature of the environment and the variability of the fragility of similar equipment packages, the damage potential must be defined statistically.

The limited data available for the environment and the limited number of tests permitted to determine fragility, especially during design, necessitates the use of estimates in both these areas. Simple ideal dynamical models of the equipment are generally used with such input excitations as sinusoids and white band random noise. With these models the nature of the various modes of failure can be qualitatively understood and the most critical areas or items of failure isolated for more detailed examination, both by analysis and laboratory tests.

Certain types of malfunction failures, such as relay chatter, chassis vibration and vibration-induced electrical noise in electron tubes, are dependent upon the relative displacements of neighboring mechanical elements and are thus amenable to analysis and controlled testing for assessment of their damage potential. The parameters of importance in these cases are the RMS and peak responses of the elements and the statistical distributions of these quantities. Little or no malfunction is produced in such cases when the response amplitudes are maintained below certain critical values. Malfunctions and damage caused by deterioration and fatigue are not easily analyzed and the damage potential must be determined experimentally. For these cases, not only the amplitude levels and their distributions are important, but also the sequencing of the applied excitation must be considered. Thus, although ideally it is desirable to define the fragility of the equipment as including both of these malfunction types, it is often more convenient to handle these effects separately, due to their distinctly different characteristics.

At the present time, sufficient controlled laboratory test data are available to show that the ideal models often used for the

equipment and the ideal sinusoidal and sine-sweep substitutes for the generally complex random environment are often inadequate for determining the damage potential of equipment, except for especially simple modes of failure. Therefore, in many cases, in order to raise equipment reliability to those levels which are compatible with the reliability established for the vehicle and its mission, true simulation of the shock and vibration environment in the laboratory is essential for qualification testing.

Thus, the test design for both fatigue and malfunction proceeds through the answers to these questions: (a) can the test apply a duplication of the load history without acceleration in level or time? This type of test may be especially appropriate for missiles and space vehicles because of the limited service life. The margin of safety may be assigned to this case with more accuracy than usual; (b) if not the test above, is there a way to accelerate the test in time only? (c) if neither of the above tests applies, consideration can be given jointly to:

1. Is there an appropriate sinusoidal equivalent or should a random test be used?
2. Is the part sufficiently linear in response to allow acceleration in level?

#### V. GENERAL CONCLUSIONS

The present lag between the reliability required of space vehicles and the reliability which can be provided in a new design, imposes serious penalties in mission capability and cost. To overcome this lag requires redoubled and concentrated effort in several areas.

First, vibration control must be considered as a major problem area from the conception of any new vehicle. This consideration should enable basic management decisions, which determine the effort required in new vibration control methods, analysis of structure, and definition of the test facility and test program requirements. These judgments must be predicated on the overall reliability target for the vehicle to insure that the scope of the vibration effort is compatible with the reliability goal.

Secondly, increased effort must be made in the dissemination of information, design manuals, etc., by the vibration specialists to the design engineers. Only with adequate information at all design levels can the required vibration resistance be designed into each small part. Repeated examples of unnecessary failures because of easily avoidable stress concentrations and inadequate support cannot continue.

Third, increased effort is required in the development of practical analytical tools for complex structure, and in the

development of a better understanding of fatigue under random loading. Continued research is needed in all areas discussed if the overall state of the art is to improve.

Fourth, communication and correlation of vibration data and experiments between all of the weapons systems contractors and interested government agencies must be accelerated. Present practices which tend to suppress data regarding severe vibration problems and which are considered "mistakes," lead to repetition of similar "mistakes" by other companies. To expedite this communication process, a centralized activity should collect vibration information from each company or agency, through informal reports and personal visits, for timely dissemination. At present, enormous amounts of experience are wasted and many experiments have been needlessly repeated because of the lack of adequate communication. The sad experiences with fatigue failures and malfunctions over the past few years conclusively demonstrate that poor communication is an extravagance which cannot be afforded in the present and future technological revolution.

LIST OF REFERENCES

1. Eldred, K. M., Roberts, W., White, R., "Structural Vibration in Space Vehicles," to be published as WADD Technical Report 61-62. (Note that this report includes work reported herein, together with considerable additional information and numerous references.)
2. Veneklasen, Paul S., "Missile Noise as a Factor in Reliability," Aero/Space Engineering Vol. 17, No. 9, September 1958.
3. Eldred, K. M., "Analysis of Noise Data for Convair, Pomona, Tartar LTV-1, SN-3 and SN-6," Paul S. Veneklasen & Associates report dated 10 September 58.
4. Lighthill, M. J., Proceedings of Royal Society of London, 1951.
5. Lighthill, M. J., Proceedings of Royal Society of London, A211; 564 (1952)
6. Richards, F. J., Ball, M. K. and Willis, J. L., "Boundary Layer Noise Research in the USA and Canada; A Critical Review," University of Southampton Department of Aeronautics and Astronautics Report No. 131, February 1960.
7. Roshko, A., "Some Measurements of Flow in a Rectangle Cutout," NACA TN 3488, August 1955.
8. Krishnamurty, K., "Acoustic Radiation from Two-Dimensional Rectangular Cutouts in Aerodynamic Surfaces," NACA TN 3487, August 55
9. Yartan, D. C., "Investigation of B-47 Bomb Bay Buffet," Boeing Document D-12675, ASTIA 150-742, dated 16 May 1952.
10. Eldred, K. M., "Base Pressure Fluctuations," JASA Vol. 33, No. 1, 59 - 63, January 1961.
11. Lunney, E. J., and Crede, C. E., "Establishment of Vibration and Shock Tests for Airborne Electronic Equipment," WADC TR 57-75, January 1958.
12. Corliss, W. R., "Propulsion Systems for Space Flight," McGraw-Hill Book Co., New York, 1960.
13. Convair Report FZS-4-149, "Method for Predicting B-58 Vibration Environment," October 1957.
14. Convair Report FZS-4-803, "B-58 Environmental Vibration Qualification Tests," February 1958.
15. Convair Report FZS-4-160, "B-58 Predicted Vibration Environment and Vibration Range Curves for Environmental Test," February 1958.

LIST OF REFERENCES, continued

16. Shanley, F. E., "Discussion of Methods of Fatigue Analysis," Rand Report P-1749, 6 July 1959.
17. Freudenthal, A. M., and Helles, R. S., "On Stress Interaction in Fatigue and a Cumulative Damage Rule," Journal of Aerospace Sciences, Vol. 26, No. 7, July 1959.



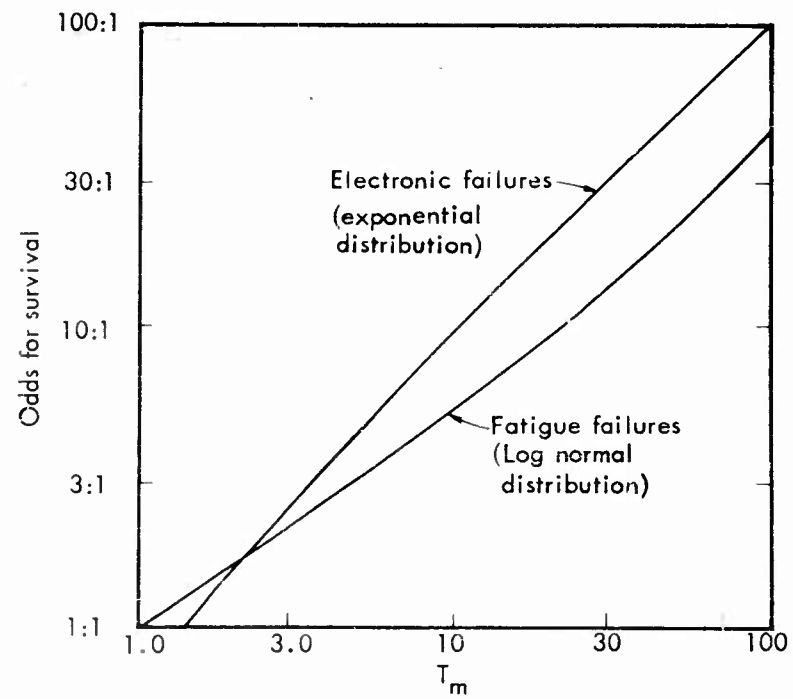


Figure 1. Odds for survival on a mission of duration of  $T$  versus a system mean time to failure  $T_m$



Figure 2

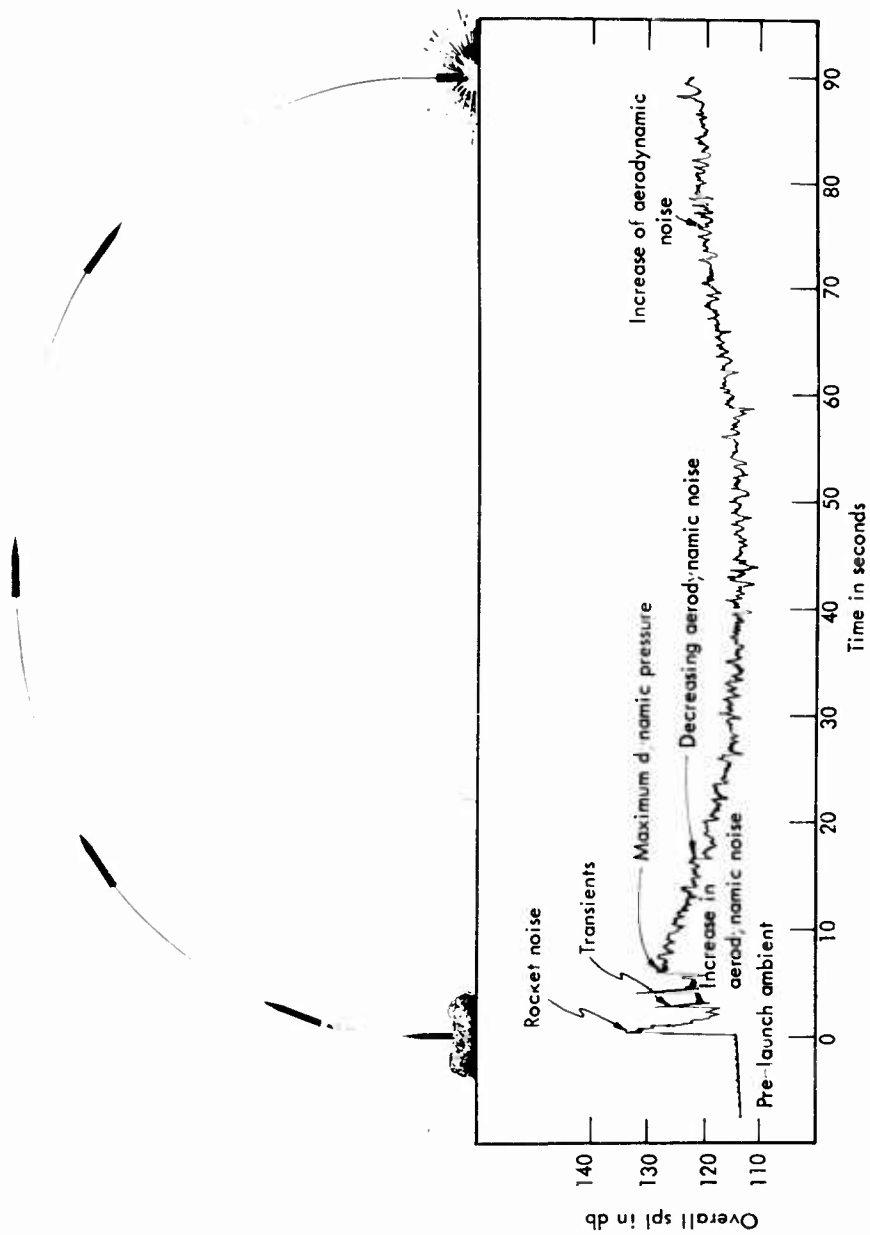


Fig. 3 - Graphic level recording of noise in a forward compartment of a small missile from Ref. 2

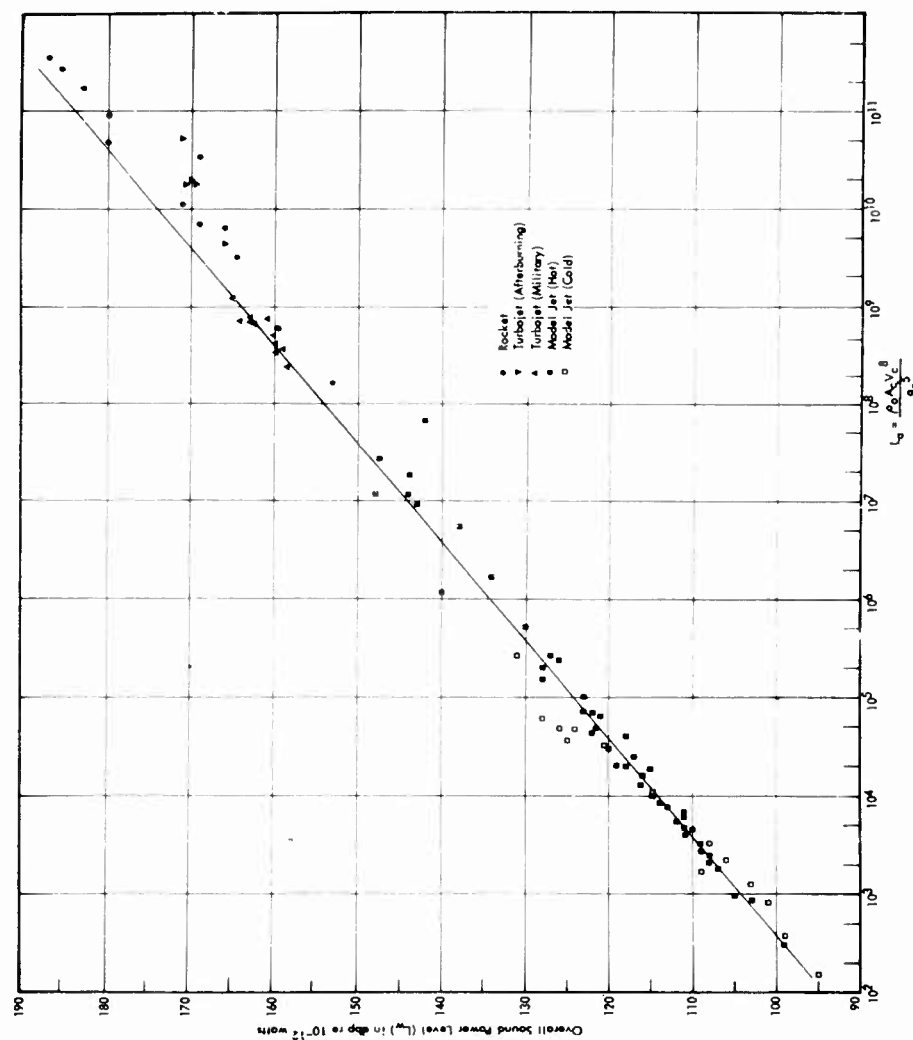


Fig. 4 - Overall sound power level for free jets of various types, versus the "Modified Lighthill Parameter"

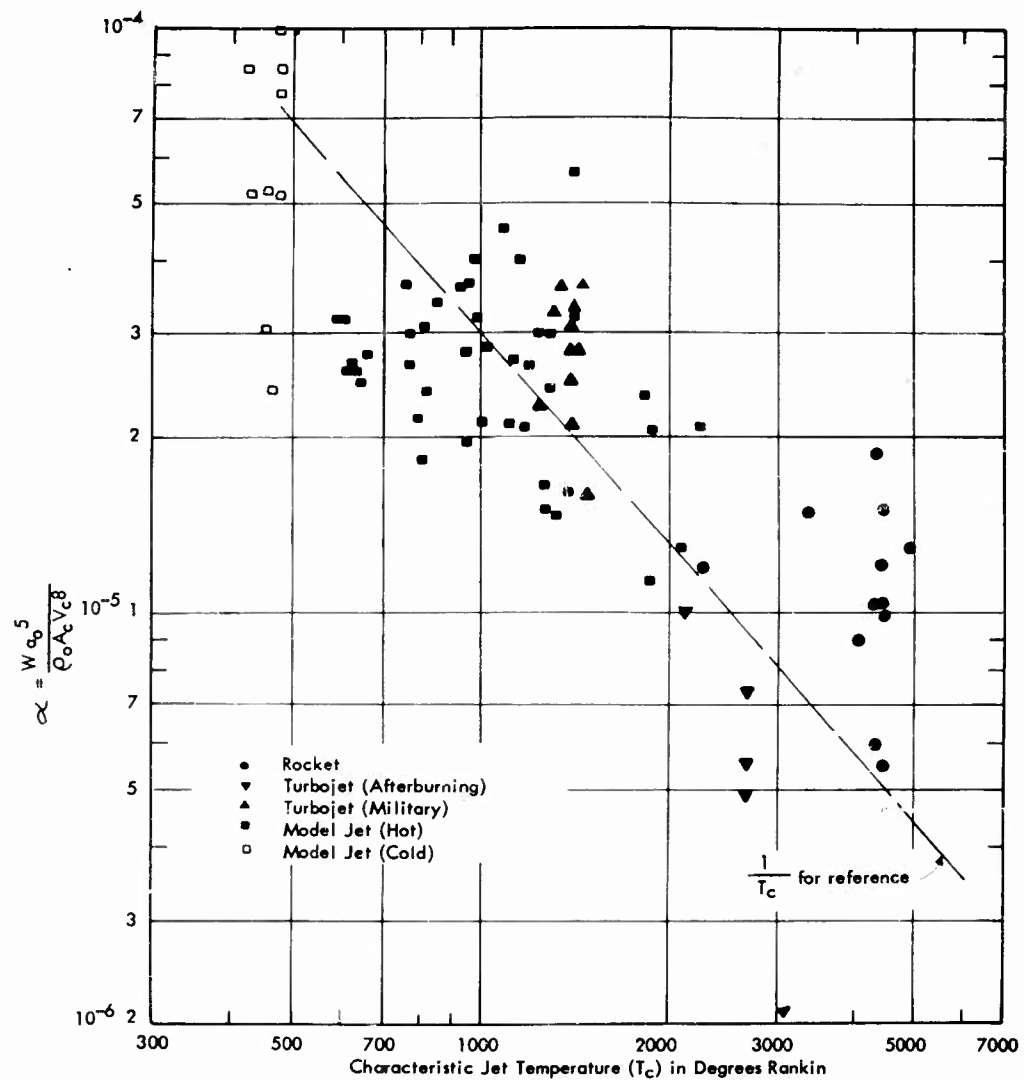


Fig. 5 - Ratio of sound power to "Modified Lighthill Parameter" as a function of jet temperature

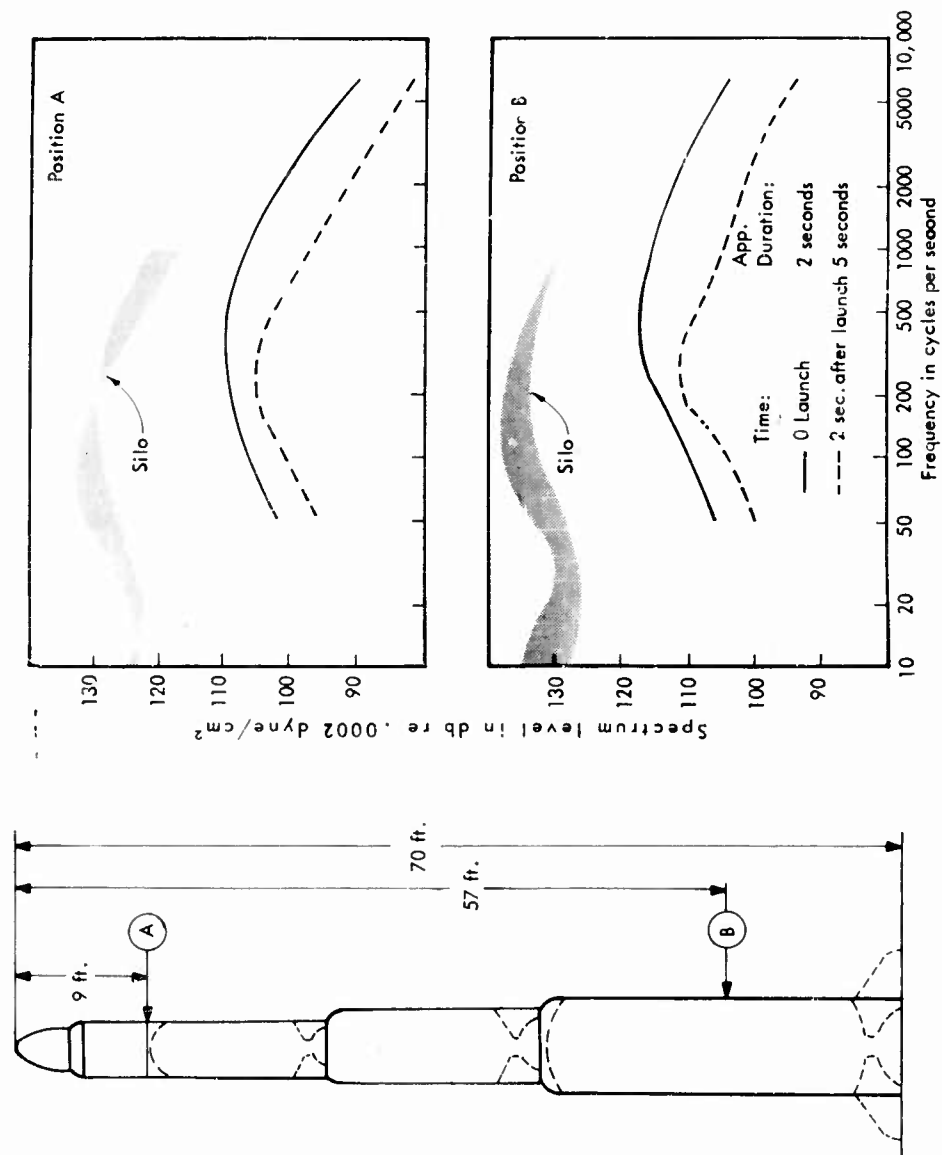


Fig. 6 - Hypothetical example of the comparison of vehicle launch noise for three launch configurations

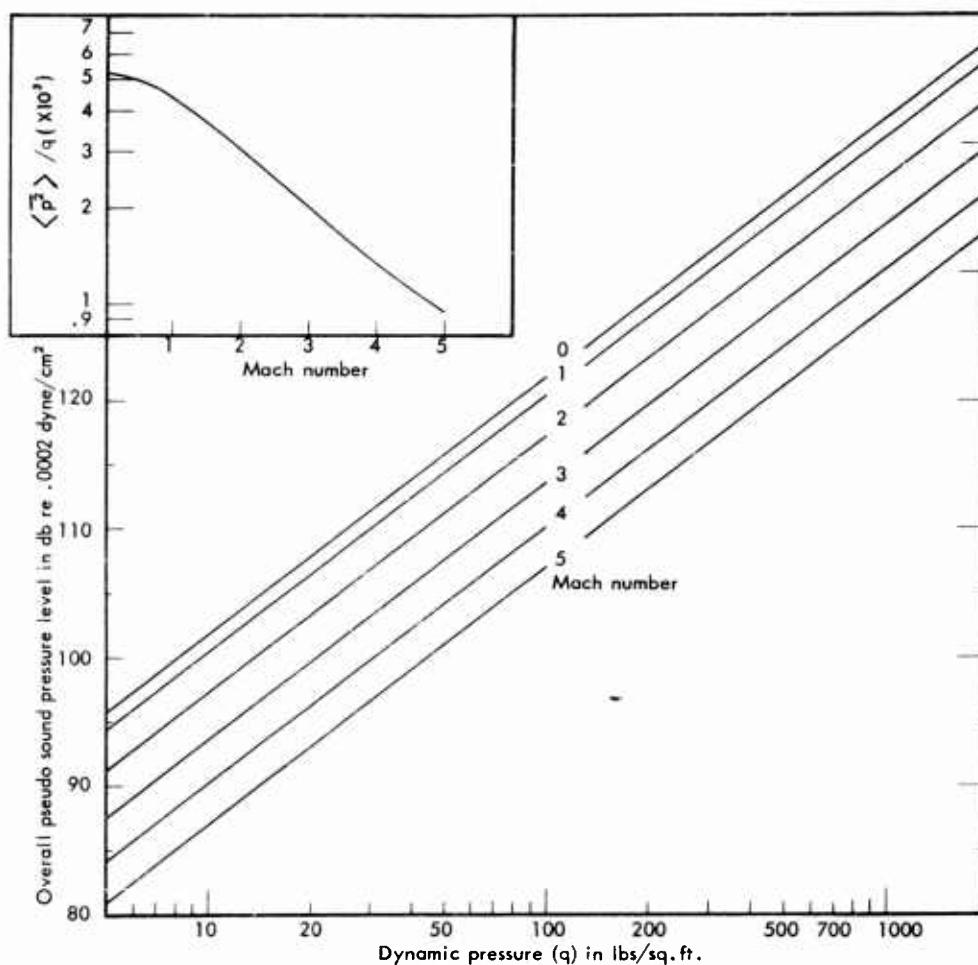


Fig. 7 - Overall psuedo sound pressure levels for boundary layer pressure fluctuations for normal flat plate turbulent flow with an estimated correction for Mach number based on variation of density throughout the boundary layer assuming insulated plate.

Note: The inset shows the ratio of rms pressure fluctuation to dynamic pressure external to the boundary layer.

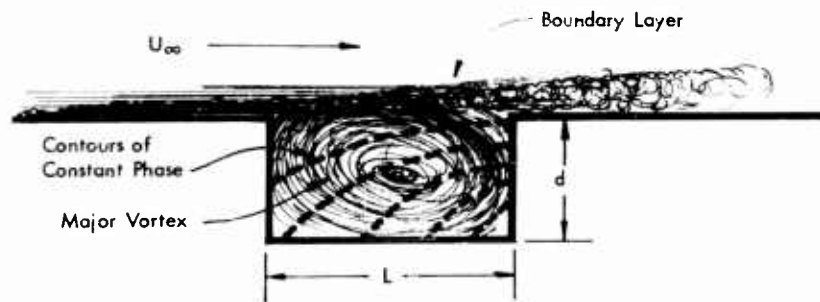
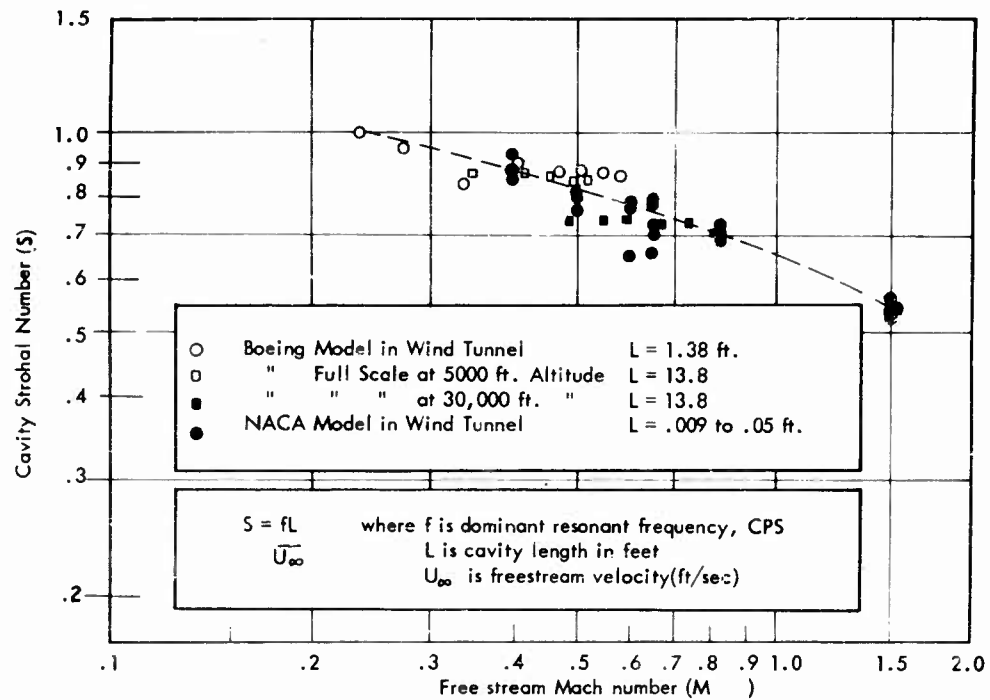


Fig. 8 - Strouhal number of fundamental cavity resonance frequency as a function of Mach number from Refs. 8 and 9



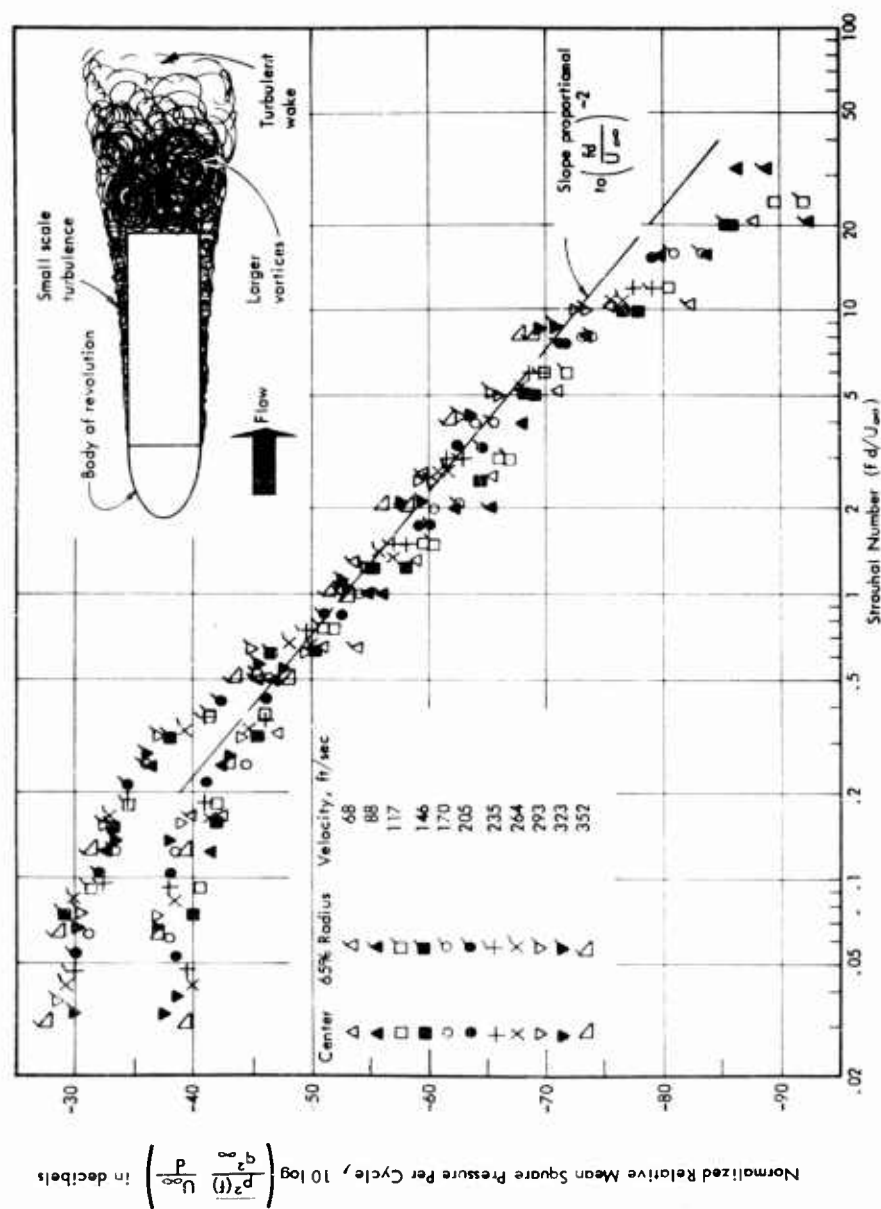


Fig. 9 - Base pressure fluctuations: Mean square pressure per cycle relative to the freestream dynamic pressure  $q$  and normalized by  $U_{\infty}/d$  for two microphone positions. Model body had 5-in. diameter and 20 1/4-in. length. See Ref. 10.

SUMMARY OF PROPULSION ENGINES FOR SPACE VEHICLES (Based on information from reference 12, with exception of Vibratory Potential)

CLASS	TYPE	VIBRATORY POTENTIAL		THRUST WEIGHT RATIO	SPECIFIC IMPULSE (sec)	MAJOR ADVANTAGES		MAJOR DISADVANTAGES		MISSION APPLICATIONS	
		Present Knowledge	Types of Vibratory Sources			Well developed; large compressor plus auxiliary machinery	Complex when clustered; may be unsafe	Energy & propellant extracted from environment	Not well understood; must be boosted to high speeds	Interplanetary	Satellite Maneuvering
Thermal Engines	Turbojet	Good	Noise in atmosphere; large compressor plus auxiliary machinery	1	1500				X		
	Recombination Ramjet	Fair	Auxiliary machinery	$10^{-3}$ - $10^{-4}$							
	Chemical Rocket	Fair	Noise in atmosphere; liquids have turbo pumps and other auxiliary machinery; both liquids and solids have rough burning, screech and other instabilities	10	240 (now) to 480					X	X
	Nuclear Heat Transfer Rocket	Fair	Turbopumps and auxiliary machinery; noise in atmosphere	2	to 1500						
	Consumable Nuclear Rocket	Poor	Turbopumps and auxiliary machinery; noise in atmosphere	10	to 3000					X	
Electrical Engines	Nuclear Bomb Propulsion	Poor	Extreme shock environment	10	1000-1700						
	Thermonuclear Rocket	Poor	Large electrical generator and auxiliary; noise in atmosphere	$10^{-1}$	to 3000						
	Plasma Jet Ion-drive	Poor	Electrical generator and aux. Large generator can operate either DC or AC; in latter case the thrust is modulated by the electrical frequency; also pumps and other aux.	$10^{-3}$	to 2500						
		Poor	Some devices are steady state; others are pulsed; most are large; require quantities to 10000 psi; large gen. and aux.	$10^{-3}$ - $10^{-4}$	to 25,000						
	Plasma Arc-celeration (magnetohydrodynamic devices)	Poor	Some devices are steady state; others are pulsed; most are large; require quantities to 10000 psi; large gen. and aux.	$10^{-5}$	to 10,000						
	Solar Sail	Poor	Should require little aux. machinery	$10^{-4}$							

Figure 10

MAJOR SOURCES OF VIBRATORY ENERGY  
IN MISSILES AND SPACE VEHICLES

<u>Source</u>	<u>Type of Forcing Function</u>	<u>Important During</u>	<u>Relative Severity*</u>
Rocket noise (generated in exhaust stream)	Continuous spectra random amplitude	(a) Launch (b) Flight below Mach 1	1 2
<b>Aerodynamic Excitation</b>			
(a) Boundary layer turbulence	Continuous spectra random amplitude	Atmospheric flight	1**
(b) Cavity resonances	Discrete frequencies dependent on flight speed	" "	1**
(c) Projection wakes	Discrete frequencies and continuous spectra	" "	3**
(d) Impingement of propulsion exhaust	Continuous spectra random amplitude	Atmospheric or space flight	2**
(e) Fluctuating wake drag	Continuous spectra random amplitude	Atmospheric flight	1**
(f) Oscillating shock waves	Primarily discrete frequencies	Primarily in low super- sonic range	1**
(g) Skin flutter	Discrete frequency	Atmospheric flight	1**
(h) Buffet and other separ- ated flows	Discrete frequency	" "	1**
Wind Shear and Gust Excitation	Continuous spectra predominately low frequency	" "	2**
Meteorite Impinge- ment	Intermittent or quasi- continuous spectra	Space flight	4
<b>Internal Vibration Excitation</b>			
(a) Propulsion system	Primarily discrete frequencies plus start- ing transients and random thrust variations	Whenever operating	1**
(b) Internal equipment	Primarily discrete frequencies	" "	3
(c) Fuel sloshing	Primarily low frequency	Whenever fuel tanks are partially filled and vehicle alters direction	2**

\* This estimate is very simplified and primarily qualitative

\*\* Occurrence and severity depend upon design and/or mission profile

Figure 11

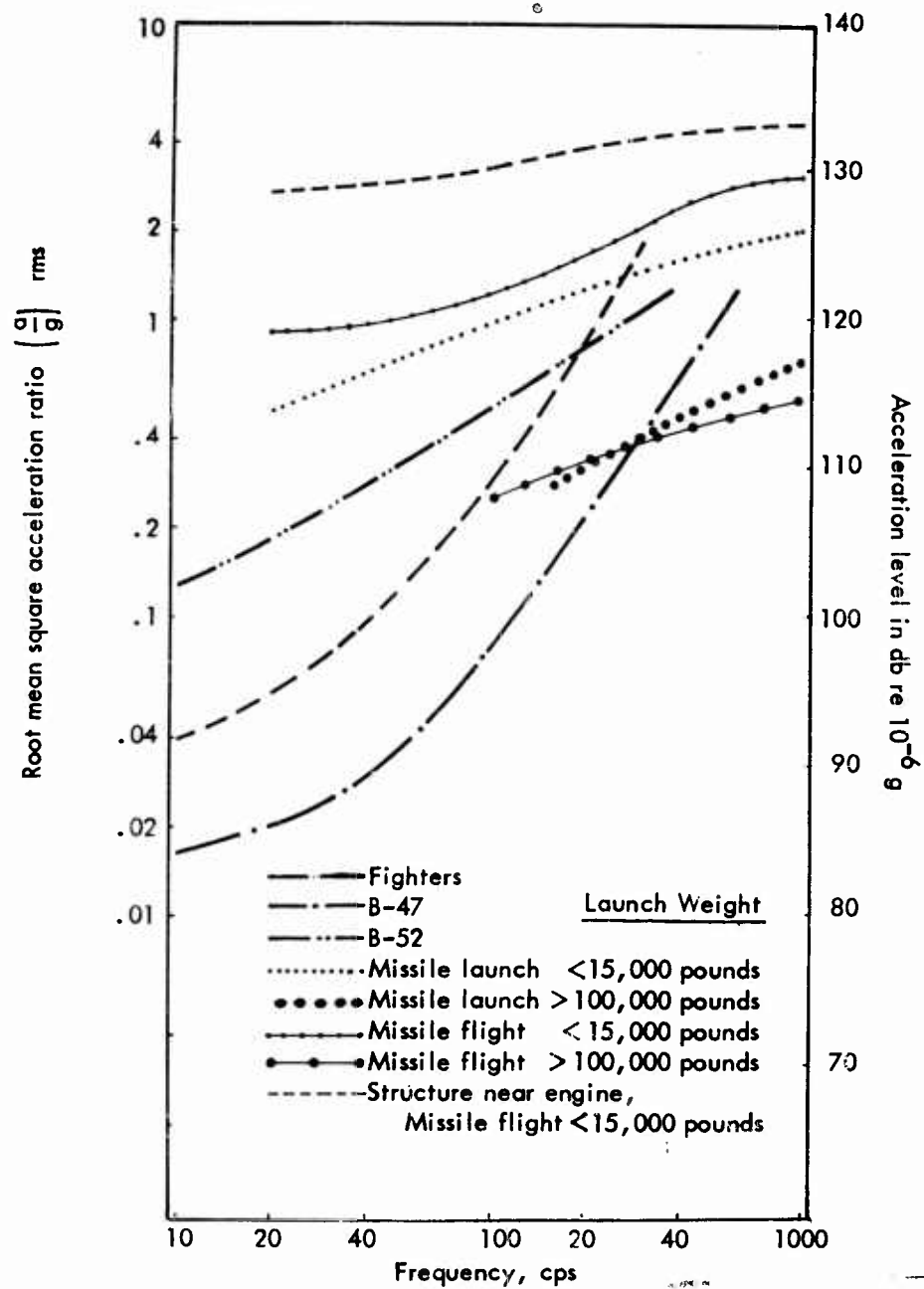


Fig. 12 - Summary of median rms acceleration ratios for various types of vehicles from Refs. 1 and 11

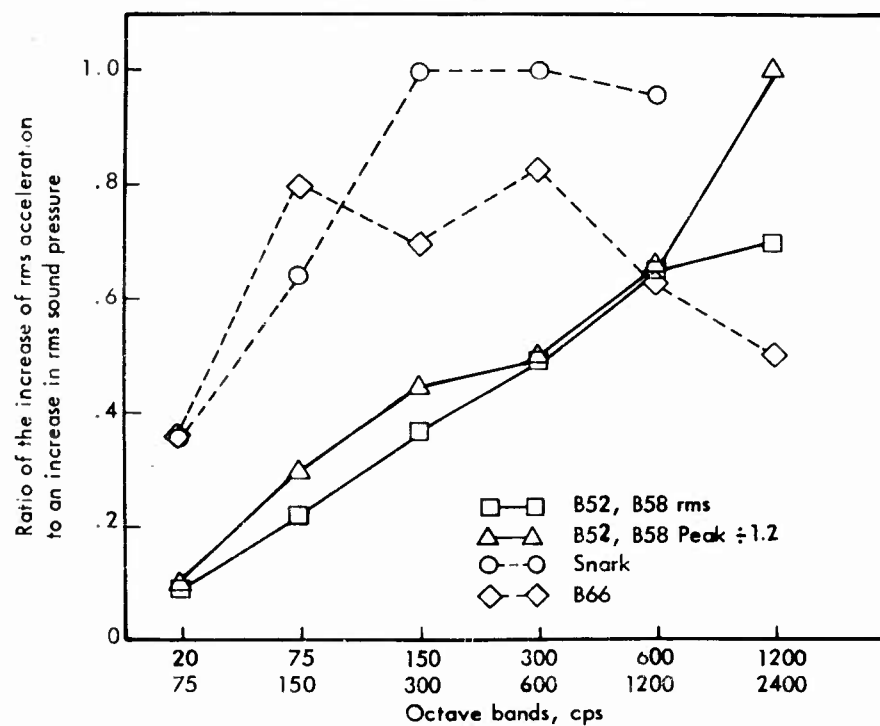
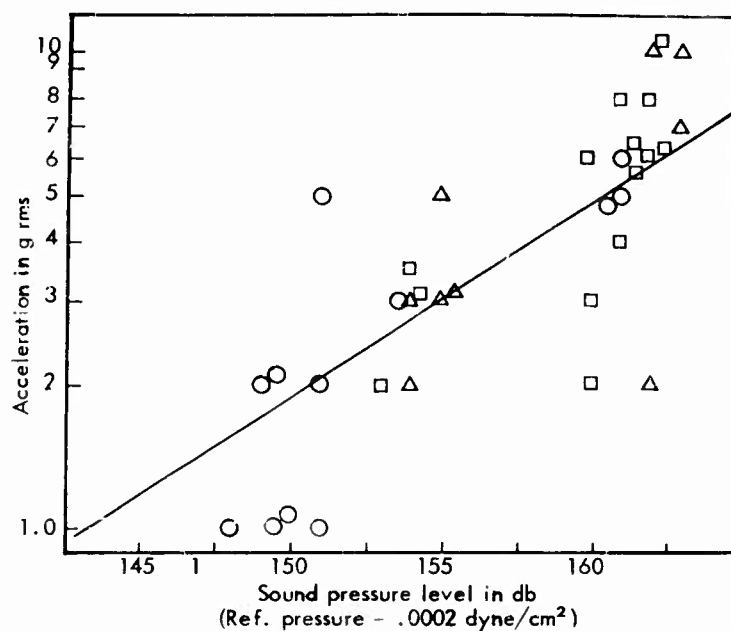


Fig. 13 - Comparison of external sound pressure levels with internal vibration levels. (a) 75 - 150 cps octave band for Snark ground firings. (b) Slopes of similar correlations from refs. 1, 13, 14, 15.

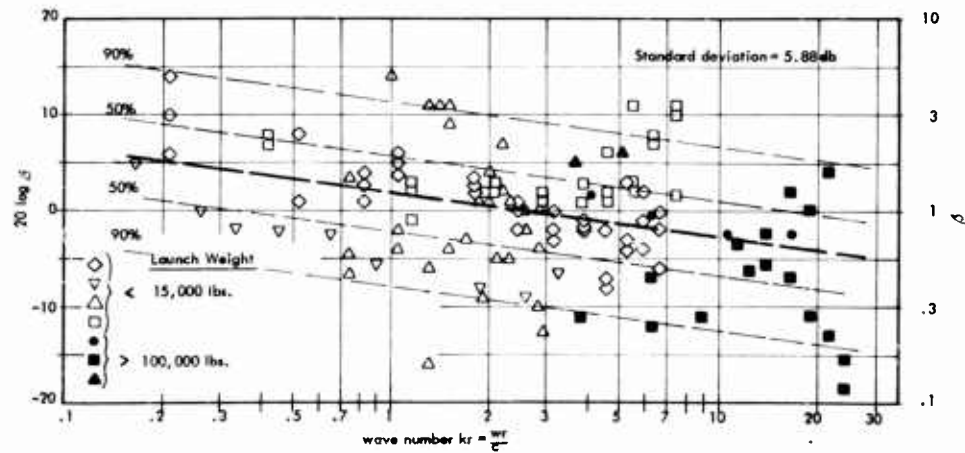


Fig. 14 - Relationship between the parameter

$$\beta^2 = 4(\alpha/g^2)W/\omega_n Q \overline{F(f)^2}$$

and the dimensionless frequency parameter  $kr$  from data for several missiles.

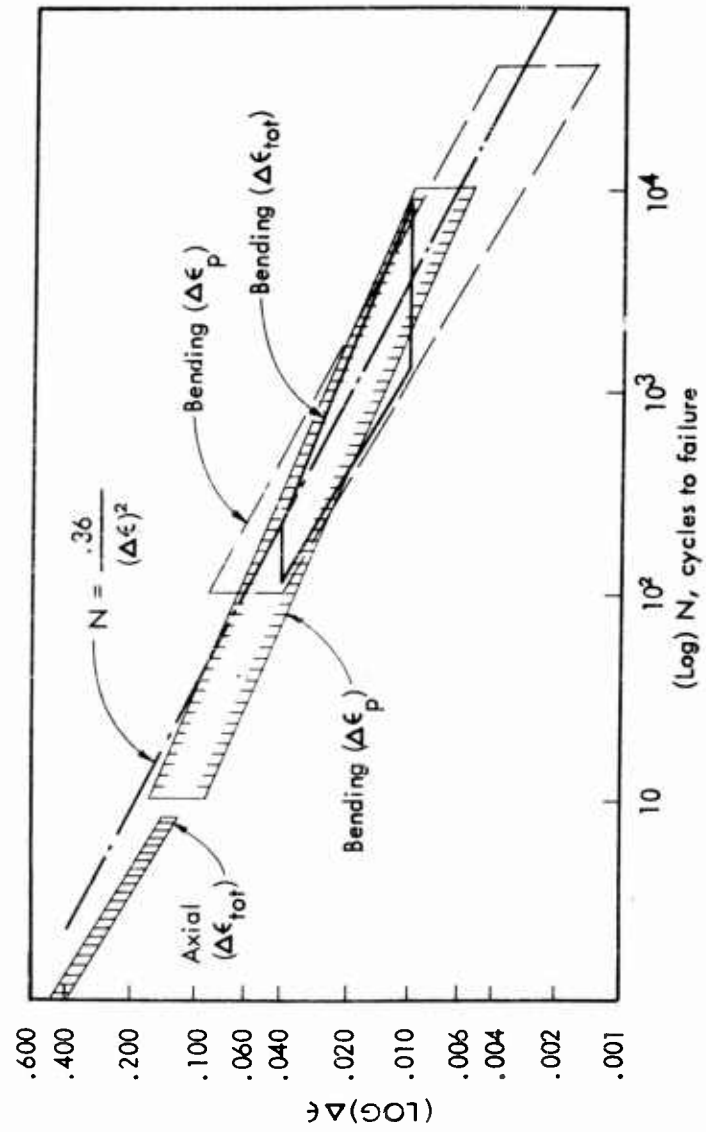


Fig. 15 - Comparison of fluctuating rms strain ( $\Delta \epsilon$ ) and the number of cycles to fatigue failure for several materials from ref. 16.

## STRUCTURAL RESPONSE TO RANDOM AND DISCRETE NOISE INPUTS

G. L. Getline  
Convair, A Division of General Dynamics Corporation  
San Diego, California

### Introduction

Although the title of this paper is somewhat restrictive, the actual discussion will be on a somewhat broader base. I plan to stand back and see if some engineering basis can be established for the handling of a particular class of random phenomena. In particular, I would like to discuss the vibratory responses of a complex structure such as an airframe or missile hull from the following standpoints:

1. How does one analyze the "random" vibratory responses of an airframe (or missile) structure when the characteristics of the vibratory inputs are unknown?
2. What do these responses mean in terms of secondary inputs to equipment installed inside the vehicle?
3. What are the important effects with respect to fatigue of the structure?
4. Is there reasonable justification for conducting "random" noise or vibration tests in the laboratory, in preference to the employment of sinusoidal inputs?



Discussion

Some time ago, we had occasion to obtain extensive flight vibration data on an F-106 airplane. The data were obtained from transducers located all over the aircraft, and installed on a wide variety of structural elements. Recording was on magnetic tape. For the most part, the characteristics of the vibratory forcing functions were unknown. The problem was, then, how to analyze the recorded data so as to provide meaningful design information.

Loosely speaking, the responses of the airframe were random, except for those due to excitation by the powerplant and accessory packages. The use of the word "random" to describe the vibratory responses of the aircraft structure is not strictly correct, however, since it implies (in the rigorous sense) the absence of periodic or quasi-periodic elements. The aerodynamic forces which cause the structure to vibrate may be truly random, although this was not investigated, but the structure responds essentially at discrete frequencies which are (in effect) natural frequencies (Reference 1). The responses, then, are quasi-sinusoids whose frequencies are fixed, but whose amplitudes vary as a function of time, as shown in Figure 1. To describe such vibrations, their amplitudes must be considered in terms of their time variation.

In order to analyze the vibration responses of the F-106 structure as recorded on magnetic tape, considering the previously mentioned qualifications, it was necessary to make a number of side investigations involving the following questions:

1. What is the minimum time over which the vibrations will converge to a quasi-stationary signal?
2. What is the maximum filter bandwidth which will provide an effective approximation of the true power spectral density?

The reason for the first question is obvious, and the answer establishes the minimum length of record required to obtain consistent data. The answer to the second question is important, because it effects a compromise between the amount of detail seen (or obscured) in the analysis and the rapidity with which large amounts of raw data may be reduced (Reference 2).

At this point I would like to diverge briefly from the main discussion. To repeat a previous statement, the purpose of the data analysis is to provide meaningful design information. I am sure that all of you who have had occasion to deal with random phenomena, and who have either read up on the subject or discussed it with a statistician or mathematician, have been exposed to the following observations:

## Getline

1. "Well, since we don't know what we're talking about anyway, let's assume we have a Gaussian (or normal) random process."
2. "Now that we know the process is Gaussian, then it is completely characterized by its power spectral density, ie, its mean square acceleration or mean square stress per cycle per second."

At this point, the consulting statistician loses interest and terminates the conversation. As far as he's concerned, he has solved your problem. (Have you ever told a design engineer that a structure must work at a particular mean square stress level? The reaction could prove interesting.) Gentlemen, you haven't solved a thing! In good faith, you couldn't design a kiddie car to a mean square (or rms) stress level. The problem is essentially this: The statistician is basically interested in averages and trends; the design engineer is always dealing with absolute values. Hence, the statistician's point of termination is the design engineer's point of departure.

In one sense, the contact between the engineer and statistician has been unfortunate. In the course of being inculcated with statistical methods of handling random data, some engineers have lost sight of their main purpose, that is, to provide meaningful design information. In fact, the averaging procedures which yield mean square numbers, effectively erase the time history of the basic data beyond reconstruction. This obscures the real character of the "vibration" and could be misleading (Reference 1).

It is my contention that what we are really interested in is not average or rms or mean square values, but rather the real time history of maximum values (Reference 3). And with this, I'll return to the main theme of this discussion.

In the first place, it is obvious that a basic requirement for the analyzer filter is that it be a constant percentage bandwidth rather than a fixed frequency bandwidth. This is necessary to provide the same size window for looking at the data independently of frequency. For example, let us refer to Figure 2. Suppose we arbitrarily select a filter with a 2 cps bandwidth. If resonance (frequency ratio of 1) is at 10 cps, the filter encompasses the frequency range 9-11 cps or frequency ratios of 0.9-1.1. For the response curve shown in Figure 2, this intersects it approximately at the so-called half-power points or at  $\sqrt{2}$  of the peak amplitude. If resonance is at 100 cps, this filter encompasses a frequency ratio of 0.99 - 1.01, which intersects the response curve very close to the peak amplitude. It is obvious that the detail seen at 100 cps is much greater than that seen at 10 cps. Further, if a fixed bandwidth filter is used, the time required to analyze data increases disproportionately as the frequency range of interest

## Getline

increases, in order to assure that major variations are not overlooked.

A most important consideration in selecting a constant percentage bandwidth filter, is to assure that the filter does not encompass significant responses for more than one frequency adjacent mode at a time. An empirical rule, deriving from the F-106 study, is that the filter may have a maximum bandwidth equal to the average damping coefficient of the structure (Reference 4). As a matter of interest, the average equivalent viscous damping coefficient ( $C/C_c$ ) of all F-106 structure, from all sources while airborne, was found to be about 7 percent.

Having selected a constant percentage bandwidth filter, it is now possible to discard the power spectrum approach entirely and work in units which can furnish useful design numbers. As mentioned previously, we are primarily interested in the real time history of maximum values. To obtain these numbers, the following procedure is used: First, the taped information is analyzed so as to provide plots of rms acceleration (or pressure or stress) versus frequency. On the basis of the previous discussion, the responses at all frequencies are now directly comparable. It should be noted, however, that the only significance of plotting rms levels (instead of some other average level) is that true rms measuring systems are available. The rms level is only a reference and has no other importance. The next step is to select the frequencies at which the responses appear interesting, eg, indicated resonances. At the selected frequencies it is then necessary to obtain statistical histories of the responses in terms of the percentage of time that particular peak rms ratios occur or are exceeded. This immediately yields the distribution of actual peak accelerations (or stresses, etc.) and the probable number of occurrences in any given time interval. In addition, it provides information as to whether the responses are sinusoidal, are beat manifestations or are random. A typical F-106 distribution is shown in Figure 3, in comparison with a Rayleigh Distribution.

To summarize the discussion to this point, what I have actually accomplished is to demonstrate that the responses of a complex structure to unknown random inputs can be simulated by sinusoidal vibrations of scheduled magnitudes. On this basis alone, the justification for random vibration testing in the laboratory appears, at the least, highly questionable!

Now that we have briefly looked at the vibratory responses of a structure when the input is unknown, let us look at the opposite case - where the input is known, but the structural responses are not. For a working example, we shall assume that we are designing a new jet aircraft and that the problem is prevention of acoustically induced structural fatigue.

The first task is straightforward, that is, recording on magnetic tape the exhaust noise from the particular engine at the appropriate locations. (I'm not going to elaborate on this since this is not a discussion of noise measurement techniques.) The noise data, like the vibration data, should be analyzed with a filter equivalent to the estimated aggregate damping of the structure, so as to provide plots of rms pressure versus frequency. At various frequencies, the statistical histories of the peak pressures should be investigated. As a matter of interest, Figure 4 shows the general statistical characteristics of exhaust noise of the GE CJ-805 engine in the near field.

The next step is to mate the acoustic pressure input with the fatigue characteristics of the structure being designed. Since we are dealing with a random forcing function, this mating must be accomplished in the light of a cumulative fatigue damage criterion. The following are some considerations:

- a. Vibratory stresses which are significant with respect to generation of a fatigue failure will be developed only in a resonant mode of the structure (Reference 5).
- b. A lightly damped structure will respond significantly in its least damped mode when subjected to random vibratory excitation. The selection of this mode is based on stress magnification, not amplitude magnification (Reference 5).
- c. The fatigue failure of a structure, when subjected to random excitation, can be interpreted in terms of a quasi-sinusoidal input whose frequency corresponds to that of the least damped mode and whose amplitude varies randomly as a function of time.
- d. A predictable relationship can be established between vibratory stress in a structure and applied vibratory pressure.
- e. A fatigue (stress-cycle) curve for the structure can be established and normalized on a non-dimensional equivalence of stress ratio and pressure ratio.
- f. The randomness of the pressure input can be defined statistically as the probable rate of occurrence of peak values of pressure.

## Getline

By use of the above ground rules, it is possible to equate the fatigue life of a structure under random excitation to its fatigue life under sinusoidal excitation. To accomplish this, there are two requirements which must be met for both types of excitation:

1. Fatigue failure is defined by an intercept of the S-N curve.
2. The total vibratory energy absorbed by the structure must be the same for either type of excitation. (Reference 6).

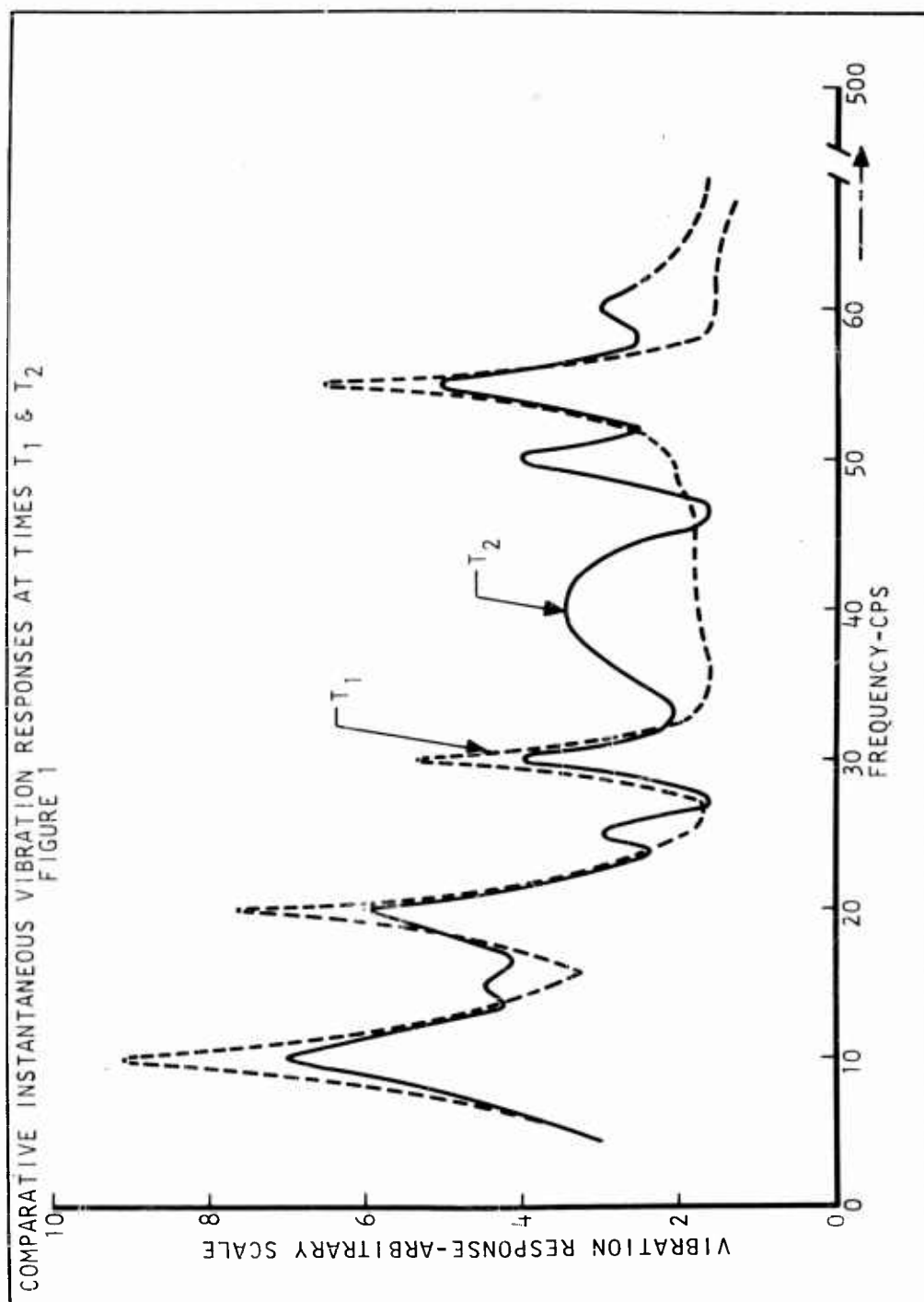
Let us now take a look at Figure 5. The acoustic pressure distribution curve is the same as shown on Figure 4, except that the scale is log-log and the axes have been reversed. Time to failure may be expressed in hours where the minimum desired fatigue lift of the structure corresponds to 100 percent. Curves A and B have the same slope, which is that of the S-N curve for the fabricated structure. As a matter of interest, this particular slope has a ratio of 6 to 1, ultimate stress to endurance stress at  $5 \times 10^8$  cycles, and was used successfully in the design of wing trailing edge structure on the Convair 880 and 990 jetliners. If line BB is drawn tangent to the pressure distribution curve, then both of the above fatigue life requirements have been fulfilled for the random excitation. If the rectangle CDE is now drawn through the point of tangency such that its effective area is equal to that under the random distribution curve, and line AA is drawn parallel to BB through point D then we have established the random-sine fatigue equivalence. In addition, for laboratory testing of structural samples, accelerated sinusoidal tests can be run by merely moving back on S-N curve AA. (Reference 6).

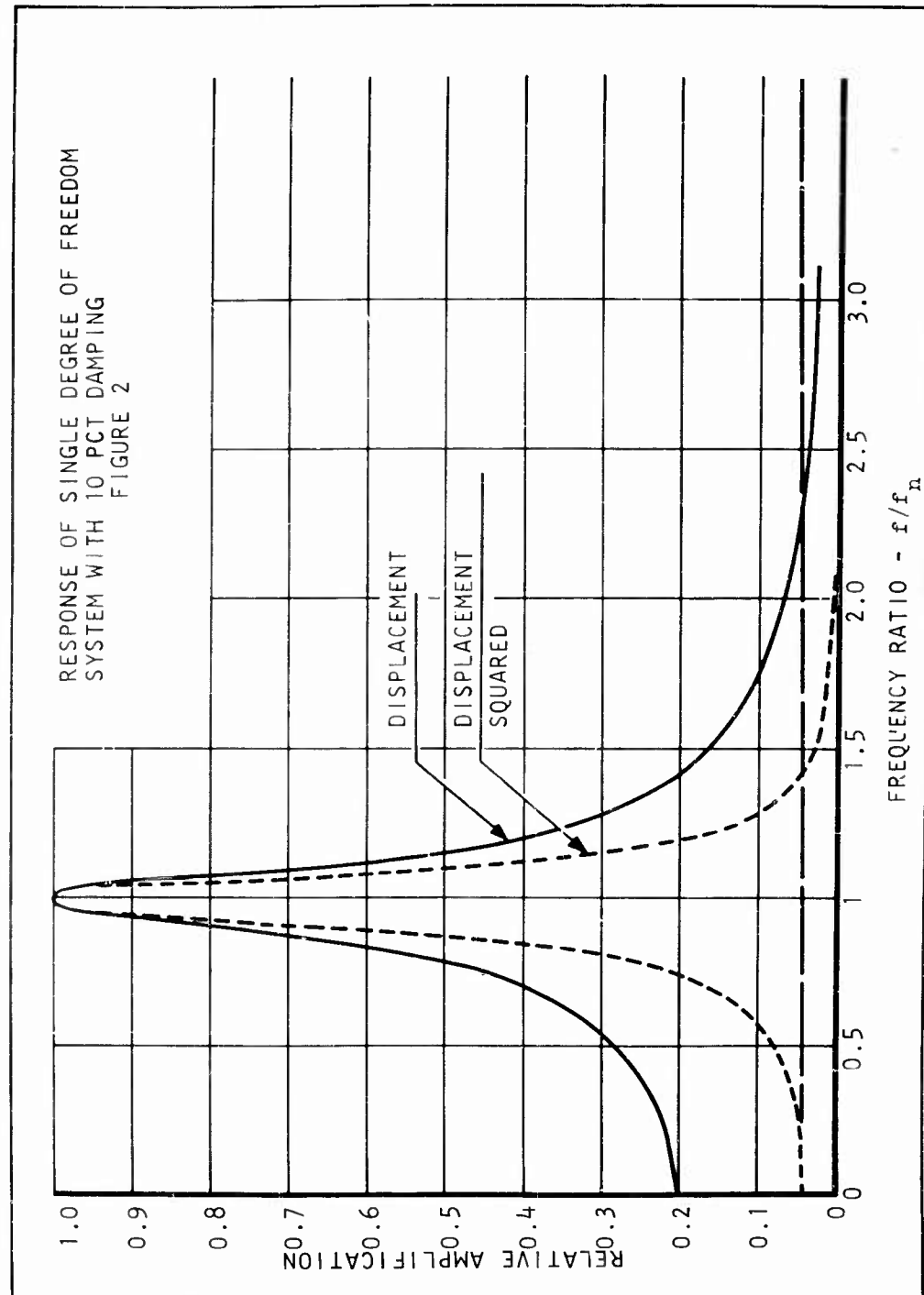
It is fully realized that the procedure just described, like other procedures of a similar nature, entails a number of assumptions. However, this much can be said of it:

- a. It requires a minimum amount of information about the structure involved.
- b. It has been checked successfully against published laboratory fatigue data.
- c. Its successful application has been demonstrated to date in the many Convair jetliners now flying the airways.

R E F E R E N C E S

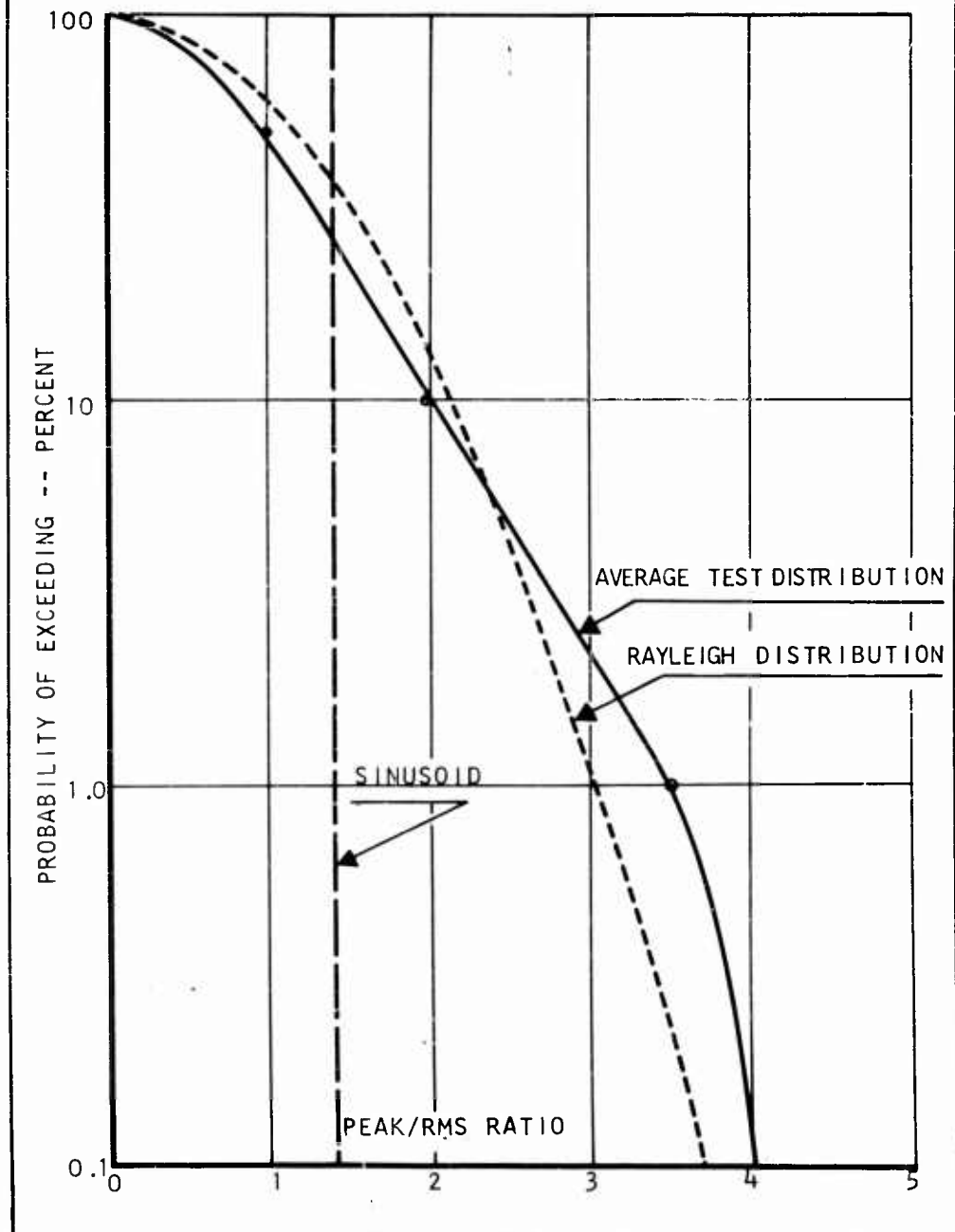
1. WADC TR 56-503; "Establishment of Vibration and Shock Tests For Missile Electronics As Derived From the Measured Environment."
2. "Random Vibration"; The Technology Press of M.I.T.
3. University of Southampton, Dept. of Aeronautics & Astronautics; "A New Framework For the Calculation of Cumulative Damage in Fatigue, Part II - Historical Theory": I. Torbe. (U.S.A.A. Report No. 111).
4. Convair-San Diego Memorandum Report DF-8-232, "F-106A Environmental Vibration."
5. University of Southampton, Department of Aeronautics & Astronautics; "Experimental Study of the Random Vibrations of an Aircraft Structure Excited by Jet Noise": Clarkson and Ford. (U.S.A.A. Report No. 128).
6. "Correlation of Structural Fatigue Relative to Discrete Frequency - Constant Amplitude and Random Acoustic Excitation"; Getline: I.E.E., Proceedings Annual Meeting, April 1958.



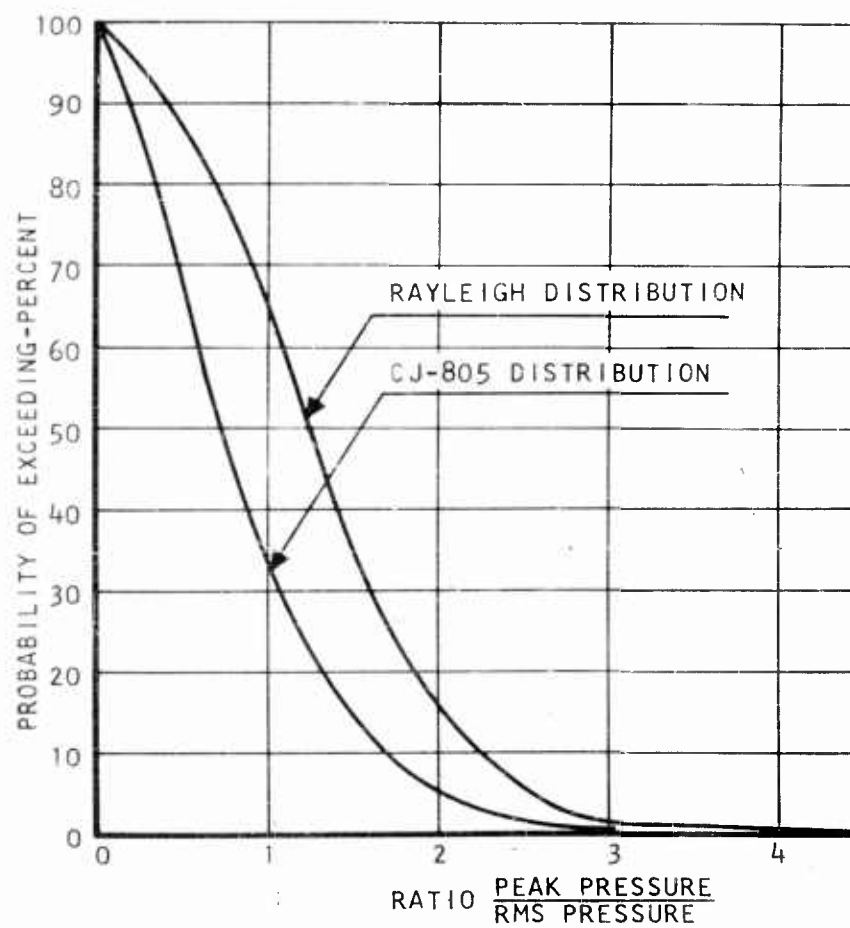


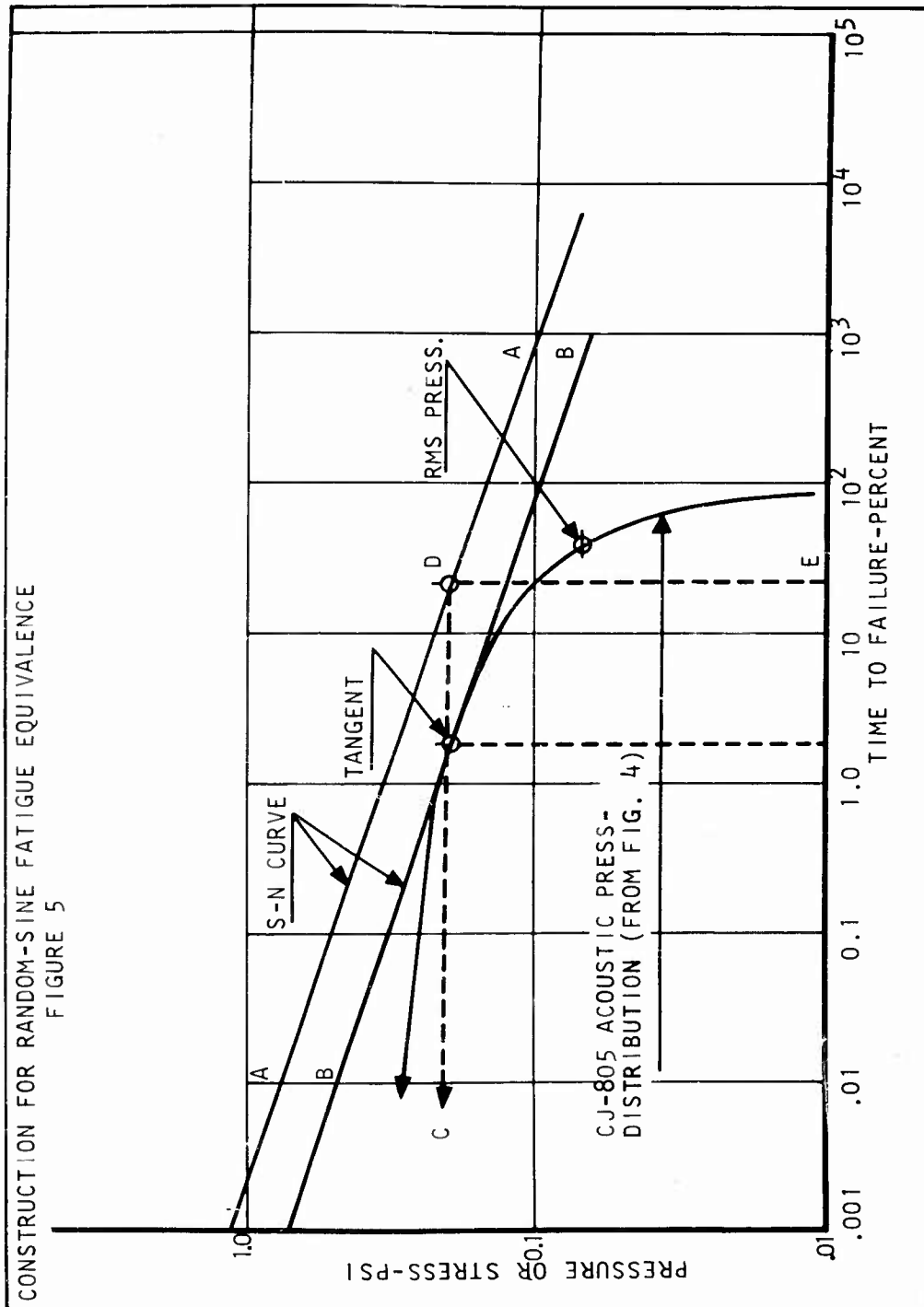


STATISTICAL VARIATION OF F-106 VIBRATION RESPONSES  
FIGURE 3



ACOUSTIC PEAK PRESSURE PROBABILITY CURVE  
FIGURE 4





## CAPTIVE MISSILE RESPONSE DUE TO RANDOM PRESSURES

H. L. Leve  
Hughes Aircraft Company  
Culver City, California

### Introduction

The environment associated with any missile flight history is composed of two parts; namely, a mean or steady part, and a fluctuating part about the mean. There are, in general, well defined procedures for predicting the response of a system to a steady environment. The fluctuating part involves random inputs into the system which permit only a statistical description of the system response. For each portion of the history over which the statistics of the system input remain essentially invariant, an analytical procedure can be formulated which will describe statistically the forces acting internally in the system, and hence evaluate the system design.

Consider the particular case of a captive missile being flown exposed to the airstream under a constant dynamic pressure. The fluctuating environment in this case is a random pressure acting over the missile, where the statistics of this environment remain essentially stationary under the described conditions. The power spectrum of this type of input, in a local region as obtained by a pressure transducer, is approximately white noise from 0 cps to a cutoff frequency in the range of 250 cps to 1,000 cps. It will be presumed that the total fluctuating pressure (that is, fluctuating force) acting on a section of the missile, in either the vertical or lateral direction, has the same spectral characteristics as the local pressures; although it does not necessarily follow that a sum composed of white noise quantities has a white noise spectrum.

A possible situation that may arise is when only one piece of response data is available for predicting the behavior of the captive missile in either the vertical or lateral direction. With just one piece of response data (for example, the rms acceleration

at the nose of the missile), only one degree of freedom can be allowed in the description of the total fluctuating pressure field. This can be done, for instance, by selecting a fixed shape for the longitudinal distribution of the pressures (for example, proportional to the planform normal to the direction of motion being considered), and such that this shape is retained at all times. The magnitude of the longitudinal pressure distribution can be described by one of its ordinates, since any other ordinate is a fixed constant times the reference ordinate. Thus the only quantity remaining to complete the description of the fluctuating longitudinal pressure distribution is the level of the white noise spectrum for the reference ordinate. From the one known piece of response data, the level of the reference ordinate spectrum can be determined as will be shown later. Having this result, all the desired response spectrums, and their associated rms values, can be found.

Since the fluctuating portions of the pressure field have zero means and considering the captive missile system to act linearly, the mean values of the responses obtained for this case are also zero. Further, it has been found from strain gage and accelerometer flight measurements that, for a stationary portion of the flight history, the deformation and acceleration responses are normally distributed. Thus the responses are completely characterized by the determination of their rms values.

If more than one piece of response data is available, then a corresponding number of degrees of freedom can be used in describing the longitudinal pressure distribution. The analysis that will be given presently for the case of one known piece of response data can be readily extended to the case in which more than one piece of response information is known. In either one of these cases there are many ways to restrain the pressure distribution, since very little is known about the characteristics of the pressure field acting upon an exposed captive missile. Thus to supplement the analysis, a study should be made into the effect of various pressure field descriptions on the rms response levels, dependent upon the number of known pieces of response data. Further, since the damping in the captive missile system is relatively difficult to ascertain, a study should be made on the sensitivity of the rms response levels to various damping levels and distributions. A study of the effect of the pressure field cutoff frequency on the rms responses would be of value also. The results of these studies will indicate the scope of the flight testing, as well as any laboratory testing, required to give reasonably accurate rms response levels. With these considerations, the analysis that follows shows a procedure for predicting the rms response levels for the particular case in which only one known piece of response data is available. The approach that will be described can be readily adapted to more complex situations, as mentioned previously. To give a clear description of random

analysis procedures, the mathematical methods used in the following analysis require only a familiarity with elementary vibration theory.

#### Random Vibration Analysis

A dynamic model for the exposed captive missile system can be arranged in the form of discrete masses, springs, and dampers. Acting on each mass section of the exposed captive missile, in either the vertical or lateral direction, will be a fluctuating force (with zero mean) which has a white noise spectrum from 0 cps to some cutoff frequency in the range of 250 cps to 1,000 cps as discussed previously. For the case in which only one piece of response data is available (for instance, the rms acceleration of the missile nose in the direction of the motion being considered), the fluctuating forces on the missile section will be allowed only one degree of freedom. This will be done in the following analysis by retaining, at all times, a fixed proportionality between the fluctuating forces on the missile sections.

Without any loss in the analysis, the model in Figure 1 may be used in place of the captive missile model.

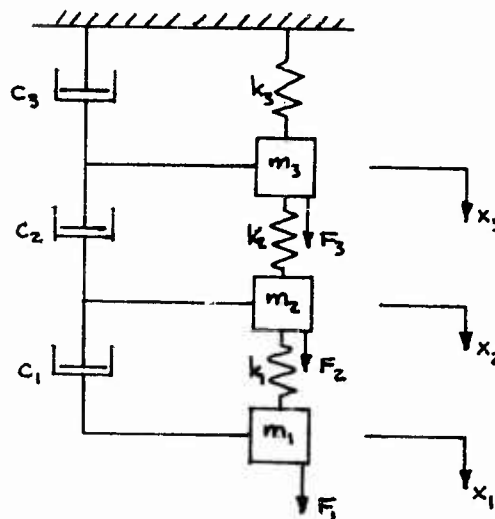


Figure 1

Dynamic Model

The differential equations governing the system in Figure 1 may be written in matrix form as

$$[M][\ddot{x}] + [C][\dot{x}] + [K][x] = [F] \quad (1)$$

The 3x1 matrices  $[x]$ ,  $[\dot{x}]$ , and  $[\ddot{x}]$  are, respectively the coordinate displacement, velocity and acceleration matrices. The 3x3 matrices,  $[M]$ ,  $[C]$ , and  $[K]$ , and the 3x1 matrix,  $[F]$ , are the mass, damping, stiffness, and external force matrices, respectively. The elements in the  $i$ -th rows of the matrices  $[F]$  and  $[x]$  are written respectively as  $F_i$  and  $x_i$ . These latter quantities, which are functions of time (that is,  $F_i = F_i(t)$  and  $x_i = x_i(t)$ ), are, respectively, the force acting on the  $i$ -th mass and the displacement of the  $i$ -th mass.

For the case of one degree of freedom in the fluctuating force field, the fluctuating forces  $F_i(t)$  may be written as

$$F_i(t) = \lambda_i F_1(t) \quad (2)$$

where  $\lambda_i$  is the constant of proportionality between the fluctuating force on the  $i$ -th mass section and the fluctuating force on mass section 1 and is prescribed a priori.

The time-wise forcing function  $F_1(t)$  can be considered as composed of a sum of sinusoids in the following manner:

$$F_1(t) = p_0 \sin(\omega_0 t + \psi_0) + p_1 \sin(\omega_1 t + \psi_1) + \dots + p_k \sin(\omega_k t + \psi_k) + \dots + p_n \sin(\omega_n t + \psi_n) \quad (3)$$

The spacing between successive frequencies in Equation (3) will be considered constant in the following analysis and of magnitude  $\Delta\omega$ . The frequency  $\omega_n$  will be considered as the cutoff frequency.

From (2) and (3), the representation for the force acting on the  $i$ -th mass section is

$$F_i(t) = \lambda_i [ p_0 \sin(\omega_0 t + \psi_0) + p_1 \sin(\omega_1 t + \psi_1) + \dots + p_k \sin(\omega_k t + \psi_k) + \dots + p_n \sin(\omega_n t + \psi_n) ] \quad (4)$$

If the expressions in (3) and (4) for each frequency are placed term-by-term in the right hand side of Equation (1), by superposition, the particular solution for the  $i$ -th displacement can be found in the following form:

$$x_i(t) = A_{i0} \sin(\omega_0 t + \psi_0 + \phi_{i0}) + A_{i1} \sin(\omega_1 t + \psi_1 + \phi_{i1}) + \dots \\ + A_{ik} \sin(\omega_k t + \psi_k + \phi_{ik}) + \dots + A_{in} \sin(\omega_n t + \psi_n + \phi_{in}) \quad (5)$$

To develop a program for obtaining the amplitudes,  $A_{ik}$  and phase angles,  $\phi_{ik}$ , in expression (5), the use of complex notation is convenient. If the term in expression (3) for  $F_i(t)$  associated with frequency level  $\omega_k$  is denoted by  $F_{ik}(t)$  (that is,  $F_{ik}(t) = p_k \sin(\omega_k t + \psi_k)$ ) then this term can be considered as the imaginary part of the complex quantity

$$\tilde{F}_{ik}(t) = p_k e^{i(\omega_k t + \psi_k)} \quad (6)$$

where the value of  $i$  in the exponent of  $e$  is  $\sqrt{-1}$ .

It follows from (2) that

$$\tilde{F}_{ik}(t) = \gamma_i p_k e^{i(\omega_k t + \psi_k)} \quad (7)$$

If the displacement of the  $i$ -th mass associated with frequency level  $\omega_k$  is denoted by  $x_{ik}(t)$  (that is  $x_{ik} = A_{ik} \sin(\omega_k t + \psi_k + \phi_{ik})$ ), then this term can be considered as the imaginary part of the complex quantity

$$\tilde{x}_{ik}(t) = A_{ik} e^{i(\omega_k t + \psi_k + \phi_{ik})} = A_{ik} e^{i\phi_{ik}} e^{i(\omega_k t + \psi_k)} \\ = X_{ik} e^{i(\omega_k t + \psi_k)} \quad (8)$$

It can be seen from (8) that

$$X_{ik} = A_{ik} e^{i\phi_{ik}} \quad (9)$$

Putting (6), (7), and (8) into (1), it is found for frequency level  $\omega_k$  that



$$\{-\omega_k^2 [M] + i \omega_k [C] + [K]\} \begin{bmatrix} X_{1k} \\ X_{2k} \\ X_{3k} \end{bmatrix} = \begin{bmatrix} P_k \\ \gamma_2 P_k \\ \gamma_3 P_k \end{bmatrix}$$

or more briefly,

$$\{-\omega_k^2 [M] + i \omega_k [C] + [K]\} [X_k] = P_k [\gamma] \quad (10)$$

Now taking

$$[X_k] = P_k [Z_k] \quad (11)$$

Equation (10) becomes

$$\{-\omega_k^2 [M] + i \omega_k [C] + [K]\} [Z_k] = [\gamma] \quad (12)$$

Equation (12), which is a set of algebraic equations, can now be solved for the complex matrix  $[Z_k]$  by using the machine program in Reference (1).

From (11) and (9), it can be seen that

$$Z_{ik} = P_k^{-1} X_{ik} = P_k^{-1} A_{ik} e^{i \phi_{ik}} = a_{ik} e^{i \phi_{ik}} \quad (13)$$

Hence the complex values  $Z_{ik} = \gamma + i \delta$  obtained in the solution of (12) for frequency level  $\omega_k$ , can be used to determine the phase angle,  $\phi_{ik}$ , and the amplitude  $A_{ik}$  for a unit value of  $P_k$  (that is,  $a_{ik}$ ). Thus

$$a_{ik} = \sqrt{\gamma^2 + \delta^2}$$

and

$$\phi_{ik} = \arctan \frac{\delta}{\gamma} \quad (14)$$

Applications of sinusoidal procedures to random vibration problems are shown in References (2) and (3). For the present purposes, the random vibration analysis of the system in Figure 1 may be begun by determining the covariances between the coordinate responses. By definition the covariance between responses  $X_i$  and  $X_j$  (which have zero means) is given mathematically as

$$\text{Cov}(x_i, x_j) = \lim_{T \rightarrow \infty} \frac{1}{T} \int_0^T x_i(t) x_j(t) dt \quad (15)$$

Using expression (5), with appropriate subscripts, in the evaluation of (15), it is found that

$$\begin{aligned} \text{Cov}(x_i, x_j) = \lim_{T \rightarrow \infty} \frac{1}{T} \int_0^T & \left[ \sum_{k=0}^n A_{ik} \sin(\omega_k t + \psi_k + \phi_{ik}) \right] \cdot \\ & \cdot \left[ \sum_{k=0}^n A_{jk} \sin(\omega_k t + \psi_k + \phi_{jk}) \right] dt \end{aligned} \quad (16)$$

Thus

$$\text{Cov}(x_i, x_j) = \sigma_{x_i x_j} = \sum_{k=0}^n \frac{1}{2} A_{ik} A_{jk} \cos(\phi_{ik} - \phi_{jk}) \quad (17)$$

In arriving at (17) from (16), the cross terms, involving unlike frequency levels, vanish in the limiting process. Thus each term in (17) is obtained as follows:

$$\begin{aligned} \lim_{T \rightarrow \infty} \frac{1}{T} \int_0^T & A_{ik} \sin(\omega_k t + \psi_k + \phi_{ik}) \cdot A_{jk} \sin(\omega_k t + \psi_k + \phi_{jk}) dt \\ & = \frac{1}{2} A_{ik} A_{jk} \cos(\phi_{ik} - \phi_{jk}) \end{aligned} \quad (18)$$

The covariance between a response and itself is termed the variance or mean square value of the response. Thus the variance or mean square value of the response  $x_i$  is given from (17) as

$$\text{Cov}(x_i, x_i) = \text{var}(x_i) = \sigma_{x_i x_i} = \sigma_{x_i}^2 = \sum_{k=0}^n \frac{1}{2} A_{ik}^2 \quad (19)$$

The result in (19) is obtained from (17) by changing the subscript  $j$  to  $i$ . The last expression in (19) indicates the well known fact that the mean square value of a sinusoid is one-half of the square of its amplitude. It can also be noted that  $\frac{1}{2} A_{ik}^2$  is the contribution to the mean square value of the response of the  $i$ -th mass from the frequency band  $\omega_k \pm \frac{\Delta\omega}{2}$ . Thus in (19) it is seen that the total mean square response of the  $i$ -th mass is the sum of the contributions from all the frequency bands of width  $\Delta\omega$ , associated with the frequency levels from  $\omega_0$  to  $\omega_n$  indicated in expressions (3), (4), and (5).

From Equation (13) it follows that

$$A_{ik} = P_k a_{ik} \quad \text{and} \quad A_{jk} = P_k a_{jk} \quad (20)$$

Substituting the expressions in (20), for  $A_{ik}$  and  $A_{jk}$  into Equations (17) and (19), it is found that

$$\sigma_{x_i x_j} = \sum_{k=0}^n \frac{1}{2} P_k^2 a_{ik} a_{jk} \cos(\phi_{ik} - \phi_{jk}) \quad (21)$$

and

$$\sigma_{x_i}^2 = \sum_{k=0}^n \frac{1}{2} P_k^2 a_{ik}^2 \quad (22)$$

Similar to the discussion following Equation (19), it is seen in Equation (3) that the contribution to the mean square value of the force  $F_i(t)$  from the frequency band  $\omega_k \pm \frac{\Delta\omega}{2}$  is  $\frac{1}{2} P_k^2$ ; that is, one-half of the square of the amplitude of the sinusoidal term in (3) associated with the frequency level  $\omega_k$ . In the frequency band from  $\omega_0$  to  $\omega_n$ , the force  $F_i(t)$  is assumed to have a white noise spectrum as indicated in earlier discussions. This means that the ordinate of the power spectrum for  $F_i(t)$  between  $\omega_0$  and  $\omega_n$  is a constant. Denoting this ordinate by  $\alpha$ , the contribution to the mean square value of  $F_i(t)$  from any frequency band of width  $\Delta\omega$ , between frequency levels  $\omega_0$  and  $\omega_n$ , is  $\alpha \Delta\omega$ ; since the area under a power spectrum between any two frequencies gives the mean square value contributed by that frequency band. It can then be seen from the above discussion that

$$\frac{1}{2} P_k^2 = \alpha \Delta\omega \quad (23)$$

Following again the discussion after (19), the mean square value of  $F_i(t)$  is the sum of the mean square contributions from all the frequency bands. Thus if the mean square value of  $F_i(t)$  is denoted by  $\sigma_{F_i}^2$  then

$$\sigma_{F_i}^2 = \sum_{k=0}^n \frac{1}{2} P_k^2 = \sum_{k=0}^n \alpha \Delta\omega = \alpha n \Delta\omega = \alpha(\omega_n - \omega_0) \quad (24)$$

Putting expression (23) into (21) and (22), it is found that

$$\sigma_{x_i x_j} = \alpha \Delta \omega \sum_{k=0}^n a_{ik} a_{jk} \cos(\phi_{ik} - \phi_{jk}) \quad (25)$$

and

$$\sigma_{x_i}^2 = \alpha \Delta \omega \sum_{k=0}^n a_{ik}^2 \quad (26)$$

In the evaluation of Equations (24), (25), and (26), only the quantity  $\alpha$ , at this stage, is unknown. The ordinate,  $\alpha$ , of the power spectrum of  $F_1(t)$  can be determined as follows from one known piece of response data; for instance, the rms (or mean square) acceleration of mass 1:

Differentiating Equation (5) twice and putting  $i=1$ , it is found that

$$\ddot{x}_1(t) = -\omega_0^2 A_{10} \sin(\omega_0 t + \psi_0 + \phi_{10}) - \omega_1^2 A_{11} \sin(\omega_1 t + \psi_1 + \phi_{11}) - \dots \\ \dots - \omega_k^2 A_{1k} \sin(\omega_k t + \psi_k + \phi_{1k}) - \dots - \omega_n^2 A_{1n} \sin(\omega_n t + \psi_n + \phi_{1n}) \quad (27)$$

Now similar to the definition in (15)

$$\text{cov}(\ddot{x}_1, \ddot{x}_1) = \sigma_{\ddot{x}_1, \ddot{x}_1} = \sigma_{\ddot{x}_1}^2 = \lim_{T \rightarrow \infty} \frac{1}{T} \int_0^T [\ddot{x}_1(t)]^2 dt \quad (28)$$

Putting (27) into (28) and performing the indicated operations, it is found that

$$\sigma_{\ddot{x}_1}^2 = \sum_{k=0}^n \frac{1}{2} \omega_k^4 A_{1k}^2 \quad (29)$$

The expression in (29) shows, as expected, that the mean square value of a sinusoidal term in (27) is one-half of the square of its amplitude.

Substituting (20) into (29) with  $i=1$  (or  $j=1$ ) gives

$$\sigma_{\ddot{x}_1}^2 = \sum_{k=0}^n \frac{1}{2} P_k^2 \omega_k^4 a_{1k}^2 \quad (30)$$

Using (23), expression (30) becomes

$$\sigma_{\ddot{x}_1}^2 = \alpha \Delta\omega \sum_{k=0}^n \omega_k^4 a_{1k}^2 \quad (31)$$

Since the mean square acceleration of mass 1,  $\sigma_{\ddot{x}_1}^2$ , is a known quantity, then

$$\alpha = \frac{\sigma_{\ddot{x}_1}^2}{\Delta\omega \sum_{k=0}^n \omega_k^4 a_{1k}^2} \quad (32)$$

Thus with (32) and the results given in Equations (24), (25), and (26), the rms (or mean square) values of the inputs and responses can now be completely determined for the system in Figure 1.

#### Mean Square Values of the Inputs and Responses

The mean square value of the force on mass 1 obtained in Equation (24) could also have been determined from the approach indicated by the definition in (15). Thus

$$\text{COV}(F_1, F_1) = \sigma_{F_1 F_1} = \sigma_{F_1}^2 = \lim_{T \rightarrow \infty} \frac{1}{T} \int_0^T [F_1(t)]^2 dt \quad (33)$$

Putting expression (3) into (33), the result in (24) will be found.

The mean square value of the force acting on any other mass can be found in a similar manner. Hence

$$\text{COV}(F_i, F_i) = \sigma_{F_i F_i} = \sigma_{F_i}^2 = \lim_{T \rightarrow \infty} \frac{1}{T} \int_0^T [F_i(t)]^2 dt \quad (34)$$

Substituting (2) into (34), it is found that

$$\sigma_{F_i}^2 = \lim_{T \rightarrow \infty} \frac{1}{T} \int_0^T [\lambda_i F_1(t)]^2 dt = \lambda_i^2 \lim_{T \rightarrow \infty} \frac{1}{T} \int_0^T [F_1(t)]^2 dt \quad (35)$$

Thus from (33)

$$\sigma_{F_i}^2 = \lambda_i^2 \sigma_{F_1}^2 \quad (36)$$

From a definition similar to that in (15), the mean square value can be determined for any interior force response; for instance, the spring force,  $f_i$ , between the  $i$ -th and  $j$ -th masses of the system shown in Figure 1. The spring force,  $f_i$ , in this case is given mathematically as

$$f_i = k_i (x_i - x_j) \quad (37)$$

where  $k_i$  is the spring stiffness.

Thus by definition

$$\text{cov}(f_i, f_i) = \sigma_{f_i f_i} = \sigma_{f_i}^2 = \lim_{T \rightarrow \infty} \frac{1}{T} \int_0^T [f_i(t)]^2 dt \quad (38)$$

Putting (37) into (38)

$$\begin{aligned} \sigma_{f_i}^2 &= \lim_{T \rightarrow \infty} \frac{1}{T} \int_0^T [k_i (x_i - x_j)]^2 dt \\ &= k_i^2 \lim_{T \rightarrow \infty} \frac{1}{T} \int_0^T (x_i - x_j)^2 dt \end{aligned} \quad (39)$$

Expanding, it is found that

$$\begin{aligned} \sigma_{f_i}^2 &= k_i^2 \left\{ \lim_{T \rightarrow \infty} \frac{1}{T} \int_0^T [x_i(t)]^2 dt + \lim_{T \rightarrow \infty} \frac{1}{T} \int_0^T [x_j(t)]^2 dt \right. \\ &\quad \left. - 2 \lim_{T \rightarrow \infty} \frac{1}{T} \int_0^T x_i(t) x_j(t) dt \right\} \end{aligned} \quad (40)$$

From (15) and the symbolism previously used, it is seen that

$$\sigma_{f_i}^2 = k_i^2 (\sigma_{x_i}^2 + \sigma_{x_j}^2 - 2 \sigma_{x_i x_j}) \quad (41)$$

The covariance and mean square values in the right hand sides of expressions (41) and (36) can be found from Equations (24), (25), (26), and (32). Thus a procedure is demonstrated for determining the mean square value of any input or response for the type of system described by Figure 1.

#### References

1. Andrews, G. J. and Levitan, E. S., "On the Vibration Isolation of a Rigid Body on Resilient Supports", Hughes Aircraft Company Report No. TM-648, 1 February 1960, Revised 9 June 1960.
2. Mains, R. M., "Mechanical Design for Random Loading", Random Vibration, edited by Stephen H. Crandall, Massachusetts Institute of Technology Press, 1958, Chapter 12.
3. Mains, R. M., "The Probable Response of Multi-Degree-of-Freedom Systems to Random Shock and Vibration", Random Vibration, edited by Stephen H. Crandall, Massachusetts Institute of Technology Press, 1958, Chapter 12.

STRUCTURAL RESPONSE TO THE NOISE  
INPUT OF THE SATURN ENGINES

J. H. Farrow  
NASA, George C. Marshall Space Flight Center  
Huntsville, Alabama

R. E. Jewell, Chrysler Corporation  
G. A. Wilhold, Chrysler Corporation

The acoustic field associated with large jet and rocket engines has become increasingly significant as a prime source of vehicle vibrations. Indications are that during lift-off portion of vehicle flight, the sound field generated in the turbulent wake of the vehicle is perhaps the most important source of structural vibration. Vibration levels have been noted to decrease considerably after the first few seconds of flight, and it is noted that this lifting of the vehicle from its pad coincides with the changing of the acoustic field from hemispherical to spherical radiation. The problem of predicting or even measuring sound induced vibrations is exceedingly complex. Many idealized situations must be assumed for the sake of simplicity. Acoustic theory assumes such things as free field conditions and plane wave fronts, and it is realized that these conditions are not met during the launch phase of vehicle flight.

The vehicle structure itself must be idealized in order to assume certain boundary conditions, modal shapes, and damping ratios. The assumption of boundary conditions affects the calculation of natural frequencies and the assumed mode shape and damping affects the calculation of vibration amplitudes.

Finally, the development of an equation which relates the impinging pressure to the induced acceleration is a straight forward approach which assumes that each mode responds as a single degree of freedom system.

The theoretical basis for this analysis is given in work done by both Doctors Powell and Dyer where methods were devised for determining the important vehicle vibrations from acoustic data. The task in this paper is to apply these methods to a specific location on the Saturn booster, calculate the expected vibration levels, and compare these values to the actual measured responses.



The noise of a rocket engine has as its origin the turbulence which exists in the exhaust stream. The result is that the sources which generate the intense acoustic field do not appear to exist within the engine, but are downstream in the volume of the exhaust. The distance from the plane of the nozzle to the location of the source is a function of frequency. Low frequencies appear farther downstream than do high frequencies. For the Saturn static tests, deflection of the exhaust stream causes the sound sources to occur to one side of the vehicle. A sketch of the geometry is shown below.

### GEOMETRY OF SATURN STATIC TEST

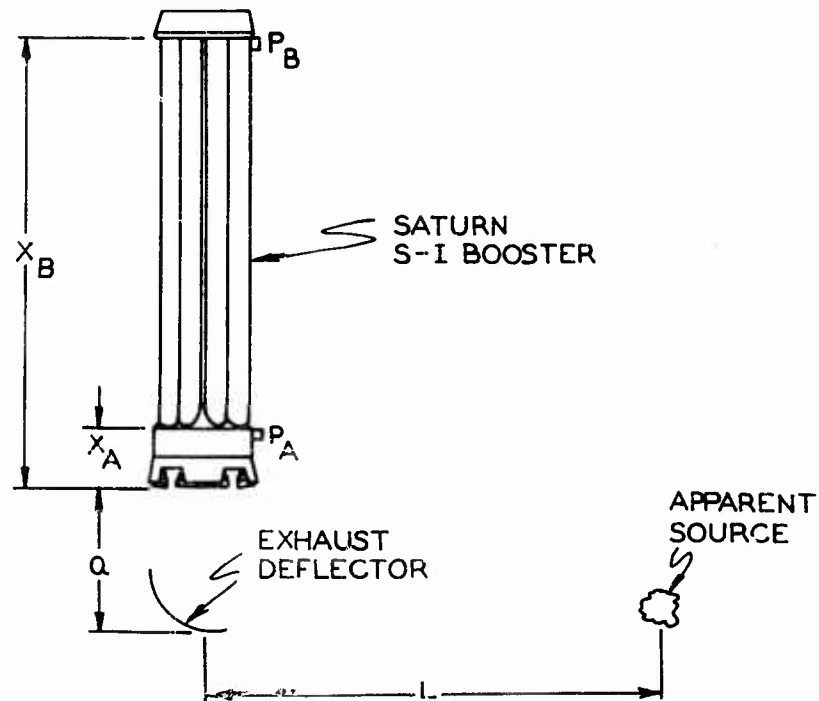


FIGURE 1

With the use of measured sound pressure levels at points A and B values of L, greater than (a), can be determined by:

$$L^2 = \frac{(X_B + a)^2 - (X_A + a)^2 (P_A/P_B)^2}{(P_A^2/P_B^2) - 1}$$

then  $X_0 \approx a + L$ .

As L decreases with increasing frequency until  $L < (a)$  then  $X_0$  may be determined directly by:

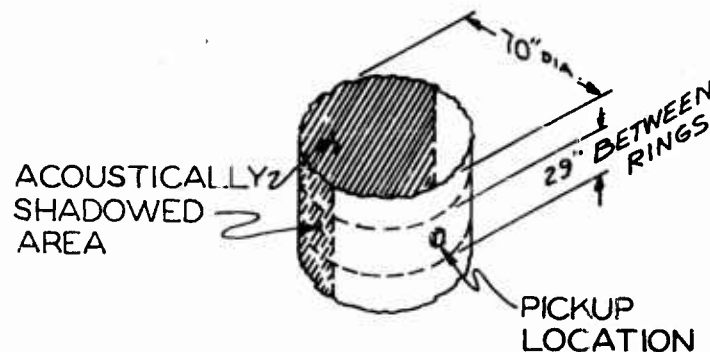
$$X_0 = \frac{X_B - X_A (P_A/P_B)}{(P_A/P_B) - 1}$$

For both cases the total distance from the source to the point in question is then given by:

$$R = X_0 + X$$

It now becomes necessary to determine, with the use of the measured data, a spectrum function at a point one foot from the source. This is accomplished by increasing the SPL at A and the SPL at B by 20 log R. With use of the spectrum function it is possible to determine the sound pressure level at any point on the surface of the vehicle.

A point thirty feet up the side of the vehicle was chosen as a location for correlating the impinging pressures with vibration measurements. The sound pressure spectra was then computed for this point. A physical description and the sound spectra are shown below for this location.



CROSS SECTION OF LOX TANK

FIGURE 2

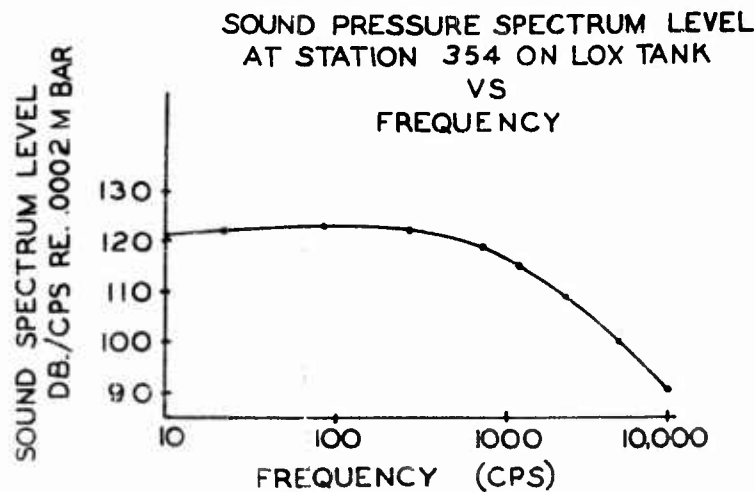


FIGURE 3

The construction of the tank consists of a circular cylinder segmented by ring frames spaced approximately twenty-nine inches apart. The ring frames are assumed to be sufficiently rigid so as to approximate supported end conditions for the material between the frames. The three modes of tank vibrations are as follows:

1. Expansion and contraction of the vehicle skin; (ring motion)
2. Translation without deformation;
3. Bending or corrugation along the vehicle skin.

The differential equation which relates the deflection of a beam to the impinging pressure is given as:

$$M_n \ddot{Y}_n + \beta_n \dot{Y}_n + \omega_{on}^2 Y_n = \int P(x, t) \alpha_n(x) dx. \quad (1)$$

This also holds for the surface of a cylinder if the deflection ( $y$ ) is a function of  $\phi$  over the surface as well as  $x$  and  $t$ . The instantaneous deflection  $y_n$  equal  $Y_{\max} \sin(\omega t + \delta)$ , therefore,  $y(x, \phi, t)$  is equal to  $\alpha_n(\phi, x) y_n(t)$  where  $\alpha_n(\phi, x)$  is the mode shape. Equation (1) is recognized to be identical to one for a simple spring mass system. The mass ( $M_n$ ) must then be put into a form of an effective or generalized mass by integrating

over the surface, in equation form:

$$M_n = \int_S \alpha_n \alpha_n^2 (\phi, x) dx d\phi. \quad (2)$$

For radial symmetry the pressure over the surface is a function of  $x$  and  $t$  and is independent of  $\phi$ . This can be written as:

$$P(x, t) = P_0 \cos(\omega t - kx) \quad (3)$$

where

$$k = \frac{2\pi f}{c}.$$

Substituting (3) into (1);

$$M_n \ddot{Y}_n + \beta \dot{Y}_n + \omega_{on}^2 Y_n = \int P_0 \cos(\omega t - kx) \alpha_n(x) dx. \quad (4)$$

If  $\alpha_n(x)$  is replaced by its mode shape  $\sin \frac{q\pi x}{l}$ , equation (4) reduces to

$$M_n \ddot{Y}_n + \beta \dot{Y}_n + \omega_{on}^2 Y_n = \int P_0 \cos(\omega t - kx) \sin \frac{q\pi x}{l} \sin n\phi dx. \quad (5)$$

Performing the necessary integration the right side of (5) becomes

$$\frac{P_0 q (1 - \cos q\pi \cos \frac{2\pi l}{\lambda})}{\pi l \left[ \left( \frac{q}{l} \right)^2 - \left( \frac{2}{\lambda} \right)^2 \right]} \cos \omega t + k, \sin \omega t.$$

Inspecting of the left hand side of (5) it is recognized that

$$Y_n = Y_{MAX} \sin(\omega t + \gamma)$$

which expands into

$$Y_n = Y_{MAX} [\sin \omega t \cos \gamma + \cos \omega t \sin \gamma] \quad (6)$$

Substituting (6) into the left side of (5), letting  $t = 0$ , and recalling that  $\ddot{Y}_{MAX} = -Y_{MAX} \omega^2$

$$(M_n \omega^2 Y_{MAX} + \omega_{on}^2 Y_{MAX}) \sin \gamma + \omega \beta_n Y_{MAX} \cos \gamma = \frac{P_0 q \left[ 1 - \cos q \pi \cos \frac{2\pi \ell}{\lambda} \right]}{\pi \ell \left[ \left( \frac{q}{\ell} \right)^2 - \left( \frac{2}{\lambda} \right)^2 \right]} \quad (7)$$

but since  $\ddot{Y}_{MAX} = -Y_{MAX} \omega^2$

then:

$$\left( -M_n \ddot{Y}_{MAX} + \frac{Y_{MAX}}{\omega^2} \omega_{on}^2 \right) \sin \gamma + \beta_n \frac{\ddot{Y}_{MAX}}{\omega} \cos \gamma = \frac{P_0 q \left[ 1 - \cos q \pi \cos \frac{2\pi \ell}{\lambda} \right]}{\pi \ell \left[ \left( \frac{q}{\ell} \right)^2 - \left( \frac{2}{\lambda} \right)^2 \right]} \quad (8)$$

Recalling that equations in the form of  $A \sin \gamma + B \cos \gamma$  have as their magnitudes the square root of the sum of the squares of the coefficients  $\sqrt{A^2 + B^2}$  then:

$$\frac{\ddot{Y}_{MAX}}{P_0 \sin \frac{q\pi \ell}{\lambda}} = \frac{q \left( 1 - \cos q \pi \cos \frac{2\pi \ell}{\lambda} \right)}{\pi \ell \left[ \left( \frac{q}{\ell} \right)^2 - \left( \frac{2}{\lambda} \right)^2 \right] \left[ \left( -M_n + \frac{\omega_{on}^2}{\omega^2} \right) + \left( \frac{\beta_n}{\omega} \right)^2 \right]}^{1/2} \quad (9)$$

Further simplification and evaluation of the effective mass results in the following final equation for resonance

$$\ddot{Y}_{MAX} = \frac{2 P_0 \sin K_n \ell (1 - \cos K_n \ell \cos K \ell)}{M_n \ell} \frac{K_n \ell}{K_n^2 \ell^2 - K^2 \ell^2} \quad (10)$$

Solutions of (10) were determined for the fundamental frequencies and several of the harmonics associated with the three modes of vibration. The important resulting vibration are plotted to show its comparison with measured data.

## Comparison of Calculated Data to Measured Data

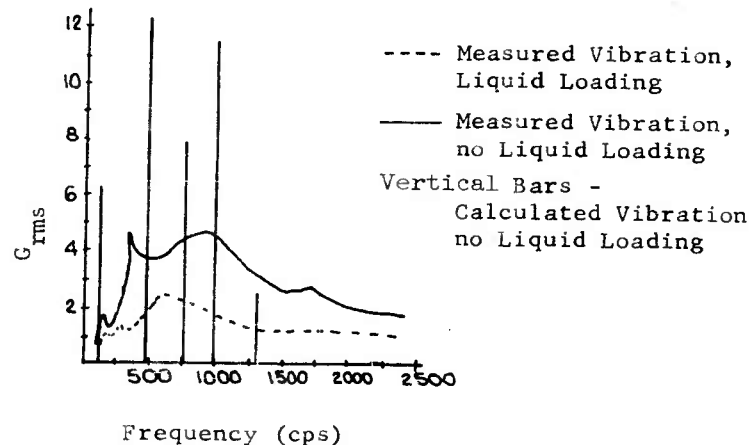


FIGURE 4

The lower curve is given for interest and represents the vibration level before the liquid level had depleted to below the location of the pickup. The upper curve represents the vibration level which exists without liquid loading for the section. The vertical bars represent the calculated vibrations utilizing equation (10). The frequencies associated with the important vibrations calculated seem to agree fairly well with the peaks in the measured spectrum. The amplitudes of the predicted vibration appears to be, in general, an order of magnitude higher than the measured vibration, however, the criteria for the original work in this field was to obtain an order of magnitude for design and test levels. From this standpoint the calculated levels appear reasonable. In addition, the equation for this correlation assumed radial symmetry of the pressure field over the surface of the vehicle. This most certainly is not the case for static test configurations. The effective shadowing of the backside of the LOX tank may have an appreciable effect on certain modes of vibration.

Farrow

This analysis neither proves nor disproves the ability to predict vibration levels from acoustic data. The results are encouraging in some respects and it is hoped that interest will be stimulated for additional studies of this kind. It may well be possible that empirical results will become sufficient in number so as to allow a categorizing of certain basic structures with the acoustic fields to which they are subjected. The final function being that of obtaining a broad profile of the structural responses.

REFERENCES

1. Crandall, S. H., "Random Vibration", M.I.T. Press, 1958
2. Bolt, Beranek & Newman, Inc., "Exterior Sound and Vibration Fields of a Saturn Vehicle During Static Firing and During Launching Final Report", Report Number 764, B.B.N Job Numbers 110402 thru 110407, Contract Number DA-19-020-ORD-5038, Aug. 1960
3. Greenspon, Joshua E., "Vibrations of Thick Shells in a Vacuum and in an Acoustic Medium", J. G. Engineering Research Associates, Report Number 1, Office of Naval Research Project Number NR 385-412, Contract Number NOnr 2733(00), Feb. 1959
4. Rayleigh, John W.S., "The Theory of Sound", Second Edition, Dover Publications, 1945
5. Thompson, W. T., "Mechanical Vibrations", Prentice-Hall, Inc., 1956
6. Lamb, H., "The Dynamical Theory of Sound", Dover Publications, Inc., 1960



## DEFINITION OF SYMBOLS

$X_A$	Distance from the plane of the exhaust nozzles to an acoustic measurement point A on the vehicle.-ft
$X_B$	Distance from the plane of the exhaust nozzles to an acoustic measurement point B on the vehicle.-ft
$a$	Distance from the plane of the exhaust nozzles to the point of impingement, of the exhaust gases on the deflector.-ft
$L$	Distance from the impingement of the exhaust gases on the deflector to the apparent source.-ft
$P_A$	Measured pressure at point A $\text{lb/ft}^2$
$P_B$	Measured pressure at point B $\text{lb/ft}^2$
$X_O$	Approximate distance from the plane of the exhaust nozzles to the apparent source.-ft
$R$	The distance from the apparent source to the point in question -ft
$M_n$	Generalized mass - slugs
$n$	Mode number-nondimensional
$Y_n$	Deflection due to the $n^{\text{th}}$ mode.-ft
$\dot{Y}_n$	First time derivative of the deflection.-ft/sec
$\ddot{Y}_n$	Second time derivative of the deflection-ft/sec <sup>2</sup>
$Y_{\text{max}}$	Maximum deflection -ft
$Y(x, \phi, t)$	Deflection as a function of $x$ , $\phi$ , and $t$ .-ft
$x$	Distance up the side of the section in question with the origin in the plane of the lower ring frame.-ft
$\phi$	Angular distance about the longitudinal axis of the vehicle-radians
$t$	Time-seconds
$Y_n(t)$	Modal deflection as a function of time.-ft
$\omega_o$	Natural angular frequency rad/sec
$\beta_n$	Appropriate damping coefficient $\frac{\text{lb sec}}{\text{ft}}$

# Farrow

$P(x,t)$	Pressure as a function of distance and time-lb/ft <sup>2</sup>
$\alpha_n(x)$	Mode shape as a function of distance-nondimension
$\gamma$	Phase angle-radians
$m$	Mass per unit length - slugs/ft
$\alpha_n(\phi, x)$	Mode shape as a function of distance and angular displacement-nondimension
$P_0$	Maximum pressure-lb/ft <sup>2</sup>
$\omega$	Angular frequency-rad/sec
$K$	Wave number-rad/ft
$f$	Frequency - sec <sup>-1</sup>
$C$	Velocity of sound in the atmosphere-ft/sec
$q$	Order number of the specific mode-nondimensional
$l$	Length between ring frame supports =ft
$\lambda$	Wave length of sound in the atmosphere-ft
$M$	Mass per unit area-slugs/ft <sup>2</sup>
$\eta$	Damping factor-nondimensional assumed 10 <sup>-2</sup>
$K_n$	Wave number of the material rad/ft

## A RATIONAL APPROACH TO THE ENVIRONMENTAL VIBRATION PROBLEM

P. T. Mahaffey  
Convair, A Division of General Dynamics Corporation  
Fort Worth, Texas

As those who work in the field are well aware, questions on vibration environment have often been answered by specifying the qualification test to be met. Not only does this side-step the question on what the environment actually is, but provides an answer in arbitrary terms. Our excuse for proceeding in this manner is that there is no way that we can predict the environment, and that we must rely on arbitrary test specifications until we can obtain actual measurements.

While this may have been true in the past, the prediction of vibration environment is no longer beyond the state of the art. The purpose of this paper is to outline an engineering approach to the problems of environment prediction and test specification derivation. Parts of this approach are already being applied at Convair-Fort Worth. Other parts are taken from plans for procedures to be applied to new projects. The procedures will apply specifically to airplane type vehicles, but much of the material is also applicable to missiles.

### BASIC CONCEPTS

If we consider the overall problem of noise and vibration on an airplane, it appears that the airframe builder should develop two types of documents. The first document should define the actual noise and vibration environment which exists on the vehicle since this information is needed at an early date for the design of equipment and structure.

The second document needed is a qualification test specification. This should be based on the environment expected, but should be tailored to perform a specific task. This task is primarily to describe the testing which must be done to demonstrate that the equipment being purchased will perform satisfactorily in

its environment. Historically, specifications like MIL-E-5272 have been applied primarily to demonstrate a satisfactory fatigue life. While this is indeed an important item, it is equally important to demonstrate satisfactory performance of the equipment under vibration and noise environment. Since the vibration level used for fatigue testing is often appreciably greater than that under normal operating conditions, we are led to the conclusion that a vibration test specification needs really to be divided into two parts - one part to demonstrate fatigue life and the other part to demonstrate proper functioning of the equipment under its actual operating environment.

Reflection on the things to be accomplished points up the importance of being able to describe the actual vibration environment in the vehicle. Such a description is needed to provide design information, and to provide the basis for a test to check for proper functioning. It is also logical to start with such a description in designing a fatigue test. Let us now look at what we might be able to accomplish toward our desired goals.

#### PREDICTION METHODS

While the problem of environmental vibration prediction is very difficult, it is by no means a hopeless one. A method for attacking this problem has been presented in reference (1) and will be reviewed briefly here. This scheme is based on relating vibration to ambient noise levels, and on dealing with the most probable resulting vibration levels. If we attempt to look too closely at specific locations in an air frame, we quickly get discouraged in trying to predict vibration levels. We usually either conclude that we can't do an acceptable job, or that the answer we get is not worth the effort required to get it. However, if we look instead at larger areas of the vehicle and concern ourselves with a description of probable vibration levels, we can begin to make progress in this problem.

It is fairly well established that most vibration in a jet powered vehicle is caused by response of the structure to engine noise. Furthermore it seems reasonable that the structural vibration levels should be in some proportion to the applied noise levels. In pursuing this line of reasoning, a quantity of measured structural vibration data was plotted against the applied noise data. As shown in reference (1), it was found that a relationship between noise and vibration definitely exists. This was particularly true when the data were examined on an octave band basis. Such a plot is illustrated in Figure (1). Acceleration in g units is plotted on a log scale against sound pressure level in decibels for a large number of measured cases. As expected, a considerable amount of scatter is present. However, when the data are analyzed by statistical methods, a definite correlation is shown between vibration level and noise level. This trend is also apparent to the eye.

Statistical analysis permits us to lay out a regression line and percent confidence lines defining the distribution of vibration points. With a series of such plots and an octave band analysis of the applied noise, it is relatively easy to construct a plot of envelopes of probable vibration level in the structural area concerned. Such a plot is shown in Figure (2).

One can thus achieve a prediction of environmental vibration in a jet powered vehicle by the following procedure:

- (1) Make a prediction of the noise levels on the external surface of the vehicle (by calculation or the use of an acoustic model, see references 2, 3, and 4).
- (2) Divide the vehicle into zones of approximately equal noise level.
- (3) Prepare for each zone a plot of the type illustrated in Figure (2). Do this by utilizing the octave band noise levels representative of the zone and a series of plots relating vibration level and noise level for each octave band of the type illustrated in Figure (1). (See reference 1 for plots which can be used for this purpose.)

#### PREDICTION DOCUMENT

A useful document describing the predicted environmental vibration levels for the vehicle can then be prepared by presenting a sketch defining the vibration zones and plots showing the probable vibration level envelope for each zone.

This can be achieved for the take-off condition within the current state of the art. With a little more work on methods for predicting in-flight noise levels and distributions, the same process can be extended to predict in-flight vibration levels. Thus the environmental document can cover both take-off and in-flight vibration levels.

In addition to the noise excited vibration, the zone vibration envelopes should also be extended to cover landing and taxi vibration, vibration due to flight through turbulent atmosphere, and any discrete frequency vibration which is known to exist. The means for arriving at these contributions to the envelope is not nearly as clear cut as for the noise excited vibration. Nevertheless, it is usually possible to arrive at some reasonable approximation for these effects.

Up to this point, no mention has been made of the manner for specifying the vibration level. Actually, there are several advantages for giving this in terms of rms g's. One of these is that rms acceleration is a rational way of describing the vibration level when accompanied by a description of peak distribution. Another

is that this form provides a convenient input for fatigue damage calculations. This will be discussed later.

One more thing that the environmental prediction document should include is a description of vehicle usage. This needs to be in the form of the number of hours expected for each of the vibration levels quoted. A description of this type is necessary to define fatigue damage.

Such an environmental prediction document needs to be prepared at an early date in the design of a vehicle, and it should be revised whenever new and pertinent information becomes available. In particular, it should be revised to reflect input from actual measurements of vibration on the vehicle as they are obtained.

#### QUALIFICATION TEST PROCEDURE

Having established a method and a form for describing the environmental vibration levels in the vehicle, let us now examine what we might do in the way of designing a rational qualification test procedure. We should recognize in the beginning that there are two things which we wish to accomplish.

The first objective is to provide a procedure which will demonstrate that the equipment will perform satisfactorily under its operating environment. This is particularly important with respect to electronic equipment. If it doesn't function properly, the length of its fatigue life is of purely academic interest.

The second objective is to demonstrate a satisfactory fatigue life for the equipment. The importance of this item will vary according to the length of the operating time required.

Considering our first objective, the most straightforward approach is as follows. Use the zone distribution set forth in the environment prediction document, and present for each zone a vibration level plot of the same type as used in that document. One has a choice here of specifying the most probable (regression line) envelope or taking a higher level. It would appear that some margin of safety should be employed and that perhaps the upper 50% confidence level envelope might be used.

Before proceeding farther, let us take a close look at the physical significance of our predicted vibration level plot. This is not a vibration spectrum. It is simply an envelope defining the probable level of vibration of a structural resonance which might occur at a particular frequency. This is illustrated in Figure (3). The significance with respect to equipment is as follows. We are saying that the equipment may be excited at any of its resonances by an input of this magnitude at a discrete frequency having a varying amplitude with a prescribed peak distribution.

Our test procedure might logically then be set up as follows. Subject the equipment to single frequency vibration of randomly varying amplitude at the rms g level specified by the predicted envelope. Vary the frequency through the appropriate frequency range while monitoring the operation of the equipment. The criterion for passing the test would be satisfactory performance of the equipment under vibration. It is to be emphasized here that this test is to be conducted at the vibration level under which the equipment has to perform. This is not necessarily the maximum level to which it is subjected.

It is apparent that such a test could also be conducted with constant amplitude sinusoidal vibration. In this case one would specify the input level according to his best estimate of equivalence between constant amplitude and randomly varying amplitude.

It is interesting to note that existing equipment could be evaluated for operation in the environment of a particular zone of the vehicle by comparing the operational fragility curve for the equipment with the environment curve for the zone. Operational fragility curve as used here means a plot of the acceleration level versus frequency under which the equipment will operate satisfactorily. With such information supplied by the equipment manufacturer, and with a prediction of the operating environment, equipment could be selected on a reasonably intelligent basis.

The purpose of the second part of our qualification test procedure is to establish that the equipment will have adequate fatigue life under its environment. For vehicles with long service lives such as aircraft, we will need to raise the level of the vibration input in order to obtain a reasonably short laboratory test time. For the sake of being specific, let us choose one hour as the laboratory test time for each run. During this hour, we wish to apply the fatigue damage accumulated during a specified period of service. Our task is then to devise a test loading which will accomplish this purpose, and which will provide a suitable margin of safety.

Let us suppose that the bulk of the fatigue damage to the equipment is incurred during maximum engine power application during take off and during ground engine checks. By analysis of expected operation procedures, the cumulative total of this time can be determined. For the sake of illustration, let us say that this number comes out to be 10 hours of take off and ground engine run time during the specified life of the equipment. The criterion for our equipment is then that it shall withstand 10 hours of vibration under this environment without failure. However, we wish to shorten our laboratory test time to one hour. So we must raise our test level in order to do the same amount of fatigue damage in the reduced time.

One way to accomplish this is illustrated in Figure (4). To arrive at our vibration level multiplying factor for the accelerated test, let us assume that the equipment lasts 10 hours at the environmental level but fails at 10:01 hours. This gives us a point on a fatigue (S-N) curve. If we also knew the location of this curve at one hour, we would know what the one hour vibration test level should be. We cannot in most cases establish the fatigue curve for the equipment, so we are forced to fall back upon basic material information. One way of handling this problem is to compute a fatigue curve for a representative material in terms of rms stress versus cycles to failure using the peak distribution defined in our environmental document. Such a curve is illustrated at the top of Figure (5).

Now let us take several frequencies and calculate the number of cycles accumulated in 10 hours. As an example, for 500 cps this would be  $1.8 \times 10^6$  cycles. Underneath our S-N plot, let us construct a plot of vibration level in rms g's versus hours. Each frequency in a particular airplane zone will have an environmental vibration level, designated  $g_0$ . The intersections of the  $g_0$  levels and the corresponding 10 hour lines effectively define points of required fatigue life. Using the appropriate slope of the S-N curve to pass through the  $g_0$ , 10 hour point provides us with a line to extrapolate to the required test level,  $g_1$ , for the one hour laboratory test. The multiplying factors for each of the other frequencies can be determined in the same manner as for the case illustrated.

The factor of safety is perhaps best brought in by choosing the environmental vibration level to correspond to one of the upper confidence lines. The upper 60% confidence line generally provides levels of approximately twice the regression line level and is perhaps a reasonable choice.

It is now possible to construct an envelope of rms g versus frequency for use in the one hour laboratory test. Again, referring to the physical meaning of the envelope, it is most logical to set up our vibrator to deliver vibration at a single frequency with randomly varying amplitude. We should seek out the major resonances of the equipment and test each of these for the prescribed period of time. To avoid duplication, perhaps sweeps should be made first, vibrating in each of the three perpendicular axes. The major resonances would be noted along with their severity. The test would then be conducted by applying the vibration at each particular resonance along the axis of greatest response. Covering the four strongest resonances in this manner should provide a fairly good fatigue test. Testing at different temperatures and under combined environments would be worked into the specification according to the best judgment of the originator. While the equipment would not be required to deliver specified performance during the fatigue test, it would be required to do so after the test.



Again, the possibility of conducting the test with constant amplitude sinusoidal vibration suggests itself. This could be done by substituting a sinusoidal test envelope whose acceleration values would produce the same fatigue damage in the same length of time. Unfortunately, this equivalence depends upon the Q value of each resonance of the equipment as well as on cumulative damage and the shape of the S-N curve, so that additional assumptions are required.

#### CONCLUDING REMARKS

A major advantage to be gained by the procedures advanced in this paper is that the specification originator has control over the amount of conservatism to be employed. For vital pieces of equipment, this can be increased. For secondary items, it can be relaxed if desired.

Also, when vibration fatigue tests are being conducted after equipment is already in service (as often happens), premature failures will occur from time to time. These raise the question of how many hours of service life the parts will actually withstand. If the test procedure has been derived on a rational basis as described above, the test time can be converted into expected service life in hours. Modification effectivity points can then be scheduled on a rational basis.

The author is aware that the methods outlined above are built on many assumptions and approximations. However, these methods do permit a rational determination of expected environmental vibration levels and of tests to be conducted on equipment. In a few cases, the tests may be unconservative. However, the author believes that these cases can be tolerated in view of the large time and monetary savings which can be achieved by avoiding excessive conservatism in the majority of the cases.

#### REFERENCES

1. Mahaffey, P. T., and K. W. Smith, "A Method For Predicting Environmental Vibration Levels In Jet Powered Vehicles", Noise Control, July-August 1960.
2. Franken, P. A., and E. M. Kerwin, Jr., "Methods Of Flight Vehicle Noise Prediction", WADC Technical Report 58-343.
3. Beranek, L. L., "Noise Reduction", Chapter 24, McGraw Hill.
4. Stepp, E. H., "Methods For Predicting The Acoustic Environment For The B-58 Weapon System", Proceedings Of The First Annual Meeting Of The Institute Of Environmental Engineers, 1957.

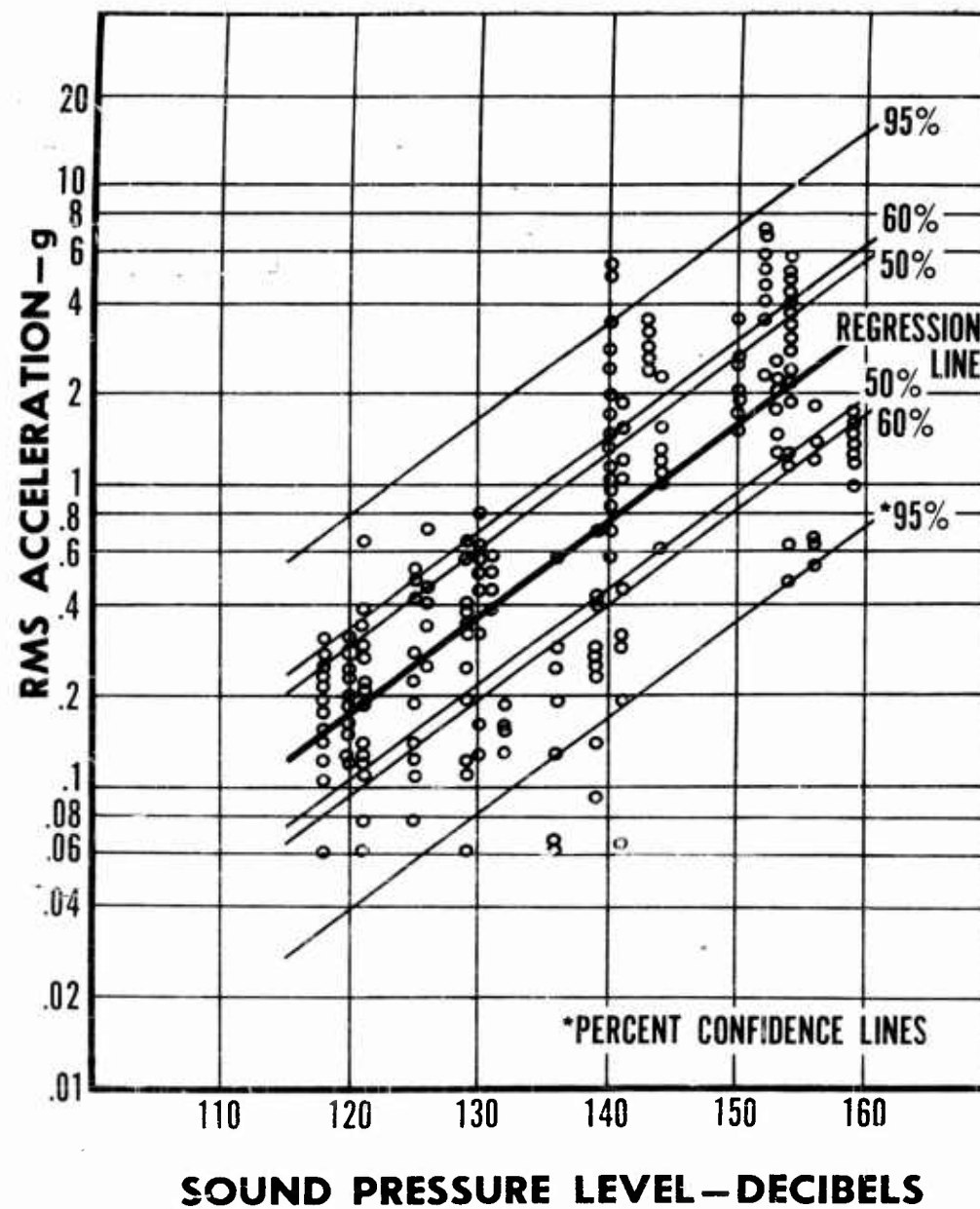


**Figure 1. Relation between structural vibration and applied noise level 300-600 cps octave band**

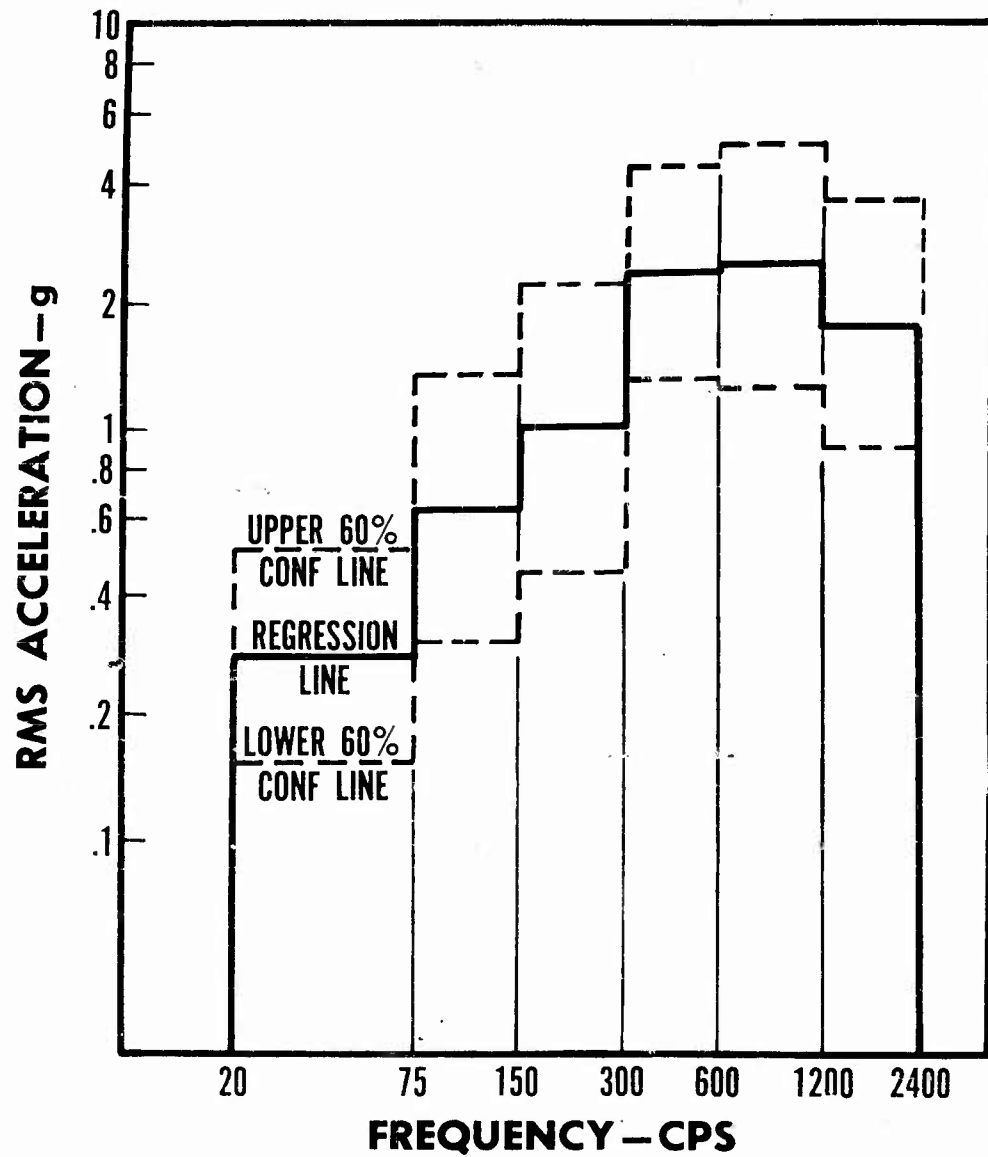


**Figure 2. Example of predicted vibration envelope for a vibration zone**

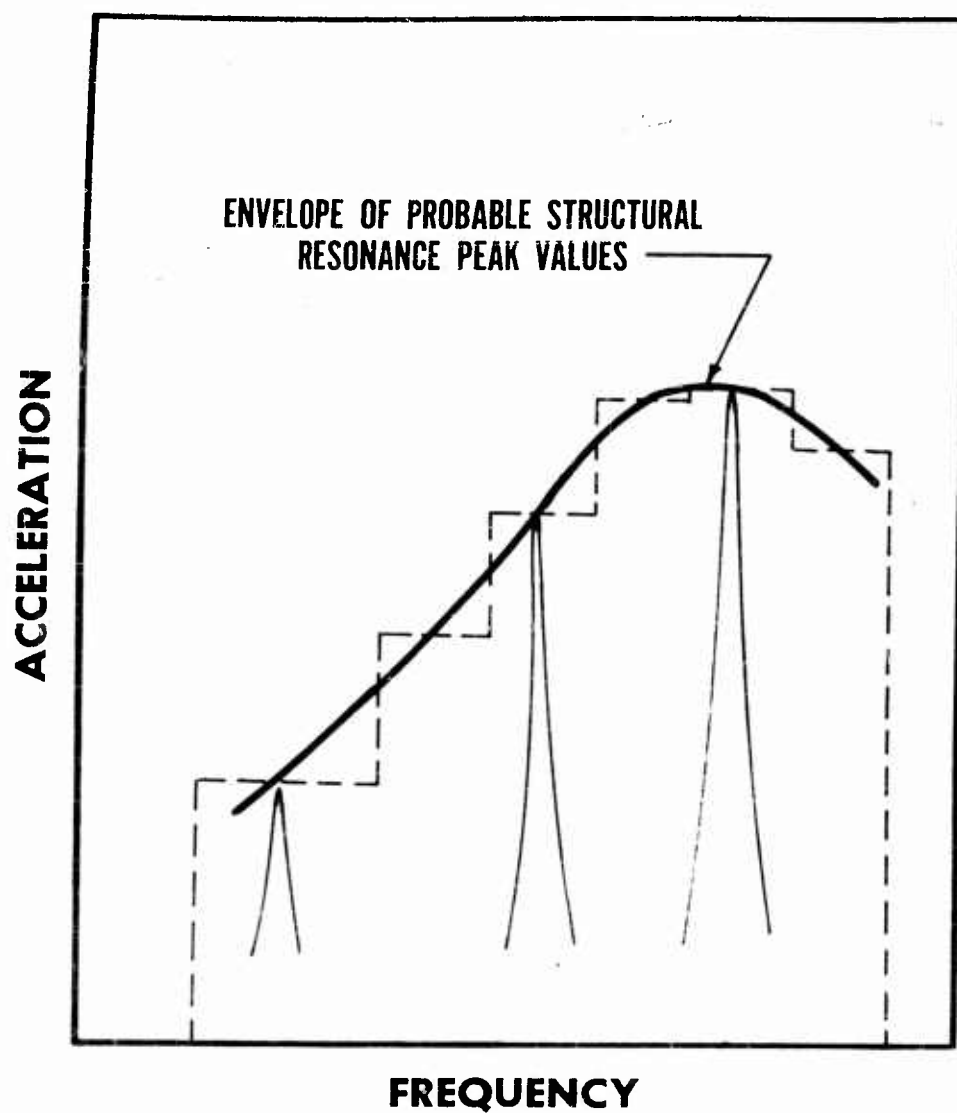


**Figure 3. Physical significance of predicted vibration envelope**

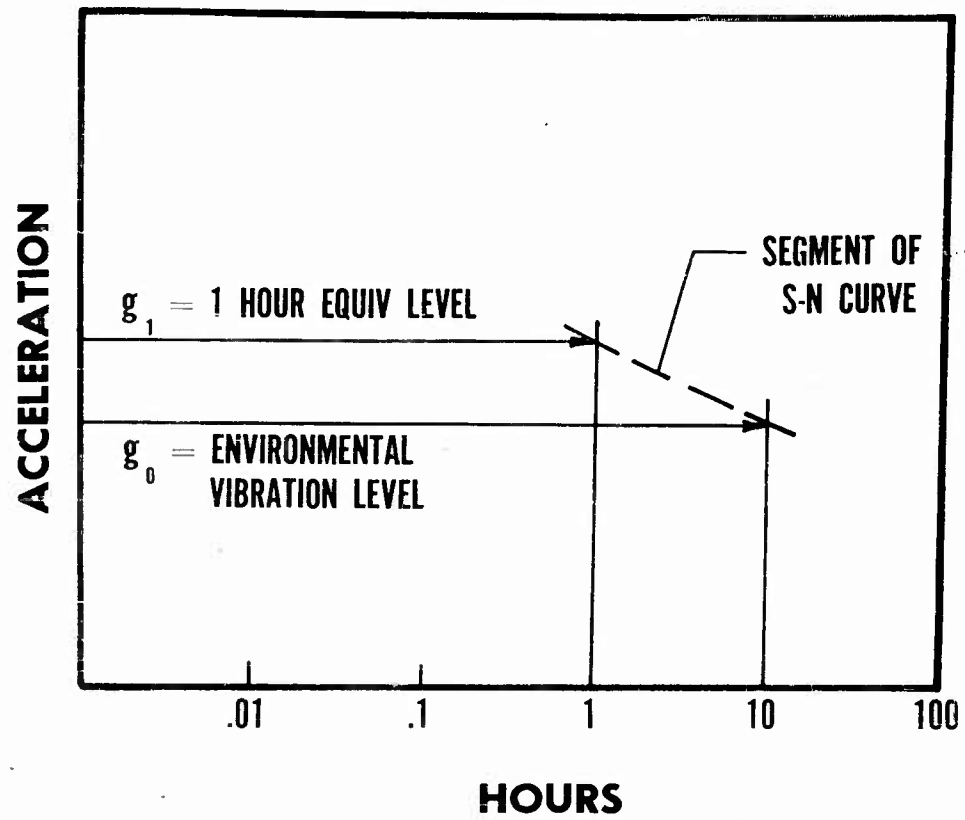


**Figure 4. Illustration of method for arriving at accelerated test level**

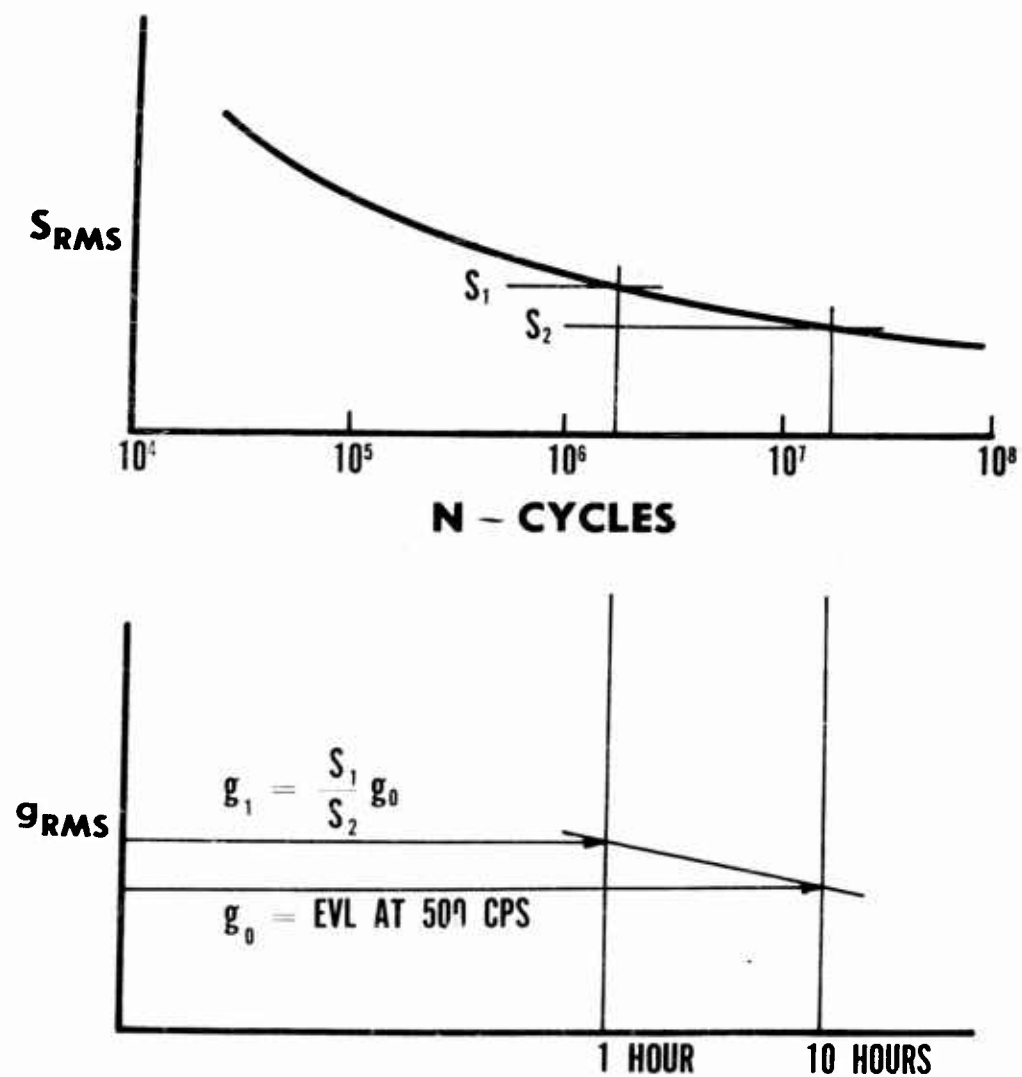


**Figure 5. Determination of vibration level for laboratory test**

OFFICE OF NAVAL RESEARCH  
AEROSPACE INDUSTRIES ASSOCIATION

SYMPOSIUM ON STRUCTURAL DYNAMICS OF  
HIGH SPEED FLIGHT

24-26 APRIL 1961

ATTENDANCE

Commander, ASD  
Attn: Lt. David R. Abel  
USAF WWSFS  
Wright-Patterson AFB, Ohio

H. Norman Abramson  
Southwest Research Institute  
8500 Culebra Road  
San Antonio, Texas

Fred C. Allen  
Douglas Aircraft Company, Inc.  
El Segundo Division  
El Segundo, California

Joel R. Alper  
Jet Propulsion Laboratory  
4800 Oak Grove Avenue  
Pasadena, California

Harry B. Amey, Jr.  
Aerojet-General Corporation  
1100 West Hollyvale Street  
Azusa, California

James E. Ancell  
North American Aviation, Inc.  
International Airport  
Los Angeles 45, California

Gary W. Anderson  
Douglas Aircraft Company, Inc.  
3000 Ocean Park Boulevard  
Santa Monica, California

James E. Anderson  
Dynamics Group, Dept. B-250  
Douglas Aircraft Company, Inc.  
827 Lapham Street  
El Segundo, California

William J. Anderson  
California Institute of Technology  
1201 East California Street  
Pasadena, California

Lowell V. Andrew, Dept. 413-60  
North American Aviation, Inc.  
12214 Lakewood Boulevard  
Downey, California

Attendance

Irving L. Ashkenas  
Systems Technology, Inc.  
1630 Centinela Avenue  
Inglewood, California

Norman N. Au  
Aerospace Corporation  
P.O. Box 95085  
Los Angeles 45, California

Frederick Baganoff  
McDonnell Aircraft Corp.  
P.O. Box 516  
St. Louis 66, Missouri

Eugene F. Baird  
Grumman Aircraft Engrg. Corp.  
Bethpage, Long Island  
New York

William F. Bangs, Code 321-1  
NASA, Goddard Space Flt. Ctr.  
Greenbelt, Maryland

Ellen J. Barndollar  
Douglas Aircraft Company, Inc.  
3000 Ocean Park Boulevard  
Santa Monica, California

Sheldon Baron  
NASA Langley Research Center  
Langley Field, Virginia

Millard V. Barton  
Space Technology Labs, Inc.  
P.O. Box 95001  
Los Angeles 45, California

Helmut F. Bauer, Aero-Dynamics  
Marshall Space Flt. Ctr., NASA  
Redstone Arsenal, Alabama

Peter M. Belcher  
North American Aviation, Inc.  
International Airport  
Los Angeles 45, California

Raymond C. Binder  
The Rand Corporation  
1700 Main Street  
Santa Monica, California

Ralph E. Blake  
Lockheed Missiles & Space Division  
Sunnyvale, California

Edward B. Borek  
The Marquardt Corporation  
16555 Saticoy Street  
Van Nuys, California

Herman F. Borges  
Directorate of Research Analysis  
AF Office of Scientific Research  
ATTN: SRLS  
Holloman Air Force Base, New Mexico

Robert B. Bost  
Temco Electronics & Missiles Co.  
Box 6191  
Dallas, Texas

Robert W. Boswinkle, Jr.  
NASA Langley Research Center  
Langley Field, Virginia

Theodore Bratanow  
North American Aviation, Inc.  
Los Angeles International Airport  
Los Angeles 45, California

D. W. Breuer  
Air Force Institute of Technology  
Wright-Patterson AFB, Ohio

Bernard Budiansky  
AVCO Corp., ATTN: LIBRARY  
201 Lowell Street  
Wilmington, Massachusetts

Kenneth L. Burgess  
The Martin Company  
P.O. Box 179  
Denver 1, Colorado

Charles J. Buzzetti  
Lockheed Aircraft Corporation  
Burbank, California



## Attendance

B. J. Cagle  
Office of Naval Research  
1030 East Green Street  
Pasadena, California

William J. Carley  
Jet Propulsion Laboratory  
4800 Oak Grove Avenue  
Pasadena, California

Edwin Y. Chow  
Jet Propulsion Laboratory  
4800 Oak Grove Avenue  
Pasadena, California

William Clark  
Grumman Aircraft Engrg. Corp.  
Bethpage, Long Island  
New York

John E. Clough  
Lockheed Aircraft Corporation  
Burbank, California

Charles W. Coale  
Dept. 53-13, Bldg. 201-2  
Lockheed Missiles & Space Div.  
3251 Hanover Street  
Palo Alto, California

Henry A. Cole, Jr.  
NASA, Ames Research Center  
Moffett Field, California

Dale E. Cooley, WFRMDD-21  
Aeronautical Systems Division  
Wright-Patterson Air Force Base  
Ohio

Jerry Counts  
Sandia Corporation  
Sandia Base  
Albuquerque, New Mexico

Delbert Ray Cox  
McDonnell Aircraft Corporation  
P.O. Box 516  
St. Louis 66, Missouri

Joseph N. Crenshaw  
Army Ballistic Missile Agency  
U.S. Army Ordnance Missile Command  
Redstone Arsenal, Alabama

Walter M. Crooks  
Lockheed Aircraft Corporation  
Burbank, California

A. S. Davison  
North American Aviation, Inc.  
4300 East Fifth Avenue  
Columbus, Ohio

Richard W. Dezelan  
Douglas Aircraft Company, Inc.  
3000 Ocean Park Boulevard  
Santa Monica, California

Robert E. Donham  
Lockheed Aircraft Corporation  
P.O. Box 551  
Burbank, California

Bud L. Duft  
Narmco Research & Development  
3540 Aero Court  
San Diego, California

John Dugundji  
Department of Aeronautics  
Massachusetts Institute of Technology  
Cambridge 39, Massachusetts

Philip M. Edge, Jr.  
NASA - Acoustics Branch  
Langley Field, Virginia

Kenneth M. Eldred  
Western Electro-Acoustic Lab., Inc.  
2222 South Barrington Avenue  
Los Angeles 64, California

Alfred E. Engelbrecht  
North American Aviation, Inc.  
International Airport  
Los Angeles 45, California

# Attendance

Albert L. Erickson  
NASA, Ames Research Center  
Moffett Field, California

Clancy F. Ewald  
Lockheed Aircraft Corporation  
P.O. Box 551  
Burbank, California

James H. Farrow  
NASA - M - S&M - SD  
Marshall Space Flight Center  
Huntsville, Alabama

Gordon B. Fox  
Douglas Aircraft Company, Inc.  
3000 Ocean Park Boulevard  
Santa Monica, California

Robert E. Freeland  
Jet Propulsion Laboratory  
4800 Oak Grove Avenue  
Pasadena, California

Frank J. Frueh  
Giannini Controls Corporation  
Astromechanics Research Div.  
657 Delaware Avenue  
Buffalo 2, New York

James P. Fulton  
Douglas Aircraft Company, Inc.  
3000 Ocean Park Boulevard  
Santa Monica, California

Y. C. Fung  
California Institute of Technology  
1201 East California Street  
Pasadena, California

Arnold E. Galef  
National Engrg. Science Co.  
709 South Fair Oaks Avenue  
Pasadena, California

Richard H. Gallagher  
Bell Aerosystems Company  
P.O. Box 1  
Buffalo 5, New York

Isadore E. Garrick  
NASA Langley Research Center  
Langley Field, Virginia

William H. Gayman  
Radioplane Div., Northrop Corp.  
8000 Woodley Avenue  
Van Nuys, California

Gordon L. Getline  
Convair  
P.O. Box 1950  
San Diego 12, California

Major Earl R. Gieseman, Jr.  
HQ USAF, Directorate of Research &  
Technology, DCS/Development  
Room 4C 339, Pentagon  
Washington 25, D. C.

Robert Louis Goldman  
The Martin Company  
Middle River  
Baltimore 3, Maryland

W. P. Gray  
Project Engineer  
Rohr Aircraft Corporation  
Chula Vista, California

James A. Griffin  
Douglas Aircraft Company, Inc.  
827 Lapham Street  
El Segundo, California

George C. Grimm, Jr.  
Douglas Aircraft Company, Inc.  
3000 Ocean Park Boulevard  
Santa Monica, California

Lawrence D. Guy  
National Aeronautics & Space Adm.  
Langley Field, Virginia

Paul Gilbert Hahn  
The Martin Company, Mail #MP-233  
P.O. Box 5837  
Orlando, Florida

Attendance

B. M. Hall  
Douglas Aircraft Company, Inc.  
2560 Walnut Avenue  
Culver City, California

Dennis J. Haluza  
U.S. Naval Ordnance Test Stn.  
China Lake, California

Thomas J. Harriman  
Giannini Controls Corporation  
1600 South Mountain Avenue  
Duarte, California

Robert J. Harter  
Douglas Aircraft Company, Inc.  
El Segundo Division  
El Segundo, California

Captain G. E. Hartley, USN  
Office of Naval Research  
T-3 Building, Room 2603  
Washington 25, D. C.

Donald D. Hasbrouck  
Hughes Aircraft Company  
M.S. A2004  
Culver City, California

Hermann J. Hassig  
Lockheed Aircraft Corporation  
P.O. Box 551  
Burbank, California

Albert L. Head, Jr.  
Chance Vought Corporation  
P.O. Box 5907  
Dallas 22, Texas

Harry Himeiblauf  
Nortronics Div., Northrop Corp.  
222 North Prairie Avenue  
Hawthorne, California

F. M. Hoblit  
Lockheed Aircraft Corporation  
P.O. Box 551  
Burbank, California

Charles H. Hodson  
North American Aviation, Inc.  
International Airport  
Los Angeles 45, California

Commander  
Aeronautical Systems Division  
ATTN: N. R. Hoffman, GAM-87  
Deputy for Development, WWDGP  
Wright-Patterson AFB, Ohio

Cornelis Hogen-Esch  
Lockheed Aircraft Corporation  
Burbank, California

Francis C. Hung  
North American Aviation, Inc.  
12214 Lakewood Boulevard  
Downey, California

Melvin W. Hunt, 413-60  
North American Aviation, Inc.  
Space & Information Systems Div.  
12214 Lakewood Boulevard  
Downey, California

Robert M. Hunt  
NASA, Marshall Space Flight Center  
M - S&M - SD  
Huntsville, Alabama

William J. Husic, Ref. FS-120  
Federal Aviation Agency  
Airframe & Equipment Branch  
Washington 25, D. C.

Philip A. Hufton, R.A.E.  
c/o Chief of Naval Operations  
Code Op-92C2  
Department of the Navy  
Washington 25, D. C.

Gabriel Isakson  
University of Michigan  
Ann Arbor, Michigan

Captain W. G. Jackson, USN  
Commanding Officer  
Office of Naval Research  
1030 East Green Street  
Pasadena, California

Attendance

David A. Jewell, USN  
David Taylor Model Basin  
Washington 7, D.C.

Neil E. Johnson  
Jet Propulsion Laboratory  
4800 Oak Grove Avenue  
Pasadena, California

Walter A. Johnson, Jr.  
Systems Technology, Inc.  
1630 Centinela Avenue  
Inglewood, California

Irving W. Jones  
Grumman Aircraft Engrg. Corp.  
Bethpage, Long Island  
New York

Gareth H. Jordan  
NASA Flight Research Center  
P.O. Box 273  
Edwards, California

Peter F. Jordan  
The Martin Company  
Baltimore 3, Maryland

Jerrard A. Joseph  
Dept. 56, Group 51  
North American Aviation, Inc.  
International Airport  
Los Angeles 45, California

James R. June  
Dept. 7100  
Boeing Airplane Company  
Wichita, Kansas

Donald F. Kalkis  
Aeronautical Systems Division  
Attn: WWRPSV-3  
Wright-Patterson AFB, Ohio

Leroy N. Kanning  
North American Aviation, Inc.  
International Airport  
Los Angeles 45, California

Saul M. Kaplan  
General Electric Co., MSVD, Rm 6850  
3198 Chestnut Street  
Philadelphia, Pennsylvania

Henry Katz  
McDonnell Aircraft Corporation  
P.O. Box 516  
St. Louis 66, Missouri

Leo E. Kazmerzak  
North American Aviation, Inc.  
4300 East Fifth Avenue  
Columbus 16, Ohio

D. L. Keeton  
Douglas Aircraft Company, Inc.  
3000 Ocean Park Boulevard  
Santa Monica, California

James S. Keith  
Chance Vought Corporation  
P.O. Box 5907  
Dallas 22, Texas

C. D. Knauer, Jr.  
Douglas Aircraft Company, Inc.  
3000 Ocean Park Boulevard  
Santa Monica, California

Eldon E. Kordes  
NASA Flight Research Center  
P.O. Box 273  
Edwards, California

W. R. Laidlaw  
North American Aviation, Inc.  
12214 Lakewood Boulevard  
Downey, California

Edward D. Lakin  
U.S. Air Force  
4202 Sylvan Drive  
Dayton 17, Ohio

David Dell Lang  
Chance Vought Corporation  
P.O. Box 5907  
Dallas 22, Texas

# Attendance

Warner Lansing  
Grumman Aircraft Engrg. Corp.  
Bethpage, Long Island  
New York

Richard H. Lassen  
North American Aviation, Inc.  
Space & Information Systems Div.  
12214 Lakewood Boulevard  
Downey, California

J. Edward Lauber, Zone 6-10  
Convair  
P.O. Box 1011  
Pomona, California

Robert E. Lawrence  
North American Aviation, Inc.  
International Airport  
Los Angeles 45, California

Stuart Y. Lee, A2-260 G&C  
Douglas Aircraft Company, Inc.  
3000 Ocean Park Boulevard  
Santa Monica, California

Eugene J. Lenk  
Douglas Aircraft Company, Inc.  
827 Lapham Street  
El Segundo, California

Trygve R. Lerwick  
Douglas Aircraft Company, Inc.  
3000 Ocean Park Boulevard  
Santa Monica, California

Howard L. Leve  
Hughes Aircraft Company  
Culver City, California

Professor Harold Liebowitz  
Asst. Dean, Graduate School  
University of Colorado  
Boulder, Colorado

Joe E. Lingerfelt  
Jet Propulsion Laboratory  
4800 Oak Grove Drive  
Pasadena, California

Ralph H. Long, Jr.  
National Science Foundation  
Engineering Sciences Program Office  
Washington 25, D. C.

John R. Love  
Douglas Aircraft Company, Inc.  
827 Lapham Street  
El Segundo, California

J. A. Luistro  
USN David Taylor Model Basin  
Washington 7, D. C.

Rose E. Lunn  
North American Aviation, Inc.  
International Airport  
Los Angeles 45, California

David R. Madill, De Havilland Aircraft  
c/o Chief of Naval Operations  
Code Op-92C2  
Department of the Navy  
Washington 25, D. C.

George P. Maggos  
The John Hopkins University  
Applied Physics Laboratory  
8621 Georgia Avenue  
Silver Spring, Maryland

P. T. Mahaffey  
Convair, Mail Zone C-75  
Grants Lane  
Fort Worth, Texas

Dennis J. Martin  
NASA Langley Research Center  
Langley Field, Virginia

E. N. Martin, A2-260  
Douglas Aircraft Company, Inc.  
Santa Monica, California

Richard E. Martin  
Convair-Astronautics, Dept. 597-1  
5001 Kearney Villa Road  
San Diego 11, California

## Attendance

Bernard Mazelsky  
Aerojet-General Corporation  
1100 West Hollyvale Street  
Azusa, California

K. L. McIntyre  
Convair/Pomona  
1675 West Fifth Avenue  
Pomona, California

Norman J. McLeod  
NASA Flight Research Center  
P.O. Box 273  
Edwards, California

James I. McPherson  
Jet Propulsion Laboratory  
4800 Oak Grove Drive  
Pasadena, California

F. W. Melching  
Dynamics Group, Dept. B-250  
Douglas Aircraft Company, Inc.  
827 Lapham Street  
El Segundo, California

Barry T. Mendelsohn, A2-260  
Douglas Aircraft Company, Inc.  
Santa Monica, California

John W. Miles  
University of California  
Los Angeles 24, California

H. D. Moran, Technical Service  
Aerospace Industries Association  
7660 Beverly Boulevard  
Los Angeles 36, California

Charles T. Morrow  
Aerospace Corporation  
P.O. Box 95085  
Los Angeles 45, California

Robert C. Murphy  
Lockheed Aircraft Corporation  
P.O. Box 551  
Burbank, California

Walter J. Mykytow, WWRMDD  
Aeronautical Systems Division  
Wright-Patterson AFB, Ohio

Donald O. Neilson  
The Boeing Company  
Transport Division  
P.O. Box 707  
Renton, Washington

C. D. Newsom  
Boeing Airplane Company  
3801 South Oliver  
Wichita, Kansas

Roland A. Newton  
Convair/Pomona  
1675 West Fifth Avenue  
Pomona, California

Lucian S. Nogawski, Dept. 413-60  
North American Aviation, Inc.  
Space & Information Systems Div.  
12214 Lakewood Boulevard  
Downey, California

Richard B. Noll  
NASA Flight Research Center  
P.O. Box 273  
Edwards, California

J. P. O'Neill  
Space Technology Labs, Inc.  
P.O. Box 95001  
Los Angeles 45, California

James G. Papadopoulos  
Army Ballistic Missile Agency  
U.S. Army Ordnance Missile Command  
Redstone Arsenal, Alabama

Lawrence N. Paul  
Lockheed Aircraft Corporation  
P.O. Box 551  
Burbank, California

Barry F. Pearce  
Systems Technology, Inc.  
1630 Centinela Avenue  
Inglewood, California

## Attendance

Jerry C. Peck  
National Engrg. Science Co.  
709 South Fair Oaks Avenue  
Pasadena, California

Robert F. Peck  
General Electric MSVD  
21 South 12th Street  
Philadelphia, Pennsylvania

R. P. Peloubet  
Convair - Mail Zone C-75  
Grants Lane  
Fort Worth, Texas'

Robert B. Penneman  
Convair  
P.O. Box 1950  
San Diego, California

Harry C. Peterson  
The Martin Company  
P.O. Box 179, Mail No. A-92  
Denver 1, Colorado

Paul W. Peterson  
Aeronutronic Div., Ford Motor Co.  
Ford Road  
Newport Beach, California

Robert S. Peterson  
Douglas Aircraft Company, Inc.  
3000 Ocean Park Boulevard  
Santa Monica, California

John D. Philbrick  
Douglas Aircraft Company, Inc.  
3000 Ocean Park Boulevard  
Santa Monica, California

Walter M. Philipp  
Bendix Corporation  
7250 Laurel Canyon Boulevard  
North Hollywood, California

George A. Pierce  
North American Aviation, Inc.  
4300 East Fifth Avenue  
Columbus 16, Ohio

William G. Pierpont  
Beech Aircraft Corporation  
9709 East-Central  
Wichita, Kansas

Samuel Pines  
Republic Aviation Corporation  
Farmingdale, Long Island  
New York

William Piper  
Naval Ordnance Laboratory  
White Oak  
Silver Spring, Maryland

Joseph C. Pohlen  
North American Aviation, Inc.  
Space & Information Systems Div.  
12214 Lakewood Boulevard  
Downey, California

John R. Post  
North American Aviation, Inc.  
4300 East Fifth Avenue  
Columbus 16, Ohio

Edward E. Postel  
Lockheed Aircraft Corporation  
P.O. Box 551  
Burbank, California

Samuel Rabinowitz  
Republic Aviation Corporation  
Farmingdale, Long Island  
New York

Guido E. Ransleben, Jr.  
Southwest Research Institute  
8500 Culebra Road  
San Antonio 6, Texas

Paul Ratner  
Grumman Aircraft Engrg. Corp.  
Bethpage, Long Island, New York

J. D. Revell  
Norair Division, Northrop Corp.  
Hawthorne, California

# Attendance

Mario H. Rheinfurth  
NASA, Marshall Space Flt. Ctr.  
Huntsville, Alabama

Carl Reichert  
WWFE, Aeronautical Systems Div.  
Wright-Patterson AFB, Ohio

James E. Rice  
Goodyear Aircraft Corporation  
1210 Massillon Road  
Akron, Ohio

Thomas M. Richardson  
Douglas Aircraft Company, Inc.  
3000 Ocean Park Boulevard  
Santa Monica, California

William M. Robe  
Convair  
3165 Pacific Highway  
San Diego, California

William H. Roberts  
Norair Division, Northrop Corp.  
1001 East Broadway  
Hawthorne, California

William P. Rodden  
Laboratories Division  
Aerospace Corporation  
P.O. Box 95085  
Los Angeles 45, California

Captain H. E. Ruble, USN  
Deputy and Assistant Chief  
Office of Naval Research  
Department of the Navy  
Washington 25, D. C.

J. Ray Ruetenik - 41-219  
Massachusetts Inst. of Technology  
77 Massachusetts Avenue  
Cambridge, Massachusetts

Hassel C. Schjelderup  
National Engrg. Science Co.  
709 South Fair Oaks Avenue  
Pasadena, California

William T. Schleich, 413-40  
North American Aviation, Inc.  
Space & Information Systems Div.  
12214 Lakewood Boulevard  
Downey, California

Raymond H. Schuett  
Convair-Astronautics, Dept. 597-1  
5001 Kearny Villa Road  
San Diego 11, California

Sidney Siegel  
North American Aviation, Inc.  
International Airport  
Los Angeles 45, California

J. C. Simmons  
Douglas Aircraft Company, Inc.  
3000 Ocean Park Boulevard  
Santa Monica, California

Richard B. Skoog  
The Boeing Company, Transport Div.  
P.O. Box 707  
Renton, Washington

Laird deL. Sloan  
Aerojet-General Corporation  
1100 West Hollyvale Street  
Azusa, California

John B. Smedfjeld  
Grumman Aircraft Engrg. Corp.  
Bethpage, Long Island  
New York

Aeronautical Systems Division  
Attn: WWRMDD (Lt. T.M. Snaring)  
Wright-Patterson AFB, Ohio

Robert R. Solverson  
Hughes Aircraft Company  
Culver City, California

Frank B. Sperling  
U.S. Naval Ordnance Test Station  
3202 East Foothill Boulevard  
Pasadena, California



## Attendance

Clayton L. Stevens  
North American Aviation, Inc.  
Space & Information Systems Div.  
12214 Lakewood Boulevard  
Downey, California

Clifton D. Stevens  
Goodyear Aircraft Corp. D/458  
1210 Massillon Road  
Akron 15, Ohio

Joseph R. Stevenson  
North American Aviation, Inc.  
International Airport  
Los Angeles 45, California

Donald J. Stone  
North American Aviation, Inc.  
12214 Lakewood Boulevard  
Downey, California

Ernest S. Stoops  
North American Aviation, Inc.  
4300 East Fifth Avenue  
Columbus 16, Ohio

Ivan R. Stoughton  
The Marquardt Corporation  
16555 Saticoy Street  
Van Nuys, California

Robert Strike  
Convair/Pomona  
1675 West Fifth Avenue  
Pomona, California

Ralph H. Stringham  
Douglas Aircraft Company, Inc.  
827 Lapham Street  
El Segundo, California

Johannes E. Sweers  
Lockheed Aircraft Corporation  
Burbank, California

Harold R. Sweet  
North American Aviation, Inc.  
International Airport  
Los Angeles 45, California

Donald B. Taylor  
The Bendix Corporation  
Bendix Mishawaka Division  
400 South Beiger Street  
Mishawaka, Indiana

Wayne H. Terrill  
Convair/Pomona  
1675 West Fifth Avenue  
Pomona, California

Roland F. Teuber  
Douglas Aircraft Company, Inc.  
3000 Ocean Park Boulevard  
Santa Monica, California

K. G. Thorsted  
U.S. Naval Ordnance Test Station  
China Lake, California

Leon A. Tolve  
Lockheed Aircraft Corporation  
Georgia Division  
Marietta, Georgia

Alfred C. Tracey  
Douglas Aircraft Company, Inc.  
3000 Ocean Park Boulevard  
Santa Monica, California

Marc Trummel  
Jet Propulsion Laboratory  
4800 Oak Grove Drive  
Pasadena, California

M. J. Turner  
Boeing Company  
P.O. Box 3707  
Seattle 24, Washington

John J. Umstetter  
Grumman Aircraft Engrg. Corp.  
Bethpage, Long Island, New York

David A. Underhill  
Convair/Pomona  
1675 West Fifth Avenue  
Pomona, California

# Attendance

Robert E. Underwood  
Douglas Aircraft Company, Inc.  
3000 Ocean Park Boulevard  
Santa Monica, California

Lt. R.E. Van Putte, GAM-87  
Engineering Office  
Directorate of Systems Engrg.  
Aeronautical Systems Division  
Wright-Patterson AFB, Ohio

H. M. Voss  
The Boeing Company  
P.O. Box 3707  
Seattle 24, Washington

Bruce R. Vernier  
Nortronics Div., Northrop Corp.  
222 North Prairie Avenue  
Hawthorne, California

Robert T. Wagner  
The Boeing Company  
P.O. Box 3707, M.S. 14-54  
Seattle 24, Washington

William J. Walker  
Jet Propulsion Laboratory  
4800 Oak Grove Drive  
Pasadena, California

Robert Walton  
Jet Propulsion Laboratory  
4800 Oak Grove Drive  
Pasadena, California

W. K. Waymeyer  
Douglas Aircraft Company, Inc.  
3000 Ocean Park Boulevard  
Santa Monica, California

Dwight L. Weathersbee, Code 4061  
U.S. Naval Ordnance Test Station  
China Lake, California

William J. Werback, Code 4061  
U.S. Naval Ordnance Test Station  
China Lake, California

Richard P. White, Jr.  
Cornell Aeronautical Laboratory, Inc.  
4455 Genesee Street  
Buffalo 21, New York

Edward Widmayer, Jr.  
The Martin Company, Mail G3212  
Baltimore 3, Maryland

Jackson E. Wignot  
Lockheed Aircraft Corporation  
Burbank, California

Norman Lee Willett  
Federal Aviation Agency  
5651 West Manchester  
Los Angeles 45, California

Robert M. Williams  
Ryan Aeronautical Company  
Harbor Drive  
San Diego, California

Maurice O. W. Wolfe, R.A.E.  
c/o Chief of Naval Operations  
Code Op-92C2  
Department of the Navy  
Washington 25, D. C.

Charles E. Woods  
U.S. Naval Ordnance Test Station  
China Lake, California

John H. Wykes  
North American Aviation, Inc.  
International Airport  
Los Angeles 45, California

Harry Yousoof  
Hamilton Standard Division  
United Aircraft  
Windsor Locks, Connecticut

Edmond F. E. Zeijdel  
Midwest Research Institute  
425 Volker Boulevard  
Kansas City, Missouri

Attendance

N. H. Zimmerman  
McDonnell Aircraft Corp.  
P.O. Box 516  
St. Louis 66, Missouri

Melvin B. Zisfein  
Giannini Controls Corp.  
Astromechanics Research Div.  
657 Delaware Avenue  
Buffalo 2, New York

# AUTHOR INDEX

Abramson, H. Norman	287	Mahaffey, P. T.	721
Amey, Harry B., Jr.	135	Mazelsky, Bernard	135
Baron, Sheldon	413	Morgan, Homer G.	413
Bauer, Helmut F.	319	Neilson, D. O.	175
Edge, Philip M., Jr.	629	Newsom, C. D.	609
Eldred, Kenneth McK.	649	Padlog, Joseph	567
Farrow, J. H.	710	Peloubet, R. P.	447
Frueh, Frank J.	1	Post, J. R.	497
Fung, Y. C.	209	Quinn, James F.	567
Gallagher, Richard H.	567	Ratner, P.	533
Getline, G. L.	686	Roberts, William	649
Grande, D. L.	609	Ruetenik, J. R.	477
Herrmann, W.	477	Topp, L. J.	609
Hunt, Robert M.	356	Voss, H. M.	252
June, R. R.	609	Wagner, R. T.	376
Jaszlica, I.	175	Wilhold, G. A.	710
Jewell, R. E.	710	White, Robert W.	649
Jones, I. W.	533	Witmer, E. A.	477
Keith, J. Stuart	85	Woods, Charles E.	268
Lansing, W.	533	Zimmerman, Norman H.	28
Leve, H. L.	698	Zisfein, <u>Melvin B.</u>	3
Lock, M. H.	209		